INJURY ASSESSMENT FOR THE HUMAN FOOT/LEG EXPOSED TO AXIAL IMPACT LOADING

A dissertation to the faculty of the
School of Engineering and Applied Science,
Department of Mechanical and Aerospace Engineering,
University of Virginia

In Partial Fulfillment of the Requirements for the Degree
Doctor of Philosophy in Mechanical Engineering

Ann Marie Bailey

Faculty Advisor:
Jeff R. Crandall, Ph.D.

Committee Members:
Jason R. Kerrigan, Ph.D.
Spyros D. Masouros, Ph.D.
Timothy L. McMurry, Ph.D.
Matthew B. Panzer, Ph.D.
Robert S. Salzar, Ph.D.

September 23, 2016

Abstract

Current injury criteria for the leg in axial loading fail to consider the effect of duration on force at fracture, which has been shown to be significant for body regions such as the femur and spine.[197,208] Consequently, application of current injury risk functions based solely on peak tibia force is limited to specific boundary and input conditions. The primary objective of this dissertation was to develop an injury criterion for use in both underbody blast (UBB) and automotive intrusion (AI) loading environments in order to encompass the loading characteristics anticipated for UBB scenarios where floor mats or other injury mitigation devices are employed. The secondary goal was to provide design criteria for expanding the range of loading durations (or frequencies) over which current anthropomorphic test device (ATD) legs provide a biofidelic force response.

Injury and response data was collected from 54 post-mortem human surrogate (PMHS) tests and from previous axial impact studies from the literature, with footplate force durations ranging from 5.1 to 89.9 ms. This test data was also used to generate force and leg compression corridors which were utilized for benchmarking a human leg finite element (FE) model. A parametric study was performed using the human leg FE model to improve understanding of the trends in fracture force observed in the PMHS experimental data and to characterize the effect of duration and pulse shape on force at fracture.

The leg injury risk function was developed using PMHS data and human leg finite element models to establish a relationship between fracture force and duration. An eventual optimization approach was used to estimate the survival model parameters for an injury risk function utilizing an injury predictor which combined peak force and impulse at peak force measured at the plantar surface of the foot. The injury risk function demonstrated a high

level of injury prediction accuracy (81.8%) for load durations ranging from 5.1 to 89.9 ms, and improved injury prediction accuracy compared to previous injury risk functions which used peak tibia force as the injury predictor by up to 18%.

To improve the utility of the injury risk function, an ATD that is biofidelic for larger range of input frequencies was needed. Recommendations for ATD leg improvements were based on the design of the Mil-Lx. Mil-Lx experimental testing was performed to provide data to benchmark an FE model of the Mil-Lx, which was then use to establish the range of frequencies for which the Mil-Lx provides biofidelic force responses at both the upper tibia and the footplate. Optimizations were performed using the finite element model and a lumped mass model (LMM) of the Mil-Lx to estimate the characteristics of the compliant materials necessary to expand the range of loading frequencies for which Mil-Lx forces match forces in the human leg. Further, several additional LMMs were developed based on the human FE model response to characterize the mass and compliance distribution which should be used in future ATD design.

Recommendations for short-term, cost-effective Mil-Lx design improvements include replacing the heel pad and tibia compliant element with 70-durometer neoprene and 90-durometer polyurethane, respectively, adding angular rate sensors on the foot and tibia, and adding an ankle rotational potentiometer. These modifications would enable the Mil-Lx to be used with the proposed force and impulse injury risk function by yielding biofidelic plantar forces for impact acceleration durations ranging from 4.5 to 100 ms. Long-term recommendations for ATD leg development are more expensive and time-consuming, and involve designing an ATD to match the characteristics of a 3-mass LMM of the human leg and including a foot or heel load cell; in theory, this design could expand this range to 5 to 156 Hz.

In summary, the duration-dependent leg injury risk function described in this dissertation increases the injury prediction accuracy by up to 18% compared to previous injury risk functions, and expands the range of load durations for which a single leg injury risk function may be used, encompassing load durations of 5.1 to 89.9 ms. Modifications to the Mil-Lx design produced improvements in the range of loading frequencies for which the Mil-Lx provided biofidelic forces, but further improvement to the design is necessary to encompass the range of load durations applicable to both the underbody blast and automotive environments and to encompass the range of durations included in the injury risk function. Nonetheless, Mil-Lx modifications outlined in the dissertation provide a temporary, cost-effective solution for providing an ATD which can utilize the proposed injury criterion for a subset of the desired frequency range. These contributions are the first step toward establishing more accurate assessment of the effectiveness of injury mitigation schemes for underbody blast, and have the potential to inform the safety design process for both automotive and military vehicles.

Approval Sheet

This dissertation is submitted in partial fulfillment of the requirements for the degree of Doctor of Philosophy in Mechanical Engineering:

Ann Marie Bailey (Author)

The dissertation has been read and approved by the examining committee:

Jeff Crandall, Ph.D. (Faculty Advisor)

Matthew Panzer, Ph.D. (Committee Chair)

Robert Salzar, Ph.D. (Committee Member)

Jason Kerrigan, Ph.D. (Committee Member)

Spyros Masouros, Ph.D. (Committee Member)

Timothy McMurry (Outside Member)

Accepted by the School of Engineering and Applied Science:

Dean, School of Engineering and Applied Science

Acknowledgements

First, I would like to thank my parents, Richard and Lisa Bailey; sisters, Stephanie and Stacie; and husband, Daniel Good, for their love, patience, and support throughout my graduate career. I would also like to thank my Center for Applied Biomechanics family, specifically “Team Rob,” for making the CAB seem like a second home throughout all the long and stressful test days and ridiculous number of hours re-processing WIAMan data. I would also like to express my gratitude for my faculty advisor, Dr. Jeff Crandall, and committee members for taking the time out of their busy schedules to meet with me. Further, I would like to acknowledge the collaboration from the U.S. Army Aeromedical Research Laboratory (Frederick Brozoski and Carol Chancey) and U.S. Medical Research Materiel Command, as well as the U.S. Department of Defense contract number W81XWH-11-2-0086 for funding the bulk of the research included in this dissertation. Additionally, I would like to thank Dr. Spyros Masouros and his colleagues at Imperial College London for letting me use their Mil-Lx model for my research. Last, but certainly not least, I would like to thank Dr. Robert Salzar for the wisdom he shared during our countless discussions about life, biomechanics, and brisance. My graduate experience certainly would not have been the same without his tireless support.

1 Table of Contents

Abstract 2
Acknowledgements 6
List of Symbols 11
List of Figures 14
List of Tables 35
Summary of Contributions 40
2 Introduction 42
  2.1 Anatomy of the Leg 45
    2.1.1 Bones 45
    2.1.2 Ankle Motion 47
    2.1.3 Muscles, Tendons, and Ligaments 48
  2.2 Loading Environment and Leg Injury 51
    2.2.1 Automotive Intrusion 51
    2.2.2 Military Underbody Blast 53
  2.3 Injury Mechanisms 59
    2.3.1 Axial Loading 59
    2.3.2 Bending 68
    2.3.3 Ankle Flexion 68
    2.3.4 Ankle Xversion 70
    2.3.5 High Rate Injury Mechanisms 71
  2.4 Injury Risk Functions 73
    2.4.1 Injury Definition and Censoring 73
    2.4.2 Injury Risk Functions for the Leg 77
  2.5 Anthropomorphic Test Devices 92
    2.5.1 Signal Comparison 96
  2.6 Discussion 97
  2.7 Objectives 100
3 Experimentation 101
  3.1 Introduction 101
  3.2 PMHS Component Experimentation 101
    3.2.1 Drop Tower Test Methodology 101

3.2.2 Linear Impactor Test Methodology 104
3.2.3 Data Processing 108
3.2.4 Results 108
3.2.5 Discussion of Results 113
3.2.6 Evaluation of Force as an Injury Predictor 117
3.2.7 Injury Location 121
3.2.8 Limitations and Conclusions 128
4 Human Leg Finite Element Modeling 130
4.1 Modified GHBMC Leg Model 130
4.2 Human Leg Finite Element Model Benchmarking 135
4.2.1 FE and Experimental Corridor Comparison 136
4.2.2 Experimental versus Finite Element Model Strain Comparison 147
4.2.3 Comparison of Injury Outcome in the Finite Element Model 151
4.3 Human FE Model Parametric Study 153
4.3.1 The Effect of Simulated Fracture on Leg Response 159
4.3.2 The Effect of Boundary Condition on Leg Response 166
4.3.3 The Effect of Pulse Shape on Leg Response 169
4.4 Discussion 173
5 Human Lumped Parameter Modeling 176
5.1 Background 176
5.2 Single Degree-of-Freedom Model 180
5.3 Two Degree-of-Freedom Model 186
5.4 Multiple Degree-of-Freedom Model with Heel Pad Compliance 190
5.5 Multiple Degree-of-Freedom Model with Wobbling Mass 197
5.6 Frequency Response 211
5.7 Conclusions 215
6 Leg Injury Criterion Development 217
6.1 Introduction and Preliminary Considerations 217
6.1.1 Injury Location Analysis 217
6.1.2 Force Measurement Location 219
6.1.3 Consideration for Covariates 224
6.1.4 Data Set and Predictor Variable Selection 229
6.2 Combining Force and Time as an Injury Predictor 239
6.2.1 Linear Regression Approach 240

6.2.2 Logistic Regression Approach 242
6.3 Piecewise Approach using Impulse and Force 245
6.3.1 Survival Analysis using Impulse for Short Durations 247
6.3.2 Injury Prediction for Long Duration Pulses 254
6.3.3 Evaluation of Piecewise Injury Criterion 258
6.4 Continuous Injury Criterion 265
6.4.1 Predictor based on Lumped-Mass Model Compression 268
6.4.2 Predictor based on Finite Element Model Foot Compression 277
6.4.3 Predictor based on Finite Element Model Strain 284
6.4.4 Optimization of Predictor using PMHS Data 286
6.4.5 Evaluation of Continuous Injury Criterion Approaches 299
6.5 Discussion 301
6.5.1 Validation of the Injury Criterion 306
6.5.2 Limitations of the Proposed Injury Criterion 309
6.6 Summary 311
7 Anthropomorphic Test Device Design 313
7.1 Introduction 313
7.2 Evaluation of Mil-LX Biofidelity 316
7.2.1 Literature Review 316
7.2.2 Experimental Testing of the Mil-Lx ATD 326
7.3 Lumped Mass Model as a Tool for ATD Design 338
7.4 Finite Element Model of the Mil-LX 350
7.4.1 Benchmarking Mil-Lx FE Model Response 358
7.5 Optimization of Mil-Lx Biofidelity using Finite Element Modeling 366
7.5.1 Selection of Materials for Adapting the Mil-Lx ATD 380
7.5.2 Comparison of Modified Mil-Lx Response to PMHS Response 387
7.6 Application of Injury Criterion to Modified Mil-Lx ATD 390
7.7 Discussion 401
7.7.1 Discussion of Modified ATD Design 404
7.7.2 Cost-Benefit Analysis of Mil-Lx Redesign 411
8 Summary 413
8.1 Limitations and Use 414
8.2 Future Work 418
8.3 Contributions 420

8.4 Publications 425
8.4.1 Conference Proceedings/Presentations 425
8.4.2 Journal Publications 426
9 References 428
10 Appendices 455
10.1 Coordinate Transformations and Scaling 455
10.1.1 Tibia Coordinate System 455
10.1.2 PMHS Data Scaling 456
10.2 Injury Summary 456
10.3 Data Summary from PMHS Tests 467
10.3.1 Fracture Timing 469
10.4 Human Finite Element Model Results 474
10.5 Statistics Equations 481
10.6 Material Property Summary 482
10.6.1 Polyurethane 483
10.6.2 Other Materials 485
10.7 Mil-Lx FE Model Response 488
10.7.1 Mil-Lx FE Original 488
10.7.2 FE-Based Optimization 498
10.7.3 Discrete Material Optimization of Mil-Lx 508

List of Symbols

Chapter 1

CORA	Cross-correlation score using equal weighting of phase, size, and shape parameters
w_i	Weighting parameter for CORA scores

Chapter 3

CORA	Cross-correlation score using equal weighting of phase, size, and shape parameters
f_i	Biofidelity score
w_i	Weighting parameter
ε	True Strain
ε_f	Failure strain
σ	True Stress
σ_Y	Yield stress
F	Force (axial)
t	Time
A	Cross-sectional area
L	Length
x	Position (or displacement)
x_f	Compression at failure
E	Elastic modulus

Chapter 4

a	Acceleration
m_i	Mass
m_w	Wobbling mass
k_i	Spring constant
k_w	Spring constant for the wobbling mass
c_i	Damping constant
c_w	Damping constant for the wobbling mass
ω_n	Natural frequency
ω_r	Resonant frequency
ω_d	Damped natural frequency
Δt_n	Time associated with the natural frequency of the leg
σ_ε	Instantaneous elastic response
r_{ankle}	Ankle radius
$t_{heel\ pad}$	Heel pad thickness
H_{ankle}	Ankle height
L_{tibia}	Length of tibia
r_{tibia}	Radius of tibia at mid-tibia
β_i	Lumped mass model scaling parameter for damping
α_i	Lumped mass model scaling parameter for stiffness
ω	Frequency in radians/second
f	Frequency in Hertz

ω_n	Natural frequency in radians/second
ω_r	Resonant frequency in radians/second
ξ	Damping ratio

Chapter 5

CORA	Cross-correlation score using equal weighting of phase, size, and shape parameters
f_i	Biofidelity score
w_i	Weighting parameter
γ_K	Kruskal's gamma
Q_Y	Yule's Q
n_d	Number of discordant pairs
n_c	Number of concordant pairs
TPR	True positive ratio
FPR	False positive ratio
FNR	False negative ratio
TNR	True negative ratio
ACC	Accuracy
PPV	Positive predictive value (precision)
FOR	False omission rate
NPV	Negative predictive value
FDR	False discovery rate
TP	True positive
TN	True negative
FP	False positive (Type I error)
FN	False negative (Type II error)

Chapter 6

m_{foot}	Mass of Mil-Lx foot assembly
m_{ankle}	Mass of Mil-Lx ankle assembly
m_{LTLC}	Mass of the Mil-Lx lower tibia load cell
m_{skin}	Mass of Mil-Lx skin attachment
m_{TCE}	Mass of the Mil-Lx tibia compliant element assembly
m_{UTLC}	Mass of the Mil-Lx upper tibia load cell
m_{knee}	Mass of the Mil-Lx knee mount assembly
$CORA_1$	Weighted overall CORA score for footplate force
$CORA_2$	Weighted overall CORA score for proximal tibia force
m_i	Mass of the i^{th} mass of the lumped mass model
k_i	Stiffness for the i^{th} compliant element of the lumped mass model
c_i	Damping for the i^{th} compliant element of the lumped mass model
z_i	SAE-z displacement of lumped mass model mass
$\dot{z}_i$	SAE-z velocity of lumped mass model mass
$\ddot{z}_i$	SAE-z acceleration of lumped mass model mass
$F_{footplate}$	Footplate force
$F_{prox\ tibia}$	Proximal tibia force
W	Strain energy density

$R(t)$	Relaxation function
c_{mn}	Coefficient for the Mooney-Rivlin hyper-elastic model
I	Strain invariant
t	time
λ_n	Time constant
δ_n	Relaxation scale factor
μ	Ogden hyper-elastic model coefficient
α	Ogden hyper-elastic model coefficient
$g(t)$	Relaxation function for the LS-Dyna Ogden model
B	Decay constant for relaxation function
G	Shear modulus
K	Bulk modulus
J	Strain invariant with volumetric portion removed
F_{plantar_z}	SAE-z component of Mil-Lx plantar force
F_{LT_z}	SAE-z component of Mil-Lx lower tibia force
a_{foot_z}	SAE-z component of Mil-Lx foot acceleration
$m_{\mathrm{belowLTLC}}$	Mass below Mil-Lx lower tibia load cell
F_{Ank_x}	SAE-x component of the force at the Mil-Lx ankle joint
F_{Ank_z}	SAE-z component of the force at the Mil-Lx ankle joint
F_{Fr_x}	Frictional force at the plantar surface of the Mil-Lx foot
M_{plantar_y}	Reaction moment at the plantar surface of the Mil-Lx foot
θ	Angle between the footplate normal and tibia shaft
ω_{LT}	Angular velocity of the Mil-Lx lower tibia
I_{foot_y}	SAE-y component of the Mil-Lx foot moment of inertia
$x_{\mathrm{ank/cg}}$	Horizontal distance between the Mil-Lx ankle joint center and foot center of gravity
m_{LT}	Mass of the Mil-Lx lower tibia
α_{LT_y}	SAE-y angular acceleration of the Mil-Lx lower tibia
a_{LT_y}	SAE-y component of the Mil-Lx lower tibia acceleration
a_{LT_z}	SAE-z component of the Mil-Lx lower tibia acceleration
I_{LT_y}	SAE-y component of the lower tibia moment of inertia
$x_{\mathrm{LT/cg}}$	Horizontal distance between the lower tibia center of gravity
$z_{\mathrm{LT/cg}}$	Vertical distance between the lower tibia center of gravity and
$r_{\mathrm{LT/foot}}$	Vector from Mil-Lx foot center of gravity to lower tibia center of gravity

List of Figures

Figure 2.1. Bones and anatomical regions of the foot and leg 46

Figure 2.2. Ankle joint motion. Note that the coordinate system aligns with the SAE J211 coordinate system[100] with the exception of the polarity of the y- and z-axes. (Accidental Injury by Springer New York. Reproduced with permission of Springer New York in the format Thesis/Dissertation via Copyright Clearance Center.)[189] 47

Figure 2.3. Diagram of the muscles of the foot and leg, showing an anterior view (left) and superficial and deep posterior views (middle and right, respectively). (Image courtesy of Creative Commons) 50

Figure 2.4. Example brake pedal pulses from frontal collision events. Acceleration and velocity plots are provided for the acceleration measured for the brake pedal and vehicle during a frontal collision. Figures were produced based on data from Kuppa et al.[115] 52

Figure 2.5. Distribution of foot and leg fractures produced from data compiled by Ye et al. for frontal collision events. Note that the pattern-filled area distinguishes the hindfoot fractures from the rest.[227] 53

Figure 2.6. Example UBB loading conditions for the seat and floor pan from live fire testing. Acceleration and velocity traces are provided for live-fire simulated UBB events. (Annals of biomedical engineering by BIOMEDICAL ENGINEERING SOCIETY Reproduced with permission of SPRINGER NEW YORK LLC in the format Thesis/Dissertation via Copyright Clearance Center.).[9,26,190] 55

Figure 2.7. Distribution of injuries for warfighters wounded in UBB events. Percentages are based on the percentage of 456 wounded soldiers with a particular injury.[3] 57

Figure 2.8. Distribution of foot/ankle injuries for warfighters wounded in UBB events. The figure shows percentages calculated based on total number of foot/ankle injuries reported from a study including 456 wounded soldiers.[3] 57

Figure 2.9 Pendulum impactor test rig used by Klopp et al., which includes a mechanism for generating muscle tension during impact (Image reproduced with permission from Taylor and Francis).[109] 62

Figure 2.10 Test fixture used by Funk et al., which utilized a pneumatic linear impactor to deliver axial impacts to the foot. (motion (Accidental Injury by Springer New York. Reproduced with permission of Springer New York in the format Thesis/Dissertation via Copyright Clearance Center.)[73] 65

Figure 2.11. Box plot of force rate for axial loading studies from the literature. Force measurement location is distinguished by color and a schematic is provided for further reference. Note that these tests used different proximal boundary conditions as well. 67

Figure 2.12. Blast (shock) wave profile based on a Friedlander waveform, which consists of an instantaneous rise in positive pressure, followed by an exponential decay of pressure which ends in a negative pressure phase. 72

Figure 2.13. Frequency of lower leg injuries generated by axially-loaded PMHS tests from the literature (238 tests).[14,73,75,82,94,108,109,135,181,191,196,231] The input and boundary conditions for these tests are provided in Table 2.2 76

Figure 2.14. Comparison of existing lower leg IRFs from literature using tibia force as an injury predictor. Note: Funk et al. 2002 and Yoganandan et al. 2014 assume a 45 year old, 75 kg male.[20,54,73,94,135,229,231] 79

Figure 2.15. Comparison of injury risk function based on plantar force and previous injury risk functions which did not distinguish between location of force measurement or measured force proximal to the location of injury. (Figures reproduced with permission from Taylor and Francis)[12] 83

Figure 2.16. Comparison of injury risk functions for foot/ankle fracture versus tibia plateau fracture. The foot and ankle injury risk curve was produced using the injury risk function developed by Yoganandan et al., and the tibia plateau injury risk curve was developed using the data from axial tibiofemoral joint impact tests performed by Banglmaier et al. [Figures produced using data from Kuppa et al.][17,116,231] 85

Figure 2.17. Diagram reproduced based on the work of von Gierke[214], which demonstrates the theoretical dependence of injury threshold (model deformation) on pulse shape, duration, and peak for various input pulses. Lines represent constant deformation response, which can be correlated with injury. 88

Figure 2.18. Injury thresholds for lung under blast loading based on peak pressure as a function of duration. (NeuroImage by Academic Press. Reproduced with permission of Academic Press in the format of Thesis/Dissertation via Copyright Clearance Center.)[51] 91

Figure 2.19. Thor-Lx ATD leg pictured with and without the flesh. (Image modified from NHTSA report.)[146] 94

Figure 2.20. Mil-Lx ATD leg with and without flesh showing instrumentation locations.[97] 95

Figure 3.1. Drop tower test fixture schematic showing the load cell plate lightly supported by polystyrene crushable supports and a weighted hammer.[94] 103

Figure 3.2. Tibia instrumentation consisting of strain gages, accelerometers, and angular rate sensors 103

Figure 3.3. Instrumentation for PMHS component impactor tests, which included strain gages, accelerometers, an acoustic sensor, and load cells. 106

Figure 3.4. Lower extremity test rig, using a pneumatic linear impactor and polyurethane pulse-shapers. The figure shows the location of the footplate and proximal tibia load cells. 106

Figure 3.5. Dynamic lateral x-ray frame from an injurious intermediate level impactor test showing fracture of the calcaneus and tibial pilon. 107

Figure 3.6. Footplate acceleration (a, b), proximal tibia force (c, d), and force-compression (e, f) response corridors for drop tower and impactor tests. Forces were mass-normalized and compressions were length-normalized to represent the response of a 50th percentile male subject. Note that tests Impactor 09 and Impactor 27 were excluded from the force-compression corridor due to eversion of the foot during the test. 110

Figure 3.7. Tibia displacement (a, b), calcaneus displacement (c), and footplate force corridors for drop tower and impactor test conditions. Tibia displacements were calculated from transformed distal tibia acceleration for the impactor study, and untransformed single-axis acceleration for the drop tower study. Calcaneus displacements were calculated from single-axis accelerometers mounted to the calcaneus. 111

Figure 3.8. Comparison of leg stiffness and proximal tibia force rate for test groups showing that leg stiffness is significantly different for different load rates. Averages are shown for normalized and non-normalized data; error bars indicate ± one standard deviation. 114

Figure 3.9. Normalized foot compression versus proximal tibia force corridors for the drop tower and impactor studies. The figure on the left shows the drop tower corridors with the Impactor Low condition overlaid for reference. The figure on the right shows the normalized foot compression versus proximal tibia force for the impactor conditions. 116

Figure 3.10. Average forces recorded for the footplate and proximal tibia at time of calcaneus fracture and time of the 2nd fracture (if applicable) for the impactor medium and high conditions. Standard error is indicated by error bars and p-values for a two-tailed t-test are shown for testing for difference in the averages. 118

Figure 3.11. Time of first fracture compared to time of peak footplate and proximal tibia forces for all injurious impactor and drop tower tests. 120

Figure 3.12. Frequency of fracture location for the drop tower and impactor PMHS studies. 122

Figure 3.13. Time-stamped images are shown from a dynamic x-ray video of a high condition impactor test. The images are shown for the time of onset of calcaneus (Image A) and tibia pilon (Image B) fractures. Time is shown in seconds, where impact with the footplate occurred at t=0 s. These images confirm the hypothesis that in the case of multiple injuries, calcaneus fractures are likely to be the first fracture when the leg is impacted at the plantar surface of the foot. 123

Figure 3.14. Medial view of a comminuted calcaneus without the presence of other fractures due to dissipation of energy (Impactor 33). 124

Figure 3.15. Medial and inferior views of a less severe calcaneus fracture accompanied by a tibia fracture radiating from the pilon (Impactor 15). 124

Figure 3.16. Dynamic x-ray snapshots at time of fracture to show variation in location of calcaneus fracture initiation. Figure A shows the calcaneus fracture initiation from the impact site for Impactor 33, which Figure B shows the calcaneus fracture initiating from the subtalar joint for Impactor 24. 127

Figure 4.1. GHBMC leg model validated by Shin, et al.,[193] which included rigid forefoot bones, deformable hindfoot bones, ligaments, and solid and shell elements to model the soft tissue. (Image from presentation by Panzer et al. 2014) 131

Figure 4.2. Stress-strain curves used to represent the stress-strain response of the heel pad for different strain rates using MAT_181 in LS-Dyna as described by Gabler et al.[78] 133

Figure 4.3. University of Virginia leg model and PMHS drop tower set-up used for comparison of FE and experimental leg response to a prescribed impact acceleration time history. 134

Figure 4.4. LS-Dyna finite element model of the impactor test set-up used for additional model benchmarking. 136

Figure 4.5. Comparison of the experimental ±one standard deviation corridor and characteristic average and the average FE proximal tibia force response for the Drop Tower A condition. 137

Figure 4.6. Comparison of the experimental ±one standard deviation corridor and characteristic average and the average FE proximal tibia force response for the Drop Tower B condition. 137

Figure 4.7. Comparison of the experimental ±one standard deviation corridor and characteristic average and the average FE proximal tibia force response for the Impactor Low condition. 137

Figure 4.8. Comparison of the experimental ±one standard deviation corridor and characteristic average and the average FE proximal tibia force response for the Impactor Medium condition. 137

Figure 4.9. Comparison of the experimental ±one standard deviation corridor and characteristic average and the average FE proximal tibia force response for the Impactor High condition. 138

Figure 4.10. Comparison of the experimental ±one standard deviation corridor and characteristic average and the average FE tibia displacement response for the Drop Tower A condition. 138

Figure 4.11. Comparison of the experimental ±one standard deviation corridor and characteristic average and the average FE tibia displacement response for the Drop Tower B condition. 138

Figure 4.12. Comparison of the experimental ±one standard deviation corridor and characteristic average and the average FE tibia displacement response for the Impactor Low condition. 139

Figure 4.13. Comparison of the experimental ±one standard deviation corridor and characteristic average and the average FE tibia displacement response for the Impactor Medium condition. 139

Figure 4.14. Comparison of the experimental ±one standard deviation corridor and characteristic average and the average FE proximal tibia displacement response for the Impactor High condition. 139

Figure 4.15. Comparison of the experimental ±one standard deviation corridor and characteristic average and the average FE foot/ankle compression response for the Impactor Low condition. 140

Figure 4.16. Comparison of the experimental ±one standard deviation corridor and characteristic average and the average FE foot/ankle compression response for the Impactor Medium condition. 140

Figure 4.17. Comparison of the experimental ±one standard deviation corridor and characteristic average and the average FE foot/ankle compression response for the Impactor High condition. 140

Figure 4.18. Weighted CORA score for plantar force compared to size score for leg compression for each combination of the 14 different input conditions. The plot on the left shows the results optimizing the weighted score using all combinations. The plot on the right shows the results optimized for leg compression size scores greater than 0.25 (Eqn. 4.1). 143

Figure 4.19. Comparison of the experimental ±one standard deviation corridor and characteristic average and the average FE calcaneus displacement response for the Impactor Low condition. 146

Figure 4.20. Comparison of the experimental ±one standard deviation corridor and characteristic average and the average FE calcaneus displacement response for the Impactor Medium condition. 146

Figure 4.21. Comparison of the experimental ±one standard deviation corridor and characteristic average and the average FE proximal calcaneus displacement response for the Impactor High condition. 146

Figure 4.22. Location of element used for comparing FE and PMHS calcaneus strain. This element is in the approximate location of the PMHS strain gages used to measure calcaneus strain in the impactor study. 148

Figure 4.23. Medial calcaneus strain for low, medium, and high impactor conditions with finite element maximum principal strain from the average input condition. 150

Figure 4.24. Example of a comparison of FE model "fracture" location indicated by high levels of maximum principal strain compared to PMHS experimental fracture. 151

Figure 4.25. Progression of maximum principal strain in the human leg FE model for the Impactor High test condition. Strain first accumulated in the calcaneus and then progressed superiorly through the talus to the tibia and fibula. Fracture occurred in the calcaneus in the location indicated in Figure 4.24. 153

Figure 4.26. Template for sinusoidal and triangular input acceleration pulses, characterized by amplitude and frequency or amplitude and duration. 154

Figure 4.27. Peak force versus leg compression for forces measured at the footplate, mid-tibia, and proximal tibia. 155

Figure 4.28. Force results from parametric study simulations where the solid lines represent the footplate force and the dashed lines represent the proximal tibia force. The left column shows the response of the model when impact velocities were constant, but peak acceleration was varied. The right column shows the results for the case where peak accelerations were the same, but velocities were different. 157

Figure 4.29. Force results from parametric study simulations where peak acceleration was kept constant at 50g while the frequency of the acceleration pulse was varied to achieve different increments of peak velocity. 158

Figure 4.30. Force results from parametric study simulations where the solid lines represent the footplate force and the dashed lines represent the proximal tibia force. For all conditions, the frequency of the sinusoidal footplate acceleration pulse was 78.1 Hz. 159

Figure 4.31. Comparison of FE model forces for models including element elimination (w/ Failure) and models for which failure was turned off in the model (No Failure). The 100g, 14 m-s^{-1}, 250g, 6 m-s^{-1}, 500g, 10 m-s^{-1}, and 500g, 12 m-s^{-1} conditions are provided to show a range of loading frequencies. 161

Figure 4.32. Maximum principal strain map for the case where fracture was indicated by element deletion (left) and for the case where fracture was turned off for the model (right). Strains are shown for the time of maximum footplate force in the model without element deletion for the 100g, 14 m-s^{-1} input condition. 162

Figure 4.33. Comparison of peak plantar force predicted by the human leg FE model with and without element deletion (ED), and plantar force at time of fracture in the element deletion model. Input conditions from left to right are arranged from low to high frequency. No fracture conditions are denoted using an asterisk. 163

Figure 4.34. Comparison of plantar impulse at time of peak plantar force predicted by the human leg FE model with and without element deletion (ED), and plantar impulse at time of fracture in the element deletion model. Input conditions from left to right are arranged from low to high frequency. No fracture conditions are denoted using an asterisk. 164

Figure 4.35. Comparison of plantar force at fracture, maximum proximal tibia force, and proximal tibia force at time of fracture for the human leg FE model. Input conditions from left to right are arranged from low to high frequency. No fracture conditions are denoted using an asterisk. 166

Figure 4.36. Comparison of peak footplate and proximal tibia forces at time of fracture in the human FE model for both the fixed and free boundary conditions. 167

Figure 4.37. Human leg FE footplate and proximal tibia forces for fixed and free proximal boundary conditions. A 100g subinjurious pulse is shown on the left and a 500g injurious pulse is shown on the right. 168

Figure 4.38. Comparison of plantar force at fracture for sinusoidal versus triangular pulse shapes for peak footplate accelerations of 500g and time-to-peak acceleration ranging from 3ms to 30ms. Forces are plotted against time-to-peak acceleration. 170

Figure 4.39. Comparison of plantar force at fracture for sinusoidal versus triangular pulse shapes for peak footplate accelerations of 500g and time-to-peak acceleration ranging from 3ms to 30ms. Forces are plotted against time of fracture. 170

Figure 4.40. Comparison of fixed and free boundary conditions and pulse shape on the relationship between calcaneus strain, plantar force, and time. Symbols represent different strain levels while colors represent differences in proximal boundary or pulse shape. 171

Figure 4.41. Comparison of fixed and free boundary conditions and pulse shape on the relationship between calcaneus strain, plantar force, and plantar impulse. Symbols represent different strain levels while colors represent differences in proximal boundary or pulse shape. 172

Figure 4.42. Fracture force versus time-to-peak for the human FE model compared to fracture and no fracture data points from PMHS axial loading tests from the *Combined Data Set* (Note that this PMHS data set will be discussed in detail in Chapter 6). 174

Figure 4.43. Example force pulses which may result in a different relationship between peak force, time-to-peak, and strain. 175

Figure 5.1. Second-order dynamic model of the leg developed by Kim et al. for use in normalizing data for corridor development (Image reproduced from Kim et al.[106] with permission from Taylor and Francis.) 178

Figure 5.2. Single-DOF, second order dynamic model of the leg, where the mass (m_1) is the mass of the leg and k_1 and c_1 are stiffness and damping parameters. F_{FP} is the footplate reaction force, z_0 is the displacement of the footplate, and z_1 is the displacement of the proximal tibia boundary. 181

Figure 5.3. CORA results for comparison of LMM based on FE response parameters and individual FE responses. M1 DZ refers to the displacement of m_1, and FPFZ refers to footplate force. 184

Figure 5.4. LMM response compared to FE response for the condition with the best average CORA score (100g, 8 m-s^{-1}, left) and worst average CORA score (500g, 12 m-s^{-1}, right). 185

Figure 5.5. Two-degree of freedom, second order dynamic model of the leg, where the mass (m_1) is the mass of the leg, and m_2 is the reaction mass (Model 2A). Model 2B represents the case where the proximal boundary of the tibia is fixed. 186

Figure 5.6. Comparison of CORA scores for cross-correlation of FE-based 2-DOF LMM and FE response for individual input conditions. 188

Figure 5.7. LMM response compared to FE response for the condition with the best average CORA score (10g, 6m/s, left) and worst average CORA score (100g, 2 m/s, right). 189

Figure 5.8. Schematics of the multiple degree-of-freedom model which includes heel pad compliance. Footplate displacement corresponds to z_0, z_1 is foot (calcaneus) displacement, z_2 is tibia displacement, and z_3 is the proximal tibia displacement. 191

Figure 5.9. Weighted overall CORA scores for displacements and forces for the 28 FE model runs compared to Model 3A optimized with fixed masses. Input conditions are ordered from low frequency to high frequency. Note that DZ refers to displacement, while FP FZ and PT FZ refer to footplate and proximal tibia forces. 193

Figure 5.10. Weighted overall CORA scores footplate and proximal tibia forces for the 28 FE model runs compared to Model 3A optimized with fixed masses. Note that FP FZ and PT FZ refer to footplate and proximal tibia forces. 194

Figure 5.11. Weighted overall CORA scores for displacements and forces for the 28 FE model runs compared to Model 3A optimized with floating masses. Note that FP FZ and PT FZ refer to footplate and proximal tibia forces. 194

Figure 5.12. Weighted overall CORA scores footplate and proximal tibia forces for the 28 FE model runs compared to Model 3A optimized with floating masses. Note that FP FZ and PT FZ refer to footplate and proximal tibia forces. 195

Figure 5.13. Floated mass LMM response compared to FE response for the condition with the best average CORA score (10g, 6m/s, left) and worst average CORA score (100g, 2 m/s, right). 196

Figure 5.14. Second order dynamic models of the leg where k_i represent spring stiffness, c_i represent damping, and m_i represent mass. Displacement is denoted by z_i. Forces measured by experimental tests are also pictured. Model 4A represents the “free” test condition while Model 4B represents the “fixed” test condition. 199

Figure 5.15. Plots showing lumped mass model fit for displacements and estimates of force for sample tests from Impactor Low, Medium, and High conditions. Results from Impactor 05, Impactor 14, and Impactor 36 are shown. Experimental (Exp) and lumped-mass model results are shown (LMM). 204

Figure 5.16. Plots showing lumped mass model (LMM) fit for displacements and estimates of force for sample experimental (Exp) tests from Drop Tower A and B conditions. Results from Drop Tower 08, and Drop Tower 15 are shown. 205

Figure 5.17. Lumped-mass model (LMM) response compared to PMHS corridors representing the response of a 50th percentile male based on experimental tests (Exp.). Results for proximal tibia force are shown. 206

Figure 5.18. Power spectral density plot for vertical calcaneus displacement for the finite element human leg model exposed to a sine wave sweep displacement function. 215

Figure 6.1. Frequency of leg injuries from 286 axial loading tests, showing a prevalence of calcaneus fractures. Injuries were classified into three categories depending on the presence of Achilles tension and the occurrence of calcaneus fracture in addition to another fracture. 218

Figure 6.2. Correlation matrix for strains and forces from the finite element leg model. Correlation coefficients are provided for proximal tibia force (PTFZ), mid-tibia force (MTFZ), footplate force (FPFZ), medial calcaneus strain (calcS1), calcaneus strain near the fracture site (calcS2), maximum calcaneus strain (MPS), 50th percentile maximum principal strain in the calcaneus (S50), and 95th percentile maximum principal strain in the tibia (S95). 222

Figure 6.3. Comparison of peak forces as measured at the footplate versus the mid- or proximal tibia in the FE model for various input acceleration conditions. While the forces are correlated, this scatterplot shows that multiple mid- or proximal tibia forces may be mapped to the same footplate force. 223

Figure 6.4. Cortical bone strain-rate dependency of stress-strain behavior from McElhaney (1966)[133] 227

Figure 6.5. Scatter plot matrix showing trends and correlations between various aspects of the combined data set. Proximal and mid-tibia forces were shown to be highly correlated, while other variables showed only slight or no visible correlation. 232

Figure 6.6. Correlation matrix for the combined data set where negative correlations are shown in red and positive correlations are shown in blue. The highest correlation was observed between mid- and proximal tibia force, while the lowest correlation was between age and injury location. 234

Figure 6.7. Correlation matrix using scaled forces for the combined data set where negative correlations are shown in red and positive correlations are shown in blue. Again, the highest and lowest correlations were between the mid- and proximal tibia forces and age and injury location, respectively. 235

Figure 6.8. Force versus force duration and time-to-peak for footplate, mid-tibia, and proximal tibia locations for the larger data set. The left column shows peak force for each of the three locations plotted against force duration, while the right column shows the peaks plotted against the time-to-peak force. 237

Figure 6.9. Relationship between plantar force at fracture versus duration and time-to-peak for injury data points. 238

Figure 6.10. Peak plantar force versus plantar force duration for the combined data set which excluded tests with non-neutral ankle positions. 239

Figure 6.11. Linear regression fits of injury data points are shown. The plot on the left shows the linear regression fit for all injury data, while the plot on the right shows the fit for only the uncensored injury data points. Note that the log of the duration and log of the force were used to produce the linear fit. 240

Figure 6.12. Histograms of the duration and force for injured data points to show the distribution of injured data points. 242

Figure 6.13. Logistic regression fits of injury data for 50% and 75% probability of injury are shown above on a log-log scale. The plot on the left shows the linear regression fit for all injury data, while the plot on the right shows the fit for only the uncensored injury data points. The linear regression fit is shown for reference. 244

Figure 6.14. Logistic regression fits of injury data are shown above for 50% and 75% probability of injury. The plot on the left shows the linear regression fit for all injury data, while the plot on the right shows the fit for only the uncensored injury data points. 244

Figure 6.15. The "All Data" logistic regression fit is shown on top of injury and no-injury data points including the tests with initial ankle flexion. Note that a log scale was used for the x-axis. 245

Figure 6.16. Diagram based on von Gierke[214], updated to show the division between regions that will use different injury predictors (blue vs. green shading). The red region highlights the "resonance region" which extends from the resonance frequency to 10 times the resonance frequency, which corresponds to 0.5-5 times the pulse length divided by the period associated with natural period. 247

Figure 6.17. Impulse versus time of peak force and duration of force calculated at peak force and at the duration of the force. The left column compares the plantar impulse at the duration of the force versus force duration (top) and time-to-peak force (bottom) for injury and no-injury data points. The right column compares the impulse at peak force for the same two time variables. 248

Figure 6.18. Demonstration of the separation between injury and no-injury points provided by plantar impulse for short force durations using the combined data set. The plot on the top shows planter impulse at force duration versus force duration, and the plot on the bottom shows plantar impulse at peak force versus force time-to-peak. 250

Figure 6.19. Diagram based on von Gierke[214], updated to show the division between regions that will use different injury predictors (blue vs. green shading). The blue region will utilize impulse as the injury predictor, while the green region will use force as the main injury predictor. The example line shown demonstrates the theoretical shape of the division between injury and no-injury assuming force as the injury predictor. 251

Figure 6.20. Survival curves showing the negative relationship between probability of injury and age for a given impulse. 254

Figure 6.21. Plantar force versus plantar force time-to-peak for the data included in the resonance region and the pulse-independent region of Figure 6.16. 255

Figure 6.22. Survival curves showing the negative relationship between age and probability of injury for a given plantar. 257

Figure 6.23. ROC curves comparing the five injury probability models validation data set. 261

Figure 6.24. Single degree of freedom LMM with a sinusoidal force input. 265

Figure 6.25. LMM used to develop response surface, which indicates the foot compression (Δz) used as the dependent variable for the response surface and used as the P_{FI} in Eqn. 6.21. In order to use force as an input, the boundary (m_0) was modeled as a small mass. 269

Figure 6.26. Response surface generated from the 2DOF LMM-based foot compression relationship with peak force (kN) and impulse at peak force (N-s). Individual data points generated by the LMM are shown for purpose of exhibiting the force-impulse grid sampling method. 270

Figure 6.27. Residuals for the fit of Eqn. 6.21 to the surface for LMM-predicted foot compression (mm) versus peak force (kN) and impulse at peak force (N-s). 271

Figure 6.28. Contour plot generated from the 3DOF LMM-based foot compression relationship with peak force and impulse with PMHS injury and no-injury data points overlaid. 272

Figure 6.29. Injury risk functions using the 3DOF LMM-based foot compression with no covariates (left) and with age as a covariate (right). Injury risk lines and 95% confidence intervals are shown for ages 25, 45, and 65 years. 274

Figure 6.30. Contours of injury probability based on the estimate of LMM foot compression using force and impulse. Contour plots A, B, C, and D were developed based on the no covariate model, and variations of the age-covariate model for 25-, 45-. And 65-year old males, respectively. 276

Figure 6.31. Forces from the human leg FE model exposed to a sinusoidal input acceleration with a magnitude of 9000 g and a frequency of 995 Hz. 278

Figure 6.32. Contour plot generated from the FE model foot compression relationship with peak force and impulse with PMHS injury and no-injury data overlaid. 280

Figure 6.33. Injury risk functions using the FE-based foot compression relationship with peak force and impulse. 281

Figure 6.34. Contours of injury probability for the force-impulse predictor variable based on FE model foot compression. Plot A shows the results from fit 3, and plots B-D show the results of fit 4 for age 25, 45, and 65. 283

Figure 6.35. Contour plot generated from the FE-based strain relationship with peak force and impulse with PMHS injury and no-injury data overlaid. 285

Figure 6.36. Schematic for discrete variable optimization for fitting PMHS injury data using survival analysis. 288

Figure 6.37. Injury risk functions based on the force-impulse predictor variable with 95% confidence intervals for the parameters estimated using the discrete variable optimization approach to fit PMHS injury data. The figure on the left shows the result of the survival analysis without covariates, and the figure on the right shows the injury risk for ages 25, 45, and 65 years. 293

Figure 6.38. Injury risk functions based on the force-impulse predictor variable with 95% confidence intervals for the parameters estimated using the maximum likelihood optimization approach to fit PMHS injury data. . The figure on the left shows the result of the survival analysis without covariates, and the figure on the right shows the injury risk for ages 25, 45, and 65 years. 294

Figure 6.39. Contours of injury probability for the force-impulse predictor variable based on Fit 3. Plot A shows the results from fit 3, and plots B-D show the results of fit 4 for age 25, 45, and 65. 296

Figure 6.40. Contours of injury probability for the force-impulse predictor variable based on Fit 3. Plot A shows the results from fit 1, and plots B-D show the results of fit 2 for age 25, 45, and 65. 298

Figure 6.41. Injury risk functions based on mass-scaled plantar force. 304

Figure 6.42. Comparison of the performance of plantar force-based injury risk functions using the combined data set. The proposed force-impulse injury risk function was shown to outperform the other models for AUC, accuracy, Kruskal's gamma, and Yule's Q. 305

Figure 6.43. Difference in probability of injury as predicted by the proposed injury risk function compared to the cross-validation injury risk functions. 308

Figure 6.44. Representation of the range of applicability of the proposed leg injury criterion with PMHS data points overlaid. The area to the left of the dashed line represents loading frequencies which may incorporate additional injury mechanisms which were not considered in the current study. 310

Figure 7.1. Simplified human and ATD leg models and theory explaining how injury mitigation materials or a boot placed in series with the leg modifies the transfer function (TF) between human and ATD leg force. 315

Figure 7.2. Comparison of Mil-Lx response (5.4 m/s) to Barbir[18] PMHS corridor (4.8 m/s) for a comparison at a lower loading condition. Note: Figure reproduced from McKay dissertation.[134] 317

Figure 7.3. Comparison of PMHS (implanted mid-tibia load cell) and Mil-Lx (upper tibia load cell) loading rates for axial impact tests.[134] 317

Figure 7.4. Mil-Lx force response to axial impacts performed at different velocities by Pandelani et al. (Plots reproduced from data presented in Pandelani's dissertation)[156] 318

Figure 7.5. Mil-Lx upper and lower tibia forces from a 5.6 m-s^{-1} impact. (Plots produced using data from Shewchenko et al.)[192] 319

Figure 7.6. Mil-Lx peak force response to varying impact velocity compared to cadaveric tibia force response. (Accidental Injury by Springer New York. Reproduced with permission of Springer New York in the format Thesis/Dissertation via Copyright Clearance Center.)[170] 320

Figure 7.7. Comparison of Mil-Lx upper tibia force to PMHS force corridors generated by Barbir et al.[18] Note that while there is reasonable agreement, the Mil-Lx test conditions consisted of slightly higher impact velocities. 323

Figure 7.8. Comparison of Mil-Lx upper tibia forces and mid-tibia forces from sub-injurious PMHS tests performed by McKay.[134] This condition was used for the development of the Mil-Lx design. 324

Figure 7.9**.** Comparison of Mil-Lx upper tibia forces and mid-tibia forces from injurious PMHS tests performed by McKay.[134] 325

Figure 7.10. Comparison of Mil-Lx upper tibia force to matched mass-normalized [63] PMHS proximal tibia force results from Henderson et al. (2013) showing that the Mil-Lx underestimates PMHS force for sub-injurious cases (Tests 17-19). 328

Figure 7.11. Comparison of PMHS normalized proximal tibia force and Mil-Lx upper tibia force corridors for the Drop Tower B loading condition. 329

Figure 7.12. Displacement response of the PMHS (solid lines) compared to the Mil-Lx (dashed lines) for the impact plate, the proximal (load cell) plate, and the tibia for drop tower test conditions 16-20. 330

Figure 7.13. Comparison of Mil-Lx and PMHS impulse for drop tower tests 16-19. Mil-Lx responses are displayed using dashed lines, while PMHS responses are displayed by solid lines. 331

Figure 7.14. Comparison of Mil-Lx tibia and hindfoot accelerations showing that the plantar force can be estimated by compensating for the mass distal to the lower tibia load cell. The sample trace provided is from Test 18, however all test cases showed similar results. 332

Figure 7.15. Comparison of estimated plantar force for the Mil-Lx and PMHS plantar force estimated using the human FE model. 333

Figure 7.16. Tibia SAE-z acceleration comparison for low condition (4.6-6.5 m s^{-1}) whole body matched pair tests reproduced from Bailey et al. (2015).[11] 334

Figure 7.17. Tibia SAE-z acceleration comparison for high condition (8.8-10.8 m s^{-1}) whole body matched pair tests reproduced from Bailey et al. (2015).[11] 335

Figure 7.18. Bode diagram for the sub-injurious drop tower conditions and the Mil-Lx tests for the same input conditions assuming a 2-pole transfer function for footplate versus proximal tibia acceleration. 337

Figure 7.19. Bode diagram for the sub-injurious drop tower conditions and the Mil-Lx tests for the same input conditions assuming a 2-pole transfer function for footplate versus proximal tibia force. 337

Figure 7.20. Lumped-mass model of the Mil-Lx which assumes no ankle compliance 339

Figure 7.21. Summary of CORA scores for the Mil-Lx LMM optimized using the input conditions from the FE parametric study compared to the human FE model force response at the footplate (FP FZ) and the proximal tibia (PT FZ). LMM parameters are described in Table 7.2. Input conditions are ordered from low to high frequency moving from left to right. 343

Figure 7.22. Summary of CORA scores for the Mil-Lx LMM optimized using the high frequency input conditions compared to the human FE model force response at the footplate (FP FZ) and the proximal tibia (PT FZ). LMM parameters are described in Table 7.3. 345

Figure 7.23. Summary of CORA scores for the Mil-Lx LMM optimized using the low frequency input conditions compared to the human FE model force response at the footplate (FP FZ) and the proximal tibia (PT FZ). LMM parameters are described in Table 7.4. 347

Figure 7.24. Summary of CORA scores for the Mil-Lx LMM optimized using all 28 input conditions compared to the human FE model force response at the footplate (FP FZ) and the proximal tibia (PT FZ). LMM parameters are described in Table 7.5. The objective function for this optimization was based on matching footplate force only. 349

Figure 7.25. Three-dimensional LS-Dyna finite element model of the Mil-Lx ATD leg adapted from the NASTRAN model developed by Newell et al. The figure on the left shows the re-meshed axisymmetric model with the original geometry from Newell et al., and the figure on the right shows the final modified Mil-Lx model for which the geometry of the foot was added.[148] 352

Figure 7.26. LS-Dyna material model fits compared to the experimental response of the Mil-Lx rubber from Newell et al.[148] 356

Figure 7.27. Diagram summarizing the location of different contact types used in the Mil-Lx model. 358

Figure 7.28. Mil-Lx experimental versus FE model response for the drop tower MLX 17 test condition. Displacements are shown on the left and forces for upper and lower tibia are shown on the right. 359

Figure 7.29. Mil-Lx FE model response compared to human leg FE model response for select conditions from the parametric study. 362

Figure 7.30. CORA scores for Mil-Lx FE model response compared to human FE model response for sinusoidal acceleration pulses described by peak acceleration and peak velocity. 363

Figure 7.31. Peak force comparison for the plantar force and upper/mid-tibia force for the human FE model with element deletion (ED) compared to the Mil-Lx FE model. 364

Figure 7.32. Probability of injury estimated using the force-impulse injury risk function and the forces and impulses estimated by the original Mil-Lx FE model and the human FE model with and without element deletion (ED). 365

Figure 7.33. Schematic of Mil-Lx design optimization using an integration of MATLAB and LS-Dyna. 368

Figure 7.34. Weighted Overall CORA scores comparing optimized Mil-Lx FE response to FE human leg response for each of the parametric study conditions within the range of 2-33 ms footplate acceleration duration. Test conditions are ordered from low to high frequency from left to right. 370

Figure 7.35. Comparison of human leg plantar force and impulse and optimized Mil-Lx plantar force and impulse from finite element models. Heel pad and tibia compliant element materials were replaced with the materials described in Table 7.13. 371

Figure 7.36. High frequency test condition for which a double hit occurs between the footplate and plantar surface of the Mil-Lx foot. This effect is likely the result of the difference in mass distribution (caused by location of the compliant element) in the Mil-Lx. 373

Figure 7.37. Weighted Overall CORA scores comparing optimized Mil-Lx FE response to shifted FE human leg response for each of the parametric study conditions within the range of acceleration durations from 1.9 to 33.3 ms. Time shift of the forces was determined by aligning peak forces. Test conditions are again ordered from low to high frequency from left to right. 374

Figure 7.38. Peak plantar force (top) and plantar impulse at time of peak plantar force (bottom) are shown for the human and optimized Mil-Lx FE models for the conditions used for the human model parametric study. Note that input conditions are ordered from low to high frequency (left to right) and ED denotes the case where element deletion was turned on for the FE model. 376

Figure 7.39. Probability of injury calculated using the proposed injury risk function is shown for the optimized Mil-Lx and human FE models. For the human FE model, probability of injury was calculated using force and impulse measured at time of peak force for the case were element deletion was turned off, and for time of fracture and time of peak force for the case were element elimination was used. Note that input conditions are ordered from low to high frequency (left to right). 378

Figure 7.40. Comparison of human leg plantar force and impulse and modified Mil-Lx plantar force and impulse from finite element models. Heel pad and tibia compliant element materials were replaced with 70-durometer neoprene and 90-durometer rubber, respectively. 382

Figure 7.41. Summary of peak forces for the Mil-Lx model using 90 durometer polyurethane for the tibia compliant element and 70 durometer neoprene for the heel pad and the human FE model for footplate (FP), proximal tibia (PT), upper tibia (UT), and mid-tibia (MT) forces. 384

Figure 7.42. Weighted CORA scores for the comparison of the Mil-Lx model results using 90 durometer polyurethane for the tibia compliant element and 70 durometer neoprene for the heel pad and the human FE model results for footplate force (FPFZ), proximal tibia force (PTFZ), and footplate impulse (FP Impulse). 385

Figure 7.43. Injury probability calculated using the force-impulse injury risk function and the results of the modified Mil-Lx and human FE models. An asterisk denotes the sub-injurious conditions. 386

Figure 7.44.Comparison of experimental Mil-Lx and PMHS corridors to the finite element proximal tibia forces from the original, FE optimized, and discrete optimized Mil-Lx models for the Drop Tower A test condition. 388

Figure 7.45. Comparison of experimental Mil-Lx and PMHS corridors to the finite element footplate (plantar) forces from the original, FE optimized, and discrete optimized Mil-Lx models for the Drop Tower A test condition. 389

Figure 7.46. Free body diagram of the Mil-Lx leg showing forces (F) and moments (M) in the x-z plane for the plantar surface of the foot (plantar), upper tibia (UT), and lower tibia (LT). 391

Figure 7.47. Odyssey UBB-simulator test rig consisting of a hammer sled with two hammers which impact the seat and foot pans of the carriage sled separately. The mass of the hammer sled is decelerated by crushing a steel tube mounted to the tracks of a Via sled system. (Annals of biomedical engineering by BIOMEDICAL ENGINEERING SOCIETY Reproduced with permission of SPRINGER NEW YORK LLC in the format Thesis/Dissertation via Copyright Clearance Center.)[9] 392

Figure 7.48. Mil-Lx force and acceleration response to a sub-injurious (top) and injurious (bottom) footplate loading condition from tests performed by Bailey et al. using the Odyssey blast simulator. Time of noticeable ankle dorsiflexion is indicated in each plot. 394

Figure 7.49. Estimated location of the center of mass, center of pressure, and center of ankle rotation location for the Mil-Lx. 397

Figure 7.50. Free body diagrams for the foot and distal portion of the tibia below the lower tibia load cell. Note that θ represents the angle between the tibia shaft and the normal to the footplate. 400

Figure 7.51. Probability of injury calculated using the McKay and Bir injury criterion and the proposed force-impulse injury criterion for the original and modified Mil-Lx FE model. Input conditions with asterisks indicate that failure occurred in the human FE model.[136] 405

Figure 7.52. Difference between human mid-tibia force and the forces estimated using the original and modified Mil-Lx FE models. Human FE model response with element deletion (ED) is also reported. 407

Figure 7.53. Peak force and impulse at peak force for the original and modified Mil-Lx FE models and for the human leg FE model with and without element deletion (ED). Individual data points are shown each of the input conditions used for the human model parametric study. 409

Figure 7.54. Contour for 50% probability of injury for age 27 as defined by the proposed injury risk function. Injury data points (outlined in black) and no-injury data points (outlined in white) are plotted for the response of the human FE model with and without element deletion (ED) and for the original and modified Mil-Lx FE model. The second plot (bottom) provides the same data, but with additional contour lines. 410

Figure 10.1. Local coordinate system for the tibia, aligned with the SAE J211 coordinate system. 455

Figure 10.2. Mass-compensated footplate force for low impactor tests 467

Figure 10.3. Leg compression for low impactor tests calculated using footplate and proximal tibia accelerometers 467

Figure 10.4. Mass-compensated footplate force for medium impactor tests 468

Figure 10.5. Leg compression for medium impactor tests calculated using footplate and proximal tibia accelerometers 468

Figure 10.6. Proximal tibia force for high impactor tests 468

Figure 10.7. Leg compression for high impactor tests calculated using footplate and proximal tibia accelerometers 468

Figure 10.8. Mass-compensated proximal tibia force for Drop Tower A tests. 468

Figure 10.9. Leg compression for Drop Tower A tests calculated using footplate and proximal tibia accelerometers 468

Figure 10.10. Mass-compensated proximal tibia force for Drop Tower B tests. 469

Figure 10.11. Leg compression for Drop Tower B tests calculated using footplate and proximal tibia accelerometers. 469

Figure 10.12. Medium Impactor condition fracture timing plots with tibia and calcaneus acoustic data and calcaneus maximum principal strain plotted over footplate and proximal tibia forces. 471

Figure 10.13. High Impactor condition fracture timing plots with tibia and calcaneus acoustic data and calcaneus maximum principal strain plotted over footplate and proximal tibia forces. 473

Figure 10.14. Polyurethane rubber engineering stress versus strain for different durometers ranging from 20 to 90 durometer. (Data from polyurethane products). 484

Figure 10.15. Polyurethane rubber stress versus strain for strain rates ranging from quasi-static to 9000 s^{-1}. (Data from Yi et al.)[228] 484

Figure 10.16. Polyurethane rubber stress versus strain for strain rates ranging from quasi-static to 9000 s^{-1}. (Data from Yi et al.)[228] 485

Figure 10.17. Nitrile rubber stress versus strain for strain rates ranging from 0.067 to 383 s^{-1}. 486

Figure 10.18. Neoprene 60-durometer rubber compressive stress versus strain for strain rates ranging from 50 to 1000 s^{-1}. Reproduced from Zhao et al.[234] 486

Figure 10.19. Neoprene 65-durometer rubber compressive stress versus strain for strain rates ranging from 50 to 1000 s^{-1}. Reproduced from Zhao et al.[234] 487

Figure 10.20. Neoprene 70-durometer rubber compressive stress versus strain for strain rates ranging from 50 to 1000 s^{-1}. Reproduced from Zhao et al.[234] 487

List of Tables

Table 2.1. Summary of the motions of the foot controlled by muscles of the foot and leg. An X denotes that the listed muscle contributes to the indicated motion of the ankle joint. 49

Table 2.2. Summary of previous axial leg impact tests 60

Table 2.3. Previous injury risk functions for axial loading of the leg 78

Table 3.1. Test matrix for drop tower test conditions containing averages and standard deviations. Measurements were taken from an accelerometer on the impact plate of the test fixture. 104

Table 3.2. Test matrix for impactor test conditions containing averages and standard deviations. Measurements were taken from an accelerometer on the test fixture footplate. 106

Table 3.3. Summary of test conditions for drop tower and impactor tests 109

Table 3.4. Averages and standard deviations for test results 109

Table 3.5. Summary of Component PMHS Test Results 112

Table 4.1. Summary of material property changes made to the GHBMC leg model by Gabler et al. (2014)[76] 132

Table 4.2. Input conditions for sensitivity study simulations 142

Table 4.3. Summary of CORA scores for comparison of experimental characteristic averages and FE response to the average input footplate acceleration pulse for proximal tibia force. 145

Table 4.4. Summary of 50th and 95th percentile calcaneus cortical bone strains from the finite element model for maximum strain and strain at time of fracture in µS. 148

Table 4.5. Frequencies (Hz) associated with input sinusoidal acceleration pulses for finite element parametric study. 155

Table 5.1. Summary of previous estimates of leg and foot compliance from dynamic models of the human leg where k[kN-m^{-1}] and c[N-s-m^{-1}]. 177

Table 5.2. Optimized scale parameters for the SDOF LMM of the leg. 183

Table 5.3. Optimized scale parameters for the 2-DOF LMM of the leg. 187

Table 5.4. Average weighted overall CORA score (standard deviation) for the 28 parametric study conditions comparing the FE model response to the LMM response from the single degree of freedom (SDOF) and two degree of freedom (2DOF) models optimized using FE model responses. 189

Table 5.5. Optimized parameters for the 3-DOF LMM of the leg based on the response of the human leg FE model. 192

Table 5.6. Average weighted overall CORA score (standard deviation) for the 28 parametric study conditions comparing the FE model response to the LMM response from the single degree of freedom (2DOF) and two degree of freedom (3DOF) models optimized using FE model responses. 197

Table 5.7. Optimized parameter values for the three-mass leg model with wobbling mass. 202

Table 5.8. Summary of CORA scores for impactor experimental test PMHS response compared to lumped-mass model response for axial displacements (DZ) of masses (m_i), proximal tibia forces (PT FZ), and footplate forces (FP FZ). 203

Table 5.9. Summary of CORA scores for drop tower experimental PMHS tests and fixed- and free-boundary finite element model response compared to lumped-mass model response for axial displacements (DZ) of masses (m_i), proximal tibia forces (PT FZ), and footplate forces (FP FZ). 207

Table 5.10. Summary of damped natural frequencies calculated for each of the LMMs of the leg. 213

Table 6.1. Summary of PMHS axial loading tests with limited ankle xversion (249 tests). This data set will be referred to as the “larger data set.” 230

Table 6.2. Summary of PMHS axial loading tests to be included in the development of the leg injury criterion (137 tests). This data set will be referred to as the “combined data set.” 231

Table 6.3. Linear regression fit parameters for the injured data points for log(Plantar Force) and log(Plantar Force Duration). 241

Table 6.4. Logistic regression coefficients for the combined data set excluding tests with initial ankle flexion or xversion. Analysis was performed on the plantar force data. 243

Table 6.5. Results of the one-by-one exclusion analysis to determine which covariates should be included in the survival model. 252

Table 6.6. Estimated parameters for the survival model using plantar impulse at peak force as the main predictor and age as a covariate for data points with plantar force times to peak of less than 11 ms (n=92). 253

Table 6.7. Comparison of impulse 95% confidence intervals (N-s) for 10-, 50-, and 90-percent probability of injury for different ages. 254

Table 6.8. Results of the one-by-one exclusion analysis to determine which covariates should be included in the survival model. 256

Table 6.9. Estimated parameters for the survival model using peak plantar force as the main predictor and age as a covariate for data points with plantar force times to peak of more than 11 ms (n=50). 256

Table 6.10. Comparison of plantar force at 10-, 50-, and 90-percent probability of injury for different ages. 257

Table 6.11. Estimated parameters for the piecewise injury risk function using Eqn. 6.3 and Eqn. 6.4. 259

Table 6.12. Summary of statistical measures for assessing the predictive capabilities of the proposed injury model compared to three existing injury probability models.[70,230,231] The best score for each measure is highlighted in bolded green type. 263

Table 6.13. Assessment of injury risk functions for 50% risk of injury using the Funk 2002 and Yoganandan 1996 data sets.[70,230,231] 264

Table 6.14. Fit parameters for Eqn. 6.21 where P_{FI} is the compression of the foot (Δz) predicted by the lumped-mass model pictured in Figure 6.28. Weibull survival model parameters are also provided with and without age included as a covariate. 273

Table 6.15. Velocity ($m\text{-}s^{-1}$) associated with high frequency input sinusoidal acceleration pulses for finite element parametric study. 277

Table 6.16. . Fit parameters for Eqn. 6.21 where P_{FI} is the compression of the foot (Δz) predicted by the finite element model of the leg measured from distal tibia to plantar surface of the foot. Weibull survival model parameters are also provided with and without age included as a covariate. 279

Table 6.17. Fit parameters for Eqn. 6.21 where P_{FI} is the 95th percentile peak strain (μS) in the cortical bone of the calcaneus predicted by the finite element model of the leg. Weibull survival model parameters are also provided with and without age included as a covariate. 284

Table 6.18. Discrete variable matrix for choosing A and B parameters for Eqn. 6.21. 287

Table 6.19. Model fit parameters and model fit statistics based on the PMHS injury data are provided for both optimization approaches for with and without the use of age as a covariate. Comparison is also provided for the use of impulse at peak force versus maximum impulse. 291

Table 6.20. Summary of test statistics and fit parameters associated with survival models for each of the previously-outlined approaches to injury criterion development. The best score for each statistic is bolded for easy reference. 300

Table 6.21. Estimated parameters for the survival model using mass-scaled plantar force as the main predictor and age as a covariate. 303

Table 6.22. Comparison of the performance of previous injury risk functions to the plantar force-based injury risk function and the proposed force and impulse-based injury criterion. 305

Table 6.23. Assessment of injury risk functions for 50% risk of injury using the Funk 2002 and Yoganandan 2015 data sets.[70,230,231] 306

Table 6.24. Summary of the cross-validation models and statistics comparing the cross-validation and proposed injury risk functions 307

Table 7.1. Mil-Lx Drop Tower Test Matrix 327

Table 7.2. Optimized parameter values for a LMM representing the Mil-Lx based on a fit of the force response of the human FE model for each of the input conditions used in the FE parametric study. 342

Table 7.3. Parameters for a LMM representing the Mil-Lx based on a fit of the high frequency (97.6-390 Hz) force response of the human FE model. 344

Table 7.4. Optimized parameter values for a LMM representing the Mil-Lx based on a fit of the low frequency (5.0-97.6 Hz) force response of the human FE model. 346

Table 7.5. Parameter values for a LMM representing the Mil-Lx optimized to fit the force response of the human FE model and weighted toward matching the footplate force response for all 28 inputs. 348

Table 7.6. Specifications for the spherical ankle joint including stiffness, damping, and stop angle. 351

Table 7.7. Mil-Lx FE model part masses compared to actual part masses 354

Table 7.8. Material parameters for the rubber materials in the Mil-Lx used in the Newell et al. Mil-Lx FE model developed by Newell et al.[148] 355

Table 7.9. Material parameters for the rubber materials used in the LS-Dyna Mil-Lx FE model using *Mat_Ogden_Rubber. 356

Table 7.10. Summary of average CORA scores for comparison of FE and experimental Mil-Lx forces and displacements. 360

Table 7.11. Description of the sinusoidal input pulses used to optimize the FE Mil-Lx model. 368

Table 7.12. Summary of *Mat_Viscoelastic material parameters and the ranges used for the FE optimization. 369

Table 7.13. Summary of *Mat_Viscoelastic optimized material parameters. 369

Table 7.14. Summary of FE materials used for discrete optimization of Mil-Lx biofidelity 381

Table 10.1. Summary of Impactor Test Injuries 457

Table 10.2. Summary of materials considered as candidates for replacing components in the Mil-Lx. 483

Summary of Contributions

Chapter 2—Experimental testing for the drop tower study was performed by Jake Christopher, Ann Bailey, and Dr. Robert Salzar. The drop tower tests were funded by U.S. Department of Defense contract number W81XWH-11-2-0086. The impactor study experimentation was performed by Brandon Perry, Dani Rapela, and Ann Bailey. The test matrix and instrumentation was designed by Ann Bailey, and Brandon Perry and Dr. Robert Salzar used an original design by Acen Jordan to design the impact test fixture. All analysis was done by Ann Bailey.

Chapter 3—Modifications to the human leg finite element model were made by Dr. Matthew Panzer, with additional modifications to the heel pad material properties made by Lee Gabler. Comparison and primary comparison of drop tower and modified finite element model results was performed by Lee Gabler and Dr. Matthew Panzer. Additional analysis and comparison of the finite element model to additional experimental data was performed by Ann Bailey. All other analysis in the chapter was performed by Ann Bailey.

Chapter 4—Optimization and model design was performed by Ann Bailey using Matlab code modified from an original code written by Dr. Taewung Kim. All analysis was performed by Ann Bailey.

Chapter 5—The injury risk function was developed by Ann Bailey in collaboration with Dr. Jeff Crandall, Dr. Timothy McMurry, Dr. Robert Salzar, and Lee Gabler. The form of the force-impulse injury predictor equation was developed by Lee Gabler for use with head velocity and acceleration and adapted by Ann Bailey under the advisement of Dr. Jeff Crandall. The reprocessing and collection of data from the literature as well as the analysis was performed by Ann Bailey.

Chapter 6—Translation of the Mil-Lx model from NASTRAN to LS-Dyna and subsequent mesh and part modifications were performed by Ann Bailey. The NASTRAN model and material testing was performed by Dr. Nicolas Newell from Imperial College London. Experimental testing, literature review, Matlab coding, modeling, and analysis were performed by Ann Bailey.

2 Introduction

The use of improvised explosive devices (IEDs) in recent military conflicts has led to a number of severe injuries from underbody blast (UBB) of military vehicles, with 26 percent of warfighters wounded in these events suffering foot and ankle injuries and another 18 percent sustaining tibia or fibula fractures.[3] While many lower extremity injuries are not life-threatening, these injuries pose problems for post-explosion evacuation in the case of UBB. In addition, lower extremity injuries have a high likelihood of long-term impairment, societal cost, and disability.[50,144,152] MacKinzie et al. estimated that a severe lower extremity injury can cost over $110,000 in associated medical costs.[128] Other research has shown that these injuries can cause ambulation issues, inability to drive, and inability to return to work even a year post-injury.[153] Understanding the injury mechanisms and injury thresholds for the leg in UBB events is a critical step toward improving future military vehicle design and protecting the warfighter.

Lower extremity injuries are also prominent in frontal collisions according to a study by the University of Virginia utilizing the National Automotive Sampling System (NASS) injury database.[1] These events will be referred to as automotive intrusion (AI) and can involve axial loading of the leg, but on a longer time scale than UBB. Lower extremity injuries in these events accounted for 44.6 percent of frontal collision injuries for properly-belted, non-ejected front seat occupants above the age of 16 from the years 1998-2010.[58] Many of the types of lower extremity injuries sustained in UBB are also sustained in frontal collisions, with a majority of the injuries (AIS2+) occurring in the ankle/foot (46.8%), and fewer occurring in the tibia/fibula shaft (9.2%).[58]

Despite having similar injury patterns, frontal collisions and underbody blast events are currently analyzed using separate injury criteria and different anthropomorphic test device (ATD) legs. For AI events, the Hybrid-III ATD leg has been primarily used to predict the response of the human leg, though the Thor-Lx is slowly being adopted in its place. Previous research has shown that the stiff nature of the Hybrid-III yields peak tibia forces of over twice those measured in the human tibia for higher loading rates.[114,135] Kuppa et al. established that for foot pan acceleration frequencies greater than 6.4 Hz, the Hybrid-III tibia force exceeds human tibia force, and can be as low as 77 percent of the human tibia force for frequencies as low as 2.5 Hz. Considering the high-frequency nature of UBB events, the Hybrid-III leg is incapable of providing an accurate estimate of human leg response for these events. Despite this fact, the Hybrid-III is the most widely-used ATD for the study of UBB within U.S. Military research groups.[151] The Mil-Lx ATD leg, though less common than the Hybrid-III, is also used by NATO groups to study UBB. The biofidelity of this leg, specifically designed for the study of UBB and tuned to match a 7 $m\text{-}s^{-1}$ impact, has not been sufficiently evaluated for the lower loading rates associated with automotive intrusion.[135] The fact that the Mil-Lx has only been validated for a narrow range of loading conditions suggests that the results it produces for cases where personal protective equipment (PPE) or floor mats are present may be untrustworthy, since these may alter the loading rate applied to the foot.

Injury criteria used for AI and UBB loading environments are also different. An injury risk function developed by McKay and Bir based on mid-tibia force is used to predict leg injury for underbody blast events using the Mil-Lx.[135] This injury risk function predicts a 10% risk of Foot and Ankle Severity Score greater than four (AFIS 4+) for a Mil-Lx upper tibia force of 2.6 kN.[135,151] Several injury risk functions exist for the automotive environment. One injury risk function developed by Yoganandan et al. which combined data from multiple PMHS test series, associates a 10% risk of an Abbreviated Injury Scale score greater than two (AIS 2+) with a Hybrid-III tibia force of 5.4 kN.[231] Though each of these injury criteria are tied to a specific ATD, it is unclear whether the validity of the injury criteria extends beyond the biofidelity range of the ATD to which it is tied.

The importance of understanding the leg's response to the overlap of automotive intrusion and underbody blast environments is imperative to the accuracy of leg injury prediction. While the current separation may suffice for events that fall purely within one loading environment or the other, when injury mitigation schemes such as floor mats or personal protective equipment (PPE) interfere with the loading event, the validity of each of the separate injury criteria or ATDs may be compromised. Using an ATD leg for a condition for which its biofidelity has not been assessed may lead to inaccuracies in injury prediction, which in turn lead to ineffectiveness of vehicle safety design. The same is true for using an injury criterion for a loading environment for which it has not been validated, though in many cases the limitations of the applicability of existing leg injury criteria are not discussed or are ignored.

The current segregation between automotive and military leg biomechanics research inhibits the ability to understand how response and injury changes over a continuum of loading conditions. Development of an injury criterion for axial impact loading of the leg which can bridge the gap between AI and UBB load rates could greatly improve the ability to design safety measures for both automotive and military vehicles. Further, the development of an ATD leg which can provide a biofidelic response across a wider range of loading conditions would reduce the need to choose between the use of an automotive or military

ATD for applications involving the use of PPE or energy mitigating floor materials. The following sections provide a review of leg injury literature and summarize the contributions and shortcomings of previous military and automotive research efforts in order to highlight the areas where additional attention should be focused.

2.1 Anatomy of the Leg

2.1.1 Bones

The human foot and leg are composed of 28 bones including the long bones that make up the leg (tibia and fibula) and the bones of the foot and ankle. The foot can be divided into three regions: the hindfoot, midfoot, and forefoot.[90] The forefoot contains the metatarsals, phalanges, and two sesamoid bones which are located inferior to the first metatarsal. The midfoot consists of five bones: the navicular; cuboid; and three cuneiforms. The hindfoot, which bears most of the load from the body while standing, is made up of the calcaneus and talus. The talocrural (also known as tibiotalar) joint connects the long bones of the leg to the foot, while the subtalar or talo-calcaneus joint links the calcaneus (heel bone) to the talus. The bones of the hindfoot and the two long bones are of particular focus to this dissertation because of their load-bearing nature.

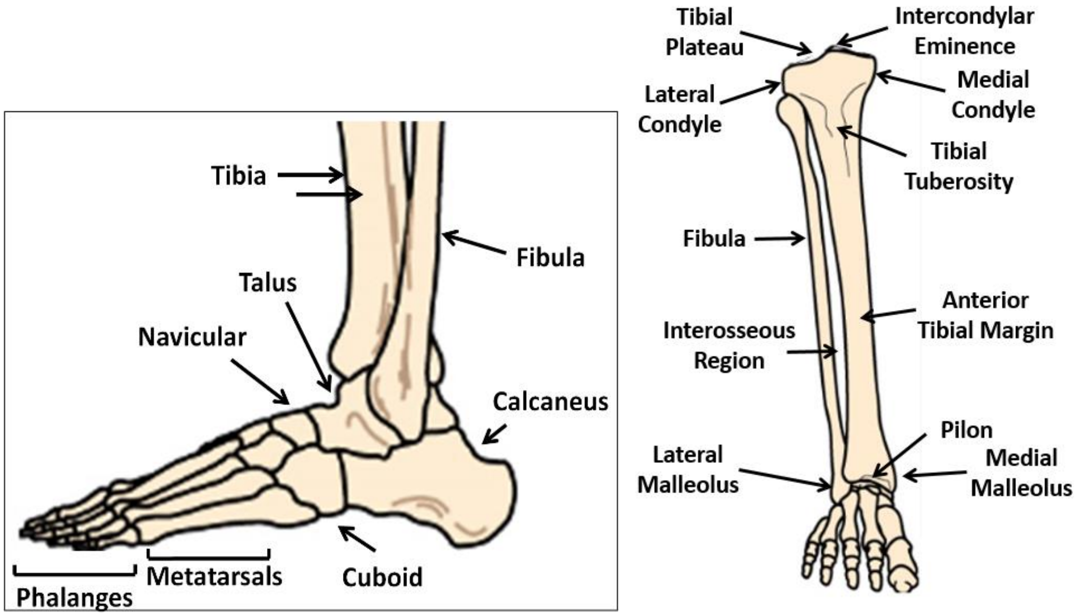
Tibia
Fibula
Talus
Navicular
Calcaneus
Phalanges
Metatarsals
Cuboid
Tibial Plateau
Intercondylar Eminence
Lateral Condyle
Medial Condyle
Tibial Tuberosity
Fibula
Anterior Tibial Margin
Interosseous Region
Pilon
Lateral Malleolus
Medial Malleolus

Figure 2.1. Bones and anatomical regions of the foot and leg

The malleoli are extensions of the inferior tibia and fibula and make up part of the colloquial "ankle." The medial malleolus is an extension of the distal tibia, and articulates with the talus. The lateral malleolus extends distally from the inferior tibiofibular joint comprised of the anterior and posterior ligaments of the lateral malleolus and the interosseous membrane of the leg.[90] The articular surface of the distal tibia in the tibiotalar joint is known as the plafond or pilon, and is a weight-bearing surface for the tibia.

Specific anatomical regions of the foot and leg which are mentioned later in the dissertation are depicted in Figure 2.1 as well. The anterior tibia margin refers to the ridge that runs along the length of the anterior aspect of the tibia shaft. The tibial tuberosity is also located on the anterior portion of the tibia and is the location of the patellar ligament attachment. The tibial plateau refers to the superior portion of the tibia which articulates with the femur, while the intercondylar eminence separates the medial and lateral condyles of the tibia. The pilon is the distal portion of the tibia, which articulates with the talus.

2.1.2 Ankle Motion

The ankle joint is free to rotate about three axes. As shown in Figure 2.2, rotation about the positive and negative x-axis is referred to as inversion and eversion, respectively. The term xversion is often used to describe the general rotation about the x-axis in either direction. Internal and external rotations refer to rotation about the axis running parallel with the tibia. Rotating the toes medially is designated as internal rotation, while moving the toes laterally is external rotation. Dorsiflexion and plantar flexion refer to y-axis rotation, where decreasing the angle between the dorsal surface of the foot and the tibia is dorsiflexion.

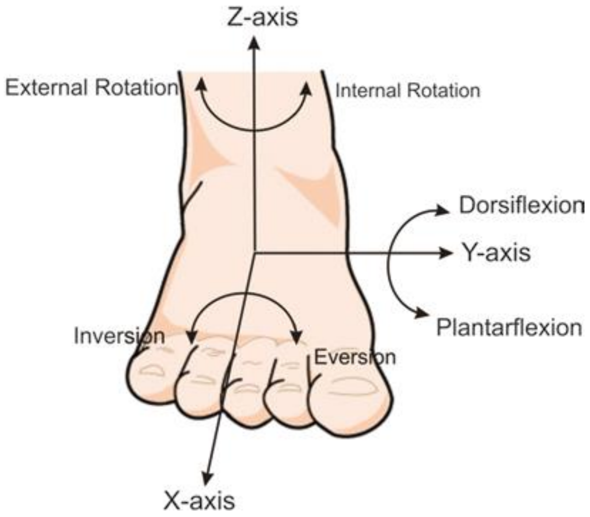

Figure 2.2. Ankle joint motion. Note that the coordinate system aligns with the SAE J211 coordinate system[100] with the exception of the polarity of the y- and z-axes. (Accidental Injury by Springer New York. Reproduced with permission of Springer New York in the format Thesis/Dissertation via Copyright Clearance Center.)[189]

Though the image in Figure 2.2 implies orthogonality between the rotation axes, a study by Inman et al. concluded that ankle motion does not strictly occur in one plane, but combines rotation about multiple axes.[98,99] Various studies have investigated the relative displacements of bones in the ankle joint as a result of ankle motion and its effect on talocrural joint contact area.[34,46,69,107,117,164] A study by Siegler et al. quantified the contribution of the talocrural and subtalar joints to the overall rotation of the ankle along different axes. This study showed that the subtalar joint contributes most during xversion and the talocrural joint contributes most during flexion. Internal and external rotation involved equal contributions from the two joints.[195]

Ankle range of motion has been quantified using both cadaveric and volunteer testing.[29,99,126,223] Using human volunteer testing, Lindsjo et al. found the range of ankle flexion to be greater when the ankle is weight-bearing; the maximum amount of dorsiflexion was found to be 32.5±6.9 degrees and 44.7±7.6 degrees for plantar flexion.[126] Inversion and eversion maximum angles were found to be around 50 degrees.[126]

2.1.3 Muscles, Tendons, and Ligaments

Muscles of interest for this dissertation include the gastrocnemius and soleus. Both muscles are located posterior to the tibia and fibula and insert into the posterior calcaneus via the Achilles tendon. Contraction of these muscles increases the plantar flexion of the ankle. The flexor hallucis longus and the flexor digitorum longus perform the function of plantar-flexing the ankle. These muscles originate on the fibula and tibia and insert into the inferior surface of the distal phalanx and phalanges, respectively.[90] Additional muscles including the fibularis tertius and tibialis anterior also contribute to dorsiflexion of the foot. Eversion of the foot is controlled by the fibularis longus, fibularis brevis and fibularis tertius.

Inversion of the foot is controlled by the tibialis posterior, flexor hallucis longus, flexor digitorum longus, and tibialis anterior. A summary of the motions controlled by different muscles of the foot and leg is provided in Table 2.1. Figure 2.3 provides a diagram of the leg with muscles identified.

Table 2.1. Summary of the motions of the foot controlled by muscles of the foot and leg. An X denotes that the listed muscle contributes to the indicated motion of the ankle joint.

Muscle	**Eversion**	**Inversion**	**Plantar Flexion**	**Dorsiflexion**
Gastrocnemius			X	
Plantaris			X	
Soleus			X	
Flexor hallucis longus		X	X	
Flexor digitorum longus		X	X	
Tibialis posterior		X	X	
Fibularis longus	X		X	
Fibularis brevis	X		X	
Tibialis anterior		X		X
Extensor halluces longus				X
Extensor digitorum longus				X
Fibularis tertius	X			X

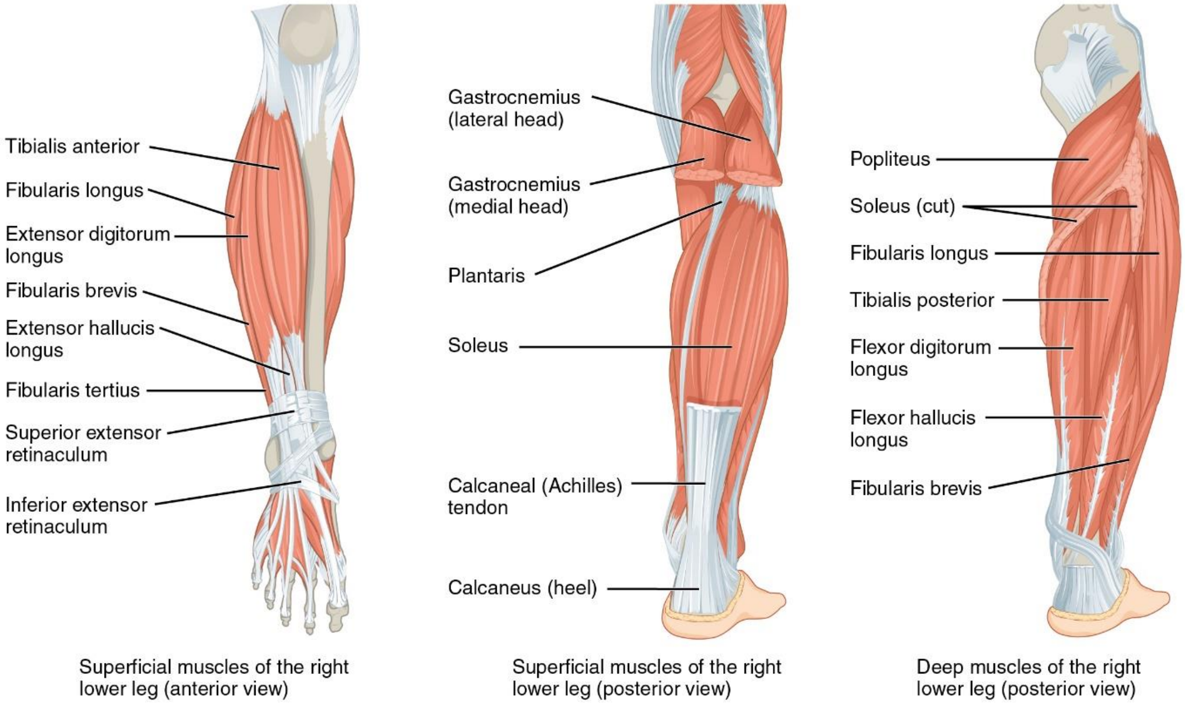
Tibialis anterior
Fibularis longus
Extensor digitorum longus
Fibularis brevis
Extensor hallucis longus
Fibularis tertius
Superior extensor retinaculum
Inferior extensor retinaculum
Superficial muscles of the right lower leg (anterior view)
Gastrocnemius (lateral head)
Gastrocnemius (medial head)
Plantaris
Soleus
Calcaneal (Achilles) tendon
Calcaneus (heel)
Superficial muscles of the right lower leg (posterior view)
Popliteus
Soleus (cut)
Fibularis longus
Tibialis posterior
Flexor digitorum longus
Flexor hallucis longus
Fibularis brevis
Deep muscles of the right lower leg (posterior view)

Figure 2.3. Diagram of the muscles of the foot and leg, showing an anterior view (left) and superficial and deep posterior views (middle and right, respectively). (Image courtesy of Creative Commons)

Ligaments are fibrous tissue that that join bones and cartilage. Ligaments of the ankle include the deltoid and calcaneonavicular ligaments on the medial side of the ankle, while the lateral side includes the lateral talocalcaneal, posterior talofibular, calcaneal fibular, anterior talofibular, and five inferior talofibular ligaments. [90] Tendons are also fibrous structures, but instead they connect muscles to bones. Tendons of the foot and ankle are largely named for the muscles to which they attach, though exceptions exist. The Achilles tendon attaches the posterior aspect of the calcaneus to the soleus, gastrocnemius, and plantaris muscles.[90] This tendons is important to note because of its use in biomechanics experiments to simulate the muscle tension involved during driver braking.[73,108]

2.2 Loading Environment and Leg Injury

2.2.1 Automotive Intrusion

Automotive intrusion (AI) refers to the resulting floor pan deformation generally caused by a frontal collision. Of the different types of automobile crashes, frontal collisions are responsible for a majority of lower limb injuries.[56] Contact with the floor pan, pedals, knee bolster, or steering wheel deliver loads to the leg, foot, and ankle in these events.[144] Lower limb injury has been shown to occur with and without floor pan intrusion in these events.

These events have been shown to involve 40-250 g of longitudinal floor pan acceleration with durations of 10-50 ms.[54,70] Relative velocities are typically less than 5 $m\text{-}s^{-1}$, and floor pan displacement can exceed 350 mm.[55] Kuppa et al. examined crash test pulses from frontal intrusion events and measured up to 27 cm of brake pedal motion relative to the vehicle (Figure 2.4).[115] While these events have the potential to produce large deformations in the foot pan, a study by Crandall et al. estimated that 90 percent of frontal collisions result in less than 3 cm of intrusion, but accounted for 61 percent of the lower limb injuries in the data set.[55]

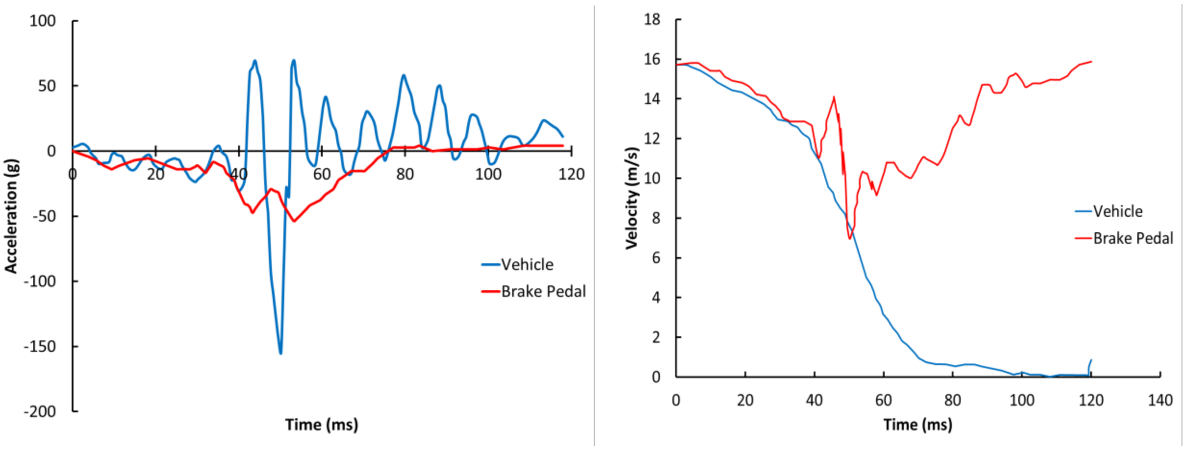

Figure 2.4. Example brake pedal pulses from frontal collision events. Acceleration and velocity plots are provided for the acceleration measured for the brake pedal and vehicle during a frontal collision. Figures were produced based on data from Kuppa et al.[115]

A report from the National Highway Traffic and Safety Administration summarized lower leg injuries from automotive intrusion events from frontal crashes from the NASS-CDS 1997-2009 database and attributed 68 percent of MAIS2+ injuries to loading from the floor pan, while brake pedal loading accounted for another 25.2 percent.[8] A more recent case study by Ye et al. concluded that despite efforts to reduce toe pan intrusion in automobiles, axial loading continues to be the leading cause of lower extremity injuries in frontal collisions, accounting for 43 percent of foot and ankle injuries. This finding is in agreement with a previous study by Dischinger et al. in 2005.[61,227] Ye et al. also reported the distribution of fractures in in the leg for the frontal collision case study, which showed that hindfoot fractures were the most prevalent, accounting for 48 percent of foot and leg fractures (Figure 2.5).

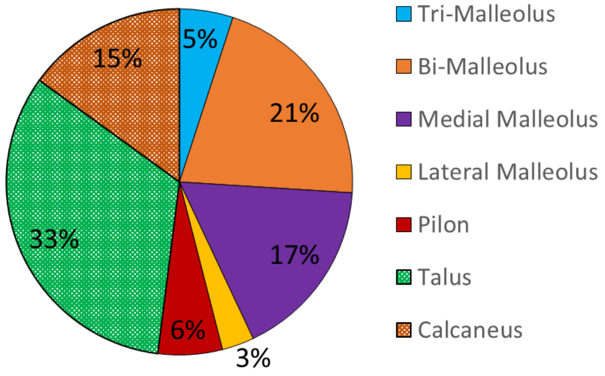

Figure 2.5. Distribution of foot and leg fractures produced from data compiled by Ye et al. for frontal collision events. Note that the pattern-filled area distinguishes the hindfoot fractures from the rest.[227]

2.2.2 Military Underbody Blast

Underbody blast (UBB) occurs when an explosive device detonates beneath a vehicle. These events are assumed to deliver a vertical load to the vehicle and subsequent vertical loading to the occupants through the floor and seat of the vehicle. The loading environment associated with UBB includes a vast array of loading rates due to differences in vehicle type, charge type, and charge size. The loads experienced by the occupant can be affected by the mass of the vehicle, structure of the vehicle, presence of floor mats or seat padding, and whether breach of the vehicle occurs. Contact with other structures within the passenger compartment may also affect the likelihood and type of injury.

Underbody blast events can be characterized as high energy events in which accelerations are high and durations are short.[177] Though much of the work performed to summarize the loading environment of UBB for U.S. military vehicles is classified, some studies have attempted to define the environment in terms of velocity and time-to-peak.[111]

Wang et al. defined the UBB environment as including floor accelerations in excess of 100 g over time spans of 3-100 ms, while others reported floor velocities of 7-30 m-s^{-1} with times to peak of less than 10 ms.[177,219] Controlled live-fire testing performed by the U.S. Army Tank Automotive Research Development and Engineering Center (TARDEC) produced floor and seat accelerations like those pictured in Figure 2.6. These pulses show that the local effects of floor deformation amount to about 30 mm of displacement for the floor pan and 75 mm for the seat. According to a North Atlantic Treaty Organization report, peak forces in the lower extremities occur around 15-25 ms after detonation, which represents the “local effects” of UBB such as floor deformation, rather than the “global” vertical translation of the vehicle.[236]

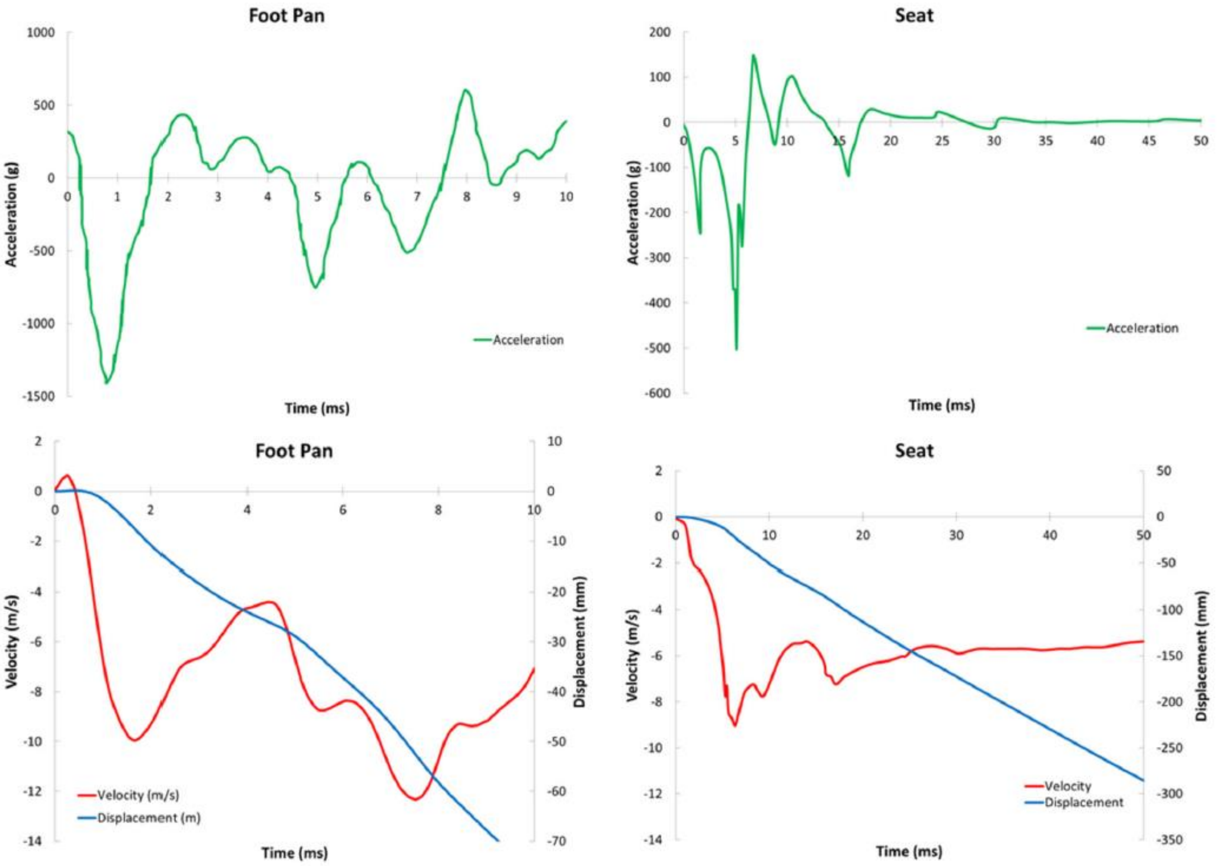

Figure 2.6. Example UBB loading conditions for the seat and floor pan from live fire testing. Acceleration and velocity traces are provided for live-fire simulated UBB events. (Annals of biomedical engineering by BIOMEDICAL ENGINEERING SOCIETY Reproduced with permission of SPRINGER NEW YORK LLC in the format Thesis/Dissertation via Copyright Clearance Center.).[9,26,190]

Though blast injury has been a focus of military injuries for centuries, UBB has only recently become a prominent research topic in biomechanics in the past twenty years due to changes in modern warfare tactics.[47,177] Improvements to military vehicle design have led to the survivability of these events such that the emphasis lies on the prevention of injury rather than survivability. Underbody blast is primarily associated with tertiary blast, which typically involves blunt or crushing loads due to objects propelled by the blast wave or structural damage to building or vehicles, though secondary blast is sometimes associated with UBB. Secondary blast is likely to occur in the case where the passenger compartment of the vehicle is breached by the blast, and shrapnel and other debris cause penetrating injuries.[41] Few injuries due to primary blast are observed in UBB events since the blast wave encounters the structure of the vehicle first.

A summary of injuries from underbody blast loading was presented by Alvarez in 2011. This briefing described lower extremity injuries including calcaneus, talus, metatarsal, and navicular fractures and even partial and full amputations of the foot and leg in more severe cases.[3] When summarizing the injuries from soldiers wounded in UBB events, 26 percent sustained foot/ankle injury, while 18 percent sustained tibia/fibula injury (Figure 2.7). A more detailed look at lower extremity injuries revealed that the calcaneus was the most commonly injured bone in the foot, accounting for 36 percent of fractures (Figure 2.8). Fracture of the metatarsals and talus were the next most common injuries, though the percentage associated with metatarsal injury may be artificially inflated due to the number of bones (and possible codes) associated with the metatarsals. In total, 45 percent of lower extremity fractures occurred in either the calcaneus, talus, or distal tibia, whereas only 18 percent were malleoli fractures, which are associated with non-axial loading vectors and ankle rotations. Only two percent of lower extremity fractures were tibia plateau fractures.[4]

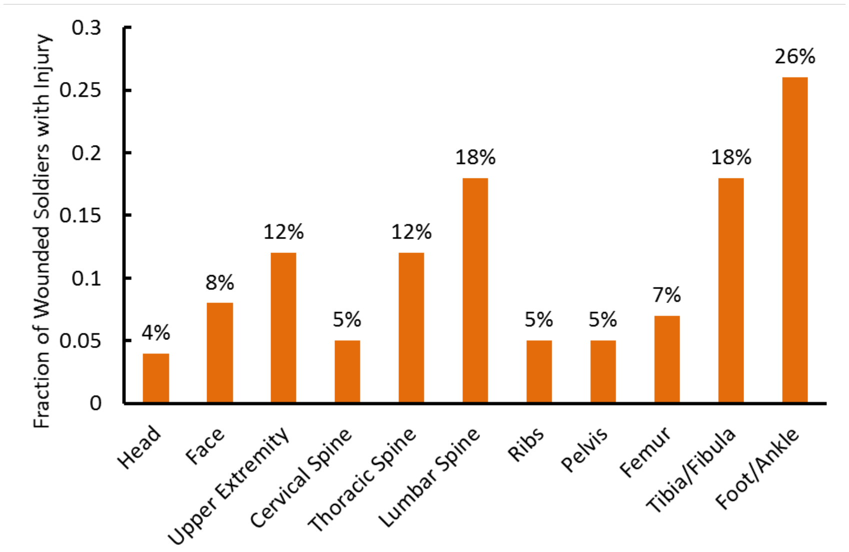

Figure 2.7. Distribution of injuries for warfighters wounded in UBB events. Percentages are based on the percentage of 456 wounded soldiers with a particular injury.[3]

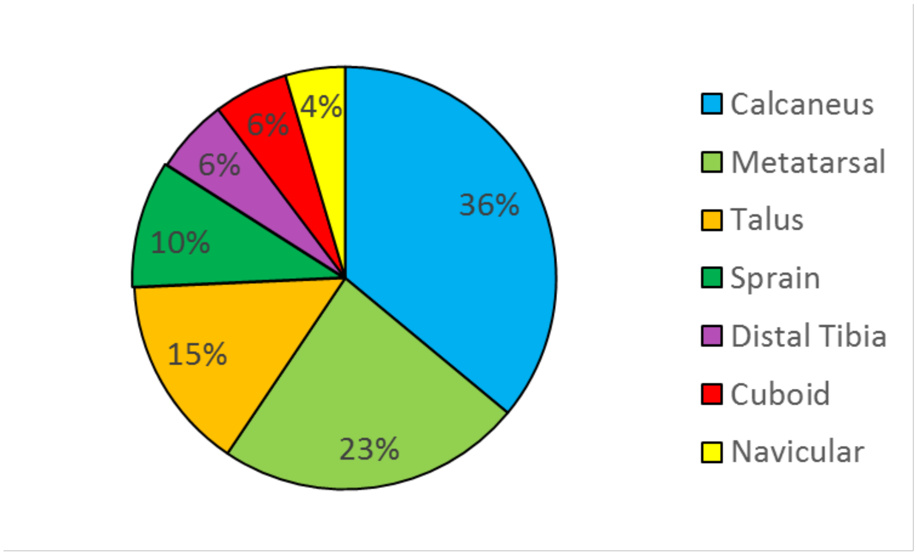

Figure 2.8. Distribution of foot/ankle injuries for warfighters wounded in UBB events. The figure shows percentages calculated based on total number of foot/ankle injuries reported from a study including 456 wounded soldiers.[3]

Ramasamy et al. performed an in-depth analysis of the injuries from recent conflicts in the Middle East from 2006-2008, which showed a concentration of lower extremity fractures for events involving UBB compared to other causes of injury. Of the 63 casualties included in the study, 89 percent of the cases resulted in severe lower extremity injuries. Thirty-five percent of casualties sustained only lower extremity injuries. Though the distribution of injuries reported in this study are slightly different from the distribution presented by Alvarez et al., in that a greater percentage of casualties sustained head/neck and femur injuries in the Ramasamy study, the prevalence of lower extremity injury is consistent.[4,178]

In addition to the long-term effects associated with automotive intrusion lower extremity injuries, the warfighter is faced with more immediate risk factors related to these injuries. Without the convenience of being rushed to the nearest hospital following an automobile crash, the threat of further danger remains a concern because of the decreased mobility caused by these injuries. The ability to move to a safer location without aid is valuable when faced with the hazards of an active warzone. Moreover, the risk of infection is elevated for UBB. A study by Ramasamy et al. reported 38 percent of calcaneus fractures caused by UBB resulted in wound infection, whereas the rate of post-operation wound infection for the general population following calcaneus fracture is less than 27 percent.[175,233]

The types of injuries to the lower extremities from UBB are similar to those associated with historical “deck slap” scenarios which occurred aboard ships subjected to underwater explosions.[176] Injuries from these events involved fractures of the calcaneus and distal tibia characteristic of loading through the plantar surface of the foot.[28,48] A clinical study by Barr et al. which summarized deck slap injuries from World War II revealed that 36 percent of those included in the study sustained foot/ankle fractures which included calcaneus, talus, and distal tibia fractures, while 25 percent sustained fractures located at the knee.[19] Balazs et al. attributes the similarity of these injuries to the vertical loading vector common to both "deck slap" and UBB events as a result of floor pan buckling.[16]

2.3 Injury Mechanisms

2.3.1 Axial Loading

The fractures that commonly result from UBB and AI are primarily associated with axial loading. This loading is a result of floor intrusion in both AI and UBB events and can involve inertial loading, entrapment, excessive motion of the joints, subsequent contact with other structures within the occupant compartment, and contributions from internal muscle forces.[54,71,73] Though the loading of the lower extremities in UBB and AI events is assumed to be primarily axial, other factors specific to individual events may introduce alterative load vectors, which in turn can lead to alternative injury mechanisms.

Calcaneus, talus, and distal tibia (pilon) fractures are commonly associated with axial loading of the foot and ankle.[71] Comminution and associated fractures of the talus, distal tibia, proximal tibia and malleoli are more common in specimens with low bone mineral density,[73] and the calcaneus is less likely to be fractured when axial loading is combined with shear loading and ankle rotation since this type of loading predisposes the leg to malleolar fractures.[71] Funk et al. also concluded that distal tibia fractures occur more frequently while calcaneus and malleolar fractures occur less frequently when the axial loading is applied to a dorsiflexed ankle.[71]

Forces applied to the calcaneus via the Achilles tendon, which causes dorsiflexion of the ankle, may also contribute to the pattern of injury. Funk et al. hypothesized that Achilles tension can increase the axial force in the tibia without affecting the compressive force on the calcaneus and talus which are more common in axial loading events. This leads to an increased likelihood of tibial pilon fractures relative to the case where Achilles tension is not applied.[73]

Various studies have been performed to characterize the tolerance of the leg in axial loading. Table 2.2 provides a summary of previous PMHS studies which applied axial loading to the leg, showing the range of input conditions, boundary conditions, and resulting forces reported by each study. As noted in the table, forces were measured at different locations on the foot/leg, which makes comparing data sets difficult.

Table 2.2. Summary of previous axial leg impact tests

Study	**Boundary Condition**	**Hammer Mass (kg)**	**Plate Velocity (m/s)**	**Max Energy (J)**	**Max Force (kN)**	**Plate Acceleration (g)**
Roberts 1993[181]	Knee fixed[+]	NR	4.1-7.5	NR	2.4-16.0[F]	65-99
Schueler 1995[191]	Whole body	38	12.5	860-3000	16.0 [F]	40-210
Begeman 1996[25]	Potted mid-tibia	16	NR	NR	4.0-8.7 [P]	NR
Crandall 1996[53]	Seated position[+]	15.5	6.5	330	0.8-3.7[M]	NR
Yoganandan 1996[231]	Ballasted to 16.8kg	25	7.6	37-580	4.3-11.4 [F,P]	20-100
Klopp 1997[109]	Potted femur[+]	15.5	1.4-5.5	15-220	1.6-10.8 [F,M]	20-290
Kitagawa 1998[108]	Fixed prox. tibia	18	3.99	50-140	7.0-9.0 [F,M]	NR
Manning 1998[130]	Fixed prox. tibia[+]	1.25	2.0-6.0	3.5-23	1.8-3.1[M]	120-210
McMaster 2000[138]	Fixed prox. Tibia[+]	NR	NR	NR	2.7-10.7[M,P]	NR
Funk 2000[75]	Potted femur[+]	33	4.3-9.5	300-1500	4.4-10.9[F,M]	300-970
Funk 2002[73]	Knee fixed	13.6-29.4	1.4-8.4	240-830	1.7-10.8 [F,M,P]	42-370
Bass 2004[20]	Free end	N/A	NR	NR	>8.6 [M]	25-200
McKay 2009[135]	Potted femur	36.7	7.2-11.8	940-2500	4.0-6.0 [M]	NR
Quenneville 2009[171]	Free end*	3.9	13.9	110	15.0 [P]	NR
Newell 2012[147]	Potted femur	42	9.0	1700	n/a	NR
Henderson 2013[94]	Prox. tibia potted	38.5, 61.2	4.4-7.2	320-1600	2.6-10.9 [P]	180-790
Gallenberger 2013[82]	Ballasted to 16.8kg[+]	3.3-12.3	2.0-9.1	6.7-240	1.4-8.1 [P]	NR

[F] Force measured at footplate

[M] Force measured at mid-tibia

[P] Force measured at proximal tibia

* Tibia only

[+]Includes dorsi/plantar flexion tests

NR=not reported

A study by Roberts et al. (1993) focused on the differences between static and dynamic axial loading tolerances of the human foot and ankle. This study utilized 12 pairs of PMHS limbs, with one limb from each pair tested in each of the two loading conditions: static or dynamic. Each limb was sectioned at mid-femur, and placed in the test fixture such that the leg was flexed and the anterior part of the distal thigh was placed against a fixed boundary. The plantar surface of the foot was placed against the footplate with an ankle dorsiflexion of 20 degrees. Quasi-static compression loads were applied until the force dropped to 50% of the peak force, indicating failure; dynamic tests were performed under constant velocity conditions ranging from 3.2-3.6 m-s^{-1}. Forces measured at the footplate indicated significantly higher force tolerances under dynamic loads compared to static loads. Injuries included calcaneus, talus, and tibia fractures, with most calcaneus and talus fractures occurring under static loads, and a majority of the static loads causing malleolar fractures indicative of the occurrence of ankle rotation.[181]

Schueler et al. (1995) performed another study aimed at estimating the tolerance of the leg, foot, and ankle, with a focus on injuries caused by frontal collisions. For this test series, 24 impact tests were performed using 12 whole body PMHS. Specimens were seated such that the legs were suspended parallel to a pendulum impactor, which impacted the plantar surface of the foot. Heel and forefoot forces were measured using load cells incorporated into a special shoe. Impact velocities ranged from 6.7-12.5 m-s^{-1}, and injuries resulting from the study included 10 calcaneus fractures, two talus fractures, and one knee joint fracture. Hybrid-III tests were performed under the same loading conditions, and the major conclusion of the study was that measurements in the Hybrid-III ATD are insufficient for predicting PMHS injury under these conditions.

Begeman et al. investigated injuries due to axial impact loading using a pneumatic impactor to impact the plantar surface of the foot of 20 component PMHS legs at velocities of 3.0-8.1 m-s^{-1}.[23] The positioning of the impactor was chosen so as to induce dorsiflexion at dynamic rates during the impact to investigate the causation of malleolar fractures in the leg during axial loading. Injuries produced by this test series included avulsion fractures of the tibia and fibula, malleolar fractures, and torn ligaments. Injured specimens were found to have experienced greater than 45 degrees of dorsiflexion during the test.

Crandall et al. performed tests specifically aimed at simulating the toe pan intrusion associated with frontal collision. Twelve PMHS tests were performed using a test sled which included pistons which were used to displace the toe pan. Load cells were incorporated into the toe pan and load cells were implanted at the mid-shaft of the tibia. Three test conditions varying toe pan intrusion were used with a target vehicle velocity of 50-60 km-h^{-1}. Findings of the study indicated that intrusion alone was not enough to predict fracture.[53]

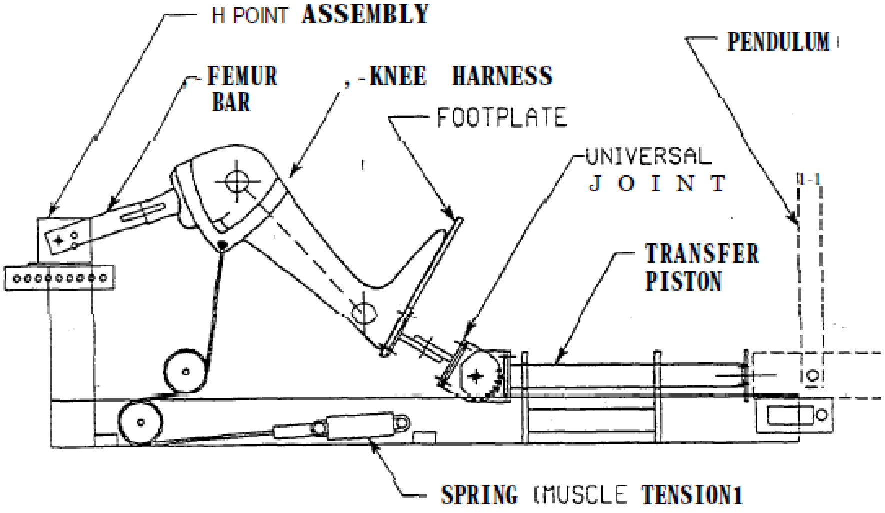

Figure 2.9 Pendulum impactor test rig used by Klopp et al., which includes a mechanism for generating muscle tension during impact (Image reproduced with permission from Taylor and Francis).[109]

Yoganandan et al. performed 26 additional PMHS component leg impact tests and combined the data with that of Roberts et al. and Begeman et al. to produce and injury risk function for the foot and ankle complex.[24,181,231] For these tests, the proximal tibia and fibula were potted, and then placed on a sled which allowed translation of the leg in the direction of impact. The foot/ankle was positioned such that the plantar surface of the foot was vertical, and a pendulum with a padded impact surface was used impact it. Force was measured at both the impact surface and proximal tibia. Injuries from this test series were not specifically outlined, but fracture forces were reported as ranging from 6.9-8.7 kN.[231]

Fifty PMHS leg tests were performed by Klopp et al. using a pendulum impactor to deliver energy to the toe pan structure of the test fixture.[109] Footplate forces, tibia forces, and specimen and footplate accelerations were collected for each test. Position of the foot was varied to study the effects of inversion, eversion, plantar flexion, and dorsiflexion on fracture force. Injuries included a mixture of malleolar, talus, tibia pilon, and calcaneus fractures.[109]

Kitagawa et al. (1998)[108] used eight pairs of PMHS lower legs to conduct axial impact tests using a pendulum impactor. These tests applied 2 kN of tension to the Achilles tendon during the impact to simulate the muscle tension induced by pressing on the brake pedal. Each specimen was sectioned at the shaft of the tibia and fibula (300 mm from section cut to plantar surface of the foot) and potted. Impact velocities ranged from 2.91 to 3.99 m-s^{-1}, and forces were measured at the impact plate and at the potted end of the tibia. Fractures induced by the impacts included ten calcaneus, five tibia pilon, one medial malleolus, and two talus fractures. Pilon fractures were found to occur in cases where calcaneus fracture did not occur. Subsequent finite element modeling suggested that the application of a preload and Achilles tension was likely to increase the likelihood of tibia fractures under axial impact loading.[108]

Manning et al. (1998) performed low energy PMHS foot impact tests for producing biofidelity corridors for the leg. Heel and forefoot (toe) impacts were performed using a pendulum. Average peak impact acceleration was 130 g for impact velocities of 4 m-s^{-1} for the heel impact condition. Toe impact tests were performed at 4 and 6 m-s^{-1}, and additional tests were performed with initial ankle eversion and inversion. Forces were measured using an implanted tibia load cell, and corridors were developed for each of the test conditions.[130]

McMaster et al. (2000) studied the results of 23 potted PHMS legs exposed to axial impact loading at different locations on the foot. Force was measured at the impactor and at the potted proximal tibia. Tension was applied to the Achilles tendon in order to simulate the plantarflexion that occurs during braking. Three impact locations were used: along the tibia axis, centered at the anterior tibial margin, and 2.5 cm anterior to the anterior tibial margin. Fractures included those typical of axial loading, which included calcaneus, talus, malleolus, and pilon fractures. The highest fracture forces occurred for the tests performed with the impactor position in line with the axis of the tibia (8.6 kN at the impactor), while lower fracture forces were measured for the other two locations (4.9 and 4.5 kN), though more tension was applied to the Achilles tendon in these tests. Malleolar fractures were found to have the lowest fracture forces, which may be indicative of the presence of shear forces which are often associated with these injuries. Pilon fractures were more common when greater Achilles tension was applied. Another significant conclusion from this work was that fracture patterns were found to be influenced by the bone mineral density of individual bones in the foot and ankle.[138]

Funk et al. (2002) focused on the effect of Achilles tension on fracture location in the ankle. A linear impactor was used to impact two PMHS test groups: one which had no tension applied to the Achilles tendon, and a second which applied tension that simulated pressing the brake pedal. Results showed that the tests with Achilles tension were more likely to have a pilon fracture because of the effect of adding force to the tibia without adding force to the calcaneus or talus. An injury risk function which incorporated Achilles tension, tibia force, age, sex, and mass was developed for the data set and will be discussed in a later section.[70]

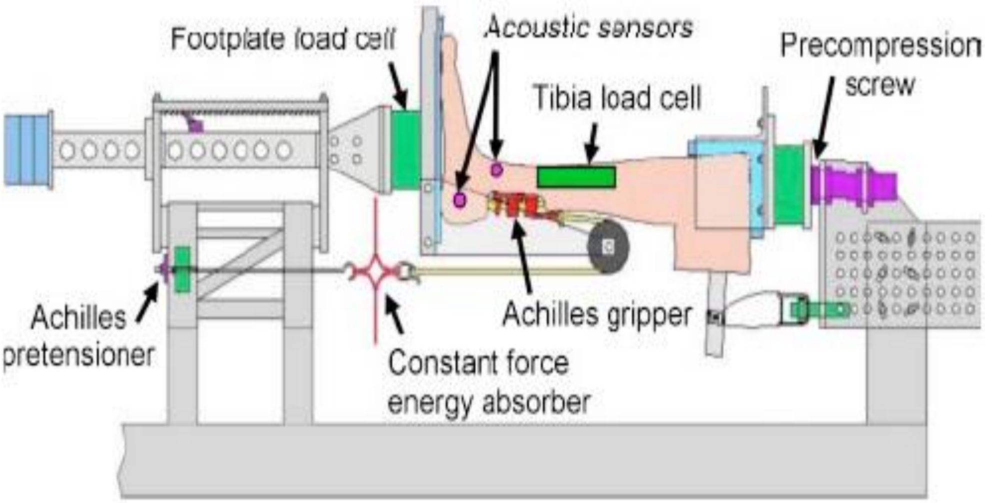
Footplate load cell
Acoustic sensors
Precompression screw
Tibia load cell
Achilles pretensioner
Achilles gripper
Constant force energy absorber

Figure 2.10 Test fixture used by Funk et al., which utilized a pneumatic linear impactor to deliver axial impacts to the foot. (motion (Accidental Injury by Springer New York. Reproduced with permission of Springer New York in the format Thesis/Dissertation via Copyright Clearance Center.)[73]

McKay and Bir (2009) focused on simulating underbody blast loading to the legs using 18 component PMHS legs sectioned at the mid-femur. A linear impactor was used to impact a floorplate on which the foot was resting. The femur was potted and attached to the Hybrid-III pelvis to simulate the proximal boundary condition of the thigh. Load cells were implanted into the tibia shaft to measure forces in the leg. Strain gages were used for estimating time of fracture. The legs were tested at three different conditions with impact velocities averaging 7.2, 9.9, and 11.6 m-s^{-1}. Fracture occurred in 12 of the 18 tests, with all legs tested at the lowest impact velocity remaining uninjured. Fractures included calcaneus, talus, malleolus, and distal tibia fractures. Various tibia and fibula fractures occurred, however these fractures are suspected to be artefactual because of their location near the implanted load cell. Injury risk functions based on force and velocity were developed, with 50% probability of injury occurring for 6.4 kN and 10.8 m-s^{-1}.[135]

Quenneville et al. performed axial impact tests on 7 pairs of denuded PMHS tibias with the goal of investigating the effect of short duration loads of less than 10 ms. The proximal end of the tibia was potted, and the distal end of the tibia was interfaced with a polyurethane talus attached to a load cell and the impact plate. Projectiles of 3.9 and 6.8 kg were used to impact the tibia at velocities ranging from 5.1-12.4 m-s^{-1} where kinetic energy was the controlled input to the system. An injury risk function based on force was developed and 7.9 kN was found to correspond to 10% risk of injury, which was greater than the previous standard of 5.4 kN for 10% risk of injury for the whole leg.[172] Though these results provide information about the strength of the tibia at these load rates, it is important to consider the strength of the leg as a system, since other bones in the foot and ankle may be more susceptible to fracture due to stress concentrations and other factors such as material properties of individual bones. Further, the effect of de-fleshing the tibia must be investigated in more detail, particularly when considering the forces associated with the overall strength of the leg.

Gallenberger et al. (2013) focused on the effects of dorsiflexion and kinetic energy on the risk of foot/ankle injury. This study performed 60 impact tests using a pendulum to impact the plantar surface of the foot of 15 PMHS legs.[82] Leg position was such that the foot was impacted by a pendulum plate at either a neutral ankle position (nominally 90 degrees from tibia axis to plantar surface of the foot) or at 20 degrees of dorsiflexion. Conclusions from this study indicated that fracture forces were approximately 1.1 kN higher for the dorsiflexion tests.[82]

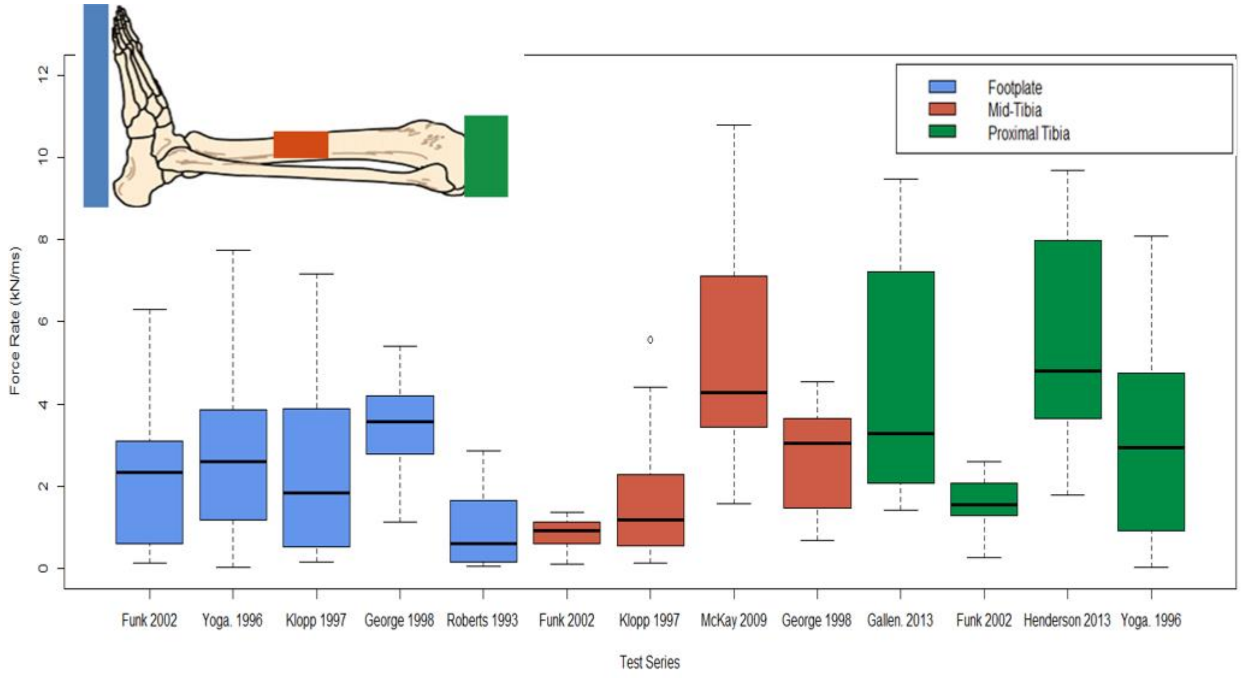

Figure 2.11. Box plot of force rate for axial loading studies from the literature. Force measurement location is distinguished by color and a schematic is provided for further reference. Note that these tests used different proximal boundary conditions as well.

The loading rates for many of these test series are summarized in Figure 2.11 to show the overlap in force rates for the studies and the differences as measured at different location. Force rates were calculated using the slope between 20- and 80-percent of the peak force. Forces measured at different locations are indicated by different colors. The highest loading rate was observed in the McKay and Bir study, while the lowest load rate was part of the Yoganandan et al. data set.[135,231] Despite the fact that the literature has explored the leg's response to axial loading for a wide range of load rates, additional experimentation is necessary to understand the force tolerance of the leg for this spectrum of load rates. Since forces were measured in different locations and different boundary conditions were used for the individual test series, it is difficult to determine whether the fractures that occurred in each test series are associated with a single force threshold or whether load rate or duration affects force at fracture.

2.3.2 Bending

It is important to note the contribution of bending to leg injury, whether anterior-posterior (AP) or medial-lateral (ML). Previous studies have shown that bending or application of moments to the tibia/fibula can affect both the injury pattern in the leg as well as the leg's injury thresholds when combined with axial loading.[71,221] The Tibia Index is based on the assumption that the tibia can be treated as a column under combined compression and bending loads, and uses the moments measured in the tibia to adjust the probability of injury.[139,222] Bending moments can be created not only by a second loading vector, but also by position of the leg. Alignment of the SAE-z axis of the tibia relative to the loading vector can cause an increase in the bending moment, which leads to an increase in tibia fracture risk for a given axial force. Further, the innate curvature of the tibia leads to inherent bending moments along the length of the tibia. These are important factors to consider when developing an injury criterion for the leg exposed to axial loading.

2.3.3 Ankle Flexion

Injuries caused by flexion of the ankle joint have included both ligamentous and bony failure. Static and dynamic PMHS testing has been performed to establish angles of flexion required to cause injury.[25,163,168,168] Begeman et al. estimated a maximum dorsiflexion angle of 45 degrees for dynamic loads applied to the forefoot, while Portier et al. found that the maximum dorsiflexion angle was 30 degrees for dynamic loading of the forefoot, with an average moment to failure of 60 Nm.[25,168] Quasi-static PMHS tests estimated higher dorsiflexion angle to failure with lower failure moments. Petit et al. found an average failure angle of 49±11 degrees and a moment of 47±17 Nm, while Parenteau later measured 44±11 degrees and 33±17 Nm.[163,166] A later study by Rudd et al. performed additional dynamic dorsiflexion PMHS tests to validate the injury risk function developed by Kuppa et al.[116,182] The most common injury from this study was fracture of the medial malleolus, which involved avulsion of the deltoid ligament. A 25 percent risk of injury was estimated for 42 degrees of dorsiflexion and 59 N-m, which agreed reasonably with previous test data.[182]

Variation of ankle position combined with axial loading can lead to alternative injury patterns for foot and leg. Flexion of the ankle from a neutral position (where the axis of the tibia is nominally 90 degrees to the floor surface) causes bending moments in the tibia and fibula as mentioned in the previous section, and changes relative the position of bones in the ankle. Axial impact testing of the dorsiflexed and plantar flexed foot-ankle complex has been performed in multiple studies.[25,55,109,168,181] Gallenberger et al. showed a 1.1 kN decrease in the force associated with 50 percent probability of injury for 20-degree dorsiflexed ankles compared to neutrally positioned ankles.[82] Klopp et al. concluded that dorsiflexion of the ankle increases the amount of compressive force required to produce fracture in the foot and ankle by increasing the contact area within the subtalar joint.[34,109] A more recent study which combined data from various axial impact tests from the literature showed that dorsiflexion had a similar effect of increasing the force associated with 50 percent risk of injury by approximately 1.18 kN for a 45 year old male with an initial 10 degrees of dorsiflexion.[12]

Plantar flexion was shown to have the opposite effect, and lowered the axial force required to cause fracture.

These trends are supported by the work of Calhoun et al., which revealed that plantar flexion and dorsiflexion change the amount of tibio-talar joint articulation, with plantar flexion decreasing contact area.[35,117] This change in contact area helps explain the positive relationship between force at fracture and dorsiflexion angle suggested by previous injury risk analyses.[12,82,109] Other literature has demonstrated that ankle flexion angles greater than 10 degrees can contribute to alternative injury mechanisms due to shear and bending.[35,72,109]

2.3.4 Ankle Xversion

Medial-lateral bending is introduced to the leg when the ankle is inverted or everted (xversion). Tolerances for ankle range of motion and moment in inversion and eversion have been estimated both statically and dynamically by Parenteau et al. and Petit et al., however, few tests exist in combination with axial loading.[163,166] Jaffredo et al., Funk et al., and Klopp et al. analyzed the effects of ankle xversion.[71,101,109] Ligamentous injuries such as tears of the lateral ligamentous complex and anterior talo-fibular ligament have been associated with inversion of the ankle and eversion has produced deltoid ligament injury.[71] Bony fractures associated with xversion combined with axial loads have largely included malleolar fractures, though a smaller number of these fractures have occurred with pure eversion or inversion.[71,163,166]

Inversion and eversion are widely accepted as an injury mechanism for malleolar fractures, though Madeley et al. deduced that inversion and eversion combined with axial loads and sometimes extreme dorsiflexion can cause these fractures.[129] Though malleolar fractures have been caused by axial loading PMHS studies, these fractures often occurred when excessive joint motion occurred when floor displacements are large and ankle joint motion was unconstrained.[181]

Shin and Untariou developed a model for estimating fracture force for the ankle under combined loading involving axial loading, ankle xversion, and ankle flexion.[193] This study resulted in an injury surface equation to demonstrate the effect of ankle position on the axial force necessary to cause fracture based on finite element model simulations. Results indicated that extreme ankle positions (non-neutral) reduce the axial force necessary to produce fracture in the leg, with maximum force at fracture occurring for zero degrees of xversion and approximately 20 degrees of dorsiflexion.[193]

2.3.5 High Rate Injury Mechanisms

The mechanisms by which the body fails under primary blast loading are largely still a mystery. Since these phenomena typically involve direct contact with a shock wave, the focus of this dissertation is limited to the loading induced by the response of the vehicle to these loads. The previously outlined injury mechanisms have involved mainly inertial based loading and application of loads at low frequencies. When shifting attention to military injuries, additional injury mechanisms come into play as a result of blast loading.

Primary blast involves direct contact with a shock wave, which can be idealized as a Friedlander waveform (Figure 2.12), which consists of an instantaneous rise in pressure, followed by an exponential decay of that pressure, and ends with a negative pressure phase. When a shock wave encounters an object, the sharp rise in pressure loads the object at a rate faster than the pressure wave can travel through the material. Injury mechanisms associated with primary blast are dictated by how the tissues of the body respond to this loading.[198]

leg.

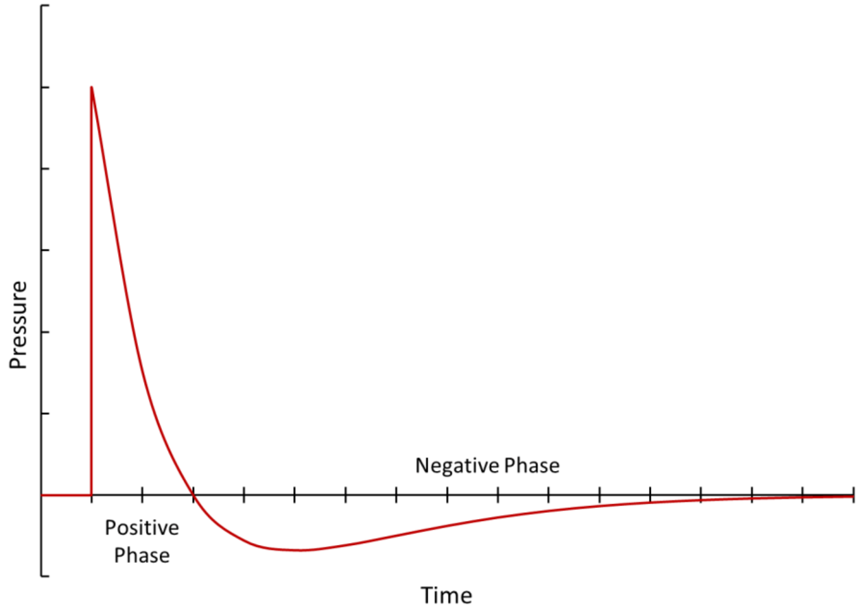

Figure 2.12. Blast (shock) wave profile based on a Friedlander waveform, which consists of an instantaneous rise in positive pressure, followed by an exponential decay of pressure which ends in a negative pressure phase.

Brisance, a term used to describe the ability of a blast wave to shatter materials, is believed to occur 0.2 to 2 ms after detonation.[174] Brisance occurs when a shock wave encounters and object and the energy is converted into an acoustic wave, which travels through the material at a velocity related to material properties (speed of sound in that material). The energy of the shock wave continues to interact with the surface of the object until it dissipates enough to travel at the speed of sound in the object's material, which often leads to extensive damage at this interface.[198] Though this injury mechanism is typically associated with direct contact with the blast wave as is the case for anti-personnel landmine detonation, the timing associated with this injury mechanism is important for inferring the limits of inertial-based axial loading injury mechanisms and blast injury mechanisms for the leg.

Spalling, a term typically used in reference to the failure of concrete due to blast loading, may also be considered as an injury mechanism. Spalling and brisance are used interchangeably in the literature, though the term brisance generally refers to the ability to shatter a material.[33,83] Spalling occurs mainly for materials which have high compressive strength, which allow a blast wave to travel through the material without exceeding fracture threshold. However, once the blast wave reaches a free surface of the material or a region of impedance mismatch, the acoustic wave is reflected. The reflected wave interacts with the impending blast wave to create a "mechanical interlocking" phenomena in the material.[125] Concrete, notorious for its high compressive strength and low tensile strength fails under this mode, which often results in fragmentation (brisance) of the concrete at the free surface and under tension.[125] Spalling has also been hypothesized as an injury mechanism in the body due to impedance mismatch between different tissues for an injury referred to as "blast lung."[161,173]

Implosion is another mechanism of injury associated with primary blast. This injury mechanism typically refers to the behavior of a material when the blast wave encounters soft tissue with pockets of air. When the shock wave encounters these hollow pockets in organs, the air in the pocket contracts and then expands, which can cause organ damage known as implosion.[122] Though implosion is mentioned as a blast injury mechanism, it has not been associated with UBB or lower extremity injury.

2.4 Injury Risk Functions

2.4.1 Injury Definition and Censoring

One of the first steps in development of injury risk functions is determination of the definition of injury. In many cases, the Abbreviated Injury Scale (AIS) is used to define the division between "injury" and "no injury" or between different severities of injuries.[86,100] Some applications for injury risk curves, may dictate division between long-term and short-term injuries, or for military purposes distinction between injuries which prevent warfighters from escaping further threats after an initial injury as in the case of UBB or anti-personnel landmines. Functional Capacity Index (FCI) and the Injury Impairment Scale (IIS) attempt to perform this role for civilian applications by providing an estimate of an injury's impairment,[128] but unfortunately no military-based immediate functional capacity scale exists.

The Foot and Ankle Severity Scale (FASS) or Ankle and Foot Injury Scale (AFIS) has been utilized in some research to classify injuries according to their severity, particularly for cases where multiple injuries exist.[20,124,131,135] Since the AIS focuses on the relative survivability or lethality of particular injuries, it is not the best choice for distinguishing between leg injuries. Many foot/ankle/leg injuries are classified with the same AIS score even though different types and combinations of foot/ankle/leg injuries can have different consequences on quality of life or ability to escape danger post-injury in the case of UBB.[86,131] For military applications in which post-injury mobility is of importance, the AFIS-S scale may be more useful for distinguishing between injuries to the foot/ankle/leg. An AFIS-S score of 4 or greater (severe injury) was used as a classification for an injury risk function developed by McKay and Bir, which is currently used for the Mil-Lx ATD leg.[135,151]

Consideration must also be given to the injury mechanism of different injuries in order to ensure that the injuries or injury categories may be distinguished from each other using the same injury predictor, or reasonably accommodated for using statistics. Historically, injury criteria have distinguished between different injuries and injury mechanisms using time or impulse data. Rupp et al. used impulse of the force measured in the Hybrid-III femur to differentiate between the use of a hip versus knee injury risk function for predicting injury.[184,187] Similarly, multiple injury criteria exist for thorax including displacement and force predictors due to different injury mechanisms leading to rib fractures and internal organ damage.[104,213]

Examination of the leg injuries produced by a combination of axial loading tests from the literature [14,73,75,82,94,108,109,135,181,191,196,231] revealed that calcaneus, talus, and distal tibia (pilon) fractures are the most common, with calcaneus fractures far outnumbering other injuries. Further analysis showed that calcaneus fractures occurred alone (67 tests), and also accompanied many of the talus and pilon fractures (Figure 2.13). Proximal tibia injuries occurred only in test series where the knee joint remained intact, and occurred only once without a calcaneus fracture.[73,135] Fractures which occurred when Achilles tension was applied during the test are also indicated in Figure 2.13.

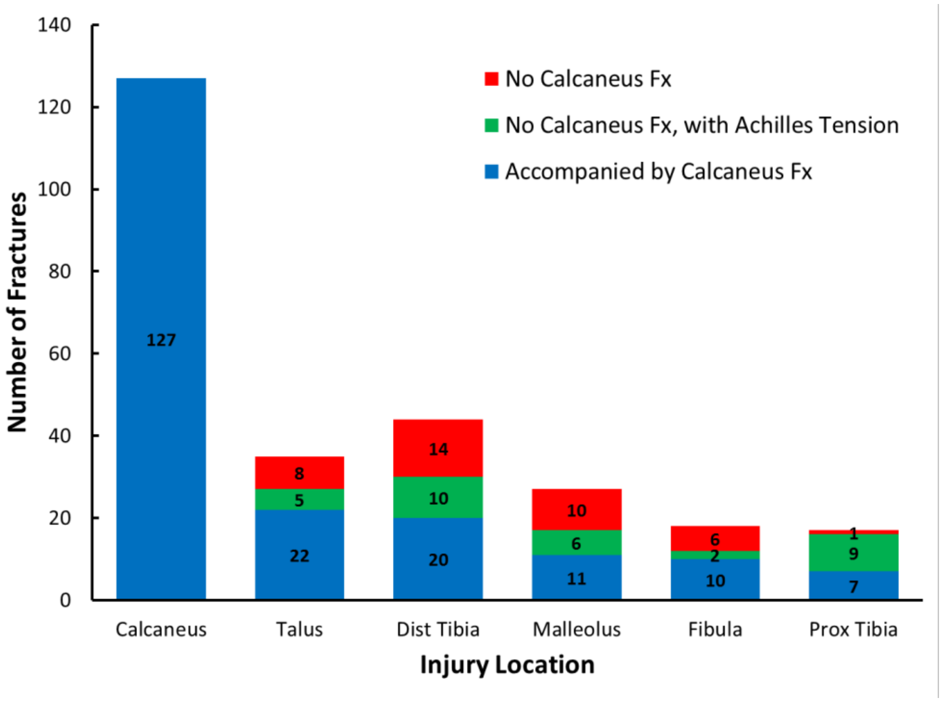

Figure 2.13. Frequency of lower leg injuries generated by axially-loaded PMHS tests from the literature (238 tests).[14,73,75,82,94,108,109,135,181,191,196,231] The input and boundary conditions for these tests are provided in Table 2.2

This summary of injuries suggests that the calcaneus has a higher tendency to fracture compared to other bones for axial impacts to the foot. Several reasons for this were discussed by Bailey et al., particularly inertial differences between the forces at the impact site (plantar surface of the foot) compared to locations further from the impact like the proximal tibia.[15] McMaster et al. showed that difference in the bone mineral density for individual bones in the hindfoot and ankle may predispose the leg, foot, and ankle to different types of fractures when exposed to axial loading.[138] Previous studies have shown that the talus is nearly twice as strong in compression as the calcaneus, with an average failure force of 6.4 kN compared to 3.8 kN.[32] Funk et al. hypothesized that the tibia and calcaneus are nearly equal in compressive strength, though inertial differences yield a higher number of calcaneus fractures when the foot is impacted.[72] These factors may influence the injury location within the leg.

For the foot and ankle, it is not reasonable to generate separate injury criteria for specific bones because of potential overlap in the injury thresholds for each bone. For example, for a given axial force a talus injury might occur in one specimen while a calcaneus fracture might occur in another due to inter-specimen variability. Geometric differences for individual bones may lead to two specimens having different fracture locations as well. These reasons suggest that injury risk functions developed for individual bones in the foot and ankle would be misleading as they would tend to be skewed by outliers in the population. Further, the injury criterion should be focused on defining the probability of any injury with a given injury mechanism rather than a specific injury which may occur at a higher threshold than another injury.

2.4.2 Injury Risk Functions for the Leg

Yoganandan et al. (1996), McKay and Bir (2009), Klopp et al. (1997), and others have generated IRFs for the leg based on various parameters measured in post-mortem human surrogate (PMHS) experiments (Table 2.3, Figure 2.14).[109,135,231] While these statistical models fit their respective injury data, it is important to consider the conditions under which the IRFs are valid before applying them to other loading scenarios. Table 2.3 provides a summary of existing IRF results for the foot/leg and their associated experimental test conditions, while Figure 2.14 shows force-based IRFs from previous studies.

Table 2.3. Previous injury risk functions for axial loading of the leg

Study	Boundary Condition	Loading Condition	Injury Predictor for 50% Injury Probability
Yoganandan 1997[232]	Potted proximal tibia, unbooted, ballasted	Pendulum	0.348*Age+0.415*Axial tibia force = 4.4 6.8kN Axial mid-tibia force
Klopp 1997[81]	Potted femur, unbooted	Pendulum	-9.75+0.13*ankleVr+0.47footplate force+0.14 dorsiflexion angle=-0.1
Funk 2002[73]	Potted proximal tibia, unbooted	Linear Impactor	45 YO 50% Male: 8.3 kN mid-tibia force 65 YO 50% Male: 6.1 kN mid-tibia force 45 YO 5% Female: 5.0 kN mid-tibia force 65 YO 5% Female: 3.7 kN mid-tibia force
Bass 2004[20]	Potted mid-femur, booted	AP Landmine Blast	8.6 kN mid-tibia force
McKay 2010[134]	Potted femur, unbooted	Linear Impactor	5.9 kN axial tibia force, 10.8 m/s velocity
Quenneville 2011[172]	Potted tibia, unbooted No foot	Linear impactor	7.9 kN = 10% risk of injury
Henderson 2013[94]	Potted proximal tibia, unbooted, ballasted	Drop Tower	7.34 kN distal tibia force 6.16 kN proximal tibia force
Gallenberger 2013[82]	Potted proximal tibia, unbooted, ballasted	Pendulum	Neutral Position: 6.8 kN prox. tibia force 20 deg dorsiflexion: 7.9 kN prox. tibia force
Yoganandan 2014[229]	Potted proximal tibia, unbooted	Pendulum	25 YO: 10.4 kN prox. tibia force 45 YO: 8.3 kN prox. tibia force 65 YO: 6.6 kN prox tibia force
Bailey 2015[15]	Combination	Combination	25 YO 50% Male: 11.5 kN footplate force 45 YO 50% Male: 10.2 kN footplate force 25 YO 50% Female: 9.1 kN footplate force 45 YO 50% Female: 8.0 kN footplate force

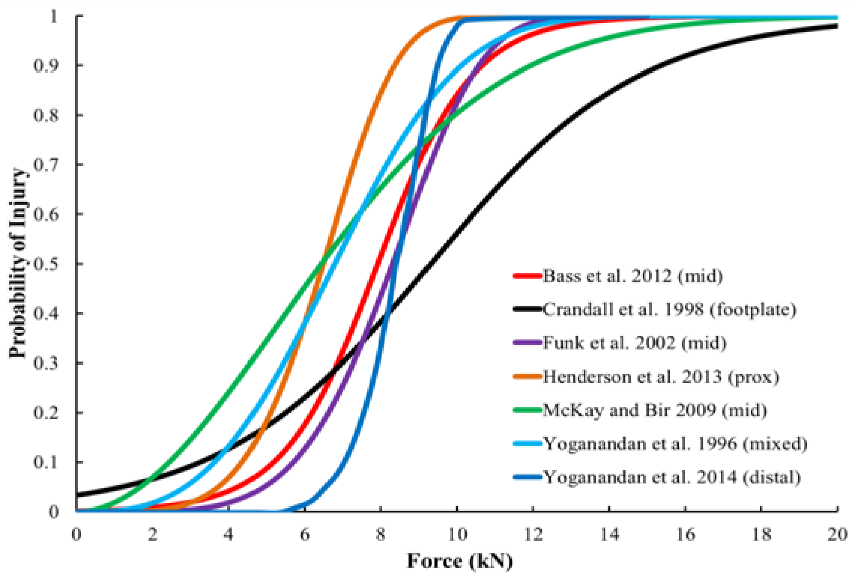

Figure 2.14. Comparison of existing lower leg IRFs from literature using tibia force as an injury predictor. Note: Funk et al. 2002 and Yoganandan et al. 2014 assume a 45 year old, 75 kg male.[20,54,73,94,135,229,231]

Comparing several previously-developed IRFs from a variety of loading rates, it is not clear which are applicable for the higher loading rates associated with UBB. While the loading rates from Henderson et al. (2013) and McKay and Bir (2009) were among the highest of those compared in Figure 2.14 the location of force measurement is proximal to the location of a majority of the injuries produced.[94,135] IRFs based on mid-tibia forces measured by implanted tibial load cells reveal differences between the McKay IRF developed at high load rates (3.2-10.8 kN/ms) and the Funk et al. (2002) data set from more moderate load rates (0.1-3 kN/ms).[73] It is unclear whether these differences are due to input pulse characteristics, quality of specimens tested, or the way injury is defined in the two models (McKay uses AFIS-S 4+ to define injury and Funk uses bony fracture in the foot/ankle complex). It is important to understand the effects of these dissimilarities in order to make progress in understanding the role of load rate or duration on leg injury.

One of the most widely-used IRFs for the leg was generated by Yoganandan et al. (1996).[231] Unfortunately, though the risk function includes a large number of tests, the data set is composed of force measurements taken from various locations, and does not account for the inertial differences between the measurement locations. Additionally, the data set included both dorsiflexed and neutral ankle positions; dorsiflexion has since been shown to increase the fracture tolerance of the ankle joint.[82,109] Furthermore, the boundary conditions in the three data sets were different, which enhances the potential for inertial differences between the tests and increases the need for a common location of force measurement. While the data from Yoganandan et al. (1996) was reanalyzed to use distal forces, the same issue exists of failing to account for the effect of ankle flexion.[229,232]

Boundary conditions in tests aimed at determining injury risk are of vital importance; however, simulating exact boundary conditions and achieving the higher loading rates required for studying UBB is challenging. McKay and Bir (2009), Funk et al. (2002), and Henderson et al. (2013) each achieved higher loading rates with three different boundary conditions, thus producing different injury patterns in select cases. All but Henderson et al. produced proximal tibia fractures, which was likely due to the presence of the knee joint in the other test series. Knowing the effect that each of these complicated boundaries has on producing stresses on potentially weaker bony regions is important for determining whether these more-proximal injuries should be considered for inclusion in an analysis focusing on injuries to the foot/ankle complex, or rather included in a separate injury criterion.[73,94,135]

Some IRFs for the leg have taken into account covariates such as age, sex, and bone mineral density (BMD).[73,108,109,181,231] While these studies have used realistic injury predictors (force) and have attempted to compensate for specimen variability, the location of force measurement in these works limits their accuracy as well as obscures the relationship established between the main injury predictor and the covariates. For example, Funk et al. measure the force at mid-tibia using an implanted load cell. While this force is realistic for determining force at fracture for the tibia and locations in close proximity to the mid-tibia, most injuries occurred at the level of the calcaneus. Further analysis shows that footplate force was better correlated with injury than mid-tibia force,[73] likely because a majority of the injuries occur in close proximity to the footplate. Load-sharing between the tibia and fibula can account for about 6 percent of the difference between the load measured at the two locations,[73,89,201] and the remainder can likely be assigned to the effect of inertia due to the mass present between the two load cells.

The studies aimed at understanding the effect of UBB on the leg[94,135] have different proximal boundary conditions and instrumentation locations than others performed at automotive conditions,[109,196,231] making it difficult to understand the effect of higher loading frequencies on the leg, foot, and ankle. At higher loading accelerations, it becomes increasingly important to measure the load closer to the region of interest because of inertial effects. As the acceleration of the leg increases, the greater the difference between the forces measured in one location versus another location due to the mass present between the load cell and region of interest. While previous IRFs may be valid for data set from which they were generated (assuming loading rates were not varied), deviations from the input or boundary conditions of that particular test setup decrease the predictive ability of that IRF for other data sets. Thus, it is important to consider this when applying an IRF to a new data set to predict injury.

A more recent study by Yoganandan et al. reanalyzed previous PMHS test data to fit the parameters of an injury risk curve based on force.[229] Though the statistical analysis followed the recommendations set by the International Organization of Standardization and smaller confidence intervals were obtained by eliminating outliers from the data set, no validation work was performed to demonstrate an improvement in injury prediction capabilities compared to the previous logistic regression injury risk function.[229,231] Age was included in the analysis and was shown to have the effect of increasing the probability of injury for a given peak force, which was consistent with previous injury risk functions which included age.[70]

An attempt to account for the rate effects on the estimation of injury risk involved combining data from five studies (82 tests), and using plantar force as the main predictor variable and dorsiflexion angle, age, sex, and mass as covariates.[12] Plantar force was chosen as the predictor variable because of its proximity to injury location in effort to reduce error in force measurement due to the presence of mass between the load cell and fracture location. The injury risk function resulting from this analysis (Figure 2.15) estimated higher forces for given probability of injury compared to previous injury risk functions which used proximal or mid-tibia force measurements. Though no validation was performed to show the utility of using plantar force over proximal or mid-tibia force, this injury risk function provided advantages over previous injury risk functions by including data from multiple load rates and not combining force data from different locations in the leg as was done by previous studies.[12,231]

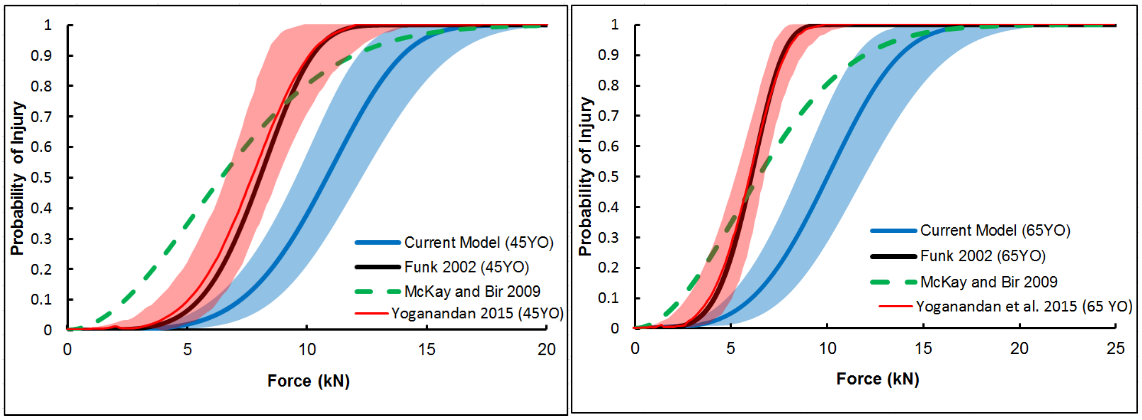

Figure 2.15. Comparison of injury risk function based on plantar force and previous injury risk functions which did not distinguish between location of force measurement or measured force proximal to the location of injury.(Figures reproduced with permission from Taylor and Francis)[12]

Kuppa et al. summarized injury criteria that were developed for various regions and bones in the leg.[116] Individual injury criteria were developed for the leg shaft; foot fractures including the calcaneus, talus, ankle, and midfoot; and tibia plateau. The tibia index and revisions of the tibia index aim to estimate risk of fracture for the tibia and fibula shaft using a combination of axial force and bending moments. Originally developed by Mertz et al. the tibia index can be calculated using Eqn. 2.1, where TI is the tibia index, F is the axial force, F_c is the critical axial force (35.9 kN for a 50th percentile male), M is the resultant anterior-posterior and medial-lateral tibia moment, and M_c is the critical resultant tibia moment (225 N-m for a 50th percentile male).[141] Crandall et al. summarized the benefits of using the tibia index, though concluded that the critical values used by Mertz were not reasonable for the entire leg. [52] A subsequent study by Funk et al. demonstrated that tibia curvature and fibula load sharing affect the assumptions used to develop the tibia index.[74] Funk et al. performed PMHS testing to estimate the degree to which the tibia index is affected by these factors and used the information to correct the ATD measurements used to calculate the tibia index (Eqn. 2.2).

$$TI = \frac{F}{F_c} + \frac{M}{M_c} < 1 \qquad \text{Eqn. 2.1}$$

$$F_{z\_human} = F_{z\_ATD} \cdot \left[1 - Fib\,load(\%)/100\%\right] = F_{z\_ATD} \cdot \left[0.925 - 0.0029 \cdot ev(\mathrm{deg})\right] \qquad \text{Eqn. 2.2}$$

The foot injury criteria summarized by Kuppa et al. included the bones most commonly fractured in the foot and ankle due to axial impact loading. The injury risk function provided by Kuppa is based on a PMHS data set combined by Yoganandan et al., which estimates a 25% and 50% risk of AIS 2+ foot/ankle fracture for 5.2 kN and 6.8 kN of force, respectively. The logistic regression equation for this relationship is provided in Eqn. 2.3. Though the Yoganandan et al. data set combined force measurements from footplate and proximal tibia locations, the injury risk function is based on lower tibia forces measured in the ATD leg.

$$p(AIS\ \ 2+) = \frac{1}{1 + e^{4.572 - 0.670F}} \qquad \text{Eqn. 2.3}$$

$$p(AIS\ \ 2+) = \frac{1}{1 + e^{(0.5204 - 0.8189F + 0.0686mass)}} \qquad \text{Eqn. 2.4}$$

It is interesting to note the differences between the magnitude of force associated with foot/ankle compared to proximal tibia injuries. The proximal tibia injury risk function was developed using data from experiments which impacted the tibiofemoral joint, with the mid-shaft of the tibia potted.[17] Comparing the foot injury risk function to the risk function for the tibia plateau and condyles (Eqn. 2.4) reveals that higher forces are associated with tibia plateau fractures. Though upper tibia forces were used for the tibia plateau injury criterion, the dissimilarity in forces associated with the different injury locations explains the prominence of foot/ankle injuries generated by axial loading events compared to more proximal injuries such as those of the tibia plateau and condyles (see Figure 2.13). The higher force at failure for the proximal leg injuries predisposes the leg to foot/ankle fractures, in addition to the inertial differences in the forces observed at the two injury sites due to impact location.

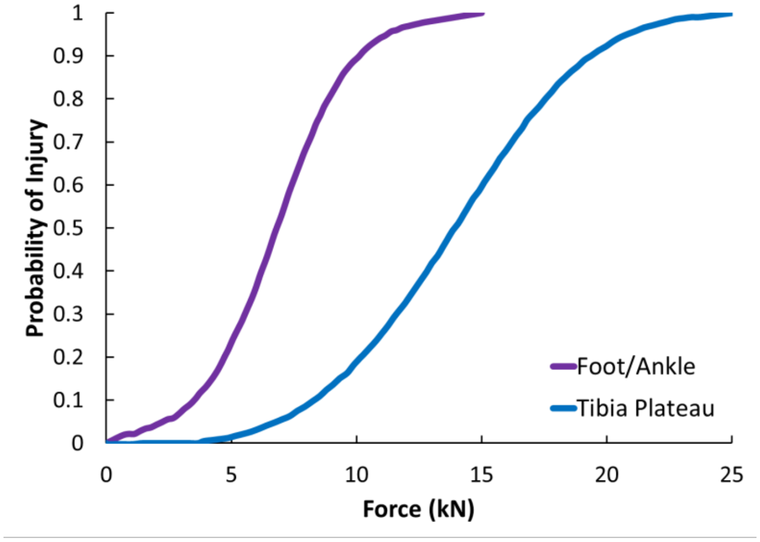

Figure 2.16. Comparison of injury risk functions for foot/ankle fracture versus tibia plateau fracture. The foot and ankle injury risk curve was produced using the injury risk function developed by Yoganandan et al., and the tibia plateau injury risk curve was developed using the data from axial tibiofemoral joint impact tests performed by Banglmaier et al. [Figures produced using data from Kuppa et al.][17,116,231]

While force is the most widely accepted injury predictor used for leg, other injury predictors have also been considered. McKay and Bir (2009) proposed a velocity-based injury metric for the leg to be used for UBB loading conditions. While impact velocity is significantly correlated with injury in McKay's test series, the velocity-based injury criterion should not be used with different boundary conditions or with different impactor masses than were used for that particular test series.[135] The velocity necessary to produce fracture may change based on the impactor mass (i.e. kinetic energy) or if the proximal boundary of the leg is fixed. Thus, it is important to consider the versatility of an injury predictor in relation to boundary conditions when choosing a predictor variable to be used in various loading scenarios. McKay and Bir also found peak compressive strain in the leg and kinetic energy to be significant predictors of injury, though force was chosen as the best predictor based on the correlation coefficient.

Klopp et al. investigated several injury predictors, which included peak heel acceleration and footplate force rate.[109] In addition to peak footplate force, these predictors were found to be significant. Further, ankle angular velocity and ankle dorsiflexion proved to be significant predictors when combined with force and force rate in multivariate regression models.

While most injury criteria for the leg have used peak force as the injury predictor, injury criteria for the head, neck, spine, and femur[140,197,208] have included duration of loading to account for the transient response of the system.[87,214] The transient response of a system refers to the response of a system to an input prior to reaching its steady state behavior. Dynamics systems have been shown to exhibit an overshoot in response to impulse and step loading. The magnitude of the overshoot is dependent upon system characteristics, such as damping, and the frequency and amplitude of the input.

Von Gierke, Stech and Payne, and King et al. have outlined the application of dynamic theory to the biomechanical response of the human body using a single degree of freedom dynamic model. King et al. demonstrated the effect of system damping on the "dynamic load factor," which is calculated by dividing the maximum spring force by the maximum excitation force, and is dependent upon the duration of the impact relative to the natural period of the system.[66] When the load duration is less than the natural period (or loading frequency is higher than the natural frequency), the force measured in the system is less than the applied force. For longer durations (exceeding twice the natural period), the dynamic load factor tends toward one, meaning that the applied force and system response force approach equivalency.[6666,197,214] For underdamped systems, transient response of a dynamic system near the natural frequency produces an overshoot in the spring force for a given peak force input. The magnitude of the overshoot depends on the system's damping characteristics.[66] The transient response can also be presented in terms of displacement inputs and deflection of the model. Figure 2.17 presents this information in terms of peak input and peak response in a way that more directly relates to the understanding of force at fracture for a given load duration. Each line in the diagram represents a constant level of peak model deflection for different pulse shapes as a function of the amplitude of the input pulse and the ratio of pulse length to the natural period for an under-damped system. Von Gierke divides the plot into regions of integral dependence, meaning that the integral of the input pulse controls the model deflection; duration dependence, where the input pulse duration is close to the natural period and is subject to resonance (overshoot); and a duration-independent region, where the input pulse produces the same amount of deflection regardless of the pulse duration.[214]

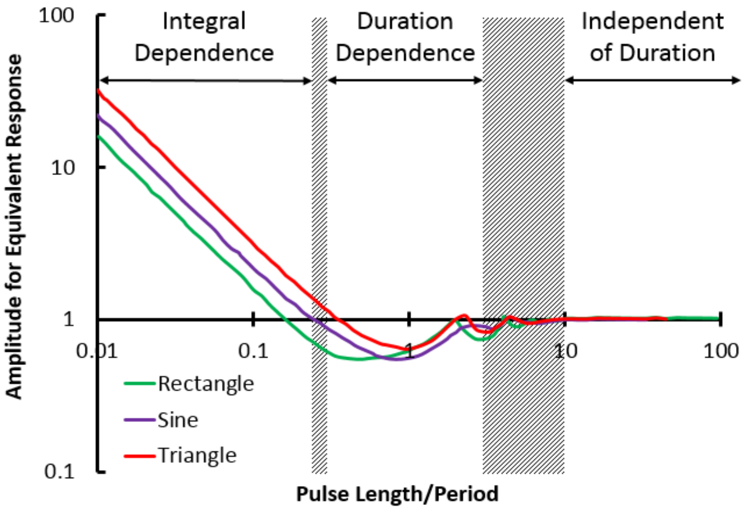

Figure 2.17. Diagram reproduced based on the work of von Gierke[214], which demonstrates the theoretical dependence of injury threshold (model deformation) on pulse shape, duration, and peak for various input pulses. Lines represent constant deformation response, which can be correlated with injury.

If the behavior of a dynamic model is applied to the response of the leg, the deflection of the model can be likened to the amount of strain in the leg. Assuming that the leg fails at a threshold of compression (or strain), the curves in Figure 2.17 relate to thresholds of injury as a function of the input in terms of peak and duration. It can then be assumed that the input is a sinusoidal force characterized by its peak and frequency (which relates to duration). In terms of developing an injury criterion based on these assumptions, the integral of force (impulse) would be expected to be a better predictor of injury for short durations of loading (for loading frequencies greater than the natural frequency). A peak force would be sufficient for predicting injury at longer durations of loading. The "resonance region," or the duration dependent portion of this curve complicates the behavior of the curve and is highly dependent upon the damping of the system. However, it is clear that for short durations of loading, peak force is insufficient for predicting model response, and therefore, injury.

Though duration of loading has not previously been incorporated into previous lower leg injury criteria, there is a precedence for duration-dependent injury criteria for other body regions such as the spine and femur.[197,208,214,220] Viano et al. demonstrated the duration-dependence of femur force-at-fracture for short duration loads (less than 20 ms), while Carothers et al. estimated a constant level of force at fracture for quasi-static loads.[36,209] Viano et al. combined these data to produce an injury criterion which used a linear regression to fit dynamic knee impact data, and a constant force level for the long duration or quasi-static data. Long and short duration loads were defined arbitrarily using a 20 ms force duration as the division point. Though Viano et al. do not justify their approach using response of dynamic models, the injury criterion they developed follows a pattern for peak versus duration that is similar to that presented in Figure 2.17. For a constant level of injury risk, peak force decreases with duration for short duration loads, and then is constant for longer duration loads.

The dynamic response index (DRI) used for estimating injury risk for the thoraco-lumbar spine exposed to axial loading also incorporates duration. DRI uses a 2nd order dynamic model to relate pelvis acceleration to compression of the spine, which is then associated with a probability of injury.[151,220] For axial loading, a DRI of 17.7 is associated with a 10% risk of AIS2+ injury, and can be calculated using Eqn. 2.5 and Eqn. 2.6. While DRI has largely been replaced by the use of lumbar forces measured in the ATD,[204] the theory is still applicable to axial loading scenarios for which it is necessary to predict the response of the body to a measured input.

$$\ddot{z}(t) = \ddot{\delta} + 2\zeta\omega_n\dot{\delta} + \omega_n^2\delta \qquad \text{Eqn. 2.5}$$

Where ζ is the damping ratio, ω_n is the natural frequency, $\ddot{z}(t)$ is the pelvis acceleration, and δ is the compression of the model.

$$DRI_z = \frac{\omega_n^2 \delta_{max}}{g} \qquad \text{Eqn. 2.6}$$

Gadd et al. explored impulse (integral of input force and acceleration) as a means of injury prediction.[79] They observed that the magnitude of the transient spike in the response trace associated with many impact tests could not be ignored in terms of its ability to cause injury, but also that the magnitude of that spike was not necessarily representative of the entire loading pulse. An additional observation was that the use of an impulse-based severity measure accounts for differences in pulse shape which are not considered when using a peak force or acceleration characterize an input. Gadd's observations emphasized the importance of incorporating duration into injury severity measures and provided the early groundwork for the Head Injury Criterion (HIC) and other soft tissue injury criteria.[79,80,120,212]

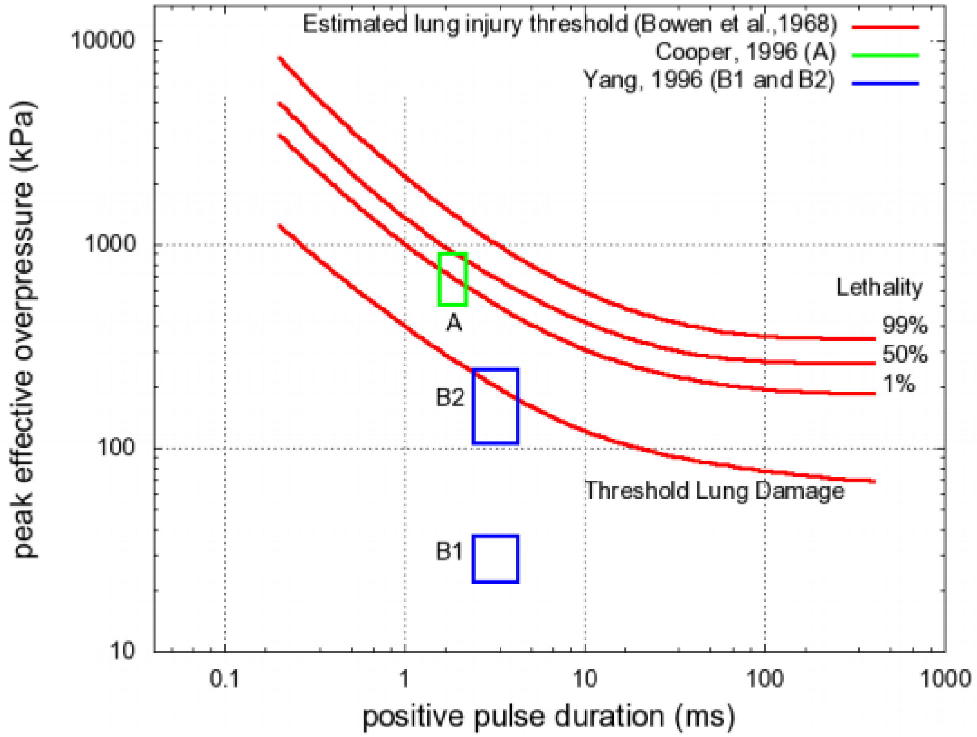

Figure 2.18. Injury thresholds for lung under blast loading based on peak pressure as a function of duration. (NeuroImage by Academic Press. Reproduced with permission of Academic Press in the format of Thesis/Dissertation via Copyright Clearance Center.)[51]

Blast injury criteria have also incorporated duration. Courtney and Courtney summarized the injury thresholds for blast lung using peak overpressure as a function of duration.[51] As duration increases, the peak pressure associated with a particular probability of injury decreases. Additional studies have hypothesized that that the same relationship holds for other body regions such as the head, when subjected to blast loading.[40,47]

Impulse and duration of loading were also considered by Rupp et al. when developing an injury criterion for the knee-thigh-hip complex. Rupp et al. noted differences in injury pattern based on duration of knee impact loading. For long duration loads, hip fractures and dislocations were observed more frequently, while knee injuries were reported more often for short duration impacts, which may be explained by the rate of mass recruitment and inertia. Rupp et al. used lumped mass models of the human and Hybrid-III legs to demonstrate frequency dependence of the biofidelity of the Hybrid-III force response.[184,186]

2.5 Anthropomorphic Test Devices

An important aspect of the development of an injury criterion is the ability to use it alongside an anthropomorphic test device (ATD) to predict injury risk. In general, ATD legs have limited biofidelity across large ranges of loading rates because of design criteria which include the ability to withstand large forces without breaking like the human body. This design criteria generally leads to ATDs composed of stiff materials such as steel and aluminum, which often do not exhibit the same load-rate dependence as the human body.

It is important to understand the limitations of particular ATDs before using them to interpret injury risk, though this concept is often ignored because of both a lack of understanding of the effects of load rate on the human body compared to the ATD as well as the absence of an ATD that can perform in a biofidelic manner across a wide range of loading rates. While automotive ATDs have a better defined loading environment for which an ATD leg must be biofidelic, military applications such as UBB can cover a vast range of loading rates which are currently outside of the range of biofidelity for automotive ATDs. A few of the prominent ATD legs that are currently used are described for reference purposes, though more detail will be provided in a later chapter.

The most commonly-used ATD leg is the Hybrid-III leg, which is used by both military and automotive industries to assess injury.[151] The 50th percentile Hybrid-III leg consists of a 4.29 kg lower leg and a 1.16 kg foot with a knee-to-floor length, foot length, and foot height of 492.8 mm, 259.1 mm, and 99.1 mm respectively.[237] Instrumentation includes a proximal and distal tibia 5-axis load cell, and a 3-axis accelerometer package located at the mid-shaft of the tibia. The Hybrid-III tibia shaft has a 9 degree posterior tilt, giving the knee an 8 mm offset from the center of the ankle.[102] This contributes to bending moments and off-axis forces in the tibia when the leg is under axial loads.

Several researchers have demonstrated the Hybrid-III's lack of biofidelity at higher loading rates.[10,113,114,135] Kuppa et al. developed a transfer function for Hybrid-II and PMHS tibia force, while Bailey et al. generated a FE-based polynomial function for predicting PMHS force from Hybrid-III force measurements.[10,114] Both of these studies indicated that the Hybrid-III's stiff construction led to overestimation of human tibia force for higher impact velocities. McKay and Bir reported that peak Hybrid-III forces exceeded 2-3 times the peak force measured in the human leg for matched input conditions.[136]

The Thor-Lx Advanced Lower Extremity (Figure 2.19) instrumentation is more extensive than that of the Hybrid-III lower leg, containing a knee shear displacement potentiometer, 5-axis upper and lower tibia load cells, a 3-axis tibia accelerometer package, Achilles load cell, 3-axis ankle rotation potentiometer, and 3-axis foot accelerometer package.[235] This leg allows for the simulation of muscle resistance in the leg by applying load via a structure representing the Achilles tendon, and incorporates a more realistic ankle joint center than the Hybrid-III. The injury criteria for the ankle and calcaneus injury was defined as a distal tibia axial force of 5.2 kN and 6.8 kN for 25- and 50-percent probability of AIS 2+ injury, respectively. Proximal tibia forces of 5.6 kN and 7 kN are associated with 25- and 50-percent probability of tibia plateau fracture for the Thor-Lx.[113]

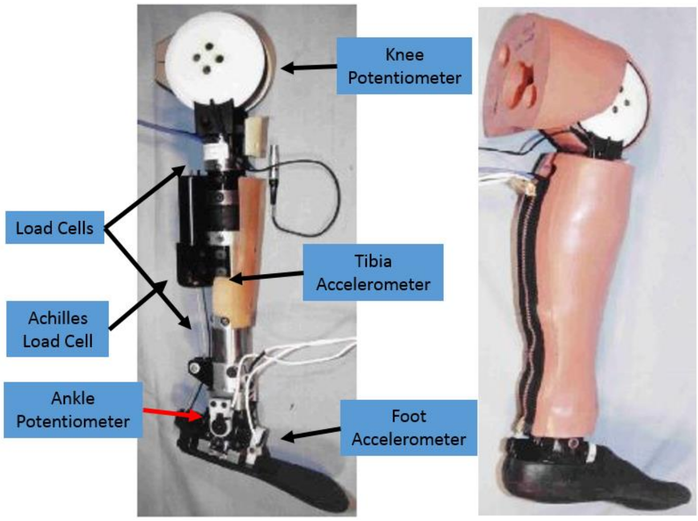

Figure 2.19. Thor-Lx ATD leg pictured with and without the flesh. (Image modified from NHTSA report.)[146]

The Mil-Lx or the Military Lower Extremity (Figure 2.20) was designed specifically for military applications because of the inadequacies of existing ATD legs when used in high-rate loading environments. The Mil-Lx contains 5-axis upper and lower tibia load cells, a 3-axis mid-tibia accelerometer, 3-axis mid-foot accelerometer, and a SAE-Z axis heel accelerometer.[97] The design of the Mil-Lx combined elements from the Hybrid-III ATD leg and the Thor-Lx leg by including a replaceable heel pad insert and a compliant puck in the shaft of the leg. The compliant element of the Mil-Lx is twice the length of that in the Thor-Lx (100 mm compared to 50 mm) and is located distal of the proximal (upper) tibia load cell.[134] Having been designed specifically for military underbody blast applications, this ATD leg has only been used by a small subset of the biomechanics community. Even within military underbody blast testing, the Hybrid-III is used more frequently than the Mil-Lx because of the Hybrid-III's availability, cost, durability, and its perceived usefulness for comparing to previous literature.[13,151]

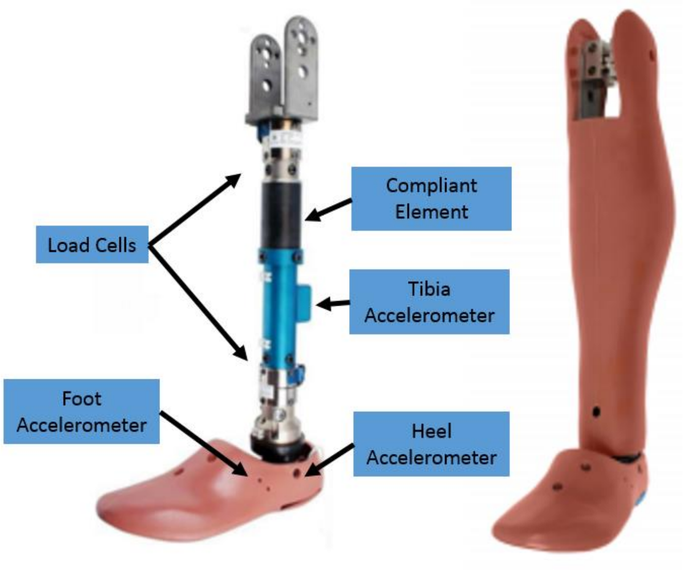

Figure 2.20. Mil-Lx ATD leg with and without flesh showing instrumentation locations.[97]

NATO standards for evaluating armored vehicles suggest evaluating probability of lower leg injury using the upper tibia force measured in the Mil-Lx are based on the injury probability function developed by McKay and Bir.[135] A Mil-Lx upper tibia force of greater than 2.6 kN, and a Hybrid-III lower tibia force of 5.4 kN from Kuppa et al. are considered injurious for axial compression.[116,135,151] The existence of separate force criteria for these two ATDs emphasizes the fact that they have different responses to the same input and were developed for different purposes. The Mil-Lx was specifically designed to be used for the study of UBB, however, the availability of the Hybrid-III makes it the most commonly used ATD leg for military testing, leading to the existence of a large amount of data with little meaning in terms of providing an estimate of human leg response or injury risk.

2.5.1 Signal Comparison

Several methods exist for quantifying the biofidelity of ATD response. Some of these methodologies include Cumulative Standard Deviation (CSD) and Correlation Analysis (CORA).[85,179] While other simpler statistics exist for the purpose of comparing two traces, such as sum of squared errors or summation of the differences for samples along the length of each curve for one or both variables, these more involved methods consider multiple aspects of curve similarity.

Rhule et al. introduced the method of Cumulative Standard Deviation and utilized it in the Biofidelity Ranking System (BioRank).[179] Cumulative Standard Deviation is calculated by summing the standard deviation for each time point of a signal compared to a reference curve. For BioRank, the cumulative variance is calculated between the ATD response and the average PMHS response and then divided by the cumulative variance for the PMHS responses. A cumulative standard deviation or cumulative variance of zero means that there is a perfect match between the signals.[179]

Correlation Analysis is a rating system developed by Gehre et al. to compare curves using corridor and cross-correlation methods.[85] The cross-correlation portion combines three individual scores: *magnitude*; *progression*; and *phase*. The magnitude score, also referred to as the *size* score, is calculated using the square of the area between the two signals. The progression rating is calculated using the cross-correlation which utilizes time-shifting of a reference curve to compare the curves which provides and estimation of the similarity of the shape of the two curves. Lastly, the phase score is calculated by comparing the value of each of the signals at two points in time within the time interval and evaluates the time shift between the signals. Each of the scores ranges between 0 and 1, with 1 being a perfect match. The overall CORA score for the cross-correlation methods combines these three individual scores with equal weighting (w_i) (see Eqn. 2.7). The CORA score may also incorporate a separate *corridor* rating, which rates each point of the curve on its position with respect to two degrees of corridor width.[85] Overall CORA scores have been classified in the 2013 International Organization of Standardization document as excellent (CORA>0.94), good (0.94≥CORA≥0.80), fair (0.8≥CORA≥0.58), and poor (CORA≤0.58).[100]

$$\boldsymbol{CORA = w_1(magnitude) + w_2(progression) + w_3(phase)} \qquad \text{Eqn. 2.7}$$

Vavalle et al. compared several methods for rating the similarity between curves and their ability to assess biofidelity. They concluded that CORA provided the most “comprehensive evaluation” of the similarity of curves based on the ability of each of the measures to evaluate different aspects of the signal characteristics.[207] In a similar study, Gayzik et al. concluded that CORA’s separation of individual scores provides beneficial information for understanding the nature of the relationship between individual signals.[84]

2.6 Discussion

The recent focus on military underbody blast (UBB) events has led to an increased desire to understand the effect of short duration, high amplitude loading on the human body. Foot and leg injuries due to axial loading are of particular interest because of proximity to application of the load through the vehicle floor. Currently, Mil-Lx and Hybrid-III ATD legs and their associated axial loading injury criteria are used to evaluate the safety of military vehicles when exposed to UBB.[151] Though it is well established that the Hybrid-III leg overestimates the force in the human tibia for higher velocities, little is known about the biofidelity of the Mil-Lx for loading conditions apart from the 7 m-s^{-1} condition used to tune the original design.[13,114,136] The uncertainty associated with the biofidelity of each of these

ATDs within the expansive UBB loading environment is cause for even greater concern when considering that floor mats, boots, and other designs for protecting the warfighter have potential to change the characteristics (e.g. magnitude, rate, duration) of the load applied to the foot in these events. These factors highlight the need for a single ATD and injury criterion that can be used to evaluate injury risk across a wide range of loading rates in order to ensure that injury mitigation strategies for military vehicles are effective.

Various injury risk functions have been developed for axial loading of the leg,[15,70,108,109,136,229,231] but fail to account for important factors which prevent their use for a wide range of load durations and frequencies. Many of the injury risk functions were developed for predicting injury in automotive intrusion events so the experimental data covers a smaller range of loading frequencies than is applicable to UBB. Additionally, the fact that the injury risk functions were based on forces measured at different locations prevents a clear understanding of the overlap between injury risk functions. Inertial differences between the location of force measurement and the location of injury may cause significant error in the estimation of injury risk depending on the input and boundary conditions.

The numerous PMHS leg axial loading studies in the literature provide a good starting point for understanding the differences between the injury risk of the leg in mitigated and unmitigated UBB events. The aforementioned similarity in the types and distribution of injuries caused by AI and UBB events suggests that data from each of these loading environments may be combined to develop an injury risk function to cover the range of loading conditions typical of mitigated and unmitigated UBB. The literature has shown that the time-to-peak for floor acceleration in UBB events can be as short as 1.25 ms. Automotive intrusion events were shown to have accelerations pulses which peaked at 50 ms. In order to encapsulate both AI and UBB loading environments, an injury risk function would need to be valid for load durations ranging from 3 to 100 ms, assuming symmetric loading and unloading.

Shortcomings of previous axial leg injury criteria are that they have failed to consider the importance of loading frequency and inertial shielding between forces measured at different locations. The studies aimed at understanding the effect of UBB on the leg[94,135] have different proximal boundary conditions and instrumentation locations than others performed at automotive conditions,[109,196,231] making it difficult to understand the effect of higher loading frequencies on the lower leg. At higher loading accelerations, it becomes increasingly important to measure the load closer to the region of interest because of inertial effects. As the acceleration of the leg increases, the greater the difference between the forces measured in one location versus another location due to the mass present between the load cell and region of interest. While previous IRFs may be valid for the data set from which they were generated (assuming loading rates were not varied), deviations from the input or boundary conditions of that particular test setup decrease the predictive ability of that IRF for other data sets. Thus, it is important to consider this when applying an IRF to a new data set to predict injury. While force is widely accepted as an injury predictor for the leg, previous studies and dynamic theory have demonstrated that force at fracture in other body regions is duration-dependent.[197,209,214] The incorporation of duration-dependence is vital to developing an injury risk function for the leg which can span the range of loading frequencies applicable to AI and UBB.

Integrating duration- or frequency-dependence into an injury criterion for the leg enhances the importance of ensuring that ATD response can be correctly interpreted for all applicable loading frequencies. Understanding the behavior of ATDs in terms of frequency response is crucial to interpreting human injury risk based on its measurements. While an ATD may produce a biofidelic force response for one loading condition, it may not necessarily be valid for another loading condition, as Kuppa et al. demonstrated for the Hybrid-III leg.[114] The Mil-Lx leg's ability to provide a biofidelic response for high velocities typical of UBB without railing the load cells and other instrumentation makes it a better candidate than other existing ATD legs for a universal ATD leg which can span the range of loading frequencies from AI to UBB.

2.7 Objectives

Using previous duration-dependent injury criteria as precedence, the objective of this dissertation is to develop a duration-dependent injury criterion for the leg exposed to axial impact loads that could be used for both mitigated and unmitigated loading from automotive and military underbody blast environments. A secondary objective is to assess the ability of an existing anthropomorphic test device leg, the Mil-Lx, to provide a biofidelic response for both automotive and military loading environments. A combination of experimental testing and analytical and finite element modeling will be used to satisfy the following specific aims of this dissertation:

1. Demonstrate the duration- and frequency-dependence of force at fracture using experimental testing and finite element modeling.
2. Create lumped-parameter models for the human leg to aid in development of injury criterion and ATD design.
3. Develop an injury criterion for the leg to incorporate duration- and frequency-dependence.

4. Compare the predictive accuracy of the proposed duration-dependent injury criterion to that of previous peak force-based injury criteria.
5. Provide an assessment of the Mil-Lx anthropomorphic test device for mitigated and unmitigated underbody blast environments and, if necessary, recommend design changes to expand the range of loading frequencies for which it can assess injury risk.

3 Experimentation

3.1 Introduction

In effort to increase the number and range of loading conditions, a number of tests were conducted at the University of Virginia Center for Applied Biomechanics using component PMHS legs. This chapter discusses two separate test series which served the purpose of providing additional leg injury data under two separate proximal tibia boundary conditions: all degrees of freedom fixed (fixed); and all degrees of freedom fixed except SAE-z translation (free), but inertially weighted. The "free" boundary tests were performed using a drop tower setup and provided additional short-duration data, which the literature previously lacked. The "fixed" boundary tests were performed using a linear impactor; these tests were used to test the statistical significance of the difference in force and impulse at fracture for different load durations.

3.2 PMHS Component Experimentation

3.2.1 Drop Tower Test Methodology

A series of 18 PMHS component leg tests were performed using a drop tower to deliver an axial load to a footplate in contact with the plantar surface of the foot, with the proximal tibia restricted to SAE-z translation. The PMHS legs, disarticulated inferior to the patella, were procured for the study via the Virginia State Anatomical Board and other tissue suppliers; screened for Hepatitis A, B, and C, and HIV; and fresh-frozen after acquisition. All test protocols were subject to review and approval by the University of Virginia Cadaver Use Committee. A pre-test DEXA and computed tomography (CT) scan were performed to screen for pre-existing fractures and verify that the bone mineral density was greater than the threshold between osteopenia and osteoporosis (T-score 2.5).[225]

First removing the soft tissue, the proximal tibia was potted in a steel cup using Fast Cast polyurethane casting resin (Goldenwest Manufacturing, Cedar Ridge, CA). The specimens were then placed in the UVA drop tower fixture with the proximal mating cup attached to a six degree of freedom load cell and an aluminum plate (load cell plate). The position of the leg was such that the plantar surface of the foot faced vertically upward in contact with a second aluminum plate (impact plate) of mass 10.2 kg. Both plates were constrained in the X- and Y- directions, but free to translate in the Z-direction (SAE coordinate system).[188] The proximal tibia boundary conditions consisted of a reaction mass comprised of the load cell, load cell plate, and the potting cup, totaling 7.2 kg, which is equivalent to the effective mass acting at the proximal tibia for a 50th percentile male determined using an FE simulation of a representative UBB event at 600g. For three cases (tests 1.5-1.7), proximal tibia was fully constrained. The stroke of the impact plate was limited by the use of shaft collars (Figure 3.1). Post-test CT scans and necropsies were performed to determine injuries caused by the impacts. Some results from this study are discussed in Section 4.

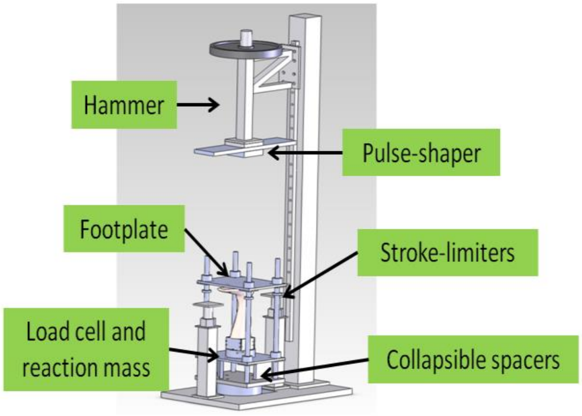
Hammer
Pulse-shaper
Footplate
Stroke-limiters
Load cell and reaction mass
Collapsible spacers

Figure 3.1. Drop tower test fixture schematic showing the load cell plate lightly supported by polystyrene crushable supports and a weighted hammer.[94]

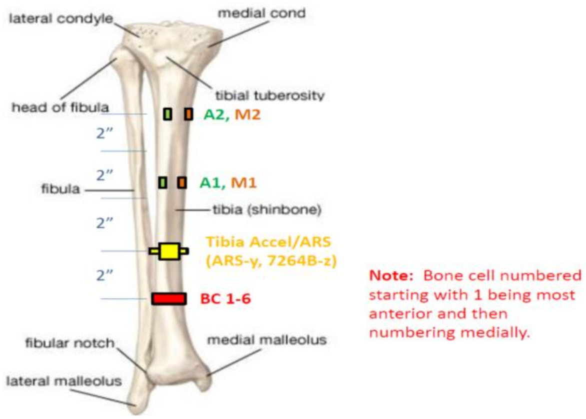
lateral condyle
medial cond
tibial tuberosity
head of fibula
A2, M2
2”
2”
fibula
A1, M1
tibia (shinbone)
2”
Tibia Accel/ARS
(ARS-y, 7264B-z)
2”
BC 1-6
Note: Bone cell numbered starting with 1 being most anterior and then numbering medially.
fibular notch
medial malleolus
lateral malleolus

Figure 3.2. Tibia instrumentation consisting of strain gages, accelerometers, and angular rate sensors

For this series, multiple input conditions were investigated. These conditions were obtained by varying drop heights, hammer masses, and pulse shaping material placed on the hammer impact surface. Drop distances ranged from 1 to 2.3 m and hammer masses ranged from 38.5 to 61.2 kg. Two different pulse shapers, as listed in Table 3.1 were placed between the hammer and impact plate to shape the acceleration: (1) a 38mm thick sheet (155x155 mm) of expanded polystyrene (E=413 kPa) and (2) a 105x120 mm block of crushable aluminum honeycomb (E=10.3 MPa) with a 6.4 mm layer of latex.

A combination of load cells, accelerometers, angular rate sensors, acoustic emission sensors, as well as a laser displacement device for capturing impact velocity and displacement were used in this study. Force, strain, and acceleration data were acquired through a TDAS (Diversified Technical Systems, Inc., Seal Beach, CA) data acquisition system at a sampling rate of 20 kHz with an anti-aliasing filter of 4 kHz. Laser displacement (Keyence America, Elmwood Park, NJ) and acoustic emission data were collected by a Synergy CS (Hi-

Techniques, Inc., Madison, WI) high speed data acquisition system at a sampling rate of 1 MHz with an anti-aliasing filter of 200 kHz.

Each specimen was instrumented with 12 strain gages (Micro-Measurements C2A-06-062LW-350) attached along the tibia diaphysis and the medial and lateral calcaneus to capture strains in the SAE-Z direction using cyanoacrylate adhesive (Figure 3.2). An SAE-Z accelerometer (Endevco 7264B-2000) and an SAE-Y angular rate sensor (ARS-8k) were attached to the tibia using a non-intrusive worm-drive clamp design.

Table 3.1. Test matrix for drop tower test conditions containing averages and standard deviations. Measurements were taken from an accelerometer on the impact plate of the test fixture.

Test Condition	Number of Tests	Hammer Mass (kg)	Impact Accel. (g)	Time-to-peak Az (ms)	Reaction Mass (kg)
Drop Tower P0	2	38.5	204.6 (21.7)	8.33 (0.60)	7.2
Drop Tower P1	3	38.5*	361.9 (150.9)	4.07 (2.98)	∞
Drop Tower A	6	61.2	515.0 (44.7)	1.5 (0.1)	7.2
Drop Tower B	7	34.2	485.4 (92.6)	2.2 (0.1)	7.2

Reported values are averages with (standard deviations)
*Includes one test using different hammer mass

A preliminary lumped-mass model (LMM) was developed based on the drop tower data in a previous paper;[94] however, a reanalysis of the data would lead to an improved understanding of leg response, particularly if the data is combined with additional PMHS data with various loading conditions. A new LMM (to be discussed later) will be fit using a different distribution of mass in order to accommodate a variety of boundary conditions and compare to the Mil-Lx ATD. Additionally, this data was used by Gabler et al. to improve the biofidelity of a human finite element model.

3.2.2 Linear Impactor Test Methodology

Additional leg component tests were performed using a pneumatic linear impactor. Extra instrumentation was added for these tests, particularly a footplate load cell, calcaneus accelerometer, and three 6-axis accelerometer-angular rate sensor cubes along the length of the tibia. Having obtained information about the injuries expected from a proximal tibia boundary allowed to translate in the SAE-z direction from the drop tower tests, a fixed proximal boundary (no translation or rotation) condition was used for the impactor tests. The potted proximal tibia boundary provides a boundary condition which can be more easily modeled compared to the Funk et al. (2002) tests which included the knee resting against a fixed boundary. These tests will improve the understanding of the response of the leg itself rather than be complicated by the behavior of the knee joint.

For these tests, a composite structure foot platen was impacted with the foot placed on the platen prior to impact. The transfer piston of the linear impactor contacted a polyurethane or Sorbothane rubber (Sorbothane, Inc., Kent, OH) pulse shaper to control the input pulse to the foot. The limbs were potted using methods similar to those used for the drop tower test, and instrumented according to Figure 3.3. Prior to and after potting, the specimen was weighed to determine specimen mass. The test rig, shown in Figure 3.4, includes a proximal tibia load cell (mounted to the potting cup), a footplate load cell, platen accelerometers, and load cell accelerometers for mass compensation. The test fixture is mounted to a reaction sled which remained in a fixed position for all tests.

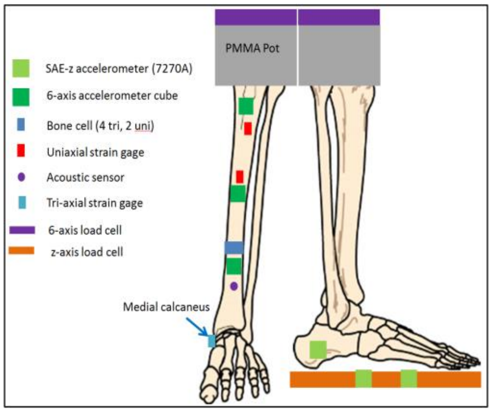
PMMA Pot
SAE-z accelerometer (7270A)
6-axis accelerometer cube
Bone cell (4 tri, 2 uni)
Uniaxial strain gage
Acoustic sensor
Tri-axial strain gage
6-axis load cell
z-axis load cell
Medial calcaneus

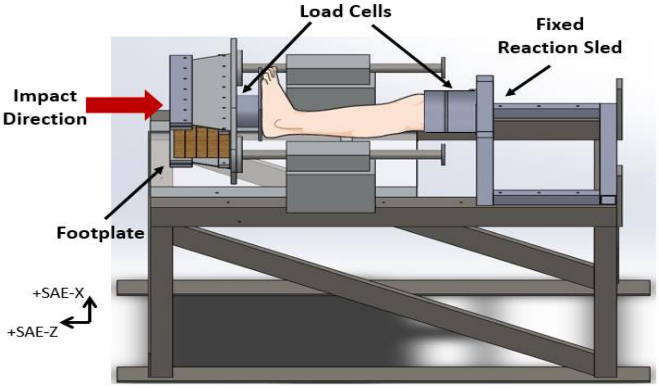
Load Cells
Fixed Reaction Sled
Impact Direction
Footplate
+SAE-X
+SAE-Z

Figure 3.3. Instrumentation for PMHS component impactor tests, which included strain gages, accelerometers, an acoustic sensor, and load cells.

Figure 3.4. Lower extremity test rig, using a pneumatic linear impactor and polyurethane pulse-shapers. The figure shows the location of the footplate and proximal tibia load cells.

The test matrix shown in Table 3.2 consists of testing 36 PMHS leg components using three different hammer velocities. The goal was to produce injury at intermediate and high levels and perform a paired Student's t test to determine whether the average force at fracture is significantly different to a significance level of p=0.05. The low tests were to be sub-injurious to provide response data for benchmarking finite element models and comparing to ATD response.

Table 3.2. Test matrix for impactor test conditions containing averages and standard deviations. Measurements were taken from an accelerometer on the test fixture footplate.

Test Condition	# of Tests	Acceleration (g)	Time-to-peak (ms)	Velocity (m/s)	Time-to-peak (ms)	Stroke Limit (mm)
Low	12	7.3 (1.4)	7.60 (0.77)	0.5 (0.1)	13.63 (0.92)	50
Intermediate	12	75.1 (7.9)	3.48 (0.04)	2.4 (0.1)	7.69 (0.25)	50
High	12	192.3 (6.1)	3.50 (0.23)	4.5 (0.5)	8.11 (0.52)	38

Reported values are averages with (standard deviations)

High speed dynamic x-ray was used during these tests to provide further information about location and progression of injury during axial loading. While previous studies used acoustic emission to estimate time of fracture,[73] the use of dynamic x-ray will provide critical information about time and location of fracture initiation, which will be valuable for providing information about how to analyze previous injury data (Figure 3.5). While the acquisition rate is lower for the dynamic x-ray (5000 Hz), it provides additional information which is helpful for interpreting the acoustic emission and strain gage data also collected for these tests.

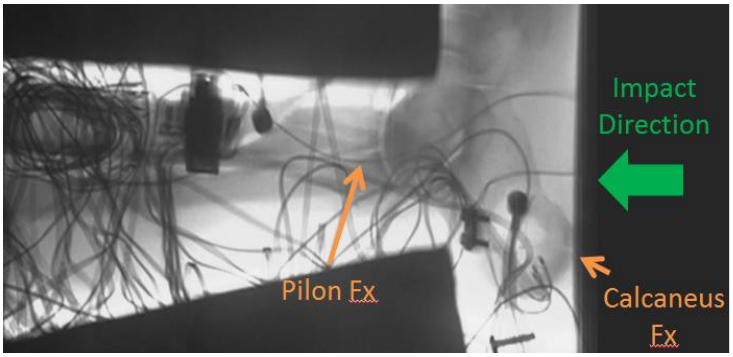

Figure 3.5. Dynamic lateral x-ray frame from an injurious intermediate level impactor test showing fracture of the calcaneus and tibial pilon.

The fixed boundary condition used in these tests enabled greater control of input conditions than was achieved using the drop tower setup. Potting the proximal tibia, though an unrealistic boundary condition, allowed for a simpler boundary condition at the proximal tibia and helped provide additional information about the response of the tibia itself as opposed to the Funk et al. study[70] which included compliance of the knee. Further, this test setup did not include a compliant interface between the aluminum footplate and the foot, which further simplified the boundary conditions to allow for assessment of how variation of input conditions affects the leg.

3.2.3 Data Processing

All data was filtered using a CFC 1000 filter[188] and accelerations were transformed to a local body-centric leg coordinate system based on landmarks described by Wu et al.,[226] and aligned with the Society of Automotive Engineers J-211 coordinate system [188]. While these transformations were possible for the impactor tests, not enough data was collected to perform these transformations for the drop tower tests due to lack of off-axis instrumentation in this test series. To reduce anatomical variability in the data, the accelerations and forces were scaled to 50th percentile human male leg mass (4.54 kg) using the Global Human Body Model Consortium (GHBMC) 50th percentile male finite element model to estimate the leg mass,[199] and using an equal velocity-equal stress scaling technique.[62] Leg compression was normalized to the length of the leg from the edge of the plate to the edge of the pot, which was approximately the most proximal point of the tibia; this distance was estimated to be 532 mm using the GHBMC model. Additionally, average responses and +/- one standard deviation corridors were produced for each test condition using the method described by Lessley et al. which uses an elliptical technique to account for variance in both variables being analyzed.[123]

3.2.4 Results

Average test conditions for both impactor and drop tower studies are provided in Table 3.3 and average results are reported in Table 3.4, separated by test condition. Force rates were estimated using the slope from 20- and 80-percent of the peak proximal tibia force for each test, and all forces reported were mass-compensated if the load cell was not stationary. Injuries from both the drop tower and impactor tests included calcaneus, talus, and distal tibia (pilon) fractures. These injuries are outlined in further detail in supplemental electronic resources and will be discussed in a future publication when necropsies have been completed. Table 3.4 shows that the highest force rates were recorded for the Drop Tower A condition, while the highest peak forces were reached with the Impactor High condition. Despite having higher impact velocities, the impactor tests had lower footplate velocities than the drop tower tests.

Table 3.3. Summary of test conditions for drop tower and impactor tests

Test Condition	Number of Tests	Impactor Mass (kg)	Impact Velocity (m/s)	Reaction Mass (kg)	Energy (kJ)
Drop Tower A	6	61.2	5.25 (0.60)	7.2	8.53 (1.80)
Drop Tower B	7	34.2	4.86 (0.35)	7.2	4.06 (0.60)
Impactor Low	12	10.5	3.48 (0.22)	∞	0.69 (0.08)
Impactor Medium	12	10.5	5.44 (0.69)	∞	1.70 (0.46)
Impactor High	12	10.5	11.13 (1.05)	∞	7.07 (1.39)

Velocities and energies are averages with (standard deviations)

Table 3.4. Averages and standard deviations for test results

Test Condition	Peak FP Acceleration	Acc. Time-to-peak	Peak FP Velocity	Vel. Time-to-peak	Peak Force[1]	Force Rate[2]
	(g)	(ms)	(m/s)	(ms)	(kN)	(N/ms)
Drop Tower A	515.0 (44.6)	1.5 (0.1)	6.7 (0.2)	3.10 (0.07)	6.29 (1.37)	7334 (1905)
Drop Tower B	485.2 (92.4)	2.2 (0.1)	5.0 (0.5)	2.82 (0.13)	8.44 (1.51)	4622 (1199)
Impactor Low	7.3 (1.4)	7.60 (0.77)	0.5 (0.1)	13.63 (0.92)	4.91 (0.8)	373 (85)
Impactor Medium	75.1 (7.9)	3.48 (0.04)	2.4 (0.1)	7.69 (0.25)	10.96 (2.36)	2226 (361)
Impactor High	192.3 (6.1)	3.50 (0.23)	4.5 (0.5)	8.11 (0.52)	14.39 (4.83)	4391 (876)

FP=Footplate
Average values are reported with (standard deviations)
Note: All acceleration and force values are for the negative SAE-z direction.
[1] Forces were mass compensated and mass normalized to a 4.54 kg component leg mass
[2] Force rates were calculated using slope between 20 and 80% of peak proximal tibia force

Response corridors are presented in Figure 3.6 A-F for footplate acceleration, proximal tibia force, and force versus leg compression. These corridor plots show the average response and +/- one standard deviation of the mean. Despite the precision of the input acceleration for each test condition and normalizing the data by mass and length scaling, variation is shown in the output responses due to specimen variability. Additional results for forces and compressions are provided in Appendix 10.3, and Table 3.5 provides a summary of individual PMHS test results. Additional injury details can be found in Appendix 10.2.

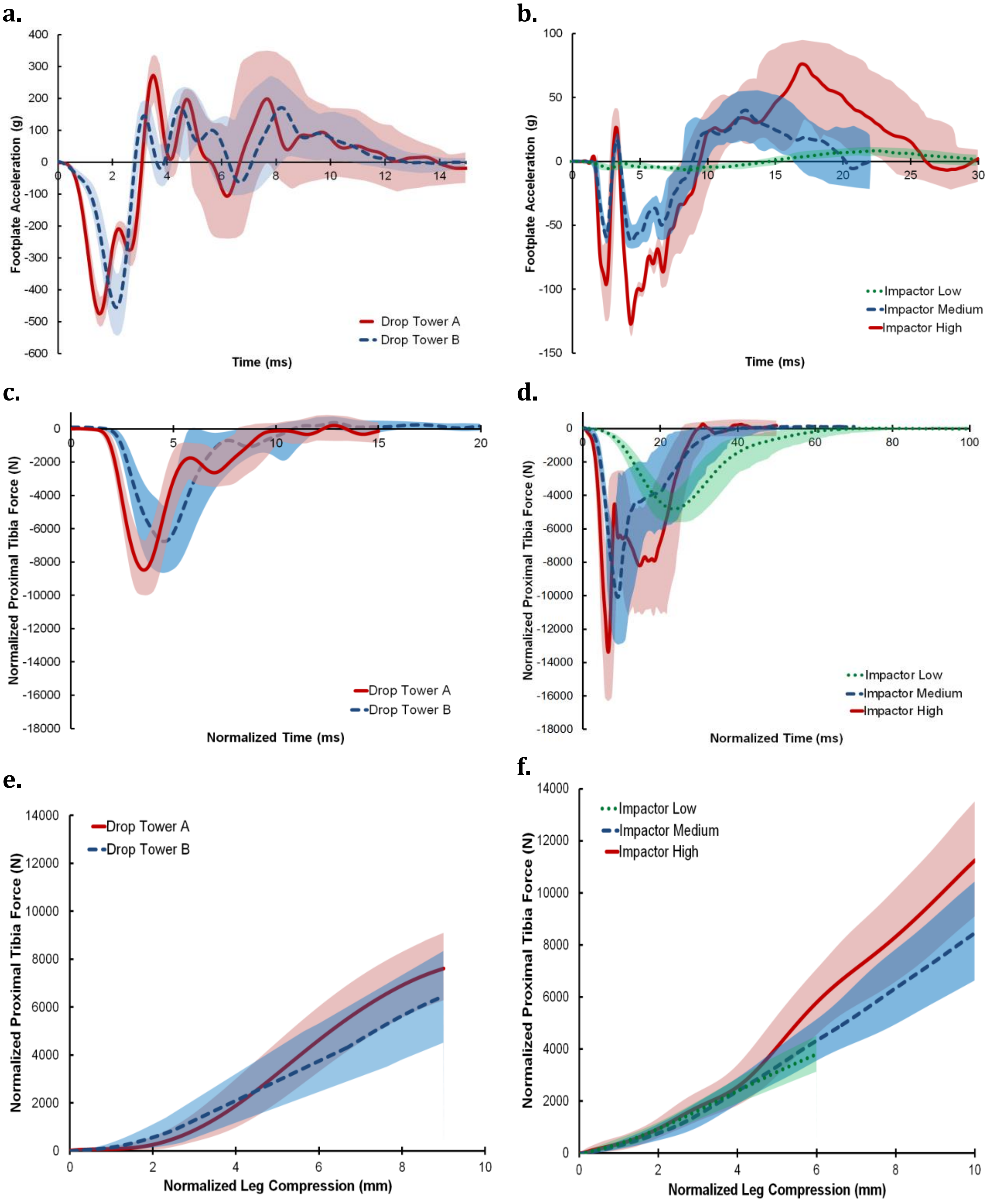

Figure 3.6. Footplate acceleration (a, b), proximal tibia force (c, d), and force-compression (e, f) response corridors for drop tower and impactor tests. Forces were mass-normalized and compressions were length-normalized to represent the response of a 50th percentile male subject. Note that tests Impactor 09 and Impactor 27 were excluded from the force-compression corridor due to eversion of the foot during the test.

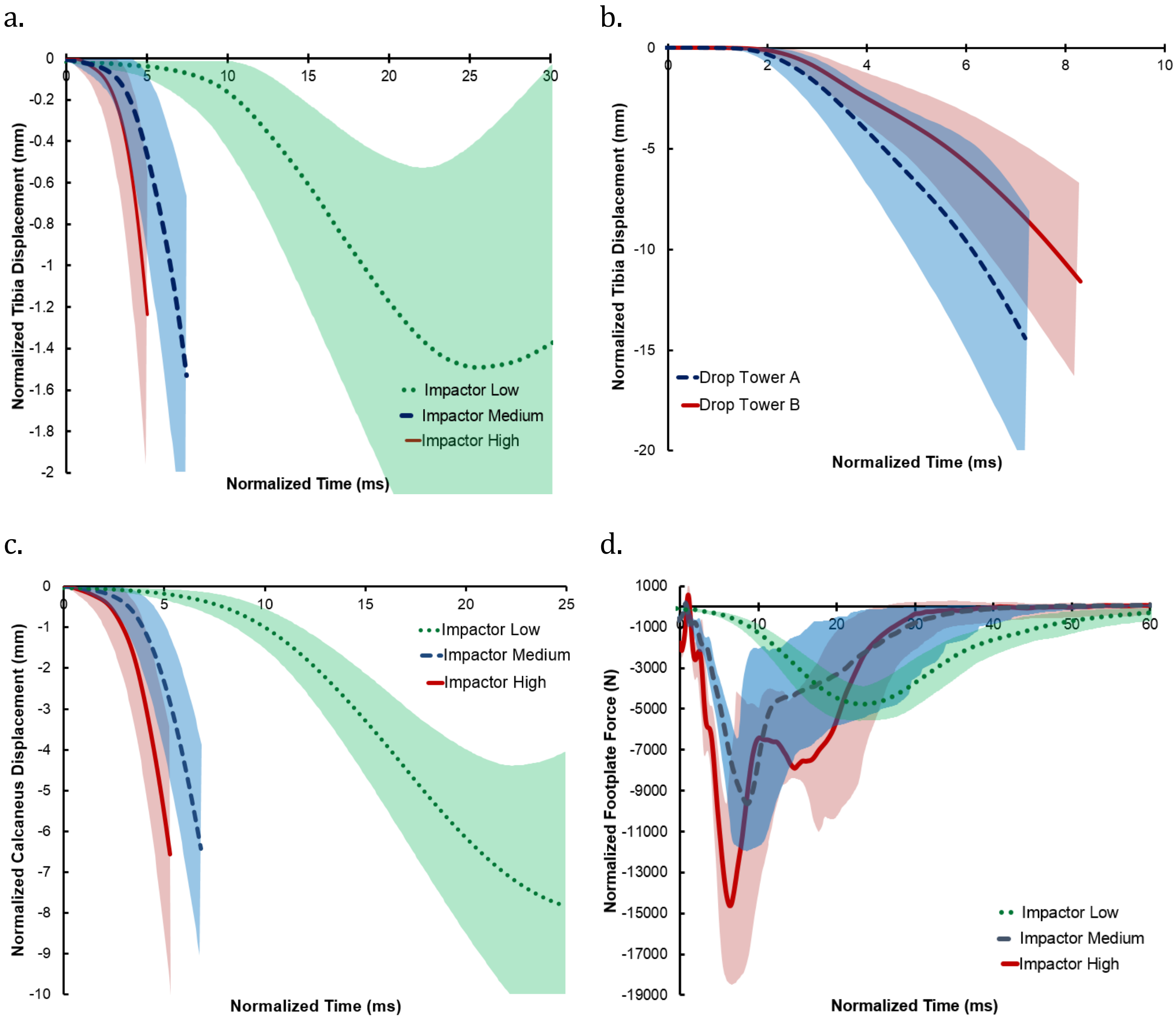

Figure 3.7. Tibia displacement (a, b), calcaneus displacement (c), and footplate force corridors for drop tower and impactor test conditions. Tibia displacements were calculated from transformed distal tibia acceleration for the impactor study, and untransformed single-axis acceleration for the drop tower study. Calcaneus displacements were calculated from single-axis accelerometers mounted to the calcaneus.

Table 3.5. Summary of Component PMHS Test Results

Test ID	Test Condition	Age	Mass	Peak Prox. Force	Force Rate	Peak AZ	Fx Strain	Strain Rate	Fracture*
		(years)	(kg)	(kN)	(N/ms)	G	(uS)	(uS/ms)	
Imp 01	Medium	62	104	11.29	2.19	72.8	-	-	C, P
Imp 02	Low	60	75	2.97	0.40	7.7	804	91	NF
Imp 03	Low	63	80	3.05	0.32	6.2	1958	273	NF
Imp 04	Low	42	104	3.29	0.44	9.4	885	116	NF
Imp 05	Low	67	72	3.53	0.45	8.8	4125	375	C
Imp 06	Low	74	73	3.60	0.35	8.8	3284	277	NF
Imp 07	Medium	28	81	14.04	3.08	66.1	4822	410	NF
Imp 08	Medium	65	97	7.83	1.73	65.0	5690	1261	C,T,P
Imp 09	Medium	66	86	8.82	2.06	67.2	4454	896	C
Imp 10	Low	56	62	3.61	0.31	5.2	2087	202	NF
Imp 11	Low	67	72	3.26	0.39	6.2	3347	335	NF
Imp 12	Low	74	73	4.76	0.24	5.7	1109	105	NF
Imp 13	Medium	60	77	9.39	1.71	74.8	4955	934	C, T, P, F
Imp 14	Medium	58	54	9.94	1.82	67.0	3285	720	NF
Imp 15	Medium	56	79	10.53	1.82	73.4	2874	775	C, P
Imp 16	Low	61	49	4.50	0.24	7.3	2160	171	NF
Imp 17	Low	61	49	4.50	0.30	6.5	1498	196	NF
Imp 18	Low	60	75	3.29	0.28	8.4	1735	134	NF
Imp 19	Low	65	95	3.75	0.32	7.6	679	78	NF
Imp 22	Medium	55	91	13.67	2.67	80.8	-	-	P, F
Imp 23	Medium	65	101	9.28	2.08	88.6	3056	900	C
Imp 24	Medium	59	64	6.67	1.89	78.2	5503	1784	C
Imp 25	Medium	65	118	12.48	1.90	83.5	4950	817	C, P
Imp 26	Medium	54	90	11.69	2.56	83.4	-	-	C, T
Imp 27	High	62	104	10.68	3.55	194.5	-	-	C
Imp 28	High	65	101	9.38	3.28	182.9	5600	2586	C
Imp 29	High	59	64	10.23	4.19	195.1	5528	1759	C
Imp 30	High	65	118	10.70	3.29	192.6	3440	727	C
Imp 31	High	65	97	8.01	5.29	186.7	6345	2187	C, P
Imp 32	High	54	90	12.59	4.55	194.6	6828	1158	C, P
Imp 33	High	28	81	18.39	5.14	182.0	6229	1980	C
Imp 34	High	60	77	11.77	4.77	192.3	7080	-	C, T
Imp 35	High	58	54	13.76	5.08	203.2	7065	1238	C, P
Imp 36	High	56	79	10.35	3.10	198.9	-	-	C, M
Imp 37	High	55	91	12.39	4.08	191.6	7135	1123	C, T, M
Imp 38	High	66	86	10.31	5.99	193.8	5530	1416	C
DT 08	A	59	118	10.44	6.93	541.4	-	-	C
DT 09	A	53	127	13.10	10.46	554.6	-	-	NF
DT 10	A	64	104	10.51	9.29	532.1	-	-	P
DT 11	A	53	127	12.86	12.16	447.5	-	-	C,T
DT 12	A	47	73	7.18	5.24	470.2	-	-	C
DT 13	A	60	104	9.21	8.09	544.2	-	-	C, P
DT 14	B	54	117	7.77	5.30	579.1	-	-	C, T
DT 15	B	47	73	6.97	6.46	605.1	-	-	C
DT 16	B	60	82	4.47	3.98	520.3	-	-	C
DT 17	B	60	82	5.05	3.30	338.8	-	-	C
DT 18	B	54	117	8.38	4.93	488.5	-	-	NF
DT 19	B	53	73	8.64	5.90	438.7	-	-	NF
DT 20	B	53	73	6.85	4.60	427.0	-	-	NF

*C=calcaneus fracture, T=talus fracture, P=Pilon fracture, t=tibia fracture, F=fibula fracture, M=malleolus fracture, NF=no fracture

Note: Since post-test necropsies were not performed for the impactor test series, only the fractures visible in the dynamic x-ray footage are reported. -Data is not normalized

Average maximum strain (or strain at failure) for the calcaneus for low, medium, and high impactor conditions was 1970±1110 µS, 4400±1060 µS, and 6080±1130 µS, respectively. Average strain rate calculated using 20- and 80-percent of the peak strain or strain at failure was 197±99 µS-ms^{-1}, 940±390 µS-ms^{-1}, and 1570±540 µS-ms^{-1} for low, medium, and high conditions, respectively. It is important to consider the limitations associated with the conclusions that can be drawn from the calcaneus strain data. Strain gages were placed in only one location on the calcaneus, and the dynamic x-ray footage shows that fracture in the calcaneus initiated at different locations. Thus, the maximum strain measured by the strain gage may not be a measure of failure strain. Further, the irregular geometry of the calcaneus results in complicated strain fields, which have potential to vary greatly from specimen to specimen.

3.2.5 Discussion of Results

The drop tower force-compression corridors show a distinct toe-region compared to those from the impactor tests. Since both test series used similar amounts of preloading (100 N in the drop tower tests and 116 N for the impactor tests), this behavior cannot be explained by differences in initial heel pad compression. Alternatively, this effect may be explained by the fact that since the proximal boundary is allowed to translate in the drop tower tests, mass is incrementally accumulated slower than for the fixed boundary. Additionally, the mass of the soft tissue of the leg may be recruited differently for the drop tower tests because of the translation allowed by the boundary condition. The limited motion in the impactor tests diminishes the leg’s soft tissue mass recruitment compared to the larger (yet still small) displacements allowed by the drop tower setup.

As expected, higher overall leg stiffness was estimated for higher leg compression rates in both test setups. Figure 3.8 shows that within each test setup, overall leg stiffness increased with force rate. For each of the impactor test conditions, force rate was significantly different, as was leg stiffness, according to Welch's t-test (α=0.05) results comparing means for individual test conditions (p<<0.01). The same was true for the two drop tower test conditions for both normalized and non-normalized data. Welch's t-test between Drop Tower B and Impactor High conditions revealed that though the force rates were not significantly different (p=0.67 for normalized data), estimated leg stiffness was significantly different (p=0.008). Further, Drop Tower A and Impactor High, and Drop Tower B and Impactor Medium conditions did not have significantly different leg stiffness (p=0.57 and p=0.10, respectively) despite having significantly different force rates (p=0.01 and p=0.002, respectively) for the normalized data. The same was true for the non-normalized data.

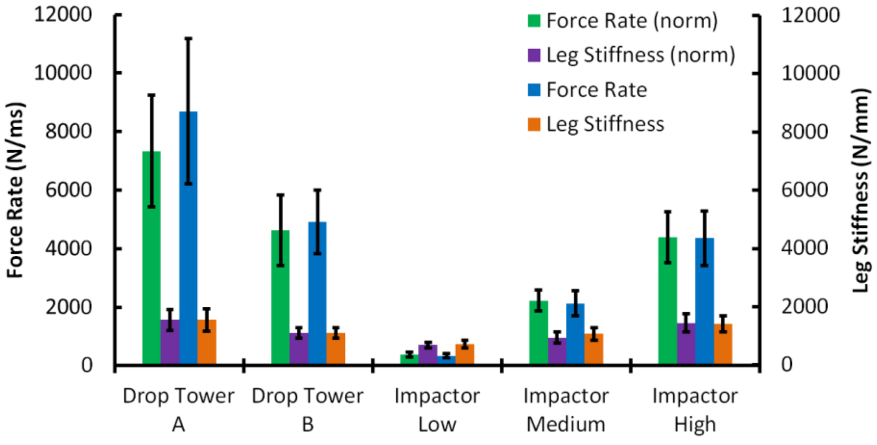

Figure 3.8. Comparison of leg stiffness and proximal tibia force rate for test groups showing that leg stiffness is significantly different for different load rates. Averages are shown for normalized and non-normalized data; error bars indicate ± one standard deviation.

These results are expected based on the concepts of momentum transfer and inertia. Despite having similar proximal tibia force rates, the estimated leg stiffness for the Drop Tower B condition is lower than for the Impactor High condition. This is due to the fact that higher forces (and larger compressions) are concentrated near the impact plate rather than transmitted to the proximal tibia where the forces are measured for the drop tower tests. When the leg is impacted at a high velocity, momentum is transferred to the foot, which produces localized deformations (or fractures) before transferring the momentum to more proximal structures. For lower momentum impacts, less deformation occurs locally before the transfer of momentum, thus accelerations close to the impact site are comparable to those at the proximal tibia, which reduces the difference between proximal and distal force rates.

Injury patterns are consistent with this concept. For tests with multiple fractured bones, calcaneus fractures occurred prior to the more proximal fractures, as evidenced by dynamic x-ray. Calcaneus fractures were a combination of both non-articular and articular, displaced and non-displaced. Comminution of the calcaneus was common in the tests in which the calcaneus was the only fractured bone (Figure 3.14, Figure 3.15). Less severe (non-articular or un-displaced) calcaneus fractures were present for the cases where pilon or talus fractures were also present. This pattern suggests that for the cases in which the calcaneus fractured to the extent that it could no longer transmit load, other fractures were not able to occur. Conversely, if the calcaneus was only slightly fractured (or not at all), the loads from the footplate were better able to transmit to other bones in the ankle to produce subsequent fractures.

To obtain a better understanding of how location of leg compression changes with load rate, tibia accelerometer data were used to estimate the percentage of leg compression associated with the foot/ankle and tibia. Results of this analysis showed that compression of the foot (heel pad and ankle compression) accounted for a majority of the total leg compression (>75%) at peak force and that as loading rate increased, the percentage of total leg compression was increasingly dominated by foot compression. The drop tower tests had a significantly larger percentage of foot compression at 20- versus 80-percent of peak force compared to the impactor tests (p=0.03). Though the results were not significant, test conditions with higher force rates had a larger proportion of foot compression at 20- compared to 80-percent of peak force. Normalized foot compression (as estimated from double integration of distal tibia and footplate accelerometers) versus proximal tibia force corridors are provided in Figure 3.9.

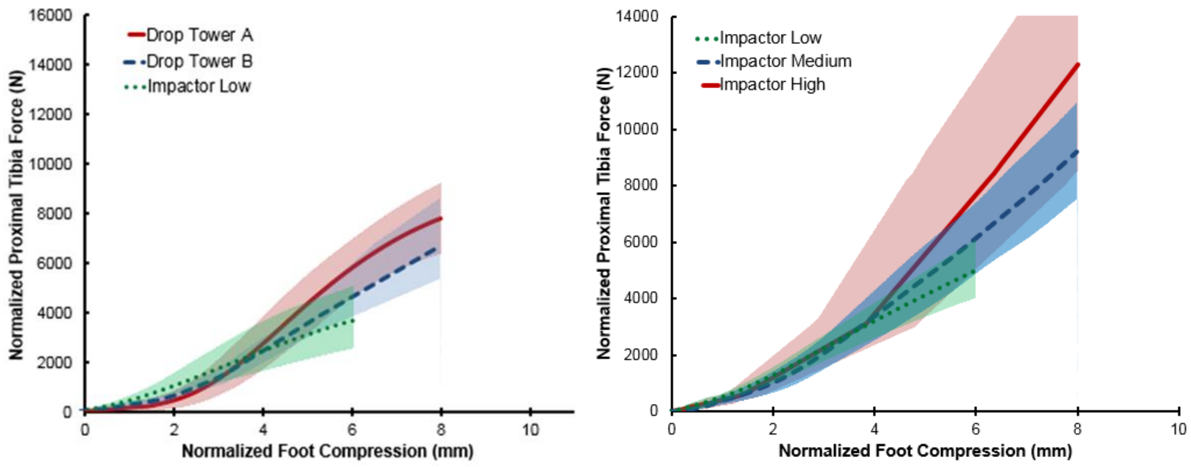

Figure 3.9. Normalized foot compression versus proximal tibia force corridors for the drop tower and impactor studies. The figure on the left shows the drop tower corridors with the Impactor Low condition overlaid for reference. The figure on the right shows the normalized foot compression versus proximal tibia force for the impactor conditions.

The leg stiffness estimated in this study, ranging from 706 N/mm for the Impactor Low condition to 1600 N/mm for the Drop Tower A condition are consistent with a study by Kuppa et al. which modeled the foot and leg as a single degree of freedom spring-mass-damper system with a spring stiffness of 963 N/mm.[114] Other studies found leg stiffness to be 174 and 142 N/mm, though loading rates are assumed to be lower than the current study.[6,42] Further, those studies which modeled the foot and leg separately as a multiple degree of freedom system for rates comparable to the current study found the leg stiffness (not including the foot) to be much higher (~8800 N/mm), while foot stiffness was estimated between 460 and 2000 N/mm.[94,106] These results are also consistent with the current study's results considering that the equivalent stiffness from combining those springs in series would range from 500-1600 N/mm.

3.2.6 Evaluation of Force as an Injury Predictor

The impactor study data was used to evaluate whether force duration affects force at fracture in the leg. Specimens in the intermediate and high loading groups were paired such that the right and left legs from 12 specimens were divided into these two groups. Since the age, sex, mass, and bone mineral density characteristics are assumed to be equal for these two groups, a t-test comparing the average force at fracture for the two groups should be sufficient. Figure 3.10 compares the impactor medium and high groups, where force duration and time-to-peak were different for each loading condition. Since the 9 ms and 15 ms groups contained leg specimens from the same whole body subjects, these two groups are directly comparable.

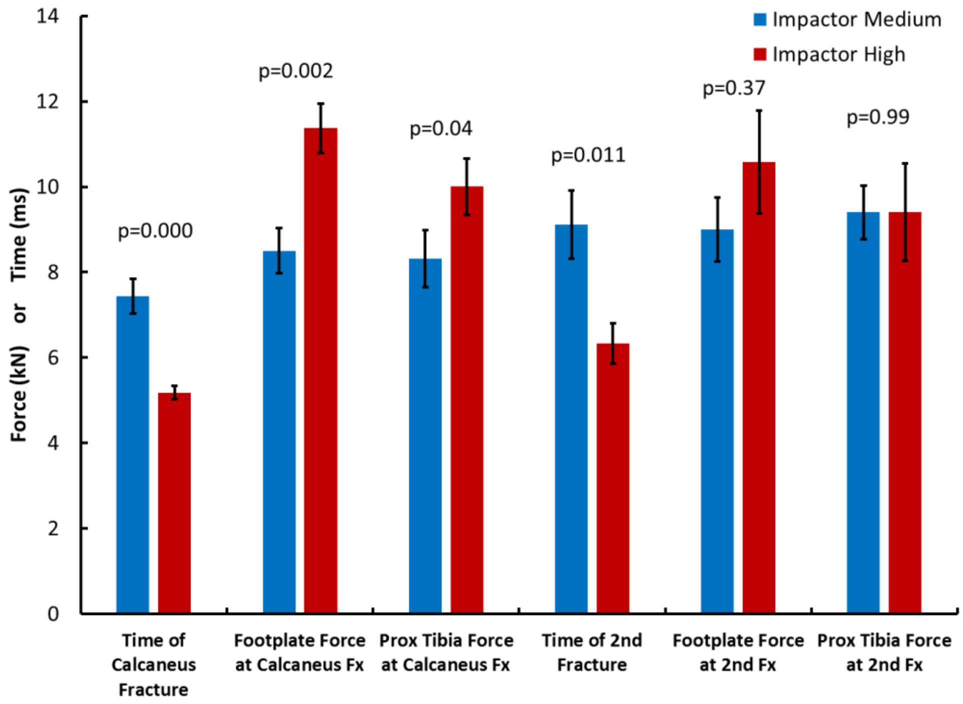

Figure 3.10. Average forces recorded for the footplate and proximal tibia at time of calcaneus fracture and time of the 2nd fracture (if applicable) for the impactor medium and high conditions. Standard error is indicated by error bars and p-values for a two-tailed t-test are shown for testing for difference in the averages.

As previously mentioned, risk of foot and leg fracture due to UBB loading is currently assessed using forces measured at the mid- and proximal tibia.[135,151,231] A previous study summarized the benefits of using force measured at the plantar surface of the foot compared to more proximal force measurements due to the frequency of calcaneus fractures in axial impact loading events and the inertial differences between the foot and proximal or mid-tibia.[12] In order to quantify the inaccuracies associated with using proximal tibia force to assess injury risk, time of fracture and time of peak footplate and proximal tibia force were compared (Figure 3.11). While the average absolute difference between time of fracture and time of peak footplate force was 0.32 ms for the impactor tests, the average difference for the proximal tibia force time-to-peak was 0.49 ms, though the difference was not significant (p=0.16). Time of peak proximal tibia force and time of fracture varied by an average of 0.86 ms for the drop tower tests despite times to fracture being less for the drop tower tests compared to the impactor tests. In all tests, time of fracture occurred prior to peak proximal tibia force indicating that peak proximal tibia force was higher than for time of fracture. Previous injury criteria based on this measure may over- or under-predict based on the censoring used in the study and the degree to which force transmission was affected by fracture.[70,82,135,231]

Having shown that peak footplate force is superior to peak proximal tibia force in terms of timing, force at fracture was compared for the impactor medium and high conditions to assess whether a single threshold of force is sufficient for predicting injury outcome when multiple loading rates are considered. Figure 3.11 showed that footplate force and proximal tibia force at the time of calcaneus fracture were also significantly different for the two loading conditions, despite efforts to minimize the effect of specimen variability. This result has major implications for the development of future leg injury criteria, considering that only peak force is currently used to estimate injury risk. Though strain rates were significantly different for the two test conditions, strain-rate dependence of bone strength cannot account for the magnitude of difference in force at fracture. Assuming that the ultimate compressive strength for cortical bone is proportional to the strain rate raised to the 0.06 power, the difference in strain rate between the two test conditions would only account for a three percent difference in strength.[38]

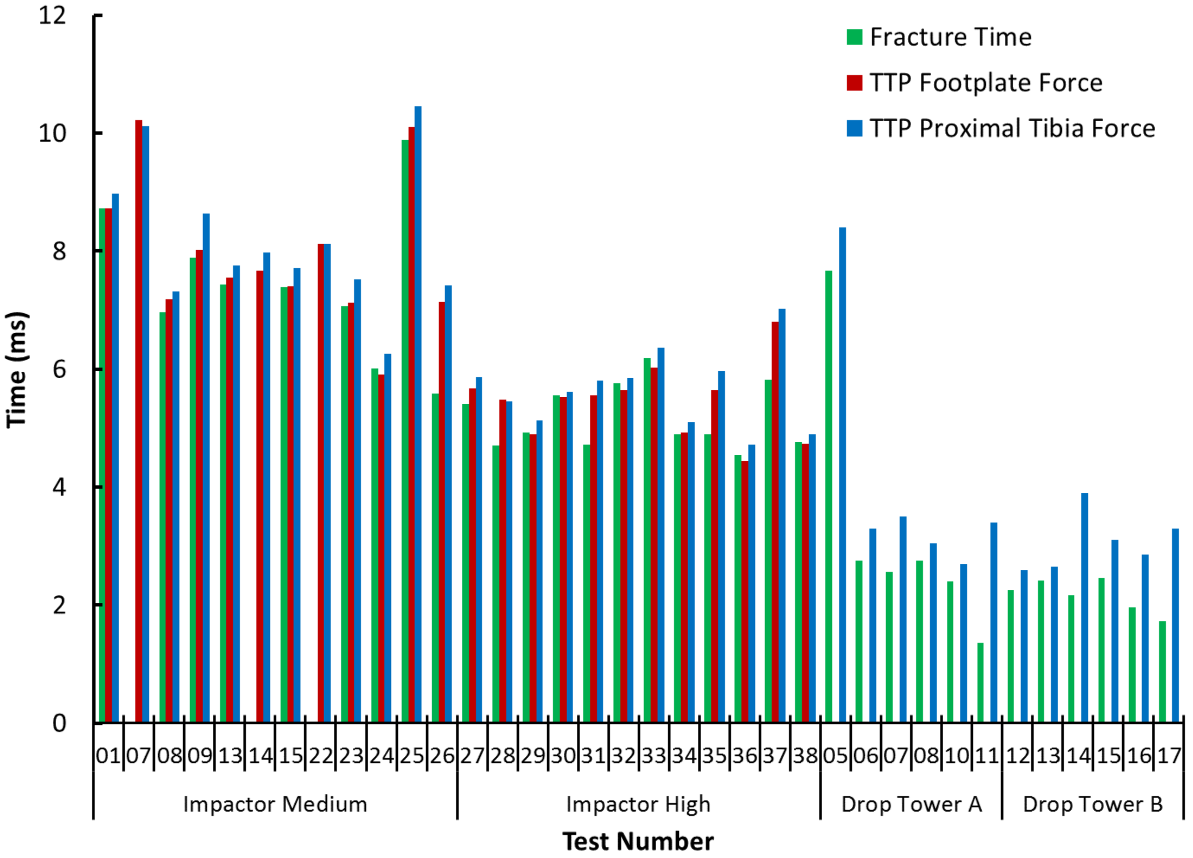

Figure 3.11. Time of first fracture compared to time of peak footplate and proximal tibia forces for all injurious impactor and drop tower tests.

An alternative hypothesis is that duration of the load affects the force at fracture since the time-to-peak force was also significantly different for the two test conditions. Interestingly, impulse to fracture (integral of force from initiation of impact to fracture) was not significantly different for the two test conditions ($p=0.76$), though impulse at time of peak force was greater for the low impactor test condition. The invariance of impulse at time of fracture between these two conditions warrants further investigation. Though previous injury criteria for the femur, neck, spine, and head have incorporated duration dependence, no duration-dependent injury criteria currently exists for axial loading of the leg.[140,197,208]

The results from this analysis suggest that force is an insufficient injury predictor when considering a larger range of load durations or frequencies. Thus, a duration- or frequency-dependent injury criterion is necessary to accurately predict injury across both automotive and underbody blast loading regimes. These results also suggest that impulse may be a useful for injury prediction, though it is important to figure out how this measurement would be interpreted by the ATD.

3.2.7 Injury Location

Injury patterns from the drop tower and impactor studies are consistent with previous studies in terms of location of fracture. Calcaneus fracture occurred in 29 of the 49 tests, with pilon fractures being the second most common fracture, occurring in 11 tests (Figure 3.12). For three tests, fracture occurred in the talus or pilon without an accompanying calcaneus fracture. Drop Tower 10 resulted in a lone pilon fracture, while Impactor 22 resulted in a pilon and fibula fracture. For the case of Drop Tower 10, the opposite leg from the same whole body specimen also sustained a pilon fracture, though a calcaneus fracture also occurred. Aside from these two occurrences, no other drop tower tests resulted in pilon fractures, but with the exception of Impactor 13, pilon and talus fractures did not occur together.

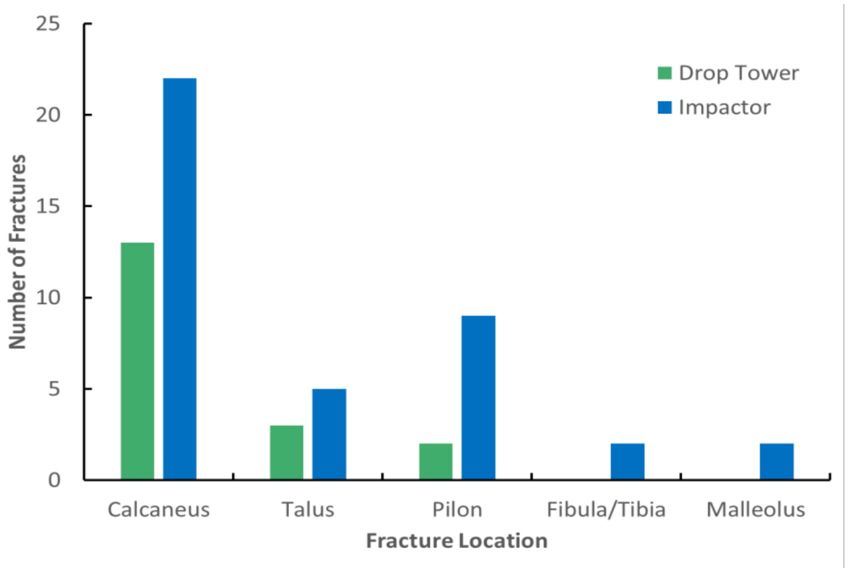

Figure 3.12. Frequency of fracture location for the drop tower and impactor PMHS studies.

For the impactor tests, there seemed to be no pattern for the occurrence of pilon fractures. Pilon fractures occurred for both medium and high test conditions, but only once in the absence of a calcaneus fracture. For tests with multiple fractured bones, calcaneus fractures occurred prior to more proximal fractures, as evidenced by dynamic x-ray (Figure 3.13).

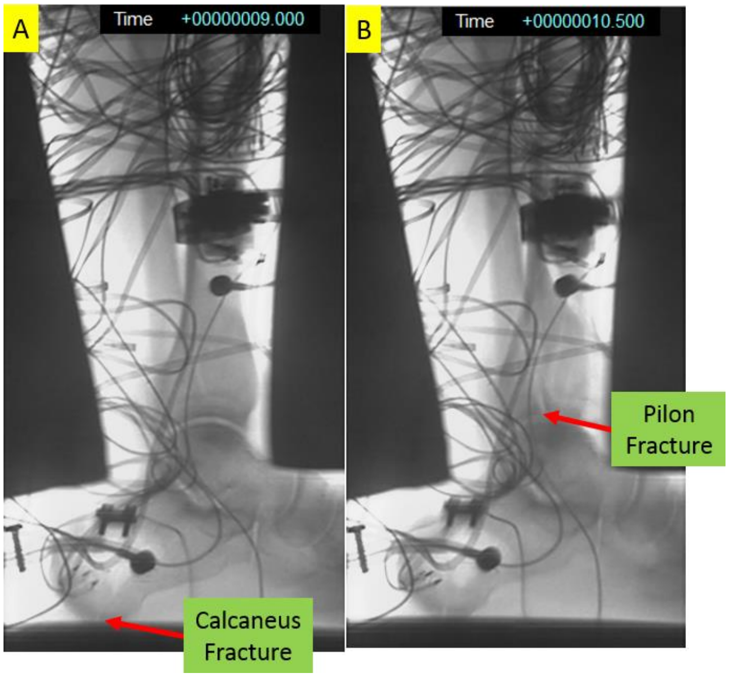

Figure 3.13. Time-stamped images are shown from a dynamic x-ray video of a high condition impactor test. The images are shown for the time of onset of calcaneus (Image A) and tibia pilon (Image B) fractures. Time is shown in seconds, where impact with the footplate occurred at t=0 s. These images confirm the hypothesis that in the case of multiple injuries, calcaneus fractures are likely to be the first fracture when the leg is impacted at the plantar surface of the foot.

Calcaneus fractures involved a combination of both non-articular and articular surfaces, and displaced and non-displaced fractures. Comminution of the calcaneus was common in the tests in which the calcaneus was the only fractured bone (Figure 3.14). Less severe (non-articular or un-displaced) calcaneus fractures were present for the cases where pilon or talus fractures were also present (Figure 3.15). This suggests that for the cases in which the calcaneus fractured to the extent that it could no longer transmit load, other fractures were not able to occur. Conversely, if the calcaneus was only slightly fractured (or not at all), the loads from the footplate were better able to transmit to other bones in the ankle to produce subsequent fractures. Though stress concentrations were likely the cause of calcaneus fracture in many instances, the variation in location of calcaneus fracture in these tests suggests that regardless of the presence of padding at the plantar surface of the foot, the calcaneus is still most likely to be fractured in these primarily axial loading events.

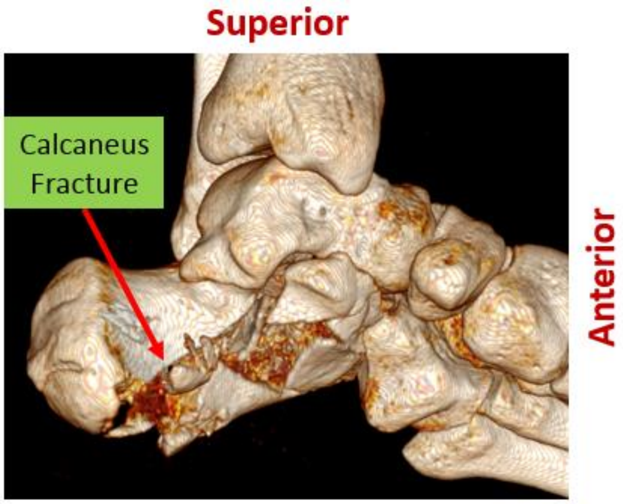
Superior
Calcaneus Fracture
Anterior

Figure 3.14. Medial view of a comminuted calcaneus without the presence of other fractures due to dissipation of energy (Impactor 33).

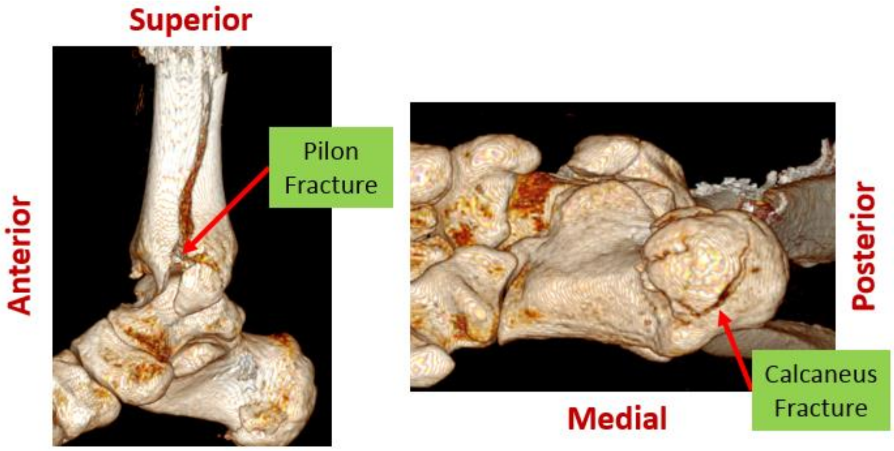
Superior
Anterior
Pilon Fracture
Posterior
Calcaneus Fracture
Medial

Figure 3.15. Medial and inferior views of a less severe calcaneus fracture accompanied by a tibia fracture radiating from the pilon (Impactor 15).

Talus fractures were less common than pilon fractures for the impactor study, but more common than pilon fractures for the drop tower study. Though the ratio of pilon to talus fractures are dissimilar for these two boundary conditions, other differences between the data sets including load rate, load duration, and characteristics of the specimen groups prevent a conclusion from being drawn about boundary conditions and injury location. In theory, however, it seems that without the fixed boundary condition which prevents the tibia from translating once impact occurs, a greater amount of energy must be applied to the leg in order that sufficient energy to fracture the pilon remains after the energy dissipation due to calcaneus fracture. Further, the energy of this impact must be applied at a fast enough rate so that the tibia cannot simply translate, which may require higher impact velocities than those used in the drop tower study.

An earlier study by Funk et al. concluded that the presence of Achilles tension increases the likelihood of pilon fracture when the leg is exposed to axial loading because of the additional force placed on the tibia rather than the entire leg. Funk et al.'s study compared the fractures resulting from two groups: one with tension applied to the Achilles tension, and one without. The group with Achilles tension sustained more pilon fractures than the group without, however, many of the pilon fractures occurred without the presence of calcaneus fracture.[70] The absence of Achilles tension in these tests suggests that the combination of the "fixed" boundary condition and the application of sufficient force and energy to create a succession of calcaneus and pilon fractures may be the cause of these differences in injury pattern among the drop tower, Funk et al., and impactor studies.

Previous studies have hypothesized that the location of fracture for axial loading of the leg depends on the bone mineral density of individual bones. McMaster et al. compared the average BMD for groups with specific injuries and the BMD of individual bones. This comparison revealed that the average calcaneus BMD for calcaneus fractures was significantly lower than the group with pilon or talus fractures. In general, the bone mineral density for other regions of the foot/leg was higher than for the calcaneus, which would tend to predispose the leg to calcaneus fractures rather than more proximal fractures both because of the relationship between BMD and bone strength and higher inertial loads closer to the location of impact. The malleolar fracture and no-fracture groups in the McMaster et al. study had the highest BMD for most regions, suggesting that in the case of the no-injury group, the specimens had higher bone strengths than the rest.[138] The fact that the malleolar fracture group had a higher average BMD suggests that the specimens may have been strong enough to resist fracture under axial loading, malleolar fractures may have occurred due to the ankle being predisposed to inversion when axial intrusion proceeds past a certain point. This tendency toward inversion was observed in the impactor study as well as previous tests in which the proximal boundary was fixed.[70,181]

Since BMD was not recorded for individual bones in the leg, it is not possible to prove that the tests resulting in talus and pilon fractures had lower tibia or talus BMD than other specimens which sustained calcaneus fractures. Another factor which may play a role in determining injury location is individual bone geometry. Stress concentrations caused by irregular edges that articulate with other bones may be a cause for fracture occurring in locations other than those expected. For example, a smaller articulation surface between the talus and tibia pilon could results in pilon or talus fracture rather than the more frequent calcaneus fracture if the area is small enough to produce stresses greater than the failure stress of either of the two bones. A study by Bruckner investigated the geometric differences of the subtalar joint and showed that the number of facets on the calcaneus can significantly affect the contact area between the calcaneus and talus.[31] This result suggests that the variations in bone geometry can affect the fracture location in the foot.

For the impactor data set, calcaneus fracture did not all originate at the same location. Dynamic x-ray showed that calcaneus fractures originated at both the contact point of the heel with the footplate (Figure 3.16A) as well as radiated from stress concentrations in the subtalar joint where the calcaneus articulates with the talus (Figure 3.16B).

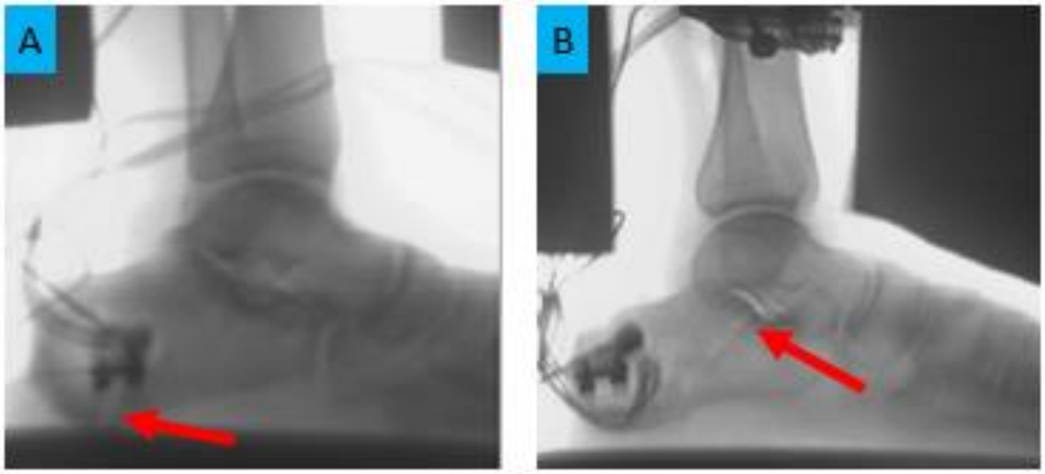

Figure 3.16. Dynamic x-ray snapshots at time of fracture to show variation in location of calcaneus fracture initiation. Figure A shows the calcaneus fracture initiation from the impact site for Impactor 33, which Figure B shows the calcaneus fracture initiating from the subtalar joint for Impactor 24.

Fracture patterns were consistent with the injuries produced by a live-fire whole body PMHS test series performed by Danelson et al to replicate UBB conditions.[60] Of 14 subjects, eight sustained calcaneus fractures and one sustained a distal tibia fracture. Drawings of the fractures produced by Danelson et al. show similar fractures to those produced by the impactor study in that the calcaneus fracture extends from the plantar surface toward the surface that articulates with the talus. The pilon fracture extends proximally from the articular surface, as the case for the pilon fractures from the impactor study.

3.2.8 Limitations and Conclusions

The drop tower and impactor studies provide a comparison of response of the leg when under free and fixed proximal boundary conditions. The simplicity of the boundary conditions used in the tests make this data ideal for validating human body finite element models for a wider range of loading rates. For all test conditions, total leg compression was dominated by foot compression (>75%) at peak force. Additionally, higher stiffness was calculated for higher load rate conditions within each test set-up, and the range of stiffness calculated for this set of experiments was consistent with previous attempts to characterize leg stiffness.[6,42,106,114] Calcaneus injuries accounted for a majority of the injuries and through the use of high speed x-ray were found to occur prior to more proximally located fractures in all tests where multiple fractures occurred.

This study's demonstration of the sensitivity of the proximal tibia's force at fracture to different proximal boundary conditions and loading rates emphasizes the fact that further effort must be focused on development of an injury criterion which is valid for a wider range of loading conditions in order to be used for AI and UBB. The major contribution these tests was the finding that magnitude of force is not a sufficient injury predictor, even when measured close to the location of fracture. Limitations of this study include that only two injurious loading conditions (impactor medium and high) were used to show the dependence of force at fracture on impact condition since the drop tower study did not measure footplate force. Nonetheless, the conclusions brought forth by these tests demonstrate the necessity of focusing on the duration-dependence of fracture force on a more continuous level in order to develop an injury criterion that can be used for the wide range of loading rates typical of AU and UBB. The next two chapters will discuss tools for understanding the response of the leg to different forces and durations (frequencies) using a finite element model of the human leg to perform a parametric study, and lumped mass models to characterize the relationship between force, duration (frequency), impulse, and leg compression (deflection).

4 Human Leg Finite Element Modeling

While the experimental data discussed in the previous section showed that load duration affects the magnitude of force at fracture, the pulse shape-dependence of the response of the human leg and continuous nature of the relationship between force and duration are not easily extracted from the data. For the purpose of providing a more deterministic understanding of the response of the human leg to a spectrum of axial loading frequencies, a finite element modeling approach was taken. An existing finite element model of the human leg was first benchmarked, then used in a parametric study to compare the response of the human leg to variations in impact conditions.

4.1 Modified GHBMC Leg Model

The Phase I GHBMC 50th percentile male leg model (version 3.5) was previously modified to incorporate rate-dependent properties, and the mesh was refined for the bony structures of the foot including the calcaneus, talus, tibia, and fibula, as described in a paper by Gabler et al.[78,200] The original model was previously validated by Shin et al., and includes deformable bones in the hindfoot, and rigid bones in the forefoot. Forty-two ligaments and 26 bones are included in the model, and cortical and cancellous bone is modeled separately.[193] The model developed by Gabler et al. will heretofore be referred to as the University of Virginia (UVA) leg model.

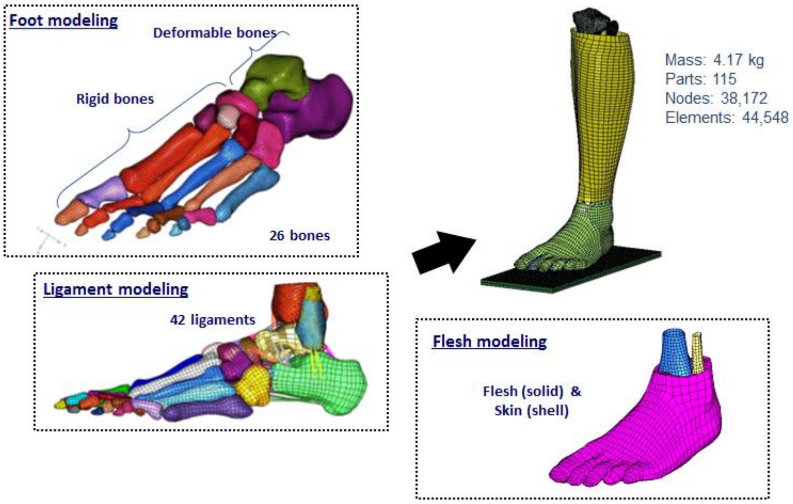
Foot modeling
Deformable bones
Rigid bones
26 bones
Mass: 4.17 kg
Parts: 115
Nodes: 38,172
Elements: 44,548
Ligament modeling
42 ligaments
Flesh modeling
Flesh (solid) &
Skin (shell)

Figure 4.1. GHBMC leg model validated by Shin, et al.,[193] which included rigid forefoot bones, deformable hindfoot bones, ligaments, and solid and shell elements to model the soft tissue. (Image from presentation by Panzer et al. 2014)

Modifications were made to the mesh and material properties of the leg model to incorporate rate-sensitivity. Mesh size for the tibia, fibula, calcaneus, and talus was decreased and rate-sensitive properties were incorporated using *Mat_Piecewise_Linear_Plasticity (Table 4.1). Bone yield stress was scaled as a function of strain rate, and failure strain was defined as 2.2 percent plastic strain for cortical bone and 13.4 percent plastic strain for cancellous bone.

Table 4.1. Summary of material property changes made to the GHBMC leg model by Gabler et al. (2014)[76]

Part	**GHBMC version 3.5**	**UVA Model**
Calcaneus Cortical Bone	*Mat_Plastic_Kinematic (ρ=2g-cm^2, E=17.5GPa, σ_Y=165MPa, ν=0.29, σ_U=165MPa)	*Mat_Piecewise_Linear_Plasticity (ρ=2g-cm^2, σ_Y=140MPa, ν=0.3, σ_U=214MPa)
Calcaneus Cancellous Bone	*Mat_Plastic_Kinematic (ρ=1.1g-cm^2, E=455MPa, σ_Y=5.3MPa, ν=0.3)	*Mat_Piecewise_Linear_Plasticity (ρ=1.1g-cm^2, E=68MPa, σ_Y=544kPa, ν=0.1, σ_U=8.24MPa)
Talus Cortical Bone	*Mat_Plastic_Kinematic (ρ=2g-cm^2, E=17.5GPa, σ_Y=165MPa, ν=0.29, σ_U=165MPa)	*Mat_Piecewise_Linear_Plasticity (ρ=2g-cm^2, σ_Y=140MPa, ν=0.3, σ_U=214MPa, ε_U=0.022)
Talus Cancellous Bone	*Mat_Plastic_Kinematic (ρ=1.1g-cm^2, E=455MPa, σ_Y=5.3MPa, ν=0.3)	*Mat_Piecewise_Linear_Plasticity (ρ=1.1g-cm^2, E=1.07GPa, σ_Y=8.564MPa, ν=0.1, ε_U=0.134)
Tibia/Fibula Cortical Bone	*Mat_Plastic_Kinematic (ρ=2g-cm^2, E=17.5GPa, σ_Y=125MPa, ν=0.3)	*Mat_Piecewise_Linear_Plasticity (ρ=2g-cm^2, σ_Y=140MPa, ν=0.3, σ_U=214MPa, ε_U=0.022)
Tibia/Fibula Cancellous Bone	*Mat_Plastic_Kinematic (ρ=1.1g-cm^2, E=455MPa, σ_Y=5.3MPa, ν=0.3)	*Mat_Piecewise_Linear_Plasticity (ρ=1.1g-cm^2, E=1.07GPa, σ_Y=8.564MPa, ν=0.1, ε_U=0.134)
Foot Flesh	*Mat_Ogden_Rubber (ρ=1g-cm^2, ν=0.49)	*Mat_Simplified_Rubber/Foam (k=2GPa)

ρ=density, ν=Poisson's Ratio, E=Young's Modulus, σ_Y=yield stress, σ_U=ultimate stress, ε_U=ultimate strain, K=bulk modulus.

Material properties for the heel pad were modified based on results from experimental PMHS heel pad compression testing performed by Gabler et al.[78] Strain rates from the study ranged from 0.001 to 13 s^{-1}. Constitutive modeling of the heel pad material was performed using a Quasi-linear viscoelastic (QLV) framework. The material model was then implemented in LS-Dyna using Mat_Simplified_Rubber (MAT_181), which uses strain-rate dependent stress-strain curves to characterize the response of the material (Figure 4.2).

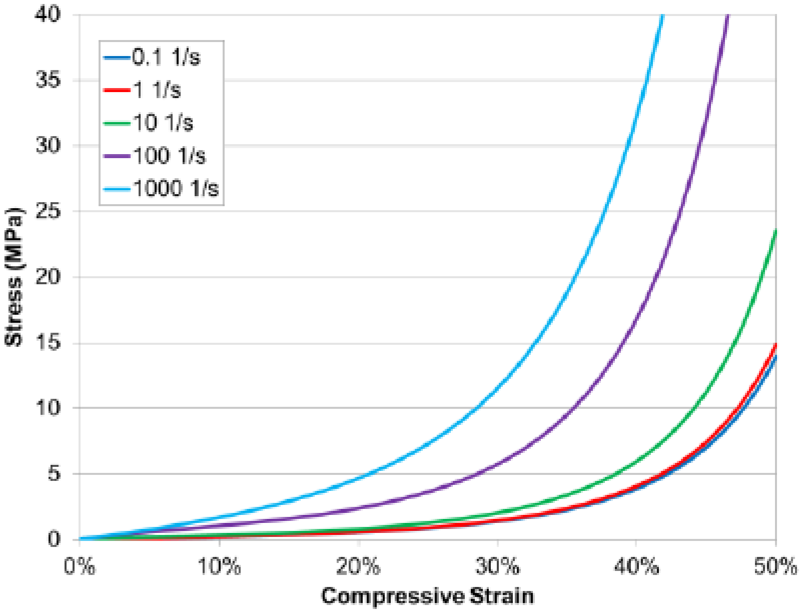

Figure 4.2. Stress-strain curves used to represent the stress-strain response of the heel pad for different strain rates using MAT_181 in LS-Dyna as described by Gabler et al.[78]

As part of the validation of the model, Gabler et al. incorporated the leg FE model into a model of the drop tower setup by attaching a free plate to the potted end of the tibia via a load cell element. A preload of 100 N corresponding to the impact plate resting on top of the foot prior to impact in the experiment was applied to an impact plate also added to the FE model (Figure 4.3). Comparison between the FE model and the physical tests was made by focusing on load cell force and distal tibia strain. Drop tower tests 11 through 18 were simulated by prescribing the impact plate acceleration and running the model for 20 ms using LS-DYNA V971 R6.1.1.

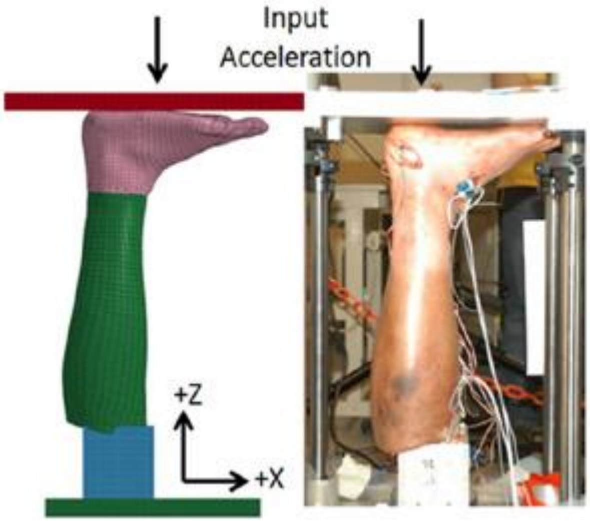

Figure 4.3. University of Virginia leg model and PMHS drop tower set-up used for comparison of FE and experimental leg response to a prescribed impact acceleration time history.

The proximal tibia force and distal tibia strain response of the original and modified FE models was compared to experimental data from the drop tower PMHS study. The changes made to the model yielded significant improvement to model response, with the average overall CORA score improving from 0.53±0.05 to 0.90±0.08 for proximal tibia force, and from 0.42±0.09 to 0.70±0.23 for anterior tibia strain. The improvement in the CORA score for proximal tibia force suggests that the modified model provides an excellent fit of the experimental data. While the average CORA score for the tibia strain shows only marginal similarity between the modified model and experimental results, it is not reasonable to assume that the FE model would be able to accurately predict such a localized strain response for individual specimens which may have different bone geometry than the FE model. Sample plots taken from the Gabler et al. conference paper are shown as a visual reference for the magnitude of improvement made between original and modified model response.

Based on the results by Gabler et al. showing obvious improvement in the ability of the FE model to predict PMHS response for higher rate axial loading, the UVA leg model was chosen for use in the modeling efforts to be described. First, however, additional validation of the model was performed using the PMHS impactor test data.

4.2 Human Leg Finite Element Model Benchmarking

The UVA 50th percentile male leg model was previously benchmarked using the drop tower PMHS tests (summarized in Section 4.1), but in order to ensure model biofidelity for other loading conditions relevant to the study, the model response was compared to PMHS response from the impactor study (Section 3.2.2). An impact plate and reaction plate were added to the model in order to replicate the boundary conditions from the PMHS tests (Figure 4.4). To match the boundary conditions from the impactor PMHS study, the proximal plate was fixed for all six degrees of freedom, and an SAE-z acceleration was prescribed to the impact plate.

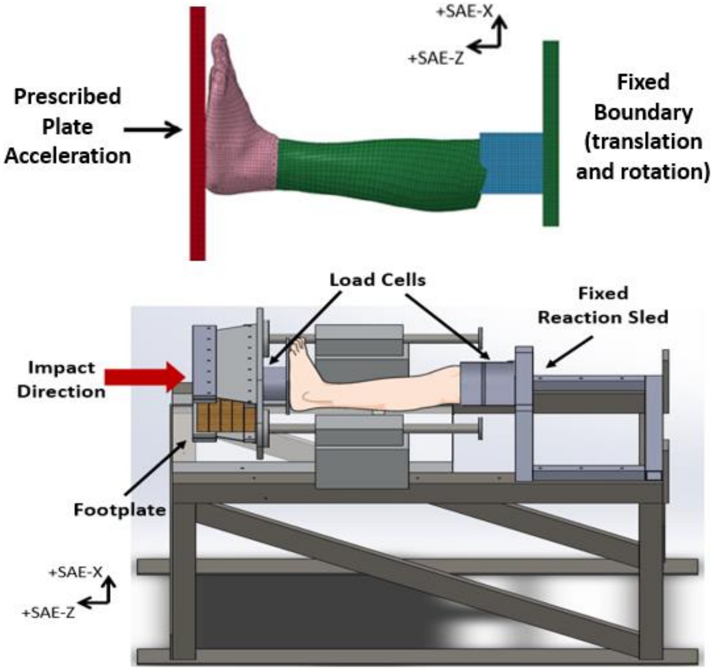
+SAE-X
+SAE-Z
Prescribed Plate Acceleration
Fixed Boundary (translation and rotation)
Load Cells
Fixed Reaction Sled
Impact Direction
Footplate
+SAE-X
+SAE-Z

Figure 4.4. LS-Dyna finite element model of the impactor test set-up used for additional model benchmarking.

4.2.1 FE and Experimental Corridor Comparison

The average impact acceleration from each of the five PMHS test conditions was applied to the FE model as a prescribed acceleration on the impact plate. Experimental PMHS response corridors (scaled to estimate the 50th percentile male response) were then compared to the finite element responses. Plots of the experimental corridors are presented in Figure 4.5 through Figure 4.17 for proximal tibia force, tibia displacement, and foot and ankle compression. Time of fracture in the finite element models is indicated for each injurious test condition.

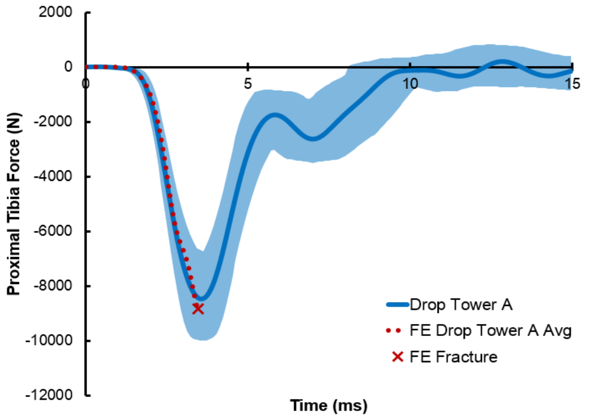

Figure 4.5. Comparison of the experimental ±one standard deviation corridor and characteristic average and the average FE proximal tibia force response for the Drop Tower A condition.

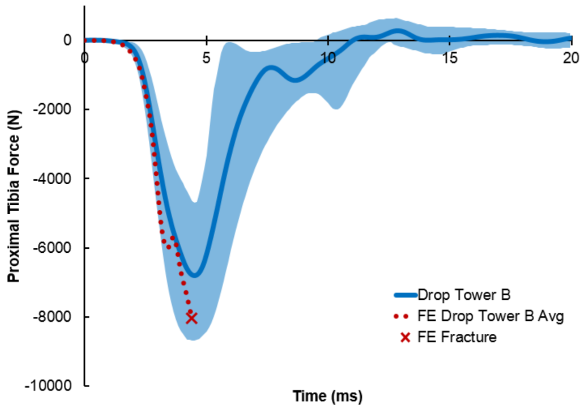

Figure 4.6. Comparison of the experimental ±one standard deviation corridor and characteristic average and the average FE proximal tibia force response for the Drop Tower B condition.

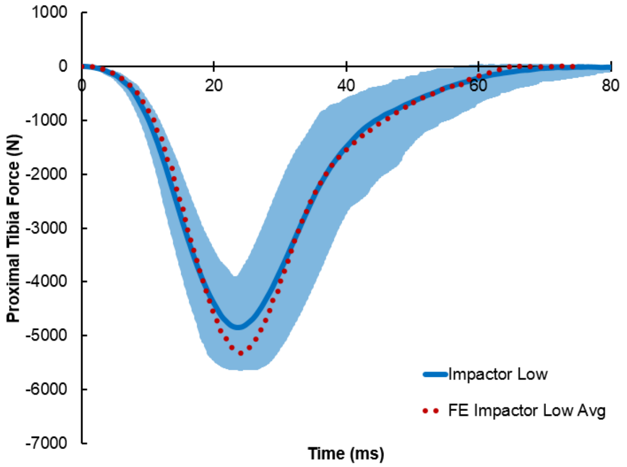

Figure 4.7. Comparison of the experimental ±one standard deviation corridor and characteristic average and the average FE proximal tibia force response for the Impactor Low condition.

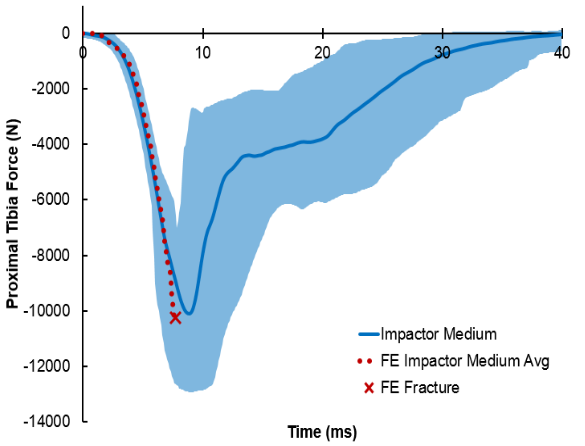

Figure 4.8. Comparison of the experimental ±one standard deviation corridor and characteristic average and the average FE proximal tibia force response for the Impactor Medium condition.

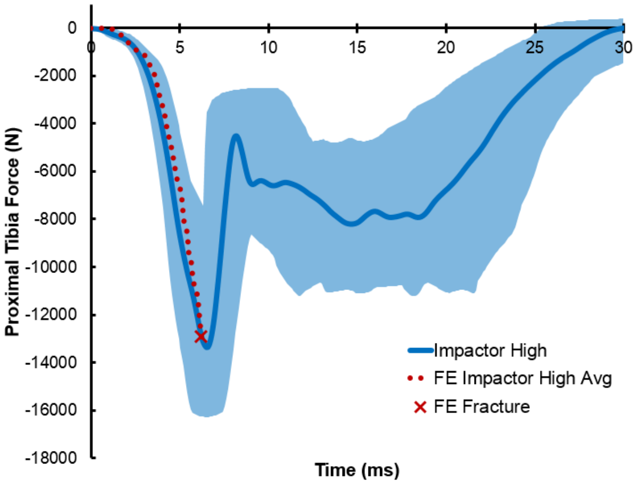

Figure 4.9. Comparison of the experimental ±one standard deviation corridor and characteristic average and the average FE proximal tibia force response for the Impactor High condition.

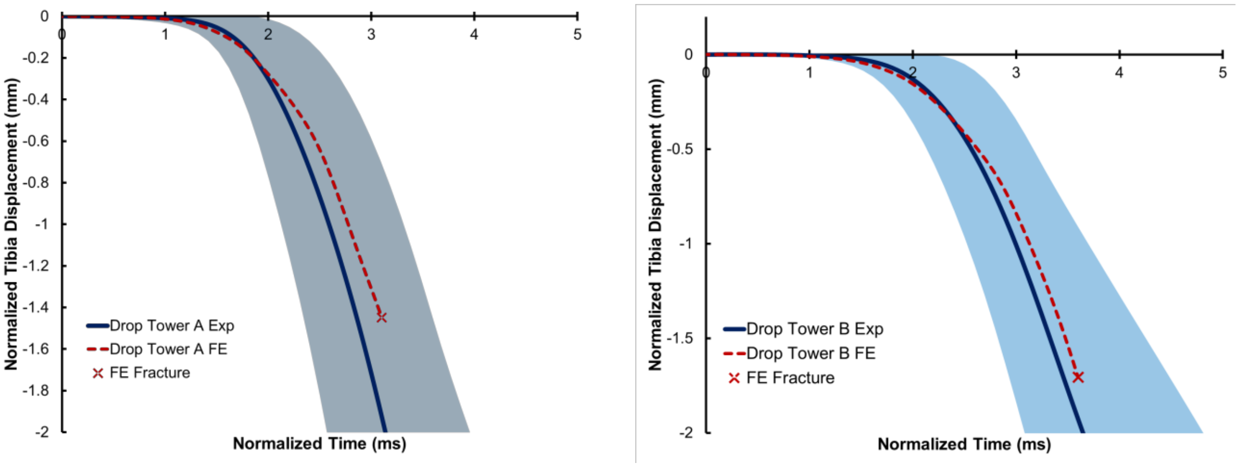

Figure 4.10. Comparison of the experimental ±one standard deviation corridor and characteristic average and the average FE tibia displacement response for the Drop Tower A condition.

Figure 4.11. Comparison of the experimental ±one standard deviation corridor and characteristic average and the average FE tibia displacement response for the Drop Tower B condition.

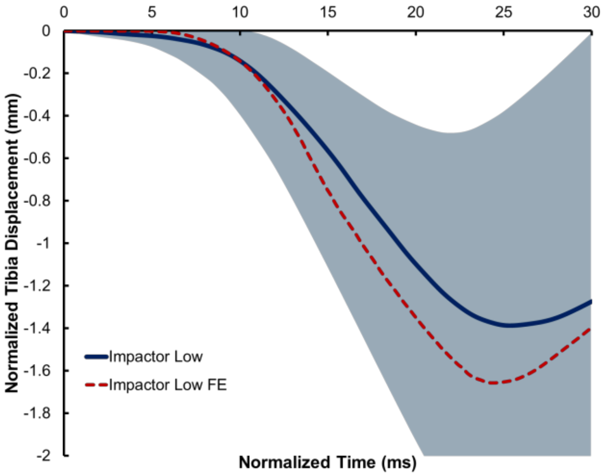

Figure 4.12. Comparison of the experimental ±one standard deviation corridor and characteristic average and the average FE tibia displacement response for the Impactor Low condition.

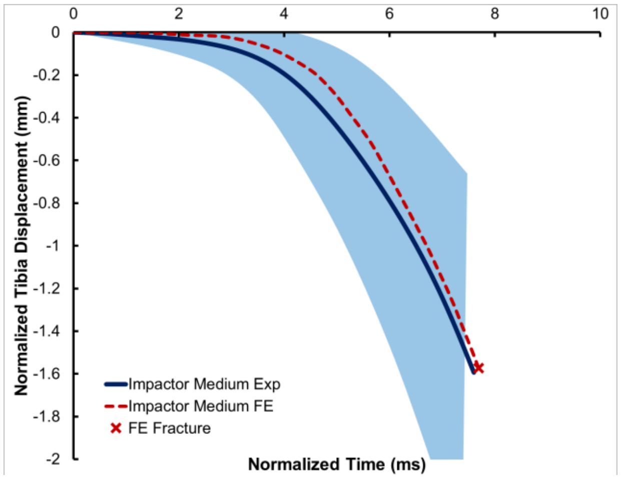

Figure 4.13. Comparison of the experimental ±one standard deviation corridor and characteristic average and the average FE tibia displacement response for the Impactor Medium condition.

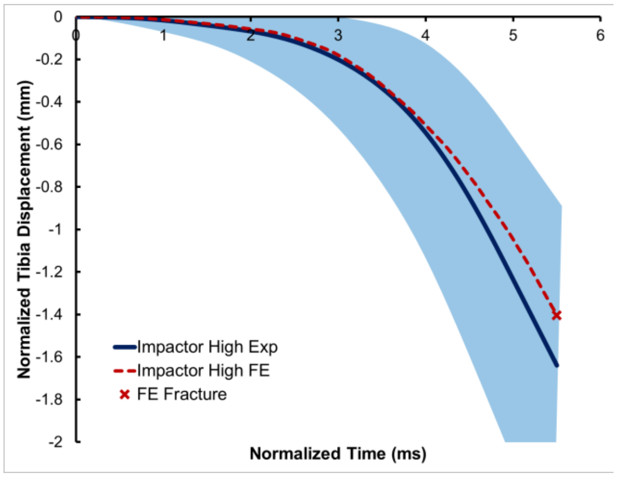

Figure 4.14. Comparison of the experimental ±one standard deviation corridor and characteristic average and the average FE proximal tibia displacement response for the Impactor High condition.

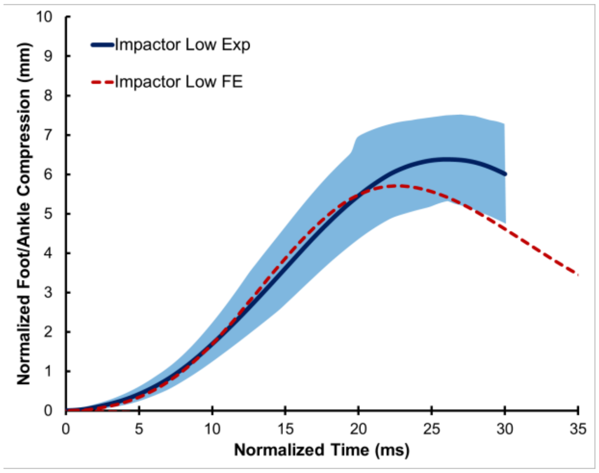

Figure 4.15. Comparison of the experimental ±one standard deviation corridor and characteristic average and the average FE foot/ankle compression response for the Impactor Low condition.

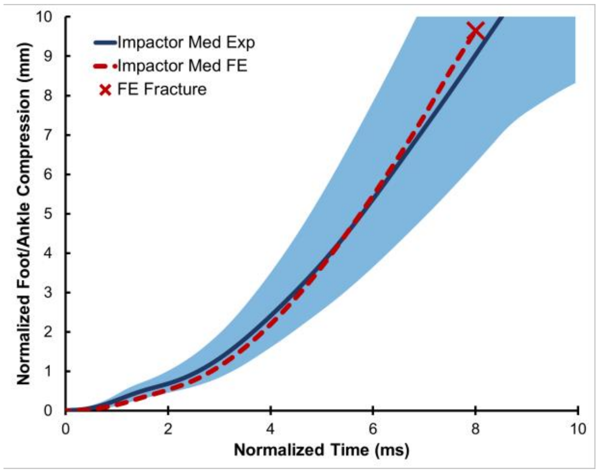

Figure 4.16. Comparison of the experimental ±one standard deviation corridor and characteristic average and the average FE foot/ankle compression response for the Impactor Medium condition.

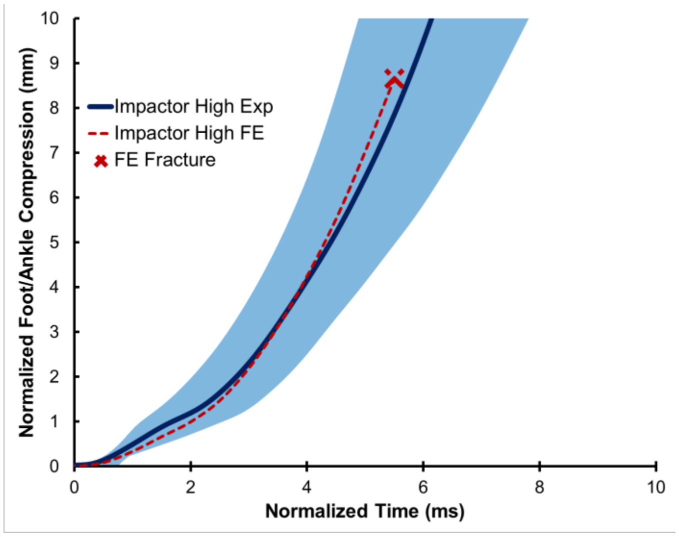

Figure 4.17. Comparison of the experimental ±one standard deviation corridor and characteristic average and the average FE foot/ankle compression response for the Impactor High condition.

Quantitative comparison of FE and experimental results was performed using Correlation Analysis (CORA), a statistical methodology developed by Gehre et al. for quantifying the likeness of curves.[85] To reiterate, CORA consists of three individual scores, "magnitude," "progression," and "phase." The overall CORA score combines these three individual scores with equal weighting (w_i) (see Eqn. 2.7). The CORA score may also incorporate a separate "corridor" rating, which rates each point of the curve on its position with respect to two degrees of corridor width.

Based on the assumption that both peak and duration affect injury tolerance by way of compression, the weights assigned to the three parts of the CORA score were determined by a finite element modeling sensitivity study. Fourteen sinusoidal force input conditions were simulated using the UVA male leg model.[78] The input conditions for the simulations are provided in Table 4.2 in terms of the magnitude and frequency of the half-sine wave applied force. Since phase shift is not expected to have an effect on displacement or compression of the leg for a given applied force, the phase portion of the CORA score was disregarded for this study.

The goal of this exercise was to determine the weighting of the parts of the CORA score such that the overall CORA score for plantar force would relate to the difference in peak leg compression caused by the two force curves being compared. To accomplish this goal, CORA scores comparing the plantar force and CORA scores comparing resulting leg compression for each combination of the 14 simulations were calculated. This resulted in 105 sets of CORA scores.

Table 4.2. Input conditions for sensitivity study simulations

Peak Applied Force (kN)	Frequency(s^{-1})
2	25
4	50
6	100
8	
12	

The relationship between the magnitude and progression scores for plantar force and the magnitude score for size was then estimated by minimizing the sum of squares error using a generalized reduced gradient nonlinear algorithm. Coefficients for magnitude and progression scores for force were constrained such that their sum was equal to one. Using all data points for this analysis showed that the comparison of the weighted CORA score for plantar force to the size CORA score for leg compression was skewed by the highly dissimilar data points with low CORA scores (Figure 4.18). To provide a better fit, data points for which the size score for leg compression was less than 0.25 were eliminated. The results of this fit showed that a weighting coefficient of 0.16 should be used for progression and 0.84 should be used for magnitude (see Eqn. 4.1). This weighting will be used in further analyses to compare forces for experimental and FE results.

$$\mathbf{CORA_{mod}}=0.84(\text{magnitude})+0.16(\text{progression}) \qquad \text{Eqn. 4.1}$$

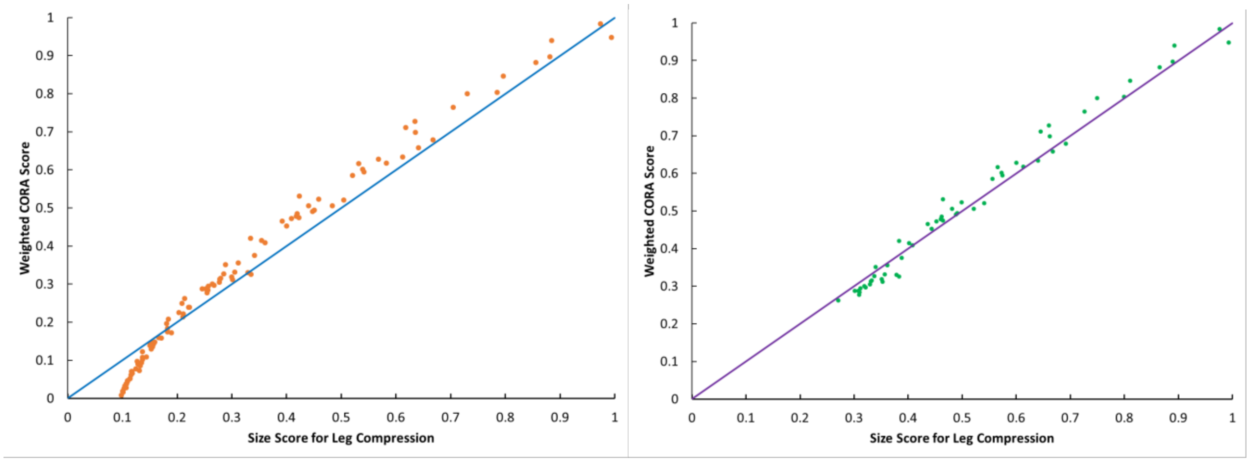

Figure 4.18. Weighted CORA score for plantar force compared to size score for leg compression for each combination of the 14 different input conditions. The plot on the left shows the results optimizing the weighted score using all combinations. The plot on the right shows the results optimized for leg compression size scores greater than 0.25 (Eqn. 4.1).

CORA scores were calculated up to time of fracture for the injurious test conditions, and up to the time that force returned to zero for the sub-injurious conditions. Traditional CORA scores and the weighted CORA scores are reported in Table 4.3. Results of the CORA comparison showed a good agreement between experimental and FE proximal tibia forces. Force magnitude scores were highest for the impactor test conditions, in particular the low impactor test condition. This is likely due to the sub-injurious nature of the low impactor test condition and the ability to use the entire loading and unloading phases of the response to calculate the CORA score. The injurious nature of the remaining test conditions may have played a role in lowering the CORA scores calculated for the other test conditions.

One hypothesis for the lower Weighted Overall scores reported for the Drop Tower test conditions compared to the impactor tests is that because of the larger displacements allowed by the test setup by allowing SAE-z translation of the proximal tibia boundary, the specimen mass differences may play a larger role in the response. Though the individual

PMHS responses were scaled by total body mass, the distribution of mass in the leg may play a role in changing the mass recruitment and therefore affect the proximal tibia force rate and magnitude. The particular mass distribution of the FE model compared to that of the individual PMHS legs, and attachment of the leg's soft tissue to the tibia and fibula in the FE model would theoretically have a greater effect on leg response in the case where the leg is allowed to translate as a result of impact to foot than if the proximal tibia were fixed. However, since the relative motion of the soft tissue and bony mass of the leg was not measured in the PMHS tests, this hypothesis cannot be tested. Nonetheless, the Overall and Weighted Overall CORA scores for all conditions were considered satisfactory for the proximal tibia force and displacement.

While proximal tibia force and tibia displacement agreed reasonably for the modified FE model and the average scaled PMHS response (Weighted Overall CORA>0.8), the FE model predicted lower calcaneus displacements. At peak calcaneus displacement for the PMHS tests for the Impactor Low condition, the modified FE model underestimated calcaneus displacement by 4.4 mm. One hypothesis for this disagreement is that it was caused by error in the alignment and double integration of the calcaneus accelerometers. Since only single-axis acceleration was recorded in the PMHS impactor tests, this acceleration (and therefore displacement) could not be transformed to the anatomic coordinate system as was done for the tibia accelerations. Another hypothesis is that this difference is related to the lack of joint cartilage in the FE model. Because of this, the initial preload applied to the leg to achieve similar initial boundary conditions to the PMHS experiments may remove more initial ankle joint laxity than exists in the actual human leg.

Table 4.3. Summary of CORA scores for comparison of experimental characteristic averages and FE response to the average input footplate acceleration pulse for proximal tibia force.

		Proximal Tibia Force			
Test Condition	**Phase**	**Magnitude**	**Progression**	**Overall**	**Weighted Overall**
Drop Tower A	1.000	0.848	0.999	0.949	0.871
Drop Tower B	1.000	0.820	0.999	0.939	0.848
Impactor Low	1.000	0.917	0.999	0.958	0.930
Impactor Medium	1.000	0.878	0.997	0.930	0.897
Impactor High	1.000	0.793	0.998	0.930	0.826

		Tibia Displacement			
Test Condition	**Phase**	**Magnitude**	**Progression**	**Overall**	**Weighted Overall**
Drop Tower A	**1.000**	**0.799**	**0.999**	**0.932**	**0.831**
Drop Tower B	1.000	0.915	0.997	0.971	0.928
Impactor Low	1.000	0.707	0.999	0.902	0.754
Impactor Medium	1.000	0.945	0.999	0.981	0.953
Impactor High	1.000	0.780	1.000	0.926	0.815

		Foot/Ankle Compression			
Test Condition	**Phase**	**Magnitude**	**Progression**	**Overall**	**Weighted Overall**
Impactor Low	1.000	0.894	0.998	0.964	0.911
Impactor Medium	1.000	0.931	1.000	0.977	0.942
Impactor High	1.000	0.879	0.999	0.959	0.898

		Calcaneus Displacement			
Test Condition	**Phase**	**Magnitude**	**Progression**	**Overall**	**Modified Overall**
Impactor Low	1.000	0.296	0.989	0.762	0.407
Impactor Medium	1.000	0.478	0.993	0.823	0.560
Impactor High	1.000	0.468	0.995	0.821	0.552

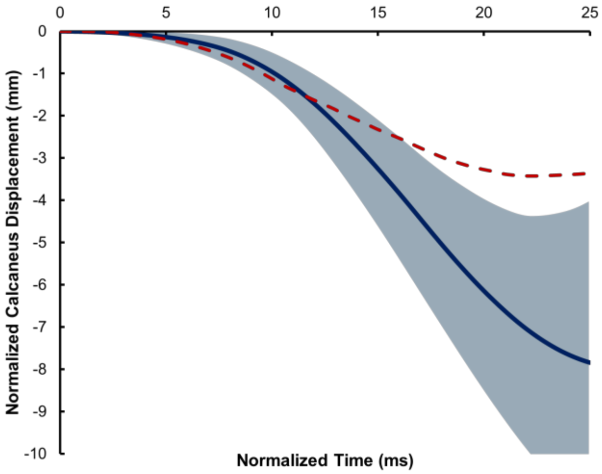

Figure 4.19. Comparison of the experimental ±one standard deviation corridor and characteristic average and the average FE calcaneus displacement response for the Impactor Low condition.

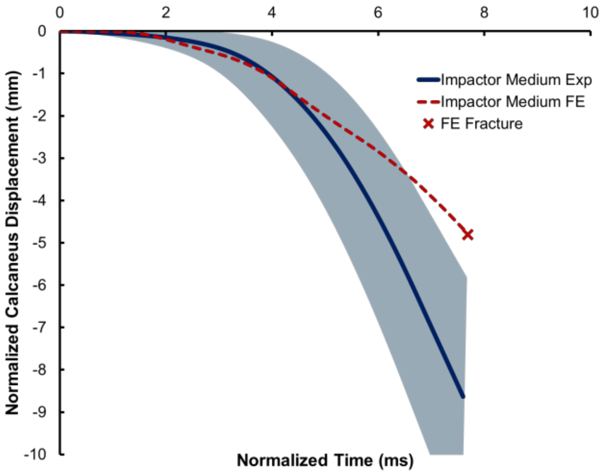

Figure 4.20. Comparison of the experimental ±one standard deviation corridor and characteristic average and the average FE calcaneus displacement response for the Impactor Medium condition.

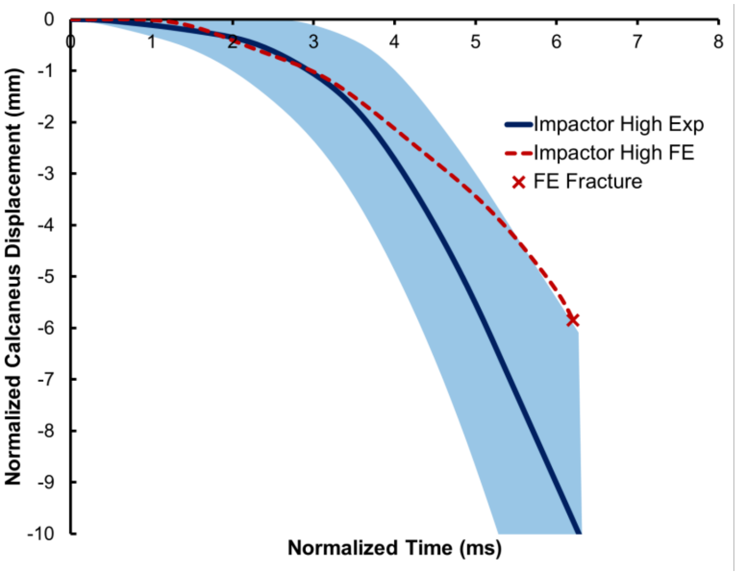

Figure 4.21. Comparison of the experimental ±one standard deviation corridor and characteristic average and the average FE proximal calcaneus displacement response for the Impactor High condition.

Gabler et al. previously postulated that this lack of cartilage could lead to premature eversion of the ankle joint in the FE model; however, analysis of the dynamic x-ray data from the impactor study suggests an alternative reason for this difference in calcaneus displacement. Visual inspection of the kinematic response of the calcaneus in the FE model compared to the PMHS tests reveals a posterior rotation of the calcaneus about the talo-crural joint in the PMHS tests as a result of the flattening of the arch of the foot. This likely occurs due to the line of action of the force acting on the tibia. The location of the calcaneus's point of contact with the impact plate posterior to the tibio-talar joint induces a moment in the talo-crural joint during this type of compression loading.

Though the FE model fails to replicate the calcaneus displacement from the experimental tests, the model still accurately models the compression of the foot and ankle. While it is not commonplace to use a model to estimate error in experimental data, in this case there is reason to believe that the calcaneus displacements calculated for the impactor experiments may be inaccurate due to the inability to transform the accelerations because of lack of off-axis instrumentation. Because of this, the decision was made to proceed with the use of the modified human leg FE model with the caveat that calcaneus displacement needs to be further validated with additional experimental data.

4.2.2 Experimental versus Finite Element Model Strain Comparison

Strains were measured on the tibia and calcaneus for both the drop tower and impactor PMHS experiments. While a direct comparison of strains in the FE model and PMHS experiments is futile unless the FE model is morphed to the geometry of the individual specimen, peak strains and strains at fracture from the PMHS tests were compared to the 50th percentile and 95th percentile calcaneus strains in the FE model. For each impactor test condition, strain-time histories were recorded for each element in the cortical shell of the calcaneus, and maximum strain was found for each element. The 50th and 95th percentile of each of these strains is summarized in Table 4.4. Strain for each element was also noted for the time of fracture as indicated by element deletion in the model. Again, the 50th and 95th percentile strains were recorded. Average maximum PMHS calcaneus strain (or strain at failure) was calculated to be 1970±1110 µS, 4400±1060 µS, and 6080±1130 µS for the low, medium, and high impactor conditions, respectively. These strains fall within the 50th-95th percentile ranges for the finite element study, but tend toward the 95th percentile strains.

Table 4.4. Summary of 50th and 95th percentile calcaneus cortical bone strains from the finite element model for maximum strain and strain at time of fracture in µS.

Test Condition	**50th at Maximum**	**95th at Maximum**	**50th at Fracture**	**95th at Fracture**
Impactor Low	1500	3500	n/a	n/a
Impactor Medium	6000	52500	2700	7400
Impactor High	10500	134400	3100	7800

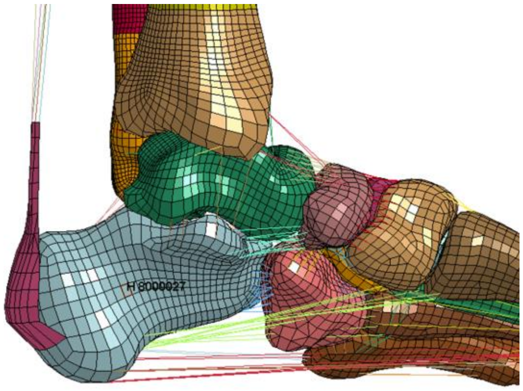

Figure 4.22. Location of element used for comparing FE and PMHS calcaneus strain. This element is in the approximate location of the PMHS strain gages used to measure calcaneus strain in the impactor study.

Individual calcaneus maximum principal strain traces for the impactor PMHS tests are provided in Figure 4.23 with the FE strain measured in an element near the strain gages' location overlaid. Location of the element assumed to be near the location of the PMHS strain gages is shown in Figure 4.22. These plots show that the strain rates are similar for the PMHS and FE model; however, the peak strains vary greatly. Average strain rate calculated using 20- and 80-percent of the peak strain or strain at failure was 197±99 μS-ms^{-1}, 940±390 μS-ms^{-1}, and 1570±540 μS-ms^{-1} for low, medium, and high conditions, respectively. Low, medium, and high finite element strain rates were 130 μS-ms^{-1}, 815 μS-ms^{-1}, 1208 μS-ms^{-1}, respectively. While finite element strain rates were lower than the average PMHS strain rates for the medial calcaneus location, they fall easily within one standard deviation of the mean.

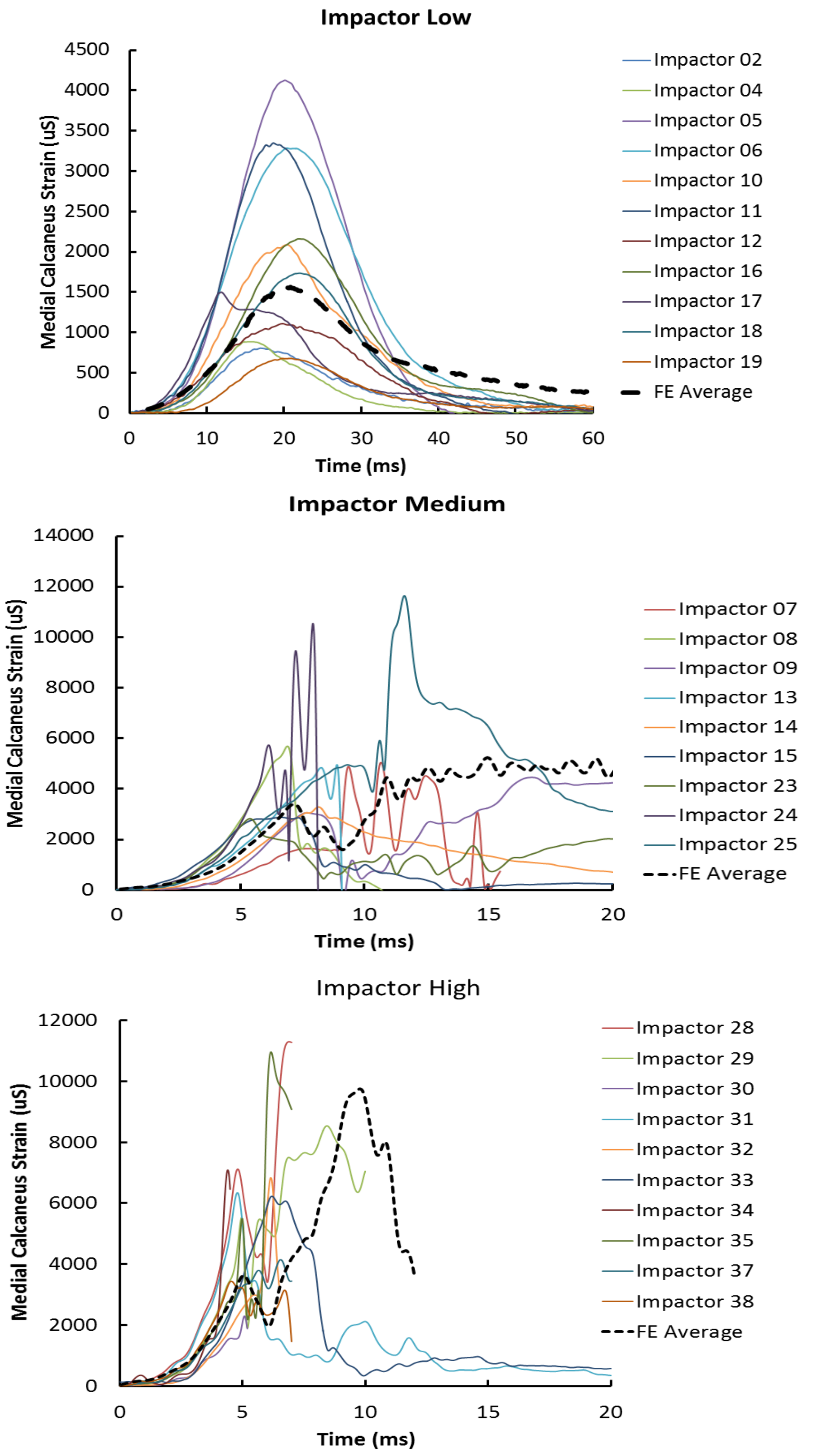

Figure 4.23. Medial calcaneus strain for low, medium, and high impactor conditions with finite element maximum principal strain from the average input condition.

4.2.3 Comparison of Injury Outcome in the Finite Element Model

While the UVA leg FE model was previously shown to predict injury for the PMHS drop tower tests. A similar comparison was performed to show the ability of the FE model to predict injury for the impactor study. The FE model indicated fracture by element deletion when the cortical bone strain exceeded 2.2 percent strain or the cancellous bone strain exceeded 12.3 percent strain in the calcaneus, talus, tibia, or fibula.[78] Mid- and forefoot fractures were not a focus of the study since they are not usually associated with pure axial loading and were treated as rigid in the FE model. Previous research has also shown that a majority of axial load applied to the foot is shunted through the hindfoot.[206]

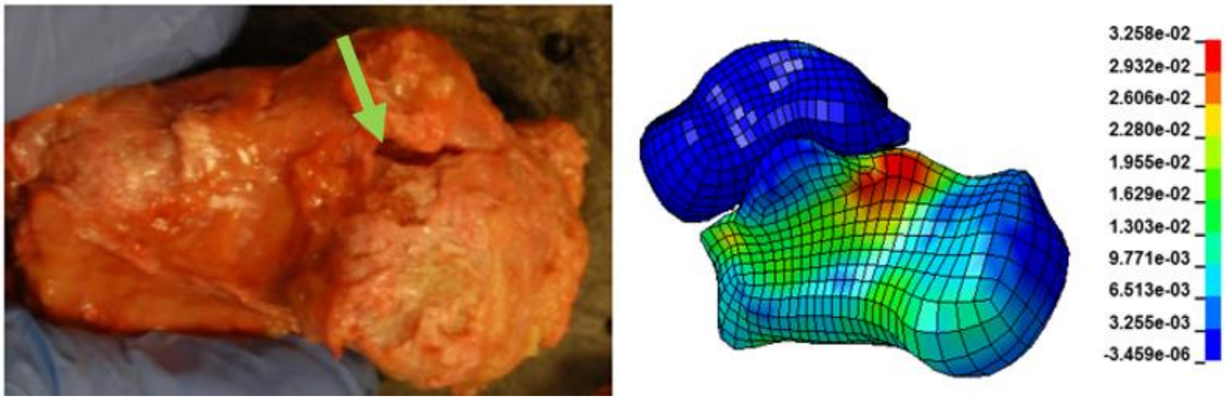

Figure 4.24. Example of a comparison of FE model “fracture” location indicated by high levels of maximum principal strain compared to PMHS experimental fracture.

The finite element model predicted injury for the impactor medium and high conditions. While these conditions produced fracture in the PMHS tests, the fracture location varied from the fracture location indicated by the FE model. As previously discussed, calcaneus fractures initiated at both the location of impact (at the footplate) as well as at the point of contact between the talus and calcaneus within the subtalar joint. A few calcaneus fractures appeared to occur in shear because of the bending moment caused by contact with the footplate and talus. While less common, these shear-induced fractures have been reported by previous studies involving axial loading.[59] Since the FE model was not morphed to recreate the specific geometry of individual specimens, it is logical to assume that the variations in fracture location due to specimen-specific stress locations cannot be captured by the model.

The current configuration of the FE model assumes the same material properties for the cortical bone of the talus, tibia, fibula, and calcaneus, which fails under the same failure strain. It is hypothesized that variations in these material properties for individual bones due to differences in bone mineral density may contribute to fracture occurring at different locations. Potential variations in the material properties within the FE model may lead to changes in fracture location. Since the purpose of using this FE model was not to predict failure, this parametric modeling effort is left for a future study.

The presence of subsequent fractures in the more proximal bones of the leg was believed to be due to the transmission of force through the calcaneus after the initial fracture (usually in the calcaneus). These fractures did not occur in the finite element model. As expected, strain in the FE model progressed from the calcaneus through the talus to the tibia (Figure 4.25). As fracture occurred in the model, elements of the calcaneus were deleted and further transmission of force to the tibia was not able to occur in the same way as for the PMHS.

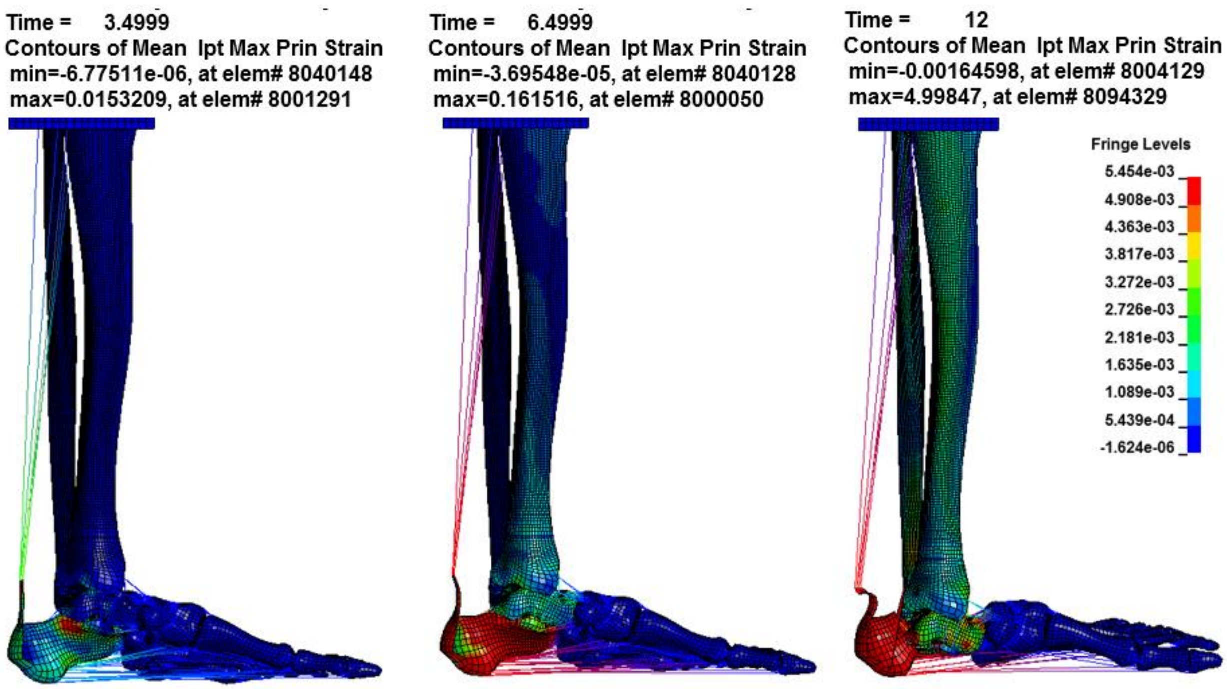
Time = 3.4999
Contours of Mean Ipt Max Prin Strain
min=-6.77511e-06, at elem# 8040148
max=0.0153209, at elem# 8001291
Time = 6.4999
Contours of Mean Ipt Max Prin Strain
min=-3.69548e-05, at elem# 8040128
max=0.161516, at elem# 8000050
Time = 12
Contours of Mean Ipt Max Prin Strain
min=-0.00164598, at elem# 8004129
max=4.99847, at elem# 8094329
Fringe Levels
5.454e-03
4.908e-03
4.363e-03
3.817e-03
3.272e-03
2.726e-03
2.181e-03
1.635e-03
1.089e-03
5.439e-04
-1.624e-06

Figure 4.25. Progression of maximum principal strain in the human leg FE model for the Impactor High test condition. Strain first accumulated in the calcaneus and then progressed superiorly through the talus to the tibia and fibula. Fracture occurred in the calcaneus in the location indicated in Figure 4.24.

4.3 Human FE Model Parametric Study

The benchmarking efforts in the previous section were able to establish that the modified human FE model provides an accurate representation of the human leg's response to load durations ranging from 5 to 80 ms. Moving forward, this model was used to characterize the response of the human leg to changes in loading amplitude and duration to fill the gaps in the data available in the literature. To accomplish this task, a parametric study was performed in which the FE model was exposed to sinusoidal acceleration pulses with amplitude and frequency varied according to Figure 4.26 and Table 4.5. Frequencies were chosen to cover the range of frequencies above and below the expected natural frequency of the leg (20-50 Hz as reported by Wakeling and Nigg), and frequencies typical of UBB and AI

(5-200 Hz).[217] This range of frequencies was established by idealizing acceleration pulses described in Section 2.1 using sinusoidal pulse shape with the same duration of loading.

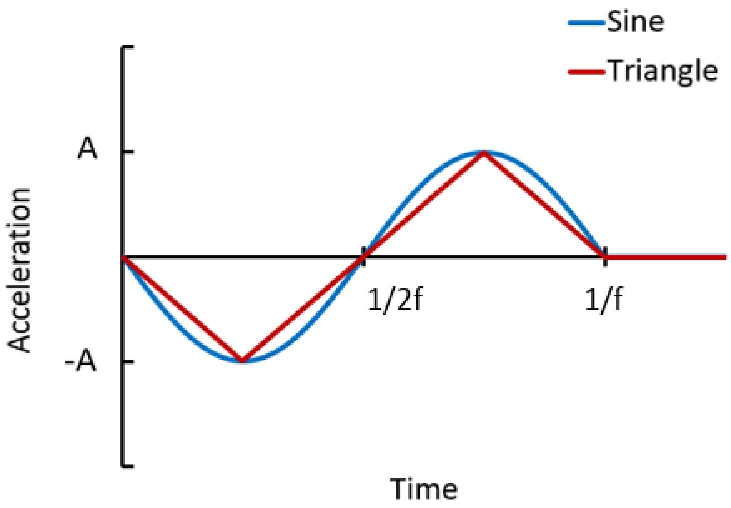

Figure 4.26. Template for sinusoidal and triangular input acceleration pulses, characterized by amplitude and frequency or amplitude and duration.

Each input condition was simulated by prescribing the footplate acceleration and using a free SAE-z translational proximal tibia boundary condition to match the PMHS drop tower study (see Figure 4.4 for coordinate system). The simulations were run without fracture (element deletion) to study the overall kinematic and kinetic response of the leg without the interference in load transmission caused by fracture. A load cell was implemented in the model at the mid-shaft of the tibia by identifying a set of nodes and elements at the cross-section of the tibia and fibula using DATABASE_CROSS_SECTION_SET. Footplate force was estimated using the contact force between the plantar surface of the foot and the footplate. Force at the location between the potting material and proximal plate was output as a joint force.

Table 4.5. Frequencies (Hz) associated with input sinusoidal acceleration pulses for finite element parametric study.

	2 m-s^{-1}	**4 m-s^{-1}**	**6 m-s^{-1}**	**8 m-s^{-1}**	**10 m-s^{-1}**	**12 m-s^{-1}**	**14 m-s^{-1}**
A=10 g	-	7.8	5.2	-	-	-	-
A=50 g	78.1	39.1*	26.0*	19.5*	15.6*	13.0*	11.2
A=100 g	156.2	78.1*	52.1*	39.1*	31.2*	26.0*	22.3*
A=250 g	390.5	195.3	130.2*	97.6*	78.1*	65.1*	55.8*
A=500 g	-	390.5	260.4	195.3*	156.2*	130.2*	111.6*

*Indicates conditions that exceeded fracture strains in the model.
-Condition was not simulated.

For each simulation, footplate, mid-tibia, and proximal tibia forces were recorded at time of fracture (as indicated by cortical bone strain exceeding 2.2 percent) and time of peak footplate force. Distal tibia, proximal tibia, calcaneus, and footplate displacements were also recorded for these times. A comparison of peak leg compression measured from footplate to the potting cup and forces measured at each of the locations was performed (Figure 4.27). For all cases, footplate force was greater than mid- and proximal tibia forces, but the ratio of footplate force to each of the other forces varied as a function of the input acceleration. These differences were expected based on the inertial differences between the force locations.

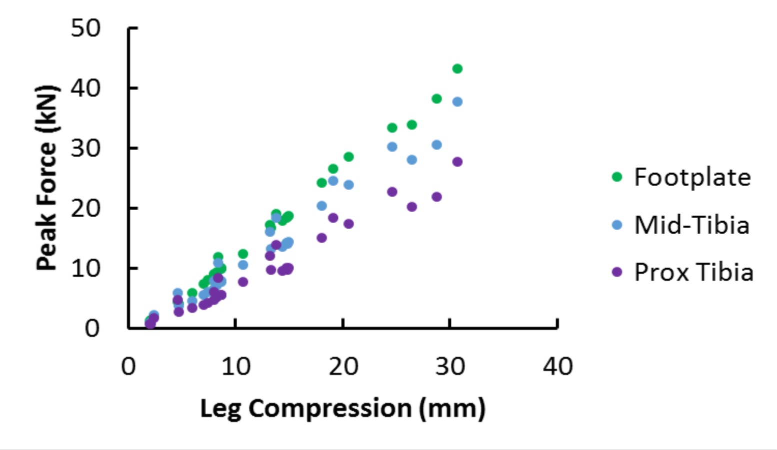

Figure 4.27. Peak force versus leg compression for forces measured at the footplate, mid-tibia, and proximal tibia.

Force plots showing footplate force (solid lines) and proximal tibia force (dashed lines) are provided to show the effect of peak velocity and peak acceleration on the force time history (Figure 4.28). The left column shows the force response for the case where peak velocity of the input pulses was kept constant, but the peak acceleration and frequency of the acceleration pulses were varied. The right column shows the force response for cases where the peak acceleration was kept constant while the peak velocity was varied by changing the frequency of the acceleration pulse.

The plots for which peak footplate velocity was kept constant demonstrate the effect of frequency on the leg. For the 2 m-s^{-1} conditions, there was an inverse relationship between peak force and peak velocity. This relationship persisted for the 500g, 8 m-s^{-1} and 250g, 8 m-s^{-1} conditions. This counterintuitive observation is a result of the frequency-dependence of the leg. The frequencies of the input accelerations for which this occurred were higher than for the 12 m-s^{-1} conditions, for which there was a positive relationship between force and peak acceleration.

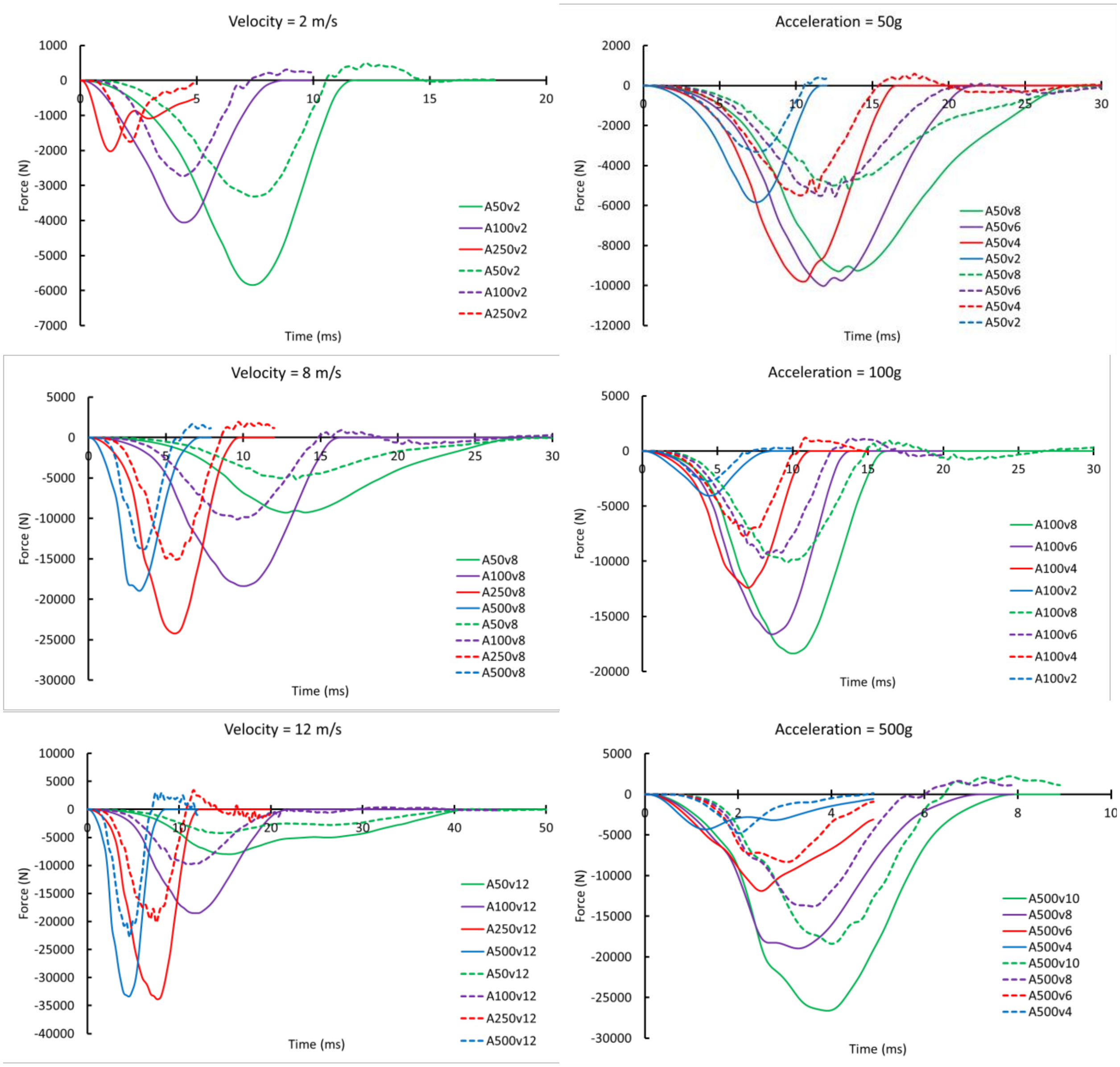

Figure 4.28. Force results from parametric study simulations where the solid lines represent the footplate force and the dashed lines represent the proximal tibia force. The left column shows the response of the model when impact velocities were constant, but peak acceleration was varied. The right column shows the results for the case where peak accelerations were the same, but velocities were different.

The change in peak force as a result of change in velocity for a given peak acceleration is shown in the right column of plots in Figure 4.28, and also in Figure 4.29. Since the shape of the input acceleration pulse is kept constant, the difference in force response is also a result of a change in frequency. Footplate forces were plotted for additional 50g inputs in Figure 4.29. Peak force increased with peak velocity for velocities less than 6 m-s^{-1}, but then gradually decreased with peak velocity for velocities larger than 6 m-s^{-1}. The behavior of the shape of the force for the 10, 12, and 14 m-s^{-1} conditions is due to rotation of the ankle since these conditions involve larger displacements than the other conditions.

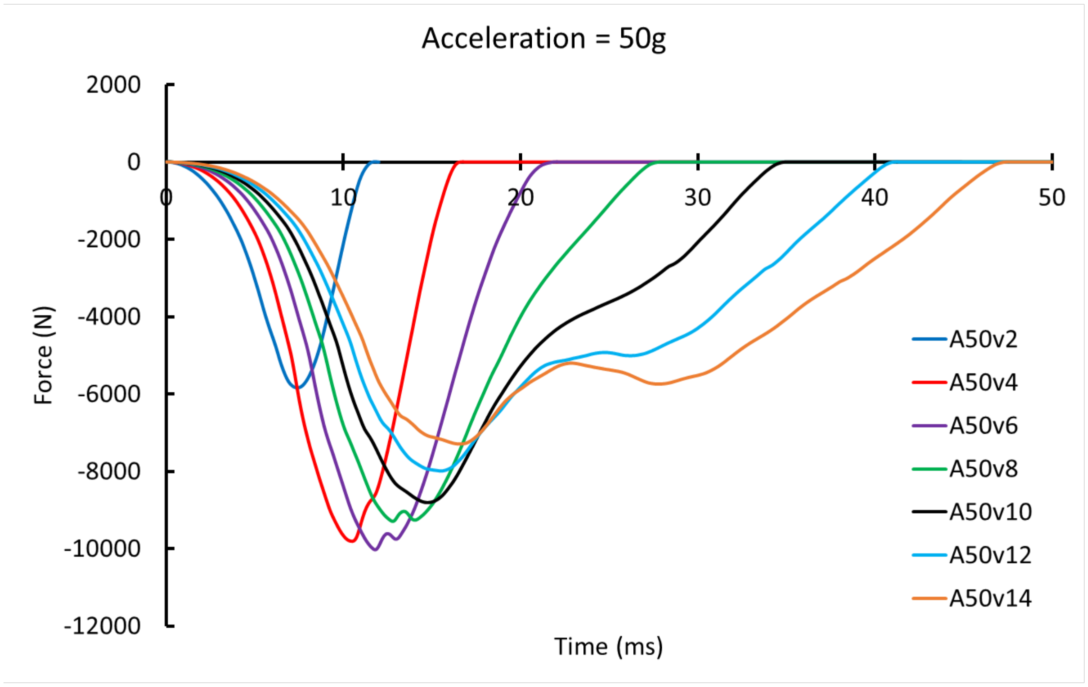

Figure 4.29. Force results from parametric study simulations where peak acceleration was kept constant at 50g while the frequency of the acceleration pulse was varied to achieve different increments of peak velocity.

Another plot was generated for which frequency of the acceleration pulse was kept constant at 78.1 Hz (Figure 4.30). Only slight variations in duration of the proximal tibia force pulses were observed (<0.5 ms). Time-to-peak footplate force increased slightly for smaller peak accelerations, though duration of the footplate force was constant. This was likely caused by the fact that force rates and strain rates were higher for the conditions with higher peak acceleration, meaning that the rate-dependency of the materials used in the model had a slight effect on the response.

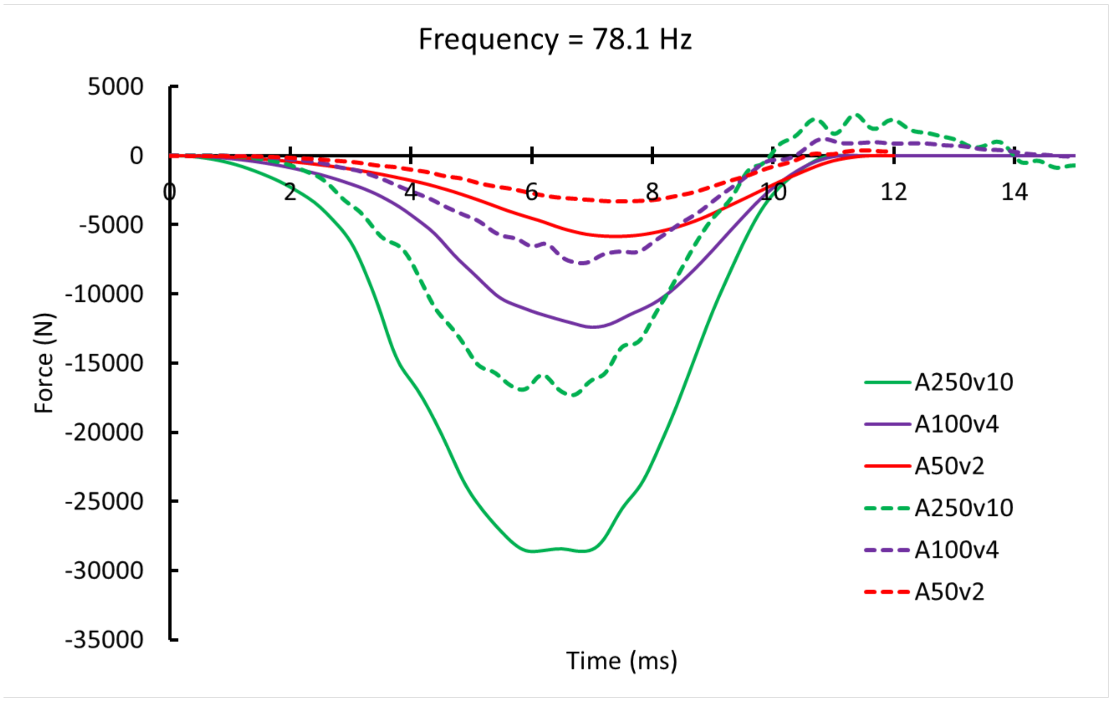

Figure 4.30. Force results from parametric study simulations where the solid lines represent the footplate force and the dashed lines represent the proximal tibia force. For all conditions, the frequency of the sinusoidal footplate acceleration pulse was 78.1 Hz.

4.3.1 The Effect of Simulated Fracture on Leg Response

The peak force response of the leg is dependent both on the frequency as well as the magnitude of the input. The force response of the leg cannot be characterized by a single parameter, so it is important that multiple parameters be considered when developing an injury criterion. Since these simulations did not include fracture, additional models which incorporated element deletion were run to compare the results. Though the process of element deletion does not necessarily cause the same effect in the model as a fracture causes in a human bone, the results were interesting in terms of the difference in duration of the pulse for the two cases. Fracture initiated in the calcaneus in the same location described by the Figure 4.24 for all simulations which indicated fracture. For more severe impacts, complete comminution of the calcaneus was observed; however, the model was unable to predict the tibia fractures that occurred in the impactor tests beacuse excessive element deletion prevented the transfer of force through the fracture. It is important to note that strain magnitudes exceeding those associated with failure were observed in the tibia for simulations where model failure was turned off.

Sample plots for four different input conditions are provided to show the effect of element deletion on force response (Figure 4.31). Results from the remaining input conditions are provided in Appendix 10.4. As expected, the force for both models tracked together until element deletion occurred. For all conditions, peak force was reduced and duration of the force was increased for the element elimination simulations. Another important observation was that for some loading conditions, the peak force was higher than the force at fracture even for the element elimination cases (see the 100g, 14 m-s^{-1} case).

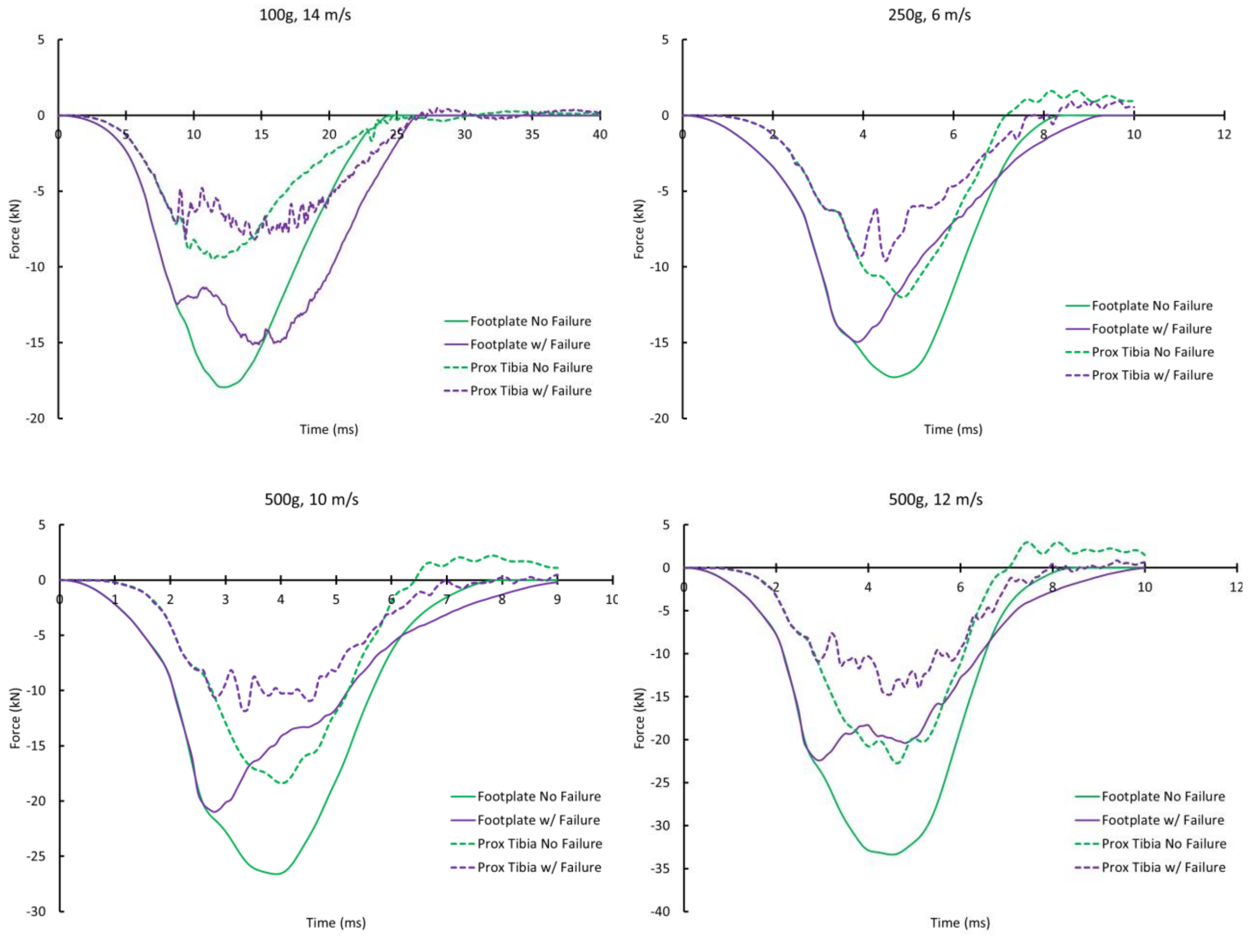

Figure 4.31. Comparison of FE model forces for models including element elimination (w/ Failure) and models for which failure was turned off in the model (No Failure). The 100g, 14 m-s^{-1}, 250g, 6 m-s^{-1}, 500g, 10 m-s^{-1}, and 500g, 12 m-s^{-1} conditions are provided to show a range of loading frequencies.

A strain map of the leg for the 100g, 14 m-s^{-1} condition is provided in Figure 4.32 for the case with element deletion and without element deletion. For the case with element deletion, the “fracturing” relieved some of the strain in the posterior portion of the calcaneus compared to the case without element deletion. Strain levels within the talus were similar for the two cases, while the strain distribution for the tibial pilon was different and involved higher strains in the case without element deletion. The element deletion led to slightly higher strains in the anterior portion of the pilon, while the other case showed higher strains in the posterior aspect of the pilon. Though these strain distributions are not validated, this comparison provides clues as to how the load may be transmitted to the tibia when fracture of the calcaneus does not occur.

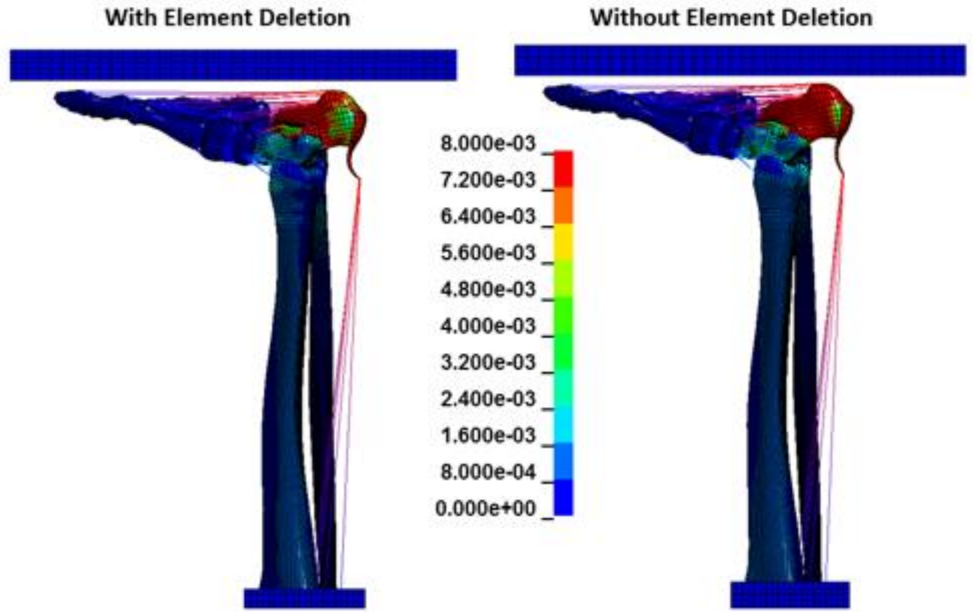
With Element Deletion
Without Element Deletion
8.000e-03
7.200e-03
6.400e-03
5.600e-03
4.800e-03
4.000e-03
3.200e-03
2.400e-03
1.600e-03
8.000e-04
0.000e+00

Figure 4.32. Maximum principal strain map for the case where fracture was indicated by element deletion (left) and for the case where fracture was turned off for the model (right). Strains are shown for the time of maximum footplate force in the model without element deletion for the 100g, 14 m-s^{-1} input condition.

Fracture in the FE model by element deletion was shown to reduce both peak plantar force and impulse for all loading conditions, as expected (Figure 4.33, Figure 4.34). For the more severe (higher velocity/higher energy) input conditions, greater differences were observed between the force at fracture and the peak force predicted by both the element deletion and non-element deletion models. The largest difference between force at fracture and peak force for the element deletion model was observed for the 250g, 14 m-s-1 condition, with the peak force exceeding the force at fracture by nearly 10 kN. Though the model with element deletion only provides an estimate of the post-fracture response of the leg, these results agree with the patterns observed in the PMHS tests in that the presence of additional energy in the impact was able to overcome drop in force due to fracture in order to reload the leg through another pathway. This explains why for some cases the peak plantar force was greater than the force at fracture.

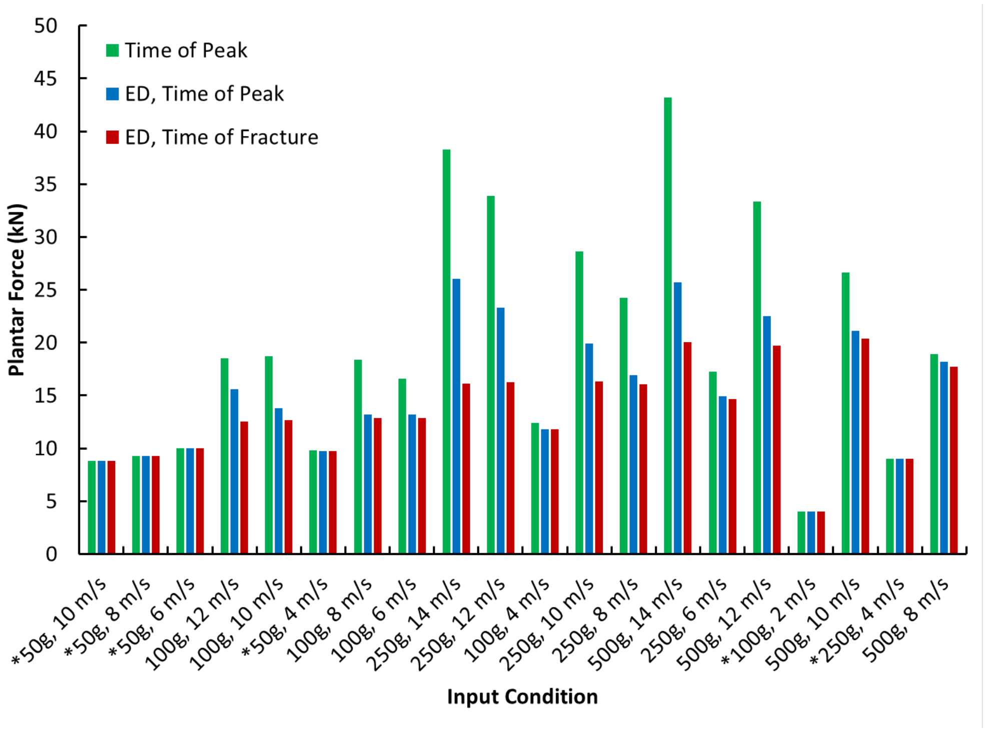

Figure 4.33. Comparison of peak plantar force predicted by the human leg FE model with and without element deletion (ED), and plantar force at time of fracture in the element deletion model. Input conditions from left to right are arranged from low to high frequency. No fracture conditions are denoted using an asterisk.

Similar trends were observed for plantar impulse, with a few exceptions. For the 100g, 12 m-s^{-1} and 250g, 10 m-s^{-1} input conditions, the impulse at time of peak was greater for the element deletion model. A brief inspection of the time-history for these plots revealed that the “fracture” induced a double peak in plantar force which the second peak had a larger magnitude than the first. For this reason, the impulse for these conditions was calculated over a larger span of time, though for a smaller magnitude of peak force.

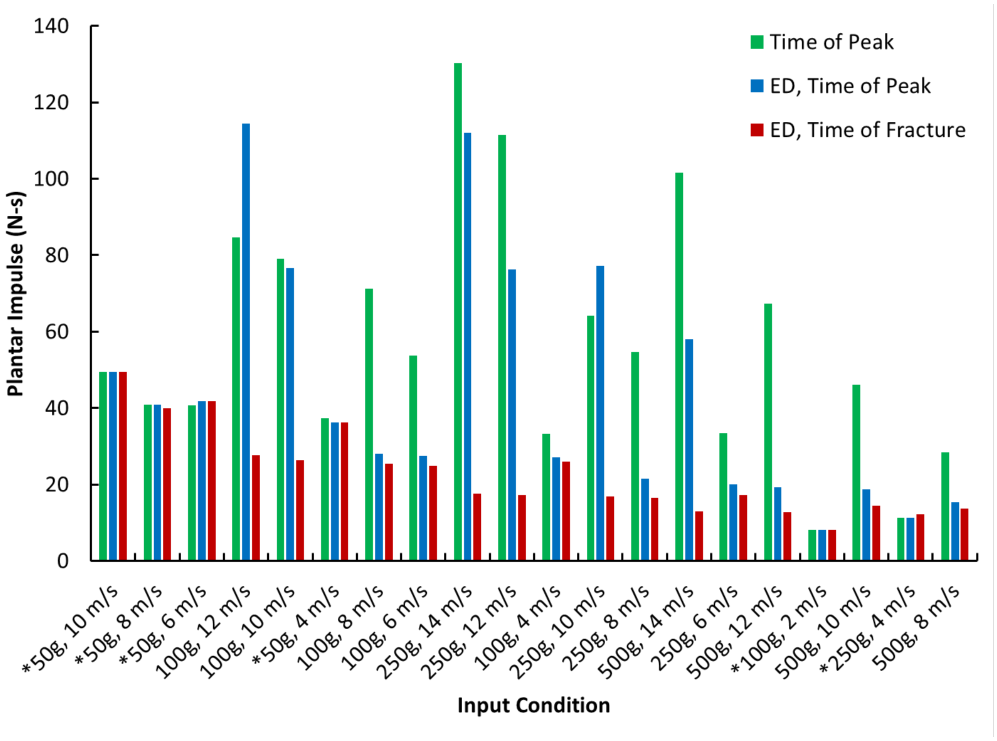

Figure 4.34. Comparison of plantar impulse at time of peak plantar force predicted by the human leg FE model with and without element deletion (ED), and plantar impulse at time of fracture in the element deletion model. Input conditions from left to right are arranged from low to high frequency. No fracture conditions are denoted using an asterisk.

These models were also used to investigate the relationship between the magnitude of plantar force and proximal tibia force for the purpose of understanding injury progression. While the previous chapter discussed the progression of injury in terms of fracture timing and forces measured at the footplate and proximal tibia, the FE model allowed for the comparison of peak forces with and without fracture. In all cases the peak plantar forces exceeded proximal tibia forces (Figure 4.35). Proximal tibia forces at fracture were lower than the peak proximal tibia forces for all input conditions, and also occurred prior to time of peak force. These results show that the proximal tibia force continues to increase after fracture. Additionally, since peak proximal tibia force occurs after time of fracture, the peak is likely affected by the energy dissipation by the fracture. Note that the conditions marked with an asterisk were sub-injurious.

In terms of injury criteria development, it is important that the force be measured near the location of injury or at least estimated near the location of injury so as to avoid inertial differences and force transmission changes due to fracture. As shown in Figure 4.35, peak proximal tibia force is dependent upon the presence of fracture in a more distal region of the leg. The differences caused by fracture and measuring force at the proximal tibia could potentially produce a situation where both a fracture and no fracture case could occur at the same peak proximal tibia force. These complications and how they relate to the importance of the location of force measurement will be further discussed in Section 6.1.

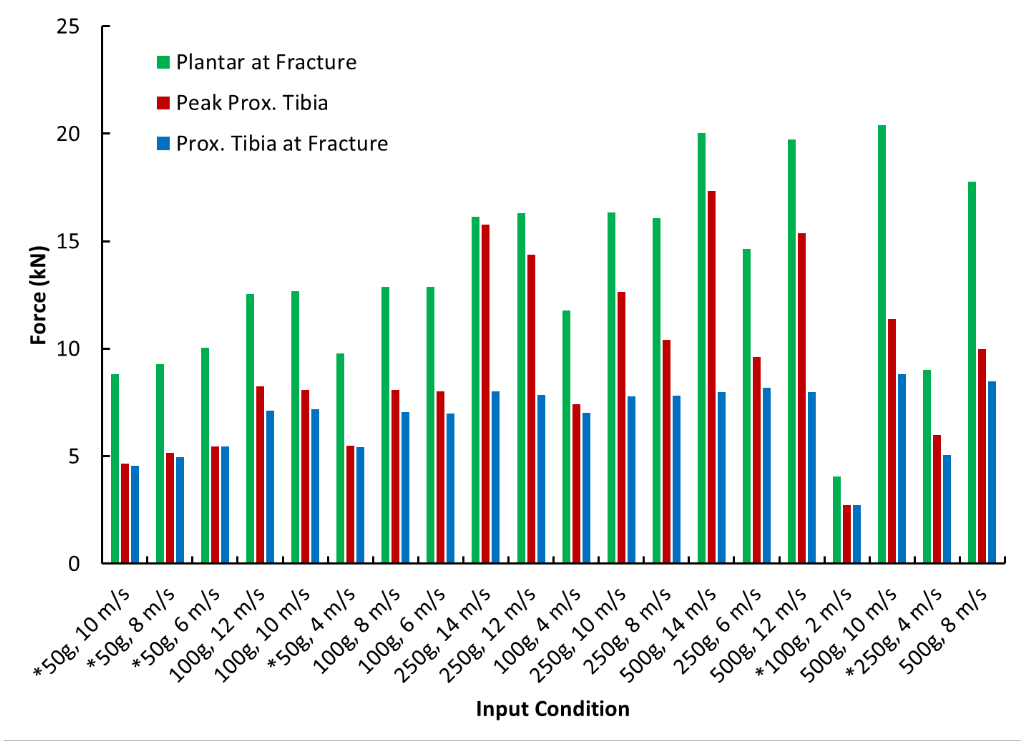

Figure 4.35. Comparison of plantar force at fracture, maximum proximal tibia force, and proximal tibia force at time of fracture for the human leg FE model. Input conditions from left to right are arranged from low to high frequency. No fracture conditions are denoted using an asterisk.

4.3.2 The Effect of Boundary Condition on Leg Response

To investigate the effect of boundary conditions on leg response, additional simulations were run using a fixed proximal boundary condition for select input conditions. Force at fracture at the footplate and proximal tibia were recorded for each of the simulations for both the free and fixed boundary conditions (Figure 4.36). Footplate force at fracture was similar for both the free and fixed boundary conditions and followed a pattern similar to an exponential decay with time of fracture. Proximal tibia forces for the two boundary conditions had more than a 5 kN difference for the same time to fracture in some cases. This difference is indicative of inertial effects which lead to differences between the force measured at impact and the force measured away from the load. In the case where the proximal boundary is fixed, a reaction force contributes to the load at the proximal tibia, but in the case where the boundary is allowed to translate, the inertia of the reaction mass dictates the proximal tibia force. The fact that there is so much difference in the proximal tibia force at fracture for the two boundary conditions emphasizes the importance of selecting an injury predictor that does not change as a result of different proximal boundary conditions. Thus, proximal tibia force should not be used for predicting foot and ankle fracture risk for this reason.

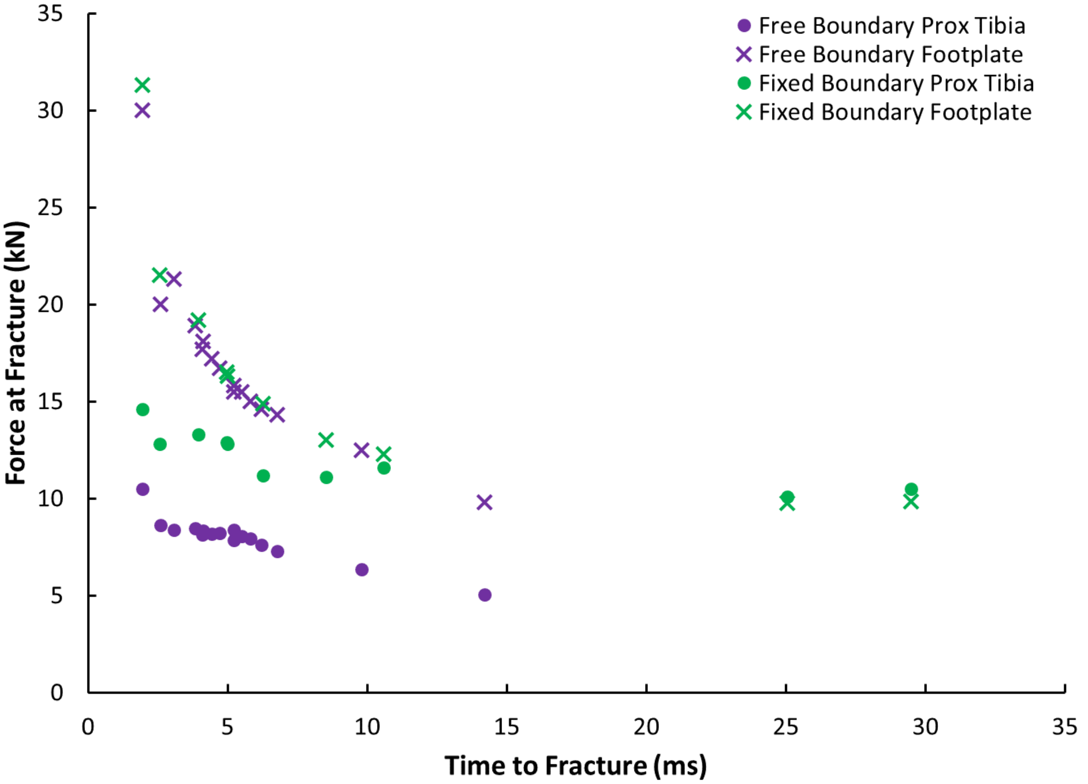

Figure 4.36. Comparison of peak footplate and proximal tibia forces at time of fracture in the human FE model for both the fixed and free boundary conditions.

Footplate and proximal tibia force response for fixed and free boundary conditions with the same input acceleration pulse are shown in Figure 4.37 for an injurious and sub-injurious input. The footplate forces were similar for both boundary conditions up to the time of peak acceleration or fracture occurred. For the injurious case, both footplate forces decreased after time of fracture, though the force leveled off for the fixed boundary case. For the fixed boundary case, footplate and proximal tibia forces were nearly equivalent after time of peak acceleration. For the free boundary condition, large differences were present for the footplate and proximal tibia forces throughout the entire positive phase of the force, and the peak difference occurred near the time of peak footplate acceleration, as expected.

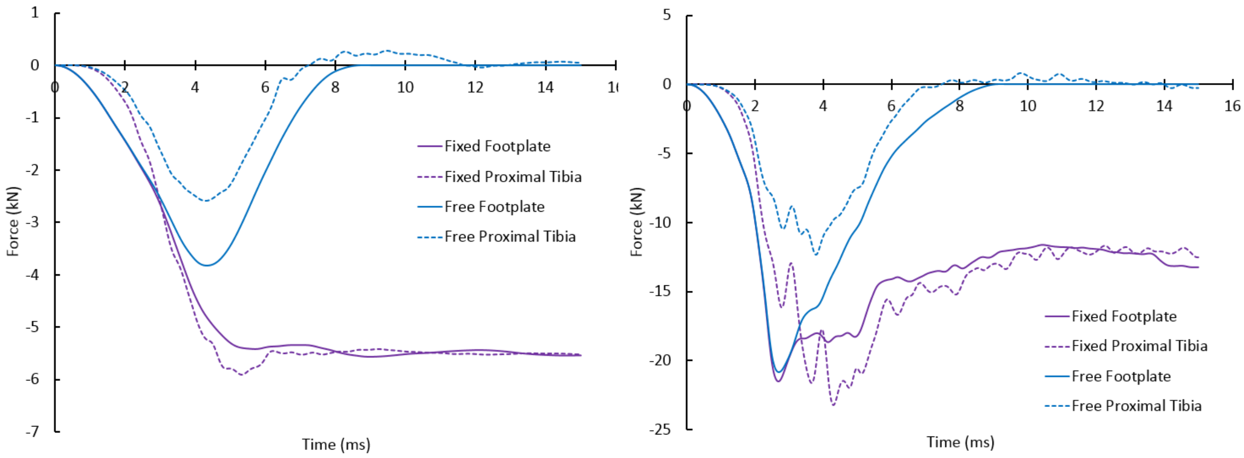

Figure 4.37. Human leg FE footplate and proximal tibia forces for fixed and free proximal boundary conditions. A 100g subinjurious pulse is shown on the left and a 500g injurious pulse is shown on the right.

These differences in the behavior of the force for different boundary conditions further demonstrate the importance of measuring force near the location of injury if it is to be used for development of an injury criterion. The fact that there is such a large difference between peak proximal tibia forces for these different boundary conditions highlights the potential error that may be interwoven into existing injury risk functions such as the one developed by Yoganandan et al., which used proximal tibia force as the injury predictor and based the risk curve parameters off of a data set which included PMHS data from tests with both fixed and free boundary conditions.[231]

4.3.3 The Effect of Pulse Shape on Leg Response

Additional FE simulations were run to investigate the effect of pulse shape on force at fracture. Sinusoidal and triangular pulse shapes were compared, with peak acceleration and frequency varied such that duration of the triangular pulses was equal to the inverse of half of the frequency using the input conditions described in Table 4.5.

Force at fracture was recorded and plotted versus time to fracture and time-to-peak acceleration to show the differences between triangular and sinusoidal pulse shapes (Figure 4.38, Figure 4.39). For a given time-to-peak acceleration, the fracture force is lower for the triangular pulse shape than the sinusoidal pulse shape. For a given time to fracture, the force at fracture is essentially equal for the two pulse shapes. This suggests that while the peaks for the two different pulse shapes are the same, the integral of the pulse shape dictates the time and force at fracture for the conditions shown. The fact that force at fracture is not constant for these conditions, but begins to level off for the longer duration conditions dictates that some aspect of time in addition to force is necessary for predicting fracture.

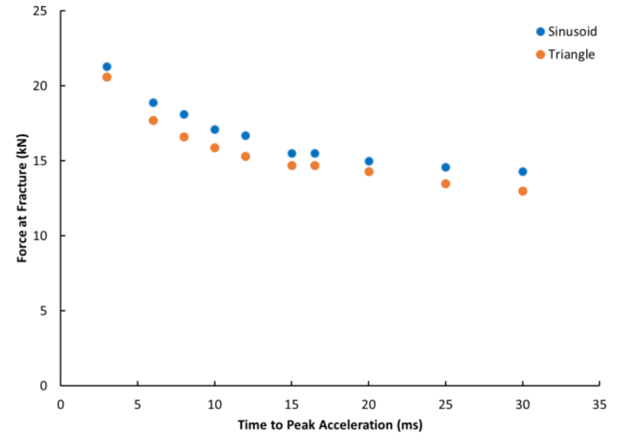

Figure 4.38. Comparison of plantar force at fracture for sinusoidal versus triangular pulse shapes for peak footplate accelerations of 500g and time-to-peak acceleration ranging from 3ms to 30ms. Forces are plotted against time-to-peak acceleration.

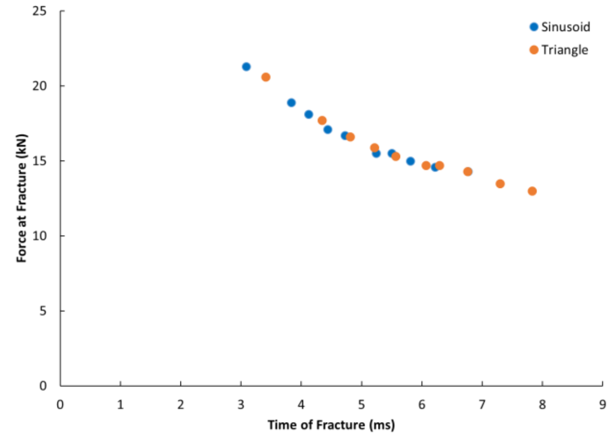

Figure 4.39. Comparison of plantar force at fracture for sinusoidal versus triangular pulse shapes for peak footplate accelerations of 500g and time-to-peak acceleration ranging from 3ms to 30ms. Forces are plotted against time of fracture.

For intermediate strain levels (prior to failure) trends between strain, force, and impulse for sinusoidal and triangular pulse shapes were investigated. Figure 4.40 and Figure 4.41 shows that the force and time or impulse associated with different strain levels varied slightly with pulse shape, though differences were minimal. Referring back to Figure 2.17, the force versus time plot for different strain values for the leg resembles the relationship between the peak displacement and input peak and duration of the single degree-of-freedom lumped mass model. Since fracture forces showed a similar trend for both triangular and sinusoidal pulse shapes, it was concluded that minimal differences in pulse shape are not enough to justify the use of separate characterization of injury risk for different pulse shapes.

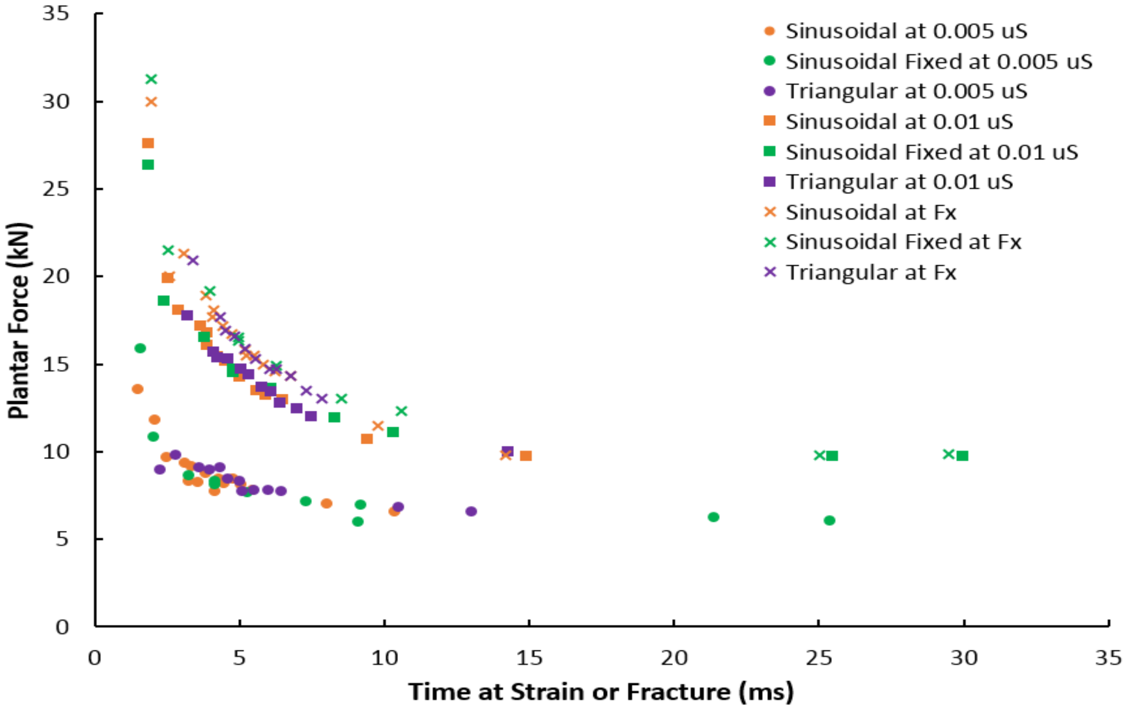

Figure 4.40. Comparison of fixed and free boundary conditions and pulse shape on the relationship between calcaneus strain, plantar force, and time. Symbols represent different strain levels while colors represent differences in proximal boundary or pulse shape.

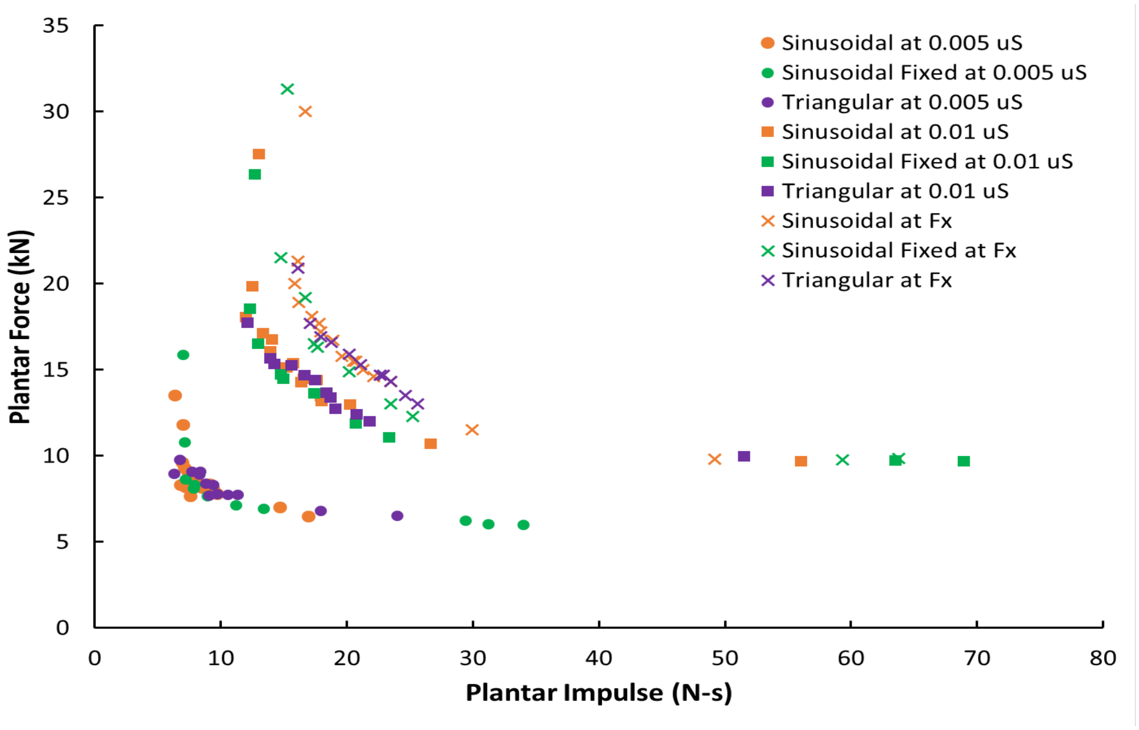

Figure 4.41. Comparison of fixed and free boundary conditions and pulse shape on the relationship between calcaneus strain, plantar force, and plantar impulse. Symbols represent different strain levels while colors represent differences in proximal boundary or pulse shape.

It should be noted that for short duration loads, impulse is less variable for a level of model calcaneus strain. For long durations, strain level would be more accurately predicted by force. Assuming that the human leg behaves similarly, the FE model provides a more continuous estimate of the effect of load duration on force at fracture and agrees with the conclusions from the PMHS impactor study. For the case of the low impactor pulse (~20 ms time-to-peak), the FE model showed that the force at fracture trends toward a constant value of force. The high and medium impactor conditions are located in the region of Figure 4.40 where force at fracture varies with duration, and falls within the area of Figure 4.41 where impulse has less variation with strain level.

4.4 Discussion

The modified human FE model was used to predict response of the leg within the range of load durations for which it was benchmarked (5-80 ms), and to extrapolate behavior of the leg to a slightly larger range of load durations (5-200 ms). Since the model is able to provide accurate results up to 80 ms, it was assumed that the rate dependency of the model properties would be less prominent at lower rates of loading. One issue with extrapolating to larger durations is that larger durations are associated with larger displacements. Because of the tendency of the ankle to evert while under large compressions, it is important to consider the motion of the ankle joint in the model when interpreting the results for the extrapolation simulations. The heel pad material model used in the FE model was based on experimental compression testing performed up to strain rates of 57 s^{-1}. For the 500g, 14 $m \cdot s^{-1}$ condition, the peak strain rate in the heel pad was 35.3 s^{-1}, so the range of strain rates for which the material model was developed was not exceeded in the parametric study.

Results of the parametric study are consistent with the experimental impactor test results in that force at fracture varies with duration of load (or loading frequency). Since failure in the FE model was indicated when a level of strain was exceeded, the relationship between force and impulse at fracture relates to a constant level of strain. The relationship between these parameters is consistent with the pattern of peak deformation of a single degree-of-freedom lumped mass model as a function of peak force and duration in that larger forces are required to cause the same amount of deflection or strain at short.[197,214] This similarity suggests that the leg may be modeled in this way to provide a characterization of the relationship between force, duration, and injury.

The results from previous PMHS axial loading tests were used to provide a visual comparison of the relationship between FE model fracture and human leg fracture. A combination of censored and uncensored fracture force and time-to-fracture (or peak force and time-to-peak force) for a set of 137 previous PMHS axial loading tests are plotted in Figure 4.42 along with FE fracture data points for a sinusoidal acceleration pulse shape. This data set will be further described in a later Chapter, but is used here to compare against the FE model results.

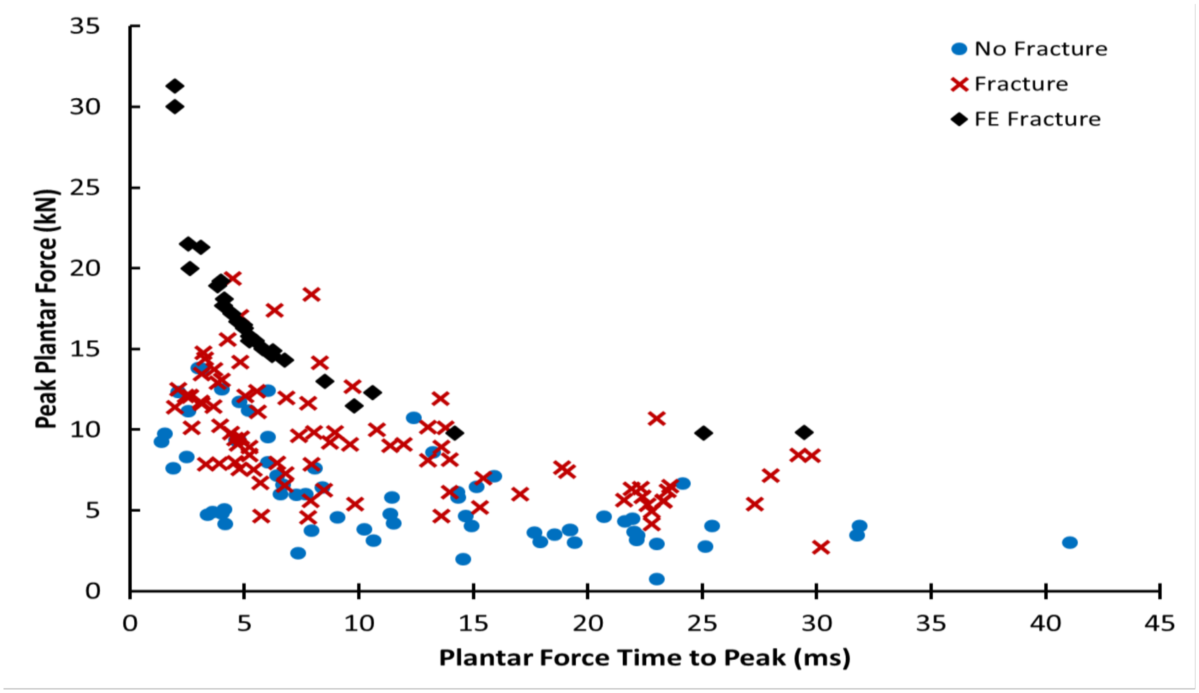

Figure 4.42. Fracture force versus time-to-peak for the human FE model compared to fracture and no fracture data points from PMHS axial loading tests from the *Combined Data Set* (Note that this PMHS data set will be discussed in detail in Chapter 6).

Footplate forces for the time of fracture in the FE model tended to be larger than a majority of the PMHS fracture data points for a given time of fracture or peak force. Since FE model fracture occurs when strains exceed a set level of plastic strain, this could indicate that the strain level used to indicate fracture for the FE model is higher than the average failure strain of the PMHS data set. On the other hand, age, geometry, mass distribution, and bone mineral density of the sample of PMHS data points factor into this difference.

Though the trend is not obvious, for short times-to-peak force, injury and no-injury PMHS data points occurred for higher force levels than for longer times-to-peak. A detailed statistical analysis is necessary to characterize this trend, but the higher forces associated with no-injury data points for short times-to-peak than for injury data points at longer times-to-peak suggest that the PMHS data is consistent with the theory of von Gierke.[214]

The parametric study showed that a change in acceleration pulse shape from sinusoidal to triangular did not significantly change the pattern of peak force versus time-to-fracture in the FE model. It should be noted, however, that only this slight variation in pulse shape was evaluated and that large variations in pulse shape such as those shown in Figure 4.43 may not yield the same pattern of force versus time-to-fracture. Moving forward, the decision was made to limit the focus of the dissertation on input pulses which resembled sinusoidal pulses for simplification, though not necessary to account for pulse shape since specimen variability is likely to be greater than the effect of slight differences in force pulse shape.

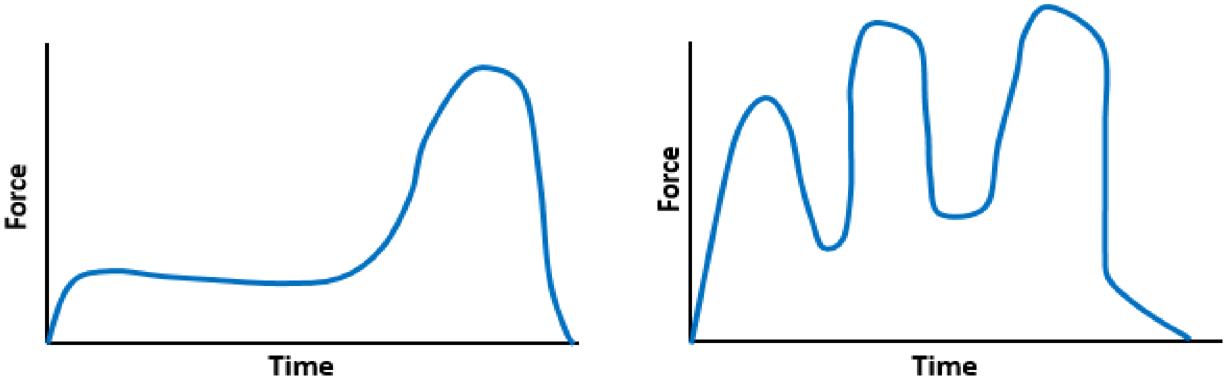

Figure 4.43. Example force pulses which may result in a different relationship between peak force, time-to-peak, and strain.

5 Human Lumped Parameter Modeling

Having demonstrated the dependence of axial leg deformation and fracture on duration and peak force using the finite element model and experimental tests, the next focus of the dissertation was to characterize this dependence so that it may be used in the development of an injury criterion. The theory proposed by von Gierke relied on the use of a single degree-of-freedom (DOF) dynamic model to predict the response of biomechanical systems. This chapter will evaluate the ability of single- and multiple-DOF dynamic models to represent and predict the response of the human leg to axial impact loads in an attempt to simplify the relationship between impact force, duration, impulse, and axial compression of the leg.

5.1 Background

Applications for a LMM of the human leg extend from athletic shoe design to understanding injury at the high rates of loading typical of underbody blast of military vehicles. While finite element (FE) models provide a more detailed estimation of leg response to axial loading, these models require longer computation time which reduces their utility for broad-scope optimization of shoe or boot design. More importantly, many existing FE models are valid only for a narrow spectrum of loading rates, making them unreliable for extrapolation or application to different loading regimes. Several studies have developed LMMs of the leg using single- and multiple-DOF approaches.[7,43,94,106,114] Some of these studies are summarized to offer a perspective on the range of stiffness estimates for the leg (Table 5.1).

Table 5.1. Summary of previous estimates of leg and foot compliance from dynamic models of the human leg where k[kN-m^{-1}] and c[N-s-m^{-1}].

Publication	DOF	Leg Compliance	Foot Compliance
Perry et al., 2014[165]	3	k=8734, c=499	k=1198, c=130
Henderson et al., 2013[94]	3	k=9058, c=0	k=2028, c=800
Kim et al., 2013[106]	3	k= 892.0, c=40.3	k= 46.8, c=567
Cheng et al., 2004[43]	2	k=141.77, c=932.4 (foot+leg)	
Cheng et al., 2004[43]	2	k=34.87, c=877.0 (foot+leg)	
Andrews and Dowling 2000[7]	1	k=173.8 (foot+leg)	
Kuppa et al., 1998[114]	1	k=963 (foot+leg+padding)	
Farley and Gonzalez 1996[67]	1	k=7-16.3 (foot+leg)	

DOF=Degrees of Freedom

The stiffness comparison in Table 5.1 demonstrates the variability in leg response to axial impact at different loading rates in addition to the sensitivity of the stiffness estimate to model setups. Models such as those developed by Liu and Nigg, McMahon and Cheng, and Farley and Gonzalez were developed for purposes of gait analysis, while others such as Kim et al. focused on understanding the effect of geometry and mass on leg response for the purposes of normalization and corridor development.[67,106,127,137] Models developed for gait analysis have estimated lower stiffness for the leg (k<1000 kN-ms^{-1}), while those developed for high rate applications such as underbody blast have estimated a higher leg stiffness (k>8000 kN-ms^{-1}).[94,165] This emphasizes the importance of designing models based on the application to ensure the model can provide the necessary level of granularity between foot and leg stiffness, which may prove important for higher loading rates.

Cheng et al. modeled the leg as a two-DOF system in order to investigate the effect of padding for mitigating injury in automotive intrusion events. This model consisted of a foot mass (2.07 kg or 1/3 of the total leg mass) and a leg/knee mass (9.43 kg or 2/3 of the total leg mass) separated by a spring (34.87 kN-m^{-1}) and damper (877.0 N-s-m^{-1}) representing the compliance of the leg.[44] A second model was developed to represent the leg with certain proximal restraints at the knee. For this model, the footplate was represented by a mass and the input condition was force acting on the footplate, and a reaction force was placed at the knee. In this case, the masses were allowed to float and the resulting model had a foot mass of 8.47 kg, and a leg/knee mass of 4.83 kg, spring constant of 141.77 kN-m^{-1}, and damping of 932.4 N-s-m^{-1}.

Kim et al. modeled the leg as a three-DOF system using data from a PMHS axial loading study performed by Funk et al. (Figure 5.1)[70,106] The model was apportioned based on the location of load cells in the experiment and stiffness and damping parameters were scaled based on geometry and bone mineral density of individual specimens. The first mass represented the mass of the foot, while the mass of the leg and tibia load cell was divided between m_2 and m_3. A cost function based on minimizing the residual forces between the model and experiments was used to estimate the parameters of the model.

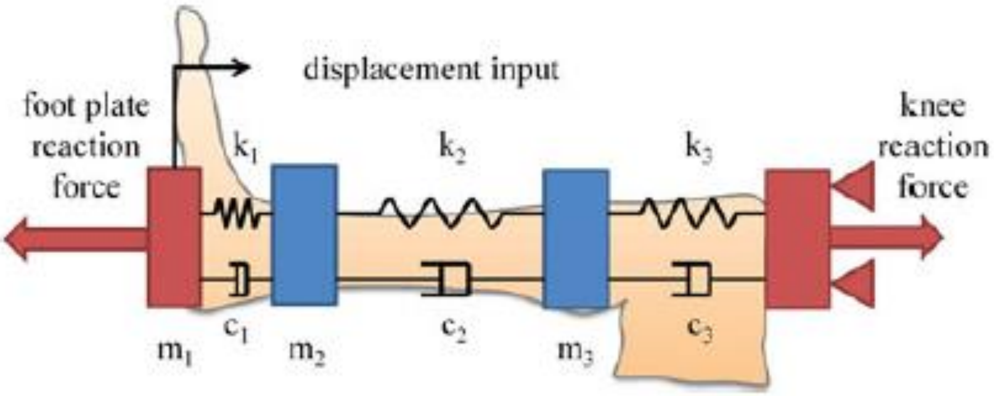

Figure 5.1. Second-order dynamic model of the leg developed by Kim et al. for use in normalizing data for corridor development (Image reproduced from Kim et al.[106] with permission from Taylor and Francis.)

A similar technique was used by Henderson et al. and Perry et al. to identify the parameters for a three-mass model of the leg. Parameters from these models were identified using select data from the drop tower study. Leg stiffness was estimated to be around 9000 kN-ms^{-1} with minimal damping, while foot stiffness was estimated to be from 1000-2000 kN-ms^{-1}.

The range in model parameters can be explained by differences in model set-up as well as differences in loading conditions for which each model was designed. Since each of these studies modeled data from different impact conditions, the models were tuned to match the response of the leg under those specific conditions. The narrower the range of input conditions, the less likely the model is able to predict the response of a separate input condition. Moving forward, the goal was to use the large range of input conditions covered by the FE parametric study to estimate the range of impact frequencies for which different LMM designs are able to capture the response of the leg.

For this portion of the dissertation, leg response to axial impact loading was characterized using both single- and multiple-DOF lumped-mass models (LMMs). Mechanical parameters for the LMM were estimated using an optimization subroutine based on maximizing correlation analysis (CORA) scores comparing LMM and finite element model responses.[94] Model validation was performed using the PMHS drop tower data.

Another use for representing the leg as a LMM is that is can be used to simplify the relationship between human and ATD force response. Rupp et al. used LMMs to represent the human and Hybrid-III femurs in effort to interpret the force response from the ATD in terms of injury risk.[187] In the case of the femur, Rupp et al. established a correlation between displacement and location of injury. For small displacements (short durations), knee fractures were found to be more common, while hip fractures were prevalent for larger displacement loads (longer durations). Lumped mass models were used to establish a relationship between the human and Hybrid-III femur. Assuming the leg can be represented in this way, a similar approach could be used to develop a transfer function from the behavior of the human leg to the ATD leg.

5.2 Single Degree-of-Freedom Model

An empirical approach was taken to develop a lumped mass model of the leg, starting with a simple model and increasing the model's complexity by adding additional parameters to improve the model's fit of the leg's response. Using this approach, it was possible to show the progression in terms of the range of frequencies for which each model could accurately predict leg response. The goal of this section was to estimate stiffness and damping parameters for a single degree-of-freedom LMM using the results from the finite element model parametric study to identify model parameters (Figure 5.2). Model 1A was used to represent the leg with a free proximal boundary condition. In the model, k_1 and c_1 represent the compliance of the entire leg (from plantar surface of the foot to proximal tibia). For Model 1A, m_1 is the mass of the leg (4.47 kg) plus the reaction mass (7.2 kg) in the case of the drop tower and FE model. The equation of motion for Model 1A is provided in Eqn. 5.1, and the equation for calculating the footplate force is shown in Eqn. 5.2. Footplate displacement corresponds to z_0 and proximal tibia displacement corresponds to z_1.

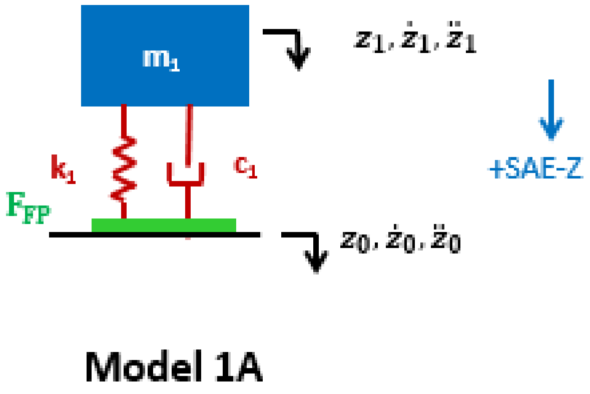

Figure 5.2. Single-DOF, second order dynamic model of the leg, where the mass (m_1) is the mass of the leg and k_1 and c_1 are stiffness and damping parameters. F_{FP} is the footplate reaction force, z_0 is the displacement of the footplate, and z_1 is the displacement of the proximal tibia boundary.

$$m_1\ddot{z}_1 + k_1(z_0 - z_1) + c_1(\dot{z}_0 - \dot{z}_1) = 0 \qquad \text{Eqn. 5.1}$$

$$F_{FP} = k_1(z_0 - z_1) + c_1(\dot{z}_0 - \dot{z}_1) \qquad \text{Eqn. 5.2}$$

Model parameters (k_1 and c_1) were identified using a reduced gradient algorithm in MATLAB (Mathworks, Natick, MA) to maximize the CORA score obtained by cross-correlating the LMM and finite element model response. For Model 1A, the finite element model footplate acceleration was used as the model input, and a combination of footplate force and proximal tibia displacement CORA scores were used to identify k_1 and c_1. The objective function for the optimization is provided by Eqn. 5.3, where h indicates the mechanical parameter being optimized (force or displacement), j is the index for the test condition, and CORA is the weighted overall cross-correlation score using a 0.84:0.16 weighting for the magnitude and progression scores.[85]

$$\textbf{Objective Function} = \max\left[\sum_{j=1}^{m}\left(\sum_{h=1}^{n}\mathbf{CORA_h}\right)_j\right] \qquad \text{Eqn. 5.3}$$

The weighted CORA score was chosen for use in the objective function because of its ability to include both the magnitude and shape changes. Traditionally sum of squared errors or maximum likelihood are used for optimizations such as this; however, incorporating the CORA progression parameter adds emphasis on the shape of the curve and uses a normalized cross-correlation method to determine the score. The magnitude parameter in the modified CORA score uses the area between the two curves to quantify the similarity of the curves. This is an improvement from the sum of squared errors approach, which can be magnified by small differences in phasing.[84] There is precedence for using the area between two curves to optimize model behavior, as this technique is used by optimization software such as LS-OPT (Livermore Software Technology Corporation, Livermore, CA). The fact that the weighted Overall CORA score is heavily weighted toward the magnitude score makes these two approaches closely related. Further, a previous study by Putnam et al. used CORA scores in an optimization routine to identify FE model parameters.[169]

Damping and stiffness parameters were limited to 1000 N-s-m^{-1} and 10000 kN-m^{-1}, respectively. The optimization was seeded to avoid converging on a local maximum within the design space. Five equally-spaced values were generated within the range of possible values for each parameter. Combinations of these values were used as the initial guess for the optimization for seeding purposes. The convergence criterion was set such that the optimization would yield a converged solution when the algorithm attempted to change the value of the objective function or model parameters by less than a prescribed tolerance.

Table 5.2. Optimized scale parameters for the SDOF LMM of the leg.

Optimization Data	Model	m_1 (kg)	k_1 (kN-m^{-1})	c_1(N-s-m^{-1})
FE Response, no Fracture	1A	11.67	1100.15	90.69

The optimized scale parameters are reported in Table 5.2 for Model 1A which used data from the FE parametric study. LMM response using the optimized model parameters was compared to average PMHS response for the Drop Tower PMHS test conditions as well as for the 28 conditions used for the FE parametric study. Weighted overall CORA scores for m_1 displacement and footplate force were calculated for each of the 28 FE parametric study input conditions (Figure 5.3). Input conditions were ordered from lowest to highest frequency to better show the range of frequencies for which the LMM was able to predict the response of the FE model. The LMM produced acceptable responses (CORA>0.8) for both displacement and force for frequencies less than 52 Hz, but was unable to produce accurate responses for higher frequencies for both the footplate force and the proximal tibia displacement. The corresponding frequencies for each of the input conditions can be found in Table 4.5.

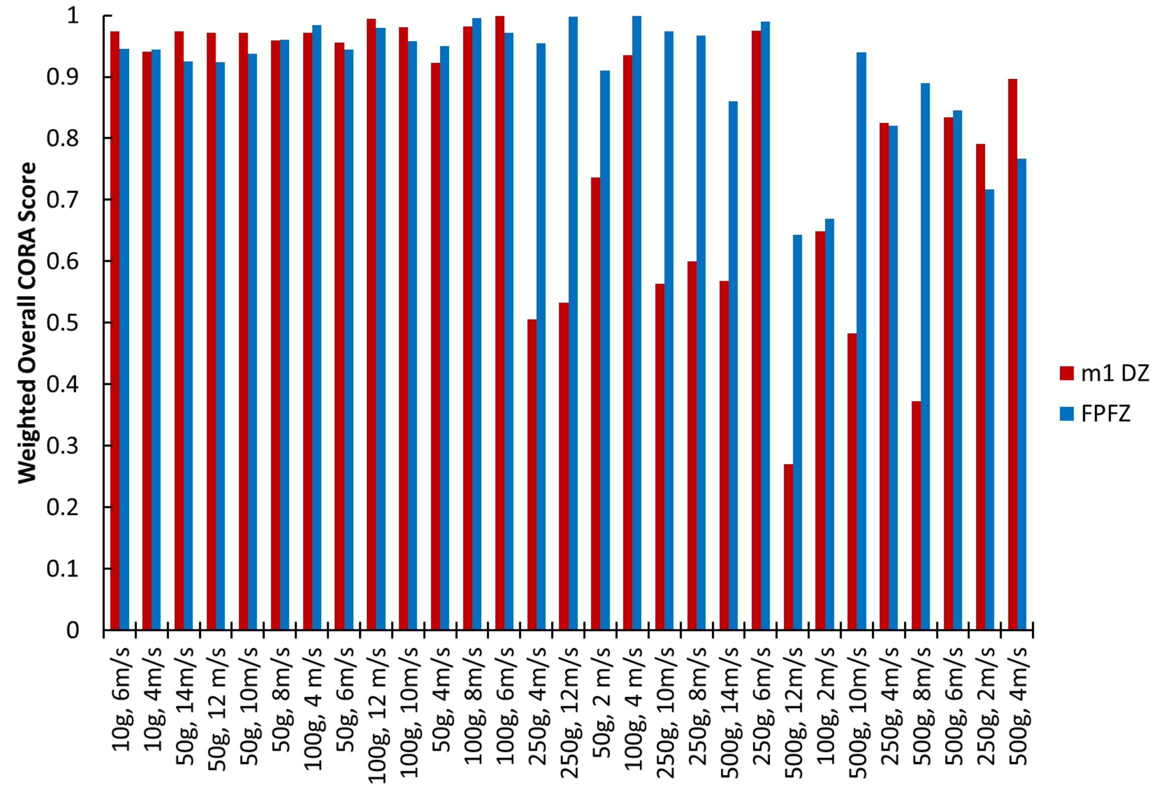

Figure 5.3. CORA results for comparison of LMM based on FE response parameters and individual FE responses. M1 DZ refers to the displacement of m_1, and FPFZ refers to footplate force.

Plots for FE and LMM response are shown in Figure 5.4 for the best and worst average CORA scores for reference of the quality of the model response compared to FE response. This particular SDOF model seems to be able to capture the displacement and force response of the leg for lower frequency loading conditions (less than 50 Hz), but struggles to provide a good fit of both displacement and force for higher frequencies. The model maintains the ability to predict footplate force responses with a weighted overall CORA score above 0.8 until frequencies of around 130 Hz, where the CORA score drops below 0.6. For these higher frequency cases the LMM force has a double peak, which highlights the lightly damped nature of the system.[30]

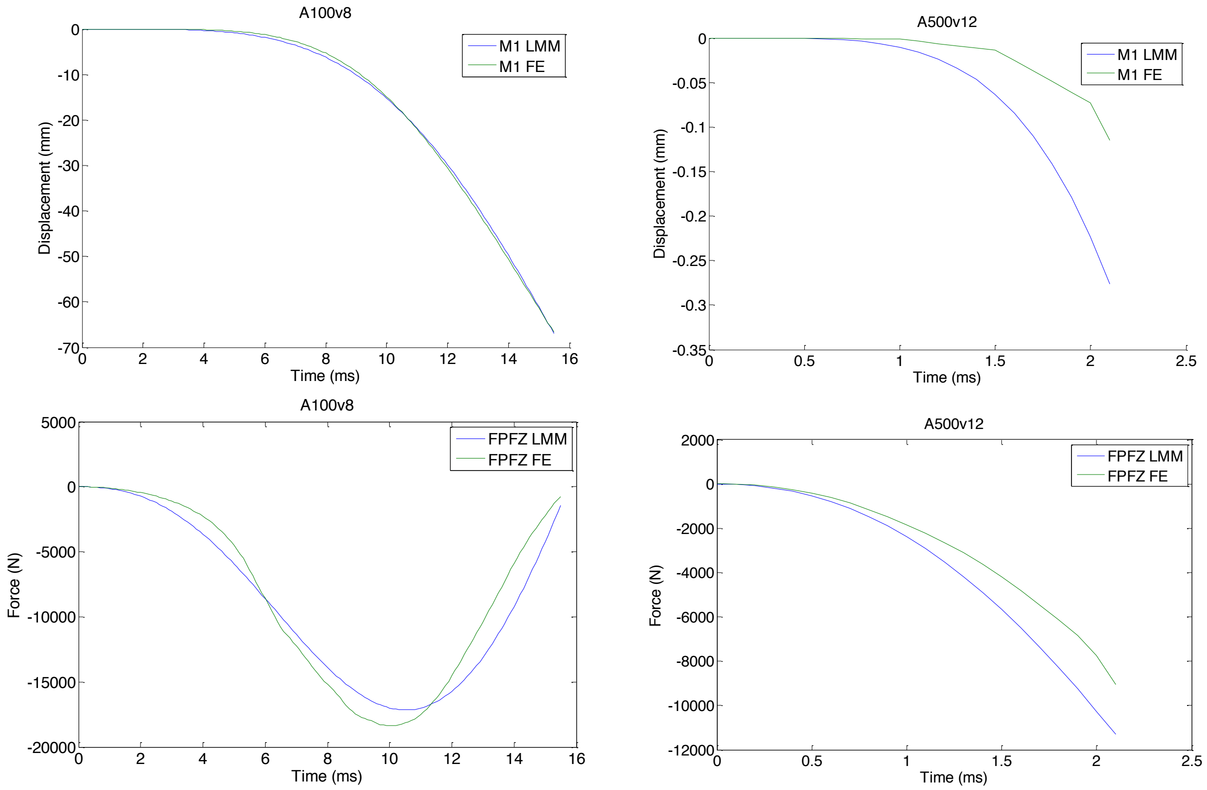

Figure 5.4. LMM response compared to FE response for the condition with the best average CORA score (100g, 8 m-s^{-1}, left) and worst average CORA score (500g, 12 m-s^{-1}, right).

The inability of the single-DOF model to predict both the displacement and force response of the leg is likely due to the model's inability to account for the recruitment of mass at different loading frequencies. While previous studies have shown that a single degree of freedom model is sufficient to model the leg under a smaller range of frequency inputs, this model is insufficient for the goals of this study.[6,44,67,114] Thus, in attempt to provide a better fit of both the displacement and force, an additional degree of freedom was added to the model. This approach is outlined in the next section.

5.3 Two Degree-of-Freedom Model

Having shown that the SDOF LMM has limitations in terms of predicting force and displacement of the leg for different frequencies of loading, an additional degree of freedom was added to the model. Using a two degree-of-freedom model (Figure 5.5) added two additional parameters for modeling the leg, which should increase the model's ability to fit the data. Further, the addition of another mass allowed for separation of leg and foot compliance. In the models in Figure 5.5, k_1 and c_1 represent the compliance of the foot, which includes heel pad and ankle compliance. Tibia/fibula compliance are modeled using k_2 and c_2. The equations of motion for Model 2A are presented as Eqn. 5.4 and Eqn. 5.5. Footplate reaction force and proximal tibia internal/reaction force can be calculated using Eqn. 5.6 and Eqn. 5.7.

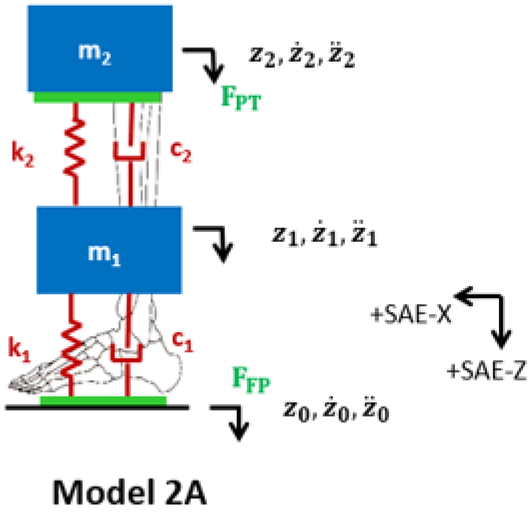
m_2
$z_2, \dot{z}_2, \ddot{z}_2$
F_{PT}
k_2
c_2
m_1
$z_1, \dot{z}_1, \ddot{z}_1$
+SAE-X
+SAE-Z
k_1
c_1
F_{FP}
$z_0, \dot{z}_0, \ddot{z}_0$
Model 2A

Figure 5.5. Two-degree of freedom, second order dynamic model of the leg, where the mass (m_1) is the mass of the leg, and m_2 is the reaction mass (Model 2A). Model 2B represents the case where the proximal boundary of the tibia is fixed.

$$m_1\ddot{z}_1 + k_1(z_0 - z_1) + c_1(\dot{z}_0 - \dot{z}_1) - k_2(z_1 - z_2) - c_2(\dot{z}_1 - \dot{z}_2) = 0 \quad \text{Eqn. 5.4}$$

$$m_2\ddot{z}_2 + k_2(z_1 - z_2) + c_2(\dot{z}_1 - \dot{z}_2) = 0 \quad \text{Eqn. 5.5}$$

$$F_{FP} = c_1(\dot{x}_1 - \dot{x}_0) + k_1(x_1 - x_0) \quad \text{Eqn. 5.6}$$

$$F_{PT} = c_2(\dot{x}_2 - \dot{x}_1) + k_2(x_2 - x_1) \quad \text{Eqn. 5.7}$$

Model scale parameters (k_i and c_i) were again identified using a reduced gradient algorithm in MATLAB (Mathworks, Natick, MA) to maximize the CORA score calculated for the LMM response and FE model response. The 28 input conditions outlined in Table 4.5 were used to optimize the model parameters using footplate acceleration as the model input, and a combination of distal tibia displacement ($\ddot{z}_1$), proximal tibia force (F_{PT}), and footplate force (F_{FP}) CORA scores in the objective function (Eqn. 5.3). The parameters optimized based on the FE model response are reported in Table 5.3.

Table 5.3. Optimized scale parameters for the 2-DOF LMM of the leg.

Optimization Data	Model	i	m_1 (kg)	k_1 (kN-m^{-1})	c_1(N-s-m^{-1})
FE Response, no Fracture	2A	1	4.47	950.58	148.79
		2	7.2	4497.1	398.54

Weighted overall CORA scores for m_1 and m_2 displacement and footplate and proximal tibia force were calculated for each of the 28 FE parametric study input conditions (Figure 5.6). Input conditions were again ordered from lowest to highest frequency to better show the range of frequencies for which the LMM was able to predict the response of the FE model. The LMM optimized based on the FE model response was able to produce weighted overall CORA scores greater than 0.78 for footplate force and greater than 0.68 for proximal tibia force for all of the 28 parametric study conditions.

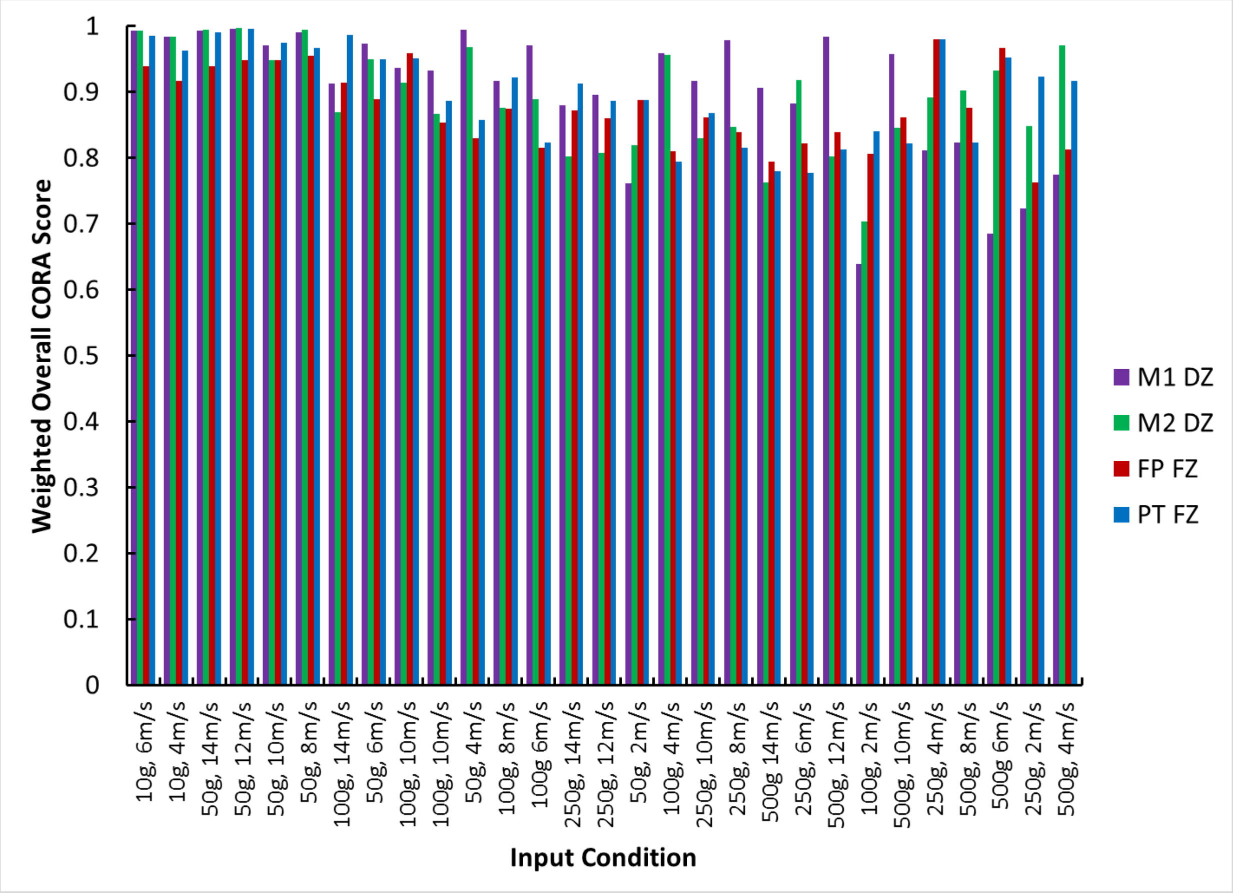

Figure 5.6. Comparison of CORA scores for cross-correlation of FE-based 2-DOF LMM and FE response for individual input conditions.

The average and standard deviation of CORA scores for all 28 test conditions showed that on average the LMM response was comparable to the FE model response for m_1 and m_2 displacements as well as footplate and proximal tibia force response (Table 5.4). Compared to the average weighted CORA scores for the single degree of freedom model, the 2DOF model performed significantly better for predicting displacement and force responses across the desired range of frequencies. The 2DOF model also provided additional detail in terms of separating foot and leg compression.

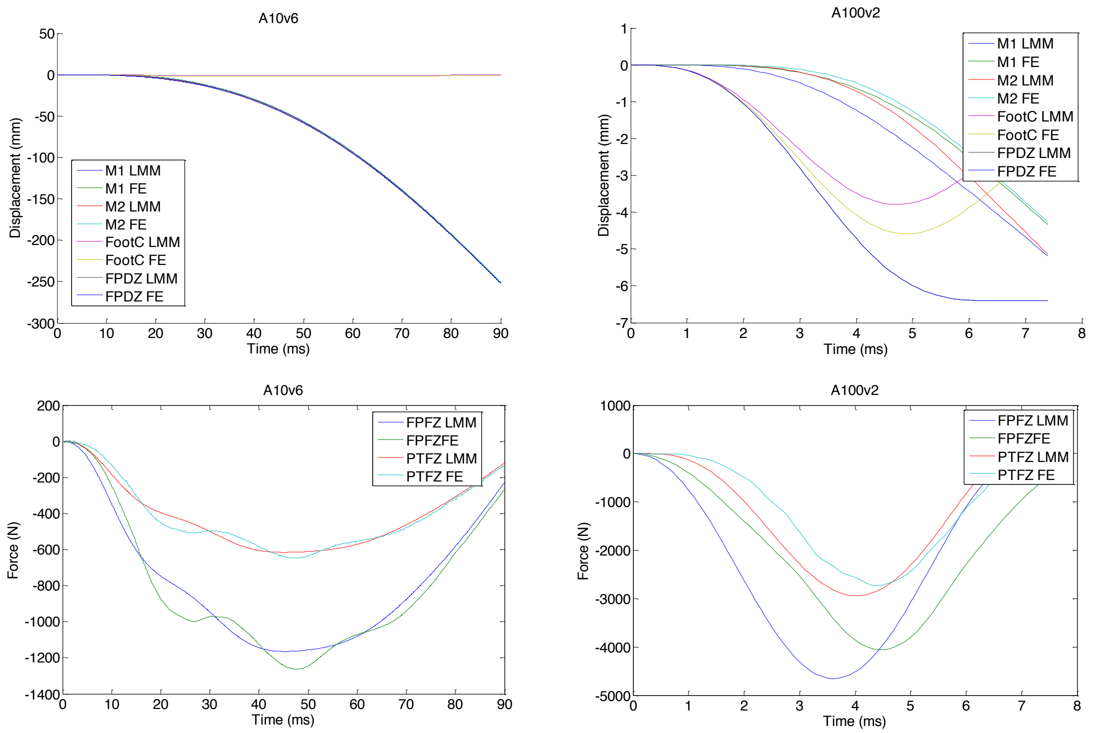

Figure 5.7. LMM response compared to FE response for the condition with the best average CORA score (10g, 6m/s, left) and worst average CORA score (100g, 2 m/s, right).

Table 5.4. Average weighted overall CORA score (standard deviation) for the 28 parametric study conditions comparing the FE model response to the LMM response from the single degree of freedom (SDOF) and two degree of freedom (2DOF) models optimized using FE model responses.

Measurement	**SDOF Model**		**2DOF Model**	
	Average	**Std. Dev.**	**Average**	**Std. Dev.**
M1 DZ	0.78	0.06	0.90	0.11
M2 DZ	-	-	0.89	0.08
Footplate Force	0.80	0.22	0.88	0.06
Proximal Tibia Force	-	-	0.85	0.09

The additional breakdown of model response allowed for a better fit of leg response to the 28 parametric study conditions compared to the SDOF LMM, though the LMM still failed to produce an acceptable match (CORA=0.8) of the human FE model response for individual conditions. Having shown that the addition of a degree of freedom improved the LMM's ability to predict leg response using pre-determined masses, the next step was to investigate how alternative mass distributions could improve model fit. While on average the 2DOF LMM provided a good fit of leg response for the impact frequencies of interest, the goal of achieving weighted CORA scores of over 0.8 for all 28 conditions was not met, though it satisfied this condition for all frequencies less than 100 Hz. Again, the corresponding frequencies for each of the input conditions can be found in Table 4.5.

5.4 Multiple Degree-of-Freedom Model with Heel Pad Compliance

The addition of another mass to the LMM provides the ability to distinguish between foot/ankle compression and heel pad compression. This additional compliance could have the potential to allow for distinction between calcaneus and pilon fractures, though this goal was not a direct aim of the dissertation. To explore the utility of including additional parameters to represent heel pad compliance, yet another LMM was developed.

A model using displacement of the footplate as the input, and three separate masses for the foot (m_1), leg (m_2), and reaction mass (m_3) was developed (Figure 5.8). The same methods were used to identify model parameters using the FE model results for which failure was not included. Footplate force, proximal tibia force, foot displacement, distal tibia displacement, and proximal tibia (pot) displacement were incorporated into the CORA-based objective function. Model equations are presented as Eqn. 5.8-Eqn. 5.10.

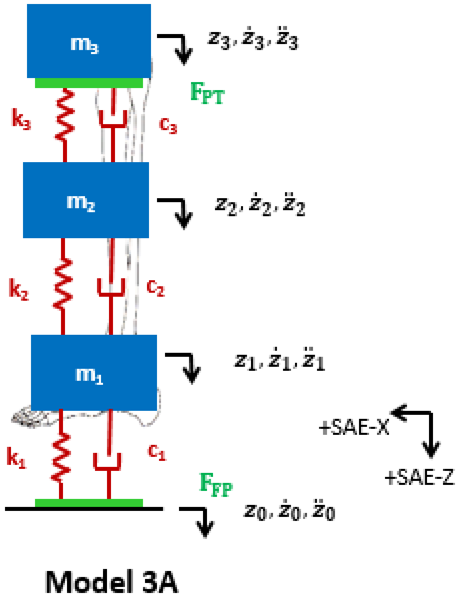
m3
$z_3, \dot{z}_3, \ddot{z}_3$
F_PT
k3
c3
m2
$z_2, \dot{z}_2, \ddot{z}_2$
k2
c2
m1
$z_1, \dot{z}_1, \ddot{z}_1$
+SAE-X
+SAE-Z
k1
c1
F_FP
$z_0, \dot{z}_0, \ddot{z}_0$
Model 3A

Figure 5.8. Schematics of the multiple degree-of-freedom model which includes heel pad compliance. Footplate displacement corresponds to z_0, z_1 is foot (calcaneus) displacement, z_2 is tibia displacement, and z_3 is the proximal tibia displacement.

$$m_1\ddot{z}_1 = -k_1(z_1 - z_0) + k_2(z_2 - z_1) - c_1(\dot{z}_1 - \dot{z}_0) + c_2(\dot{z}_2 - \dot{z}_1) \quad \text{Eqn. 5.8}$$

$$m_2\ddot{z}_2 = -k_2(z_2 - z_1) + k_3(z_3 - z_2) - c_2(\dot{z}_2 - \dot{z}_1) + c_3(\dot{z}_3 - \dot{z}_2) \quad \text{Eqn. 5.9}$$

$$m_3\ddot{z}_3 = -k_3(z_3 - z_2) - c_3(\dot{z}_3 - \dot{z}_2) \quad \text{Eqn. 5.10}$$

The optimal solutions are provided in Table 5.5 for Model 3A, along with the results from a separate optimization for which m_1 and m_2 were allowed to float (meaning the masses were not constrained to a single value, but rather included as an additional parameter in the optimization) with the constraint that the sum of the masses was equal to the total mass. This additional analysis was performed to investigate the effect of designating the masses in the model based on the assumed leg and foot masses. The mass associated with the foot (m_1)

did not change significantly, though some of the mass from the reaction mass shifted to the leg mass (m_2).

Table 5.5. Optimized parameters for the 3-DOF LMM of the leg based on the response of the human leg FE model.

Model 3A			
i	**m_i (kg)**	**k_i (kN-m^{-1})**	**c_i (N-s-m^{-1})**
1	1.225	1670.64	116.81
2	3.249	2760.96	298.42
3	7.2	9550.15	392.03
Model 3A with Floated Leg Masses			
i	**m_i (kg)**	**k_i (kN-m^{-1})**	**c_i (N-s-m^{-1})**
1	1.105	1400.3	184.2
2	4.377	3940.4	109.6
3	6.25	7090.3	267.2

The weighted overall CORA scores for LMM forces and displacements compared to those from the human FE model are summarized in Figure 5.9 through Figure 5.12. The CORA bar graphs showed that both LMMs provided a good fit of the human FE model force responses for frequencies less than 130 Hz, with the average footplate and proximal tibia force CORA scores being 0.93±0.07 and 0.92±0.08 for the fixed mass model and 0.93±0.06 and 0.93±0.06 for the floated mass model, respectively. While most input conditions yielded force CORA scores greater than 0.8 for both of the models, the average CORA score associated with displacement of the foot mass (m_1) was significantly increased by allowing the masses to float ($p=0.04$). The average CORA score for m_1 displacement increased from 0.82 to 0.89 when changing from the assigned masses to the floated masses design.

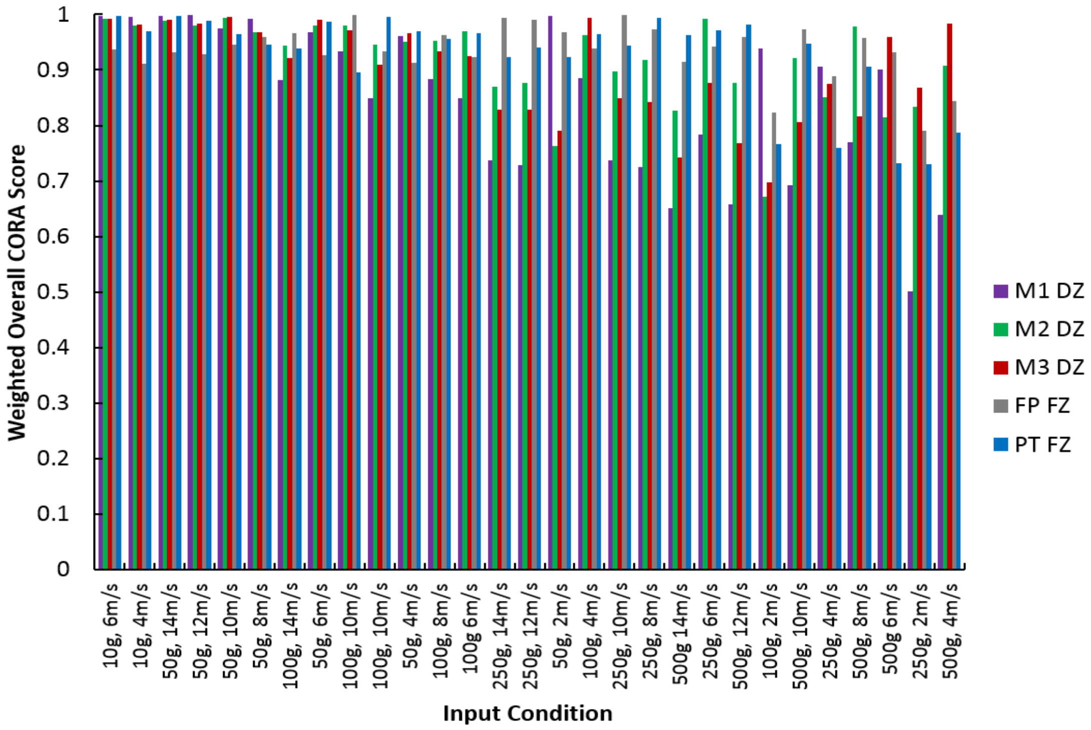

Figure 5.9. Weighted overall CORA scores for displacements and forces for the 28 FE model runs compared to Model 3A optimized with fixed masses. Input conditions are ordered from low frequency to high frequency. Note that DZ refers to displacement, while FP FZ and PT FZ refer to footplate and proximal tibia forces.

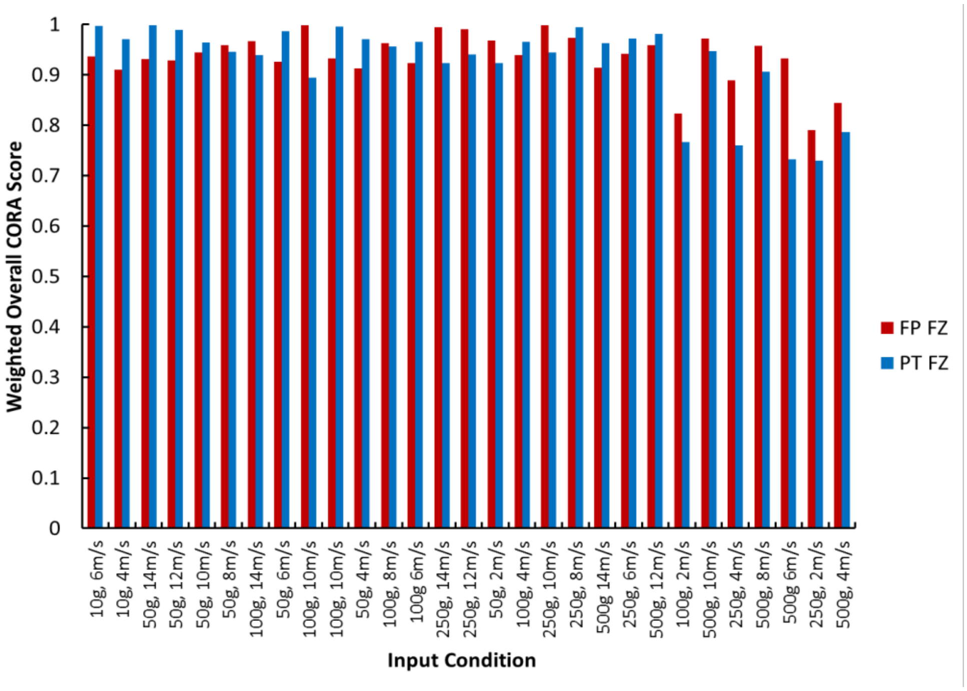

Figure 5.10. Weighted overall CORA scores footplate and proximal tibia forces for the 28 FE model runs compared to Model 3A optimized with fixed masses. Note that FP FZ and PT FZ refer to footplate and proximal tibia forces.

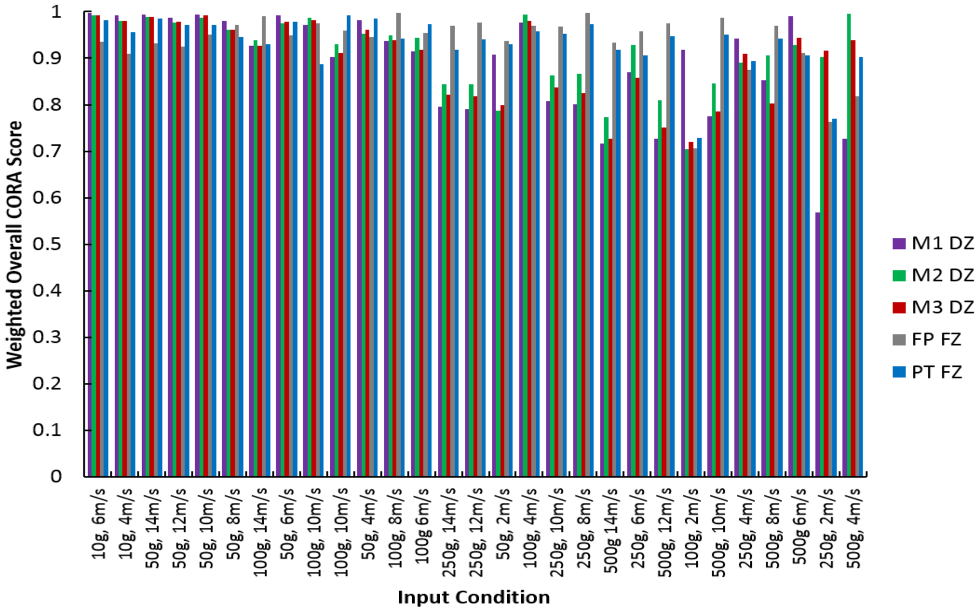

Figure 5.11. Weighted overall CORA scores for displacements and forces for the 28 FE model runs compared to Model 3A optimized with floating masses. Note that FP FZ and PT FZ refer to footplate and proximal tibia forces.

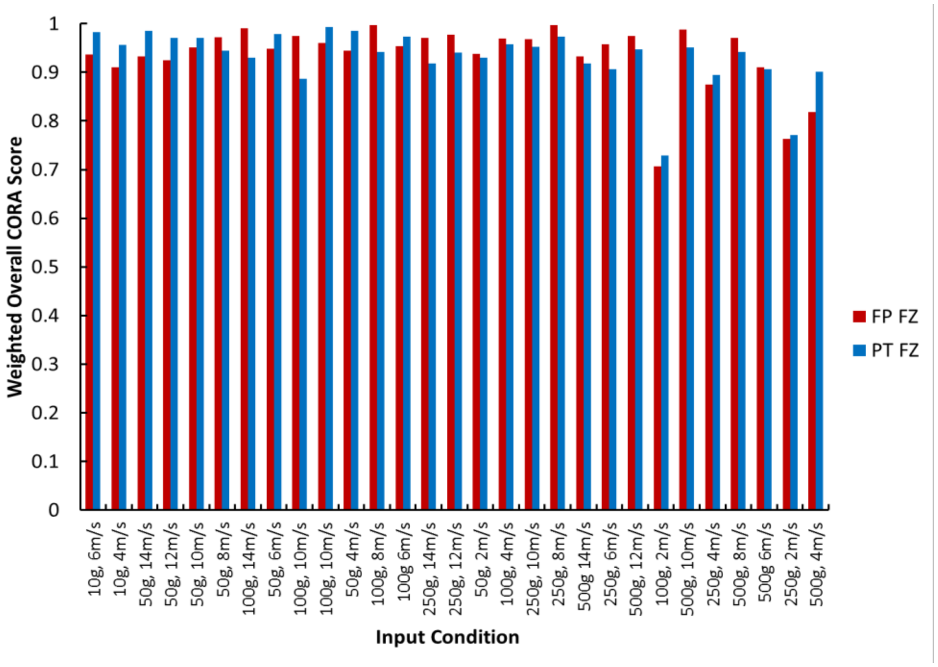

Figure 5.12. Weighted overall CORA scores footplate and proximal tibia forces for the 28 FE model runs compared to Model 3A optimized with floating masses. Note that FP FZ and PT FZ refer to footplate and proximal tibia forces.

Response of the floated mass model is shown in Figure 5.13 for the input conditions with the best and worst CORA scores. The best average CORA score, occurred for a low frequency condition, (10g, 6 m-s^{-1}). The worst average CORA score was calculated for the 100g, 2 m-s^{-1} condition, for which the LMM overestimated the footplate force and slightly overestimated the proximal tibia force. CORA scores above 0.9 were calculated for both the footplate and proximal tibia forces for loading frequencies below 156 Hz. Though the 500g, 10 m/s and 250g, 4 m/s conditions also produced force CORA scores above 0.8, the range of loading frequencies for which the model provides valid results should be limited to frequencies from 5-156 Hz.

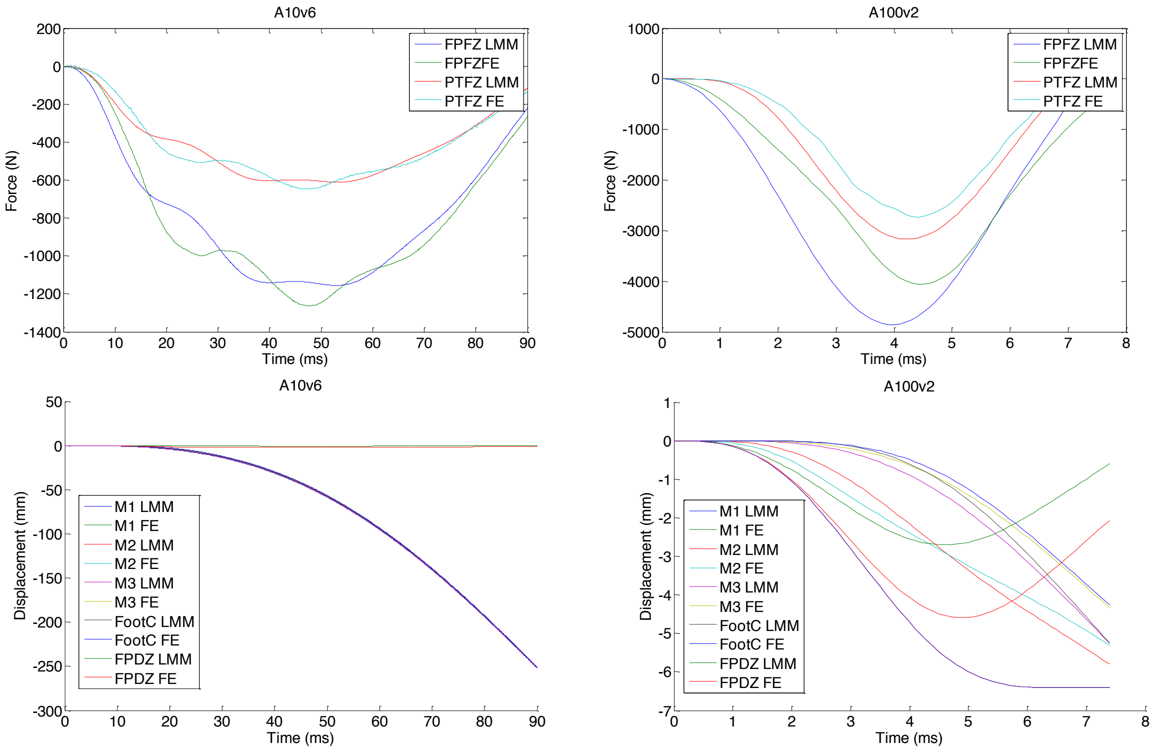

Figure 5.13. Floated mass LMM response compared to FE response for the condition with the best average CORA score (10g, 6m/s, left) and worst average CORA score (100g, 2 m/s, right).

Average and standard deviations for the CORA scores for the 28 parametric study conditions were compared for the 2-DOF model and 3-DOF model with floated masses. Average force CORA scores were significantly greater for the 3DOF model than the 2DOF model. While the average foot displacement CORA score was less for the 3DOF model, the difference was not statistically significant.

Table 5.6. Average weighted overall CORA score (standard deviation) for the 28 parametric study conditions comparing the FE model response to the LMM response from the single degree of freedom (2DOF) and two degree of freedom (3DOF) models optimized using FE model responses.

Measurement	**2DOF Model**		**3DOF Model**	
	Average	**Std. Dev.**	**Average**	**Std. Dev.**
Foot Displacement	0.90	0.11	0.89	0.11
Tibia Displacement	--	--	0.91	0.08
Prox. Tibia Displacement	0.89	0.08	0.90	0.09
Footplate Force	0.88	0.06	0.93*	0.06
Proximal Tibia Force	0.85	0.09	0.93*	0.06

*Significant difference

The addition of the third mass improved the fit of the LMM to the human FE model response and provided additional ability to distinguish between tibia and foot displacement. While the model was optimized using the entire sets of input conditions used for the FE model parametric study, the LMM struggles to provide an accurate fit of both human leg displacement and force data for the higher frequencies. Thus, it is recommended that model 3A only be used for loading frequencies ranging from 5-156 Hz. Though Model 3A provides a better fit of the human leg response, the structure of Model 2A allows for a more direct application to ATD development and will be discussed in a later chapter.

5.5 Multiple Degree-of-Freedom Model with Wobbling Mass

While the previous MDOF models were developed based on the finite element model response in order to optimize the model parameters for an expanded range of loading conditions, a separate model was developed using the experimental PMHS data to incorporate the effect of the soft tissue mass of the leg. Because of the compliant link between the bony mass and soft tissue mass of the leg, changes in stroke and velocity of the input may affect the recruitment of the soft tissue mass differently. Further, accounting for the leg's soft tissue mass separately could allow for distinguishing between the response of two specimens of the same total mass, but a different distribution of mass whether due to excess adipose tissue in the leg or the anthropometry. This model was developed in order to obtain specimen specific LMMs to gain insight in to the role of the soft tissue mass whereas the previous models accounted for the soft tissue effects by the distribution of the mass between the foot, leg, and reaction masses.

Two second-order lumped-mass models were developed based on experimental data from component PMHS axial impact tests from a previous study by Bailey et al.[14] The models consisted of three masses: one to represent the foot, one to represent the bony mass of the leg, and a third mass to represent the leg's soft tissue mass. An additional mass was added to represent the knee and reaction mass of the femur for the "free" boundary condition, as was the case for a previous study by Kim et al.[106] Compliances of the heel pad, foot and ankle, and leg were modeled as three separate sets of springs and dampers (Figure 5.14). The masses were defined such that m_1 is the mass of the foot and ankle (below the distal tibia accelerometer), m_2 is the mass of the leg from the distal to the proximal tibia, and m_3 is the reaction mass (6.2 kg). Stiffness and damping associated with the heel pad were represented by k_1 and c_1, while k_2 and c_2 represented the stiffness and damping of the foot and ankle. Tibia/fibula compliance was denoted by k_3 and c_3, and the soft tissue mass of the leg was modeled using a "wobbling mass" (m_w) attached to the bony tibia/fibula mass (m_2).[127] The equations of motion for the system under an imposed acceleration time history at the distal boundary are given by Eqn. 5.11-Eqn. 5.14.

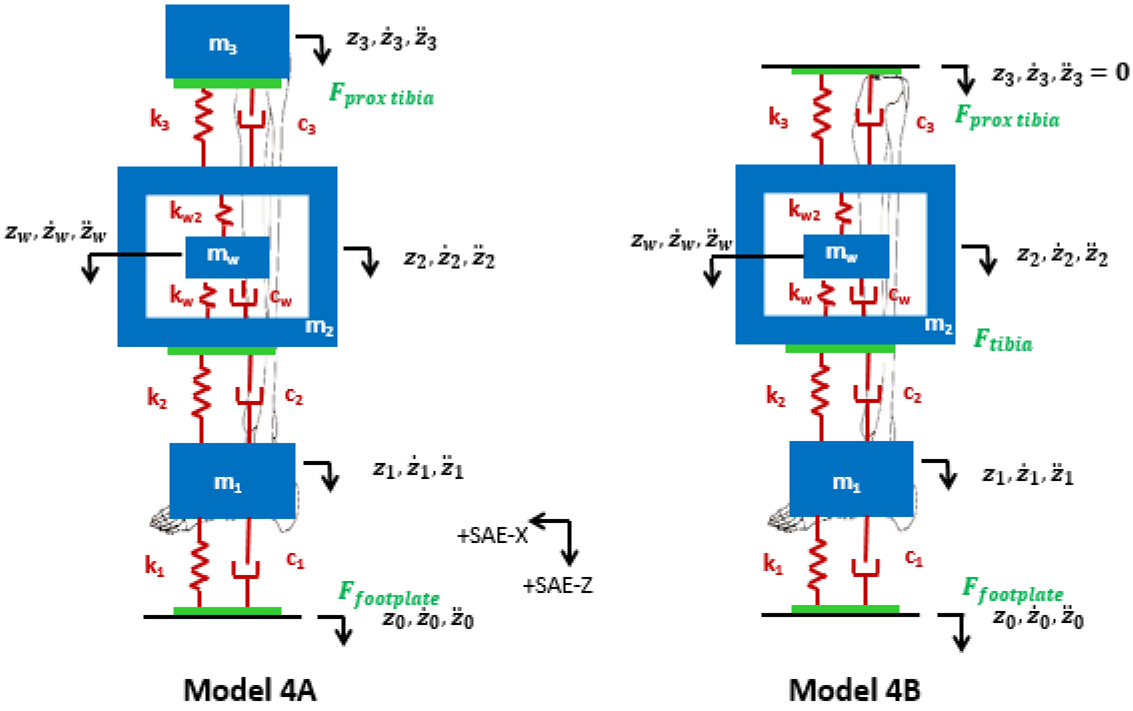
m3
z3, ż3, z̈3
Fprox tibia
k3
c3
kw2
zw, żw, z̈w
mw
z2, ż2, z̈2
kw
cw
m2
k2
c2
m1
z1, ż1, z̈1
+SAE-X
+SAE-Z
k1
c1
Ffootplate
z0, ż0, z̈0
Model 4A
z3, ż3, z̈3 = 0
Fprox tibia
k3
c3
kw2
zw, żw, z̈w
mw
z2, ż2, z̈2
kw
cw
m2
Ftibia
k2
c2
m1
z1, ż1, z̈1
k1
c1
Ffootplate
z0, ż0, z̈0
Model 4B

Figure 5.14. Second order dynamic models of the leg where k_i represent spring stiffness, c_i represent damping, and m_i represent mass. Displacement is denoted by z_i. Forces measured by experimental tests are also pictured. Model 4A represents the "free" test condition while Model 4B represents the "fixed" test condition.

$$m_1\ddot{z}_1 = -k_1(z_1 - z_0) + k_2(z_2 - z_1) - c_1(\dot{z}_1 - \dot{z}_0) + c_2(\dot{z}_2 - \dot{z}_1) \quad \text{Eqn. 5.11}$$

$$m_2\ddot{z}_2 = -k_2(z_2 - z_1) + k_3(z_3 - z_2) - c_2(\dot{z}_2 - \dot{z}_1) + c_3(\dot{z}_3 - \dot{z}_2) + c_w(\dot{z}_w - \dot{z}_2) + (k_w + k_{w2})(z_w - z_2) \quad \text{Eqn. 5.12}$$

$$m_3\ddot{z}_3 = -k_3(z_3 - z_2) - c_3(\dot{z}_3 - \dot{z}_2) \quad \text{Eqn. 5.13}$$

$$m_w\ddot{z}_w = -(k_w + k_{w2})(z_w - z_2) - c_w(\dot{z}_w - \dot{z}_2) \quad \text{Eqn. 5.14}$$

For Model 4B shown in Figure 5.14, $\ddot{z}_3$, $\dot{z}_3$, and z_3=0, which eliminates Eqn. 5.13.

Model parameters (k_i, c_i) were identified using a reduced gradient algorithm in MATLAB (Mathworks, Natick, MA) to maximize the CORA score obtained by cross-correlating the LMM response and experimental data. CORA is an objective rating method that is used to assess the relative correlation between two time varying signals, with scores are limited between values of 0 and 1 (perfect fit).[85] The 36 impactor tests were used to optimize for the model parameters based on footplate, calcaneus, and tibia displacement, and footplate and proximal tibia force CORA scores. The optimization was seeded with several different initial guesses to avoid converging on a local maximum within the design space. The convergence criterion was set such that the optimization would yield a converged solution when the algorithm attempted to change the value of the objective function or model parameters by less than a prescribed tolerance. The objective function for the optimization is given in Eqn. 5.3, where h indicates the mechanical parameter being optimized (force or displacement), j is the index for the test number, and CORA is the overall cross-correlation score calculated by averaging the equally-weighted magnitude, phase, and progression scores.[85]

A parameter-dependent modeling technique similar to the one used by Kim et al.[106] was used to scale the LMM parameters using geometric and mass characteristics based on experimental test subjects to scale the model to a 50th percentile male reference leg. Only response prior to the time of fracture was used in the optimization, and damping and stiffness parameters were limited to 1000 N s m^{-1} and 20000 kN m^{-1}, respectively. Parameters associated with the wobbling mass were treated as constants where k_w=6000 N-m^{-1}, k_{w2}=10000 N-m^{-1}, and c_w=650 N-s-m^{-1}. Liu et al. used these parameters, derived from tendon properties, in a previous model.[127] The reference mass of 0.63 kg for the bony mass of the tibia and fibula (m_2) was estimated using the GHMBC leg model and was scaled using tibia length and estimated tibia radius at mid-tibia. Eqn. 5.15 through Eqn. 5.22 summarize the relationship between the scale parameters (α_i and β_i) and the model parameters (k_i and

c_i), based on heel pad thickness ($t_{\text{heel pad}}$), ankle radius (r_{ankle}), ankle height (H_{ankle}), tibia radius (r_{tibia}), and tibia length (L_{tibia}) in meters.

$$k_1 = \alpha_1(1\text{m}^2)(t_{\text{heel pad}})^{-1} \qquad \text{Eqn. 5.15}$$

$$k_2 = \alpha_2(r_{\text{ankle}})^2(H_{\text{ankle}})^{-1} \qquad \text{Eqn. 5.16}$$

$$k_3 = \alpha_3(r_{\text{tibia}})^2(L_{\text{tibia}})^{-1} \qquad \text{Eqn. 5.17}$$

$$c_1 = \beta_1(0.5 * m_1) \qquad \text{Eqn. 5.18}$$

$$c_2 = \beta_2(0.5 * m_1 + 0.5 * m_2) \qquad \text{Eqn. 5.19}$$

$$c_3 = \beta_3(0.5 * m_2) \qquad \text{Eqn. 5.20}$$

$$m_2 = 0.63\ (L_{\text{tibia}}/0.4067\text{m})\ (r_{\text{tibia}}/0.01215\text{m}) \qquad \text{Eqn. 5.21}$$

$$m_w = m_{\text{leg}} - m_2 \qquad \text{Eqn. 5.22}$$

Model validation was performed using data from PMHS leg tests performed by Henderson et al. for which data was collected and processed in a similar manner to the impactor data.[94] For these tests, a 5.6 kg plate was attached to the potted proximal tibia and allowed to translate in the SAE-z direction after a hammer impacted the footplate in contact with the plantar surface of the foot. Instrumentation and specimen prep were similar to those of the impactor tests. Thirteen tests from the drop tower study were grouped into two conditions based on impactor mass and velocity, and labeled as Drop Tower A (tests 08-13) and Drop Tower B (tests 14-20). Additional response corridors were generated for these data and CORA scores were calculated for forces and displacements for the 13 drop tower tests and for the characteristic averages for each of the two conditions.

Optimized parameter values based on experimental PMHS impactor tests are presented in (Table 5.7). The optimal α_i and β_i are reported along with the average k_i and c_i for each impactor test condition as well as for the drop tower and FE validation conditions. Averages and standard deviations are based on 12 low impactor tests, 11 medium impactor tests, 10 high impactor tests, and 12 drop tower tests. Some experimental PMHS tests were omitted from the analysis due to missing data and/or excessive ankle rotation during the test.

Table 5.7. Optimized parameter values for the three-mass leg model with wobbling mass.

Data	**i**	**m_i (kg)**		**i**	**α_i (kN m^{-2})**	**β_i (kg s^{-1} m^{-1})**	**k_i (kN m^{-1})**		**c_i (Ns m^{-1})**	
		Avg.	**S.D.**				**Avg.**	**S.D.**	**Avg.**	**S.D.**
Low Impactor	1	0.94	0.14	1	51.0	2910	3140	440	137	20
	2	0.57	0.05	2	4.49e4	2190	620	80	165	20
	w	1.34	0.25	3	4.85e7	9310	17500	2060	263	24
Medium Impactor	1	1.17	0.20	1	51.0	2910	2950	390	171	29
	2	0.58	0.07	2	4.49e4	2190	620	100	193	28
	w	1.80	0.35	3	4.85e7	9310	17700	2150	272	34
High Impactor	1	1.14	0.22	1	51.0	2910	2970	520	166	33
	2	0.59	0.06	2	4.49e4	2190	620	90	189	29
	w	1.72	0.42	3	4.85e7	9310	18500	1880	274	29
Drop Tower	1	1.37	0.30	1	51.0	2910	2980	670	200	44
	2	0.60	0.07	2	4.49e4	2190	610	120	217	34
	w	3.03	0.81	3	4.85e7	9310	19300	2620	281	33
FE Model	1	1.23	0	1	51.0	2910	2450	0	178	0
	2	0.63	0	2	4.49e4	2190	630	0	203	0
	w	2.62	0	3	4.85e7	9310	18800	0	293	0

Note: Parameters were identified assuming k_w=6 kN-m^{-1}, k_{w2}=10 kN-m^{-1}, and c_w=650-Ns m^{-1}.

Performance of the lumped-mass model was quantified using CORA scores comparing displacements and forces estimated by the lumped-mass model and those measured in the experimental impactor tests. These scores (Table 5.8) show good agreement (Overall CORA>0.9) between the model and the experimental results for all three impactor test conditions and all forces and displacements except tibia displacement for the low condition. These results also show that the highest CORA scores occurred for the medium impactor test condition, while the drop tower conditions had the lowest scores. Example plots are presented to show the response of the LMM compared to normalized experimental PMHS results (Figure 5.15, Figure 5.16). Additional plots of the LMM response compared to corridors normalized to represent the response of the 50th percentile male are shown in Figure 5.17.

Table 5.8. Summary of CORA scores for impactor experimental test PMHS response compared to lumped-mass model response for axial displacements (DZ) of masses (m_i), proximal tibia forces (PT FZ), and footplate forces (FP FZ).

Average Displacement CORA Scores using Scaled Parameters						
Test Condition	**Data**	**Magnitude**	**Progression**	**Phase**	**Overall**	**Overall (Weighted)**
Low Impactor	**m_1 DZ**	0.709	0.996	1.000	0.902	0.766
	m_2 DZ	0.550	0.976	1.000	0.842	0.635
	FP FZ	0.825	0.995	1.000	0.940	0.859
	PT FZ	0.826	0.994	1.000	0.940	0.859
Medium Impactor	**m_1 DZ**	0.793	0.996	1.000	0.930	0.833
	m_2 DZ	0.744	0.986	1.000	0.910	0.792
	FP FZ	0.874	0.991	1.000	0.955	0.897
	PT FZ	0.819	0.988	1.000	0.936	0.853
High Impactor	**m_1 DZ**	0.726	0.995	1.000	0.907	0.780
	m_2 DZ	0.793	0.987	1.000	0.927	0.832
	FP FZ	0.734	0.977	1.000	0.904	0.782
	PT FZ	0.802	0.984	1.000	0.929	0.839

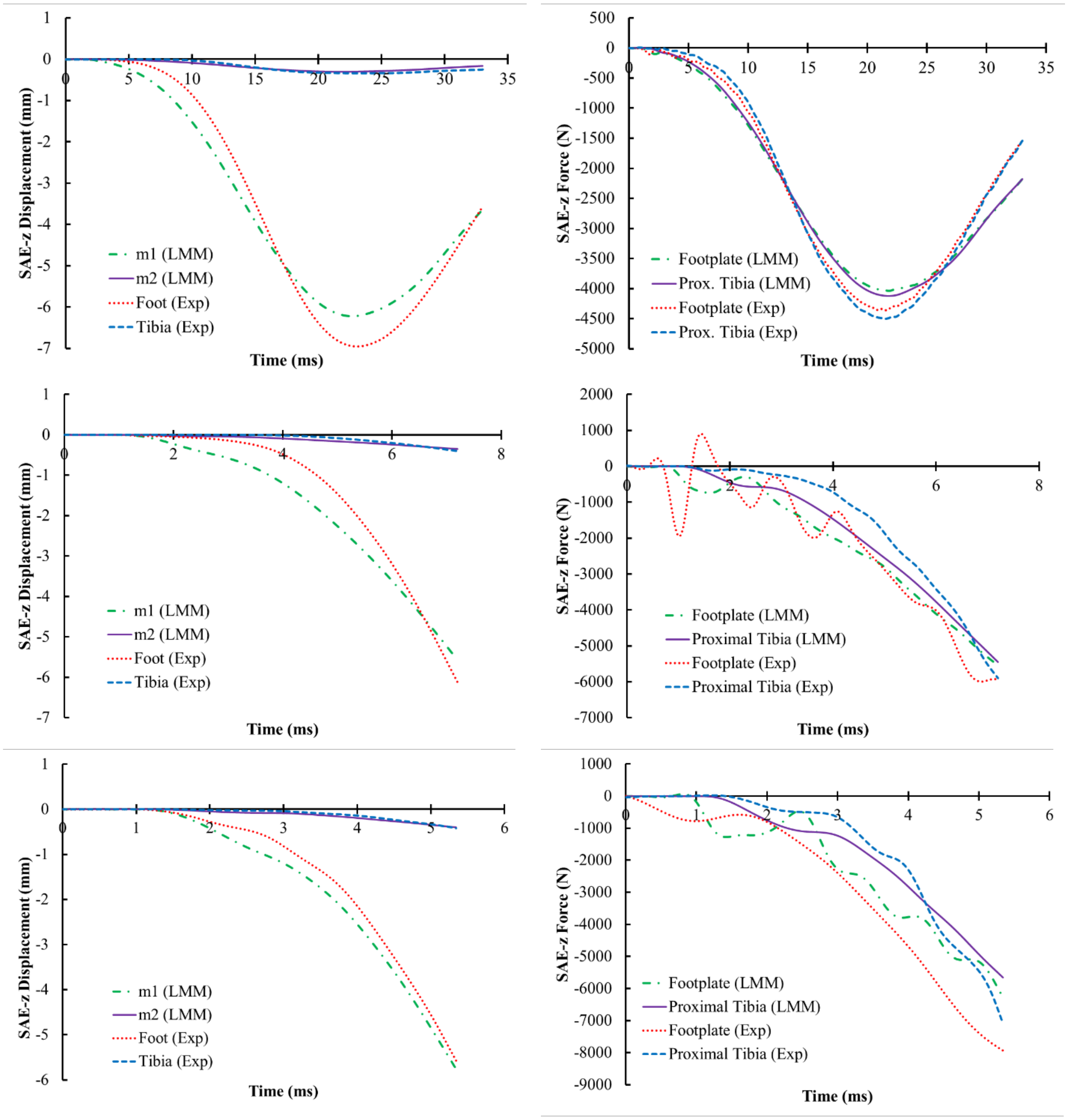

Figure 5.15. Plots showing lumped mass model fit for displacements and estimates of force for sample tests from Impactor Low, Medium, and High conditions. Results from Impactor 05, Impactor 14, and Impactor 36 are shown. Experimental (Exp) and lumped-mass model results are shown (LMM).

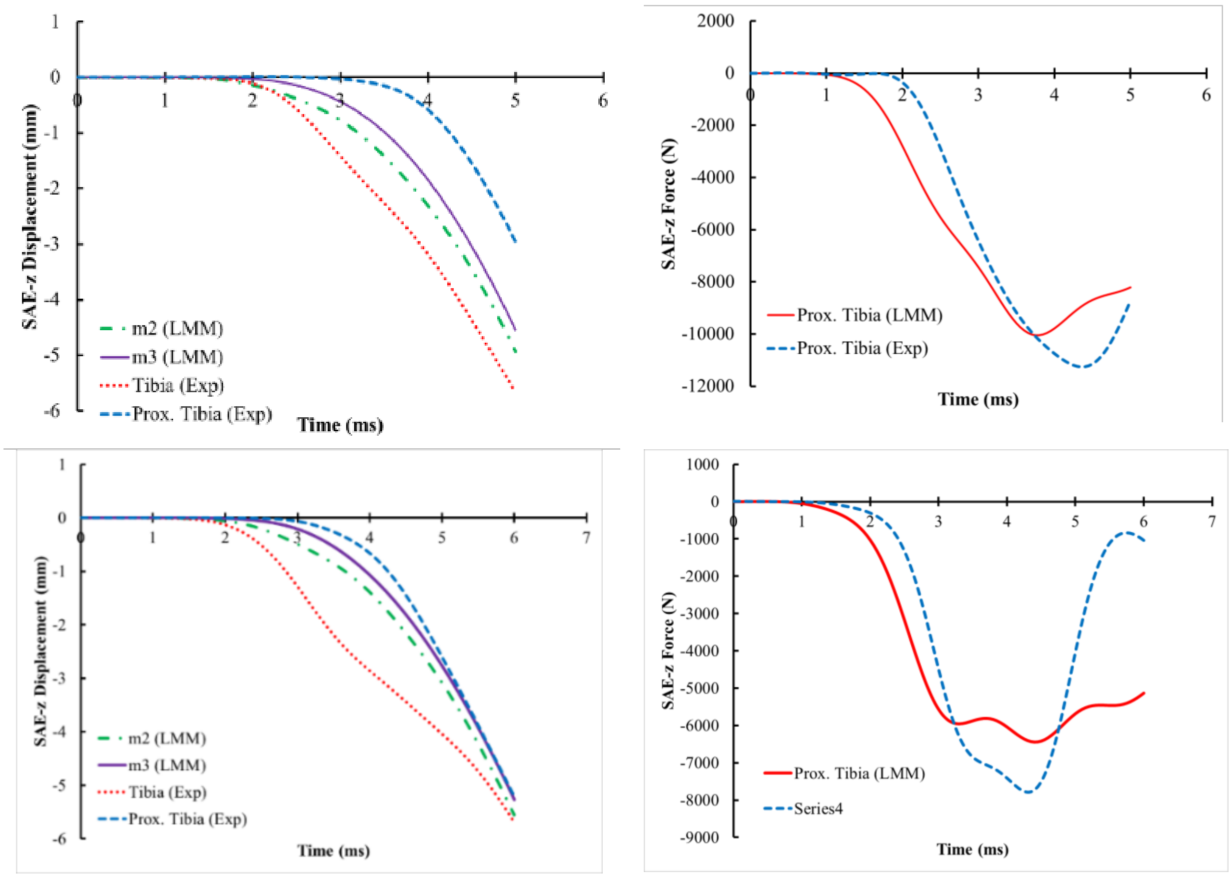

Figure 5.16. Plots showing lumped mass model (LMM) fit for displacements and estimates of force for sample experimental (Exp) tests from Drop Tower A and B conditions. Results from Drop Tower 08, and Drop Tower 15 are shown.

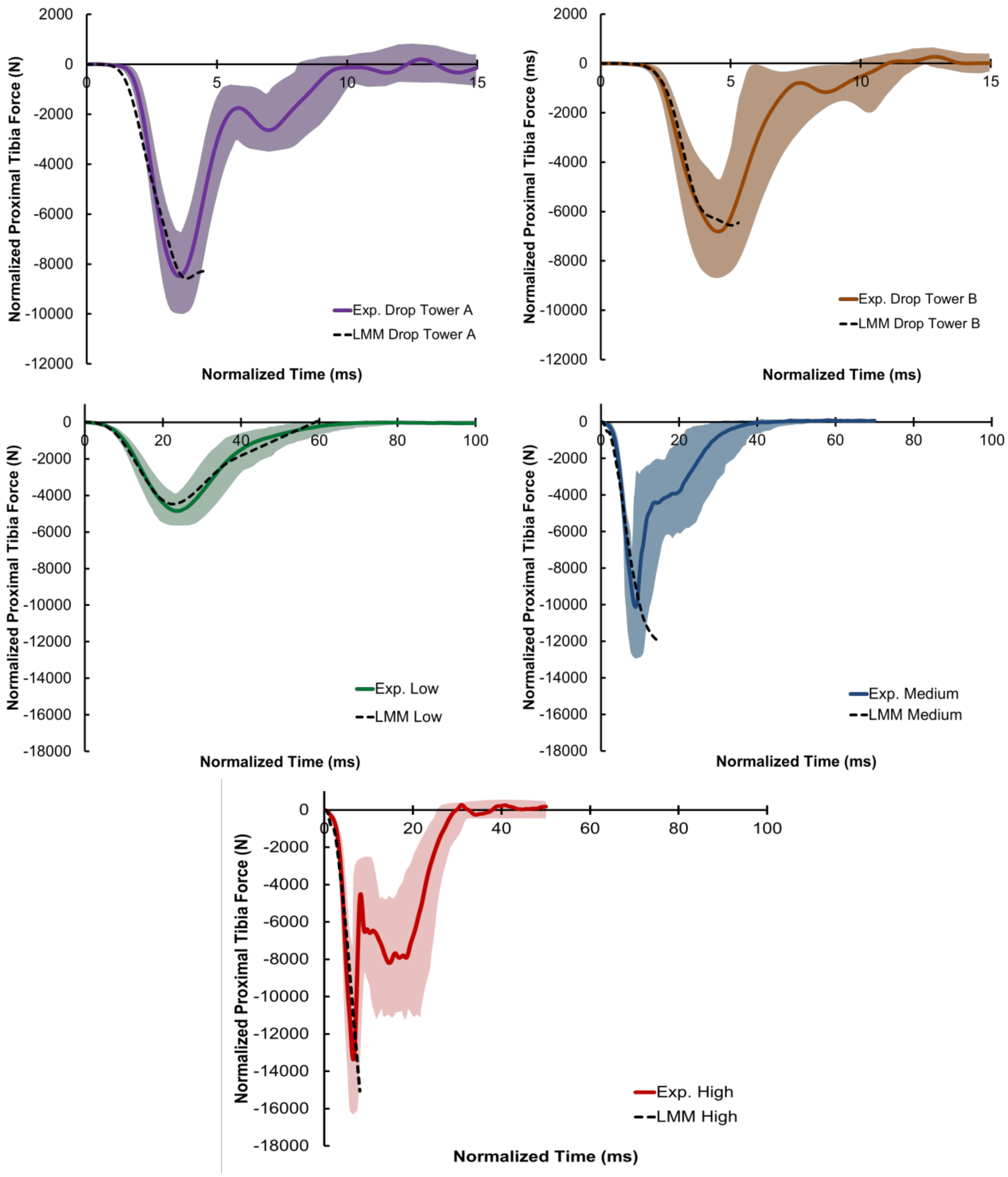

Figure 5.17. Lumped-mass model (LMM) response compared to PMHS corridors representing the response of a 50th percentile male based on experimental tests (Exp.). Results for proximal tibia force are shown.

The PMHS drop tower tests were used for validation of the lumped-mass model. The CORA scores for the drop tower conditions were lower than those comparing the model response to the PMHS response from the impactor study. Since calcaneus (foot) displacement and footplate force were not measured in the drop tower study, only proximal tibia force and distal and proximal tibia displacements were compared to the LMM response. The weighted overall CORA score for the proximal tibia force was highest for the drop tower conditions, and displacement of the distal tibia had the least accurate fit. It should be noted that the displacement for the distal tibia was calculated by double integrating a single axis accelerometer aligned with the SAE-z axis of the tibia. Despite these lower CORA scores for the validation conditions, the model has reasonable accuracy for predicting proximal tibia force and the individual displacement of the distal and proximal tibia.

Table 5.9. Summary of CORA scores for drop tower experimental PMHS tests and fixed- and free-boundary finite element model response compared to lumped-mass model response for axial displacements (DZ) of masses (m_i), proximal tibia forces (PT FZ), and footplate forces (FP FZ).

		Average CORA Scores using Scaled Parameters				
Test Condition	**Data**	**Magnitude**	**Progression**	**Phase**	**Overall**	**Overall (Weighted)**
Drop Tower A	**m_2 DZ**	0.662	0.996	1.000	0.873	0.695
	m_3 DZ	0.702	0.996	1.000	0.899	0.731
	PT FZ	0.754	0.994	0.936	0.895	0.778
Drop Tower B	**m_2 DZ**	0.691	0.994	1.000	0.895	0.721
	m_3 DZ	0.693	0.998	1.000	0.897	0.724
	PT FZ	0.726	0.990	0.879	0.865	0.752

The LMM and response corridors developed in this study provide a unique characterization of the human leg for a broader range of loading rates and load durations than previously existed. Further, the LMM's development based on three separate loading conditions and geometric parameter-dependence which enables scaling to a specified anthropometry, increase its utility compared to other models. Previous LMMs characterized the leg for specific loading conditions, which limits their use in a broader range of applications.[7,43,67,94,106,114,127] The narrow range of loading rates used to develop previous models, as well as the incorporation of a wobbling mass to represent soft tissue in the current model, may explain some of the differences between the parameters identified for the current model and previous models.

The heel pad stiffness estimated by this model is 2450 kN-m^{-1}, assuming a heel pad thickness of 14.5 mm. A previous study by Aerts et al. found the heel pad stiffness to be 1080 kN-m^{-1},[2] Pain et al. and Chi et al. estimated the heel/foot stiffness to be 965 kN-m^{-1} and 125 kN-m^{-1}, respectively.[45,154] While all of these foot and heel stiffness estimates are lower than those presented in the current model, the lack of specialized instrumentation and difference in loading rate may explain these discrepancies. Many of the models developed from gait analysis data do not have the granularity provided by PMHS impact test instrumentation, which predisposes those analyses to estimate foot/ankle stiffness as a whole rather than separating out the effect of the heel pad. Calculating the overall stiffness of the heel pad and foot and ankle from the current model gives a stiffness of approximately 500 kN m^{-1} at quasi-static rates, which agrees reasonably with previous studies, particularly when considering the addition of the damping element effects.

Tibia stiffness estimated by the model is also consistent with the literature. Using the tibia stiffness (18800 kN m^{-1}) coupled with a tibia length of 407 mm and a tibia cross-sectional area of 463 mm^2, as measured from the GHBMC leg model, approximates an elastic modulus for the tibia of 16.5 GPa. This approximation is in agreement with a study by

Kemper et al. that estimated the tibia cortical bone elastic modulus for compression to be 16.4 GPa.[103]

The assessment of model fit using CORA showed that despite being optimized to fit the impactor test data, the model also was able to fit the response of the validation data, though with lower CORA scores. The breakdown of the CORA scores shown in Table 5.9 revealed average CORA magnitude scores were lowest for the drop tower conditions, with the lowest scores occurring for m_2 (tibia) displacement. One likely reason for this is that drop tower displacements were measured using a single accelerometer on the tibia, which was unable to be transformed to the local coordinate system of the tibia due to the lack of instrumentation necessary to perform the calculation. Phase differences between experimental and model-predicted proximal tibia forces also contributed to lower Overall CORA scores for the drop tower tests. Phase CORA scores ranged from 0.6 to 1.0 for the drop tower tests, with experimental forces lagging the model-predicted forces. Further investigation is necessary to understand how the model should be altered to better fit the data for this alternative boundary condition.

One assumption made during the development of the model was the stiffness and damping associated with the wobbling mass. The model was found to be relatively insensitive to changes in the wobbling mass stiffness (<0.03% average change in the CORA magnitude score for forces and displacements for a 200% increase in k_w); however, changes in the wobbling mass itself had a greater effect on the proximal tibia force (<0.2% average change in forces and displacements for a 200% increase in wobbling mass) for the high impactor condition. As expected, the model's sensitivity to these changes was greater for the drop tower conditions because of the larger displacements allowed by the free proximal boundary. For the drop tower tests, doubling k_w led to a 4% average change, and the doubling m_w led to a 5% average change in in CORA magnitude for proximal tibia force. This difference in the effect of changing the wobbling mass parameters for the fixed versus the free boundary condition provides one possible reason for the phase differences observed between the drop tower experimental forces and the model-predicted forces.

Another assumption was that the human leg behaves linearly for the loading rates involved. This assumption was evaluated using the UVA leg model and the principle of superposition.[78] Three sinusoidal acceleration pulses with different amplitudes and frequencies, and a fourth pulse consisting of the sum of those three pulses were applied to the foot (in the -SAE-z direction) of the FE model in four separate simulations.[78] The sum of the model's force response to the first three pulses was compared to the model's response to the fourth pulse. These curves agreed reasonably for the case where a preload of 100N was applied to the leg (4% peak force difference); however, superposition did not hold for the case where the leg was not preloaded (17% peak force difference). Since all PMHS tests involved an initial pre-compression, and the model is to be used for applications in which the leg is subject to initial loading from the leg's mass due to gravity, it is believed that the assumption of the leg's linearity is reasonable.

The leg model developed in this study using PMHS axial impact test data spanning a range of load rates from 0.24 to 5.99 kN ms^{-1} provides a simplified tool for understanding the response of the leg for applications ranging from automotive intrusion to UBB. The broader range of loading rates used for development of this model enable the model to more accurately capture the frequency-dependence of the leg compared to previous models developed based on a narrow range of load rates. Further, geometric-dependence of the model parameters allows for prediction of specimen-specific responses. Future applications of this analytical tool, along with the response corridors generated by this study, include anthropomorphic test device (ATD) design and assessment of the effectiveness of injury mitigation materials. The mass breakdown of this model and the characteristics of the compliance of elements of the leg emulate the segmented structure of current ATD legs such as the Mil-Lx and Thor-Lx.[134,146] Changing the properties of elements within these designs such as mass distribution or material properties to match those of the dynamic model could potentially improve ATD biofidelity across a larger range of loading rates than currently exists. Additionally, this LMM could be used to assess the effectiveness of floor mats and boots for mitigating injury in UBB events.

5.6 Frequency Response

Matlab was used to calculate the resonant and damped natural frequencies associated with the LMMs, particularly the MDOF model with the wobbling mass. First, the state space equations were derived using theory published by Lellement et al.[118] These equations are presented in matrix form in Eqn. 5.23 through Eqn. 5.32 for Model 1, where theta was used to represent the first derivative of the displacement to turn the equations into first order equations for the state space representation. Next, Matlab was used to find the eigenvalues of A, which were then used to calculate the damped natural frequencies and resonant frequencies of the model using Eqn. 5.28 through Eqn. 5.31. Eqn. 5.32 was used to convert the frequency to units of Hertz, where f is the frequency in Hertz, and ω is the frequency in rad-s^{-1}.

$\dot{\theta}(\mathrm{t}) = \mathbf{A}\theta(\mathrm{t}) + \mathbf{B}\mathrm{u}(\mathrm{t})$ where $\theta = \dot{z}$ and u(t) is the force input Eqn. 5.23

$$\mathbf{A}_1 = \begin{bmatrix} 0 & 0 & 0 & 0 & 1 & 0 & 0 & 0 \\ 0 & 0 & 0 & 0 & 0 & 1 & 0 & 0 \\ 0 & 0 & 0 & 0 & 0 & 0 & 1 & 0 \\ 0 & 0 & 0 & 0 & 0 & 0 & 0 & 1 \\ \frac{-k_2}{m_1} & \frac{k_2}{m_1} & 0 & 0 & \frac{-c_2}{m_1} & \frac{c_2}{m_1} & 0 & 0 \\ \frac{k_2}{m_2} & \frac{-k_2-k_3-k_w-k_{w2}}{m_2} & \frac{k_3}{m_2} & \frac{k_w+k_{w2}}{m_2} & \frac{c_2}{m_2} & \frac{-c_2-c_3-c_w}{m_2} & \frac{c_3}{m_2} & \frac{c_w}{m_2} \\ 0 & \frac{k_3}{m_3} & \frac{-k_3}{m_3} & 0 & 0 & \frac{c_3}{m_3} & \frac{-c_3}{m_3} & 0 \\ 0 & \frac{k_w+k_{w2}}{m_w} & 0 & \frac{-k_w-k_{w2}}{m_w} & 0 & \frac{-c_w}{m_w} & 0 & \frac{c_w}{m_w} \end{bmatrix} \qquad \text{Eqn. 5.24}$$

$$\mathrm{B}_1 = \begin{bmatrix} 0 & 0 & 0 & 0 & 0 & 0 & 0 & 0 \end{bmatrix}^{\mathrm{T}} \qquad \text{Eqn. 5.25}$$

$$\dot{\theta} = \begin{bmatrix} \dot{\theta}_1 & \dot{\theta}_2 & \dot{\theta}_3 & \dot{\theta}_4 & \dot{\theta}_5 & \dot{\theta}_6 & \dot{\theta}_7 & \dot{\theta}_8 \end{bmatrix}^{\mathrm{T}} \qquad \text{Eqn. 5.26}$$

$$\theta = \begin{bmatrix} z_1 & z_2 & z_3 & z_w & \dot{z}_1 & \dot{z}_2 & \dot{z}_3 & \dot{z}_w \end{bmatrix}^{\mathrm{T}} \qquad \text{Eqn. 5.27}$$

Eigenvalues of A are in the form of Eqn. 5.28 where $j = \sqrt{-1}$.

$$\lambda_i = \alpha_i + j\beta_i \qquad \text{Eqn. 5.28}$$

$\xi_i = \frac{-\alpha_i}{\sqrt{\alpha_i{}^2+\beta_i{}^2}}$ where ξ_i is the i$^{\mathrm{th}}$ modal damping ratio Eqn. 5.29

$$\omega_{n_i} = \sqrt{\alpha_i{}^2 + \beta_i{}^2} \qquad \text{Eqn. 5.30}$$

$$\omega_{r_i} = \omega_{n_i}\sqrt{1 - 2\xi_i} \qquad \text{Eqn. 5.31}$$

$\omega = 2\pi f$ Eqn. 5.32

Table 5.10 summarized the results of the calculations described above for the wobbling mass model as well as for the simpler models. The first damped natural frequency of the multiple-DOF models ranged from 23-44 Hz while the largest damped natural frequencies ranged between 210-900 Hz. These lowest frequencies align with the range of natural frequencies Wakeling and Nigg reported for the leg of 20-50 Hz.[217] Another study by Wakeling et al. found the natural frequencies associated with the soft tissue mass of the entire leg ranged from 10-50 Hz, with the average natural frequency associated with lower leg musculature ranging from 20-22 Hz.[218] These frequencies are significantly lower than the natural frequencies calculated for the tibia alone, which have been reported by previous studies to range between 300-1200 Hz.[22,95,202] The highest natural frequencies for the LMMs fall in this range.

Table 5.10. Summary of damped natural frequencies calculated for each of the LMMs of the leg.

Model	Damped Natural Frequencies (Hz)
SDOF Model 1A	306.9
2DOF Model 2A	43.6 211.6
3DOF Model 3A	40.4 302.6 436.3
4DOF Model 4A	23.3 184.4 897.3

Previous studies have performed modal analysis on individual bones of the human leg to estimate resonance frequencies.[105,143,203,210] Khalil and Viano used experimental impact testing to investigate the dynamic response of the human femur, while studies by Hobatho et al. and Thomsen used finite element modeling to estimate the resonant frequencies of the human tibia.[95,105,203] Since the resonance frequencies for the entire leg were of interest to this study rather than the resonant frequencies of the individual bones, the automated method of finite element model modal analysis was not used. Instead, the human leg FE model was subjected to prescribed impact and vibration conditions in order to estimate the natural frequencies of the leg.

A linear frequency sweep from 2-200Hz was used as a prescribed displacement boundary condition on the "pot" affixed to the proximal end of the tibia. Magnitude of the oscillating displacement was 20 mm. A power spectrum density plot was generated for the resulting calcaneus vertical displacement response to estimate the natural frequencies associated with the human leg FE model (Figure 5.18). The first and second peaks in the power spectral density plots estimate resonance frequencies of 22.2 and 47.6 Hz. The first frequency matches closely with the first natural frequency estimated for the 4DOF LMM, while the second frequency is similar to the first frequency estimated by the 2DOF and 3DOF LMMs.

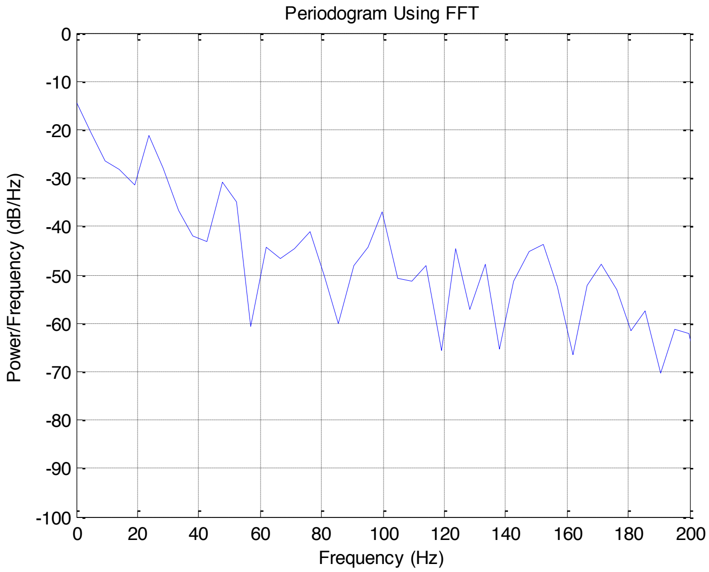

Figure 5.18. Power spectral density plot for vertical calcaneus displacement for the finite element human leg model exposed to a sine wave sweep displacement function.

5.7 Conclusions

Several iterations of lumped mass models were developed for characterizing the leg's frequency response. These models revealed that the human leg response to axial loading can be characterized for loading frequencies ranging from 5 to 56 Hz using the single-DOF model provided in Section 5.2. As additional degrees of freedom were added to the LMM, the model's ability to fit the response of the human leg improved. The 2-mass model was able to produce force CORA scores greater than 0.8 for frequencies below 156 Hz and the 3-mass model improved those CORA scores to exceed 0.90 for the same range of frequencies. A final model was constructed using PMHS data and included a "wobbling mass" to account for inter-specimen mass distribution differences. This model was found to provide a satisfactory fit of the PMHS data and is intended to provide information about scaling of PMHS data, though additional information is necessary to fully validate the model.

The natural and resonant frequencies associated with each of these models were calculated, with the lowest damped natural frequencies ranging from 22.3 to 43.6 Hz for the multiple-DOF models. A subsequent finite element model analysis estimated the first resonant frequency to be 22.2 Hz, which reasonably agrees with the frequencies estimated by the LMMs. These frequencies will be used to inform the decisions made during the development of a duration-dependent injury criterion to be discussed in the next chapter.

Information obtained from this exercise also provides valuable information which can be used for ATD leg design purposes. Modeling the leg as a single-DOF model is similar to using the Hybrid-III leg to predict human leg response. As with the Hybrid-III leg, the single-DOF model should only be used to predict the response of the leg for a narrow range of loading frequencies, particularly low frequencies. A study by McMaster et al. demonstrated the ability to model the Hybrid-II leg as a single-DOF LMM and used this model to develop a transfer function between the forces measured by the ATD and those measured in PMHS legs.

The 2-mass model is representative of the Thor-Lx and Mil-Lx ATD legs, which contain a compliant puck located in the tibia shaft. This chapter demonstrated that while a 3-mass model produces a better fit of the human leg response, the 2-mass model is still able to produce satisfactory results for the range of loading frequencies from 5-156 Hz. Chapter 7 will focus on using this information to provide recommendations for the improvement of the current Mil-Lx design.

6 Leg Injury Criterion Development

6.1 Introduction and Preliminary Considerations

The previous chapters of this dissertation focused on demonstrating the frequency-dependence of the leg's response to axial impact loading. The PMHS testing performed in Chapter 3 showed a significant difference in force at fracture between two loading conditions with different force durations. Chapter 4 focused on using a finite element model to obtain a more continuous relationship between peak force and duration (frequency) and the strain and compression response of the leg. In Chapter 5, several lumped-mass models were developed to characterize the response of the leg to impact loads typical of automotive intrusion and UBB. This chapter will utilize the tools and information from these previous chapters to outline several approaches for combining force and time into a single injury predictor to be used for development of an injury criterion for the leg exposed to axial impact loading.

The first step toward developing an injury criterion to encompass a larger range of loading frequencies is to examine existing PMHS data in terms of durations and peaks rather than peak load alone. The objective of this chapter is to demonstrate the duration dependence of a force-based injury threshold for the leg and produce an injury criterion that can be used for short duration events characteristic of UBB as well as longer duration events such as automotive intrusion.

6.1.1 Injury Location Analysis

Prior to developing an injury criterion for the leg, it is important to specify the injuries to be targeted. Data was collected from 286 previous axial loading component PMHS leg tests,[73,82,94,109,138,181,191,231] and injuries were studied to determine the best location for injury predictor measurements (i.e. force measurement location). Injuries from these tests included mainly calcaneus, talus, and distal tibia (pilon) fractures, with calcaneus fractures far outnumbering other injuries. Further analysis showed calcaneus fractures occurred alone (127 tests), and also accompanied many of the talus and pilon fractures. Proximal tibia injuries occurred only in tests in which the knee joint was included,[73,135] and occurred only once without a calcaneus fracture or Achilles tension added (Figure 6.1). This injury location study suggested that mid-tibia or proximal tibia force may not be able to fully capture the force at fracture since most injuries occur distal to the tibia, and also makes a case for concentrating on injuries occurring in the foot and ankle.

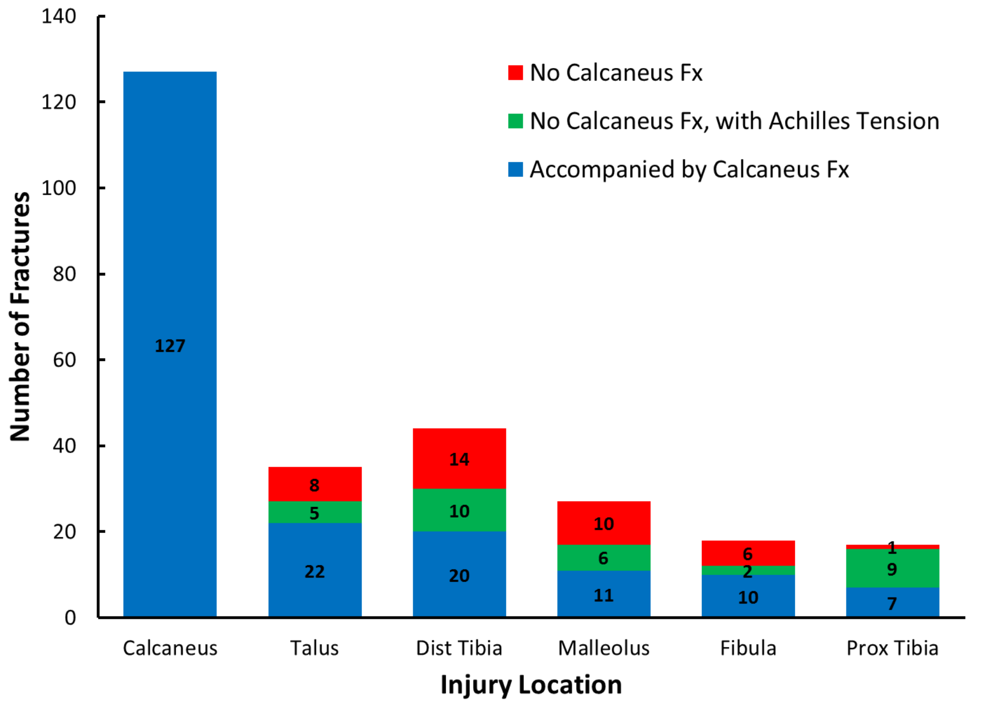

Figure 6.1. Frequency of leg injuries from 286 axial loading tests, showing a prevalence of calcaneus fractures. Injuries were classified into three categories depending on the presence of Achilles tension and the occurrence of calcaneus fracture in addition to another fracture.

Additional injury location information was provided by the linear impactor study described in Section 3.2.2. Dynamic x-ray and acoustic sensors were used to determine time of fracture for individual bones in the foot/leg. Figure 3.13 showed time-stamped images of a dynamic x-ray from a test where multiple injuries occurred. Image A showed the time that calcaneus fracture onset occurred, which agreed with the time of fracture estimated by the acoustic sensor placed on the calcaneus. Image B showed the onset of tibia pilon fracture. The sequencing of these injuries was replicated by all tests in which multiple fractures occurred, with the trend being that distal fractures occurred prior to more proximal fractures. Assuming that this trend holds for other studies, it can be concluded that calcaneus fracture is more likely than more proximal fractures such as talus and pilon fractures. Thus, it can be assumed that injuries subsequent to fracture of the calcaneus were a result of further load transmission through the fractured calcaneus for cases in which the impact contained sufficient energy to cause additional fractures. This justifies a focus on forces and accelerations measured at the plantar surface of the foot rather than at the mid- or proximal tibia for injury prediction, with the caveat that additional factors such as Achilles tension, flexion or xversion of the ankle, or off-axis loading may alter the location of injury as discussed in previous literature.[15,70,71,109]

6.1.2 Force Measurement Location

Force has been measured primarily in three locations by PMHS leg axial loading studies: the footplate, at the mid-shaft of the tibia, and at the proximal end of the tibia. These locations have different advantages and disadvantages in terms of ease of instrumentation, interpretation, and existence of equivalent measures in the ATD. Measuring force at the footplate is complicated by the need to inertially-compensate the force since the load cell is moving. Additionally, because of the high accelerations or high forces measured at the impact site, high capacity load cells are required for measuring footplate loads in most cases. The advantages of measuring the load at the footplate is that the input force is known, and one does not have to rely on calculations to determine the input force.

Mid-shaft tibia load cells, often referred to as implanted load cells, require careful alignment to reduce the likelihood of artefactual fractures. Further, the additional mass that the load cell adds to the tibia and its disruption of the transmission of force through the naturally curved bone interfere with the natural response of the leg to axial loading. Though the effect on load transmission has not been quantified, there is ample evidence of the causation of artefactual tibia and fibula fractures in literature from McKay and Bir, Klopp et al, and Funk et al.[70,109,135] Moreover, unless a fibula load cell is also implanted, load transmitted through the fibula must be estimated and added to the force measured by the implanted load cell for accurate assessment of the loads transmitted through foot to the leg. The advantage of measuring force at mid-tibia is that this force is easily measured in existing ATDs for direct comparison.

Proximal tibia forces are the most convenient to measure in these tests because of their location away from the impact site. In many cases, the load cell can be attached easily to the potted end of the tibia or placed in contact with the knee. Disadvantages of measuring forces at the proximal tibia is that these forces are inertially shielded from the impact and often fail to capture the higher forces present at more distal locations. As discussed in the previous section, a majority of the fractures caused by axial impacts to the foot are located in the foot and ankle. Furthermore, when estimating force at time of fracture for high acceleration impacts, the proximal tibia force will often continue to rise after fracture occurs due to the inertia of the mass between the fracture location and the load cell.

In using peak force (not force at fracture) to estimate injury risk, there is little difference between the use of each of these force measurement locations based on the finite element model. Maximum principal strains from various elements of the calcaneus cortical shell were compared to the peak forces measured at the footplate (FPFZ), mid-tibia (MTFZ), and proximal tibia (PTFZ) for each of the FE simulations run for the parametric study. The correlation matrix in Figure 6.2 shows that mid- and proximal tibia forces were slightly less correlated with each of the calcaneus strains compared to footplate force. However, differences in the correlation coefficient were 0.01 or less. Assuming that the strains predicted by the FE model are correlated with risk of fracture in the human calcaneus, proximal tibia force, mid-tibia force, and footplate force are nearly equivalent in their ability to predict fracture risk.

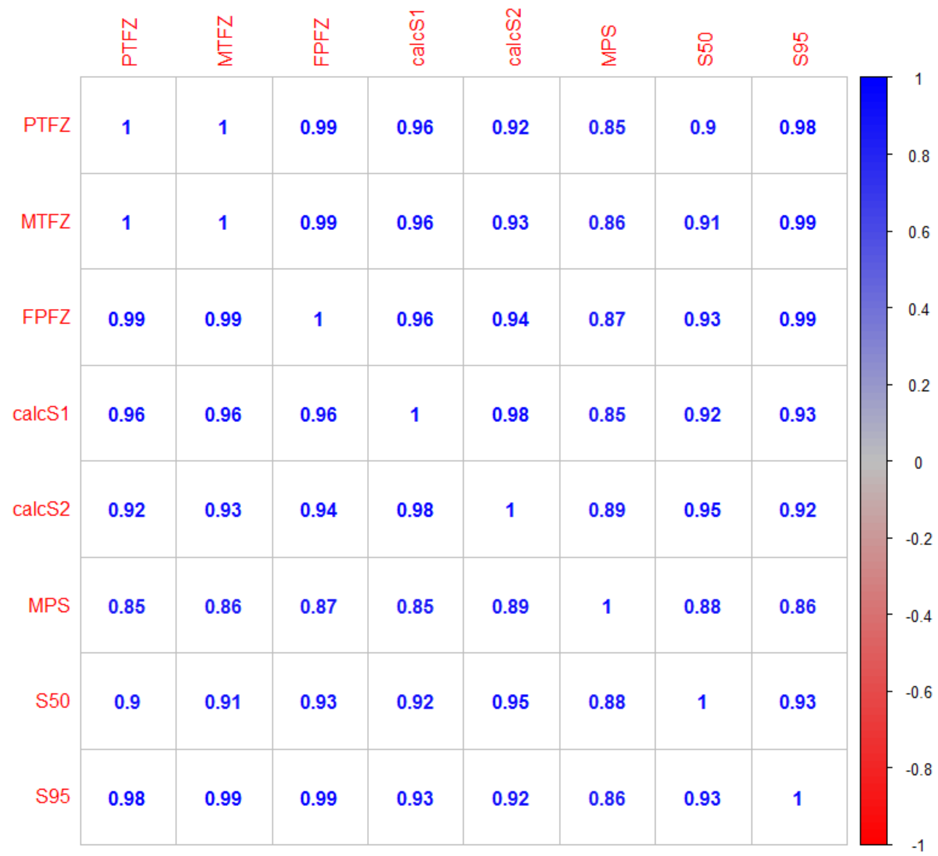

	PTFZ	MTFZ	FPFZ	calcS1	calcS2	MPS	S50	S95
PTFZ	1	1	0.99	0.96	0.92	0.85	0.9	0.98
MTFZ	1	1	0.99	0.96	0.93	0.86	0.91	0.99
FPFZ	0.99	0.99	1	0.96	0.94	0.87	0.93	0.99
calcS1	0.96	0.96	0.96	1	0.98	0.85	0.92	0.93
calcS2	0.92	0.93	0.94	0.98	1	0.89	0.95	0.92
MPS	0.85	0.86	0.87	0.85	0.89	1	0.88	0.86
S50	0.9	0.91	0.93	0.92	0.95	0.88	1	0.93
S95	0.98	0.99	0.99	0.93	0.92	0.86	0.93	1

1
0.8
0.6
0.4
0.2
0
-0.2
-0.4
-0.6
-0.8
-1

Figure 6.2. Correlation matrix for strains and forces from the finite element leg model. Correlation coefficients are provided for proximal tibia force (PTFZ), mid-tibia force (MTFZ), footplate force (FPFZ), medial calcaneus strain (calcS1), calcaneus strain near the fracture site (calcS2), maximum calcaneus strain (MPS), 50th percentile maximum principal strain in the calcaneus (S50), and 95th percentile maximum principal strain in the tibia (S95).

Unfortunately, the FE strain-force analysis only tells part of the story. When fracture occurs in the leg, some of the energy is dissipated by the formation of the fracture. In the case of axial impacts to the foot, if fracture occurs in the calcaneus, the forces measured superior to the calcaneus may be less than if no fracture occurred. Load transmission through the fracture not only affects the peak of the proximal forces, but also the timing (Figure 6.3). When using tests for which timing of fracture is unknown (left censored data), using peak mid- or proximal tibia force may skew the statistical analysis toward associating a lower probability of injury with a given force value.

For example, an uninjured specimen may reach a peak proximal tibia force of 5 kN when the peak footplate force is 10 kN due to differences in inertia at the two locations. For a higher acceleration impact, the calcaneus may fracture at 12 kN of footplate force, but because of the disruption caused by the fracture, the peak force measured by the proximal tibia load cell may only peak 4 kN. In this case, a higher force at the location of fracture (footplate) may be mapped to a lower force at the proximal tibia than would have actually been measured had fracture not occurred. This "mapping" concept becomes further complicated when considering that different impact accelerations can cause the same peak force at the proximal tibia to be mapped to different peak forces at the footplate (which is likely to be closer to the location of fracture).

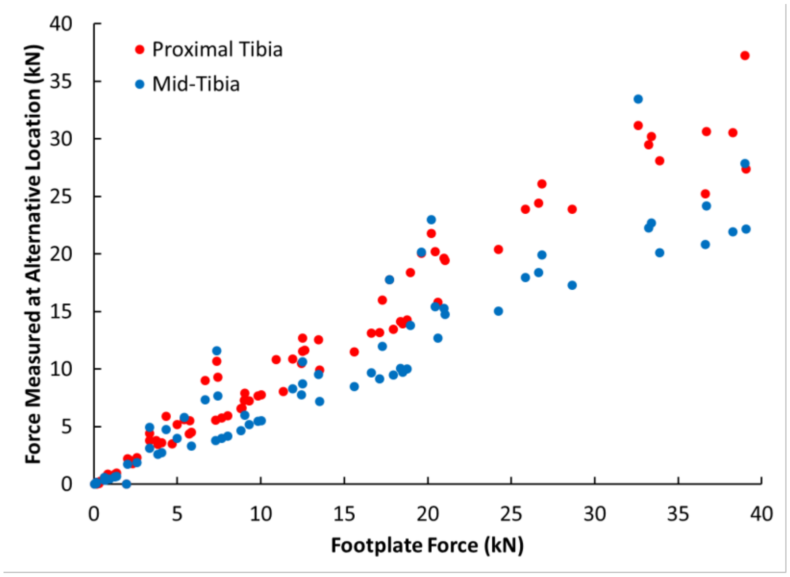

Figure 6.3. Comparison of peak forces as measured at the footplate versus the mid- or proximal tibia in the FE model for various input acceleration conditions. While the forces are correlated, this scatterplot shows that multiple mid- or proximal tibia forces may be mapped to the same footplate force.

To demonstrate this concept, peak mid- and proximal tibia forces were plotted against peak footplate force as predicted by the FE model for various loading conditions ranging in input acceleration frequency from 5 to 830 Hz (Figure 6.3). Both fracture and no-fracture simulations were included in the plot. For peak footplate forces within the range of realistic forces expected for automotive intrusion and UBB (approximately less than 25 kN), a difference of up to 10 kN could be measured between two mid- or proximal tibia forces measured for the same peak footplate force. This suggests not only the importance of measuring force close to the location of fracture, but also demonstrates the amount of error that could be incorporated into an injury risk function that combines forces measured at different locations for varied rates of loading.

6.1.3 Consideration for Covariates

As previously mentioned, bone mineral density (BMD), age, gender, and loading rate are all factors which can affect the injury tolerance of a particular bone. After determining the main predictor variable, covariates can be chosen in such a way as to reduce the variance in the relationship between injury and the main predictor.[96] Before attempting to add covariates to a survival model, it is important to understand how the covariates relate to each other as well as how they physically relate to the main predictor variable. Simply assuming each covariate has a linear effect on injury outcome could greatly affect the predictive capability of the IRF despite the model fitting the data set from which it was generated. For this analysis, BMD, age, sex, loading rate, and dorsiflexion angle were considered.

Bone Mineral Density (BMD)

Bone mineral density has been correlated with both the toughness and strength of bone by many studies.[5,89,119,121,132,183] McCalden et al. determined that the decrease of cancellous bone strength has a 92% correlation with apparent density of bone,[132] while other studies have used quantitative computed tomography (QCT) to assess bone density and found BMD accounts for 48-77% of variability in femur strength.[119] Bone mineral density alone, however, cannot completely define the overall toughness or strength of bone because of its complex structure consisting of both crystalline and fibrous microstructures as well as a macrostructure containing trabecular and cortical bone.[121,180] Since BMD alone cannot account for specimen variability in bone strength, using surrogates such as age and sex which have relationships with both BMD and cause other microstructural changes may prove better able to reduce the variance in an injury prediction model.[5,121,180,183]

Age and Sex

Age and gender have been found to have various effects on injury, particularly bony injury; however, their individual effects are difficult to distinguish.[57,132,183] For example, there is a higher rate of BMD loss in peri- and post-menopausal women than in men across all ages,[21] and as previously discussed, BMD has been correlated with ultimate strength of bone. Additionally, bone, independent of BMD, is associated with increased fracture risk because of age-related changes to the musculo-skeletal system; further, the cross-link density of collagen structures in bone increases with age, causing a decreased ability to dissipate energy before fracture occurs.[180] As bone ages, remodeling of bone increases the density of osteons and gradually elevates the number of locations for crack formation; these factors contribute to the likelihood of brittle fracture of bone.[180] Age-related bone resorption affects men and women differently as well. Ruff et al. showed that only men compensate for loss of cortical thickness due to bone resorption, while the cortical thickness in women tends to decrease with age.[21,183] These trends seem to indicate that both age and sex affect injury susceptibility, and careful consideration needs to be given to how to treat them both separately and as co-dependent variables in an injury analysis.

Mass

Mass of the specimen also contributes to variance in force at fracture. For a given acceleration input, a specimen with greater mass will have greater inertia, which will increase the force measured for that impact. Thus, when using an injury predictor such as force, the data must be scaled accordingly, such that the fracture force is normalized to a common specimen mass to avoid estimating higher tolerances for given impact conditions. This scaling can be accomplished multiple ways: by scaling data prior to statistical analysis, or by scaling the predictor variable in the survival analysis. In the injury criterion proposed by Funk, mass raised to the negative two-thirds power was used in place of a linear relationship between force and injury to account for the relationship between mass, force, and velocity.

Mass and Sex

It is also important to consider mass, particularly when considering sex as a covariate. Without compensating for mass in the injury analysis, the effect size of sex as a covariate may be artificially increased. Rather than the sex covariate corresponding to the effect of the difference in bone structure and bone strength between males and females, it then becomes a catch-all for the effects of mass and sex differences on fracture tolerance.

Load-Rate Dependence

Another consideration for a covariate is load-rate dependence since bone's ultimate strength varies with strain rate.[133] While some of the variability due to loading rate may be accounted for by measuring the force close to the location of injury, it is difficult to determine the effect of loading rate on the material properties of bone when one cannot completely compensate for other variables' effect on injury probability. Response to impact loading not only depends on the stiffness of the body being loaded, but also on the inertial and viscous resistances, which heavily depend on load rate.[211]

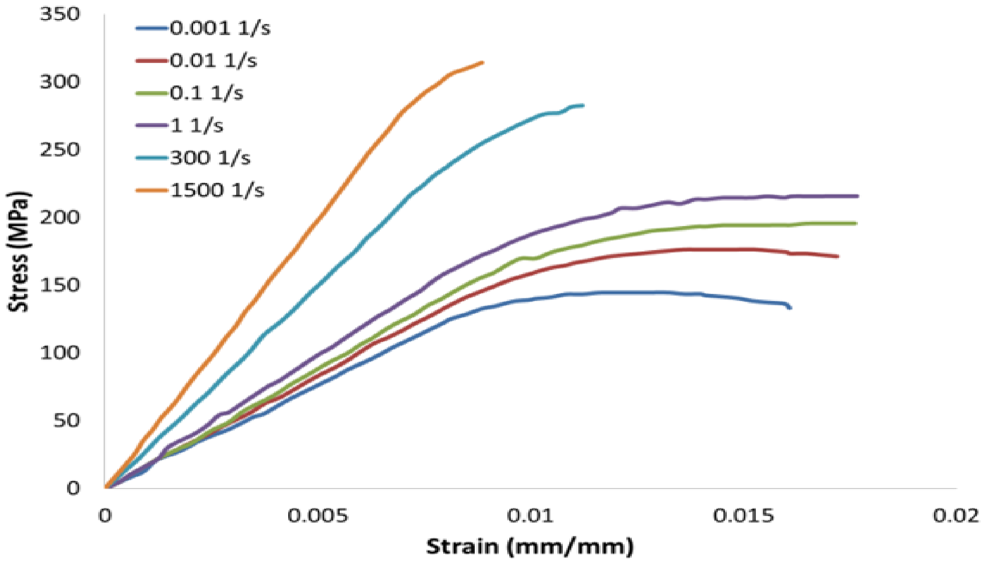

Figure 6.4. Cortical bone strain-rate dependency of stress-strain behavior from McElhaney (1966)[133]

Early literature showed that cortical bone properties are strain-rate dependent.[37,39,65,133,224] Carter and Hayes determined that ultimate strength of the bone is proportional to strain rate to the 0.06 power[37] and McElhaney concluded that the modulus of elasticity and ultimate strength of bone are proportional to strain rate (see Figure 6.4).[133]

Since the effect of strain rate is so small for the range of loading rates applicable to automotive intrusion, many studies have not considered loading rate as a predictor variable or covariate in their analysis; however, when developing an injury criterion to be used for a variety of applications from automotive intrusion to UBB, it is important to be able to account for these effects, or at least quantify their potential effect.

Additionally, the effect of strain rate or loading rate on soft tissues such as the heel pad must not be neglected. Previous studies have shown that the fat pad on the plantar surface of the calcaneus has viscoelastic properties, and because of its location between the impacting load and the bony structures of the foot/ankle complex, has the ability to control the loading profile. Work by Gabler et al., Natali et al., and Erdemir et al. has determined viscoelastic heel pad property models, and Gabler has shown through the use of FE modeling that heel pad properties significantly affect the ability of an FE model to predict failure.[64,78,145] Stiffening of the heel pad under high-rate compressive loading influences the amount of energy transmitted to the bony structure of the foot, thus having a potential effect on probability of injury. While strain rate may have a seemingly trivial effect on the properties of bone, the viscoelastic nature of soft tissues may prove to be significant.

Ankle Position

As previously mentioned, ankle position plays an important role in injury type and injury mechanism.[71] While xversion of the ankle predisposes the leg to malleoli fractures, plantar flexion and dorsiflexion have been shown to change the amount of tibio-talar joint articulation, with plantar flexion decreasing contact area.[35,117] This change in contact area helps explain the positive relationship between force at fracture and dorsiflexion angle suggested by previous injury risk analyses.[12,82,109] Gallenberger et al. suggested that 20 degrees of dorsiflexion increases the force at fracture by 1.1 kN at 50-percent probability of injury, while a similar increase in force at fracture was estimated by Bailey et al.[15,82] The statistical significance of the effect of flexion within these injury risk analyses, in addition to the underlying understanding of change in contact area associated with ankle flexion, suggest that it should be accounted for as a covariate. Other literature has demonstrated that ankle flexion angles greater than 10 degrees can contribute to alternative injury mechanisms due to shear and bending.[35,72,109]

Ankle xversion has been previously associated with malleolar fractures.[71,109] These fractures are usually associated with shear and bending rather than axial loading. Because ankle xversion plays such a major role in determining the type of fracture and introduces an alternative injury mechanism, it is important to understand the role of this variable in the injury criterion.

6.1.4 Data Set and Predictor Variable Selection

Data from 454 axial loading PMHS leg tests was collected from 11 previous PMHS studies and those outlined in Chapter 3.[14,57,70,81,94,109,136,138,181,229] Tests which included an initial eversion or inversion of the ankle greater than 10 degrees were eliminated from the data set due to the presence of alternative injury mechanisms for the leg under these conditions.[35,71,109] The remaining 249 tests are summarized in Table 6.1. Impact velocities ranged from 0.003 to 11.5 m-s^{-1} with forces measured from 0.8-20.5 kN.

Table 6.1. Summary of PMHS axial loading tests with limited ankle xversion (249 tests). This data set will be referred to as the "larger data set."

Study	Boundary Condition	Velocity (m/s)	Impulse (Ns)	Force (kN)	Sample Size	
					Male	Female
Roberts et al. 1993	Potted prox. tibia*	0.003-7.5	17-490000	2.4-16.2	14	6
Schueler et al.	Whole body	3.15-3.7	18.2-80.7	7.7-20.5	18	6
Yoganandan et al. 1996	potted prox. tibia	1.8-7.6	14-89	0.9-13.6	24	2
Klopp et al. 1997	Seated position*	1.4-5.5	33-100	2.7-19.3	18	11
Funk et al. 2000	Potted mid-femur*	4.3-9.5	25-78	4.4-10.9	2	15
Funk et al. 2002	Knee fixed	1.4-8.4	23-115	1.7-11.9	18	17
McKay et al. 2009	Hybrid-III knee	6.8-11.5	34-58	7.4-14.8	8	2
Henderson et al. 2013	Potted prox. tibia	4.4-7.8	36-67	10.5-15.9	19	0
Impactor	Fixed prox. tibia	0.4-5.2	68-133	2.8-17.8	36	0
Gallenberger et al. 2013	Potted prox. tibia*	3.2-9.1	13-52	3.9-6.1	19	2
Crandall et al. 1996	Seated position*	13-16.6+	96-120	0.8-2.7	8	0
Thor 2014	Knee fixed	1.3-1.8	133-146	2.9-3.7	4	0

*Includes dorsi/plantar flexion tests

+Delta-V reported in publication

Additional tests were removed from this data set to ensure that the data was similar enough to use for development on an injury risk function. First, since it was previously determined that plantar force, rather than tibia force, is the best correlated with strain in the leg, the tests which did not report plantar or footplate force were removed. Secondly, tests which included Achilles tension were also eliminated because of the additional force added to the tibia.[70,108] In some cases, force-time history was not reported or sufficiently described. These tests were also removed. Lastly, tests which included greater than 10 degrees of dorsiflexion were eliminated because of the effect of dorsiflexion on ankle joint contact area, which has been associated with an increase in force at fracture.[82,109] After eliminating tests with insufficient data, that did not meet the inclusion criteria, or exhibited artefactual fracture, the combined data set contained 137 tests (Table 6.2). From here forward, this data set will be referred to as the "combined data set."

Table 6.2. Summary of PMHS axial loading tests to be included in the development of the leg injury criterion (137 tests). This data set will be referred to as the "combined data set."

Study	**Boundary Condition**	**Velocity (m/s)**	**Impulse (Ns)**	**Force (kN)**	**Sample Size**	
					Male	**Female**
Yoganandan et al. 1996	potted prox. tibia	1.8-7.6	14-89	0.9-13.6	22	2
Klopp et al. 1997	Seated position*	1.4-5.5	33-100	2.7-19.3	18	10
Funk et al. 2000	Potted mid-femur*	4.3-9.5	25-78	4.4-10.9	2	5
Funk et al. 2002	Knee fixed	1.4-8.4	23-115	1.7-11.9	9	10
Henderson et al. 2013	Potted prox. tibia	4.4-7.8	36-67	10.5-15.9	19	0
Impactor	Fixed prox. tibia	0.4-5.2	68-133	2.8-17.8	36	0
Thor 2014	Knee fixed	1.3-1.8	133-146	2.9-3.7	4	0

*Includes dorsi/plantar flexion tests

A scatterplot matrix was generated to inspect the degree to which variables in the data set were correlated (Figure 6.5). Variables included in the scatterplot included: bone mineral density (BMD); injury (coded as 1 for injury and 0 for no-injury); injury location (classified according to the most proximal injury with 1 being a calcaneus fracture and 5 being a proximal tibia fracture); proximal boundary (with 1 denoting a fixed boundary and 0 indicating a free boundary); sex (with 1 indicating a male; and 0 denoting a female); age (in years); whole body mass of the specimen (in kg); impact velocity (in m-s^{-1}); load rate (measured at the footplate in kN-ms^{-1}); footplate force (in kN); mid-tibia force (in kN); and proximal tibia force (in kN).

A correlation matrix was also produced to quantitatively assess the correlation between these variables (Figure 6.6). Since bone mineral density was not reported for all tests, this variable was left out of the correlation matrix. Variables with positive correlations are shown in blue, while negative correlations are shown in red. The most notable correlation in the data set are that proximal tibia force and mid-tibia force are highly correlated (R^2=0.91), while floor force and mid-tibia force and floor force and proximal tibia force are less correlated. Injury was found to be most correlated with floor force (R^2=0.54) as compared to proximal tibia force (R^2=0.47) and velocity (R^2=0.45), which were the next highest correlated. It is interesting to note that mid-tibia force was the least correlated with injury when compared against floor and proximal tibia forces. This may result from the fact that implanted tibia load cells only measure the force transmitted through the tibia and neglect the force in the fibula.

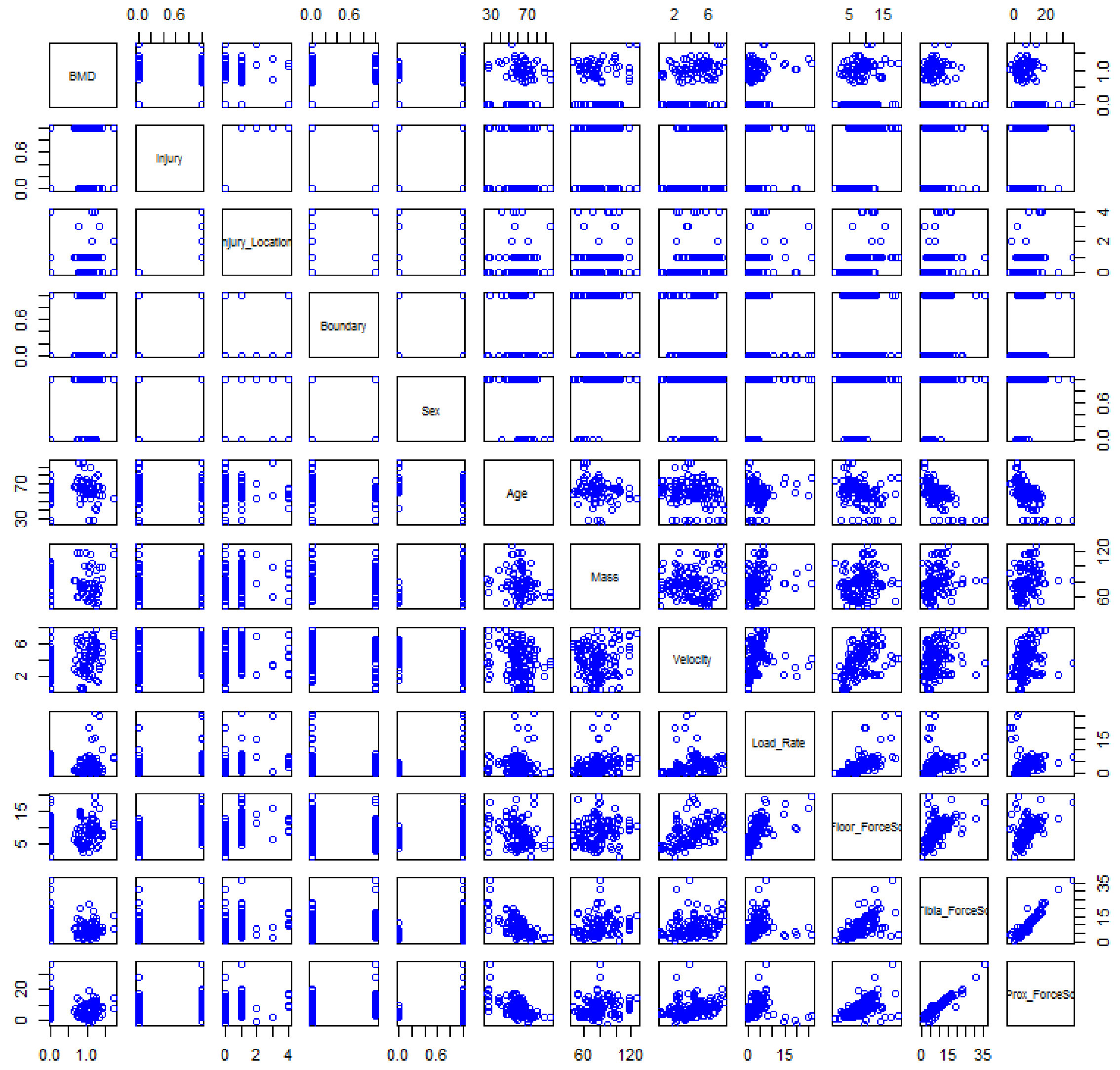

Figure 6.5. Scatter plot matrix showing trends and correlations between various aspects of the combined data set. Proximal and mid-tibia forces were shown to be highly correlated, while other variables showed only slight or no visible correlation.

Mass and sex were found to be slightly correlated for the data set (R^2=0.5), as expected. Age and sex were slightly negatively correlated (R^2=0.4), meaning that the average age of the female specimens was slightly greater than that of the male specimens. Though this relationship is not causal, it may be an artifact of the inclusion criteria for many of the data sets requiring non-osteoporotic specimens. Velocity and load rate were not significantly correlated (R^2=0.25) for the data set, which speaks to the variety of boundary conditions and impactor masses used in the data set. Negative correlations were calculated for age and each of the forces, which was expected based on the assumption that fracture occurs at peak force, though this relationship is better understood using a regression or survival analysis rather than correlations.

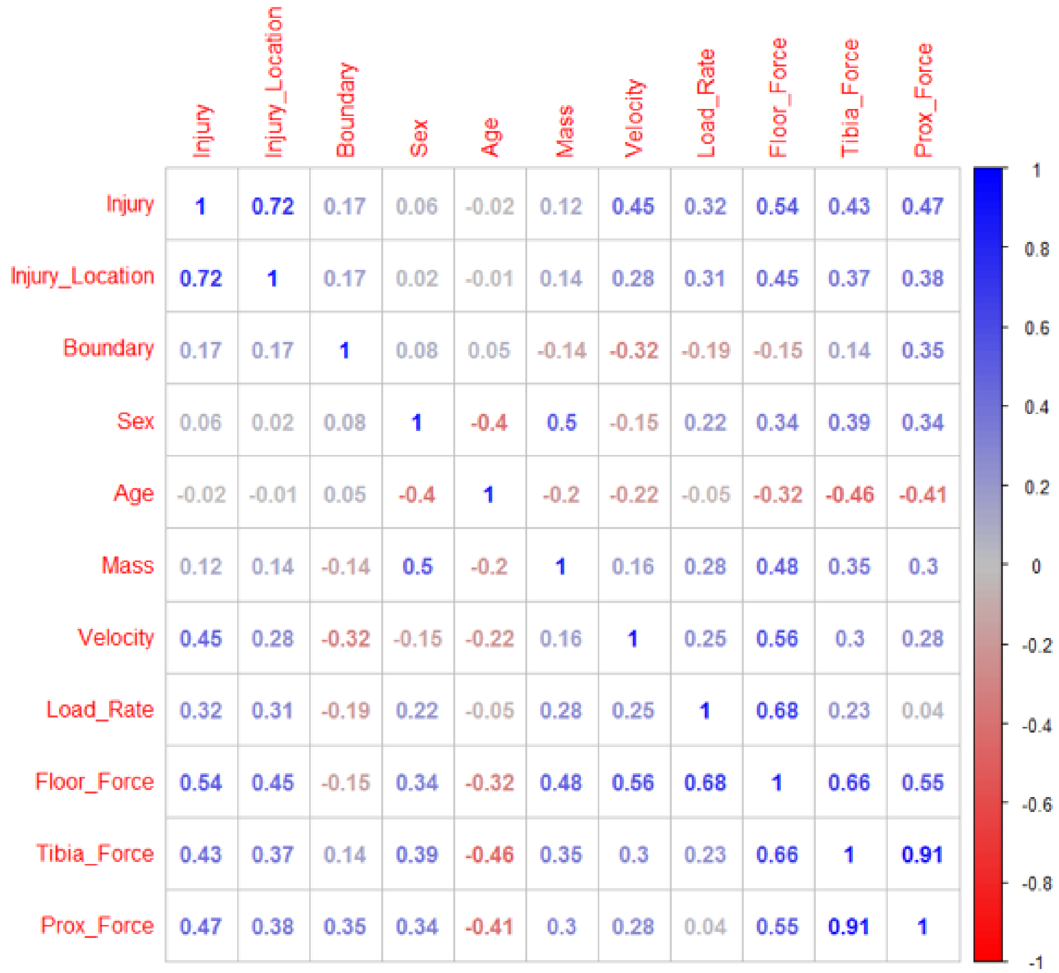

	Injury	Injury_Location	Boundary	Sex	Age	Mass	Velocity	Load_Rate	Floor_Force	Tibia_Force	Prox_Force
Injury	1	0.72	0.17	0.06	-0.02	0.12	0.45	0.32	0.54	0.43	0.47
Injury_Location	0.72	1	0.17	0.02	-0.01	0.14	0.28	0.31	0.45	0.37	0.38
Boundary	0.17	0.17	1	0.08	0.05	-0.14	-0.32	-0.19	-0.15	0.14	0.35
Sex	0.06	0.02	0.08	1	-0.4	0.5	-0.15	0.22	0.34	0.39	0.34
Age	-0.02	-0.01	0.05	-0.4	1	-0.2	-0.22	-0.05	-0.32	-0.46	-0.41
Mass	0.12	0.14	-0.14	0.5	-0.2	1	0.16	0.28	0.48	0.35	0.3
Velocity	0.45	0.28	-0.32	-0.15	-0.22	0.16	1	0.25	0.56	0.3	0.28
Load_Rate	0.32	0.31	-0.19	0.22	-0.05	0.28	0.25	1	0.68	0.23	0.04
Floor_Force	0.54	0.45	-0.15	0.34	-0.32	0.48	0.56	0.68	1	0.66	0.55
Tibia_Force	0.43	0.37	0.14	0.39	-0.46	0.35	0.3	0.23	0.66	1	0.91
Prox_Force	0.47	0.38	0.35	0.34	-0.41	0.3	0.28	0.04	0.55	0.91	1

Figure 6.6. Correlation matrix for the combined data set where negative correlations are shown in red and positive correlations are shown in blue. The highest correlation was observed between mid- and proximal tibia force, while the lowest correlation was between age and injury location.

Noticing that mass and force were somewhat correlated (R^2=0.48), a second correlation matrix was created using mass-normalized forces and force rate (Figure 6.7). As expected, the correlation between mass and each of the forces decreased. Correlation between sex and the forces decreased as well, showing that the potential effect of sex on fracture force is dominated by inherent mass differences between males and females. Correlation between footplate force and injury increased from 0.54 to 0.56, but correlation between mid-tibia and proximal tibia forces decreased. This result is likely due to the effect of inertia on forces measured in different locations. These correlations do not provide enough information from which to draw conclusions and will be revisited later in the dissertation. The fact that boundary condition was not highly correlated with any of the others variables is promising for the data set, considering this would imply that the test series was a significant contributor to the data's behavior.

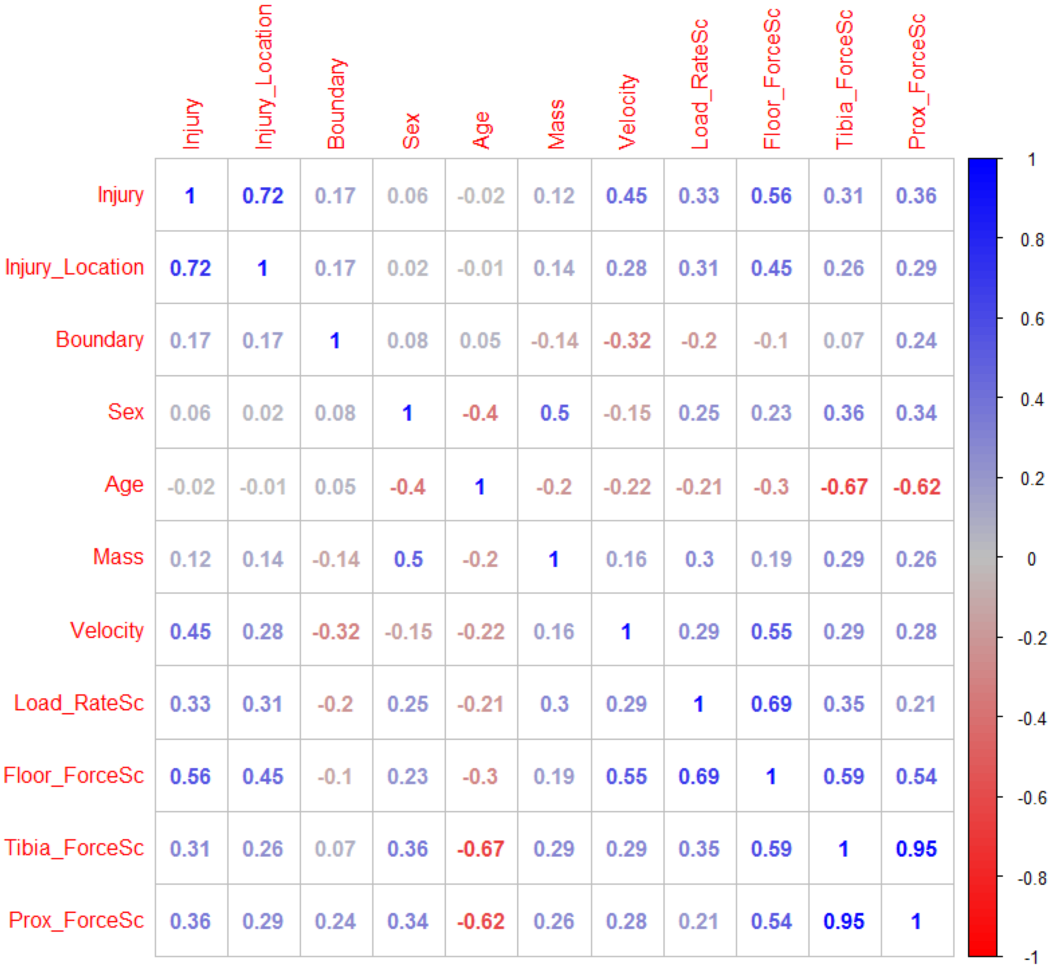

	Injury	Injury_Location	Boundary	Sex	Age	Mass	Velocity	Load_RateSc	Floor_ForceSc	Tibia_ForceSc	Prox_ForceSc
Injury	1	0.72	0.17	0.06	-0.02	0.12	0.45	0.33	0.56	0.31	0.36
Injury_Location	0.72	1	0.17	0.02	-0.01	0.14	0.28	0.31	0.45	0.26	0.29
Boundary	0.17	0.17	1	0.08	0.05	-0.14	-0.32	-0.2	-0.1	0.07	0.24
Sex	0.06	0.02	0.08	1	-0.4	0.5	-0.15	0.25	0.23	0.36	0.34
Age	-0.02	-0.01	0.05	-0.4	1	-0.2	-0.22	-0.21	-0.3	-0.67	-0.62
Mass	0.12	0.14	-0.14	0.5	-0.2	1	0.16	0.3	0.19	0.29	0.26
Velocity	0.45	0.28	-0.32	-0.15	-0.22	0.16	1	0.29	0.55	0.29	0.28
Load_RateSc	0.33	0.31	-0.2	0.25	-0.21	0.3	0.29	1	0.69	0.35	0.21
Floor_ForceSc	0.56	0.45	-0.1	0.23	-0.3	0.19	0.55	0.69	1	0.59	0.54
Tibia_ForceSc	0.31	0.26	0.07	0.36	-0.67	0.29	0.29	0.35	0.59	1	0.95
Prox_ForceSc	0.36	0.29	0.24	0.34	-0.62	0.26	0.28	0.21	0.54	0.95	1

Figure 6.7. Correlation matrix using scaled forces for the combined data set where negative correlations are shown in red and positive correlations are shown in blue. Again, the highest and lowest correlations were between the mid- and proximal tibia forces and age and injury location, respectively.

Next, the relationship between injury and non-injury data points was assessed qualitatively by plotting force against time-to-peak force and force duration, for the three force measurement locations (Figure 6.8). A log-log scale was used in order to show all data, including the quasi-static data from Roberts et al. on the same plot. From the data set shown, it is clear that force alone is insufficient for separating the injured and non-injured test data. The negative correlation between time and peak force for the injury points, particularly for the footplate (plantar) and mid-tibia force locations, emphasizes the necessity of incorporating duration or frequency-dependence into an injury criterion for the leg. This behavior is consistent with the theories of Stech and Payne and von Gierke discussed in the introductory chapter.[197,214,216]

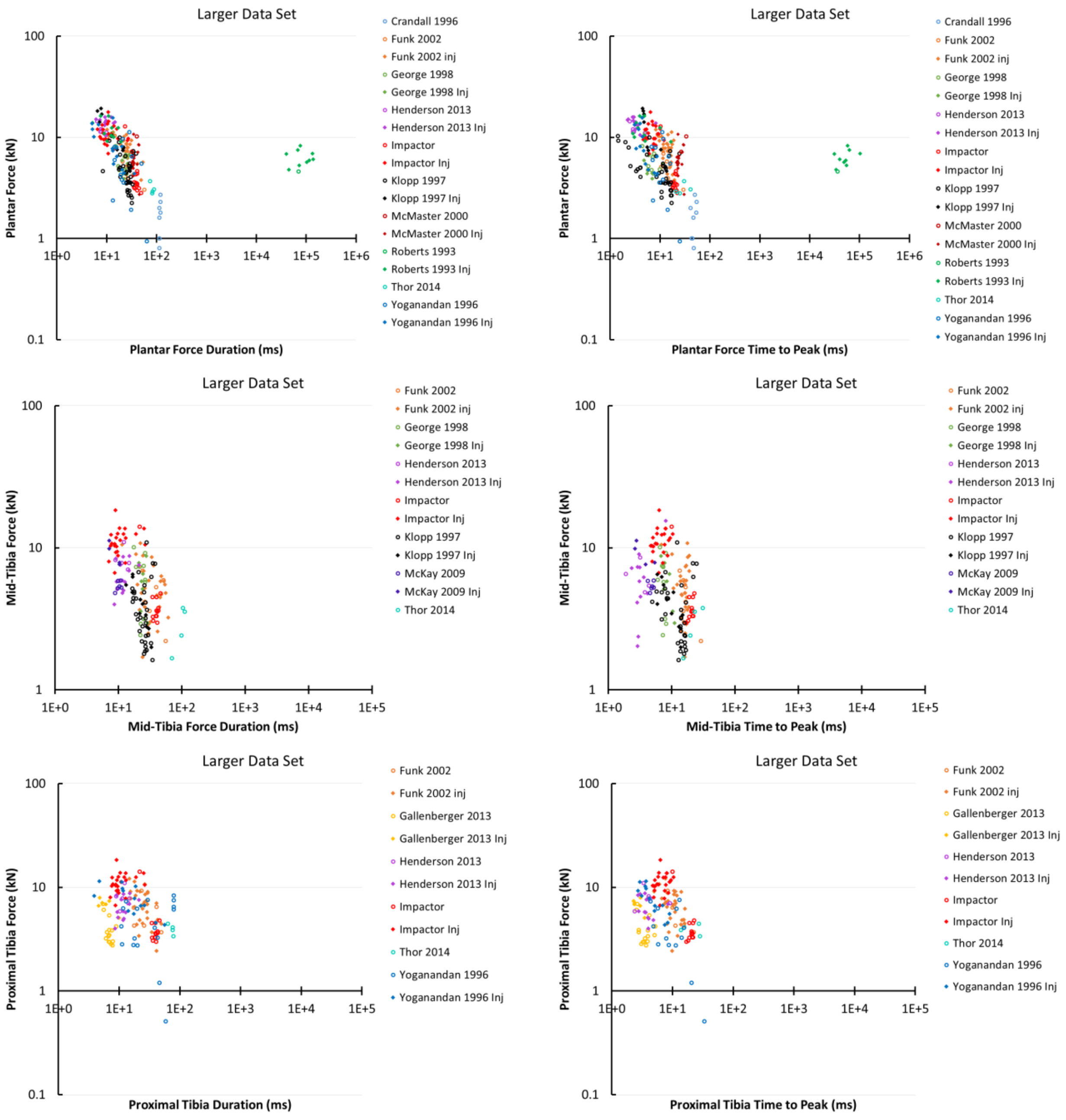

Figure 6.8. Force versus force duration and time-to-peak for footplate, mid-tibia, and proximal tibia locations for the larger data set. The left column shows peak force for each of the three locations plotted against force duration, while the right column shows the peaks plotted against the time-to-peak force.

Having previously provided justification for using plantar (footplate) force to predict injury for these injuries, and having outlined the disadvantages associated with the other force measurement locations, further analysis was focused on plantar forces. A closer look at peak plantar force versus duration for the injury tests shows an unmistakable negative relationship between assumed force at fracture and time (duration or time-to-peak) for the larger data set (Figure 6.9). Figure 6.10 shows the injury data points for the combined data set to demonstrate the relationship between plantar force and plantar force duration still holds for the smaller data set which excluded non-neutral ankle positions. The seemingly log-linear relationship between the short duration injury data points further suggests that time must somehow be included in the leg injury criterion to be able to accurately predict injury for the case where different loading frequencies are possible.

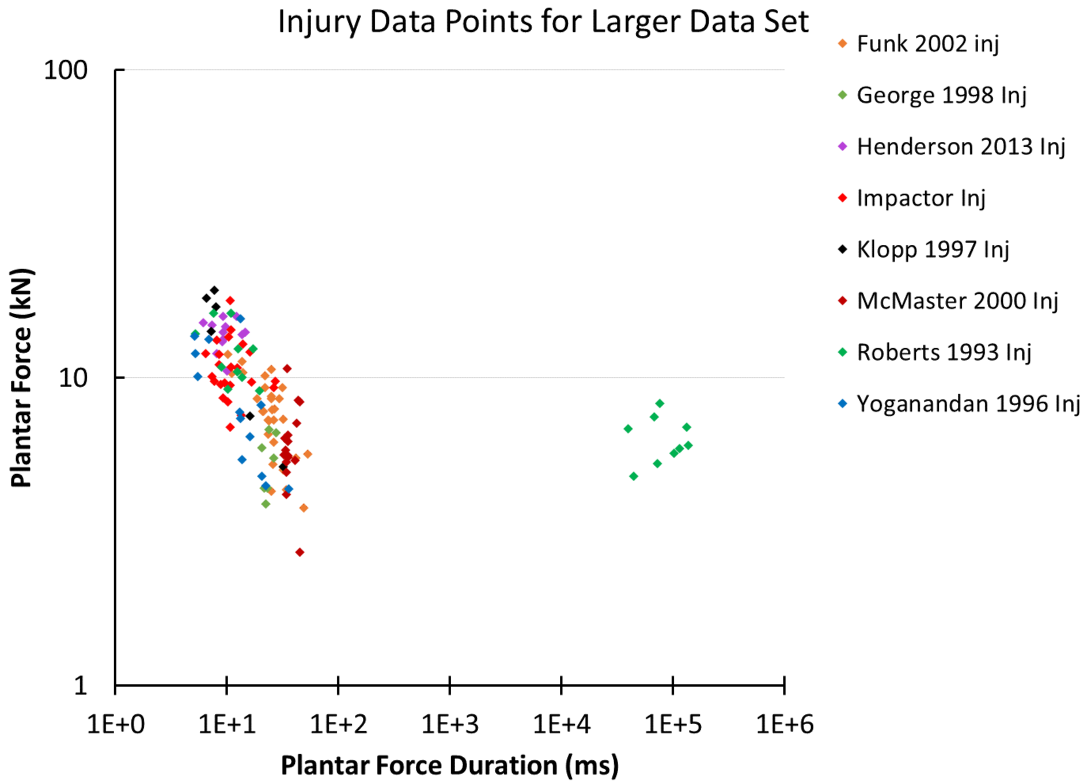

Figure 6.9. Relationship between plantar force at fracture versus duration and time-to-peak for injury data points.

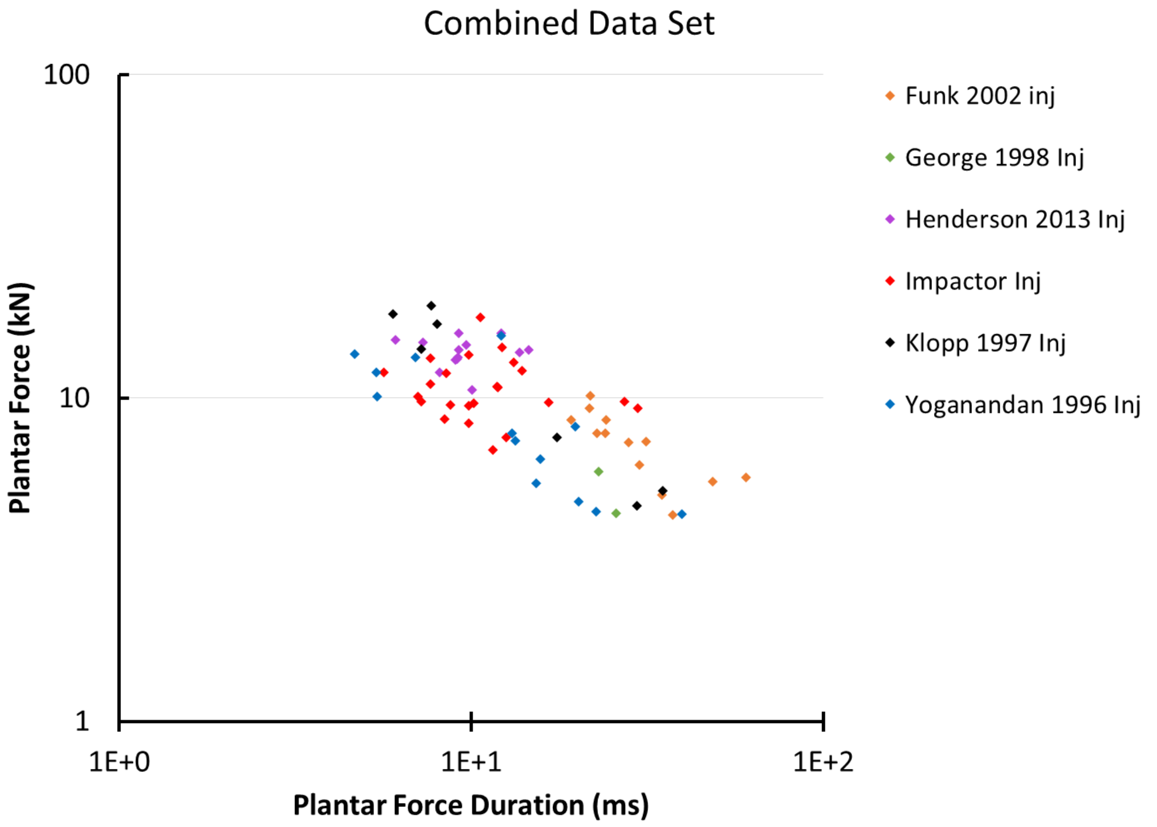

Figure 6.10. Peak plantar force versus plantar force duration for the combined data set which excluded tests with non-neutral ankle positions.

6.2 Combining Force and Time as an Injury Predictor

The first step to developing a new injury criterion for the leg was to determine an injury predictor for the data set. Section 3.2.6 concluded that a statistically significant difference existed between the averages for force-at-fracture for two different force durations, while impulse for the same two groups was not significantly different. The previous section showed that this trend continued when other data sets were combined for different effective loading frequencies. This section will discuss two preliminary methods by which to characterize the relationship between force and duration in an effort to combine them into a single injury predictor.

6.2.1 Linear Regression Approach

Linear regression was used as an initial step toward characterizing the relationship between force at fracture and duration. A linear regression was performed to establish the relationship between peak plantar force and plantar force duration for injury data points. Visual inspection of the data suggested that a log transformation be used. The line fitted through the data would be assumed as the average relationship between fracture force and force duration. Scatter about the line may be explained by random error and/or covariates which play a role in altering the force at fracture. Figure 6.11 shows the linear regression fit for the injury data points for the larger data set as well as for the uncensored data points (with quasi-static tests excluded). Table 6.3 provides the parameters for the regression lines.

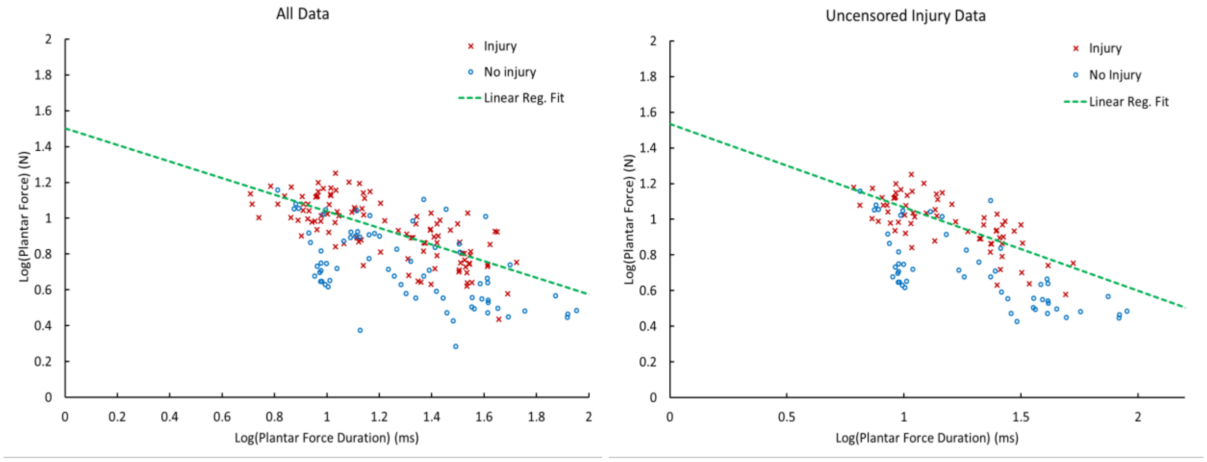

Figure 6.11. Linear regression fits of injury data points are shown. The plot on the left shows the linear regression fit for all injury data, while the plot on the right shows the fit for only the uncensored injury data points. Note that the log of the duration and log of the force were used to produce the linear fit.

Similarity in the fit of the two regression fits suggests that peak force may be used as a surrogate for force at fracture when uncensored data was not present. Previous work showed that force at fracture and first peak force were coincident because of the effect of fracture on load transmission, with a drop in force often occurring as a result of fracture.[70] This observation was consistent with the findings from the impactor and drop tower studies. For some boundary and input conditions, however, it is possible for the specimen to reload after fracture to develop a higher force after the initial fracture time. However, this was not observed for tests used in the combined data set. Care was taken to use the first peak rather than later peak forces which may have been related to subsequent fracturing.

Table 6.3. Linear regression fit parameters for the injured data points for log(Plantar Force) and log(Plantar Force Duration).

Data Set	**Slope**		**Intercept**		**R^2**
	Fit	**S.E.**	**Fit**	**S.E.**	**Fit**
All Injury Data	-0.463	0.043	1.501	0.0535	0.53
Uncensored Injury Data	-0.468	0.053	1.534	0.064	0.56

A shortcoming of this approach for estimating force at fracture at a function of time is that it assumes that the data is normally distributed. For example, having more data points for short duration events than long duration events could skew the linear regression fit. Histograms of the duration and force data are provided in Figure 6.12 and show that this approach is flawed because of the non-normal distribution of the injury data, particularly in the distribution the force duration. Further, the linear regression approach neglects to account for the probability of non-injury points along the regression line. The next section will discuss an alternative method for estimating the relationship between force, duration, and injury.

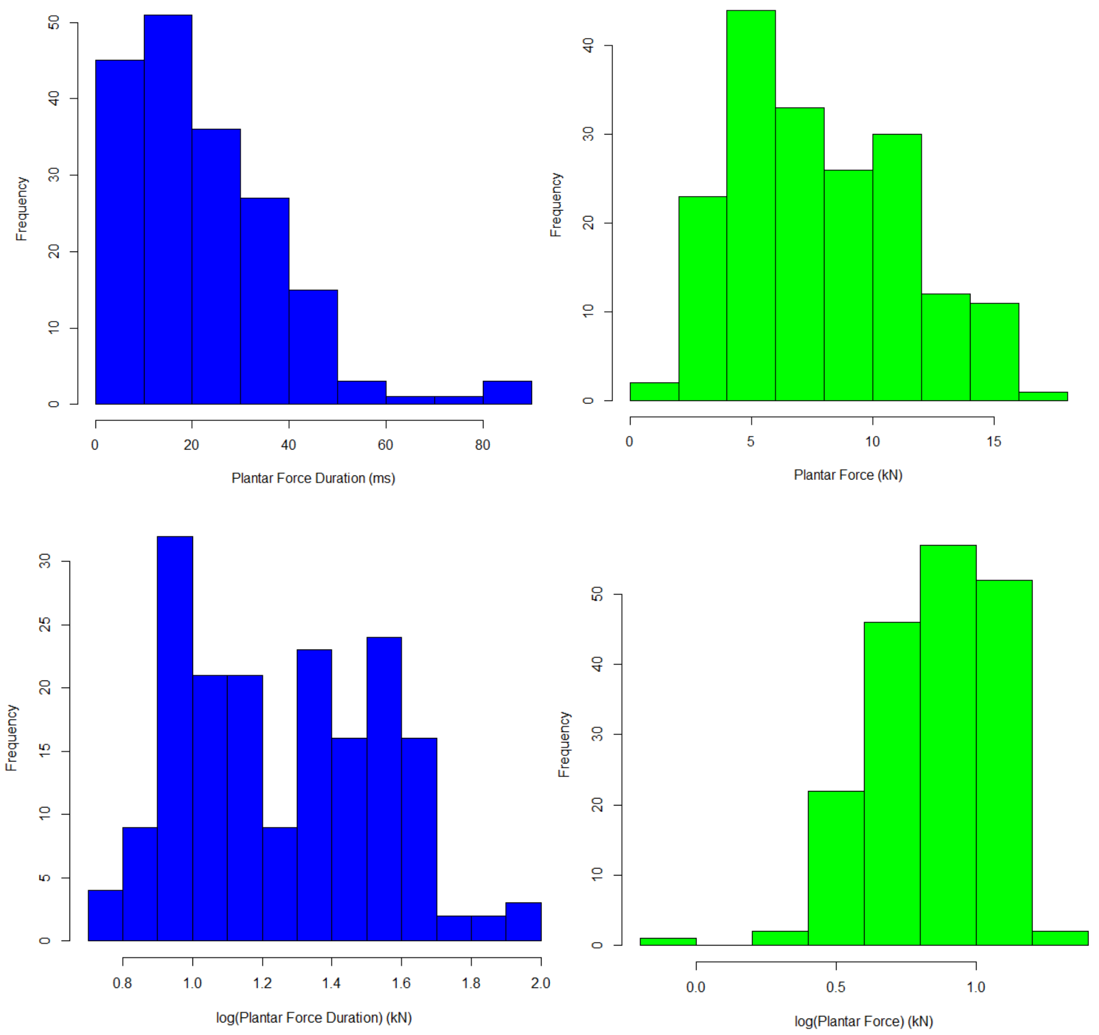

Figure 6.12. Histograms of the duration and force for injured data points to show the distribution of injured data points.

6.2.2 Logistic Regression Approach

Logistic regression was used in a second approach to estimating the relationship between force and duration in terms of injury probability. The nature of logistic regression lends itself to this type of problem because of the dichotomous nature of the data set and the presence of multiple independent variables. Additionally, logistic regression does not require the variables to be normally distributed.[93] While only injury data points were considered for the linear regression approach, no-injury data points could be considered in the logistic regression analysis. Since logistic regression treats a categorical outcome (injury or no-injury) as the dependent variable and relies on the value of the dependent variables to estimate the probability that an outcome will be one category or another, it is not necessary to exclude the left censored data as was done for the linear regression analysis.

Table 6.4 provides the logistic regression parameters for both data sets for reference purposes, and Figure 6.13 shows a comparison of the linear regression fit to the logistic regression lines for 50- and 75-percent probability of injury on a log-log scale. These plots indicate that the linear regression lines roughly capture the line of 75% probability of injury. Figure 6.14 shows the logistic regression lines for 50- and 75-percent probability of injury, revealing that at large durations, the force for a given probability of injury levels-off for the range of durations shown. When the dorsiflexed quasi-static tests[181] included in the larger data set are added to the plot (Figure 6.15), it is apparent that the logistic regression relationship is unrealistic for quasi-static loading conditions. This result suggests that while the logistic regression relationship works well for the shorter duration loads (<100 ms), long durations events must be treated differently, or an alternative approach taken to combine injury predictors.[216]

Table 6.4. Logistic regression coefficients for the combined data set excluding tests with initial ankle flexion or xversion. Analysis was performed on the plantar force data.

Data Set	**Intercept**		**Log (Force)**		**Log (Force Duration)**	
	β_0	**S.E.**	β_1	**S.E.**	β_2	**S.E.**
All Data, Neutral	-10.172	2.120	8.306	1.380	2.866	0.899
Uncensored Data	-17.009	3.677	12.826	2.326	5.064	1.490

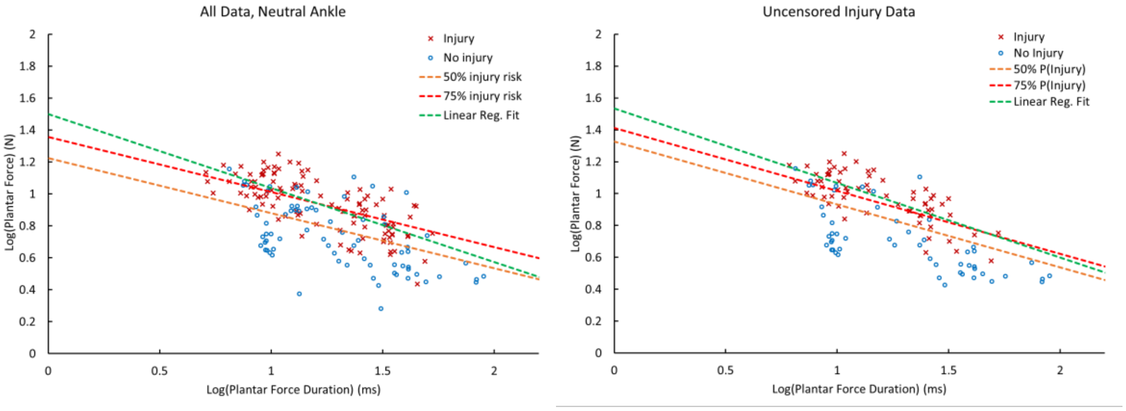

Figure 6.13. Logistic regression fits of injury data for 50% and 75% probability of injury are shown above on a log-log scale. The plot on the left shows the linear regression fit for all injury data, while the plot on the right shows the fit for only the uncensored injury data points. The linear regression fit is shown for reference.

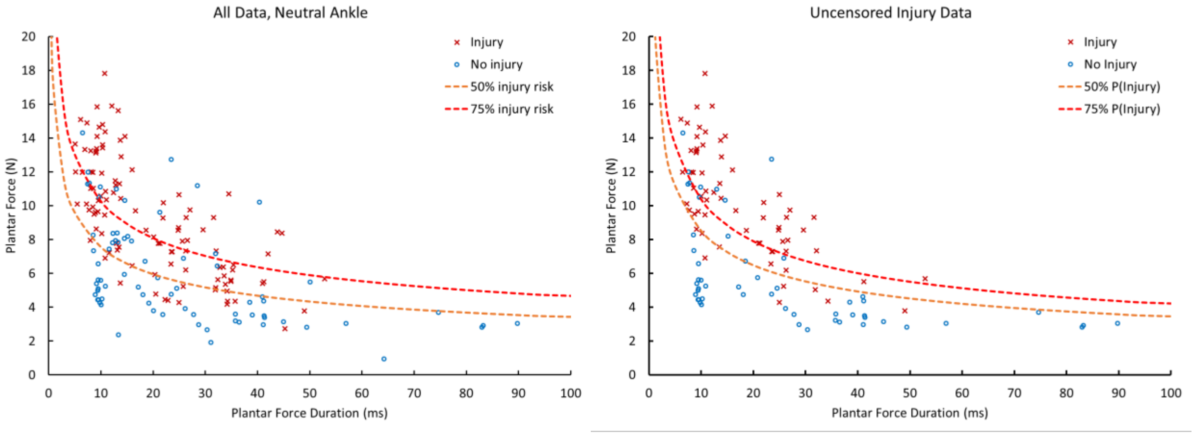

Figure 6.14. Logistic regression fits of injury data are shown above for 50% and 75% probability of injury. The plot on the left shows the linear regression fit for all injury data, while the plot on the right shows the fit for only the uncensored injury data points.

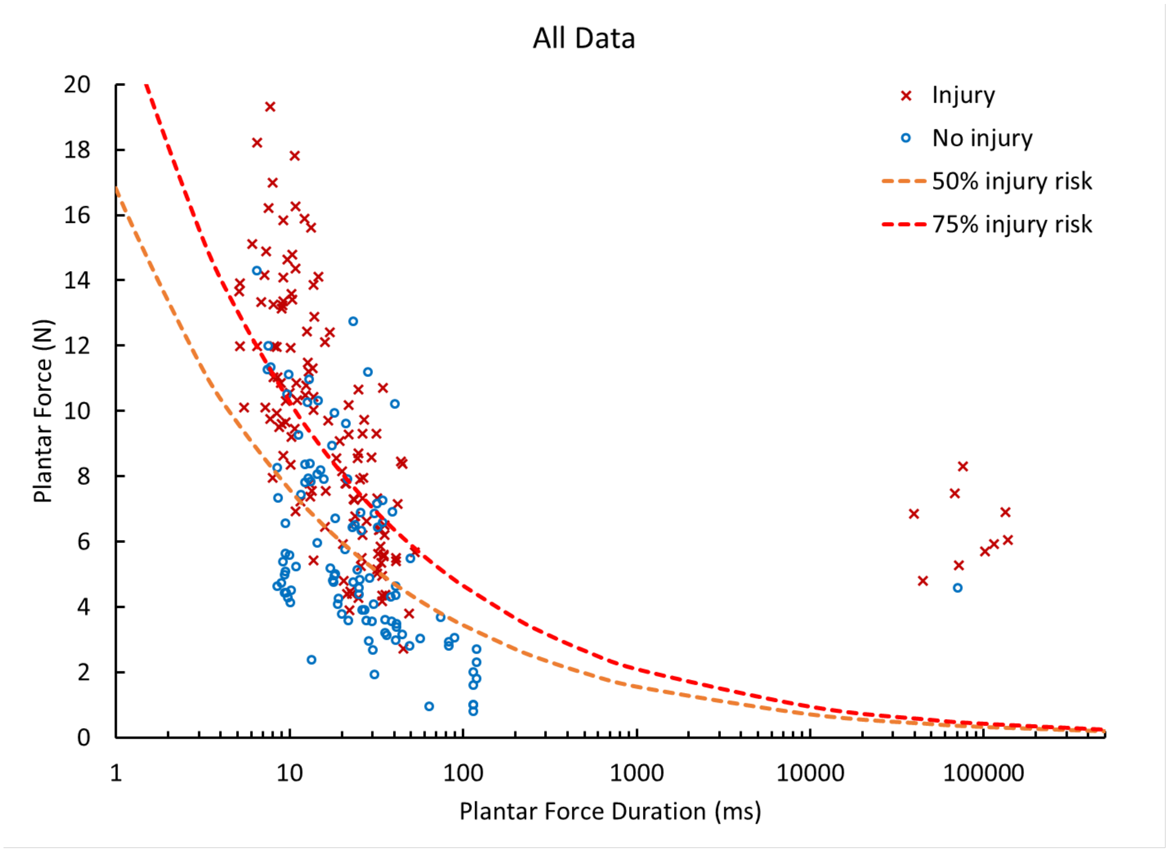

Figure 6.15. The "All Data" logistic regression fit is shown on top of injury and no-injury data points including the tests with initial ankle flexion. Note that a log scale was used for the x-axis.

6.3 Piecewise Approach using Impulse and Force

The inability of the logistic regression to fit both the dynamic and quasi-static data suggests that a piecewise approach may be taken for development of an injury criterion which will accurately capture injury behavior for both long and short duration events. This section provides two methodologies for developing a piecewise injury criterion for the leg using the results of the logistic regression and impulse as injury predictors. The precedent and foundation for developing a piecewise injury criterion comes from Viano et al. and relies on the theory of Stech and Payne and von Gierke as discussed in the introduction.[197,208,216]

The von Gierke theory shows that resonant frequency can be used to distinguish between the regions in which different aspects of the input pulse dominate a model's behavior. Wakeling and Nigg (2001) estimate the resonant frequency of the leg to be between 20 and 50 Hz.[217] The lowest damped natural frequencies estimated using the finite element and lumped parameter models described in Chapter 3 were also in this range (22.3-43.6 Hz). Using information obtained from the FE parametric study using the modified human leg FE model, this range of frequencies are associated with footplate force durations of 15-22 ms. Based on this estimation, the response of the leg should be independent of pulse duration for pulse durations greater than 150-220 ms (an order of magnitude greater than the time associated with the resonant frequency as established by von Gierke).[197,216]

To ensure that the injury criterion does not underestimate the probability of injury, it is important to carefully investigate the region associated with resonance where force at fracture should be at its minimum. Hence forward, the region associated with durations from the resonant frequency to one order of magnitude greater than the natural frequency (i.e. 20-200 ms) will be referred to as the "resonance region," which is highlighted in red in Figure 6.16. The diagram in Figure 6.16 is based on von Gierke.[214] and has been updated to show the division between regions of pulse duration that will use different injury predictors. The example line shown demonstrates the theoretical shape of the division between injury and no-injury assuming force as the injury predictor and that the leg can be modeled as a single degree-of-freedom model. Because of the complicated nature of the resonance region, these durations will be treated differently depending on the injury predictor.

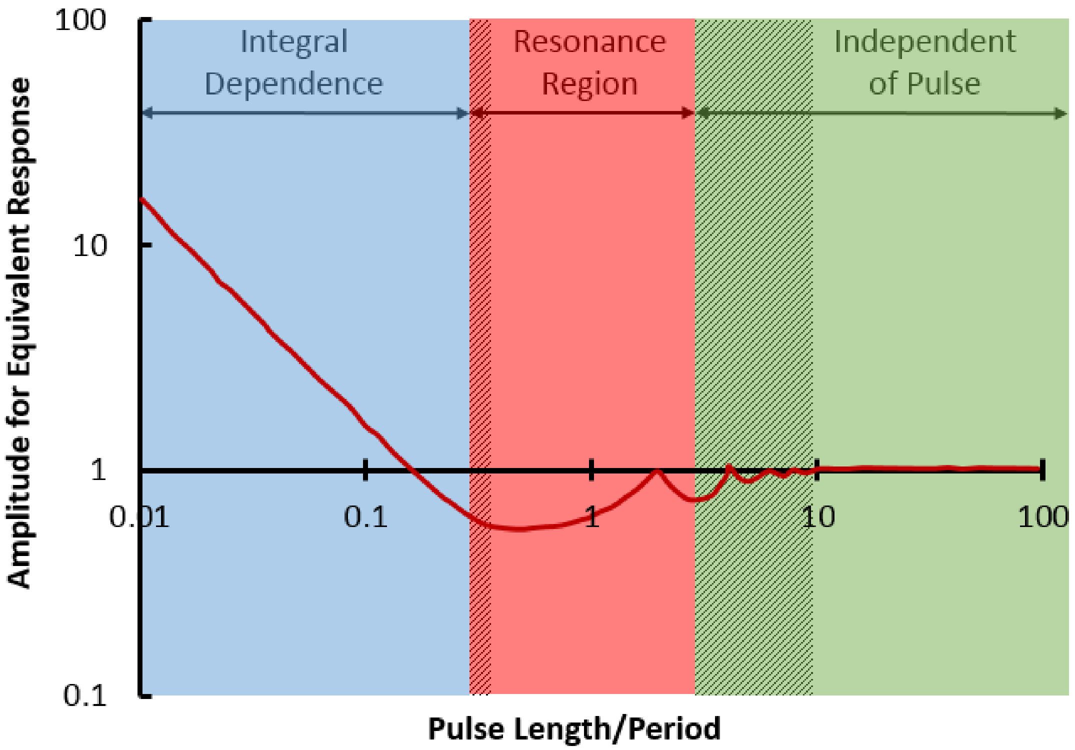

Figure 6.16. Diagram based on von Gierke[214], updated to show the division between regions that will use different injury predictors (blue vs. green shading). The red region highlights the "resonance region" which extends from the resonance frequency to 10 times the resonance frequency, which corresponds to 0.5-5 times the pulse length divided by the period associated with natural period.

6.3.1 Survival Analysis using Impulse for Short Durations

The previous section summarized the regions which should be separated in terms of injury predictors using Figure 6.16. The goal of this section is to outline an approach for predicting injury risk in the integral-dependent using impulse as an injury predictor. The theory proposed by von Gierke suggests that the integral of the input pulse (i.e. impulse in the case of an input force) is predictive of model response for frequencies higher than the natural frequency of the leg (see Figure 2.17).[216] In keeping with this theory, plantar impulse was calculated for each test in the combined data set and plotted versus duration and time-to-peak. Both impulse at peak force and impulse at force duration were calculated. Figure

6.17 shows plots of the combinations of these variables for the combined data set excluding xversion tests, and focused on durations of less than 100 ms.

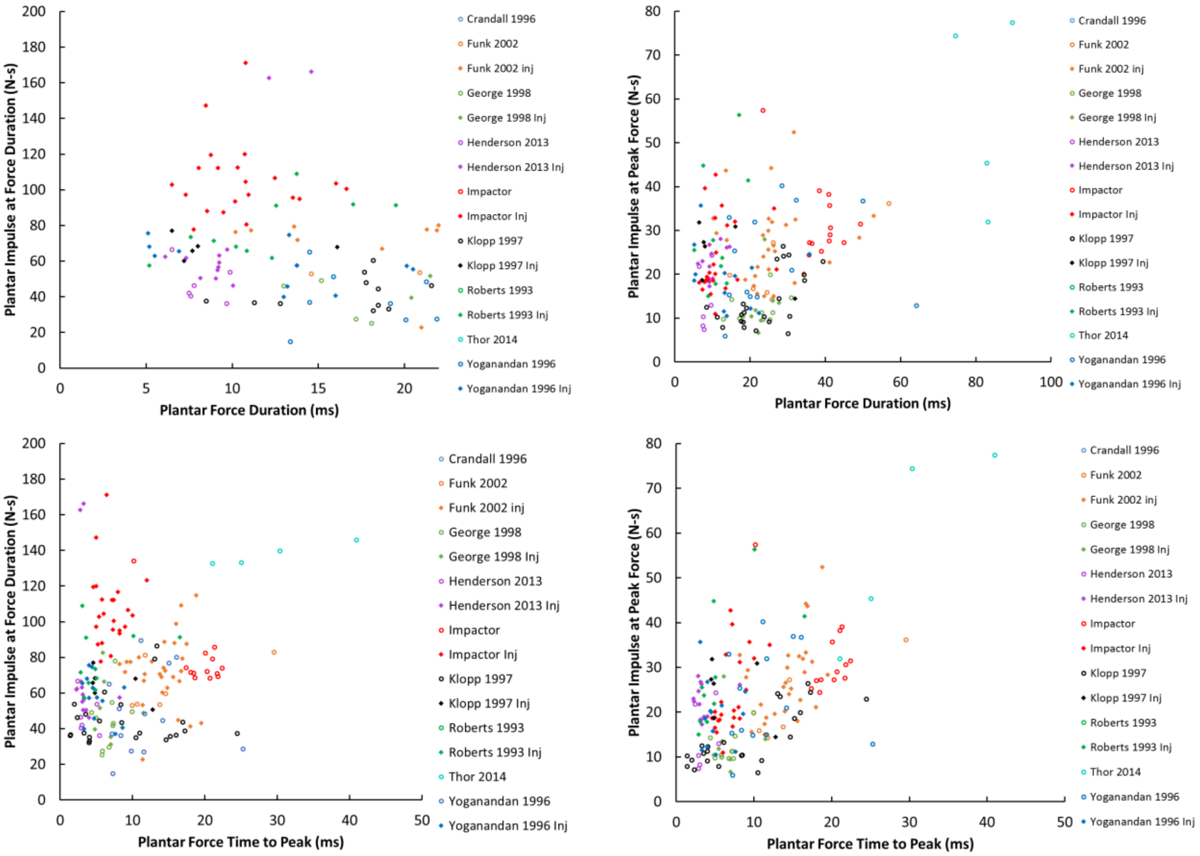

Figure 6.17. Impulse versus time of peak force and duration of force calculated at peak force and at the duration of the force. The left column compares the plantar impulse at the duration of the force versus force duration (top) and time-to-peak force (bottom) for injury and no-injury data points. The right column compares the impulse at peak force for the same two time variables.

In Figure 6.17, more no-injury than injury data points have impulses at duration of less than 60 N-s for force durations less than 21 ms (the pulse duration associated with the resonance frequency of the leg). For longer durations (and time-to-peaks), there is less grouping between injury and no-injury data points. This is consistent with the theory of von

Gierke in which the integral of the input pulse controls the response.[216] To simplify the presentation of the data shown in Figure 6.17, the data was classified into injury and no-injury and the scale for the duration was changed to include force durations of less than 22ms (Figure 6.18). This plots shows more clearly the distinction between injury and no-injury points that impulse provides for this region. Since injury is clearly not dependent upon impulse for the resonance region, the resonance region will be grouped with the longer durations as shown in Figure 6.19.

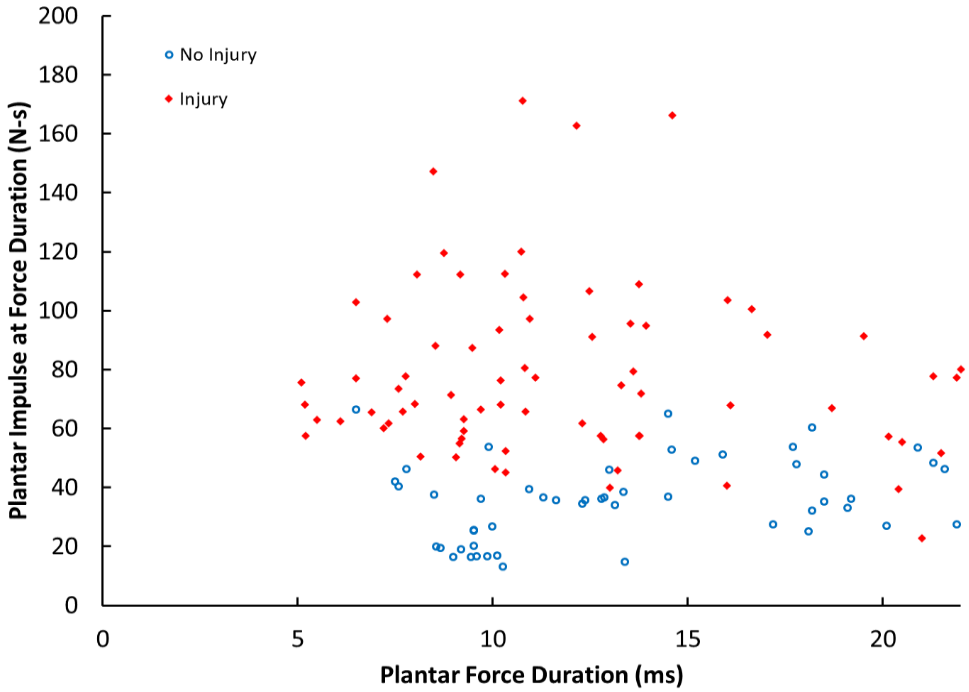

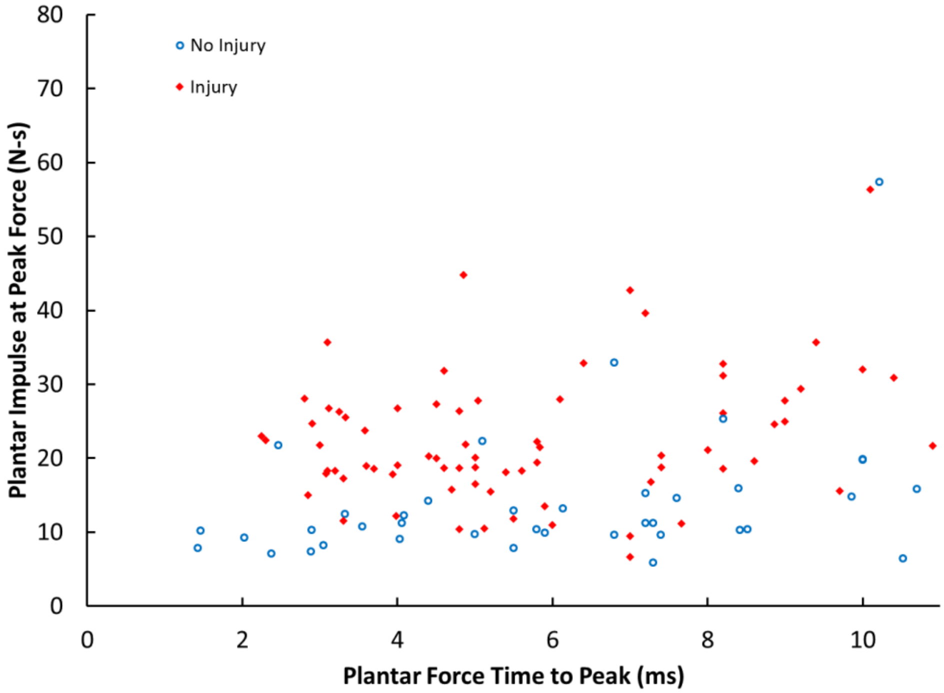

Figure 6.18. Demonstration of the separation between injury and no-injury points provided by plantar impulse for short force durations using the combined data set. The plot on the top shows planter impulse at force duration versus force duration, and the plot on the bottom shows plantar impulse at peak force versus force time-to-peak.

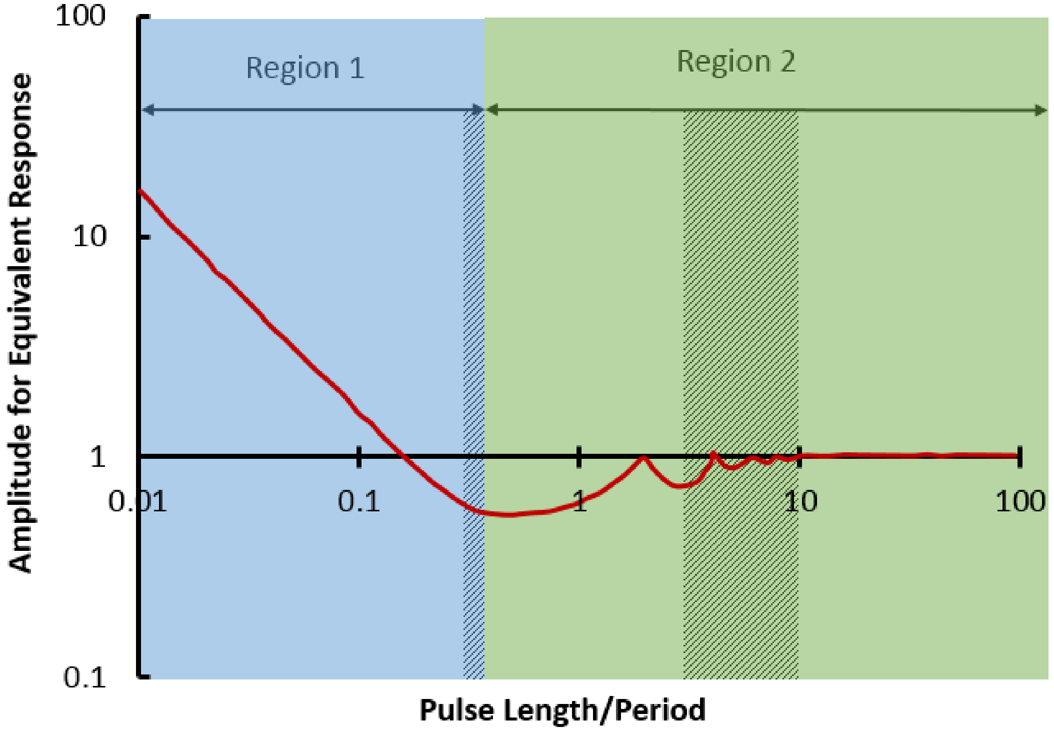

Figure 6.19. Diagram based on von Gierke[214], updated to show the division between regions that will use different injury predictors (blue vs. green shading). The blue region will utilize impulse as the injury predictor, while the green region will use force as the main injury predictor. The example line shown demonstrates the theoretical shape of the division between injury and no-injury assuming force as the injury predictor.

To quantify the relationship between impulse and injury, a survival analysis was performed using impulse as the main predictor variable for data points with plantar force times to peak of less than 11 ms (time-to-peak footplate force associated with an estimated damped natural frequency of the leg). For this analysis, no-injury data points were considered right censored, and injury points were considered left censored if time to fracture was unknown. When time of fracture was known, the data point was treated as uncensored. Age, sex, mass, and dorsiflexion angle were considered as variables affecting fracture tolerance in the foot/leg. Age in years was treated as a continuous covariate, while sex was treated as a categorical variable (i.e. females were denoted by 0, and males by 1). Flexion angle in degrees was included as a continuous covariate due to previous studies demonstrating its ability to increase force at fracture;[82,109] dorsiflexion was treated as positive, while plantar flexion angles were assigned negative values. Data was mass-scaled to prevent the previously-discussed complications arising from using sex as a covariate.

Each of the three predetermined covariates were included in the survival model, and a one-by-one exclusion analysis was performed to determine which covariates contributed to the explanation of variance in the survival model. Akaike's Information Criterion (AIC) and the log-likelihood (ln(L)) were used to compare each of the models. For this analysis the least significant covariate in each survival analysis was eliminated until all covariates were deemed to be significant.

Table 6.5. Results of the one-by-one exclusion analysis to determine which covariates should be included in the survival model.

Model Details			P-value for Covariate		
# of Covariates	**AIC**	**ln(L)**	**Age**	**Dorsiflexion**	**Sex**
3	237.73	-113.9	6.00e-3	0.633	0.517
2	235.96	-114	6.54e-3		0.485
1	234.49	-114.2	6.81e-3		
0	238.81	-117.4			

Age was found to be the only significant covariate, and contributed to a lower AIC score and higher log-likelihood than the model with no covariates. The survival model coefficients are shown in Table 6.6. This result was expected based on the nature of the data set and the inclusion criteria. Since the data set included only tests which were performed with an initial neutral ankle position (as defined by less than ±10 degrees of flexion), the effect of initial dorsiflexion should not be significant for the data set. Additionally, since the impulse data was mass-normalized, the mass-based difference between male and females should be minimized. Sex-based differences involving age-related trends in BMD reduction were likely reduced by the fact that many of the included studies excluded osteoporotic PMHS, resulting in a lack of significance for the sex covariate. Further investigation showed that the correlation coefficient for age versus BMD for the data set was 0.036 for males and 0.16 for women, which explains this result.

$$\mathrm{P}_{\mathrm{inj}} = 1 - \exp\left(-\mathrm{Impulse}^{\gamma} \exp\left[\frac{-(\beta_0 + \beta_{\mathrm{age}}\mathrm{Age})}{\gamma}\right]\right) \qquad \text{Eqn. 6.1}$$

A summary of the results of the impulse-based survival analysis are shown Table 6.5 with the inclusion of age as a covariate. Eqn. 6.1 provides the form of the equation for calculating the probability of injury (P_{inj}) using the survival model parameters (γ, β_0, β_{age}).

Table 6.6. Estimated parameters for the survival model using plantar impulse at peak force as the main predictor and age as a covariate for data points with plantar force times to peak of less than 11 ms (n=92).

Parameter	γ	**Intercept**	**Age (yr)**
β_i	2.246	3.734	-0.0123
SE		0.273	4.54e-3
P-value		0.000	6.81e-3
Log-likelihood: -114.2 χ^2: 6.31; Model P-value: 0.012			

Survival curves are provided in Figure 6.20. As expected, the probability of injury for a given impulse increased with age. A comparison of impulse magnitude associated with 10-, 50-, and 90-percent probability injury for ages 25, 45, and 65 is shown in Table 6.7. At 50-percent probability of injury, the difference in impulse required to produce injury for a 25-year old compared to a 65-year old was more than 11 N-s. Confidence intervals for the injury risk function for age 65 was smaller than that for age 25 because of the skew towards older specimens in the sample population.

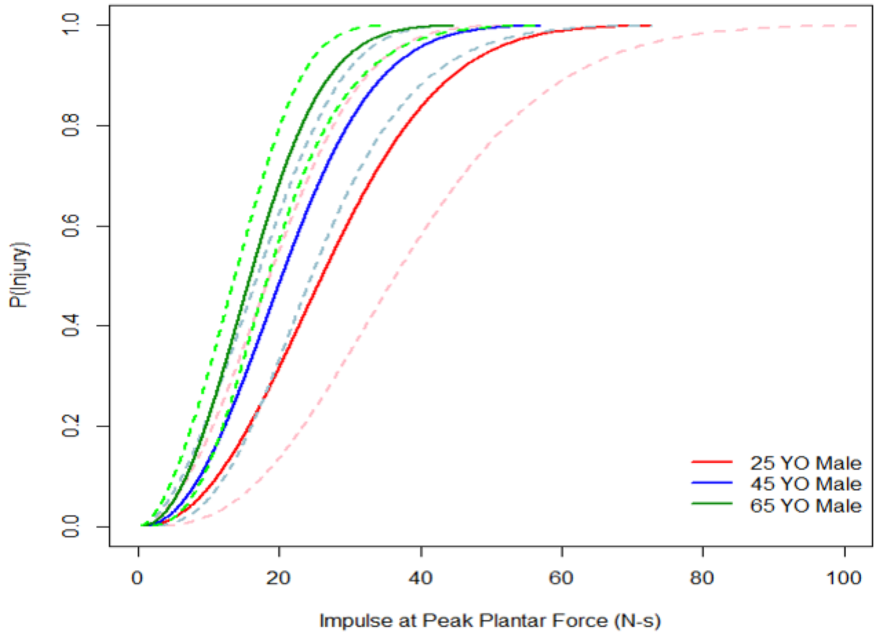

Figure 6.20. Survival curves showing the negative relationship between probability of injury and age for a given impulse.

Table 6.7. Comparison of impulse 95% confidence intervals (N-s) for 10-, 50-, and 90-percent probability of injury for different ages.

Probability of Injury	**10%**	**50%**	**90%**
25YO Male	11.30±6.42	26.14±10.36	44.62±16.64
45YO Male	8.84±3.55	20.44±4.18	34.89±6.71
65YO Male	6.91±2.41	15.99±2.51	27.29±4.66

6.3.2 Injury Prediction for Long Duration Pulses

According to von Gierke, the response of the leg to longer durations of loading should be pulse-independent, meaning that the input pulse magnitude (peak force) should be an appropriate injury predictor for this region.[216] This section focuses on providing an estimate of injury risk based on peak force for the resonance and pulse-independent regions for the piecewise injury criterion. Figure 6.21 is provided to show the plantar force versus time-to-peak data for the resonance and the pulse-independent regions. This figure demonstrates that there is little correlation (R^2=0.07 for a linear regression on the injury points) between force and time-to-peak for this region, and (with few exceptions) a value of force could potentially be used to distinguish between injury and no-injury data points.

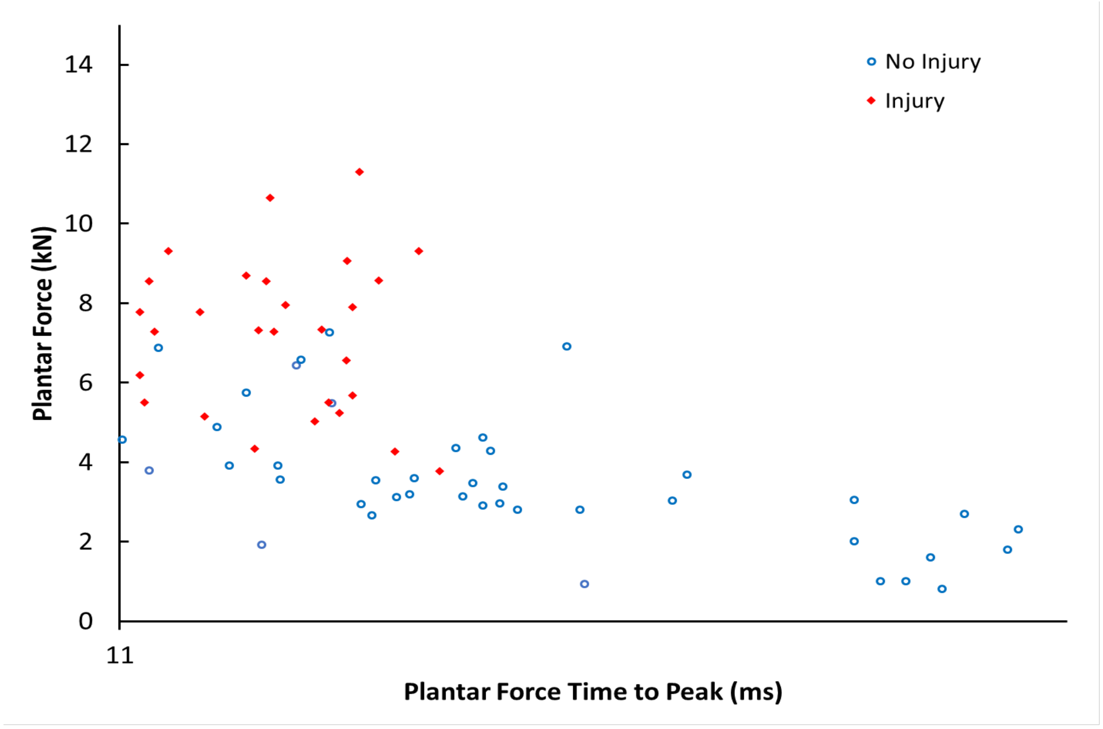

Figure 6.21. Plantar force versus plantar force time-to-peak for the data included in the resonance region and the pulse-independent region of Figure 6.16.

To develop an injury probability model for this region, peak force was used as the main predictor variable in a survival analysis. Survival model censoring was the same as for the impulse-based survival model. Age, sex, and ankle flexion angle were considered as covariates and one-by-one elimination was used to arrive at the format of the final survival model. Comparison of results from the covariate elimination analysis is provided in Table 6.5. Again, sex and dorsiflexion angle were found to have an insignificant effect on the model fit ($p>0.05$), and were removed.

Table 6.8. Results of the one-by-one exclusion analysis to determine which covariates should be included in the survival model.

Model Details			P-value for Covariate		
# of Covariates	**AIC**	**ln(L)**	**Age**	**Dorsiflexion**	**Sex**
3	53.21	-21.6	0.091	0.640	0.597
2	51.44	-21.7	0.089		0.432
1	50.11	-22.1	0.034		
0	52.98	-24.5			

The best-performing model in terms of log-likelihood and AIC included only age as a covariate. The equation for probability of injury based on plantar force is provided by Eqn. 6.2, and estimated parameters for this survival model are provided in Table 6.9.

$$\mathrm{P_{inj}} = 1 - \exp\left(-Force^{\gamma}\exp\left[\frac{-(\beta_0 + \beta_{age}Age)}{\gamma}\right]\right) \qquad \text{Eqn. 6.2}$$

Table 6.9. Estimated parameters for the survival model using peak plantar force as the main predictor and age as a covariate for data points with plantar force times to peak of more than 11 ms (n=50).

Parameter	**γ**	**Intercept**	**Age (yr)**
β_i	6.013	2.664	-0.0107
SE		0.335	5.06e-3
P-value		0.000	3.46e-2
Log-likelihood: -22.1 χ^2: 4.88; Model P-value: 0.027			

Age was found to increase the probability of injury for a given plantar force, as expected, and in agreement with the results for the impulse survival model (Figure 6.22). Results tabulated from the injury risk function for various ages and probabilities of injury are also reported (Table 6.10). The difference in force estimated for 50-percent probability of injury between 25- and 65-year olds was 3.59 kN. These results agree closely with those reported by Yoganandan et al. (2014) for an optimized injury risk function based on age. Yoganandan et al. estimated 50% probability of injury for 25-, 45-, and 65-year olds to be 10.4, 8.3, and 6.6 kN, respectively.[229] It should be noted that despite the fact that results for age 25 are reported, the confidence interval is large because of the lack of data points for this age group.

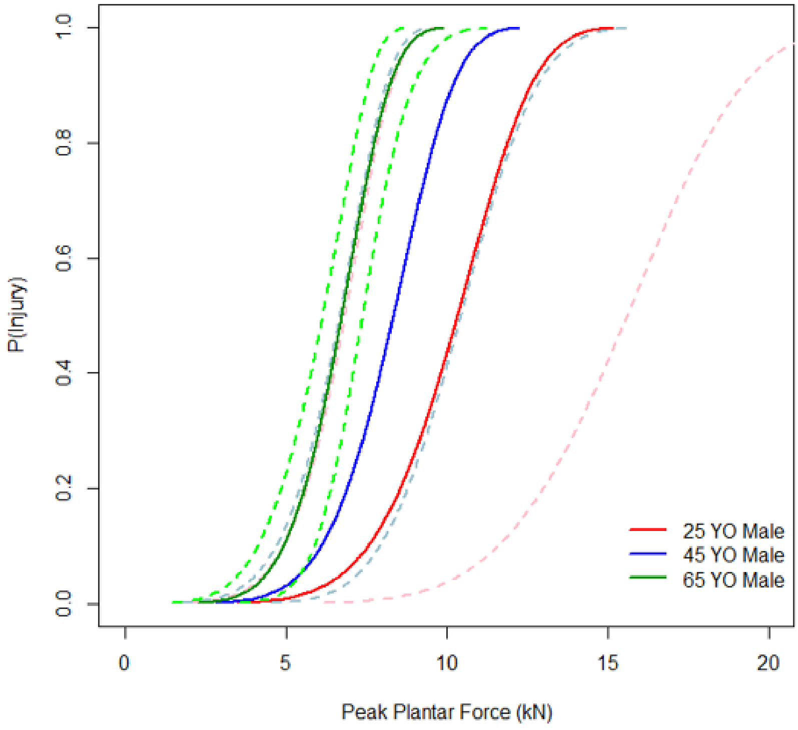

Figure 6.22. Survival curves showing the negative relationship between age and probability of injury for a given plantar.

Table 6.10. Comparison of plantar force at 10-, 50-, and 90-percent probability of injury for different ages.

Probability of Injury	**10%**	**50%**	**90%**
25YO Male	7.56±4.03	10.34±5.28	12.63±6.57
45YO Male	6.11±1.82	8.35±2.09	10.20±2.62
65YO Male	4.93±0.96	6.75±0.65	8.24±0.74

Since data points with flexion angles exceeding ±10 degrees were eliminated from the analysis, no quasi-static data (Roberts et al.)[181] was available to evaluate the fit of the model for the pulse-independent region. While this limits the applicability of the proposed injury criterion, it is assumed that the injury probability estimated by the model would be over-predicted rather than under-predicted as was the case for the model which included tests with more extreme flexion angles. Despite this shortcoming, the proposed model still satisfies the requirements of estimating injury probability for UBB and automotive intrusion events.

6.3.3 Evaluation of Piecewise Injury Criterion

The two injury risk functions developed based on impulse at peak force and peak force were combined to form a single, piecewise injury risk function to be used for a larger range of loading durations than previously existed. A summary of the form of the injury risk function is provided by Eqn. 6.3 and Eqn. 6.4. I_{maxF} refers to the impulse at maximum plantar force (N-s), F_{max} is the peak plantar force (kN), and α and γ are parameters for the Weibull distribution. Eqn. 6.4 expresses the relationship between α and the β-coefficients for the covariates. In the case of both the force and impulse survival models, only one covariate (age) is used.

$$P_{inj} = \begin{cases} 1 - exp[-\alpha_I (I_{maxF})^{\gamma_I}] & \text{if ttp} \leq 11 \text{ ms} \\ 1 - exp[-\alpha_F (F_{max})^{\gamma_F}] & \text{if ttp} > 11 \text{ ms} \end{cases} \qquad \text{Eqn. 6.3}$$

$$\alpha = exp\left[-\beta_0 - \sum_{i=1}^{n} (\beta_i * P_{inj})\right] \qquad \text{Eqn. 6.4}$$

The estimated parameters for piecewise injury risk function are summarized together in Table 6.11 for easy reference. This function will be referred to as the *piecewise injury risk function* thus forward. The time-to-peak used to distinguish between the two regions was determined using the average time-to-peak force from the human leg FE model for the loading frequencies within the range of resonance frequencies estimated using the LMMs.

Table 6.11. Estimated parameters for the piecewise injury risk function using Eqn. 6.3 and Eqn. 6.4.

Parameter	Impulse	Force
β_0	2.246	6.013
β_{age}	3.734	2.664
γ_I	-0.0123	-0.0107

Several statistical analyses were performed to compare the proposed injury probability model with four previous models developed by Funk et al. (2002) and Yoganandan et al. (1996 and 2015), and Kuppa et al.[70,116,230,231] These models were chosen for comparison based on their prominence in the literature and inclusion of covariates to account for population variance. The goal of these analyses was to estimate the predictive abilities of each of the injury probability models in order to determine whether the proposed piecewise model (Bailey 2016) is a better tool for predicting injury across a larger range of load durations. A validation data set comprised of 137 PMHS axial loading tests (110 males, 27 females) spanning a range of loading duration from 1.4 to 41 ms, an average age of 60.0±13.2 years, and an average body mass of 77.9±17.64 kg was used to compare the injury probability models. A probability of injury for each data point was estimated using each of the four injury probability models. Equations are provided below for each of the risk functions.

Yoganandan 1996 Injury Model:

$$\mathbf{P_{inj} = 1 - exp(-e^{(ln(F_{prox}) - 2.036)/0.332})} \qquad \text{Eqn. 6.5}$$

Kuppa 2001 Injury Model:

$$\mathbf{P_{inj}} = \frac{\mathbf{1}}{\mathbf{1} + \boldsymbol{e}^{\mathbf{4.572 - 0.670}\boldsymbol{F_{tibia}}}}) \qquad \text{Eqn. 6.6}$$

Funk 2002 Injury Model:

$$\mathbf{P_{inj} = 1 - exp(-e^{-47.3 + 4.99 * ln(F_m) - 0.964(sex) - 0.055(mass) + 0.079(age) - 0.473(Ach.tens.)})} \qquad \text{Eqn. 6.7}$$

Yoganandan 2015 Injury Model:

$$\mathbf{P_{inj} = 1 - exp(-F_{prox} e^{-[9.5591 + 0.0118(age)]^{4.4643}})} \qquad \text{Eqn. 6.8}$$

Area under the receiver operator characteristic (ROC) curves was calculated using R software. Area under the ROC curve (AUC) gages the ability of the model to predict injury and uses the relationship between sensitivity and specificity. Figure 6.23 shows the ROC curves for each of the five injury probability models, and AUC values are reported in Table 6.12. An AUC of 0.80-0.90 is considered a “good” fit of the validation data, while an AUC of 0.7-0.8 is considered a “fair” fit of the validation data.[142] The proposed model performed the best according to this statistic, suggesting that it has the best ability to distinguish between injury and no-injury data points compared to the other three models.

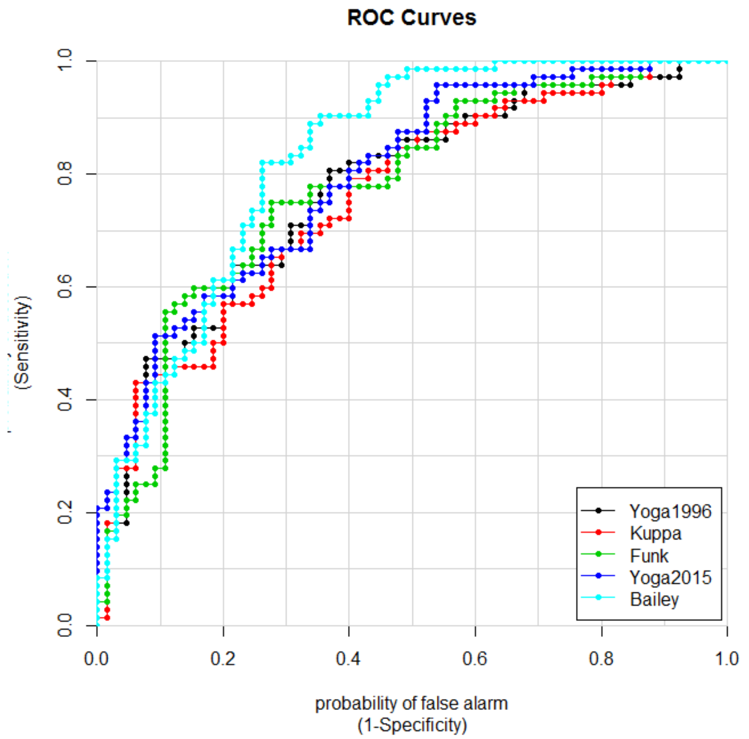

Figure 6.23. ROC curves comparing the five injury probability models validation data set.

Kruskal's gamma (γ_K) (Eqn. 6.9) evaluates the injury model's ability to distinguish between injured and non-injured data points, and is based on the number of observation pairs classified as concordant or discordant. A discordant pair consists of an injury data point for which the injury criterion predicts a lower risk of injury than a non-injury data point. Concordant pairs have the opposite relationship.[49,104] Yule's Q (Q_Y) is a similar statistic to Kruskal's gamma for evaluating a model's predictive ability, but also factors in the ratio of true and false predictions (Eqn. 6.10). Each of the four injury probability models were compared using these two statistics, which indicated the proposed model out-performed the previous models for the validation data set.

$$\boldsymbol{\gamma_K} = \frac{\mathbf{n_c} - \mathbf{n_d}}{\mathbf{n_c} + \mathbf{n_d}} \qquad \text{Eqn. 6.9}$$

$$\mathbf{Q}_{\boldsymbol{Y}} = \frac{\boldsymbol{TP} * \boldsymbol{TN} - \mathbf{FN} * \mathbf{FP}}{\boldsymbol{TP} * \boldsymbol{TN} + \mathbf{FN} * \mathbf{FP}} \qquad \text{Eqn. 6.10}$$

where n_c is the number of concordant pairs, and n_d is the number of discordant pairs.

Additional descriptors related to the AUC were tabulated and are provided in Table 6.12. The number of true positive (injury correctly identified), true negative (no-injury correctly identified), false positive (injury predicted, but specimen was not injured), and false negative (no-injury predicted, but specimen was injured) results are shown. Injury probability as estimated by each of the injury models of greater than 50% was treated as a “positive” indication of injury. The number of false positive tests refers to the number of Type I errors, while the number of false negative tests is indicative of the number of Type II errors. Sensitivity is described by the true positive rate (TPR) and refers to the model’s ability to correctly indicate injury. Specificity is described by the true negative rate (TNR) and refers to the model’s ability to correctly identify no-injury cases. Accuracy combines these two measures to indicate how likely the model is to correctly identify a data point. The score for the best-performing injury model for each test statistic is highlighted in green in **Table 6.12**, and reveals that the proposed model (Bailey 2016) scores are best for most statistics.

The Funk et al. injury model had the highest true negative ratio and the lowest false positive ratio, which indicates that it was best able to correctly identify the no-injury tests; however, the Bailey 2016 model is better able to correctly identify the injury tests. In other words, a model which over-predicts probability of injury is preferable to a model which underestimates probability of injury. While with additional injury data is necessary to provide further validation, this statistical analysis has demonstrated that the proposed injury probability model improves injury prediction capabilities and expands upon the range of load durations for which a single injury probability model is applicable.

Table 6.12. Summary of statistical measures for assessing the predictive capabilities of the proposed injury model compared to three existing injury probability models.[70,230,231] The best score for each measure is highlighted in bolded green type.

Injury Assessment	Yoganandan 1996	Kuppa 2001	Funk 2002	Yoganandan 2015	Bailey 2016
True Positive (TP)	41	35	42	43	51
False Positive (FP)	13	12	9	14	16
True Negative (TN)	52	53	56	51	49
False Negative (FN)	31	37	30	29	21
Concordant (n_c)	93	88	98	94	100
Discordant (n_d)	44	49	39	43	37
True Positive Ratio (TPR)	0.5694	0.4861	0.5833	0.5972	**0.7083**
True Negative Ratio (TNR)	0.8000	0.8154	**0.8615**	0.7846	0.7538
False Positive Ratio (FPR)	0.2000	0.1846	**0.1385**	0.2154	0.2462
False Negative Ratio (FNR)	0.4306	0.5139	0.4167	0.4028	**0.2917**
Positive Predictive Value (PPV)	0.7593	0.7447	**0.8235**	0.7544	0.7612
Negative Predictive Value (NPV)	0.6265	0.5889	0.6512	0.6375	**0.7000**
False Discovery Rate (FDR)	0.2507	0.2553	0.1765	0.2456	0.2388
False Omission Rate (FOR)	0.3735	0.4111	0.3488	0.3625	**0.3000**
Accuracy (ACC)	0.6788	0.6423	0.7153	0.6861	**0.7299**
Kruskal's Gamma (γ_K)	0.5423	0.5145	0.5521	0.5859	**0.6615**
Yule's Q (Q_Y)	0.6821	0.6137	**0.7941**	0.6876	0.7630
AUC	0.7712	0.7573	0.7761	0.7929	**0.8308**

While it is understood that validating a model using data used to develop the model is not recommended, the fact that data from each of the other studies (Yoganandan 1996, Funk 2002, and Yoganandan 2015) were contained within the validation data set, makes this comparison analysis useful. Additional analysis was performed to compare the predictive ability of the new injury model for each of the smaller data sets (or portions of the data sets since only partial data sets could be acquired). The same analysis was performed using all tests from the Funk 2002 study, and a partial data set for the Yoganandan 1996 study since both the 1996 and 2015 data sets were essentially the same (Table 6.13). Since the Yoganandan et al. data set did not measure force at the tibia, the Kuppa 2001 and Funk 2002 injury risk functions were not able to be compared for this data set.

Table 6.13. Assessment of injury risk functions for 50% risk of injury using the Funk 2002 and Yoganandan 1996 data sets.[70,230,231]

Funk 2002 Data Set					
Injury Assessment	**Yoga. 1996**	**Kuppa 2001**	**Funk 2002**	**Yoga. 2015**	**Bailey 2016**
Accuracy (ACC)	**0.6286**	0.3714	0.5428	0.6000	**0.6286**
Kruskal's Gamma (γ_K)	0.3678	0.1609	0.2759	0.3908	**0.5632**
Yule's Q (Q_Y)	**0.7526**	0.3115	0.6471	0.2414	0.5172
AUC	0.6839	0.5805	0.6379	0.6954	**0.7816**
Yoganandan 2015 Data Set					
Injury Assessment	**Yoga. 1996**	**Kuppa 2001**	**Funk 2002**	**Yoga. 2015**	**Bailey 2016**
Accuracy (ACC)	0.6667	-	-	**0.7500**	0.7083
Kruskal's Gamma (γ_K)	0.7203	-	-	**0.8741**	0.4545
Yule's Q (Q_Y)	0.6800	-	-	**0.8824**	0.7073
AUC	0.8601	-	-	**0.9371**	0.7273

The results of this secondary analysis show that the proposed piecewise model out-performed the other four models for three of the four statistics reported for the Funk et al. data set. However, the Yoganandan 2015 model performed best for the Yoganandan 1996 data set for all statistics. Further investigation showed that many of the incorrectly classified tests from the Yoganandan data set had time-to-peaks near 11 ms. This result suggests that the proposed piecewise injury risk function is limited by the assumption that a single time-to-peak can be used to separate injury predictors. While there are clear advantages to using both impulse and force to estimate probability of injury, the piecewise approach does not account for variance in the population with regards to resonance frequency. When using this approach to develop an injury criterion, a discontinuity is present in the probability of injury with respect to force duration. To correctly represent the data, the duration associated with the transition between force and impulse as an injury predictor should be represented by a distribution, rather than a single time. The next section focuses on several methods by which to remove this discontinuity from the injury criterion.

6.4 Continuous Injury Criterion

To avoid the issues brought about by using a piecewise injury criterion, alternative methods for combining force and impulse into a single injury predictor were investigated. Since the theory for using force and impulse for different durations of loading was based on the assumption that the leg can be modeled as a lumped-mass model, and that deflection or compression of this model can be associated with a probability of fracture, an attempt was made to use the analytical solution of the LMM to relate force and impulse.

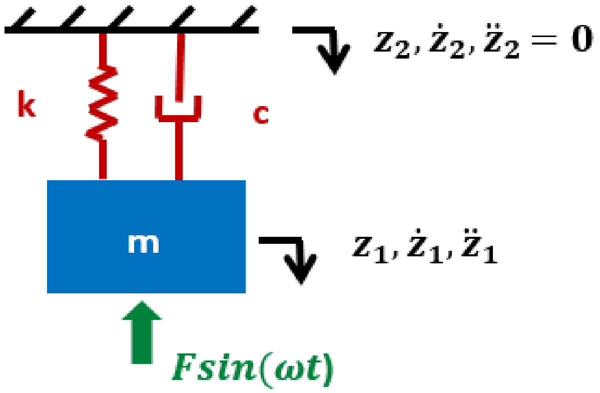
$z_2, \dot{z}_2, \ddot{z}_2 = 0$
k
c
m
$z_1, \dot{z}_1, \ddot{z}_1$
$Fsin(\omega t)$

Figure 6.24. Single degree of freedom LMM with a sinusoidal force input.

Given the model pictured in Figure 6.24 the equation of motion for the mass is given by Eqn. 6.14 for a sinusoidal force input to the system.

$$m\ddot{z}(t) + c\dot{z}(t) + kz(t) = F\sin(\omega t)\left[1 - H\left(t - \frac{\pi\omega}{F}\right)\right] \qquad \text{Eqn. 6.11}$$

This equation can be written in terms of the natural frequency of the model (ω_n) and the damping ratio (ζ) as shown in Eqn. 6.14.

$$\omega_n = \sqrt{\frac{k}{m}} \qquad \text{Eqn. 6.12}$$

$$\zeta = \frac{c}{2\sqrt{km}} \qquad \text{Eqn. 6.13}$$

$$\ddot{z}(t) + 2\zeta\omega_n\dot{z}(t) + \omega_n^2 z(t) = \frac{F}{m}\sin(\omega t)\left[1 - H\left(t - \frac{\pi\omega}{F}\right)\right] \qquad \text{Eqn. 6.14}$$

The particular solution for Eqn. 6.14, assuming an underdamped system is given by Eqn. 6.15, and the total solution is described by Eqn. 6.16.

$$z_p(t) = \frac{F/m}{\sqrt{(\omega_n^2 - \omega^2)^2 + (2\zeta\omega_n\omega)^2}}\sin(\omega t - \tan^{-1}\left(\frac{2\zeta\omega_n\omega}{\omega_n^2 - \omega^2}\right)) \qquad \text{Eqn. 6.15}$$

$$z(t) = Ae^{-\zeta\omega_n t}\sin(\omega_d t + \phi) + X\sin(\omega t - \theta) \qquad \text{Eqn. 6.16}$$

Where the following substitutions have been made for simplification of the expression and assuming that z(0)=0 and $\dot{z}(0)$=0:

$$\theta = \tan^{-1}\left(\frac{2\zeta\omega_n\omega}{\omega_n^2 - \omega^2}\right) \qquad \text{Eqn. 6.17}$$

$$\phi = \tan^{-1}\left(\frac{\omega_d(X\sin(\theta))}{-\zeta\omega_n\sin(\theta) - \omega X\cos(\theta)}\right) \qquad \text{Eqn. 6.18}$$

$$A = \frac{-X\sin(\theta)}{\cos(\phi)} \qquad \text{Eqn. 6.19}$$

$$X = \frac{F/m}{\sqrt{(\omega_n^2 - \omega^2)^2 + (2\zeta\omega_n\omega)^2}} \qquad \text{Eqn. 6.20}$$

Eqn. 6.15 shows that deflection of the model for a sinusoidal input force is dependent upon the natural frequency (ω_n), damped natural frequency (ω_d), damping ratio, and the forcing frequency. To find the peak deflection of the model for a given force amplitude (F) and forcing frequency (ω), the derivative of Eqn. 6.15 must be found. Since a sinusoidal input was assumed, this derivative is a complicated combination of both a sinusoid and exponential function, for which the closed form of the solution is unknown. Adding additional degrees of freedom to the lumped-mass model in order to capture the behavior of the leg at a larger range of loading frequencies further complicates the calculation of maximum model compression. To circumvent this issue, it was necessary to make an assumption about the form of the equation describing the relationship of LMM compression and parameters measured by previous PMHS experiments and ATDs.

Since the previously-described piecewise injury criterion proved that using impulse for short duration loads and peak force for longer duration loads provided a better fit of the injury data in terms of ability to predict fracture, it was assumed that as the duration of the force approached the critical duration for changing injury predictors, the predictor should be more of a combination of impulse and force. Thus, Eqn. 6.21 was designed such that the predictor variable (P_{FI}) was equal to the sum of two exponential functions with inverse decay rates, which approach critical values of peak force (F) or impulse (I). Fit parameters (A and B) would be related to values of force or impulse required to characterize a surface formed by the predictor variable, peak force, and impulse. Exponential decay functions were incorporated based on the exponential relationship between peak force and amplitude of model deflection in the transient part of Eqn. 6.16. The form of Eqn. 6.21 was adapted from the work of Gabler et al. who used the equation to characterize the relationship between strain in the brain and rotational head acceleration and velocity.[77,162]

$$P_{\mathrm{FI}} = \frac{F}{A}\exp\left(-\frac{F/_{A}}{I/_{B}}\right) + \frac{I}{B}\exp\left(-\frac{I/_{B}}{F/_{A}}\right) \qquad \text{Eqn. 6.21}$$

Ideally, P_{FI} would equal the probability of fracture, but since this an unknown quantity for a given experimental test, other parameters were used in place of it. First, a response surface was generated based on fitting the peak compression of a LMM representing the leg versus peak force and impulse. This approach was taken based on the assumption made by von Gierke for using the LMM as a model for the human body in relation to tolerances of accelerations. A second and third approach used the FE model of the leg to characterize foot compression and calcaneus strain in terms of force and impulse. Lastly, the parameters, A and B from Eqn. 6.21, were identified based on a probability of injury predicted by a survival model using two optimization approaches.

6.4.1 Predictor based on Lumped-Mass Model Compression

The first approach for using Eqn. 6.21 to combine impulse and force into a single predictor variable was to use peak compression of a lumped mass model as the injury predictor. To populate a response surface based on the LMM (Figure 6.25), MATLAB was used to calculate the maximum foot compression (Δz) for 1,020 sinusoidal force inputs. Amplitude of forces ranged from 1-15 kN in increments of 1 kN (Figure 6.26). Frequency associated with the sinusoidal inputs was chosen such that peak force and peak impulse were equally spaced in a grid pattern so that maximum impulse associated with the sinusoidal force input ranged from 20 to 300 N-s. Density of the grid was increased for the region associated with higher frequencies in order to better characterize the surface.

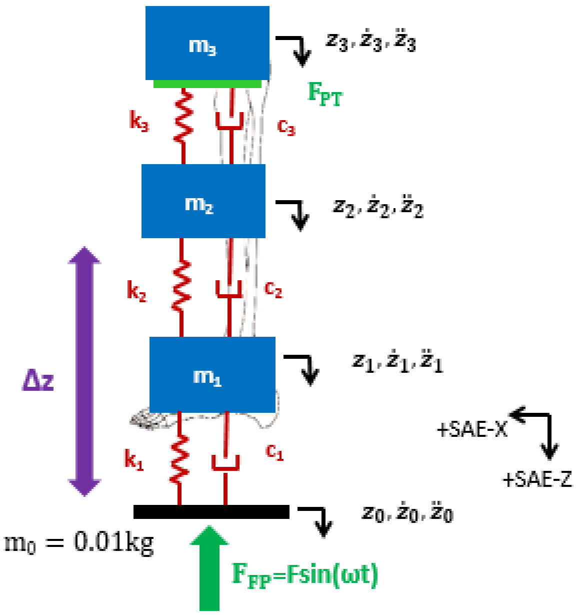
m3
$z_3, \dot{z}_3, \ddot{z}_3$
F_{PT}
k3
c3
m2
$z_2, \dot{z}_2, \ddot{z}_2$
k2
c2
Δz
m1
$z_1, \dot{z}_1, \ddot{z}_1$
+SAE-X
+SAE-Z
k1
c1
$z_0, \dot{z}_0, \ddot{z}_0$
$m_0 = 0.01$kg
F_{FP}=Fsin(ωt)

Figure 6.25. LMM used to develop response surface, which indicates the foot compression (Δz) used as the dependent variable for the response surface and used as the P_{FI} in Eqn. 6.21. In order to use force as an input, the boundary (m_0) was modeled as a small mass.

The LMM used for generation of the response surface was the 3DOF model discussed in Section 5.4. This model was chosen based on its ability to distinguish between foot compression and tibia compression, since it is hypothesized that compression of the foot (which includes heel pad and ankle compression) correlates with strain and therefore, injury. Parameters associated with this model can be found in Table 5.7 for Model 3A with floated masses.

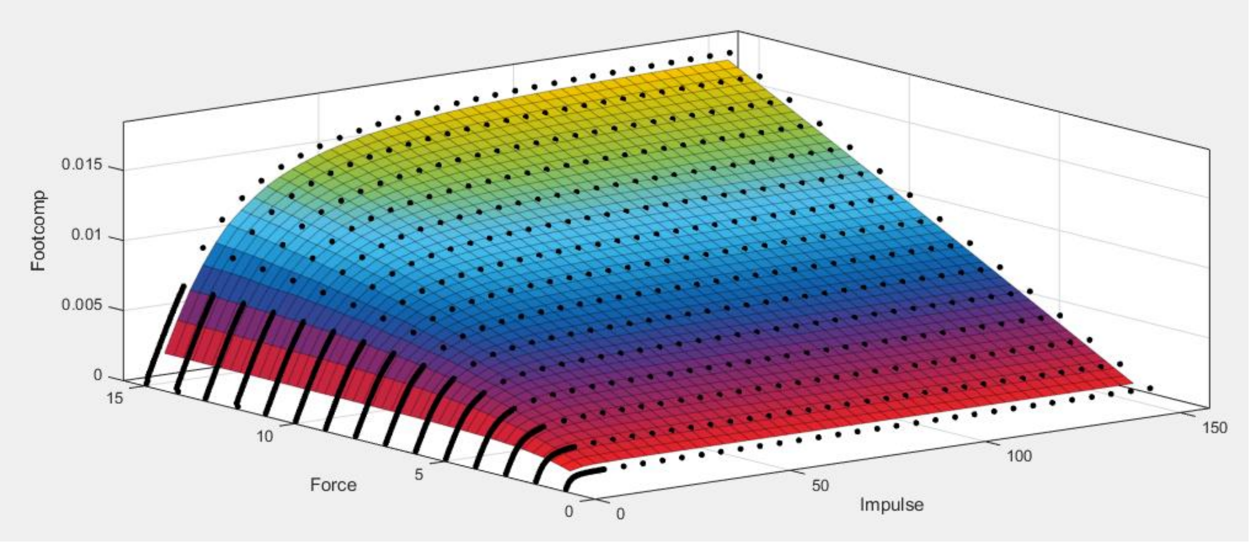

Figure 6.26. Response surface generated from the 2DOF LMM-based foot compression relationship with peak force (kN) and impulse at peak force (N-s). Individual data points generated by the LMM are shown for purpose of exhibiting the force-impulse grid sampling method.

The predictor equation parameters A and B for Eqn. 6.21 were fit for the response surface based on LMM foot compression as a function of force and impulse at peak force (Table 6.14). Root mean square error (RMSE) was found to be 0.254 mm for the equation fit. A plot of the residuals from the fit of Eqn. 6.21 to the surface for LMM-predicted foot compression shows that compression of individual conditions was predicted within 0.6 mm of the actual model compression (Figure 6.27). This residual error is less than 10 percent of the foot compression at fracture, and less than the standard error of foot compression at fracture measured in the impactor PMHS tests, which is taken to be an acceptable magnitude of error.

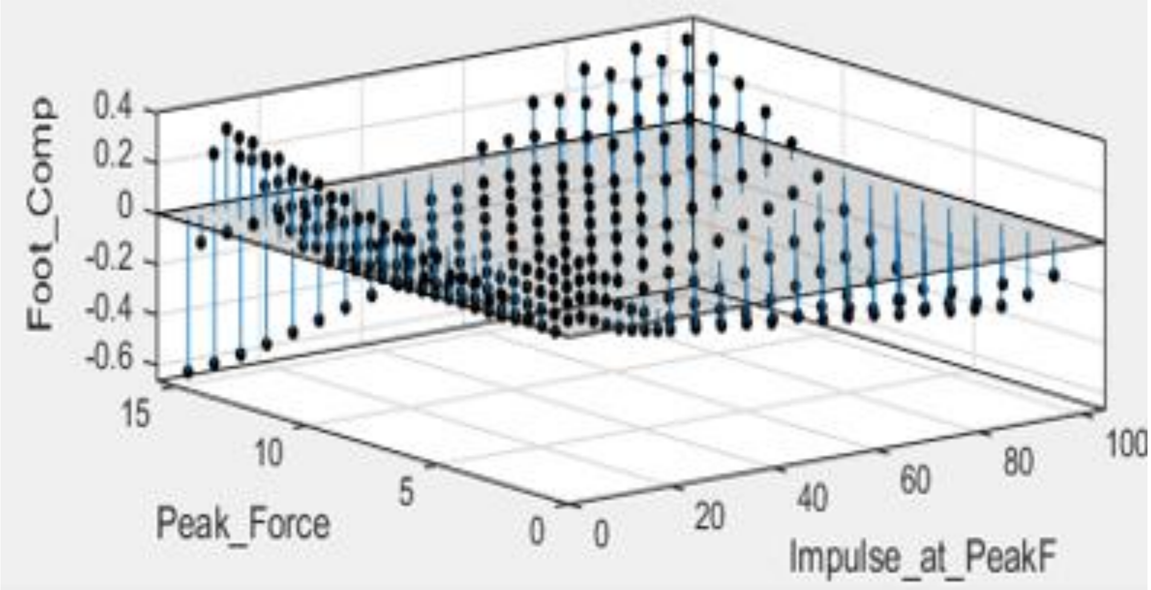

Figure 6.27. Residuals for the fit of Eqn. 6.21 to the surface for LMM-predicted foot compression (mm) versus peak force (kN) and impulse at peak force (N-s).

A contour plot was generated based on the fit of the response surface using Eqn. 6.21, and PMHS injury and no-injury data points were overlaid for a visual reference of how the deflection predicted by the LMM fits the overall pattern of the injury data (Figure 6.28). A scale is not provided for the color contours since this figure is only intended for qualitatively assessing the relationship between force and impulse provided by the surface fit parameters A and B compared to the actual injury data.

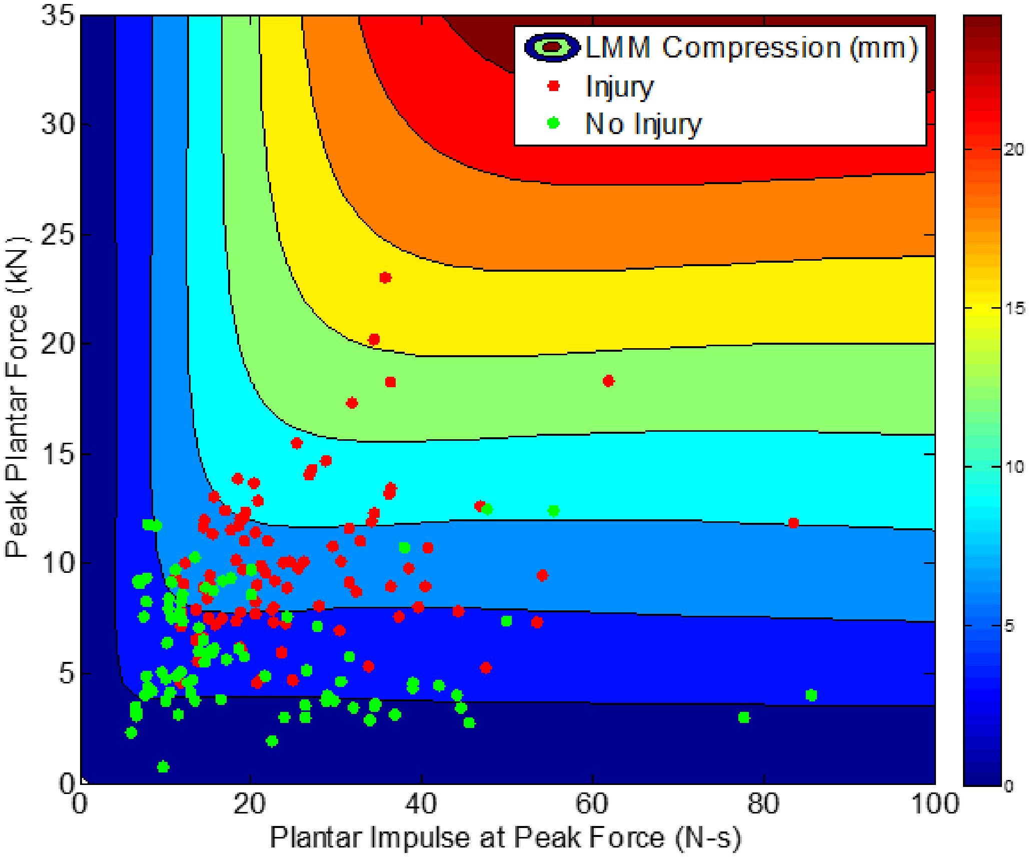

Figure 6.28. Contour plot generated from the 3DOF LMM-based foot compression relationship with peak force and impulse with PMHS injury and no-injury data points overlaid.

A survival analysis using the value of the predictor equation (P_{FI}) as the main injury predictor was then performed on the collection of PMHS data to quantitatively assess the fit of Eqn. 6.21 as an injury predictor. The equation for probability of injury (P_{inj}) using a Weibull survival analysis is provided in Eqn. 6.22 for no covariates, and Eqn. 6.23 with age as a covariate in the accelerated failure formulation. The parameters for the fit of the surface and survival analysis (with and without age as a covariate) are provided in Table 6.14.

$$\mathrm{P_{inj}} = 1 - \exp\left(-\mathrm{P_{FI}}^{\gamma} \exp\left[\frac{-\beta_0}{\gamma}\right]\right) \qquad \text{Eqn. 6.22}$$

$$\mathrm{P_{inj}} = 1 - \exp\left(-\mathrm{P_{FI}}^{\gamma} \exp\left[\frac{-(\beta_0 + \beta_{age}Age)}{\gamma}\right]\right) \qquad \text{Eqn. 6.23}$$

Table 6.14. Fit parameters for Eqn. 6.21 where P_{FI} is the compression of the foot (Δz) predicted by the lumped-mass model pictured in Figure 6.28. Weibull survival model parameters are also provided with and without age included as a covariate.

Predictor Variable Fit			
Parameter	**Fit**	**95% Confidence Interval**	
		Lower	**Upper**
A	0.8183	0.8160	0.8205
B	1.1890	1.1800	1.199
Weibull Survival Model Fit (no Covariates)			
Parameter	γ	**Intercept**	**Age (years)**
β_i	2.372	2.160	n/a
SE	n/a	5.670e-2	n/a
P-value	n/a	0.000	n/a
Log-likelihood: -64.3; AUC: 0.8667			
Weibull Survival Model Fit (Age as a Covariate)			
Parameter	γ	**Intercept**	**Age (years)**
β_i	3.248	2.833	-1.180e-2
SE	n/a	1.767e-1	2.86e-3
P-value	n/a	0.000	3.77e-5
Log-likelihood: -58; χ^2:12.69 ; AUC: 0.8904			

Graphs of the injury risk functions based on LMM estimate of foot compression are provided in Figure 6.29 for the no covariate survival model and for the accelerated failure survival model including age as a covariate. Log-likelihood and AUC suggest that the covariate model better represents the injury data. This model shows that as age increases, the (estimated) foot compression necessary to cause fracture decreases. Foot compression associated with 50% probability of injury was estimated to be 11.3±2.5 mm, 8.9±1.1 mm, and 7.1±0.7 mm for 25-, 45- and 65-year olds, respectively. These values are reasonable considering the foot compressions associated with fracture in the impactor PMHS study.

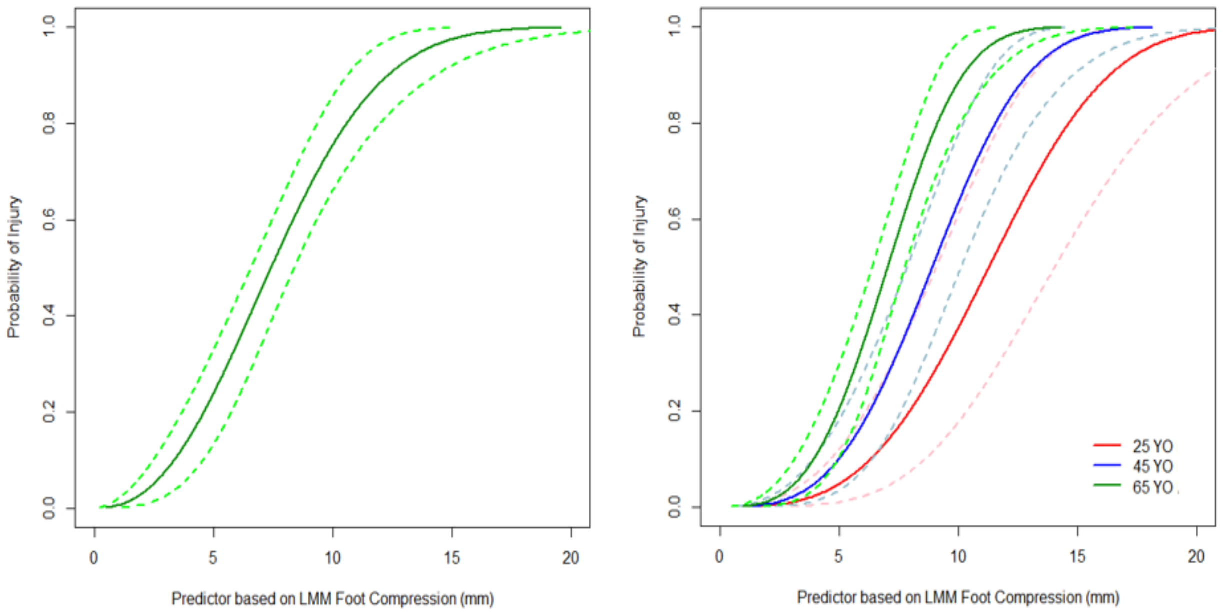

Figure 6.29. Injury risk functions using the 3DOF LMM-based foot compression with no covariates (left) and with age as a covariate (right). Injury risk lines and 95% confidence intervals are shown for ages 25, 45, and 65 years.

For the purpose of relating injury probability back to measurable quantities in the ATD, contour plots of probability of injury as predicted by the survival models were generated with impulse and force as the x- and y- axes. Plots were generated for the fit including no covariates as well as for the 25-, 45-, and 65-year old age-modified injury risk function (Figure 6.30). The point at which the impulse and force converge for a 45-year old for 50% probability of injury is around 16.2 N-s and 8.6 kN. These values are similar to the values of impulse (20.1) and force (8.3) associated with 50% probability of injury estimated by the piecewise injury criterion for a 45-year old. This suggests that while the piecewise approach makes assumptions about the resonance frequency of the leg, the force estimate for 50% probability of injury is not significantly affected, though impulse associated with 50%

probability of injury was overestimated by the piecewise approach compared to the continuous approach.

A

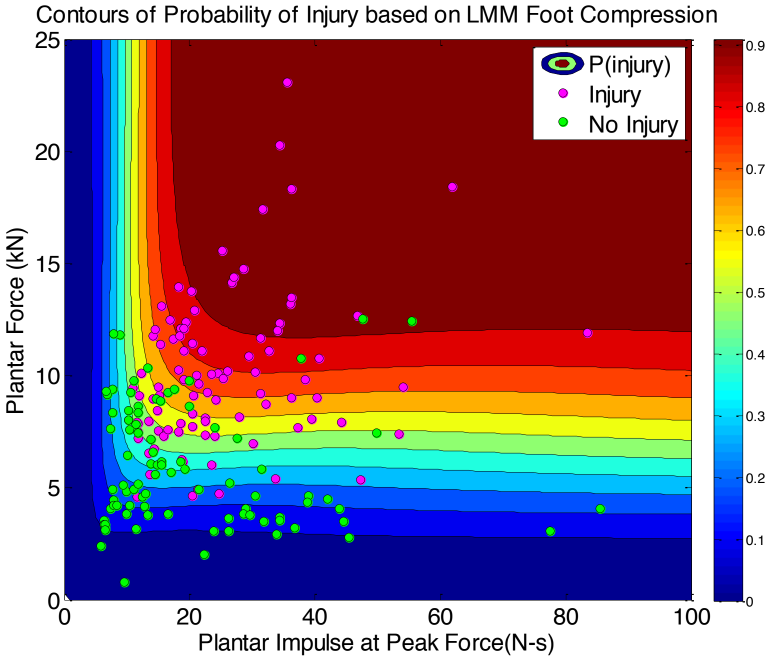

B

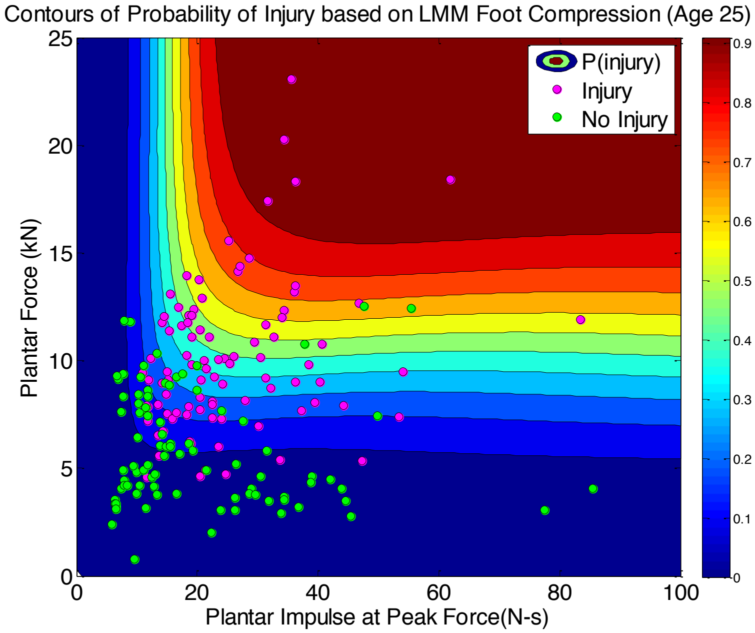

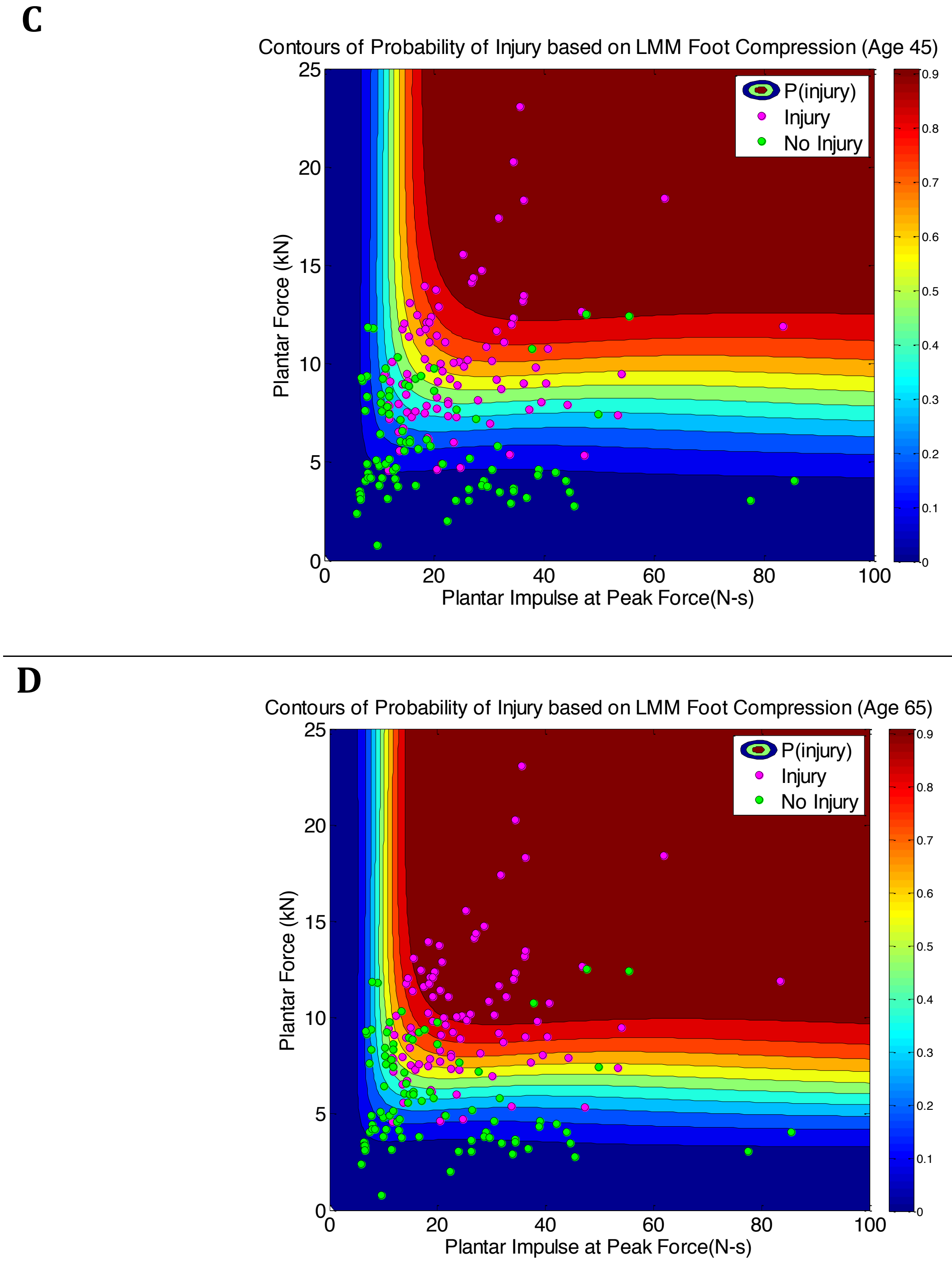

Figure 6.30. Contours of injury probability based on the estimate of LMM foot compression using force and impulse. Contour plots A, B, C, and D were developed based on the no covariate model, and variations of the age-covariate model for 25-, 45-. And 65-year old males, respectively.

6.4.2 Predictor based on Finite Element Model Foot Compression

Foot compression as predicted by the finite element model of the leg was used in the same capacity as LMM-estimated foot compression. Difference in displacement between the distal tibia and footplate was calculated for the SAE-z direction based on the FE simulations from the parametric study. A response surface using FE foot compression, peak force, and impulse at peak force was developed and the parameters A and B were estimated for Eqn. 6.21 using the curve fitting tool in MATLAB. Again, Eqn. 6.21 was found to fit the response surface reasonably well, with RMSE calculated to be 1.6 mm. The fact that RMSE is greater than that of the LMM foot compression fit is due to the fact that the LMM is not a perfect model of the leg (and FE leg).

Additional high frequency FE simulations were run to expand the range of data to be used for the equation fit. The additional simulations used peak accelerations of 1000-9000g and frequencies ranging from 166-1100 Hz to populate high force-low impulse region where little data was present from the previous parametric study (Table 6.15). It is important to note that these loading frequencies were outside the range for which the model was validated, which is a point that will be discussed later in the section.

Table 6.15. Velocity (m-s^{-1}) associated with high frequency input sinusoidal acceleration pulses for finite element parametric study.

	f=166 Hz	f=330 Hz	f= 498Hz	f=664 Hz	f=830 Hz	f=995 Hz	f=1100 Hz
A=1000 g	19.5*	-	-	-	-	-	-
A=2000 g	39.1*	19.5*	13.0*	9.8	7.8	-	-
A=3000 g	-	29.3*	19.5*	14.6	11.7	9.8	8.5
A=4000 g	-	39.1*	26.0*	19.5	15.6	13.0	11.3
A=5000 g	-	-	32.5*	24.4*	19.5	16.3	14.2
A=6000 g	-	-	39.3*	29.3*	23.4	19.5	17.0
A=7000 g	-	-	45.8*	34.3*	27.5*	22.9	-
A=8000 g	-	-	-	39.2*	31.9*	26.7	-
A=9000 g	-	-	-	44.1*	35.3*	30.0	-

*Indicates conditions that exceeded fracture strains in the model.
-Condition was not simulated.

As expected, as the input frequency was increased, duration of the forces decreased. Increasing the magnitude of the acceleration input produced higher forces, with small impulses due to the high frequency of the input acceleration. Figure 6.31 shows the force response from a 9000 g and 995 Hz input acceleration. Duration of the footplate force was approximately 1 ms, and the phase lag between the peak footplate force and peak tibia forces was approximately 0.6 ms with peak tibia forces occurring around the same time that footplate force returned to zero. Despite the high peak footplate force (43.5 kN), the failure strain for the calcaneus was not exceeded in the model. These high frequency FE data points were combined with those from the initial parametric study to ensure that the response surface fit was not skewed toward the lower frequency data.

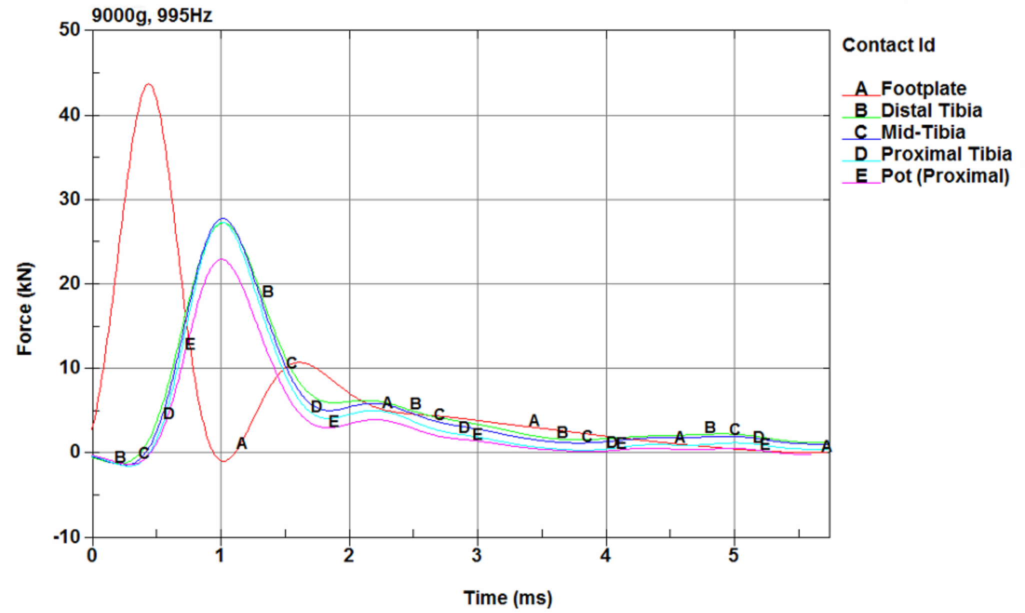

Figure 6.31. Forces from the human leg FE model exposed to a sinusoidal input acceleration with a magnitude of 9000 g and a frequency of 995 Hz.

Parameters based on the fit of the response surface for peak plantar force, impulse at peak force, and FE-based foot compression are provided in Table 6.16 along with the Weibull survival model parameters estimated based on using the force-impulse predictor variable as the main predictor. Parameters and model fit statistics are provided for the survival model with and without age as a covariate. Higher log-likelihood and a higher AUC were calculated for the survival model using age, and age was found to be a significant covariate ($p<<0.05$).

Table 6.16. . Fit parameters for Eqn. 6.21 where P_{FI} is the compression of the foot (Δz) predicted by the finite element model of the leg measured from distal tibia to plantar surface of the foot. Weibull survival model parameters are also provided with and without age included as a covariate.

<table>
<tr><th colspan="5">Predictor Variable Fit</th></tr>
<tr><th colspan="2" rowspan="2">Parameter</th><th rowspan="2">Fit</th><th colspan="2">95% Confidence Interval</th></tr>
<tr><th>Lower</th><th>Upper</th></tr>
<tr><td colspan="2">A</td><td>1.078</td><td>1.022</td><td>1.133</td></tr>
<tr><td colspan="2">B</td><td>1.524</td><td>1.43</td><td>1.618</td></tr>
<tr><th colspan="5">Weibull Survival Model Fit (no Covariates)</th></tr>
<tr><th>Parameter</th><th>γ</th><th>Intercept</th><th colspan="2">Age (years)</th></tr>
<tr><td>β_i</td><td>2.371</td><td>1.891</td><td colspan="2">n/a</td></tr>
<tr><td>SE</td><td>n/a</td><td>5.670e-2</td><td colspan="2">n/a</td></tr>
<tr><td>P-value</td><td>n/a</td><td>0.000</td><td colspan="2">n/a</td></tr>
<tr><td colspan="5">Log-likelihood: -64.4; AUC: 0.8658</td></tr>
<tr><th colspan="5">Weibull Survival Model Fit (Age as a Covariate)</th></tr>
<tr><th>Parameter</th><th>γ</th><th>Intercept</th><th colspan="2">Age (years)</th></tr>
<tr><td>β_i</td><td>3.232</td><td>2.562</td><td colspan="2">-1.180e-2</td></tr>
<tr><td>SE</td><td>n/a</td><td>1.782e-1</td><td colspan="2">2.880e-3</td></tr>
<tr><td>P-value</td><td>n/a</td><td>0.000</td><td colspan="2">4.51e-5</td></tr>
<tr><td colspan="5">Log-likelihood: -58.1; χ^2:12.52 ; AUC: 0.8904</td></tr>
</table>

Again, a contour plot was created to show the behavior of the curve fit compared to the PMHS injury data, and the age-dependent injury risk function was plotted to show the width of the confidence intervals. (Figure 6.32, Figure 6.33). Width of the confidence intervals associated with age 25, 45, and 65 were 3.82, 1.74, and 1.05 mm, respectively for 50% probability of injury.

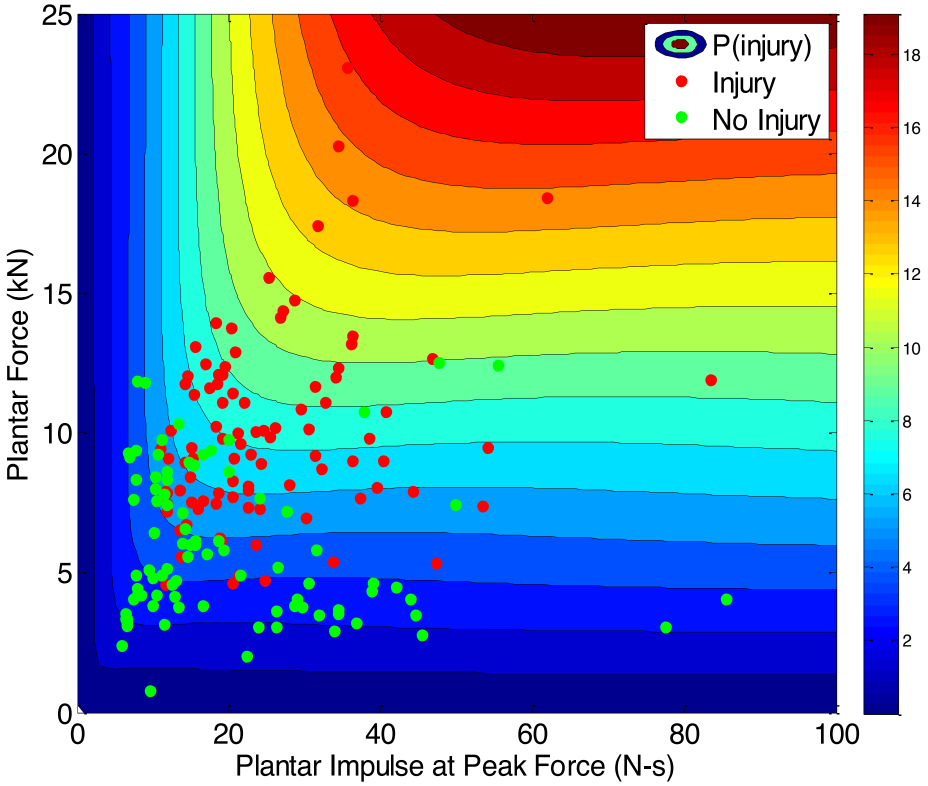

Figure 6.32. Contour plot generated from the FE model foot compression relationship with peak force and impulse with PMHS injury and no-injury data overlaid.

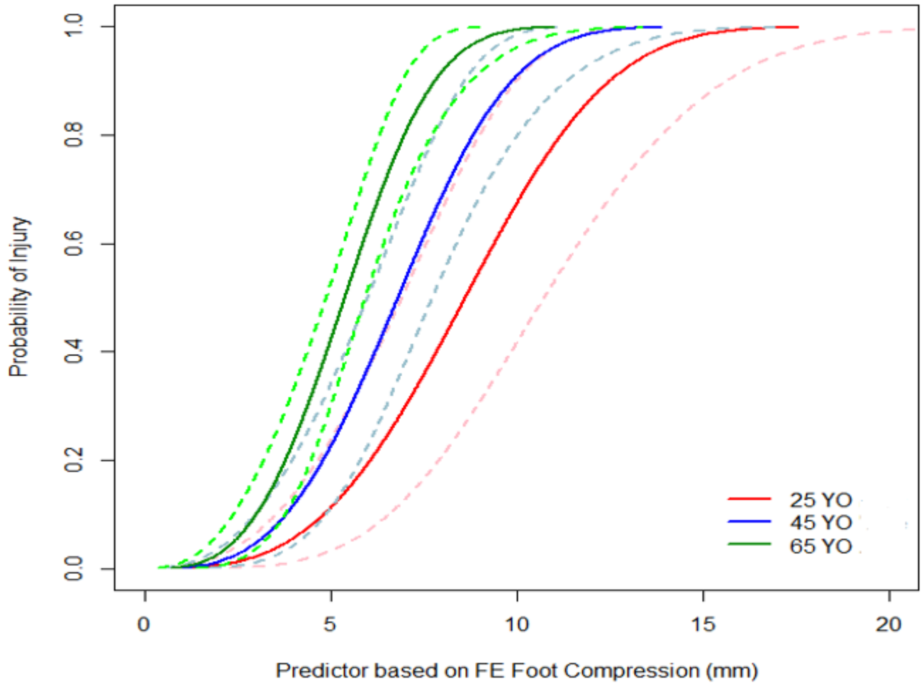

Figure 6.33. Injury risk functions using the FE-based foot compression relationship with peak force and impulse.

Consistent with the previous survival model, this model shows that as age increases, the (estimated) foot compression necessary to cause fracture decreases. Foot compression associated with 50% probability of injury was estimated to be 8.6 mm, 6.8 mm, and 5.4 mm for 25-, 45- and 65-year old males, respectively. These values are slightly lower than those predicted by the LMM-based model, which is likely due to the fact that the FE model accounts for the bottoming-out of heel pad flesh at higher forces and impulses, whereas the behavior of the LMM does not exhibit this non-linear behavior.

A

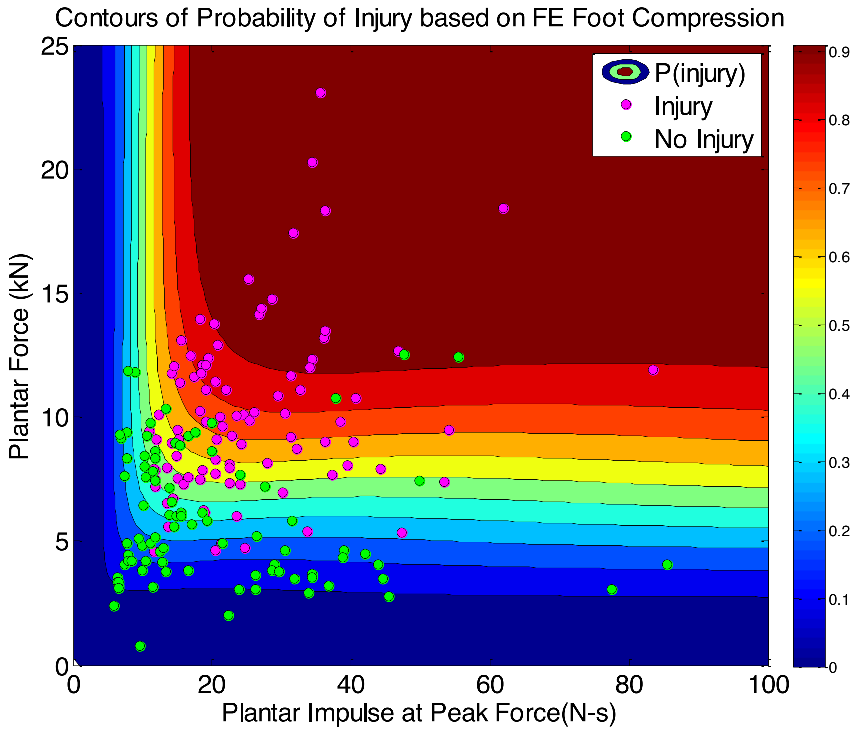
Contours of Probability of Injury based on FE Foot Compression
P(injury)
Injury
No Injury
Plantar Force (kN)
25
20
15
10
5
0
0
20
40
60
80
100
Plantar Impulse at Peak Force(N-s)
0.9
0.8
0.7
0.6
0.5
0.4
0.3
0.2
0.1
0

B

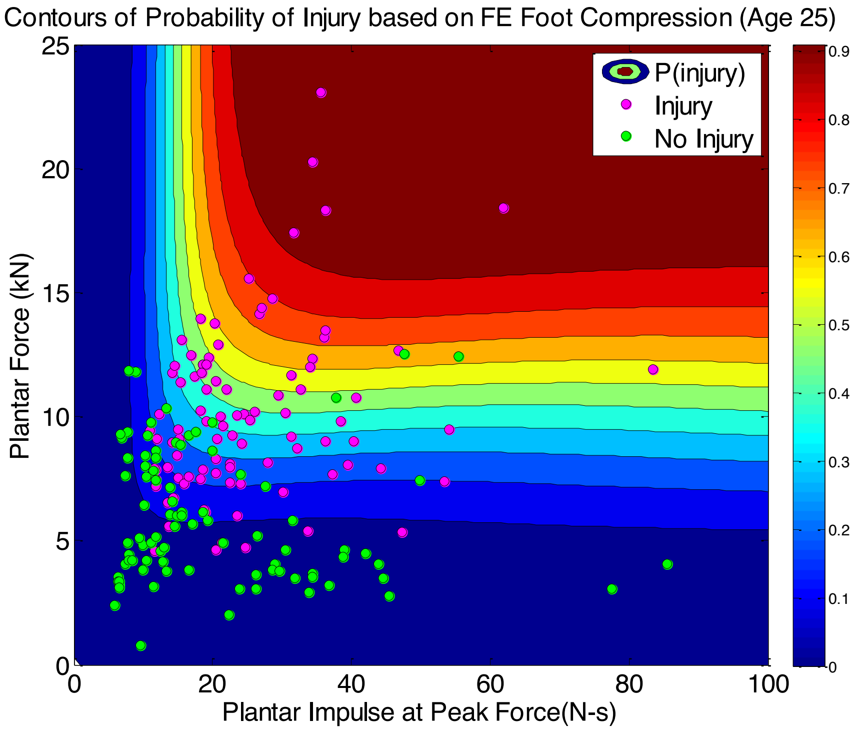
Contours of Probability of Injury based on FE Foot Compression (Age 25)
P(injury)
Injury
No Injury
Plantar Force (kN)
25
20
15
10
5
0
0
20
40
60
80
100
Plantar Impulse at Peak Force(N-s)
0.9
0.8
0.7
0.6
0.5
0.4
0.3
0.2
0.1
0

C

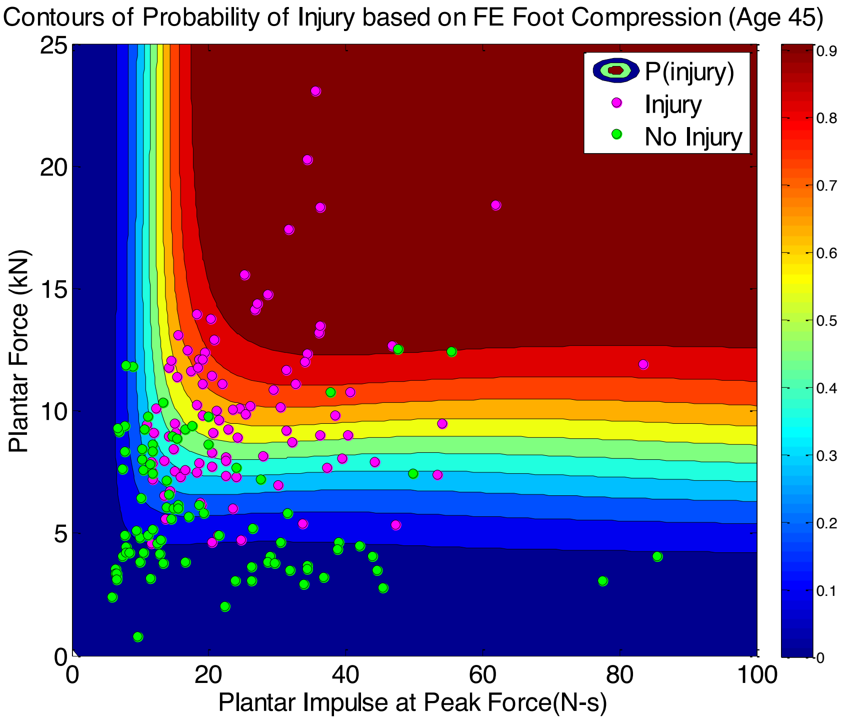

D

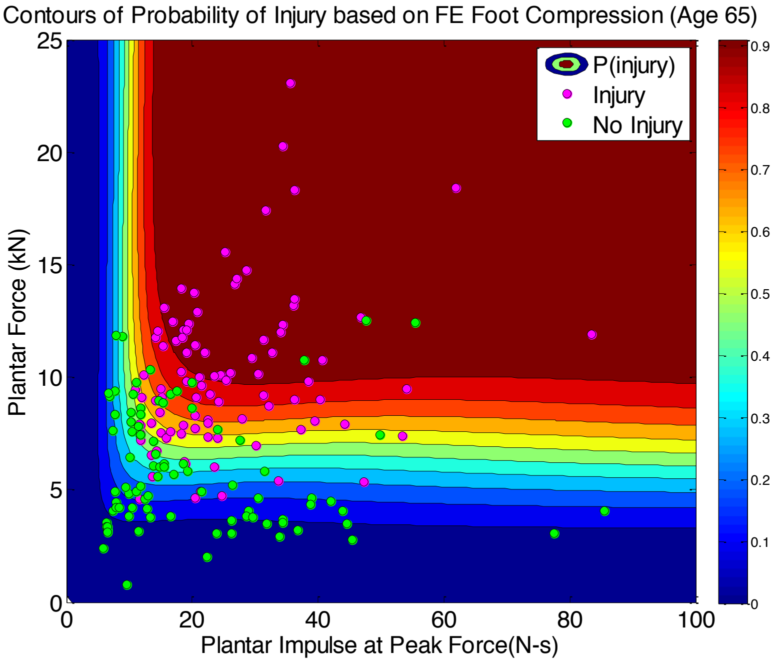

Figure 6.34. Contours of injury probability for the force-impulse predictor variable based on FE model foot compression. Plot A shows the results from fit 3, and plots B-D show the results of fit 4 for age 25, 45, and 65.

6.4.3 Predictor based on Finite Element Model Strain

In addition to basing the injury predictor on foot compression, finite element model strain results were used to fit Eqn. 6.21. Peak maximum principal strains from each element of the cortical bone of the calcaneus were recorded, and the 95th percentile strain was used to develop a response surface with peak force and impulse at peak force using results from the parametric study. Parameters A and B were estimated for Eqn. 6.21 using the curve fitting tool in MATLAB to characterize the response surface. Eqn. 6.21 was found to fit the calcaneus strain response surface reasonably well, with RMSE of 355.3 μS.

Table 6.17. Fit parameters for Eqn. 6.21 where P_{FI} is the 95th percentile peak strain (μS) in the cortical bone of the calcaneus predicted by the finite element model of the leg. Weibull survival model parameters are also provided with and without age included as a covariate.

Predictor Variable Fit			
Parameter	**Fit**	**95% Confidence Interval**	
		Lower	**Upper**
A	7.923e-3	7.317e-3	8.528e-3
B	1.439e-2	1.388e-2	1.490e-2
SSE=7.576; Adjusted R^2=0.9757; RMSE=0.3553			
Weibull Survival Model Fit (no Covariates)			
Parameter	**γ**	**Intercept**	**Age (years)**
β_i	2.323	6.735	n/a
SE	n/a	5.730e-2	n/a
P-value	n/a	0.000	n/a
Log-likelihood: -65; AUC: 0.8712			
Weibull Survival Model Fit (Age as a Covariate)			
Parameter	**γ**	**Intercept**	**Age (years)**
β_i	3.326	7.424	-1.210e-2
SE	n/a	1.674e-1	2.710e-3
P-value	n/a	0.000	8.21e-6
Log-likelihood: -58; χ^2:13.89 ; AUC: 0.8872			

The contour plot and injury risk function based on the FE calcaneus strain-based injury predictor resemble those created for the foot compression-based injury predictors. Again, age had a negative relationship with the predictor variable, and the relationship between A and B produced corridors which were able to distinguish between the low impulse, high force injury and no-injury data points from the PMHS data set.

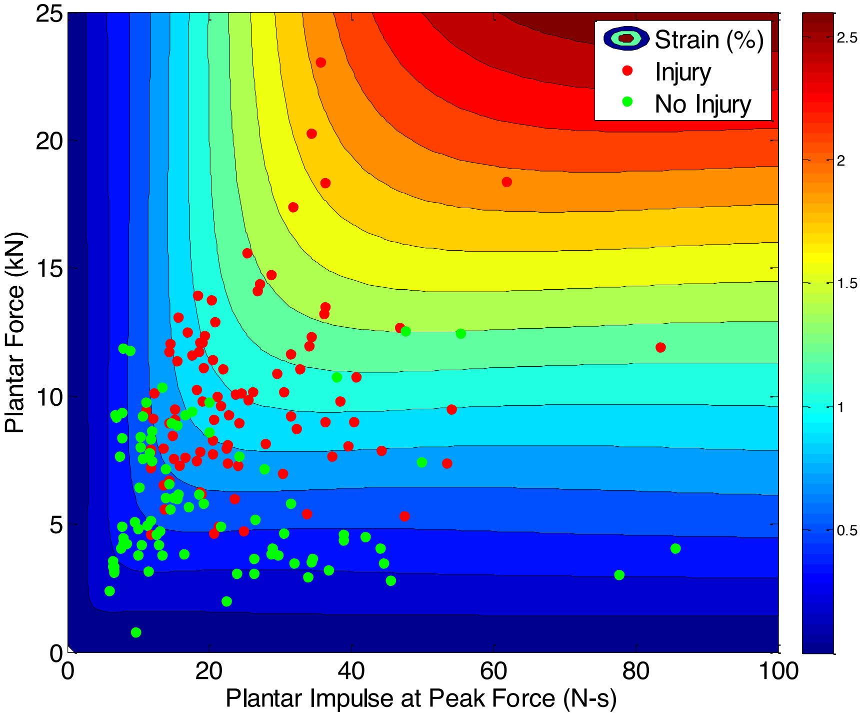

Figure 6.35. Contour plot generated from the FE-based strain relationship with peak force and impulse with PMHS injury and no-injury data overlaid.

According to the injury risk function developed based on calcaneus strain estimated by force and impulse, 50% probability of injury occurs at 1.05±0.59, 0.84±0.23, and 0.67±0.11 percent strain for 25-, 45-, and 65-year olds, respectively. It is important to note that the finite element model strains used for development of the response surface were from simulations for which failure (element elimination) was turned off. Thus, strains could exceed the theoretical failure strains without disrupting the response of the leg. The strain values predicted by the FE model, may not coincide with the strains measured in the PMHS specimens since strain distributions are highly dependent upon bone geometry. Regardless, the strain timing and general shape of the maximum principal strain curves measured in the impactor PMHS tests were similar to those estimated by the finite element model for the same approximate location, and trends in peak strain were consistent between the PMHS and FE model for each of the three loading conditions. Though the absolute magnitude of the strain associated with the force-impulse predictor may not be directly used to estimate risk of fracture, the relationship it estimates for force, impulse, and probability of injury provides valuable insight on the collection of PMHS injury data. Nonetheless, the strain associated with 95% probability of injury was around 2.3 percent strain, which falls within the range of strains associated with cortical bone failure (0.4-4 percent strain) and is reasonably close to the strain used by the Gabler et al. FE model to indicate failure (2.2 percent strain).[76,167]

6.4.4 Optimization of Predictor using PMHS Data

After investigating the effectiveness of Eqn. 6.21 for characterizing the behavior of physical aspects of leg response (compression and strain), the same form of the equation was used as a more direct estimate of probability of fracture by using the injury and no-injury data from the PMHS combined data set. Two methods were used to optimize the predictor variable function to the PMHS data using Weibull survival parameters. The form of the injury risk function for a Weibull survival model is given by Eqn. 6.24, where Inj_i is the injury status (1 for fracture or 0 for no fracture), $\mathrm{P}_{\mathrm{FI}_i}$ is the predictor value calculated using Eqn. 6.21, and λ and k are Weibull fit parameters.

$$\mathrm{P}\left[\mathrm{Inj}_i = 1 | \mathrm{P}_{\mathrm{FI}_i}\right] = 1 - \exp\left[-\left({}^{\mathrm{P}_{\mathrm{FI}_i}}\!/_{\lambda}\right)^{k}\right] \qquad \text{Eqn. 6.24}$$

Since the goal was to use a combination of the Weibull survival model and assumed relationship between force, impulse, and injury probability, to fit the PMHS injury data, A, B, λ, and k needed to be estimated. The first approach utilized maximization of AUC as an objective function and discrete variable optimization to choose A and B parameters (Figure 6.36). The objective function is given by Eqn. 6.25, and Eqn. 6.26 provides the formulation for calculating AUC. A matrix of 150,000 combinations of A and B was generated (Table 6.18), and P_{FI} was calculated for each pair of A and B. A survival analysis was run using 100*P_{FI} as the main injury predictor for each combination of A and B, and AUC was calculated based on the λ and k estimated by R. The combination of A, B, λ, and k parameters which produced the largest AUC value was chosen as the optimal solution. The predictor variable was scaled so as to represent a value similar to percent probability of injury. This analysis was repeated using age as a covariate, and peak force and impulse at peak force were used for Eqn. 6.21.

Table 6.18. Discrete variable matrix for choosing A and B parameters for Eqn. 6.21.

	A	B
Minimum	1	1
Maximum	300	500
Grid Spacing	1	1

$$\text{Objective} = \max\{\text{AUC} \mid A, B, \lambda, k\} \qquad \text{Eqn. 6.25}$$

$$\text{AUC} = \frac{1}{mn}\sum_{i=1}^{m}\sum_{j=1}^{n} 1_{pi>pj} \qquad \text{Eqn. 6.26}$$

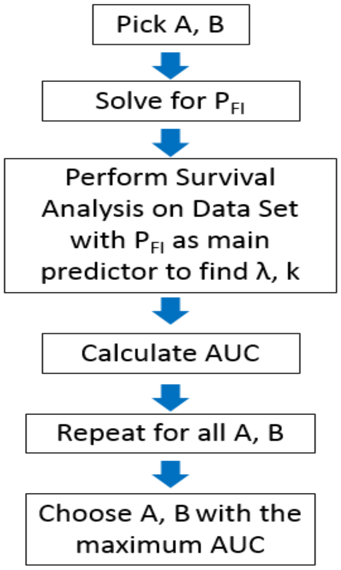
Pick A, B
Solve for P_{FI}
Perform Survival Analysis on Data Set with P_{FI} as main predictor to find λ, k
Calculate AUC
Repeat for all A, B
Choose A, B with the maximum AUC

Figure 6.36. Schematic for discrete variable optimization for fitting PMHS injury data using survival analysis.

The second approach involved fitting all parameters (A, B, λ, and k) at once by maximizing the log-likelihood of the Weibull survival model fit with $100*P_{FI}$ as the injury predictor. This approach allowed λ and k to be independent of the choice of A and B, which permitted convergence to a more optimal solution in terms of model fit as assessed by log-likelihood. The equations used to calculate log-likelihood for are given by Eqn. 6.31 through Eqn. 6.33, where β_0 and γ are the fit parameters for the Weibull survival function, and A and B are included in P_{FI} per Eqn. 6.21. Likelihood associated with injury is calculated using the set of injury tests (I'), and using the set of tests with no injury (N) to calculate the likelihood of no injury. The combination of these likelihoods is used to calculate the likelihood for the survival model. Log of the likelihood function (Eqn. 6.30) was maximized for purposes of the optimization to provide a more stable numerical solution.

$$L_{\text{no-injury}} = \prod_{i \in N}^{n} \left\{1 - \left[1 - \exp\left(-{P_{FI}}_i^{\gamma} e^{-\gamma\beta_0}\right)\right]\right\}$$ Eqn. 6.27

$$L_{\text{injury}} = \prod_{i \in I'}^{n} \left\{1 - \exp\left(-{P_{FI}}_i^{\gamma} e^{-\gamma\beta_0}\right)\right\}$$ Eqn. 6.28

$$L_S = L_{\text{no-injury}} L_{\text{injury}}$$ Eqn. 6.29

$$\ln(L_S) = \sum_{i \in N}^{n} \left\{1 - \left[1 - \exp\left(-{P_{FI}}_i^{\gamma} e^{-\gamma\beta_0}\right)\right]\right\} + \sum_{i \in F}^{n} \left\{1 - \exp\left(-{P_{FI}}_i^{\gamma} e^{-\gamma\beta_0}\right)\right\}$$ Eqn. 6.30

The analysis was also performed using an accelerated failure formulation to adjust for age as a covariate. Likelihood and log of the likelihood functions are provided in Eqn. 6.31 through Eqn. 6.34, where β_0 is the intercept fit parameter, and β_{age} is the coefficient associated with age for the survival model fit. The objective function for the optimization using maximum likelihood is provided in Eqn. 6.35 where x is the injury outcome and n is the number of data points.

$$L_{\text{no-injury}} = \prod_{i\in N}^{n}\Big\{1 - \Big[1 - \exp\Big(-P_{FI_i}^{\gamma}\, e^{-\gamma(\beta_0+\beta_{age}Age)}\Big)\Big]\Big\} \tag*{Eqn. 6.31}$$

$$L_{\text{injury}} = \prod_{i\in F}^{n}\Big\{1 - \exp\Big(-P_{FI_i}^{\gamma} e^{-\gamma(\beta_0+\beta_{age}Age)}\Big)\Big\} \tag*{Eqn. 6.32}$$

$$L_S = L_{\text{no-injury}} L_{\text{injury}} \tag*{Eqn. 6.33}$$

$$\begin{aligned}\ln(L_S) = &\sum_{i\in R}^{n}\Big\{1 - \Big[1 - \exp\Big(-P_{FI_i}^{\gamma} e^{-\gamma(\beta_0+\beta_{age}Age)}\Big)\Big]\Big\}\\ &+ \sum_{i\in L}^{n}\Big\{1 - \exp\Big(-P_{FI_i}^{\gamma} e^{-\gamma(\beta_0+\beta_{age}Age)}\Big)\Big\}\\ &+ \sum_{i\in U}^{n}\Big\{\gamma P_{FI_i}^{\gamma-1}\exp\Big[\Big(-\gamma(\beta_0+\beta_{age}Age\Big) - P_{FI_i}^{\gamma}\, e^{-\gamma(\beta_0+\beta_{age}Age)}\Big]\Big\}\end{aligned} \tag*{Eqn. 6.34}$$

$$\hat{\ell}\big(\beta_0, \beta_{age}, \gamma, A, B \,\big|\, x\big) = \max\left\{\frac{1}{n}\sum_{i=1}^{n} \ln L_S(x_i \mid \beta_0, \beta_{age}, \gamma, A, B)\right\} \tag*{Eqn. 6.35}$$

Solutions obtained from the outlined methods show that higher AUC values were obtained using the maximum likelihood optimization (Table 6.19). The largest AUC (0.9079) was associated with the maximum likelihood method using impulse at peak force with age as a covariate. All AUCs obtained from the optimized approach were greater than those obtained from the piecewise solution and the Yoganandan and Funk injury criteria discussed in Section 6.3.3.

Table 6.19. Model fit parameters and model fit statistics based on the PMHS injury data are provided for both optimization approaches for with and without the use of age as a covariate. Comparison is also provided for the use of impulse at peak force versus maximum impulse.

Ref #	**Model Description**	**Parameter**	**Estimates**		**Model Statistics**		
			Value	**S.E.**	**log(L)**	**AUC**	**ACC**
1	Discrete optimization using impulse at peak force and peak force with no covariates	A	2.10		-64.7	0.8699	0.7810
		B	3.60				
		β_0	1.173	5.69e-2			
		γ	2.344				
2	Discrete optimization using impulse at peak force and peak force with age as a covariate	A	7.06		-58.1	0.8906	0.8175
		B	10.00				
		β_0	0.683	0.178			
		β_{age}	-0.0118	2.88e-3			
		γ	3.234				
3	Maximum likelihood optimization using impulse at peak force and peak force with no covariates	A	5.74		-64.7	0.8714	0.7737
		B	10.00				
		β_0	0.163	5.70e-2			
		γ	2.339				
4	Maximum likelihood optimization using impulse at peak force and peak force with age as a covariate	A	6.723		-57.8	0.8897	0.8175
		B	10.917				
		β_0	0.704	0.171			
		β_{age}	-0.0119	2.78e-2			
		γ	3.300				
1	Discrete optimization using peak impulse and peak force with no covariates	A	2.1		-67.4	0.8630	0.7737
		B	15.1				
		β_0	1.077	5.27e-2			
		γ	2.504				
2	Discrete optimization using peak impulse and peak force with age as a covariate	A	2.1		-61	0.8791	0.8100
		B	13.8				
		β_0	1.681	5.27e-2			
		β_{age}	-9.88e-3	2.52e-3			
		γ	3.513				
3	Maximum likelihood optimization using peak impulse and peak force with no covariates	A	1.57		-66.47	0.8543	0.7810
		B	8.752				
		β_0	1.474	5.27e-2			
		γ	2.556				
4	Maximum likelihood optimization using peak impulse and peak force with age as a covariate	A	1.52		-61	0.8788	0.8110
		B	10.00				
		β_0	2.003	1.57e-1			
		β_{age}	-9.88e-3	2.52e-3			
		γ	3.576				

Injury risk function plots based on P_{FI} were generated for purposes of visually representing the confidence intervals associated with the survival models developed using PMHS data (Figure 6.37, Figure 6.38). Additionally, these plots show the trend in increasing probability of injury with an increase in age for a given value of the predictor variable. At 50% probability of injury, the predictor value increase from 11.5±2.80 to 8.9±1.31, and 6.9±0.79 for age 25, 45, and 65, respectively for the discrete optimization fit. For the survival model based on the maximum likelihood fit, the injury predictor value associated with 50% probability of injury was 11.6±2.78, 8.9±1.29, and 6.9±0.79 for ages 25, 45, and 65, respectively.

Width of the 95% confidence intervals at 50% probability of injury were 5.6, 2.62, and 1.58 for the discrete approach and 5.56, 2.58, and 1.58 for the maximum likelihood approach for ages 25, 45, and 65. The results from the discrete optimization and maximum likelihood survival models suggest that the approaches reached approximately the same solution. The slightly better fit of the maximum likelihood approach was expected because of the additional flexibility allowed for the variables.

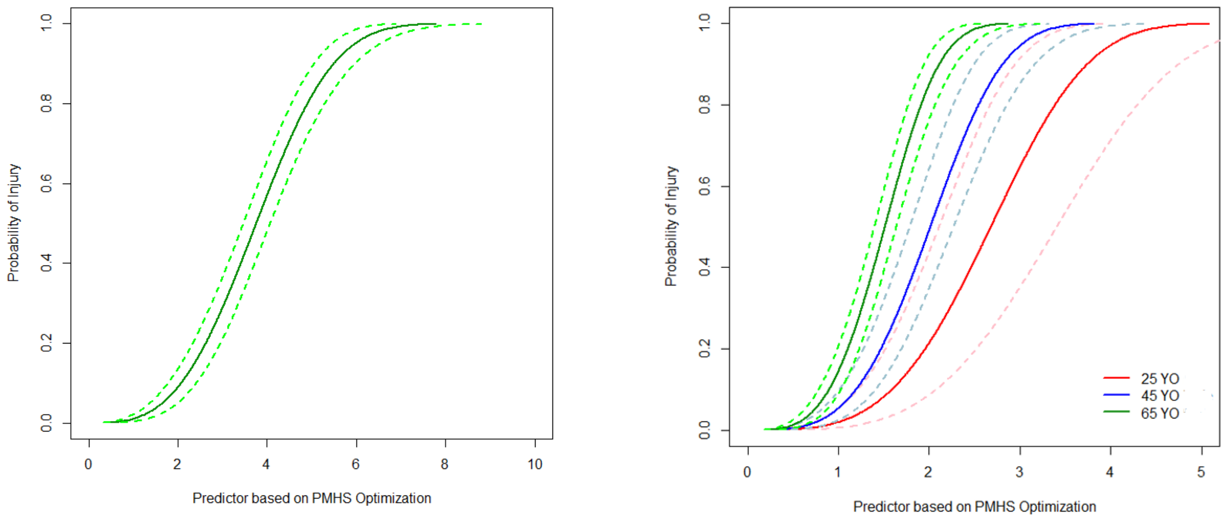

Figure 6.37. Injury risk functions based on the force-impulse predictor variable with 95% confidence intervals for the parameters estimated using the discrete variable optimization approach to fit PMHS injury data. The figure on the left shows the result of the survival analysis without covariates, and the figure on the right shows the injury risk for ages 25, 45, and 65 years.

It is important to note that the magnitude of the predictor was significantly different for the no-covariate survival fit. This was due to the fact that the predictor variable was not based on a physical measurement, but instead served as a value proportional to probability of injury based on the PMHS data. It should be noted that values are similar between the two no-covariate fits, and the age-covariate fits since the discrete variable parameters were used as the starting point for the maximum likelihood optimization. Although additional seed values were used, the optimization for the alternative starting points converged to solutions with lower AUC and maximum likelihood values.

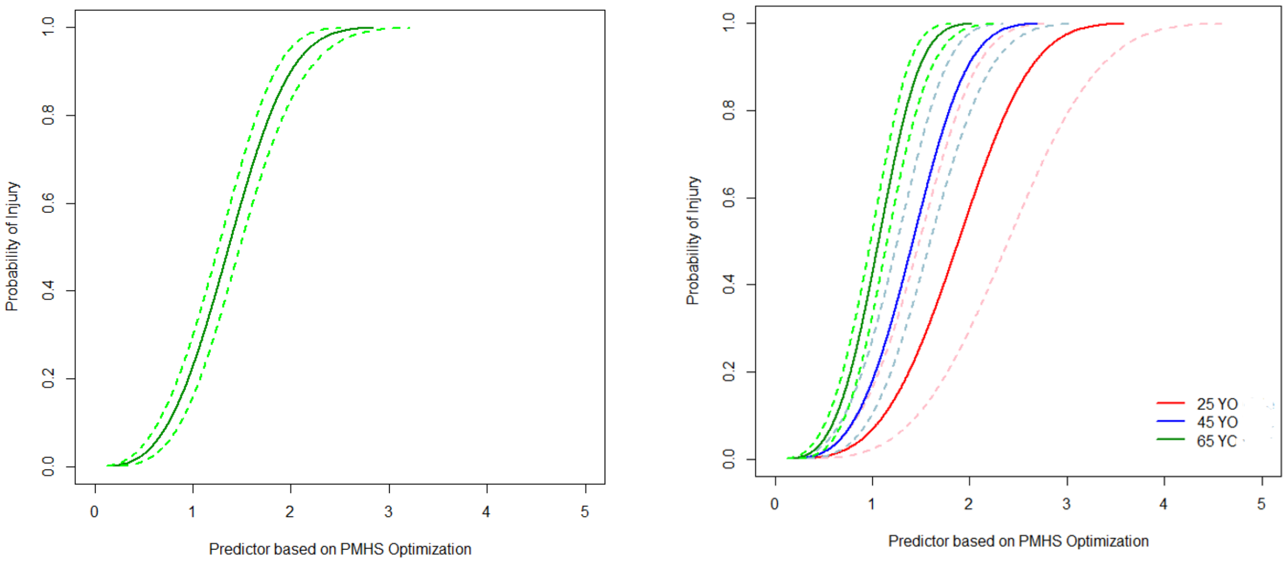

Figure 6.38. Injury risk functions based on the force-impulse predictor variable with 95% confidence intervals for the parameters estimated using the maximum likelihood optimization approach to fit PMHS injury data. . The figure on the left shows the result of the survival analysis without covariates, and the figure on the right shows the injury risk for ages 25, 45, and 65 years.

The reported injury risk function plots do not provide information for estimating the input required to cause injury since the scale of the injury predictor is dependent upon the magnitude of the parameters A and B chosen by the optimization. The utility of these plots lies mainly in the visual representation of the width of the confidence intervals for the risk curves. A more worthwhile display of the information provided by the injury risk function parameters is a contour plot of probability of injury with force and impulse as the x- and y-axes. These plots are provided for each of the fits summarized in Table 6.19 (Figure 6.40, Figure 6.39). For the age-adjusted injury risk functions, the contour plots are presented for age 25, 45, and 65, which show that the contours for probability of injury shift down (lower force) and to the right (lower impulse) as age increases. Contours with smaller widths indicate a more vertical injury risk curve with respect to the injury predictor.

A

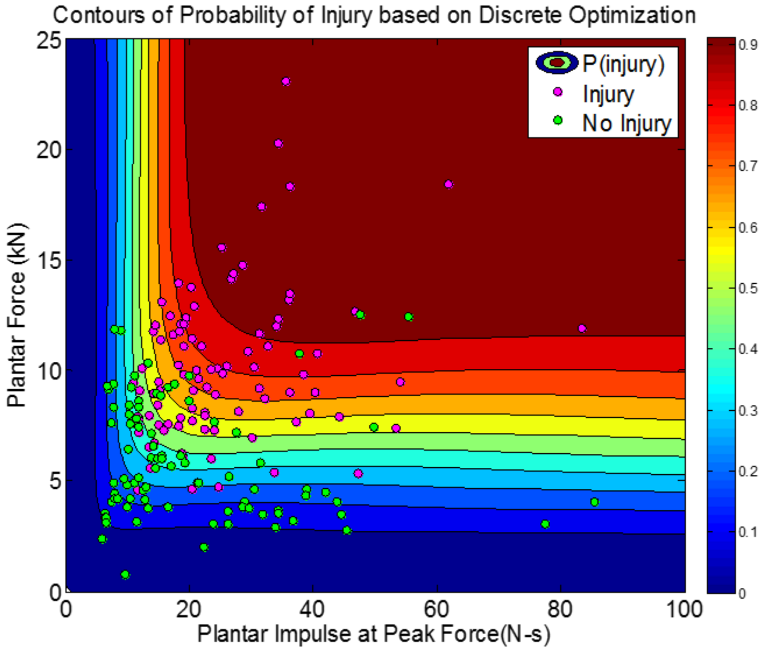
Contours of Probability of Injury based on Discrete Optimization
P(injury)
Injury
No Injury
Plantar Force (kN)
Plantar Impulse at Peak Force(N-s)
0
5
10
15
20
25
0
20
40
60
80
100
0
0.1
0.2
0.3
0.4
0.5
0.6
0.7
0.8
0.9

B

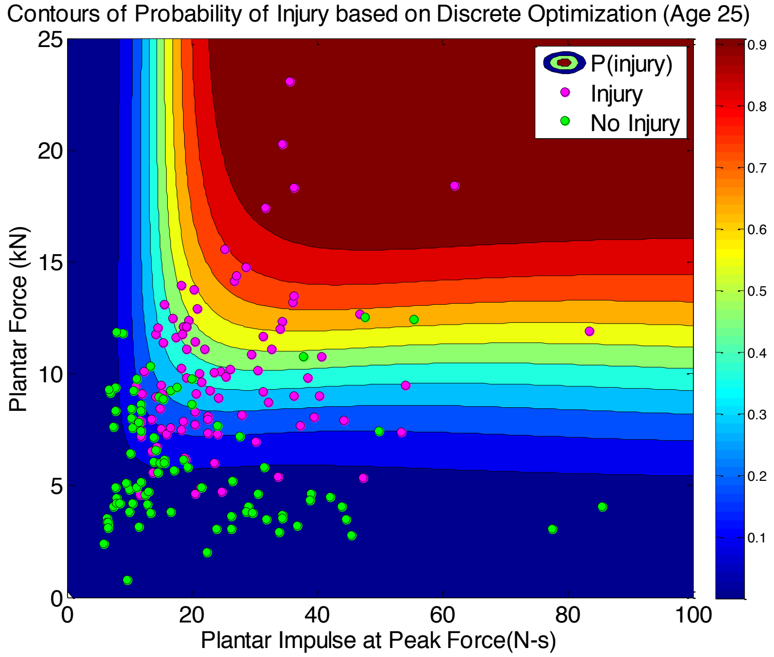
Contours of Probability of Injury based on Discrete Optimization (Age 25)
P(injury)
Injury
No Injury
Plantar Force (kN)
Plantar Impulse at Peak Force(N-s)
0
5
10
15
20
25
0
20
40
60
80
100
0.1
0.2
0.3
0.4
0.5
0.6
0.7
0.8
0.9

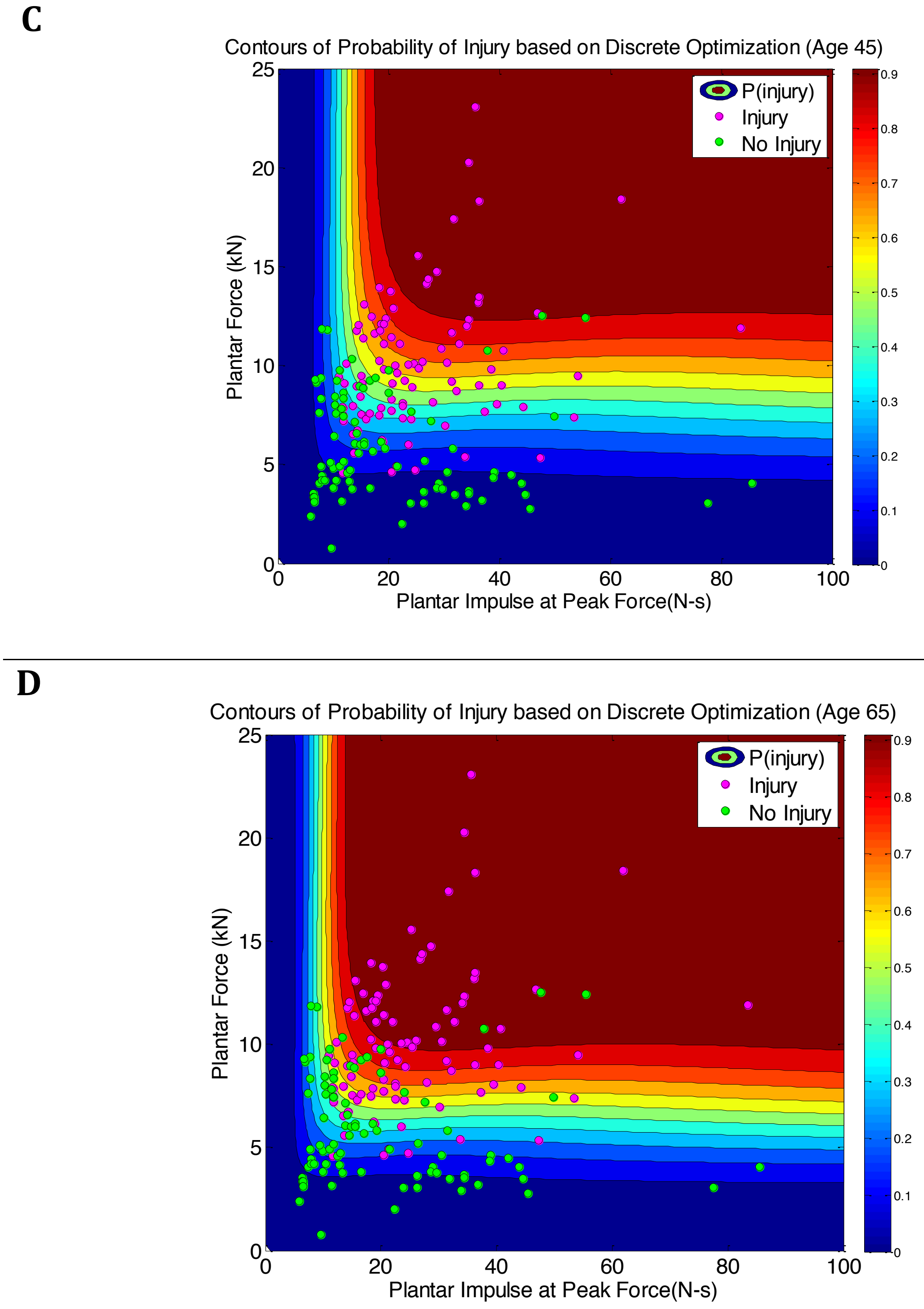

Contours of Probability of Injury based on Discrete Optimization (Age 45)

Contours of Probability of Injury based on Discrete Optimization (Age 65)

Figure 6.39. Contours of injury probability for the force-impulse predictor variable based on Fit 3. Plot A shows the results from fit 3, and plots B-D show the results of fit 4 for age 25, 45, and 65.

A

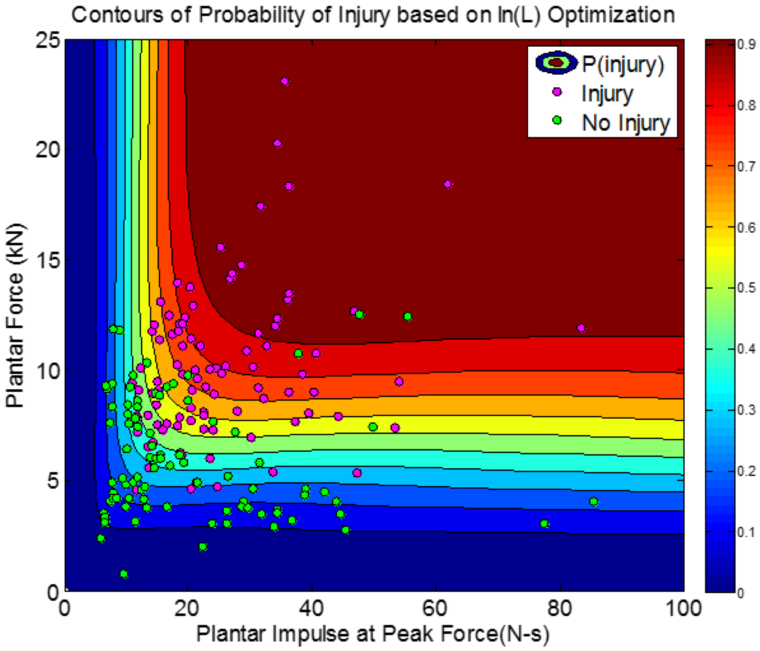
Contours of Probability of Injury based on ln(L) Optimization
Plantar Force (kN)
Plantar Impulse at Peak Force(N-s)
25
20
15
10
5
0
0
20
40
60
80
100
P(injury)
Injury
No Injury
0.9
0.8
0.7
0.6
0.5
0.4
0.3
0.2
0.1
0

B

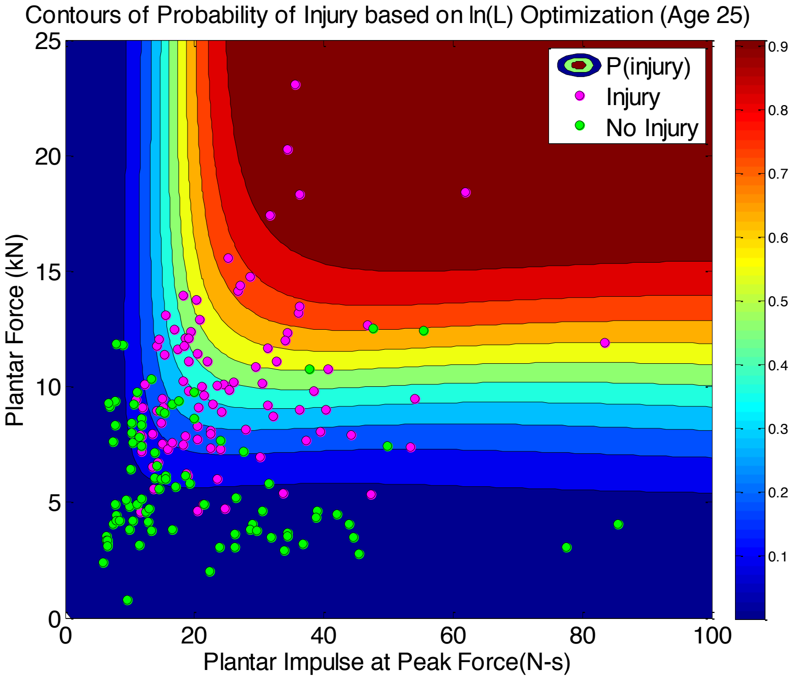
Contours of Probability of Injury based on ln(L) Optimization (Age 25)
Plantar Force (kN)
Plantar Impulse at Peak Force(N-s)
25
20
15
10
5
0
0
20
40
60
80
100
P(injury)
Injury
No Injury
0.9
0.8
0.7
0.6
0.5
0.4
0.3
0.2
0.1

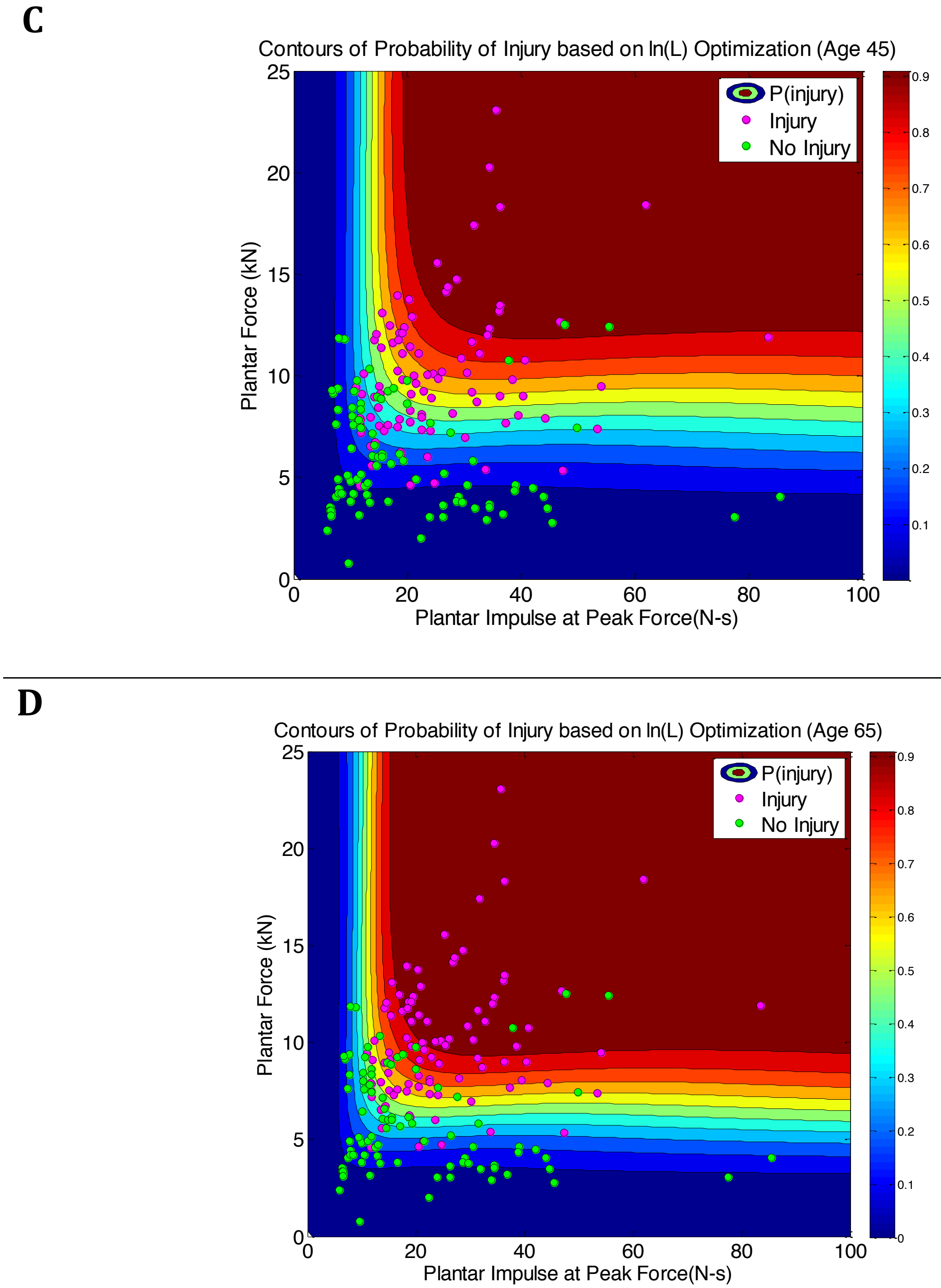

Figure 6.40. Contours of injury probability for the force-impulse predictor variable based on Fit 3. Plot A shows the results from fit 1, and plots B-D show the results of fit 2 for age 25, 45, and 65.

Though slight differences were observed in the magnitude of the force-impulse predictor variable with respect to probability of injury for the two optimization approaches, this difference is merely an artifact of the log-likelihood optimization favoring an overall lower predictor due to the nature of its calculation, while AUC has less dependence on magnitude and more dependence on classification. Nonetheless, both optimization approaches estimated A and B parameters with approximately the same ratio (0.58 for the discrete approach with no covariate, and 0.57 for the log-likelihood approach with no covariate).

6.4.5 Evaluation of Continuous Injury Criterion Approaches

As expected, injury risk functions based on the force-impulse predictor variable produced higher AUC values than previous injury criteria, perhaps because of the increased number of fit parameters. Five parameters were used to fit the models described using a covariate. The use of these additional parameters is justified based the large sample size (n=137) compared to previous injury risk functions. As a rule of thumb, the sample size used to fit a model should be 10-15 times the number of parameters used to fit the model. Further justification is based on the physical relationship of the predictor variable with causation of fracture since the form of the force-impulse predictor variable equation was shown to provide a good fit of both strain and compression data.

The ratio of A:B ranged between 0.55 and 0.71 for the different approaches taken. This ratio controls the rate of decay of the exponentials in the predictor variable function, and therefore controls the relative influence force and impulse have over injury probability. Higher ratios of A:B shift the contours toward lower impulse levels and higher force levels. If the ratio of F/A and I/B is thought of as an effective frequency associated with the damped natural frequency of the leg, a higher ratio of A:B suggests a higher natural frequency of the system. Lower natural frequencies are associated with longer pulse durations, which means that in terms of the piecewise injury criterion, the duration cutoff between impulse and force as an injury predictor would be longer for a higher A:B ratio.

Each of the previously-outlined age-modified injury risk functions using Eqn. 6.21 to relate force and impulse to a quantity associated with injury probability were assessed using AUC, accuracy, and log-likelihood calculated using the combined data set (Table 6.20). The AUC and accuracy of the piecewise model are included in Table 6.20 for reference. Log-likelihood was the same for all models except the one developed based on maximizing the log-likelihood, which was not significantly different from the other results. Accuracy was highest for the models based on foot compression and using the optimization approaches, though the other methods still resulted in higher AUC values than were calculated for any of the previous injury risk functions discussed in the evaluation of the piecewise model. Log-likelihood of the model fit became the distinguishing point for deciding which injury risk function should be recommended for future use. The injury risk function developed using maximization of log-likelihood was chosen as the best performing injury risk function for the combined data set, though AUC for the fit was slightly lower than for the discrete optimization fit.

Table 6.20. Summary of test statistics and fit parameters associated with survival models for each of the previously-outlined approaches to injury criterion development. The best score for each statistic is bolded for easy reference.

Approach	**A**	**B**	**AUC**	**Log Likelihood**	**ACC**
Piecewise model with Age	n/a	n/a	0.8308	n/a	0.7297
LMM foot compression with Age	0.8183	1.1890	0.8904	-58.1	**0.8175**
FE Foot Compression with Age	1.078	1.524	0.8904	-58.1	**0.8175**
FE Calcaneus Strain with Age	7.923e-3	14.390e-3	0.8872	-58.1	0.7883
PMHS Discrete Opt with Age	7.090	10.000	**0.8906**	-58.1	**0.8175**
PMHS ln(L) Optimization with Age	6.723	10.917	0.8897	**-57.8**	**0.8175**

6.5 Discussion

The PMHS optimization using discrete optimization based on AUC to estimate the value of parameters for the predictor variable function and survival analysis was chosen as the approach for development of the injury criterion. Since each of the other approaches outlined in the previous sections were based on model results rather than PMHS injury data, there are limited ways to justify the results compared to the PMHS data. Though each of the models (LMM and FE) were created and validated using PMHS data, the point at which injury occurs based on each of these measures cannot be validated using the data set since most of these tests do not provide information about foot compression or strains. However, the ratio of A:B was similar for each of these approaches, and the ratio of the optimized parameter values suggested that the fit based on foot compression closely matched the chosen model.

Age was chosen as a lone covariate after investigating sex and dorsiflexion angle as covariates in the analysis. Sex and dorsiflexion angle were found to have an insignificant effect on the model ($P>0.05$) in terms of explaining variance. Since the effect of sex on injury generally involves the effect of mass differences between males and females and changes in BMD with age, it was determined that the data set used for the analysis should not be greatly affected by sex differences. Since force and impulse were mass-scaled the correlation between mass and sex is diminished. Further, the specimen selection process for many of the included studies involved a BMD quality assessment in which osteoporotic specimens were not included. This would have the effect of reducing the sex-influenced aspect of the relationship between BMD and age. Though differences exist in the geometry of male and female bones[150] which could cause female legs to fracture at lower forces than male legs, this effect was not significant enough in the data set to justify inclusion as a covariate, perhaps because of the limited number of female specimens in the data set.

The decision was made to incorporate age as a covariate rather than include its effect as part of the predictor variable. Including age as a covariate allows for the compensation of age-related changes by scaling the failure criteria or predictor variable. By using this approach, the assumption was made that the overall failure response of the leg scales with age. Inclusion of the age in the predictor variable accounts for scaling of the structural response. While in reality many factors affect the structural response of the leg, such as bone mineral density, and size of the bone in terms of cortical thickness, length, and cross-sectional area, these affects were not directly included in the predictor variable. This is a limitation of the statistical model chosen to represent the data, though this limitation persists throughout the literature.[70,104,229,231]

The use of Eppinger's mass-normalization approach for scaling the forces from the PMHS data is also a limitation. Scaling the forces improved the fit of the survival model; however greater reduction in the variance associated with the population may have been achieved using alternative scaling techniques. Alternative scaling techniques using cross-sectional area of cortical bone or bone mineral density should be investigated, and future work should account for differences in the body structure and anthropometry of specimens of the same mass in order to investigate the validity of using mass as a way to normalize specimen response.

Although impulse at force duration was investigated as a possible injury predictor, the decision was made to use impulse at peak force because of the effect injury may have on the relaxation of the force pulse. Further, the use of the entire duration to calculate impulse prevents the use of uncensored data, which provides more information to the survival analysis than assuming all data is censored. Statistics for the models which used peak impulse rather than impulse at peak had less desirable AUC and accuracy values, though the models still out-performed previous injury risk functions for the combined data set.

In order to show the advantage of using the force- and impulse-based predictor variable over strictly using peak force, an additional survival analysis was performed using mass-scaled plantar force with an accelerated failure covariate of age. Injury risk functions and the model parameters from these analyses show larger confidence intervals, and lower log-likelihood and AUC values for the combined data set (Figure 6.41, Table 6.21). This suggests that the proposed force-impulse injury criterion provides a better fit of the data than force alone provides, which is consistent with the impactor PMHS test results and the theory based on the transient response of dynamic models. Accuracy for the plantar force based injury risk function was 0.7664, which suggests that even the use of plantar force rather than mid-tibia or proximal tibia force can improve injury prediction for a wider range of loading frequencies. This is consistent with the conclusions of a previous plantar force-based injury risk function published by Bailey et al.[12]

Table 6.21. Estimated parameters for the survival model using mass-scaled plantar force as the main predictor and age as a covariate.

Parameter	**γ**	**Intercept**	**Age (years)**
β_i	2.941	2.818	-1.14e-2
SE		0.191	3.09e-3
P-value		0.000	2.38e-4

Log-likelihood: -84; χ^2: 11.93; AUC:0.8410

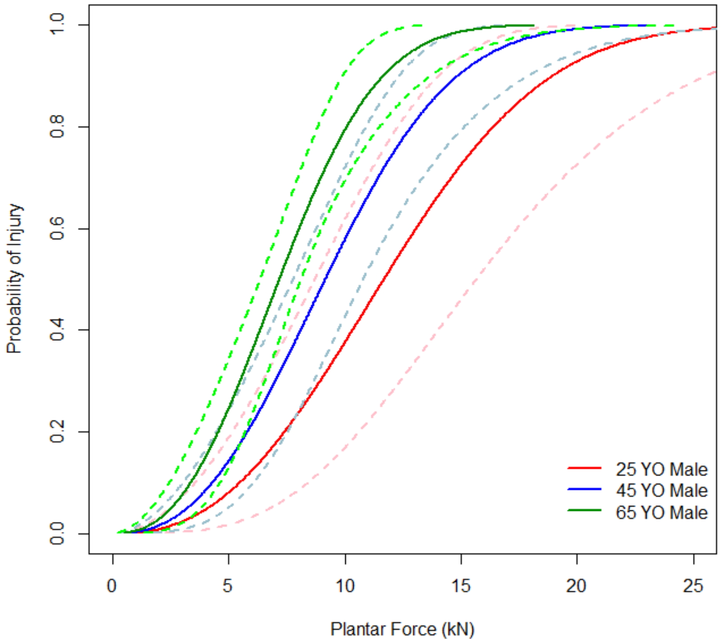

Figure 6.41. Injury risk functions based on mass-scaled plantar force.

An overview of the predictive capabilities of previous injury risk functions which used footplate force as the predictor variable shows that the proposed force-impulse injury criterion performs best in terms of AUC and accuracy for the combined data set (Table 6.22). Accuracy, Kruskal's gamma, Yule's Q and AUC were calculated for each of the three plantar force-based IRFs based on the validation data set (Figure 6.42). For each of the four statistics, the proposed force-impulse based injury criterion performed best. As the accuracy and AUC values were above 0.8, the proposed injury criterion provides a clear advantage over the other two injury risk functions.

Table 6.22. Comparison of the performance of previous injury risk functions to the plantar force-based injury risk function and the proposed force and impulse-based injury criterion.

Injury Risk Function	Parameters Used	AUC	Accuracy
Bailey et al. 2015	force, age, dorsiflexion, sex, mass	0.8470	0.7007
Plantar Force	force, age	0.8410	0.7664
Force-Impulse (Proposed)	force, impulse, age	**0.8906**	**0.8175**

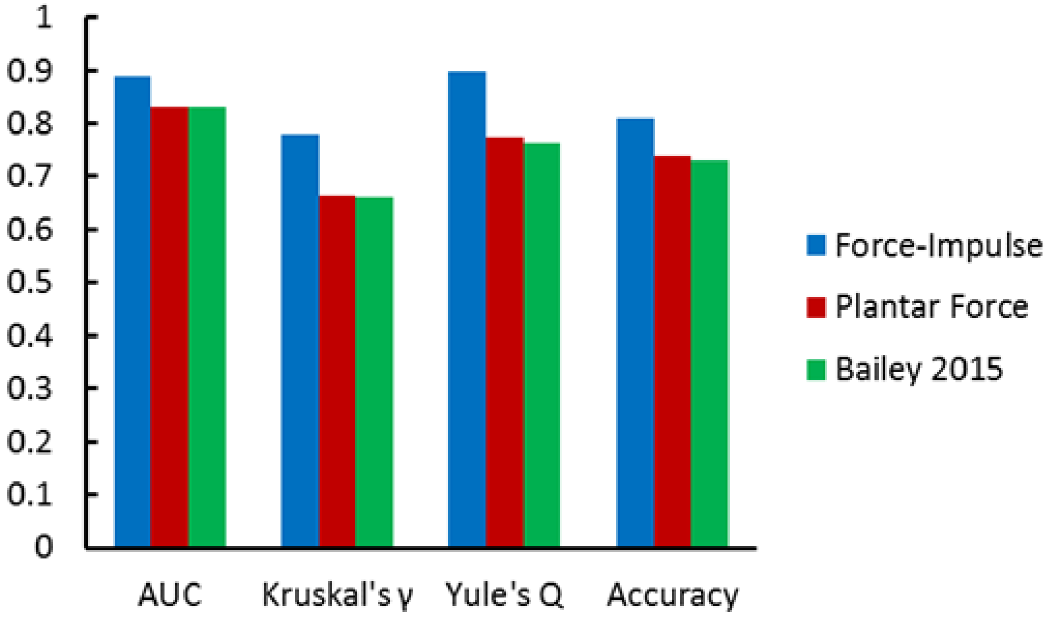

Figure 6.42. Comparison of the performance of plantar force-based injury risk functions using the combined data set. The proposed force-impulse injury risk function was shown to outperform the other models for AUC, accuracy, Kruskal's gamma, and Yule's Q.

The analysis from the piecewise injury risk function which compared the injury risk function to previous IRFs using subsets of the combined data set was revisited for the force-impulse IRF. While the piecewise IRF performed better than the other four IRFs for the Funk 2002 data set, it failed to perform better for the Yoganandan 2015 data set. The statistics provided in Table 6.23 conclude that the proposed force-impulse IRF is better able to predict injury than the other four IRFs for the Funk 2002 data set, improving prediction accuracy by more than 17%. For the analysis using the Yoganandan 2015 data, the Yoganandan 2015 IRF's higher Kruskal's gamma and AUC suggest that while it is better able to rank the data points according to injury and no-injury, the proposed IRF is better able to predict injury or no-injury based on the cutoff of 50% probability of injury (83% compared to 75% accuracy). Nonetheless, both IRFs provide good fits of the data with AUC greater than 0.8.[142]

Table 6.23. Assessment of injury risk functions for 50% risk of injury using the Funk 2002 and Yoganandan 2015 data sets.[70,230,231]

Funk 2002 Data Set					
Injury Assessment	**Yoga. 1996**	**Kuppa 2001**	**Funk 2002**	**Yoga. 2015**	**Bailey Force-Impulse**
Accuracy	0.6286	0.3714	0.5428	0.6000	**0.8000**
Kruskal's Gamma (γ_K)	0.3678	0.1609	0.2759	0.3908	**0.5060**
Yule's Q (Q_Y)	0.7526	0.3115	0.6471	0.2414	**0.8113**
AUC	0.6839	0.5805	0.6379	0.6954	**0.7529**
Yoganandan 2015 Data Set					
Injury Assessment	**Yoga. 1996**	**Kuppa 2001**	**Funk 2002**	**Yoga. 2015**	**Bailey Force-Impulse**
Accuracy	0.6667	-	-	0.7500	**0.8333**
Kruskal's Gamma (γ_K)	0.7203	-	-	**0.8741**	0.8322
Yule's Q (Q_Y)	0.6800	-	-	0.8824	**0.9223**
AUC	0.8601	-	-	**0.9371**	0.9161

6.5.1 Validation of the Injury Criterion

To validate the proposed injury criterion, a cross-validation technique was used. Twenty tests from the combined data set were randomly selected and removed from the data set. A new set of parameters was then estimated by maximizing the log-likelihood of the model fit for this reduced data set. Five different models were generated in this way and are summarized in Table 6.24. The ratio of A:B, which is theoretically related to the natural period of the leg, was similar for each of the five cross-validation models (0.64±0.27), and the ratio of A:B for the proposed model based on the whole combined data set (0.62) fell within one standard deviation of the average for the cross-validation ratios. Additionally, the difference between the AUC for the cross-validation models for the cross-validation data sets compared to the AUC for the proposed injury risk function using the cross-validation data sets was less than 0.005. Accuracy of the proposed injury risk function, when calculated for each of the cross-validation data sets exceeded 0.795, which is less than a two percent reduction in accuracy compared to the performance of the proposed IRF for the combined data set. Accuracy was higher for cross-validation sets CV1 and CV3 than for the combined data set. Thus, it was concluded that the cross-validation models were sufficiently similar to the proposed model.

Table 6.24. Summary of the cross-validation models and statistics comparing the cross-validation and proposed injury risk functions

Parameter	CV1	CV2	CV3	CV4	CV5
A	7.256	6.896	6.867	6.349	6.903
B	11.597	10.626	10.314	10.653	10.744
B_0	0.771	0.704	0.6779	0.664	0.7098
β_{age}	-0.0148	-0.0119	-0.0117	-0.0106	-0.0122
γ	3.626	3.192	3.732	3.072	3.280
AUC for CVDS using Cross-validation IRF	0.895	0.887	0.904	0.889	0.891
AUC for CDS using Cross-validation IRF	0.889	0.892	0.899	0.889	0.891
Accuracy for CVDS using Proposed IRF	0.887	0.803	0.899	0.795	0.812
AUC for CVDS using Proposed IRF	0.894	0.884	0.903	0.882	0.886

CVDS=Cross-validation data set
CDS=Combined Data Set

Each of the models was then used to estimate probability of injury associated with each of the points in the combined data set. The error between the probabilities estimated using each of the five cross-validation models and the proposed model were calculated and are presented in Figure 6.43. Less than a six percent difference was calculated for the probability of injury using the different cross-validation data sets, and the average error associated with each of the cross-validation data sets was not significantly different than for the rest of the cross-validation models. The error estimated for these cross-validation provides an estimate of the prediction error associated with the proposed injury risk function.

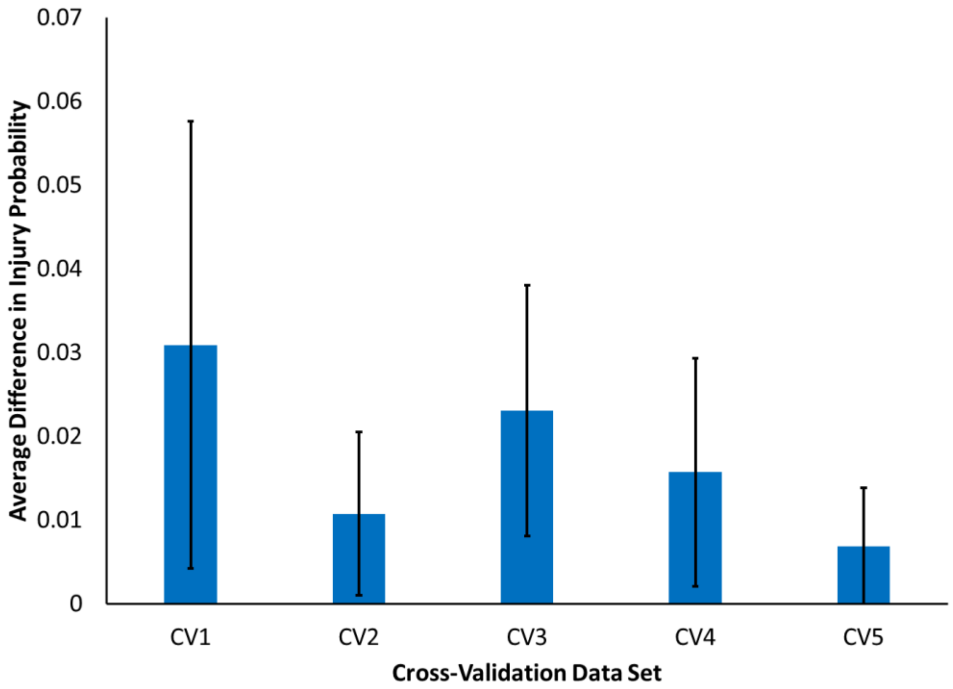

Figure 6.43. Difference in probability of injury as predicted by the proposed injury risk function compared to the cross-validation injury risk functions.

The fact that the injury risk functions developed using the cross-validation data sets did not significantly change the probability of injury associated with individual data sets suggests that the proposed injury risk function is not overly tied to the data set. Rather, the cross-validation analysis infers that the proposed injury risk function is likely to provide accurate predictions for a data set independent of the combined data set which was used to estimate the parameters of the function.

6.5.2 Limitations of the Proposed Injury Criterion

The proposed injury risk function is summarized by Eqn. 6.36 where F represents the peak plantar force, and I represents the impulse at peak force.

$$P_{inj} = 1 - \exp\left(- \exp[-3.30(0.704 - 0.0119 * \mathrm{Age})] \left[\frac{F}{6.72} \exp\left(- \frac{F/_{6.72}}{I/_{10.92}} \right) + \frac{I}{10.92} \exp\left(- \frac{I/_{10.92}}{F/_{6.72}} \right) \right]^{3.30} \right) \qquad \text{Eqn. 6.36}$$

The exponential nature of the injury criterion implies that as impulse approaches zero, the force required to cause injury is infinite. Since no-injury data is available for this high force-no-impulse region, a limitation must be placed on the validity of the injury criterion for that region. As mentioned in the introduction, injury mechanisms analogous to spalling or brisance come into play for the extreme loading frequencies associated with primary blast. Since there is currently no methodology for understanding or predicting when this phenomena will occur in the human body, this loading regime must be excluded from the scope of the proposed injury criterion. According to Ramasamy et al., these injuries occur at times less than 2 ms after detonation.[174] Thus, durations of less than 2 ms must be excluded from the range of applicability of the proposed injury criterion. Further, the PMHS data used to develop the injury risk function spanned durations of 5.1-89.9 ms, so care should be taken to limit the use of the injury risk function outside of this range. The dashed line in Figure 6.44 represents this range of durations in terms of force and impulse for the short durations. The proposed injury criterion is not validated for impulses to the left of this line.

A secondary limitation was placed on the range of validity for the injury criterion by limiting peak force to 23 kN since there were no PMHS data points beyond this force level. In order to predict the injury probability associated with this “un-validated” region, additional studies must be performed to focus on higher frequency input conditions or injury mechanisms such as energy deposition and spalling as they relate to the human leg. As these phenomena are associated with primary blast rather than underbody blast, these injury mechanisms were considered outside the scope of the current study, and were not addressed in the injury analysis.

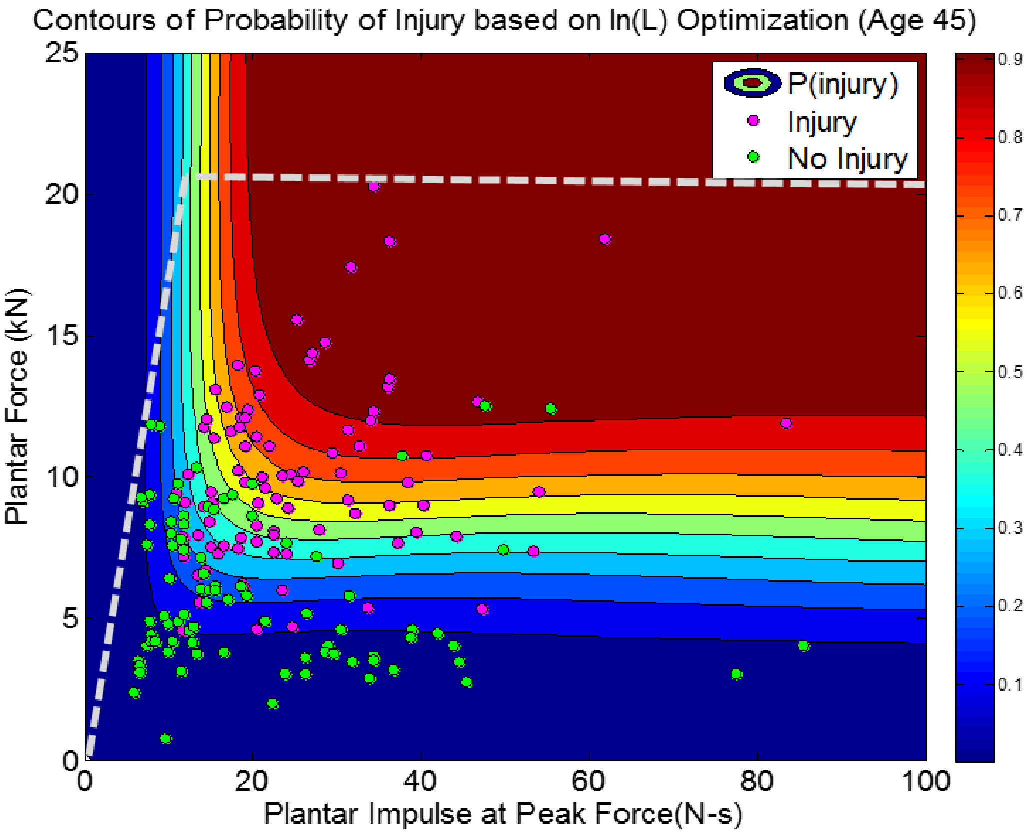

Figure 6.44. Representation of the range of applicability of the proposed leg injury criterion with PMHS data points overlaid. The area to the left of the dashed line represents loading frequencies which may incorporate additional injury mechanisms which were not considered in the current study.

Another consideration for placing bounds on the validity of this injury risk function is that as the duration of the load increases, and the foot/ankle has more time to react to the load, the ankle tends to evert. In the finite element model, noticeable eversion occurs when leg compression exceeds 17 mm. Thus, for longer durations or larger impulses, alternative injury mechanisms related to ankle rotation may be present, which have a tendency to lower the axial force required to cause fracture because of the superposition of shearing loads.[71,75] Force durations of 5-90 ms were included in the data set used to develop the injury criterion; thus, the use of the injury criterion should be limited to these same durations.

Use of the injury criteria should be limited to axial loading events with less than 10-degrees of flexion or xversion, in which the load is applied to the plantar surface of the foot with roughly a +/- 10-degree angle between the loading vector and the z-axis of the tibia as defined by Appendix 10.1.1. As previously discussed, flexion and rotation of the ankle joint alters the contact area within the joint, which can cause different injury patterns and affect the foot/leg's fracture force. Further, alternative loading vectors can affect the shear and bending loads experienced by the foot/leg, which may predispose the foot/leg to ligamentous injuries or a different injury mechanism. For this reason, the proposed injury criterion should be used alongside other injury criteria such as the tibia index.

6.6 Summary

The proposed force- and impulse-based injury criterion provides an accurate prediction of injury risk for forces with durations ranging from 5 to 90ms and assumes a sinusoidal force pulse shape. Accuracy of injury prediction for the proposed IRF was shown to be greater than that of previous injury risk functions in the literature, by 8% for Yoganandan 2015 data set, 18% for the Funk 2002 data set, and by 5% for the combined data set. Statistics also showed that the proposed force-impulse IRF provided better injury prediction accuracy than a strictly plantar force-based IRF developed using the same set of data.

Limitations of the injury criterion include that it assumes a sinusoidal force pulse shape and that an exponential equation form was used as an assumption for fitting the response surface for force, impulse, and peak compression of the foot and ankle. It was also assumed that foot and ankle compression correlates to strains in the foot and can be used as an injury predictor. Only axial loading was considered for development of the injury criterion, thus it should be considered valid only for cases where the loading vector is applied to the plantar surface of the foot within +/- ten degrees of the SAE-z aligned axis of the tibia. Injuries which may occur as a result of the addition of a bending moment in the tibia or off-axis loading from alternative ankle positions cannot be predicted by the proposed injury criterion since the superposition of these loads has been shown to reduce the axial force necessary to cause fracture.[71,109,194] The tibia index and other injury criteria would be required in addition to the proposed axial injury criterion. Thus, it is necessary for the ATD to provide biofidelic measurements for both footplate and tibia forces. The presence of Achilles tension may also lead to error in the estimation of injury risk using the proposed injury criterion. As previously discussed, studies by Funk et al. and Kitagawa et al. demonstrated that the application of force through the Achilles tension causes higher forces in the tibia, which can cause additional compressive loads in the tibia while affecting force on the calcaneus less.[70,108]

The ability to use the proposed injury criterion is highly dependent upon the existence of a biofidelic ATD leg which can replicate both the magnitude and timing of force in the human leg across all relevant loading conditions. The proposed injury criterion also relies upon the ability to measure force at the plantar surface of the foot rather than at a more proximal location as is the case for the Mil-Lx and Thor-Lx ATDs. The following chapter discusses the ability of an existing ATD leg (the Mil-Lx) to provide a biofidelic plantar force estimate for use with the proposed injury criterion.

7 Anthropomorphic Test Device Design

7.1 Introduction

Numerous studies have noted the inadequacies of existing anthropomorphic test device (ATD) legs, particularly under high rate axial loading applications [11,18,27,114,170]. The Hybrid-III leg has been shown to measure more than twice the force measured in the human leg,[136] while the forces in the Mil-LX have been shown to inaccurately represent the response of the human leg in the presence of boots.[160] With respect to dynamic theory, if the dynamic system that represents the ATD is not equivalent to that of the human, the ratio of overshoot for dynamic impacts can lead to differences in force measurement in the ATD compared to the human leg for different impact frequencies. As the fraction of critical damping decreases, the amount of overshoot increases, which lead to a decrease in the accuracy of the ATD measurement. Further, different injury mitigation materials can affect the relative force response of the human and ATD. Rupp et al. developed LMMs of the PMHS and Hybrid-III femurs in order to demonstrate the effect of the stiffness of the ATD when interfaced with knee bolster materials with different force-deflection characteristics. Force-limiting materials yield the same force in the Hybrid-III and cadaver for different deformations. Bolster materials with linear or exponential force-deflection characteristics yield higher forces in the Hybrid-III than in the cadaver.[184,185] Failure to accurately account for these differences can lead to over- or underestimation of injury risk using the ATD, particularly since only peak force is used for current leg injury criteria.

Anthropomorphic test device leg biofidelity is necessary when considering application of an injury criterion to the response of an ATD. For typical leg injury risk functions and associated injury criteria, peak force measured in the ATD leg is used to assess whether injury would occur in the human leg. The Hybrid-III leg, which is typically used in automotive crash testing, produces peak forces of more than double the human force response for higher rate loading events such as underbody blast (UBB);[27,170] thus, use of the Hybrid-III for an unknown loading environment outside of its biofidelity range can lead to inaccurate assessment of injury probability for the human. Kuppa et al. summarized the relationship between the Hybrid-II leg and the human leg using SDOF LMMs. Results from their study revealed that the Hybrid-II over-predicts force for force rise times of less than 55 ms, and under-predicts human leg force for rise times between 55 and 200 ms. These inaccuracies were linked to the difference in compliance of the ATD leg compared to the human leg.[114]

The Mil-Lx, an ATD leg designed for predicting human leg response in UBB scenarios, has similar issues, though instead of over-predicting human leg forces, it under-predicts forces for lower loading rates than for which it was designed.[170] This behavior causes major concern when considering that injury mitigation strategies for UBB tend to lower the loading rates and lengthen the duration of the input acceleration to the leg. An injury mitigation design utilizing force response of the Mil-Lx would yield inaccurate results, and a potentially dangerous situation for warfighters relying on that design for protection.

One potential solution for this problem is a transfer function or response surfaces which could utilize LMMs or FE models of the human and ATD legs to map the ATD force to human force which could then be used for estimating injury risk. This approach, however, falls short when contemplating how the addition of injury mitigation structures would affect the response of the human leg and ATD leg differently, as was the case for femur loads and material property of the knee bolster. Figure 7.1 helps to explain this concept using a simplified, un-damped, single-DOF LMM to represent both the human and ATD legs. The behavior of springs in series makes it necessary to characterize the injury mitigation or boot materials used in order to be able to use the ATD to predict the response of the human. Thus, in order to use the ATD for development of injury mitigation schemes for scenarios such as UBB, it is necessary for the ATD leg to provide a biofidelic response across all applicable rates of loading. The main goals for this chapter are to propose an approach for improving the biofidelity of an existing ATD (the Mil-Lx) and to suggest low-cost design changes for the Mil-Lx leg using finite element model optimization.

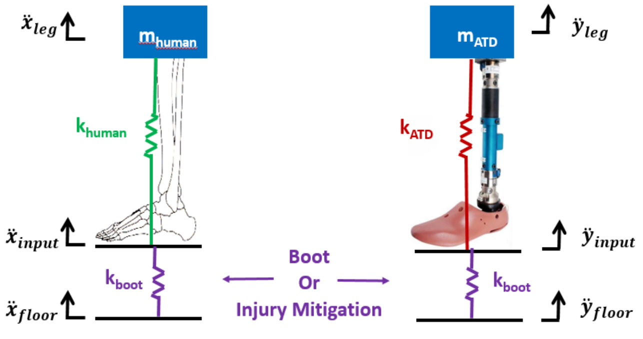

$$k_{eff\,human} = \frac{1}{k_{human}} + \frac{1}{k_{boot}} \qquad k_{eff\,ATD} = \frac{1}{k_{ATD}} + \frac{1}{k_{boot}}$$

$$F_{human} = \frac{k_{human}}{k_{ATD}} F_{ATD}$$

$$TF = \frac{k_{human}}{k_{ATD}}$$

$$TF_{boot} = \frac{k_{eff\,human}}{k_{eff\,ATD}} = \frac{\frac{1}{k_{human}} + \frac{1}{k_{boot}}}{\frac{1}{k_{ATD}} + \frac{1}{k_{boot}}} = \frac{k_{ATD}(k_{human} + k_{boot})}{k_{human}(k_{ATD} + k_{boot})}$$

$$\frac{k_{ATD}(k_{human} + k_{boot})}{k_{human}(k_{ATD} + k_{boot})} \neq \frac{k_{human}}{k_{ATD}}$$

$$\boxed{TF_{boot} \neq TF}$$

Figure 7.1. Simplified human and ATD leg models and theory explaining how injury mitigation materials or a boot placed in series with the leg modifies the transfer function (TF) between human and ATD leg force.

7.2 Evaluation of Mil-LX Biofidelity

To evaluate the biofidelity of the Mil-Lx for the range of load durations applicable to UBB and automotive intrusion, experimental and finite element modeling approaches were taken. First, the ATD's performance was assessed based on previous studies from the literature. Additional experimental tests were then performed under test conditions matching experimental PMHS tests discussed in Chapter 3. Lastly, a finite element model of the Mil-Lx was adapted, benchmarked, and used for further assessment of the Mil-Lx's ability to replicate the response of the human leg to axial loads.

7.2.1 Literature Review

The original design process for the Mil-Lx involved tuning its response by changing the compliant element material in the tibia shaft and the heel pad insert material using a 7.1 m-s^{-1} footplate impact condition.[18] The Mil-Lx response was initially compared to PMHS response at lower impact velocities; however, the Mil-Lx's biofidelity at those rates was never quantified for a matched input condition. McKay compared the Mil-Lx response to previous PMHS impact data from Barbir et al.,[18] but those tests were not necessarily performed under the same input conditions and show a lack of consistency between the timing of the PMHS corridor and the Mil-Lx upper tibia force (Figure 7.2). McKay showed that load rates were similar for PMHS and Mil-Lx forces at impact velocities ranging from 5.4-11.5 m-s^{-1} (see Figure 7.3), but no comparison of peak forces or duration of the forces was made. Moreover, the measurements used to assess Mil-Lx biofidelity were located proximal to the injuries that most commonly occur for these impact conditions (i.e. foot/ankle injuries such as calcaneus, talus, and distal tibia). Thus, further investigation is required to evaluate the biofidelity of the Mil-Lx for loading conditions other than the one used for its initial development.

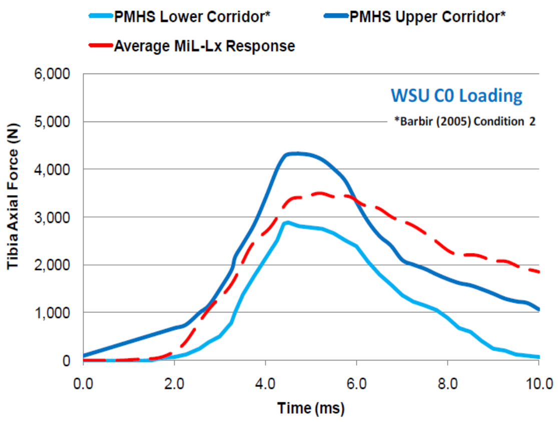

Figure 7.2. Comparison of Mil-Lx response (5.4 m/s) to Barbir[18] PMHS corridor (4.8 m/s) for a comparison at a lower loading condition. Note: Figure reproduced from McKay dissertation.[134]

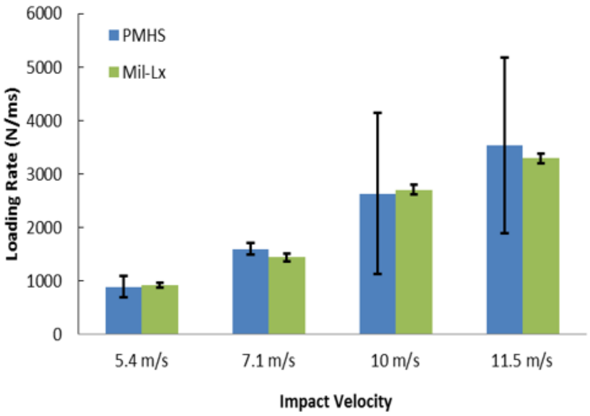

Figure 7.3. Comparison of PMHS (implanted mid-tibia load cell) and Mil-Lx (upper tibia load cell) loading rates for axial impact tests.[134]

Pandelani et al. performed several tests on the Mil-Lx leg to evaluate its repeatability and biofidelity for UBB conditions.[155,158] These tests involved comparing the Mil-Lx and Hybrid-III upper tibia force for axial impact velocities ranging from 1.5-8.8 m-s^{-1}, and showed that Mil-Lx forces were considerably lower than Hybrid-III forces. The Mil-Lx was found to be more repeatable than the Hybrid-III with less than 5 percent difference in peak force from the average peak force compared to 8 percent for the Hybrid-III at a lower velocity.[158] The Mil-Lx upper and lower tibia force versus time plots for these velocities were provided in Pandelani's dissertation, and are reproduced in Figure 7.4 for reference.[156] These plots show that lower tibia peak force was higher than upper tibia peak force. The sharp onset of lower tibia force compared to the more gradual rise of upper tibia force is caused by the compression of the compliant element located between the two load cells. The double peak observed at higher velocities has been attributed to the scenario when the tibia element fully compresses or "bottoms-out," which allows the lower tibia force to reload.[134]

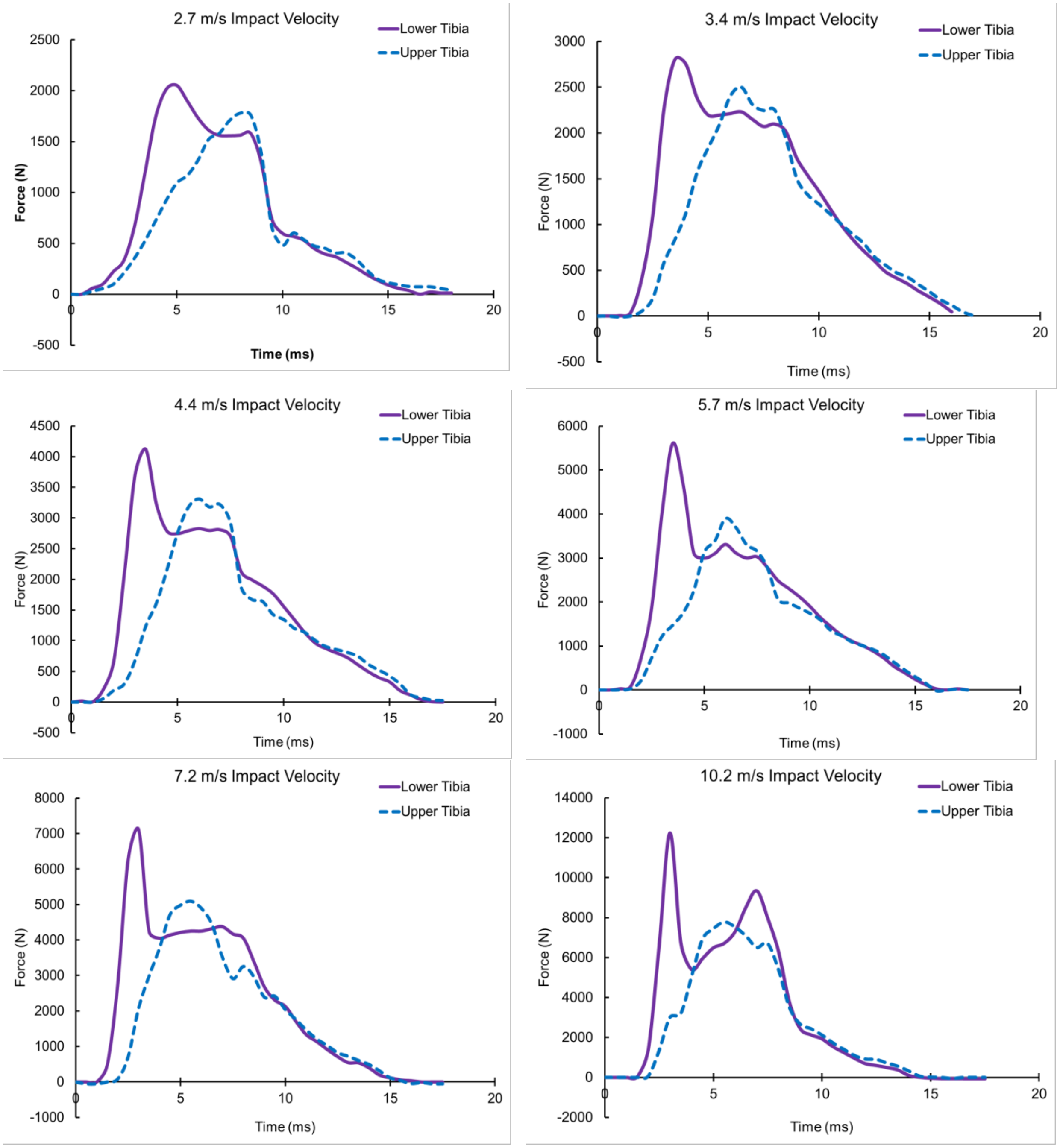

Figure 7.4. Mil-Lx force response to axial impacts performed at different velocities by Pandelani et al. (Plots reproduced from data presented in Pandelani's dissertation)[156]

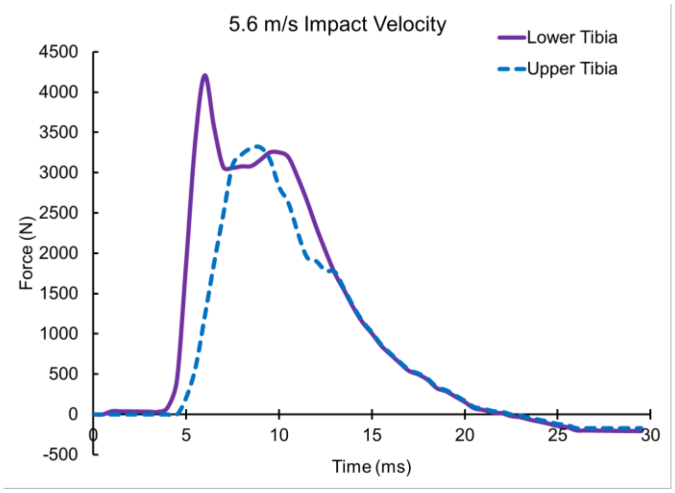

Figure 7.5. Mil-Lx upper and lower tibia forces from a 5.6 m-s^{-1} impact. (Plots produced using data from Shewchenko et al.)[192]

Quenneville et al. evaluated the Mil-Lx by performing impact tests with and without the Mil-Lx foot and compared the response to PMHS test results.[170] For these tests, a 6.8 kg projectile was used to deliver axial impact loads to the Mil-Lx leg with durations ranging from 3-10 ms and velocities of 2-7 m-s^{-1}. Figure 7.6 shows that the Mil-Lx measured forces closer to the peak proximal tibia force in the human leg for velocities ranging from 1-9 m-s^{-1}. This bilinear response of the peak Mil-Lx forces can be explained by the “bottoming-out” of the compliant tibia element. Since only peak forces are provided, a comparison cannot be made between PMHS and Mil-Lx force-time histories in order to assess the compatibility of the Mil-Lx with the proposed injury criterion. The bilinear response of the Mil-Lx, because of the behavior of the leg when the tibia compliant element is fully compressed, suggests that the Mil-Lx may be limited in is ability to be modeled as a linear system over the full range of AI and UBB conditions. Because of this, the ability to develop a transfer function from Mil-Lx to PMHS force becomes more complicated in the same manner that a force-limiting knee bolster affects interpretation of ATD femur force.

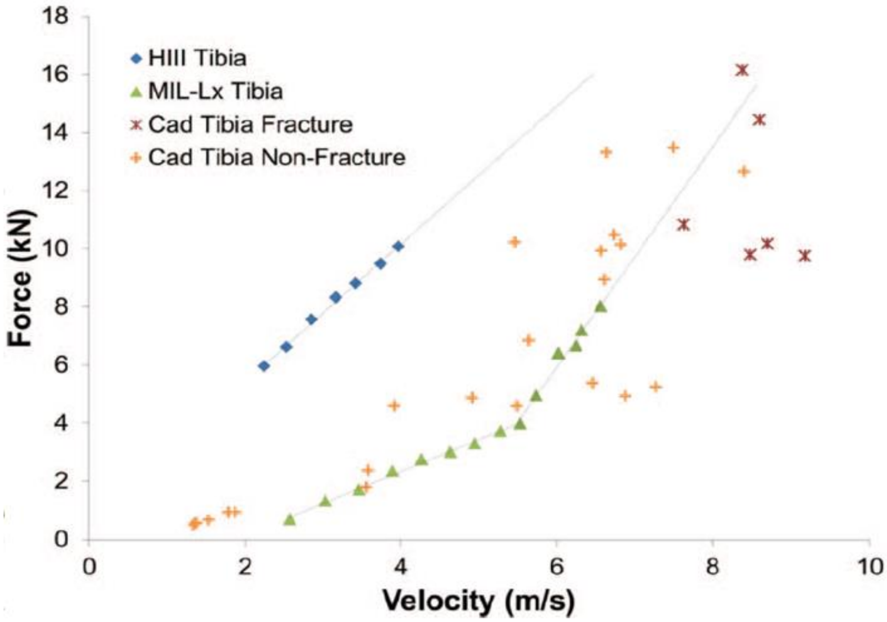

Figure 7.6. Mil-Lx peak force response to varying impact velocity compared to cadaveric tibia force response. (Accidental Injury by Springer New York. Reproduced with permission of Springer New York in the format Thesis/Dissertation via Copyright Clearance Center.)[170]

A few studies have utilized the Mil-Lx ATD leg to evaluate the protection of boots and blast mats from axial loading due to UBB.[147,160,192] Newell et al. compared the response of the Mil-Lx and Hybrid-III donned with military boots on blast mats for velocities ranging from 2.8-9.1 m-s^{-1}. This study concluded that a larger difference in Hybrid-III peak force was measured between blast mat and no-blast mat cases than for Mil-Lx peak forces, but the two ATDs ranked the different blast mats in the same order in terms of mitigating force. Shewchenko et al. found similar results in that the Mil-Lx and Hybrid-III assessed different risk of injury in the presence of energy absorbing floor mats, though neither study compared the results to the response of a human leg under these conditions.[192]

Pandelani compared the response of the Mil-Lx with and without military boots at different impact velocities. This study showed that the presence of the boot decreased the peak force measured at the Mil-Lx upper tibia for impact low velocities, but as the impact velocity was increased, higher peak upper tibia forces were measured in the Mil-Lx when the boot was present.[158] This effect may be attributed to the placement and stiffness of the compliant element in the Mil-Lx and relates back to the discussion in Section 7.1 about the necessity of biofidelity in the leg. The ability of an ATD leg to produce a biofidelic response when personal protective equipment (PPE) is present is extremely important when using ATDs to assess the ability of the PPE to attenuate energy. Pandelani et al. conclude that the insensitivity of the Mil-Lx caused by the tibia compliant element to the presence of boots could lead to over-estimation of the protectiveness of injury mitigation systems.[157]

As concluded in the previous chapter, peak force is not sufficient for estimating probability of injury for this expanded range of loading frequencies. Thus, the Mil-Lx must be able to accurately replicate the timing of the force response of the leg in addition to the magnitude of the force. Further, since preliminary results have shown that inertial differences between the proximal tibia and plantar foot forces can be significant, and that plantar foot force has been shown to have a stronger correlation with injury risk in the PMHS foot and ankle,[73] it is important that a the ATD leg not only provide a biofidelic response at the proximal tibia for use in assessing potential intrusion-type injuries, but also must measure biofidelic forces at a more distal location such as the plantar surface of the foot or heel.

To evaluate the biofidelity of the Mil-Lx leg PMHS and Mil-Lx response data from McKay et al. was obtained by digitizing the plots provided in McKay's dissertation.[134] PMHS force traces were grouped according to loading condition and plotted against the Mil-Lx upper tibia forces from tests performed at the same loading condition (Figure 7.8-Figure 7.9). Despite the similarity in average load rate for each condition found by McKay, the PMHS and Mil-Lx force responses were found to be in disagreement when the data was examined more closely. The sub-injurious test condition from Barbir et al. (4.8 m-s^{-1}) on the left side of Figure 7.7 produced a peak Mil-Lx upper tibia force outside of the +/- one standard deviation corridor. In terms of estimating injury risk, the timing and peak force difference between the Mil-lx and the ATD could lead to inaccurate estimates of injury risk.

Assuming that the lower peak forces for the test conditions in Figure 7.9 were a result of artefactual fracture at the location of the tibia load cell, eliminating these tests would cause the peak forces and timing of the remaining PMHS tests (10.4 and 9 m-s^{-1} for the plot on the left, and 11.3 and 11.5 m-s^{-1} for the plot on the right) not to align with the Mil-Lx force response. Peak forces for the PMHS occurred prior to peak force in the Mil-Lx, which indicates that impulse would be overestimated by the Mil-Lx. Moreover, the Mil-Lx's underestimation of PMHS peak force for the plot on the left suggests that there is potential for underestimation of probability of injury for that test condition. The infrangibility of the Mil-Lx should lead to higher peak forces compared to the peak force for the PMHS tests in which fracture occurred. Ideally, a biofidelic ATD force should track with the response of the PMHS up to the point of fracture, and depending on the overmatch of the input condition, the ATD peak force may continue to increase beyond the force at fracture for the PMHS.

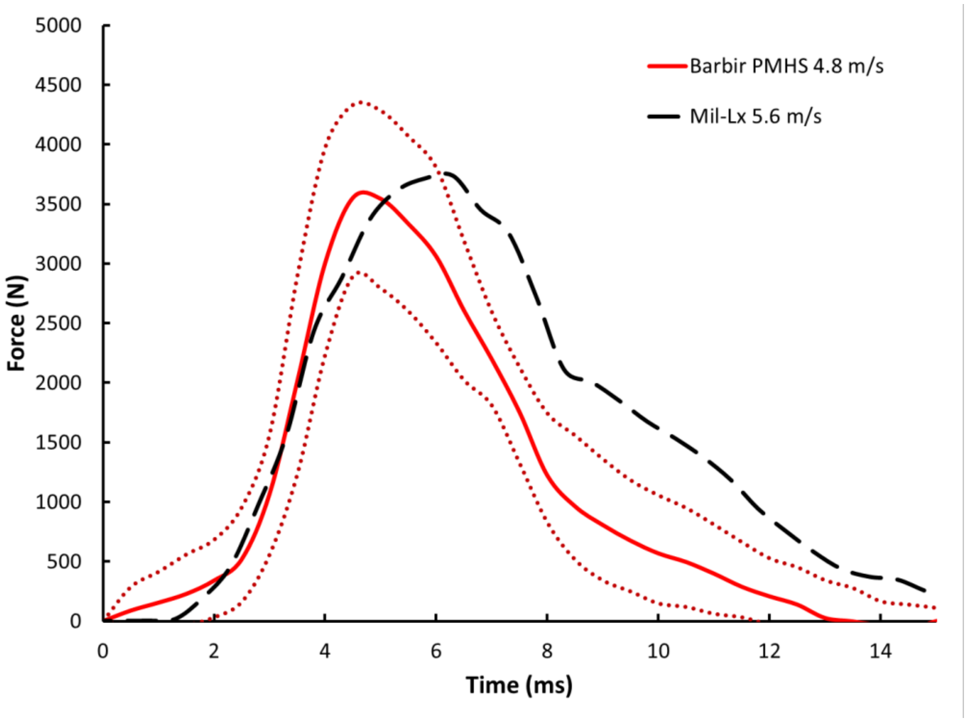

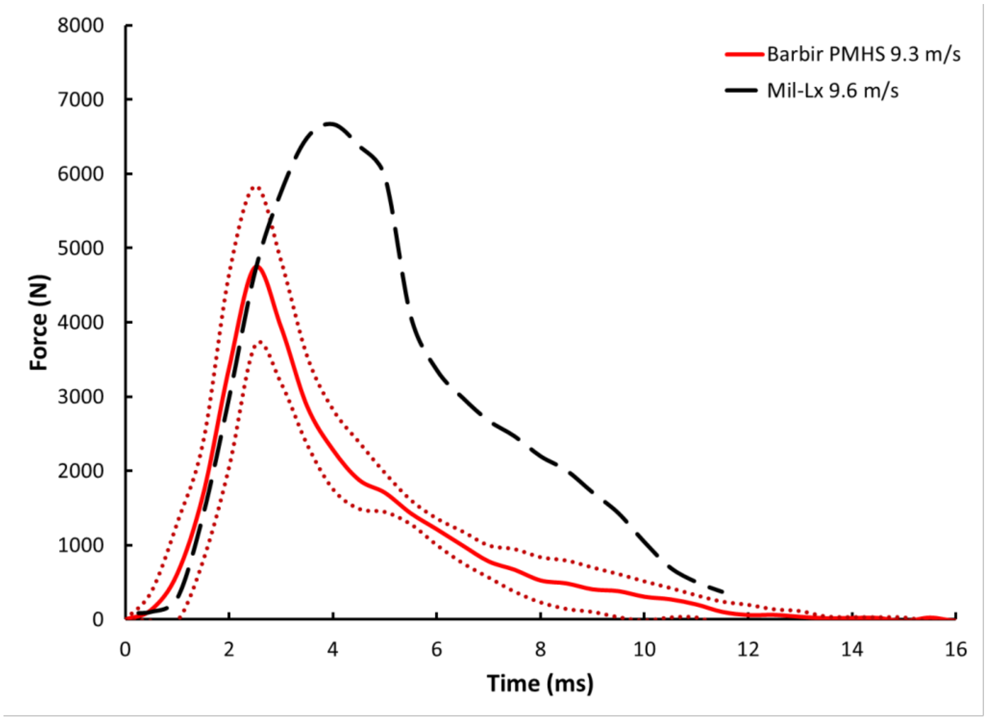

Figure 7.7. Comparison of Mil-Lx upper tibia force to PMHS force corridors generated by Barbir et al.[18] Note that while there is reasonable agreement, the Mil-Lx test conditions consisted of slightly higher impact velocities.

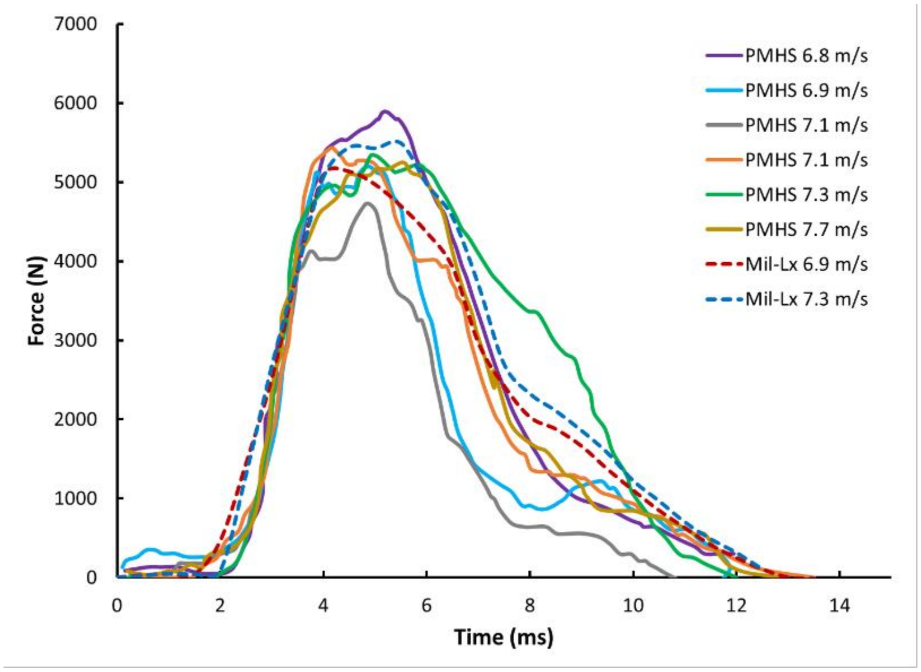

Figure 7.8. Comparison of Mil-Lx upper tibia forces and mid-tibia forces from sub-injurious PMHS tests performed by McKay.[134] This condition was used for the development of the Mil-Lx design.

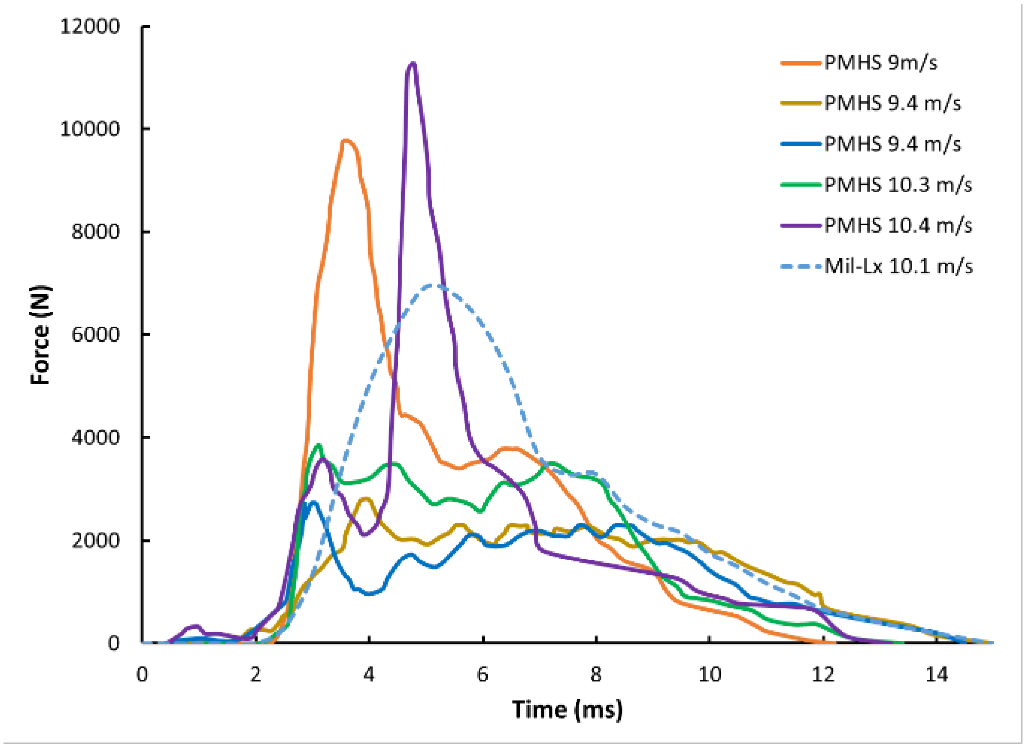

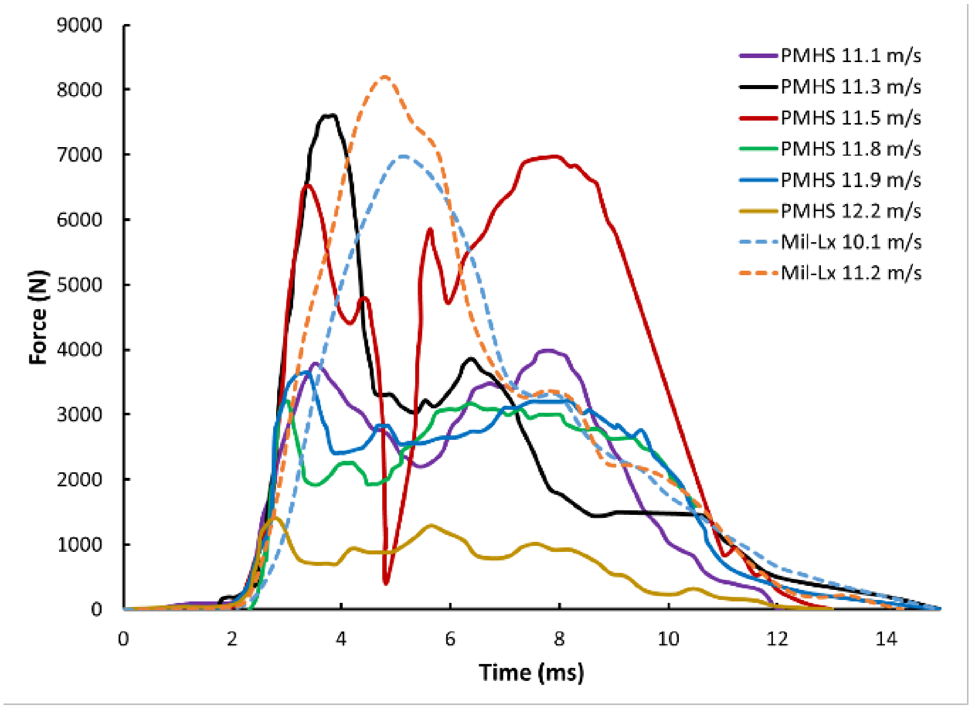

Figure 7.9. Comparison of Mil-Lx upper tibia forces and mid-tibia forces from injurious PMHS tests performed by McKay.[134]

Though the primary application for the Mil-Lx ATD is vertical loading, Pandelani et al. compared the response of the Mil-Lx and Hybrid-III legs exposed to out-of-position (OOP) loading including nominal (90°-90° foot-tibia, tibia-femur angles) acute and obtuse foot-tibia and tibia-femur angles.[157] While UBB loads are assumed to be primarily vertical in nature, warping of the floor pan and soldier seating position can expose the leg to non-vertical load vectors in these events.[60] Results of Pandelani's study revealed that the Mil-Lx is less sensitive to OOP loads than the Hybrid-III, which can lead to errors using the revised tibia index (RTI) calculated for a given input condition/leg position. A particularly large difference in RTI was observed for the 53°/90° test condition, which corresponded to a 91% difference in probability of injury estimated by the Mil-Lx compared to the Hybrid-III. These results are expected based on the presence of the compliant tibia element in the Mil-Lx design and the fact that RTI was developed for use with the Hybrid-III. The lack of comparison of the Mil-Lx and PMHS response limits the conclusions that can be made about the biofidelity of the Mil-Lx exposed to alternative loading vectors and out-of-position postures. The implications of these postures in terms of estimating injury risk will be discussed in a later chapter. Nonetheless, it is important to note that the lack of available injury criteria for the Mil-Lx limit its usefulness for loading conditions outside of the vertical loading conditions for which it was initially validated.

7.2.2 Experimental Testing of the Mil-Lx ATD

To evaluate the biofidelity of the Mil-Lx in terms of its ability to predict injury using the proposed injury criterion, further experimental testing was required. The drop tower test set-up was replicated from Section 3.2.1. An aluminum mounting block was machined to interface with the knee mounting bracket of the Mil-Lx. This block was designed such that its mass matched the mass of the proximal load cell plus the estimated mass of the potting cup and potting material from the PMHS tests. The tibia shaft of the Mil-Lx was aligned at a right angle to the impact and load cell plates, so that it aligned directly with the impact direction.

The Mil-Lx was outfitted with the full set of instrumentation which included: a heel accelerometer (SAE-z), mid-foot accelerometers (SAE-x,y,z), tibia accelerometers (SAE-x,y,z), a lower tibia load cell (6-axis), and an upper tibia load cell (6-axis). Test rig instrumentation included a footplate accelerometer and a proximal plate accelerometer for the SAE-z direction. Data was collected using a DTS SlicePro data acquisition system (Diversified Technical Solutions, Seal Beach, CA) at a sample rate of 100 kHz.

Four test conditions from the PMHS drop tower tests described in Section 3.2.1 (tests 1.16-1.19) were replicated using the Mil-lx as the test subject (Table 7.1). To match the conditions, the same hammer mass, drop height, pulse shapers, and reaction masses were used; however, due to the nature of the test rig and its dependence on the test subject, impact plate displacement histories were slightly different (Overall CORA>0.87).

Table 7.1. Mil-Lx Drop Tower Test Matrix

Test Name	Hammer Mass (kg)	Drop Height (m)	Reaction Mass (kg)	Impact Az (g) in (ms)	Lower Tibia Fz (kN)	Upper Tibia Fz (kN)
MLX 16	34.2	1.5	7.2	640 in 1.8	6.302	5.522
MLX 17	34.2	1	7.2	560 in 1.2	5.065	4.710
MLX 18	34.2	1.4	7.2	770 in 1.1	6.551	5.212
MLX 19	34.2	1.25	7.2	560 in 1.9	5.464	4.888

Mass-normalized PMHS results were compared to the individual Mil-Lx results. Figure 7.10 shows that the Mil-Lx under-estimated the peak response of the PMHS upper tibia force for the sub-injurious cases (Tests 18 and 19), but was more predictive of the response for the injurious cases. While the two sub-injurious cases have higher peak forces than the injurious tests, it is expected that the Mil-Lx should continue to behave like the PMHS beyond the point of fracture. The fact that the Mil-Lx peak upper tibia force was more than 2 kN less than that of the sub-injurious PMHS cases causes concern that the Mil-Lx may be unable to accurately predict injury because of its lack of biofidelity. Rather than predicting the response of the injurious cases, the Mil-Lx should mimic the response of the sub-injurious cases and over-estimate the peak forces associated with the injurious tests.

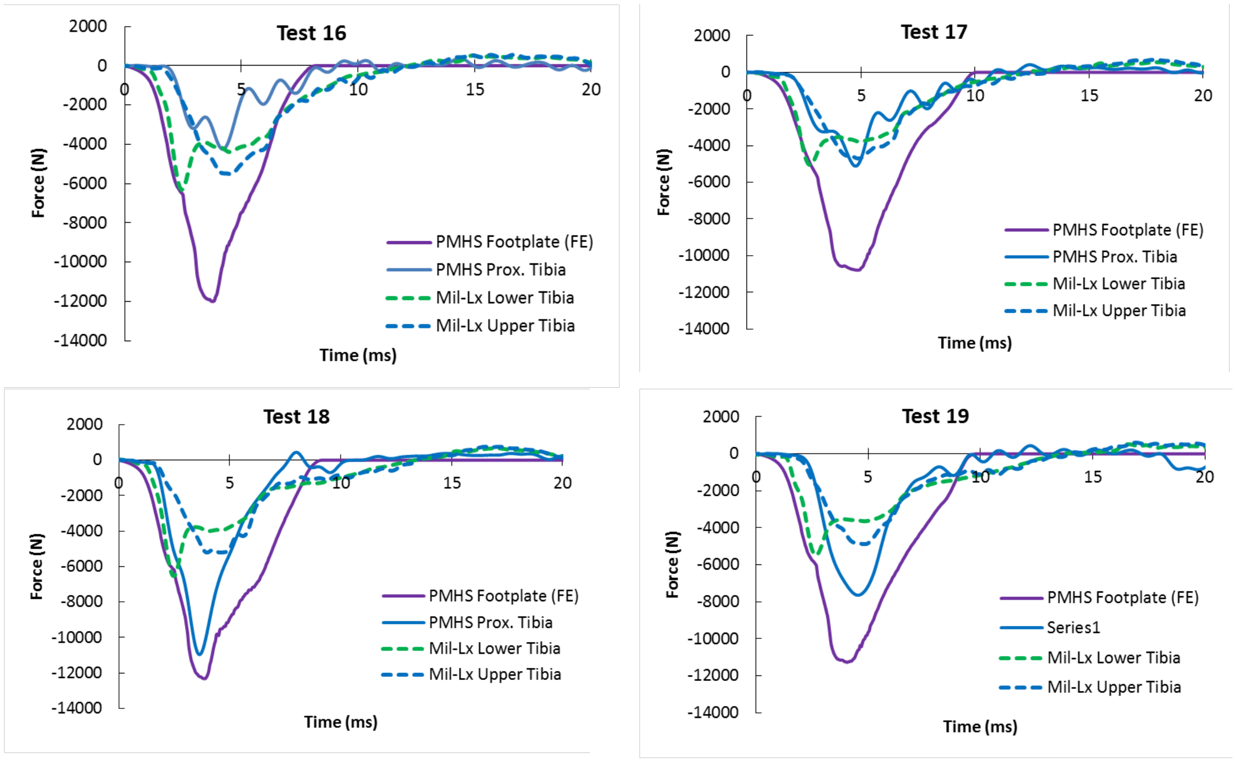

Figure 7.10. Comparison of Mil-Lx upper tibia force to matched mass-normalized [63] PMHS proximal tibia force results from Henderson et al. (2013) showing that the Mil-Lx underestimates PMHS force for sub-injurious cases (Tests 17-19).

Average response for the four mass-normalized PMHS proximal tibia forces and the Mil-Lx upper tibia force response were calculated with ±one standard deviation corridors

(Figure 7.11). This plot shows that even for the average response, the Mil-Lx under-predicts the human force. An overall CORA score of 0.826 was calculated for the PMHS and Mil-Lx average responses with a breakdown of 0.763, 0.724, and 0.990 for phase, magnitude, and progression scores, respectively. The weighted CORA score was 0.728.

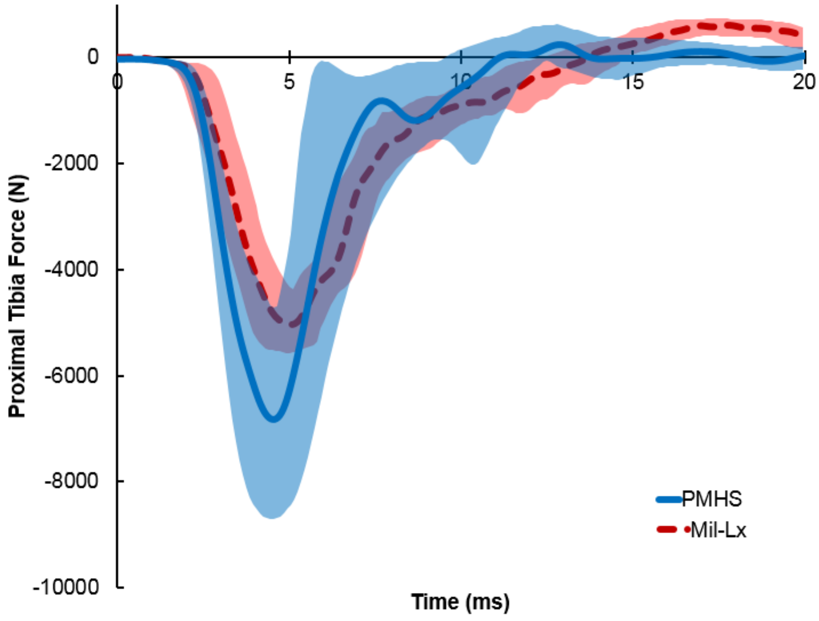

Figure 7.11. Comparison of PMHS normalized proximal tibia force and Mil-Lx upper tibia force corridors for the Drop Tower B loading condition.

Displacements were calculated for the impact plate, proximal plate, and tibia for both the PMHS and Mil-Lx using SAE-z accelerations (Figure 7.12). As shown in Figure 7.12, tibia displacement tracked closer with impact plate displacement than the proximal plate displacement for the Mil-Lx, and the PMHS tibia displacement tracked more closely with the impact plate. This difference highlights the fact that the location of the compliant element in the tibia shaft of the Mil-Lx is not realistic since much of the compliance in the leg is located in the foot and ankle rather than the tibia.

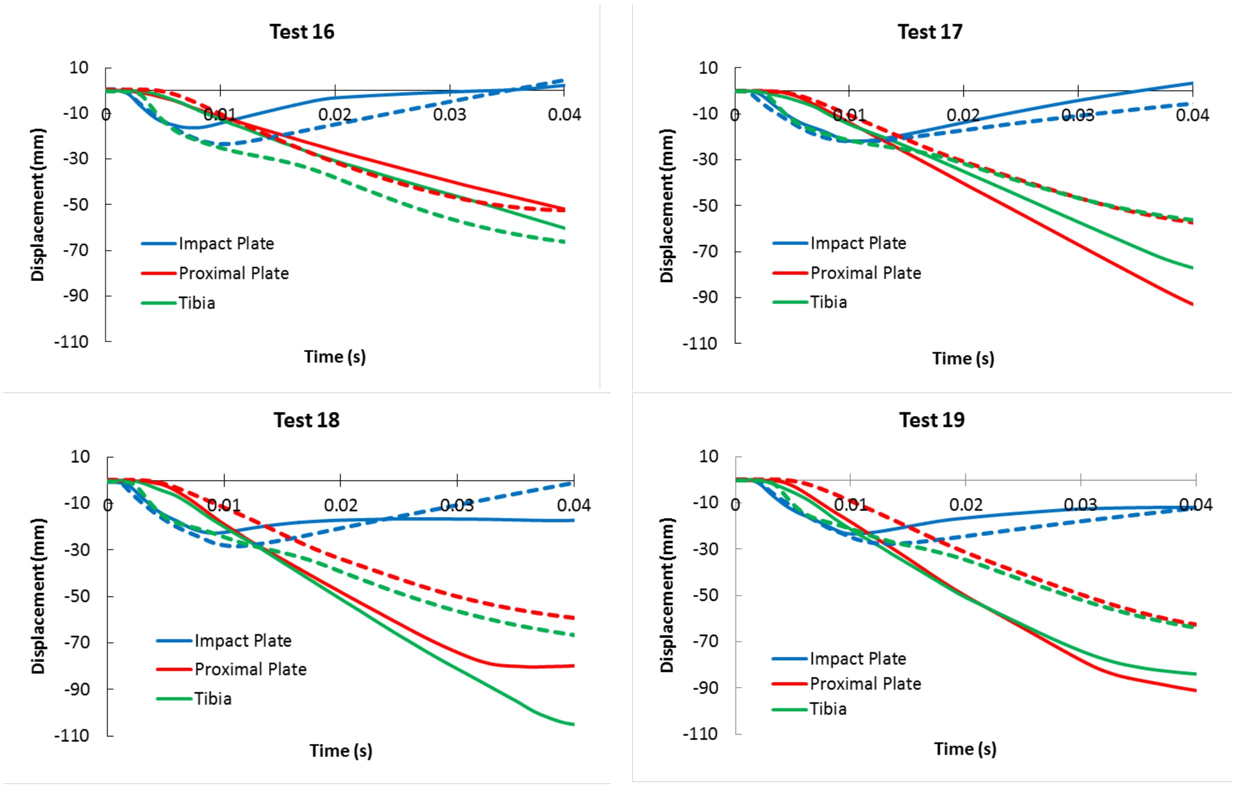

Figure 7.12. Displacement response of the PMHS (solid lines) compared to the Mil-Lx (dashed lines) for the impact plate, the proximal (load cell) plate, and the tibia for drop tower test conditions 16-20.

Despite this difference, one might argue that only the biofidelity of the force measurement is required to assess injury probability using the Mil-Lx. However, as discussed in Chapter 6 force biofidelity at more distal location is desired for predicting injury in the foot and ankle for this type of loading condition. Thus, it is necessary to investigate whether more distal instrumentation in the Mil-Lx, such as the lower tibia load cell and foot accelerometers, have the ability to produce a biofidelic estimate of the force at the plantar surface of the foot.

First, impulse was calculated for the proximal and footplate locations for the Mil-Lx and PMHS tests results. Since force at the footplate was not measured in the drop tower tests, this force was estimated using the UVA leg model.[78] These results are shown in Figure 7.13. For the sub-injurious cases, peak impulse for the PMHS proximal tibia compared to the Mil-Lx upper tibia was within 5 N-s despite the drastic underestimate of peak force provided by the Mil-Lx. Lower tibia impulse was not comparable to footplate impulse.

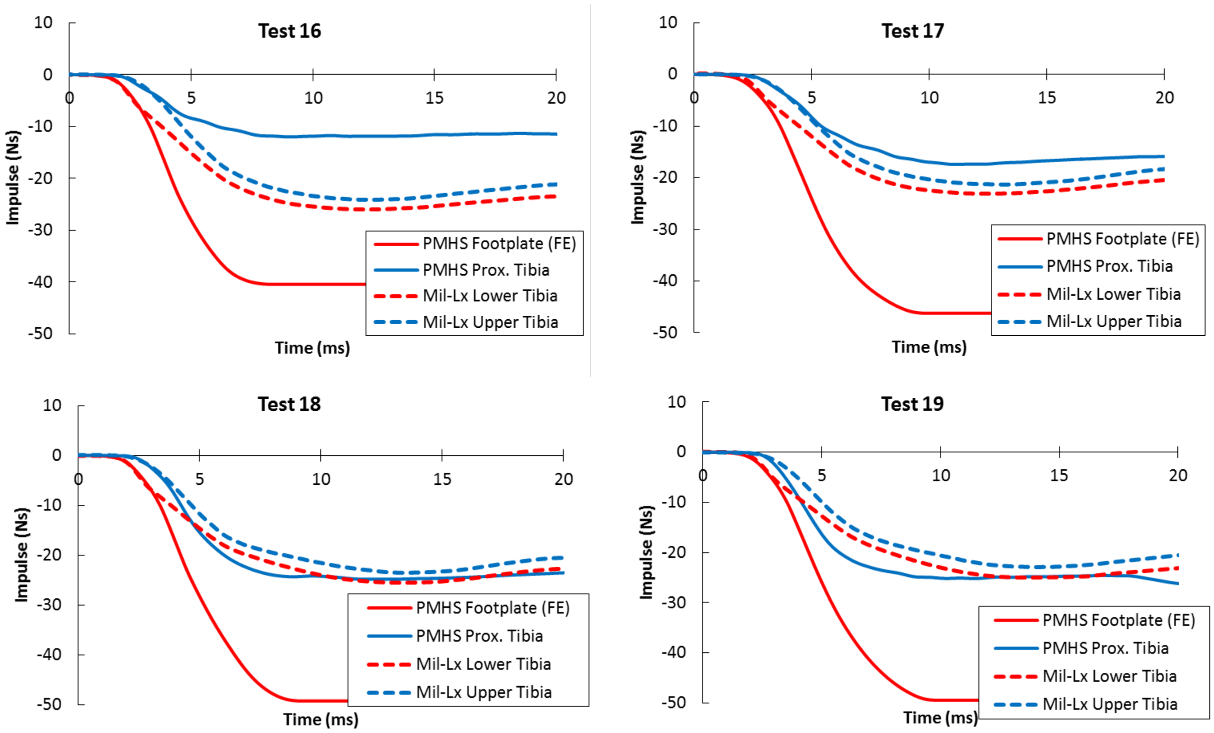

Figure 7.13. Comparison of Mil-Lx and PMHS impulse for drop tower tests 16-19. Mil-Lx responses are displayed using dashed lines, while PMHS responses are displayed by solid lines.

One method for estimating the footplate or plantar force in the Mil-Lx would be to mass-compensate the lower tibia load cell force using the foot acceleration from the Mil-Lx. This assumes that the foot and ankle behaves as a rigid body. A comparison of the tibia and hindfoot accelerations shows little difference, which suggests that this assumption is justified (Figure 7.14). Using the mass distal to the lower tibia load cell and the acceleration of the Mil-Lx hindfoot to estimate the plantar force in the Mil-Lx (Eqn. 7.1), the resulting forces and impulses for the matched pair tests were again compared (Figure 7.15).

$$F_{\mathrm{plantar}} = F_{\mathrm{Lower\ Tibia}} + m_{\mathrm{foot}}a_{\mathrm{foot}} \qquad \text{Eqn. 7.1}$$

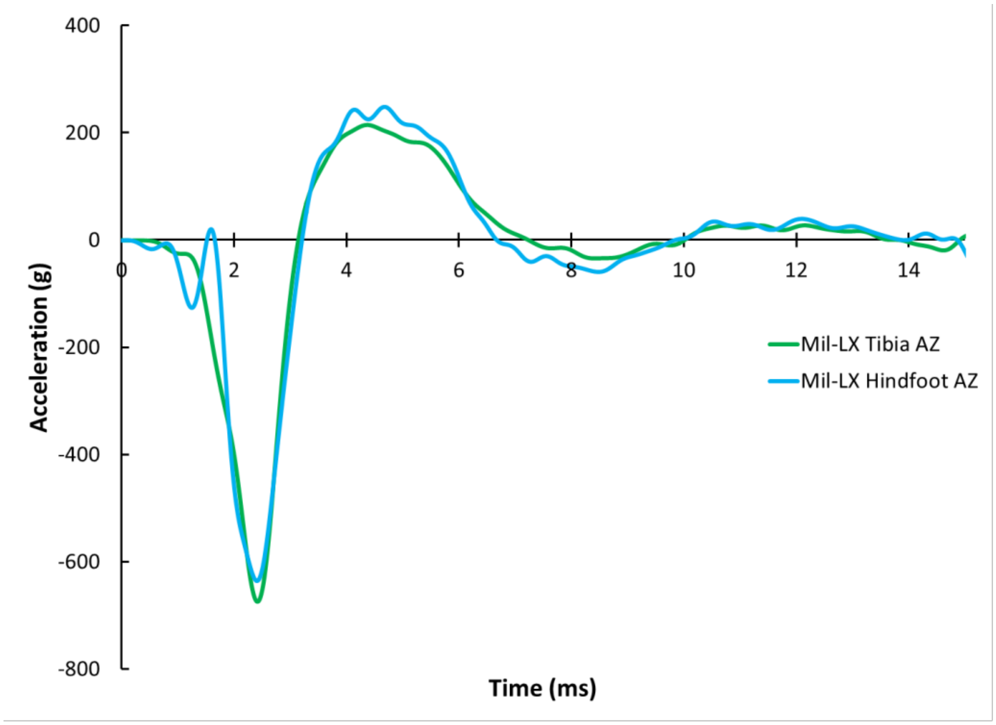

Figure 7.14. Comparison of Mil-Lx tibia and hindfoot accelerations showing that the plantar force can be estimated by compensating for the mass distal to the lower tibia load cell. The sample trace provided is from Test 18, however all test cases showed similar results.

Peak estimated Mil-Lx footplate forces were consistently higher than footplate forces estimated using the FE model for the PMHS tests. Timing of the estimated forces showed the estimated Mil-Lx forces peaking and relaxing before the peak PMHS footplate force was reached. This phenomena is likely due to the overall compliance of the Mil-Lx tibia being less stiff than the PMHS and having a different mass distribution. Since a majority of the mass of the Mil-Lx leg is located distal of the compliant element it is reasonable for Mil-Lx footplate force to be higher than for the human leg in which only the foot mass is distal to the most compliant region (the ankle). The difference in compliance between the ankle and the Mil-Lx tibia compliant element yields the dissimilarity in force relaxation as well.

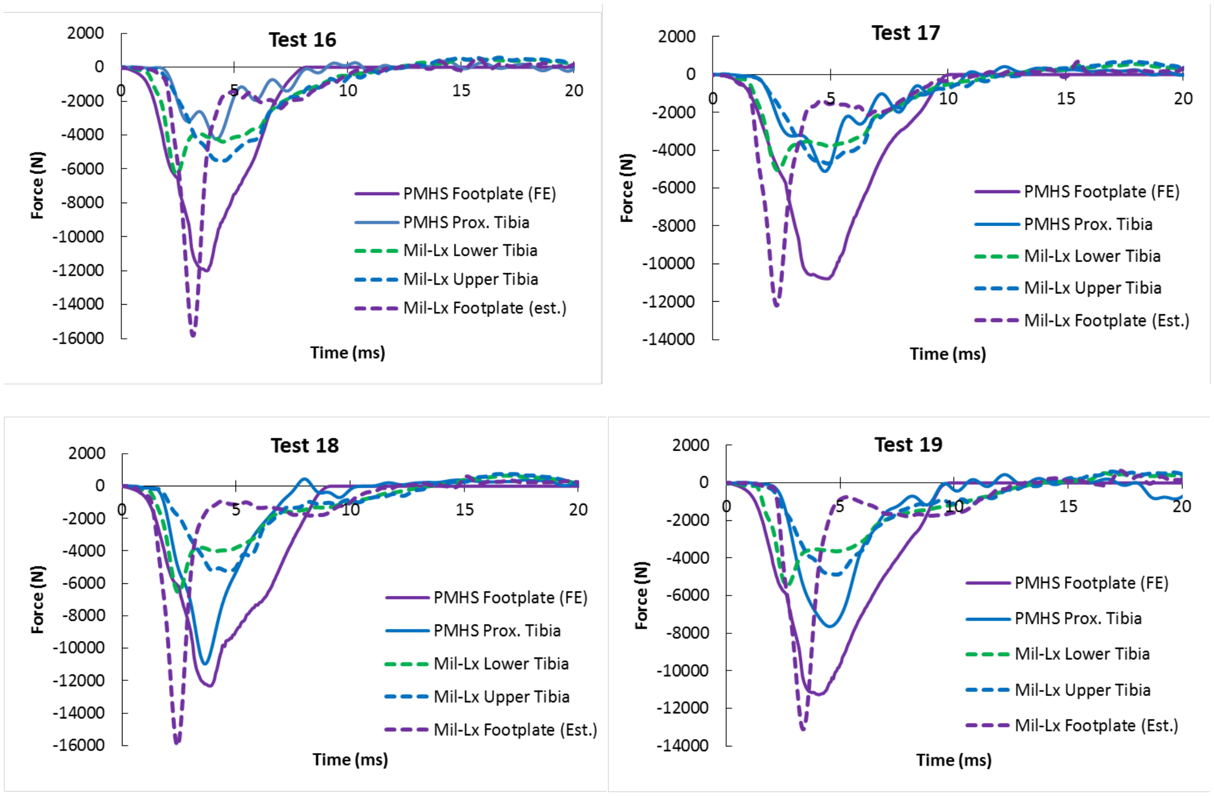

Figure 7.15. Comparison of estimated plantar force for the Mil-Lx and PMHS plantar force estimated using the human FE model.

The results presented for these experimental Mil-Lx tests show that the Mil-Lx tibia acceleration is actually more representative of the foot acceleration than the tibia acceleration as measured in the PMHS. Again, this is due to the location of the tibia compliant puck. To be more representative of the human leg, the Mil-lx compliant element should be placed distal of the tibia accelerometer and tibia shaft mass to represent the ankle compliance. Moving the location of the compliant element would also more correctly model the mass distribution of the human leg. A previous matched pair study using whole body PMHS exposed to simulated UBB loads and a Hybrid-III ATD outfitted with a Hybrid-III and Mil-Lx leg showed further evidence of this discrepancy between Mil-Lx and PMHS tibia acceleration.[11] This study showed that for a booted test condition, the PMHS tibia SAE-z acceleration was overestimated by the Mil-Lx. Corridors comparing results from these tests are provided in Figure 7.16 and Figure 7.17 for low and high acceleration test conditions, respectively.

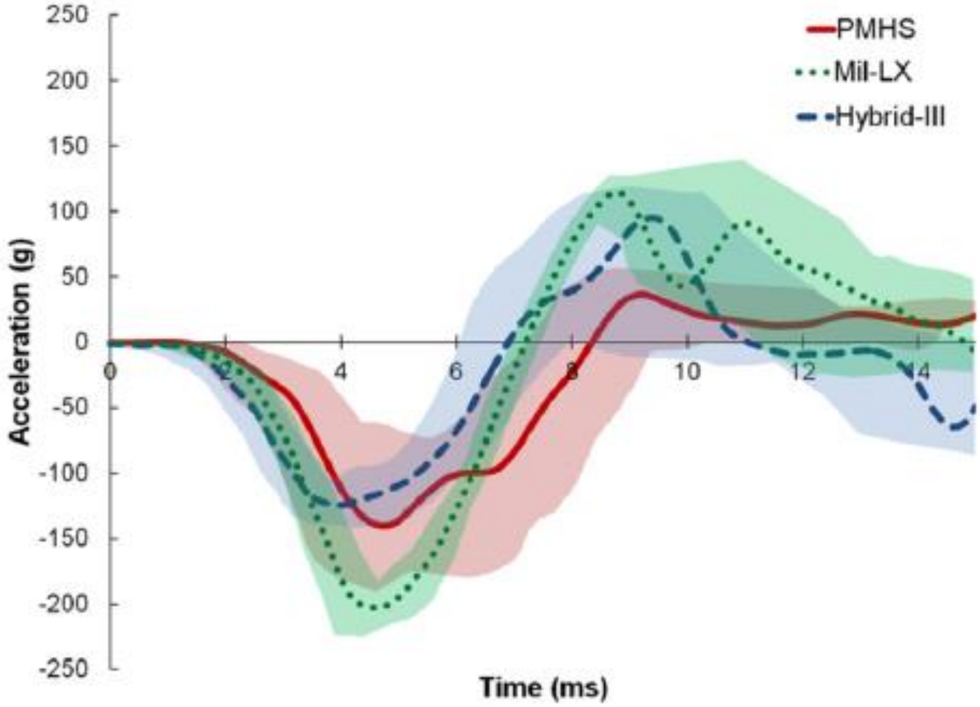

Figure 7.16. Tibia SAE-z acceleration comparison for low condition (4.6-6.5 m s^{-1}) whole body matched pair tests reproduced from Bailey et al. (2015).[11]

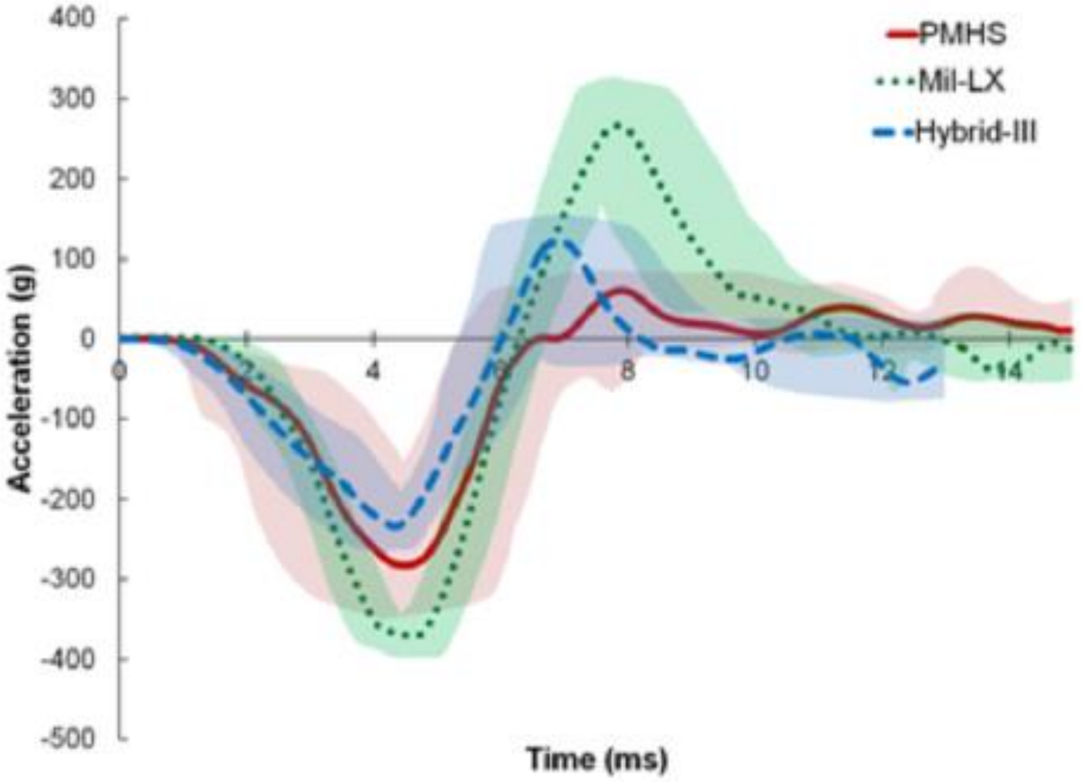

Figure 7.17. Tibia SAE-z acceleration comparison for high condition (8.8-10.8 m s^{-1}) whole body matched pair tests reproduced from Bailey et al. (2015).[11]

These results, in combination with previous comparisons of PMHS and Mil-Lx response, suggest that major changes be made to the Mil-Lx design in order to correctly mimic the behavior of the human leg. In summary, the position and stiffness of the tibia compliant element prevent the leg from producing biofidelic responses at the level of the foot and ankle, despite similarities in the force response measured at the upper/proximal tibia. The comparison to the drop tower PMHS results provides an example of a test condition within the realm of UBB, but different from the 7 m-s^{-1} condition for which the Mil-Lx response was initially designed to match. The inability of the Mil-Lx to match this condition and its failure to allow for a biofidelic estimation of PMHS plantar force established the need to explore options for improving the biofidelity of the ATD without further experimentation at different loading rates/frequencies.

MATLAB was used to examine the frequency response of the human leg compared to the Mil-Lx. Bode diagrams for the experimental Mil-Lx and PMHS drop tower tests further emphasize the phasing caused by the compression of the tibia compliant element. Figure 7.18 shows the frequency diagrams for the 2-pole transfer function between the footplate and proximal tibia accelerations, and Figure 7.19 shows Bode plots for the 2-pole transfer function between footplate acceleration and proximal tibia force. The shape of the magnitude Bode plot for the PMHS tests indicates larger system damping than in the Mil-Lx. The plot also indicates that the natural frequency of the PMHS is greater than that of the Mil-Lx, which implies that while the Mil-Lx has less damping than the PMHS, it is generally more compliant than the PMHS. These systematic differences between the Mil-Lx and PMHS imply that a transfer function must be used to predict the response of the human leg using the current ATD design for the range of loading frequencies other than those for which it was designed.

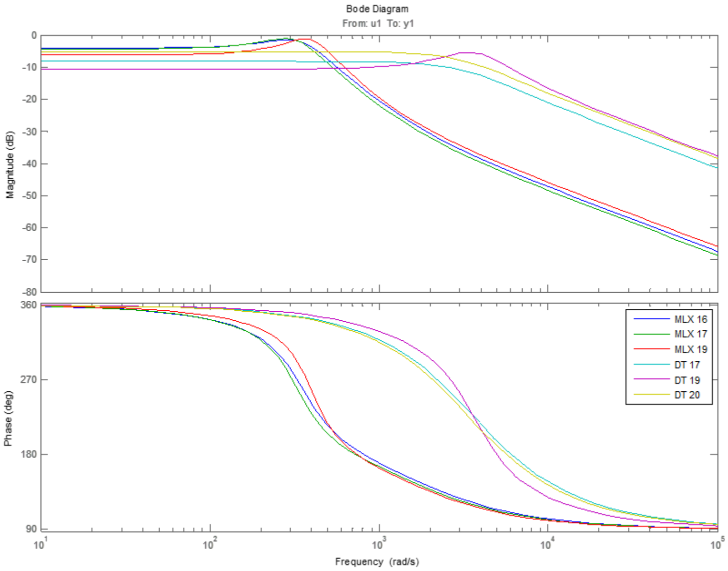

Figure 7.18. Bode diagram for the sub-injurious drop tower conditions and the Mil-Lx tests for the same input conditions assuming a 2-pole transfer function for footplate versus proximal tibia acceleration.

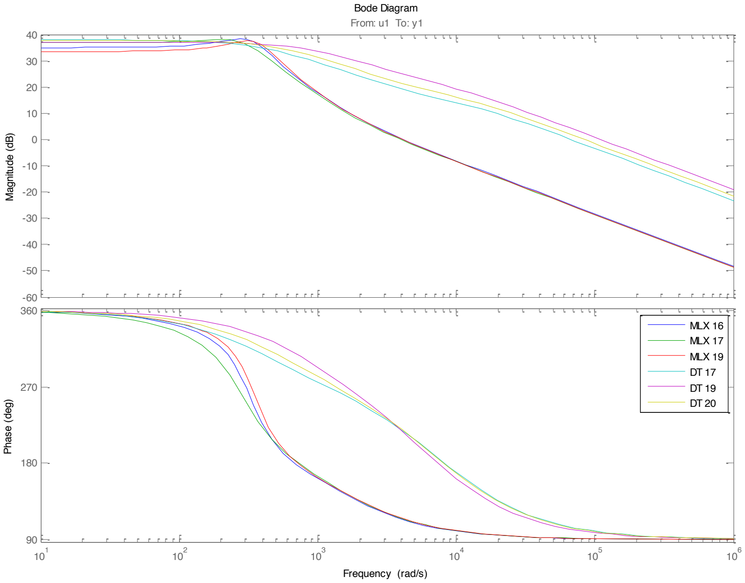

Figure 7.19. Bode diagram for the sub-injurious drop tower conditions and the Mil-Lx tests for the same input conditions assuming a 2-pole transfer function for footplate versus proximal tibia force.

The differences in the frequency response of the Mil-Lx and human legs are not surprising considering the difference in mass distribution and the large compliance in the Mil-Lx leg provided by the tibia compliant element. The next sections of this chapter focus on minimizing the difference in response of the ATD and human leg using a lumped mass model.

7.3 Lumped Mass Model as a Tool for ATD Design

Given that the Mil-Lx design has been tuned for a limited set of loading conditions, it is necessary to determine whether the Mil-Lx's segmented design can provide a biofidelic response when exposed to other loading conditions and when injury mitigation is used. The response of the Mil-Lx leg is primarily controlled by the material properties of the heel pad and the compliant element located between the upper and lower tibia load cells.[134] The goal of this part of the dissertation was to use a dynamic model of the Mil-Lx to optimize the biofidelity of the current design of the Mil-Lx at both the plantar surface of the foot and proximal tibia for various loading frequencies so that it may be used to more accurately assess injury probability using the injury criterion developed as part of this dissertation.

Having discussed the shortcomings of the current configuration of the Mil-Lx, the next step was to determine whether the segmented design of the Mil-Lx is capable of providing biofidelic forces across the rates for which the injury criterion was developed. In Chapter 5, it was demonstrated that a second-order LMM is capable of modeling the response of the leg to axial impacts ranging from 5 to 90 ms in force duration, with impact velocities of 3.4 to 11.2 m-s^{-1}.

The structure of the Mil-Lx lends itself well to being modeled as a LMM because of its segmented structure. Similar to the way the MDOF LMM of the leg was divided, the Mil-Lx's foot may be represented by a mass. However, because of the lack of compliance built into the ankle joint of the Mil-Lx additional mass from the tibia shaft must also be included with the foot mass. The remainder of the tibia mass and the knee joint may be grouped into a second mass in the LMM, separated from the first mass by a spring and damper. Thus, a 2-DOF model (Figure 7.20) may be used to represent the current design of the Mil-Lx. While the different mass distribution in the Mil-Lx compared to the human leg complicates the relationship between the human LMM and the Mil-Lx LMM, this LMM design still allows the prediction of the footplate force using the lower tibia force. The advantage of this model design will be discussed in more detail in Section 7.6.

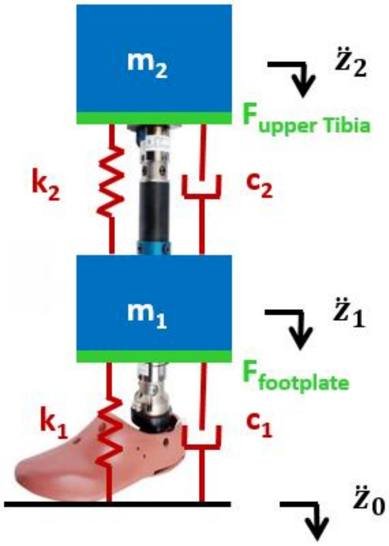

Figure 7.20. Lumped-mass model of the Mil-Lx which assumes no ankle compliance

Ideally, an ATD with the same characteristics as the optimized LMM of the human leg would provide the best results in terms of matching the response of the human leg. Despite the fact that the mass distribution of the human leg and Mil-Lx leg are different because of the placement of the tibia compliant element in the Mil-Lx, a LMM may still be used as a tool for optimizing the biofidelity of the current Mil-Lx design without making major changes to its structure. Thus, the model in Figure 7.20, which most closely represents the structure of the Mil-Lx, was used to identify the characteristics (k_i, c_i) of the compliant materials in the Mil-Lx necessary to improve Mil-Lx biofidelity. The mass for the Mil-Lx LMM was distributed such that m_1 includes the mass of the foot (m_{foot}), ankle assembly (m_{ankle}), lower tibia load cell (m_{LTLC}), skin (m_{skin}), and half the mass of the tibia compliant element assembly m_{TCE}. The other half of the tibia compliant element assembly, upper tibia load cell (m_{UTLC}), and knee mount (m_{knee}) are included in m_2 (Eqn. 7.2, Eqn. 7.3).

$$\mathbf{m_1 = m_{foot} + m_{ankle} + m_{LTLC} + 0.5 * m_{TCE} + 0.5 * m_{skin}} \qquad \text{Eqn. 7.2}$$

$$\mathbf{m_2 = m_{knee} + m_{UTLC} + 0.5 * m_{TCE} + 0.5 * m_{skin}} \qquad \text{Eqn. 7.3}$$

The same optimization methodology used for identifying the parameters of the human LMM (Chapter 5) was used to identify k1, k2, c1, and c2 such that the sum of the CORA score for the calculated Mil-Lx upper tibia force and the average PMHS proximal tibia force, and the CORA score for the calculated Mil-Lx footplate force and average PMHS footplate force was maximized across the average inputs from each input condition (Eqn. 7.4-Eqn. 7.6). Footplate force in the LMM was assumed equivalent to the force generated by the spring and dashpot between the input displacement and the foot mass (m_1). Proximal tibia force in the LMM, corresponding to upper tibia force in the Mil-Lx, was calculated using the acceleration of m_2 and the mass above the upper tibia load cell (7.314 kg) which consisted of the leg bracket, mounting plate, and half of the mass of the upper tibia load cell. The same group of human leg FE simulation results was used for the optimization, which spanned sinusoidal acceleration frequencies of 5 to 200 Hz.

$$\mathbf{Objective\ Function} = \mathbf{max}\left[\sum_{\mathbf{j=1}}^{\mathbf{m}}\left(\sum_{\mathbf{h=1}}^{\mathbf{n}}\mathbf{CORA_h}\right)_{\mathbf{j}}\right] \qquad \text{Eqn. 7.4}$$

$$\mathbf{CORA_1} = \mathbf{f}[\mathbf{c_1}(\dot{\mathbf{z}}_\mathbf{1} - \dot{\mathbf{z}}_\mathbf{0}) + \mathbf{k_1}(\mathbf{z_1}-\mathbf{z_0}), (\mathbf{F_{footplate}})_{\mathbf{PMHS}}] \qquad \text{Eqn. 7.5}$$

$$\mathbf{CORA_2} = \mathbf{f}[\ddot{\mathbf{z}}_\mathbf{2}(\mathbf{7.314\ kg}), (\mathbf{F_{Prox\ Tibia}})_{\mathbf{PMHS}}] \qquad \text{Eqn. 7.6}$$

The first set of model parameters presented below in Table 7.2 were estimated by optimizing the objective function consisting of the equally weighted sum of footplate and proximal tibia force weighted CORA scores for all input conditions used in the FE parametric study. Masses were fixed for the optimization and were based on the mass distal and proximal to the compliant element. The stiffness of k_1, representing the heel pad, was significantly higher than that estimated for the compliant element. Though the model was able to provide a good fit (CORA>0.8) of the human FE model data for one of the two force locations in most cases, particularly frequencies ranging from 5-62 Hz, both forces were not accurately predicted by the model, which was one of the goals for improving the design of the Mil-Lx. Figure 7.21 shows the LMM force response compared to the human FE model response along with CORA scores for each input condition.

Table 7.2. Optimized parameter values for a LMM representing the Mil-Lx based on a fit of the force response of the human FE model for each of the input conditions used in the FE parametric study.

i	m_i (kg)	k_i (kN m^{-1})	c_i (Ns m^{-1})
1	3.245	1251.9	127.4
2	9.300	2315.1	497.1

One observation for the response of the Mil-Lx based LMM is that it tended to provide a better fit of the human FE leg footplate force for lower frequencies (5-150 Hz), for which the average CORA score was 0.95. The CORA scores for proximal tibia force increased for higher frequencies, though the LMM was unable to provide a good fit for either force for the 100g, 2 m-s^{-1} condition. Average CORA score for proximal tibia force was highest among the loading frequencies ranging from 78-195 (avg. CORA=0.91), but was only 0.75 for frequencies less than 78 Hz.

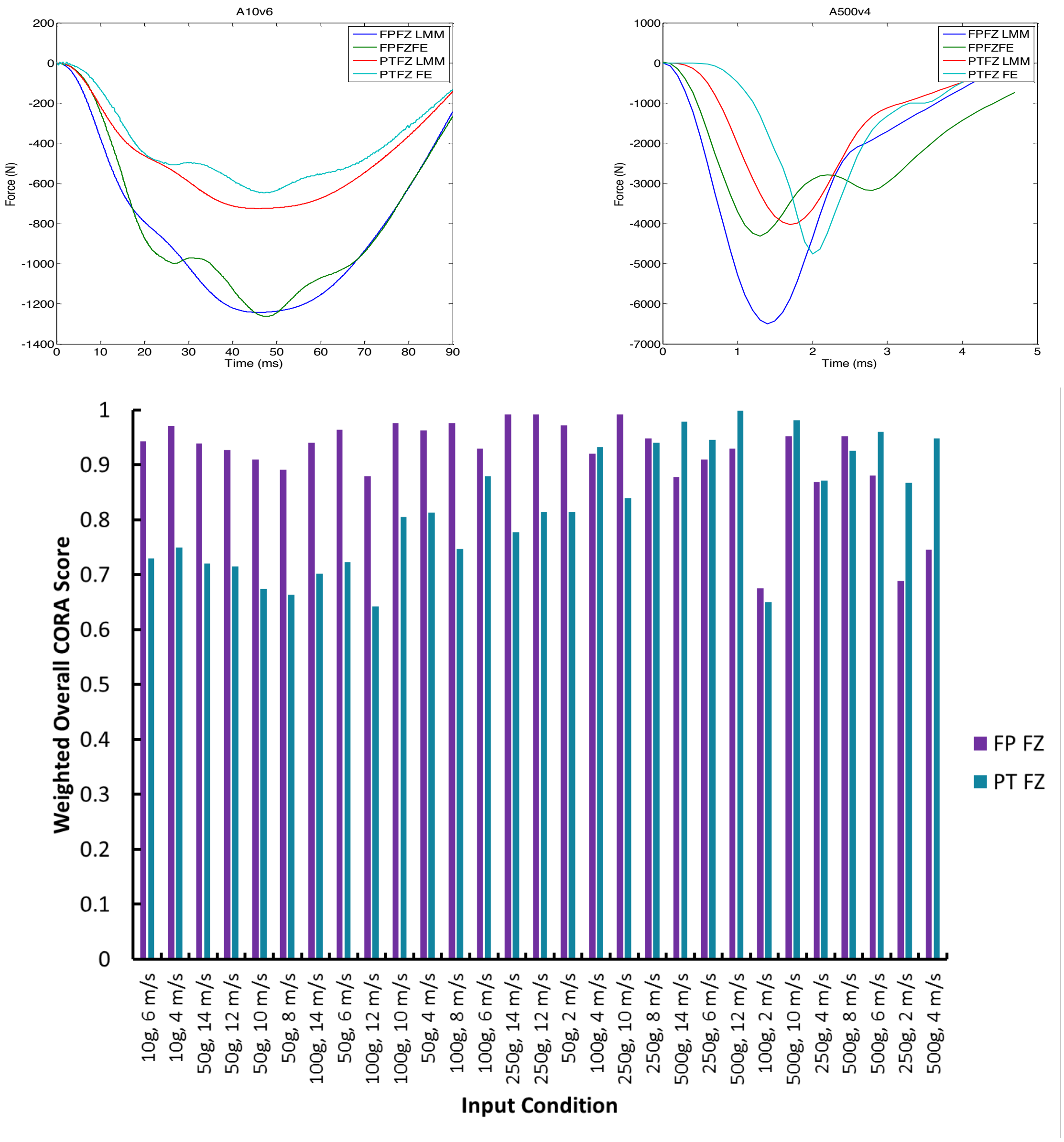

Figure 7.21. Summary of CORA scores for the Mil-Lx LMM optimized using the input conditions from the FE parametric study compared to the human FE model force response at the footplate (FP FZ) and the proximal tibia (PT FZ). LMM parameters are described in Table 7.2. Input conditions are ordered from low to high frequency moving from left to right.

Having observed that the Mil-Lx based LMM was unable to model the response of the human leg for the entire range of input conditions, the range of frequencies used to fit the LMM was reduced in order to potentially improve the fit for a smaller range of frequencies.

A second set of model parameters (presented below in Table 7.3) were estimated using only the high frequency (>100 Hz) input conditions to train the model and using an equal weighting of footplate and proximal tibia force CORA scores in the objective function. Masses were fixed for the optimization and were again based on the mass distal and proximal to the compliant element. Weighted overall CORA scores for the footplate force and proximal tibia forces are presented in Figure 7.22.

Table 7.3. Parameters for a LMM representing the Mil-Lx based on a fit of the high frequency (97.6-390 Hz) force response of the human FE model.

I	m_i (kg)	k_i (kN m^{-1})	c_i (Ns m^{-1})
1	3.245	1122.2	78.1
2	9.300	4326.5	256.4

The average CORA score for the footplate force was 0.89 for the input conditions with frequencies greater than 100 Hz, but only 0.70 for frequencies below 100 Hz. Optimizing the model over a smaller range of frequencies increased the fit of the footplate and proximal tibia forces from average CORA scores of 0.86 and 0.89 to 0.89 and 0.90, respectively, compared to the model described by Table 7.2. As expected, the fit for the loading frequencies less than 100 Hz decreased from average CORA scores for footplate and proximal tibia forces from 0.95 and 0.77 to 0.89 and 0.70, respectively. Optimizing over this smaller range of frequencies, however, did provide a statistically significant improvement in model fit for the smaller range of frequencies based on a t-test between the average CORA scores for the footplate ($p=0.39$) or for proximal tibia forces ($p=0.16$).

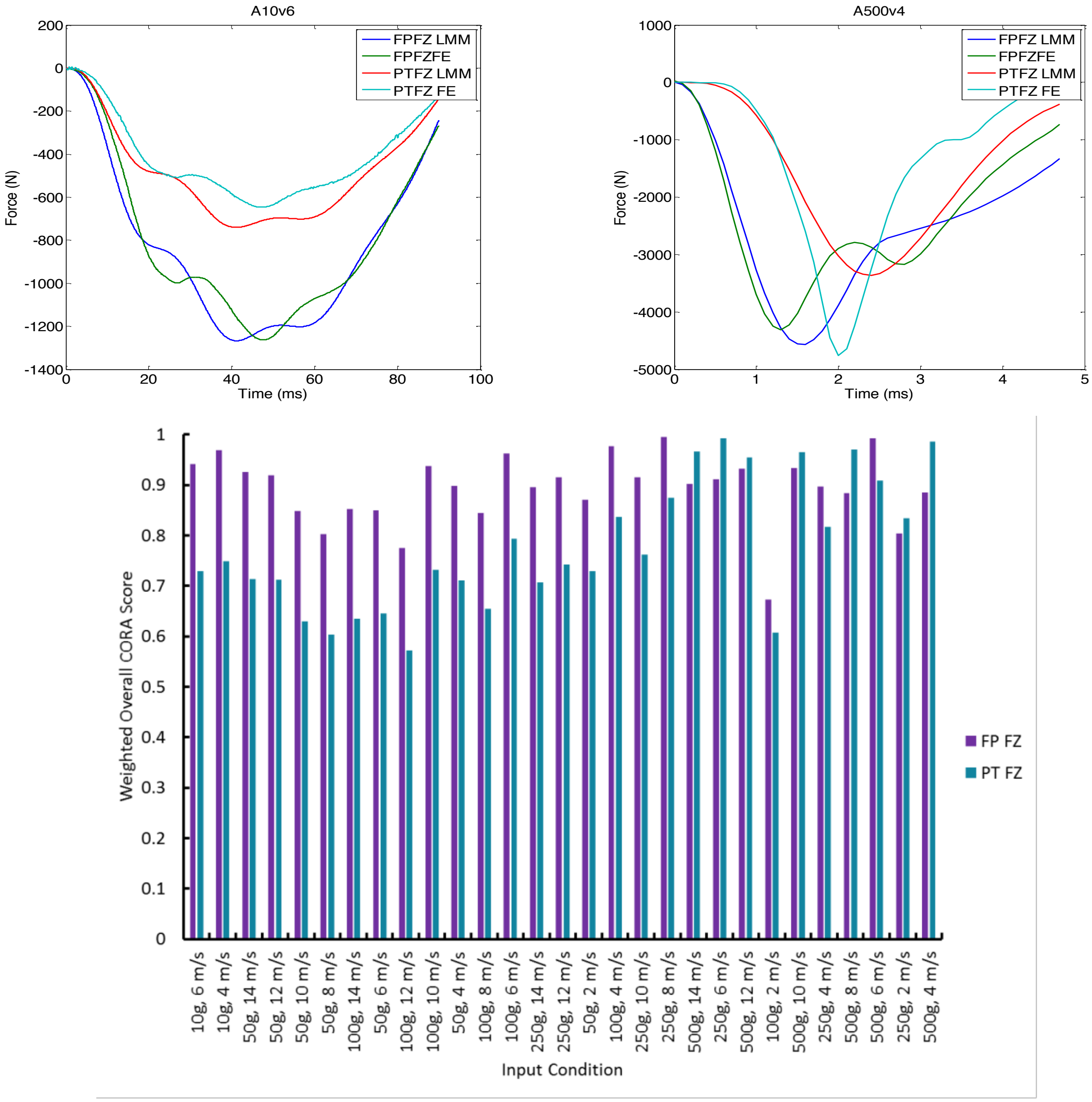

Figure 7.22. Summary of CORA scores for the Mil-Lx LMM optimized using the high frequency input conditions compared to the human FE model force response at the footplate (FP FZ) and the proximal tibia (PT FZ). LMM parameters are described in Table 7.3.

Next, a new set of LMM parameters were identified using only loading frequencies less than 100 Hz to fit the model parameters. This set of model parameters is presented below in Table 7.4, and was generated in order to compare the model's tendency to fit human response for low versus high frequency loads. If the model fit improved significantly for the lower frequency fit, then it may be hypothesized that a more complex model must be used to capture the response of the leg for higher loading frequencies.

Table 7.4. Optimized parameter values for a LMM representing the Mil-Lx based on a fit of the low frequency (5.0-97.6 Hz) force response of the human FE model.

i	m_i (kg)	k_i (kN m^{-1})	c_i (Ns m^{-1})
1	3.245	1460.0	492.8
2	9.300	5638.8	571.3

For the loading frequencies less than 100 Hz, the fit of the LMM footplate forces significantly improved (0.76 to 0.86), but the fit of the proximal tibia forces significantly (p=0.002) decreased from an average CORA score of 0.95 to 0.86. From an overall standpoint, decreasing the range of frequencies used to fit the model did not provide an advantage over the first model, which provided a slightly worse fit over twice the range of loading frequencies.

From this exercise, it seems that the current mass distribution of the Mil-Lx is predisposed to provide a better estimate of footplate force for low loading frequencies, and a better estimate of proximal tibia force for higher frequency loads. This is likely due to the fact that as the human leg is impacted, the mass of the foot is readily recruited, but the compliance in the ankle joint delays the recruitment of the tibia mass until a larger displacement is reached. In the case of the Mil-Lx mass distribution, there is a larger mass distal of the compliant element, which is recruited along with the foot mass. At high loading frequencies, the Mil-Lx LMM recruits a much larger mass than the human leg, leading to inaccurate footplate forces. At lower frequencies, with larger footplate displacements, both masses are recruited, but the LMM proximal tibia force is less than the human proximal tibia force since there is less mass reacting against the compliant element than reacts against the ankle compliance in the human leg.

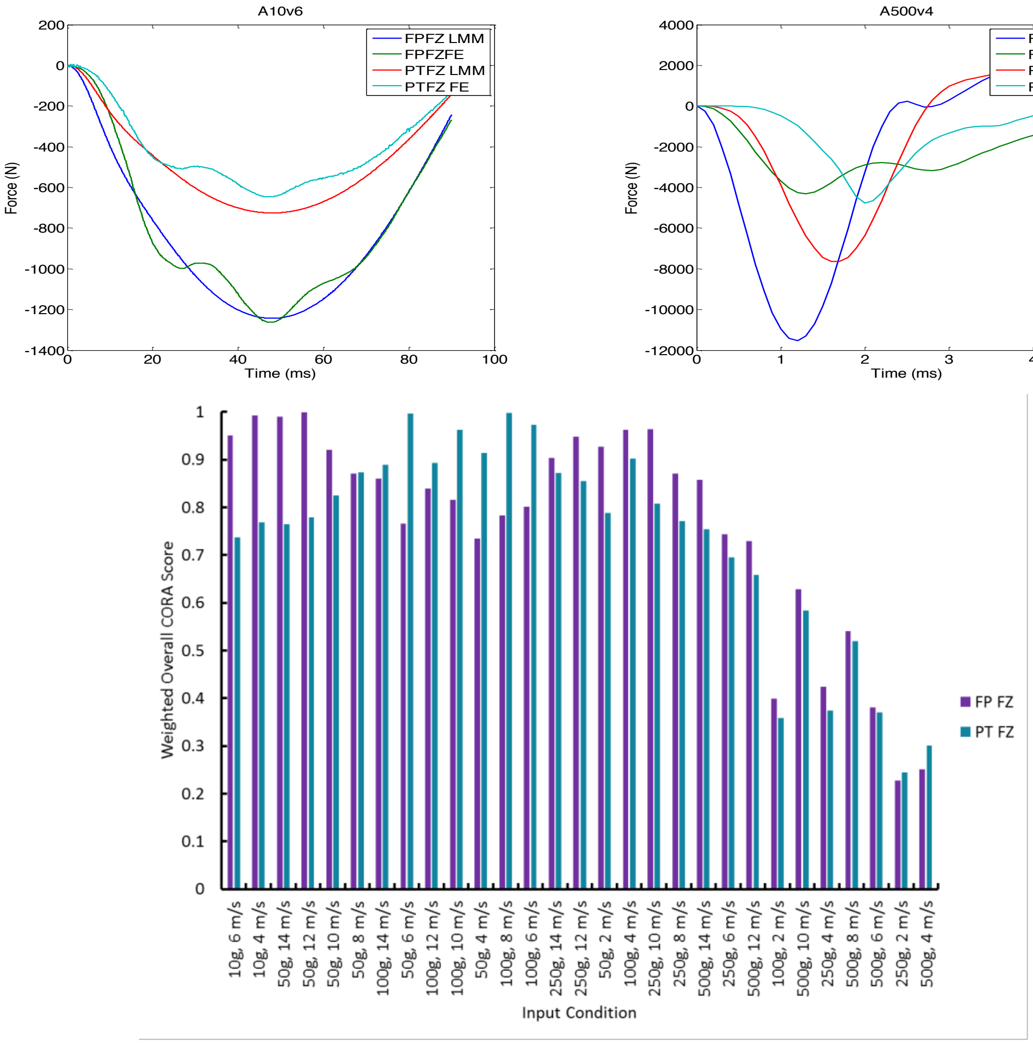

Figure 7.23. Summary of CORA scores for the Mil-Lx LMM optimized using the low frequency input conditions compared to the human FE model force response at the footplate (FP FZ) and the proximal tibia (PT FZ). LMM parameters are described in Table 7.4.

Because of the difficulty fitting both the footplate and proximal tibia forces, the objective function was then weighted toward maximizing the CORA score for the footplate force. The footplate force CORA score was given a weight of 3 times the weight of the proximal tibia force CORA score, and the optimization was performed using all 28 input conditions. For this model, it was assumed that the Mil-Lx flesh mass was divided evenly between m_1 and m_2. Not surprisingly, this model provided the best fit of footplate force, with the weighted overall CORA score being greater than 0.8 for all except four conditions, which had frequencies of greater than 195 Hz. Since the goal was to provide accurate injury prediction for frequencies of 5-200 Hz, this simplified formulation of the Mil-Lx would nearly fulfill these requirements.

Table 7.5. Parameter values for a LMM representing the Mil-Lx optimized to fit the force response of the human FE model and weighted toward matching the footplate force response for all 28 inputs.

i	**m_i (kg)**	**k_i (kN m^{-1})**	**c_i (Ns m^{-1})**
1	3.245	1292.1	37.3
2	9.300	258.03	643.5

The parameters summarized in Table 7.5 provide an improvement in the fit of the footplate force compared to the previous models. The average CORA score for the footplate force was 0.92 for the entire set of loading conditions, and 0.94 for the conditions with frequencies ranging from 5-195 Hz. Plantar force average CORA score was 0.84 for the same range of frequencies. Both footplate and proximal tibia force CORA scores were above 0.8 for the set of inputs with frequencies ranging from 31-130 Hz. As with the first set of optimized parameters, proximal tibia force was underestimated for the low frequency inputs.

The parameters for k_1 and c_1 are similar to those estimated for the model based on the human leg mass distribution. The k_2 value, however, was approximately a quarter of the stiffness associated with the human leg LMM. This difference in the stiffness of k_2 was necessary to provide the same proximal tibia force response because of the difference in the mass distribution between the human and Mil-Lx legs. Again, this highlights the fact that the tibia compliant element should be moved to a more distal location in order to represent ankle compliance since the human tibia is much stiffer than the ankle joint.

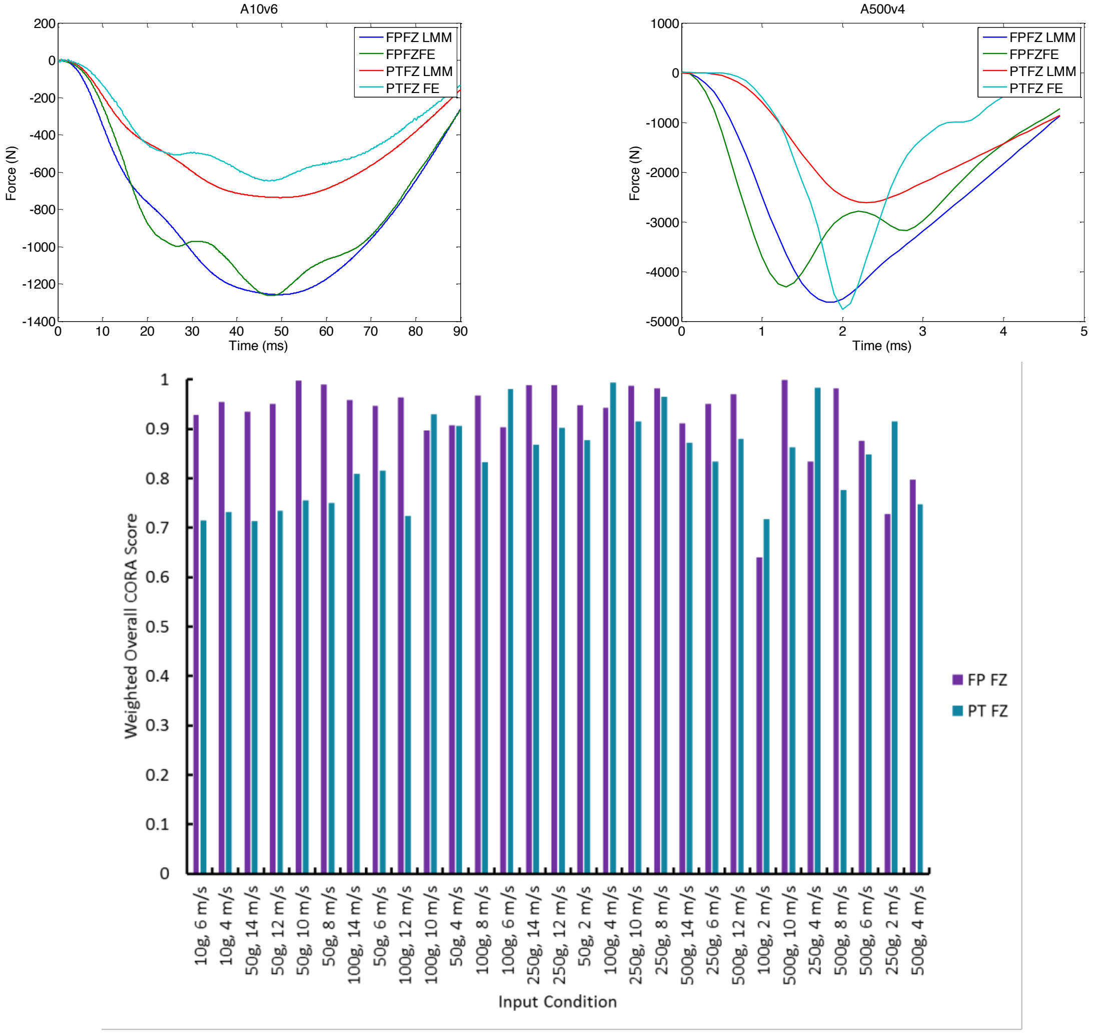

Figure 7.24. Summary of CORA scores for the Mil-Lx LMM optimized using all 28 input conditions compared to the human FE model force response at the footplate (FP FZ) and the proximal tibia (PT FZ). LMM parameters are described in Table 7.5. The objective function for this optimization was based on matching footplate force only.

The results of the comparison of LMM response to PMHS response show that while the current configuration of the Mil-Lx is incapable of providing biofidelic plantar force measurements, if the Mil-Lx were modified to match the compliances of the LMM it may provide a more biofidelic response for plantar force in order to be used with the proposed force and impulse-based injury criterion. Based on the LMM analysis, it seems that producing biofidelic plantar and proximal tibia forces for the entire range of impact conditions used is beyond of the abilities of the current configuration of the Mil-Lx because of the placement of the compliant puck. The larger mass located distal to the compliant element leads to different patterns of double hits compared to the human leg. Other potential configurations of springs and dashpots may be used to model different material properties in the Mil-Lx, but for simplification purposes, these were not considered in this preliminary effort to model the Mil-Lx.

Results of this preliminary LMM analysis suggest that the current Mil-Lx design can only provide a good fit of one of the two forces across footplate acceleration durations of 2.5-100 ms. The current configuration should be able to provide accurate results for both proximal tibia and footplate force for durations ranging from 3.8-16 ms. The following section will utilize a finite element model of the Mil-Lx to perform as similar study to attempt to increase the range of frequencies for which the Mil-Lx can provide biofidelic plantar and proximal tibia forces.

7.4 Finite Element Model of the Mil-LX

The previous section demonstrated that there are inconsistencies between the human and Mil-lx force response. To better understand the differences between the human leg and the Mil-Lx for a larger range of load durations, a finite element model of the Mil-Lx was utilized. A NASTRAN axisymmetric Mil-Lx model developed by Newell et al. was translated into a 3-dimensional model in LS-Dyna V971 R6.1.1 (LSTC, Livermore, CA) (Figure 7.25).[148]

The model consisted of five materials, including three hyper-elastic rubber materials and two elastic materials.

Several modifications were made to the Newell et al. model. First, the model geometry was re-meshed to incorporate smooth transitions between cylindrical parts and improve mesh quality using Hypermesh (Altair, Troy, MI). Secondly, the full geometry of the foot and ankle was added to the model. The geometry from the LSTC Hybrid-III leg was sectioned proximal to the lower tibia load cell and added to the model. The Mil-Lx ankle, modeled as a single part in the Newell et al. model, was modeled using a spherical joint between the ankle shaft and the steel portion of the lower tibia shaft. The rotational stiffnesses and damping as well as the joint stops were defined using the same criteria as are used for the Hybrid-III ankle (Table 7.6). Since the foot and ankle structure of the Hybrid-III was reused in the Mil-Lx design, this was considered a valid approach to improving the Newell et al. model of the Mil-Lx. Lastly, the mass of the leg flesh was added by increasing the density of the aluminum tibia shaft and the steel portion above the upper tibia load cell since this mass was omitted from the Newell et al. model.

Table 7.6. Specifications for the spherical ankle joint including stiffness, damping, and stop angle.

Joint Axis	**X**	**Y**	**Z**
Joint Stiffness (kN-rad^{-1})	500.00	500.000	500.000
Joint Damping (kN-rad^{-1}ms^{-1})	1.44	1.36	1.36
Stop Angle (rad)	±45.00	±23.00	±23.00

Mesh density of the foot flesh and heel pad was increased because of the proximity to the application of the load and because of the potential for large deformations in these materials. Overall mesh density of the model was increased from the original Newell et al. model and mesh quality was improved by using a consistent mesh throughout the cylindrical portion of the model. To ensure that mesh density did not affect the results of the model, the mesh density was doubled and compared against the less-dense modified mesh. Less than a 3 percent difference was noted for the peak upper tibia force and the peak footplate force for the two models when subjected to a prescribed footplate acceleration of 500g with a peak velocity of 10 m-s^{-1}.

The modified model (Figure 7.25) is comprised of 16 parts, 114,148 elements, with a total mass of 5.21 kg for the leg, not including the mass of the knee bracket, which was lumped into the mass of the mounting block. For replication of experimental boundary conditions, the Mil-Lx model was incorporated into a model which included a rigid impacting plate (50 kg), and a reaction mass consisting of a rectangular mounting block which included the mass of the experimental mounting block (1.88 kg), plus the mass of the Mil-Lx knee bracket (0.22 kg), and a reaction plate (5.8 kg).

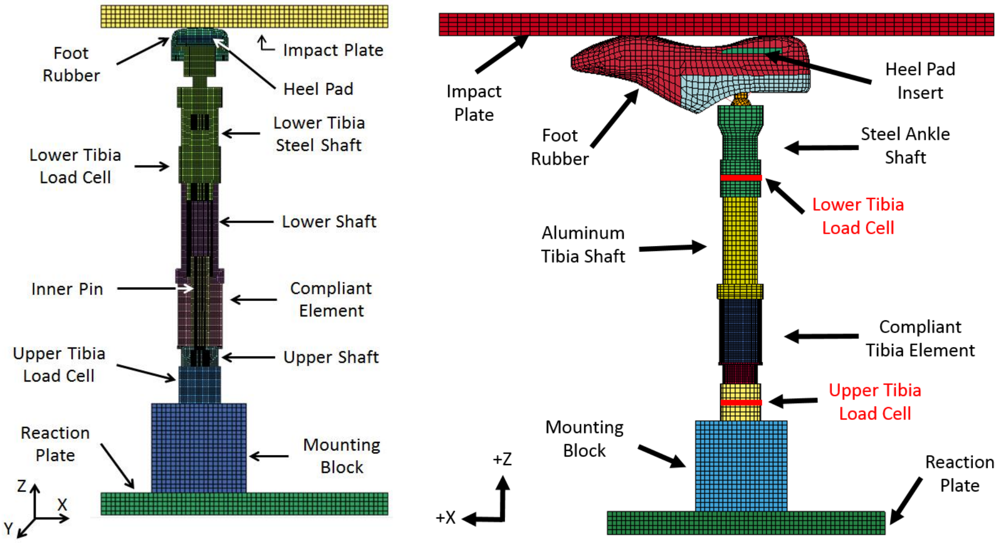
Foot Rubber
Impact Plate
Heel Pad
Lower Tibia Steel Shaft
Lower Tibia Load Cell
Lower Shaft
Inner Pin
Compliant Element
Upper Tibia Load Cell
Upper Shaft
Reaction Plate
Mounting Block
Z
X
Y
Impact Plate
Heel Pad Insert
Foot Rubber
Steel Ankle Shaft
Lower Tibia Load Cell
Aluminum Tibia Shaft
Compliant Tibia Element
Upper Tibia Load Cell
Mounting Block
+Z
+X
Reaction Plate

Figure 7.25. Three-dimensional LS-Dyna finite element model of the Mil-Lx ATD leg adapted from the NASTRAN model developed by Newell et al. The figure on the left shows the re-meshed axisymmetric model with the original geometry from Newell et al., and the figure on the right shows the final modified Mil-Lx model for which the geometry of the foot was added.[148]

The masses of individual parts of the model compared to the masses measured from the physical Mil-Lx leg are shown in Table 7.7. Parts which included the mass of the leg skin are indicated. The mass was divided such that half of the mass was located distal to the upper tibia load cell and half was located proximal to the upper tibia load cell. A sensitivity study was performed to show the effect of this assumption of mass distribution. Since the Mil-Lx leg was not completely disassembled, the total mass of the foot and compliant element assembly are reported rather than individual pieces. The density of the mounting block which was used in the experimental Mil-Lx drop tower tests was increased slightly to account for the mass of the knee mount bracket which was not explicitly modeled. Upper and lower tibia load cells were incorporated using DATABASE_CROSS_SECTION_SET, and contact force between the foot flesh and impactor plate was used to estimate plantar or footplate force in the model.

Original material properties for the Newell et al. Mil-Lx FE model are provided in Table 7.8 for the Mooney-Rivlin strain energy density (Eqn. 7.7) and relaxation (Eqn. 7.8) functions. Since the Hyper-elastic material model which incorporates relaxation uses a different formulation than the material model from NASTRAN, the stress-strain and relaxation curves provided in Newell's dissertation were used to generate the material parameters for the form used in LS-Dyna. The LS-Dyna material model parameters are summarized in Table 7.9.

Table 7.7. Mil-Lx FE model part masses compared to actual part masses

Part	FE Mass	Physical Mass	Material
Impactor	49.832	50	Aluminum
Base Plate	5.795	5.8	Aluminum
Aluminum Tibia	0.834*	0.413	Aluminum
Steel Lower Tibia	1.262[#]*	1.157[#]	Steel
Upper Aluminum	0.060	0.442	Aluminum
Aluminum Inner Pin	0.159		Aluminum
Compliant Element	0.121		CE Rubber
Steel Upper	0.463	0.463	Steel
Foot Heel Pad	0.030	0.030	Heel Pad Rubber
Foot Foam	0.767	1.119	Foot Rubber
Foot Skin Upper	0.032		Foot Rubber
Foot Plate	0.202		Steel
Foot Cylinder	0.173		Steel
Ankle Shaft	0.054		Steel
Skin	-	1.053	N/A
Pot	2.610[#]	1.860	N/A
Knee Bracket		0.223	N/A
Total Mass	12.562	12.560	

[#] Includes mass of the lower tibia load cell

* Includes part of the mass of the leg skin (50% tibia, 50% pot)

-CE=compliant element

$$W = \sum_{m=0}^{N}\sum_{n=0}^{N} c_{mn}(I_1 - 3)^m \, (I_2 - 3)^n \qquad \text{Eqn. 7.7}$$

$$R(t) = 1 - \sum_{n=1}^{N} \delta_n \left[1 - e^{\left(-t/\lambda_n\right)}\right] \qquad \text{Eqn. 7.8}$$

Table 7.8. Material parameters for the rubber materials in the Mil-Lx used in the Newell et al. Mil-Lx FE model developed by Newell et al.[148]

Hyper-elastic Coefficients						
Parameter (MPa)	**Heel Pad**		**Foot Rubber**		**Compliant Element**	
C10	1.934		0.029		3.181	
C01	-0.915		-0.011		0.000	
C11	-1.613		-2.067		0.000	
C20	2.373		3.017		-0.307	
C30	0.446		0.523		0.090	
Relaxation Parameters						
n	**λ (s)**	**δ**	**λ (s)**	**δ**	**λ (s)**	**δ**
1	0.120	0.214	0.0949	0.218	0.072	0.214
2	1.96	0.149	1.29	0.168	0.657	0.137
3	23.1	0.147	16.20	0.157	4.500	0.127
Density (g-cm^{-3})	1.08		1.15		1.25	

The *Mat_Hyperelastic_Rubber material card was first used to generate coefficients for hyper-elastic material models, but yielded coefficients which produced unstable results. Next, the *Mat_Ogden_Rubber material card was used to fit the model parameters using the stress-strain and relaxation curves for the materials. Up to three sets of coefficients (α, μ) were fit for each material, and the fits were compared and are shown in Figure 7.26. The number of parameters for the models was selected based on the assessment of stability of the model, as well as the root mean squared error (RMSE) of the model fit to the experimental stress-strain data are provided in Table 7.9. Relaxation parameters were also fit to the data using the guidance provided by Newell's dissertation, and are shown in Table 7.9.

Table 7.9. Material parameters for the rubber materials used in the LS-Dyna Mil-Lx FE model using *Mat_Ogden_Rubber.

	Hyper-elastic Coefficients					
	Heel Pad		**Foot Rubber**		**Compliant Element**	
i	**μ_i (ms^{-1})**	**α_i (MPa)**	**μ_i (ms^{-1})**	**α_i (MPa)**	**μ_i (ms^{-1})**	**α_i (MPa)**
1	1.83e-3	2.84	8.47e-3	5.34	1.92e-1	1.92e-2
2	1.10e-5	10.53	-9.69e-3	4.47	2.09e-4	5.06
3						
	Relaxation Parameters					
	Heel Pad		**Foot Rubber**		**Compliant Element**	
i	**β_i (ms^{-1})**	**G_i (MPa)**	**β_i (ms^{-1})**	**G_i (MPa)**	**β_i (ms^{-1})**	**G_i (MPa)**
1	0.00	4.55e-3	0.00	2.86e-3	0.00	1.13e-2
2	0.10	0.00	0.10	0.00	0.10	0.000
3	1.00	3.22e-3	1.00	2.03e-3	1.00	8.09e-3
Density (g-cm^{-3})	1.08		1.15		1.25	

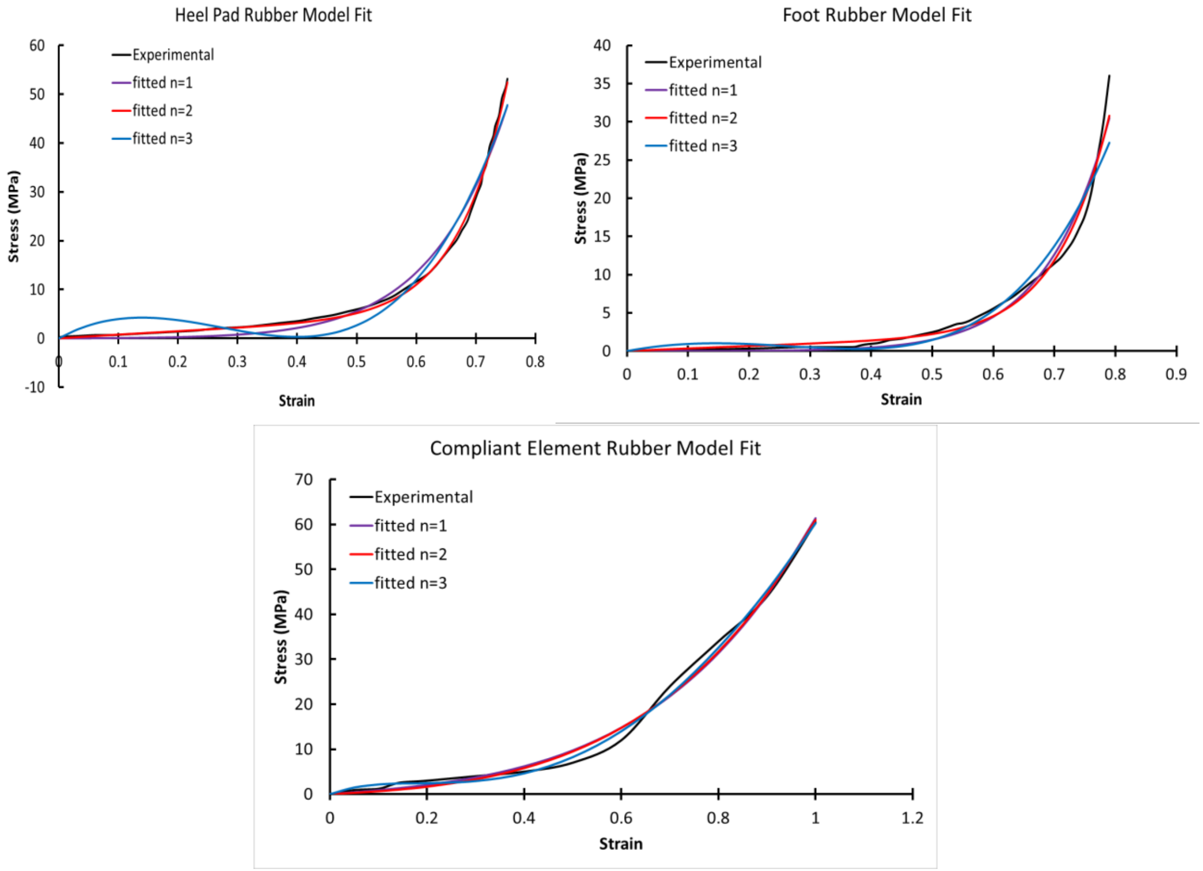

Figure 7.26. LS-Dyna material model fits compared to the experimental response of the Mil-Lx rubber from Newell et al.[148]

Equations for the strain energy density (W) and relaxation (g) as defined in the LS Dyna User's Manual for the Ogden Rubber material card are provided in Eqn. 7.9 and Eqn. 7.10, respectively.[92]

$$\mathrm{W} = \sum_{\mathrm{i}=1}^{3} \sum_{\mathrm{j}=1}^{\mathrm{n}} \frac{\mu_i}{\alpha_j} ({\lambda_i}^{\alpha_j} - 1) + K(\mathrm{J} - 1 - \ln(\mathrm{J})) \qquad \text{Eqn. 7.9}$$

$$\mathrm{g(t)} = \sum_{\mathrm{i}=1}^{\mathrm{N}} \mathrm{G_i e^{(-\beta_i t)}} \qquad \text{Eqn. 7.10}$$

A combination of Automatic_Surface_to_Surface and Tied_Nodes_to_Surface contacts were used in the model to interface between different model parts. Guidance for the type of contact was taken from Newell's dissertation where contacts were described as either "touching" or "glued." Tied contacts were placed between the structures that were designated as "glued" and automatic contacts were placed between other structures (Figure 7.27).

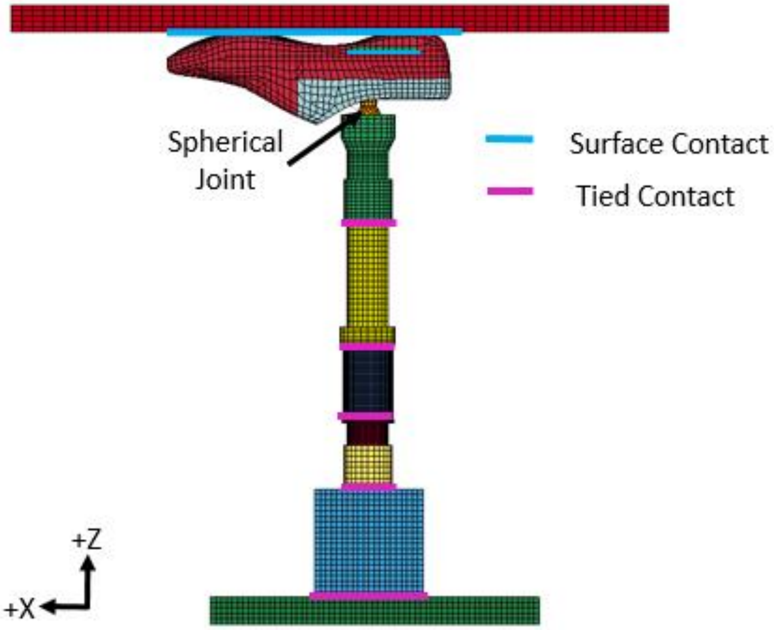

Figure 7.27. Diagram summarizing the location of different contact types used in the Mil-Lx model.

7.4.1 Benchmarking Mil-Lx FE Model Response

The LS-Dyna Mil-Lx model was then benchmarked using available test data from the tests described in Section 7.2.2. The experimental drop tower tests were simulated using the Mil-Lx FE model by prescribing footplate acceleration in order to benchmark the model's response to vertical impact loading. Figure 7.28 shows the response of the Mil-Lx FE model compared to the experimental results for displacements of the proximal tibia and tibia shaft as well as upper and lower tibia forces.

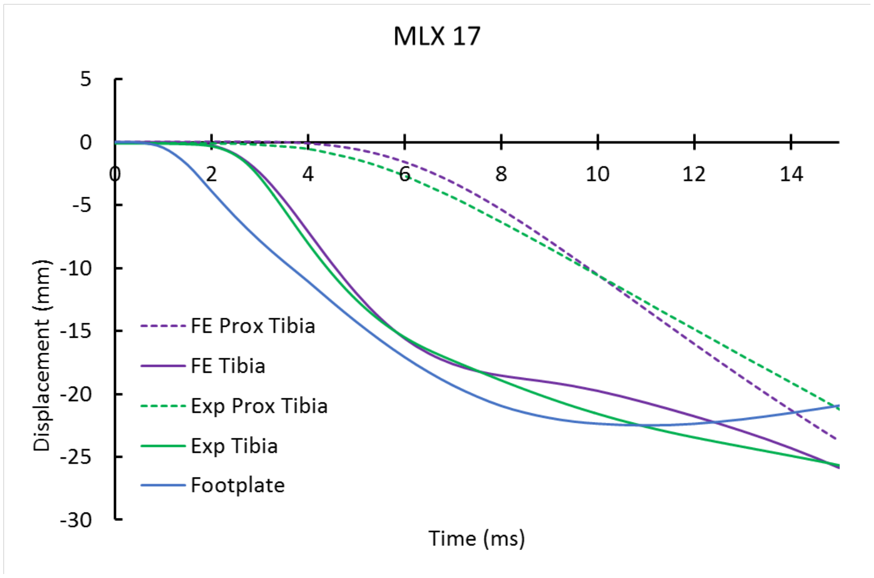

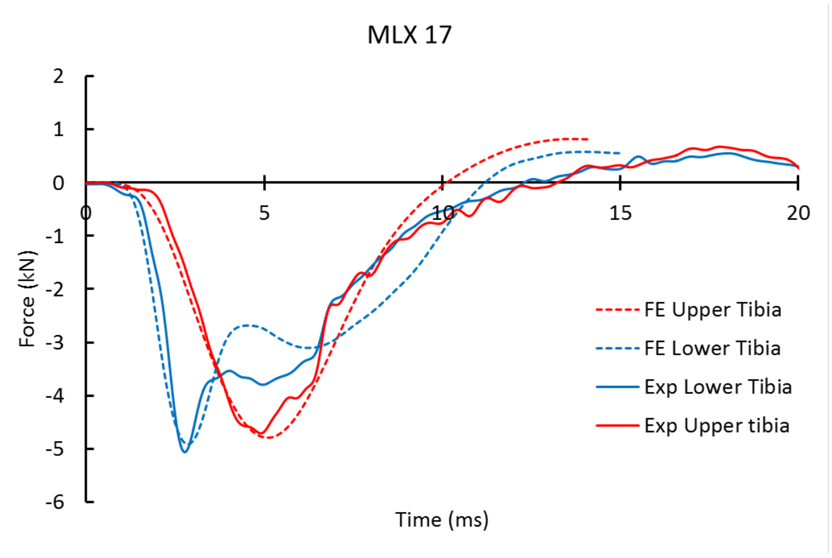

Figure 7.28. Mil-Lx experimental versus FE model response for the drop tower MLX 17 test condition. Displacements are shown on the left and forces for upper and lower tibia are shown on the right.

CORA scores were calculated for upper and lower tibia forces comparing the model and the experimental results to quantify the accuracy of the FE model. These scores are provided in Table 7.10. Scores were highest for the upper and lower tibia forces. The Mil-Lx model demonstrated excellent ability to replicate the force loading phase, however, the FE model tibia compliant element relaxed faster than for the actual Mil-Lx. This caused slightly inaccurate behavior of the relaxation of the upper and lower tibia forces. The weighted overall CORA score for the loading portion of the time-history was 0.90 compared to 0.75 for the unloading portion. Displacements for the tibia shaft and proximal tibia pot were also compared using CORA as a method of ensuring that the model's materials were behaving as expected in the overall model. These CORA scores were greater than 0.825, which was considered satisfactory for the model considering that the displacements were calculated using the accelerometer data from the experimental tests. Again, the relaxation characteristics of the materials, particularly the tibia compliant element, affected the overall performance of the model. Despite the shortcomings in terms of relaxation, the model was deemed acceptable for use in later simulations because of its ability to accurately predict the loading phase and the peak forces in the tibia, which is of particular interest in terms of predicting injury risk using the proposed injury risk function.

Table 7.10. Summary of average CORA scores for comparison of FE and experimental Mil-Lx forces and displacements.

		Mil-Lx Upper Tibia Force			
Test Condition	**Phase**	**Magnitude**	**Progression**	**Overall**	**Weighted Overall**
Upper Tibia Force	0.836	0.946	0.997	0.926	0.954
Lower Tibia Force	0.964	0.995	0.983	0.980	0.993
Tibia Displacement	1.000	0.792	1.000	0.930	0.825
Proximal Pot Disp.	1.000	0.853	0.998	0.950	0.876

Having demonstrated the Mil-Lx FE model's ability to match the displacement and force behavior of the Mil-Lx for the drop tower conditions, the next step was to assess its ability to match the forces in the human leg for the range of loading conditions applicable to UBB and

AI. To better understand the range of loading frequencies for which the Mil-Lx leg provides biofidelic responses, the Mil-Lx finite element model proximal tibia force and footplate force were compared to the force response of the previously-validated UVA human leg model.[78] The Mil-Lx model was subjected to footplate acceleration inputs matching those from the parametric study performed using the human FE model. Human and Mil-Lx FE model forces at the proximal tibia and footplate were then compared using the weighted overall CORA score.

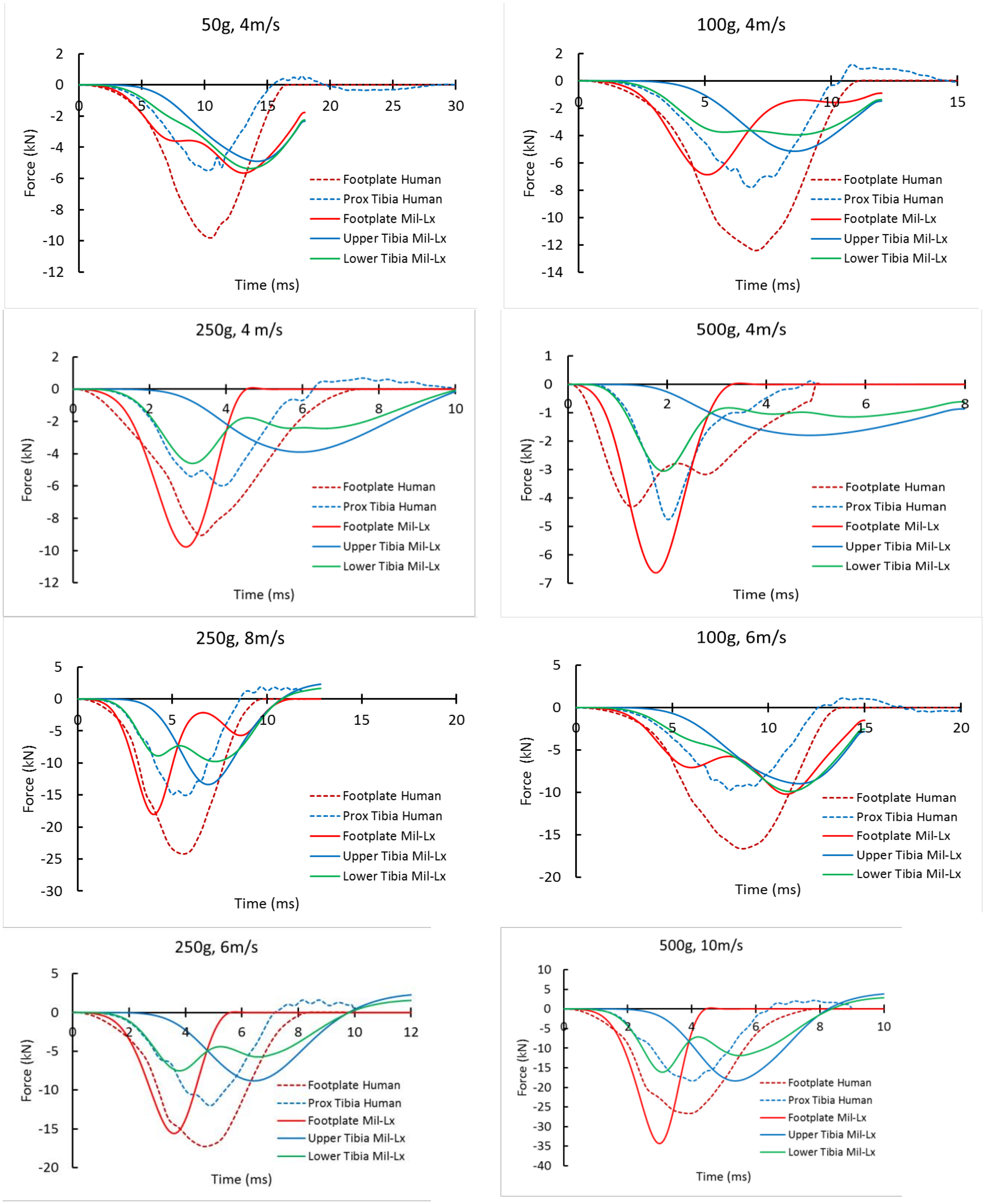

Figure 7.29. Mil-Lx FE model response compared to human leg FE model response for select conditions from the parametric study.

The FE model comparison showed that the Mil-Lx was unable to match the human FE model response for both footplate and proximal tibia forces. In all cases, the Mil-Lx upper tibia force lagged behind the human proximal tibia force because of the compression of the compliant element in the Mil-Lx tibia. For some of the higher velocity test conditions, the lower tibia force magnitude and shape reasonably matched the human tibia force, though a phase shift was present. Because of the obvious phase shift between the Mil-Lx upper tibia force and the human tibia forces, the curves were shifted to align peak force before the CORA scores were calculated.

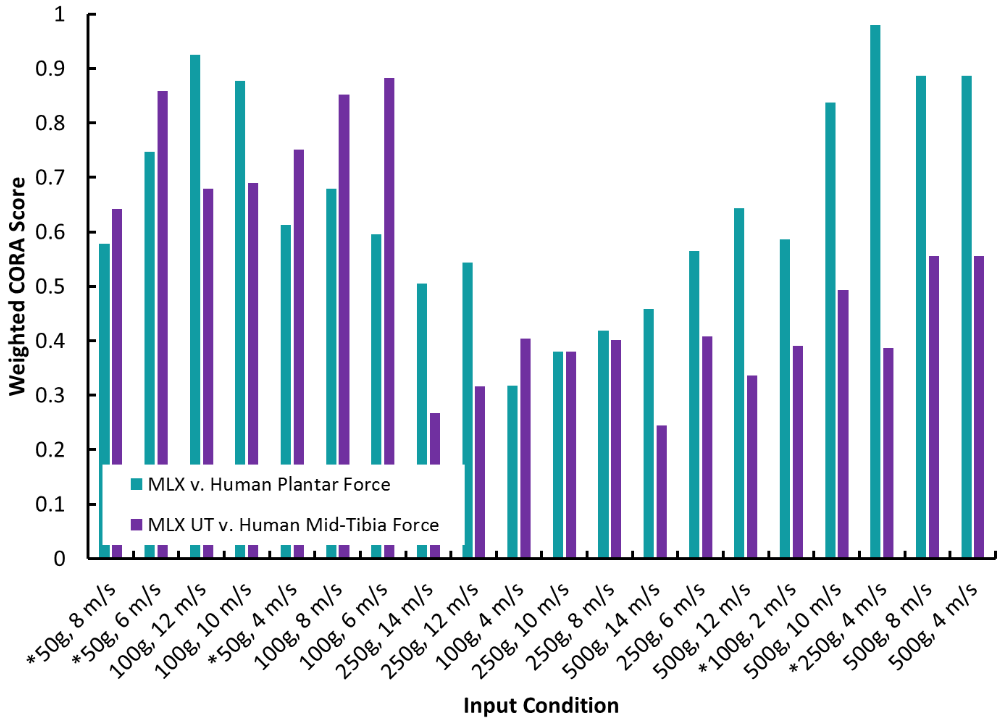

Figure 7.30. CORA scores for Mil-Lx FE model response compared to human FE model response for sinusoidal acceleration pulses described by peak acceleration and peak velocity.

Higher CORA scores were calculated for the load durations greater than 9.6 ms, though few scores exceeded 0.8. Surprisingly, CORA scores for plantar force were highest for loading durations less than 3.2 ms. Mid-tibia forces were severely under-predicted for this range of frequencies, with average CORA scores of less than 0.5. Overall, the original Mil-Lx model provided a poor fit of the human leg FE model forces in terms of CORA scores and was unable to produce biofidelic results at both the footplate and upper tibia.

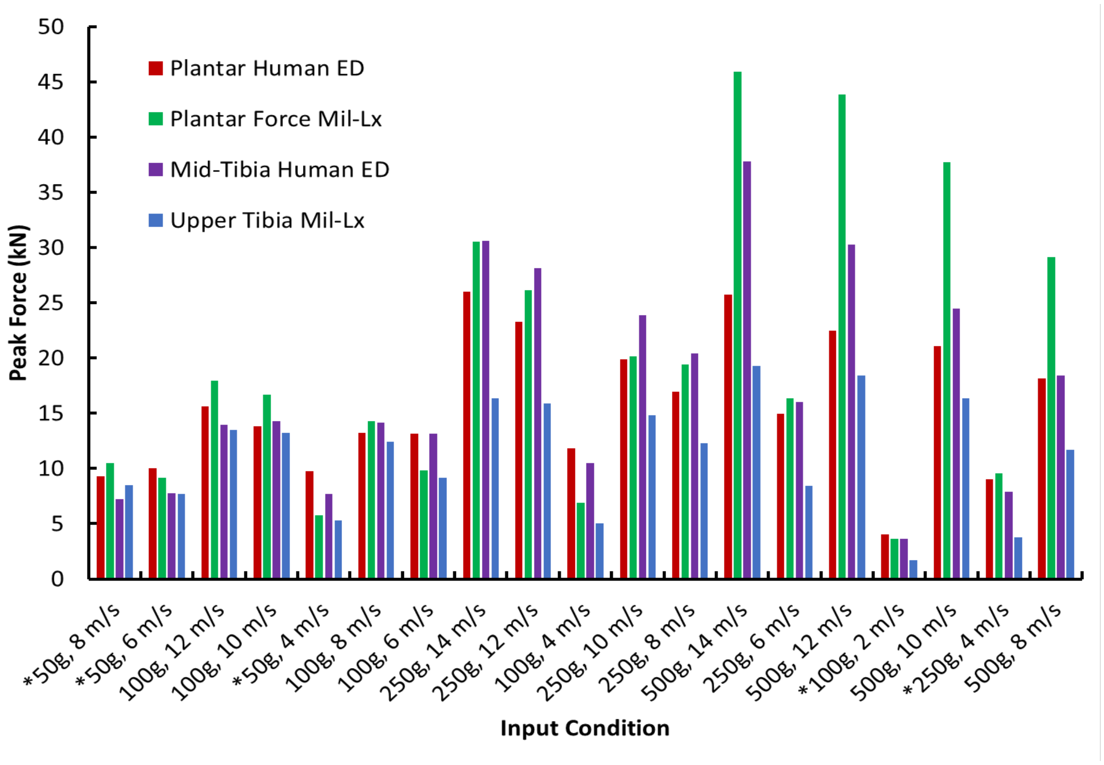

Figure 7.31. Peak force comparison for the plantar force and upper/mid-tibia force for the human FE model with element deletion (ED) compared to the Mil-Lx FE model.

Peak forces for the footplate, mid-tibia, and proximal tibia locations were tabulated and compared for the human leg FE model and the Mil-Lx FE model (Figure 7.31). Both CORA scores and peak forces showed that the Mil-Lx provides a poor estimation of human plantar and mid-tibia force across this spectrum of loading frequencies. For durations greater than

12.8 ms, the Mil-Lx provided a reasonable estimate of peak human mid-tibia force with an average error of 1.2 kN. Average error in mid-tibia force estimate increased to 8.3 kN for durations greater than 12.8 ms. One important note is that the Mil-Lx was designed to match the mid-tibia force response for a single 7 m-s^{-1} loading condition. Subsequent benchmarking of the Mil-Lx was performed using PMHS data from unknown loading frequencies and using PMHS data for which fracture occurred. Though Figure 7.31 compares the Mil-Lx force to the forces from the human model with element deletion, it is likely that the post-fracture human model behavior is not correct. Regardless, the lack of fracture in the Mil-Lx should lead to higher forces measured in the Mil-Lx than the human, which is not the case for the input conditions shown in Figure 7.31.

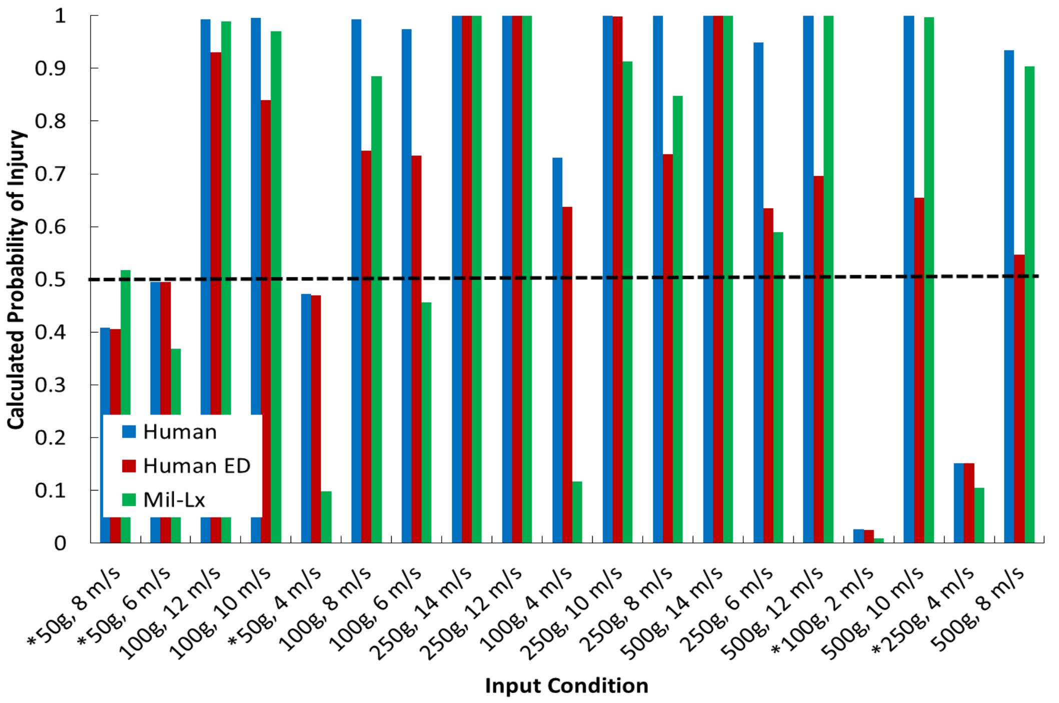

Figure 7.32. Probability of injury estimated using the force-impulse injury risk function and the forces and impulses estimated by the original Mil-Lx FE model and the human FE model with and without element deletion (ED).

Probability of injury calculated using the force-impulse injury risk function for the Mil-Lx model compared to the human FE model showed that the Mil-Lx provided a poor estimation of injury risk (Figure 7.32). This result was expected based on the fact that the plantar forces and impulses for the human leg were not accurately estimated by the Mil-Lx. No pattern was observed in terms of a frequency-dependence of the Mil-Lx's ability to estimate injury risk.

7.5 Optimization of Mil-Lx Biofidelity using Finite Element Modeling

To improve the biofidelity of the Mil-Lx, the FE model was used to optimize the material properties of the ATD such that both plantar and proximal tibia force for the human could be predicted by the Mil-Lx. From the process of optimizing the performance of the LMM of the Mil-Lx, we see that there are obvious limitations in terms of the range of loading frequencies for which the Mil-Lx can provide a reasonable estimate of human response. Changing the configuration of the Mil-Lx so that the majority of the compliance of the leg is located near the foot and ankle could potentially improve the leg's performance in terms of providing biofidelic force response at proximal and distal locations. Ideally, the mass and compliance distribution in the Mil-Lx should match that of the human leg, which is recommended for future design of ATD legs; however, fully redesigning an ATD is both financially expensive and time-consuming. Instead, the FE model will be used to determine the material properties for the tibia compliant element and heel pad such that the Mil-Lx can produce biofidelic forces at both the plantar surface of the foot (for using the proposed injury risk function) and also at the proximal tibia for an expanded range of loading frequencies.

For this optimization, the parameters necessary for the FE model of the Mil-Lx to produce force responses to match the human FE model response were identified for five sine wave acceleration inputs, equally spaced within the design space in terms of amplitude and frequency (Table 7.11). The optimization routine used methods similar to a study by Putnam et al., which used a combination of LS-Dyna and Isight optimization software in order to base model fit on CORA scores.[169] Instead, a custom MATLAB script was written to interface with LS-Dyna to iteratively update material properties using a reduced gradient algorithm and simultaneously run Mil-Lx FE simulations on the Center for Applied Biomechanics computational cluster. Five input conditions were simulated using the Mil-Lx finite element model. LS-Prepost was then used to process plantar and upper tibia forces from each of the five models. Next, a Matlab function was used to calculate the CORA scores for each of the model forces compared to the human FE model forces for the same five conditions. The value of the objective function (Eqn. 7.12), which combined an evenly weighted sum of the CORA scores (Eqn. 7.11, Eqn. 4.1) for each condition was used with the *fmincon* algorithm in Matlab to generate a new set of material parameters for the next iteration (Figure 7.33).

$$\mathbf{f_i = 0.5 * CORA_{proximal\ tibia\ force} + 0.5 * CORA_{footplate\ force}} \qquad \text{Eqn. 7.11}$$

$$\mathbf{Objective\ Function} = \mathbf{max}\left(\sum_{\mathbf{i=1}}^{\mathbf{n}} \mathbf{w_i f_i}\right) \qquad \text{Eqn. 7.12}$$

$$\sum_{\mathbf{i=1}}^{\mathbf{n}} \mathbf{w_i} = \mathbf{1} \qquad \text{Eqn. 7.13}$$

n=# of test conditions used in the optimization

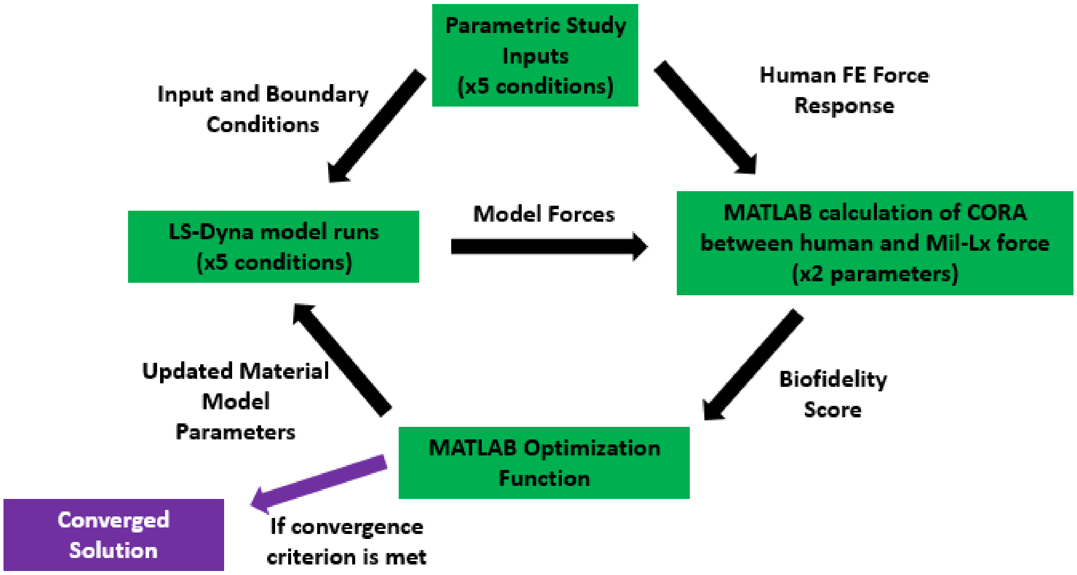
Parametric Study Inputs (x5 conditions)
Human FE Force Response
Input and Boundary Conditions
LS-Dyna model runs (x5 conditions)
Model Forces
MATLAB calculation of CORA between human and Mil-Lx force (x2 parameters)
Updated Material Model Parameters
Biofidelity Score
MATLAB Optimization Function
Converged Solution
If convergence criterion is met

Figure 7.33. Schematic of Mil-Lx design optimization using an integration of MATLAB and LS-Dyna.

Table 7.11. Description of the sinusoidal input pulses used to optimize the FE Mil-Lx model.

Input Pulse ID	Peak Acceleration (g)	Frequency (Hz)	Duration (ms)
Pulse A	100	39.1	12.8
Pulse B	100	156.2	3.2
Pulse C	250	198.3	2.5
Pulse D	250	58.6	8.5
Pulse E	500	111.3	4.5

The LS-Dyna *Mat_Viscoelastic (006) material model was used for the optimization, with limits for the parameters G_0, G_∞, and β as described in Table 7.12. Eqn. 7.14 describes the shear relaxation behavior for the LS-Dyna material model, and the relationship of the three parameters.

$$G(t) = G_\infty + (G_0 - G_\infty)e^{-\beta t} \quad \text{Eqn. 7.14}$$

Table 7.12. Summary of *Mat_Viscoelastic material parameters and the ranges used for the FE optimization.

Material	G0 (GPa)		GI (GPa)		Beta (ms^{-1})	
	Min	Max	Min	Max	Min	max
Compliant Element	1e-4	1e-2	1e-4	1e-2	1e-3	1e-2
Heel Pad Rubber	1e-4	1e-2	1e-4	1e-2	1e-3	1e-2

The optimization resulted in the material parameters shown in Table 7.13. It should be noted that only the material properties for the heel pad and compliant element were altered during the optimization in order to minimize the cost of the changes to be made to the existing Mil-Lx design. The optimization code was run starting from four different initial parameter sets. Progress of the optimization was tracked using the value of the objective function compared to each set of model parameters tried by the optimization code.

Table 7.13. Summary of *Mat_Viscoelastic optimized material parameters.

Material	Ro ($kg\text{-}mm^3$)	Bulk (GPa)	G0 (GPa)	GI (GPa)	Beta (ms^{-1})
Compliant Element	1.25e-6	2.80e-1	1.45e-2	6.00e-3	2.47e-2
Heel Pad Rubber	1.08e-6	2.00e-1	9.40e-3	4.64e-3	4.06e-2

Force and impulse response of the optimized Mil-Lx model compared to human force and impulse responses are shown in Figure 7.35 for a low (50g, 10 $m\text{-}s^{-1}$) and high (500g, 10 $m\text{-}s^{-1}$) frequency pulse and for the best fit condition (100g, 10 $m\text{-}s^{-1}$). CORA scores comparing FE Mil-Lx and FE human responses calculated up to time of peak force for each of the conditions are summarized in Figure 7.34. The complete set of optimized Mil-Lx and human leg response plots are provided in Section 10.7.

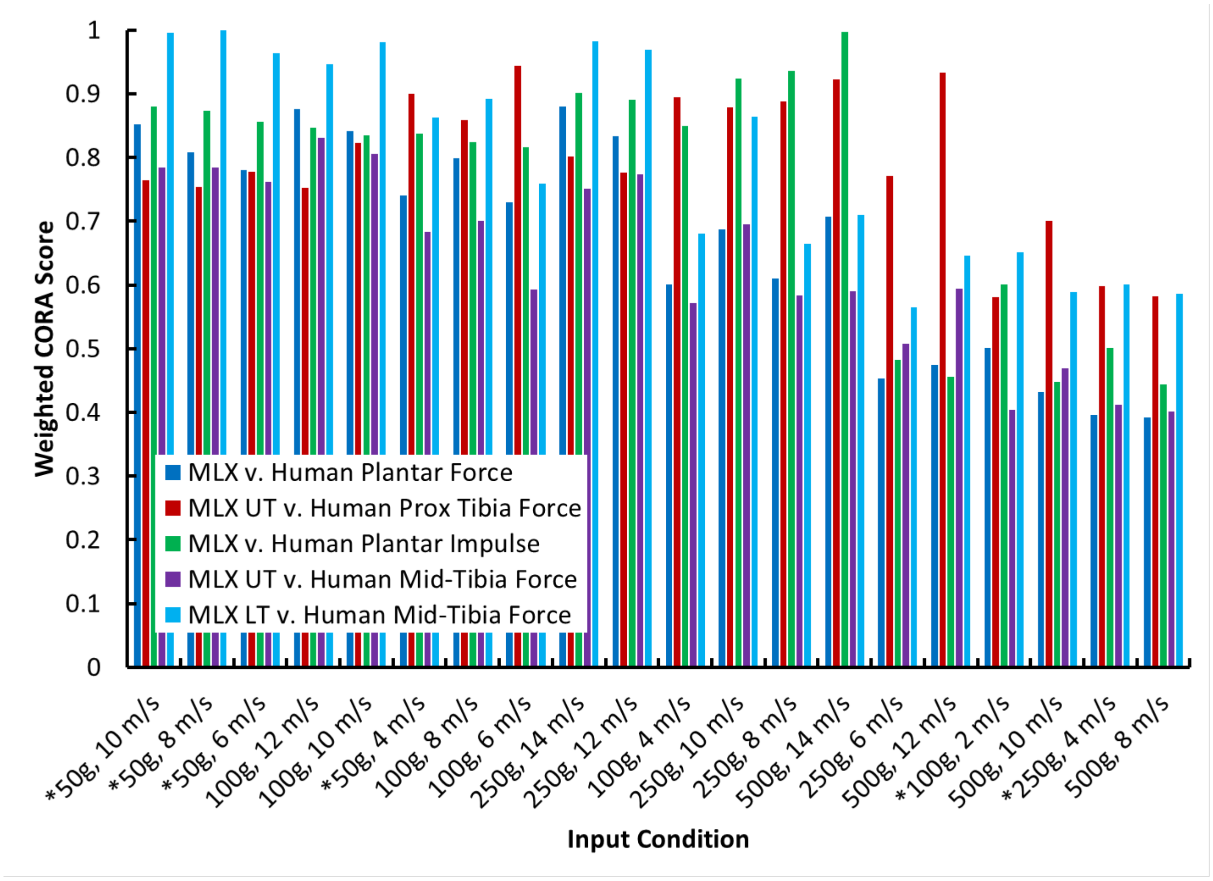

Figure 7.34. Weighted Overall CORA scores comparing optimized Mil-Lx FE response to FE human leg response for each of the parametric study conditions within the range of 2-33 ms footplate acceleration duration. Test conditions are ordered from low to high frequency from left to right.

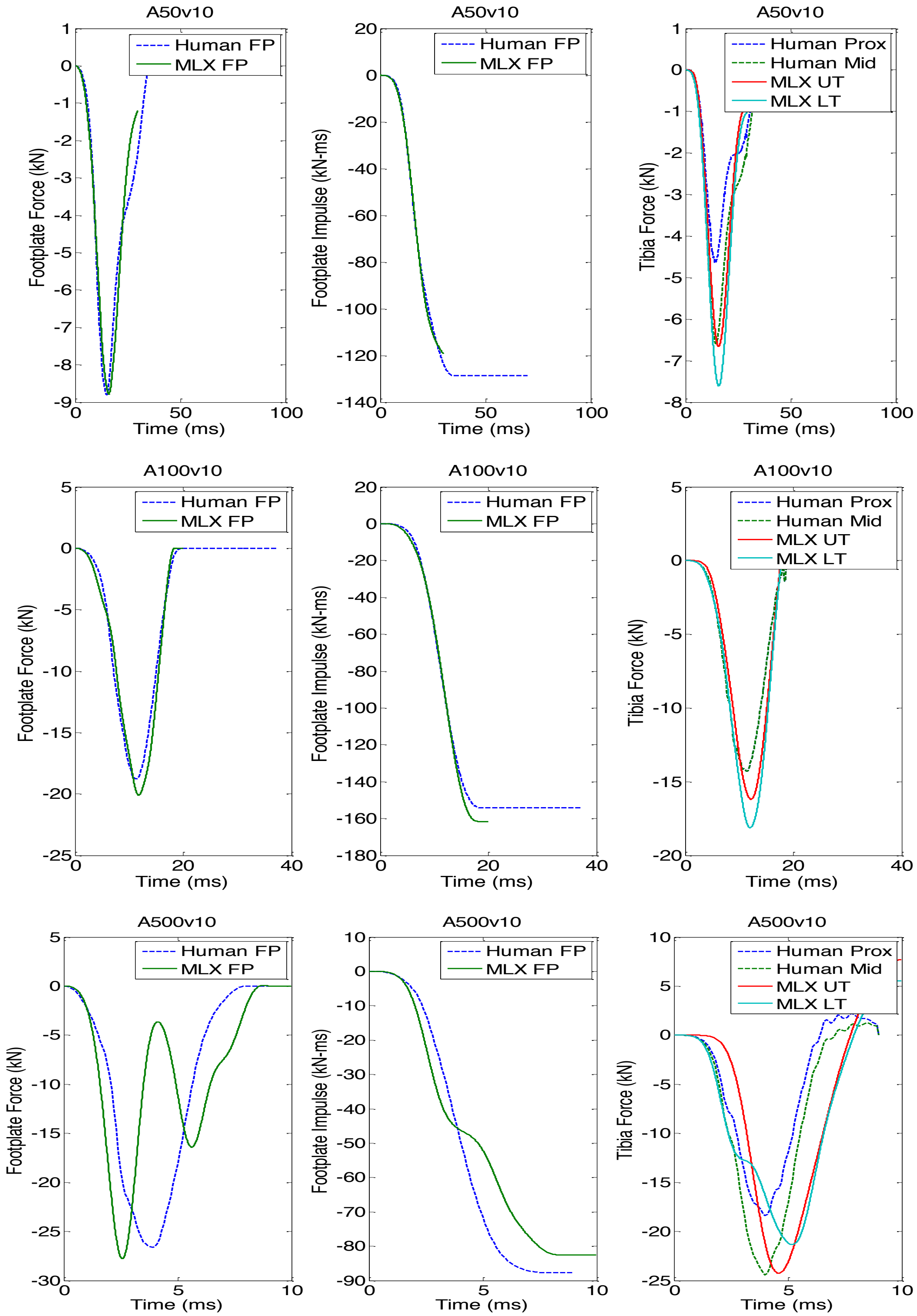

Figure 7.35. Comparison of human leg plantar force and impulse and optimized Mil-Lx plantar force and impulse from finite element models. Heel pad and tibia compliant element materials were replaced with the materials described in Table 7.13.

The optimized Mil-Lx FE model produced a better fit of the human leg footplate force and impulse for the lower frequencies, and a better fit of the proximal tibia force for the higher frequencies. The average CORA score for the plantar force comparison was 0.48 for inputs with a duration less than 5 ms, and 0.78 for inputs with a duration greater than 5 ms. The inability to provide biofidelic forces at both locations can be explained by the mass distribution of the Mil-Lx. For higher loading frequencies with small footplate displacements, the load is concentrated near the foot and ankle for the human leg. Since a majority of the mass located in the human leg is proximal to the foot and ankle, the higher frequency inputs tend not to engage this mass because of the compliance of the ankle joint. For the Mil-Lx, the compliant element is located proximal to the bulk of the Mil-Lx mass, which causes this mass to be recruited by even the high loading frequencies with small footplate displacements because of the stiffness of the structure. This effect is observed in the high frequency conditions where double impacts occur between the plantar surface of the foot and the footplate (see Figure 7.36 and others plotted in the appendix for reference). These double impacts start to occur for durations around 6.4 ms according to the conditions used in the study.

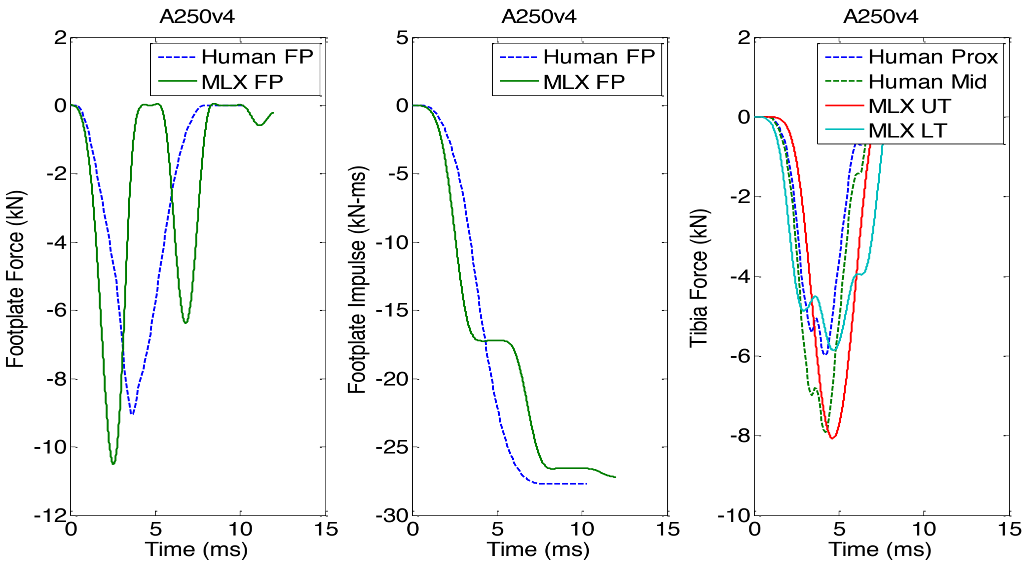

Figure 7.36. High frequency test condition for which a double hit occurs between the footplate and plantar surface of the Mil-Lx foot. This effect is likely the result of the difference in mass distribution (caused by location of the compliant element) in the Mil-Lx.

Weighted CORA scores for Mil-Lx upper tibia force compared to human proximal tibia force were reasonable for acceleration durations greater than 3.3 ms, with an average weighted CORA score of 0.84 for durations greater than 3.3 ms and only 0.62 for durations less than 3.3 ms. The comparison of interest, however, is that of Mil-Lx upper tibia force compared to human mid-tibia force since this is the measurement for which McKay and Bir designed the original Mil-Lx. Figure 7.34 shows that lower weighted CORA scores are again associated with the higher loading frequencies. Examination of the plots provided in Appendix 10.7 show that these lower CORA scores may be due to the time-shift that is present due to the compression of the compliant element in the Mil-Lx tibia. Figure 7.37 shows the weighted CORA scores calculated for the case where the curves were time-shifted so that peak forces aligned. This improved the average CORA score for the Mil-Lx upper tibia force compared to the human mid-tibia force from 0.63 to 0.82. Since only the peak upper tibia loads are used by the McKay and Bir injury criterion, the phasing of the Mil-Lx force compared to the human force is unimportant for injury risk calculation in this case. Thus, the ability of the modified Mil-Lx model to produce high weighted CORA scores for the time-shifted condition is acceptable.

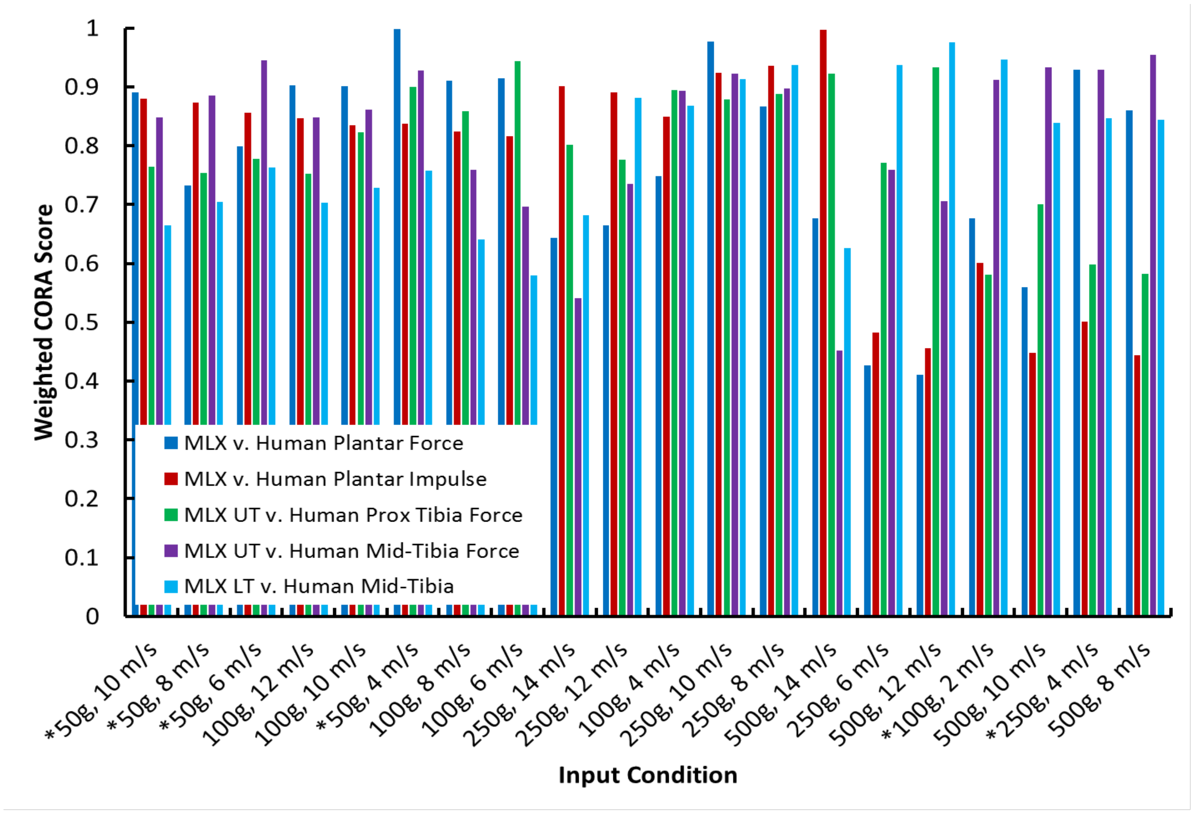

Figure 7.37. Weighted Overall CORA scores comparing optimized Mil-Lx FE response to shifted FE human leg response for each of the parametric study conditions within the range of acceleration durations from 1.9 to 33.3 ms. Time shift of the forces was determined by aligning peak forces. Test conditions are again ordered from low to high frequency from left to right.

Weighted CORA scores for Mil-Lx upper tibia force compared to human mid-tibia force averaged 0.82 across all loading conditions, with a slightly higher average for acceleration durations less than 5 ms compared to greater than 5 ms (0.83 compared to 0.81). Not surprisingly, the Mil-Lx lower tibia force compared to the human mid-tibia force produced low CORA scores for the high frequency input conditions (CORA average 0.61 for durations less than 5 ms) since the lower tibia load cell is below the compliant puck. Higher CORA scores were observed for lower frequencies, with an average of 0.89. Again, this is due to the double peaks which occur for the higher frequency loads.

While CORA scores are helpful in terms of quantifying the ability of the optimized Mil-Lx to match the response of the human leg, perhaps it is more important to quantify the ability of the optimized Mil-Lx to predict injury. Peak force for each of the Mil-Lx simulations was recorded and compared to those from the human FE model both with and without element deletion. For the element deletion (ED) cases, the force at "fracture" and peak forces were recorded.

Significant differences existed between the peak plantar forces and plantar impulse at peak force for the human and Mil-Lx. The greatest difference in peak plantar force (7.1 kN) between the Mil-Lx and human response without element deletion occurred for the 500g, 14 m-s^{-1} condition. For the element deletion case, the greatest peak force difference was 10.8 kN for the 250g, 8 m-s^{-1} condition. Unlike the comparison between the Mil-Lx and the human model without element deletion, in the second case, the Mil-Lx force is greater than the force from the human model with element deletion. Again, it is important to acknowledge that the element deletion case may not necessarily represent the response of the human leg for which fracture has occurred, though it is reasonable to assume that a lower peak force would be measured for the case in which fracture occurs in the human leg. In most cases, Mil-Lx peak plantar force was greater than that measured in the element deletion FE model for the human leg; exceptions occurred for some of the cases for which a double peak in the plantar force was observed.

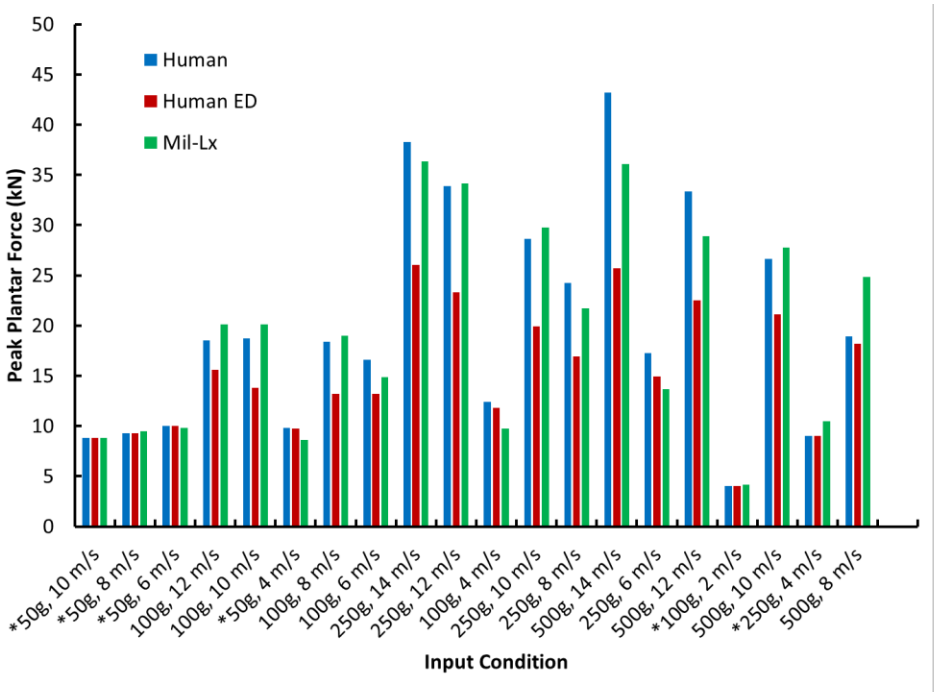

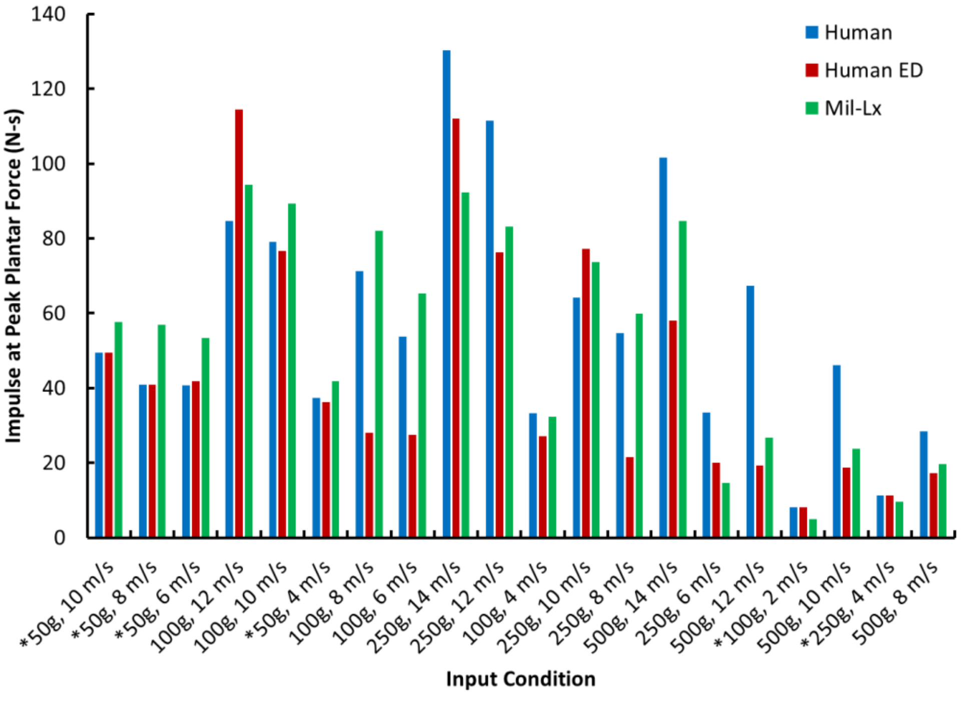

Figure 7.38. Peak plantar force (top) and plantar impulse at time of peak plantar force (bottom) are shown for the human and optimized Mil-Lx FE models for the conditions used for the human model parametric study. Note that input conditions are ordered from low to high frequency (left to right) and ED denotes the case where element deletion was turned on for the FE model.

A more useful comparison of the Mil-Lx and human response is that of injury prediction capability. While the previous comparison of Mil-Lx upper tibia force to human mid- and proximal tibia force showed that it may still be possible to use the McKay and Bir injury criterion with the optimized version of the Mil-Lx, the purpose of modifying the Mil-Lx design was to be able to use it to predict injury probability as defined the proposed force-impulse injury risk function. Using the peak plantar forces and impulse at peak force predicted by the Mil-Lx and human FE models, probability of injury was estimated for each input condition using the proposed force-impulse injury risk function. The average age of the United States enlisted military population, 27 years, was used as the age for the injury risk function.[205] Figure 7.39 summarizes the results of these calculations. Test conditions which did not produce fracture in the human FE model are denoted using an asterisk.

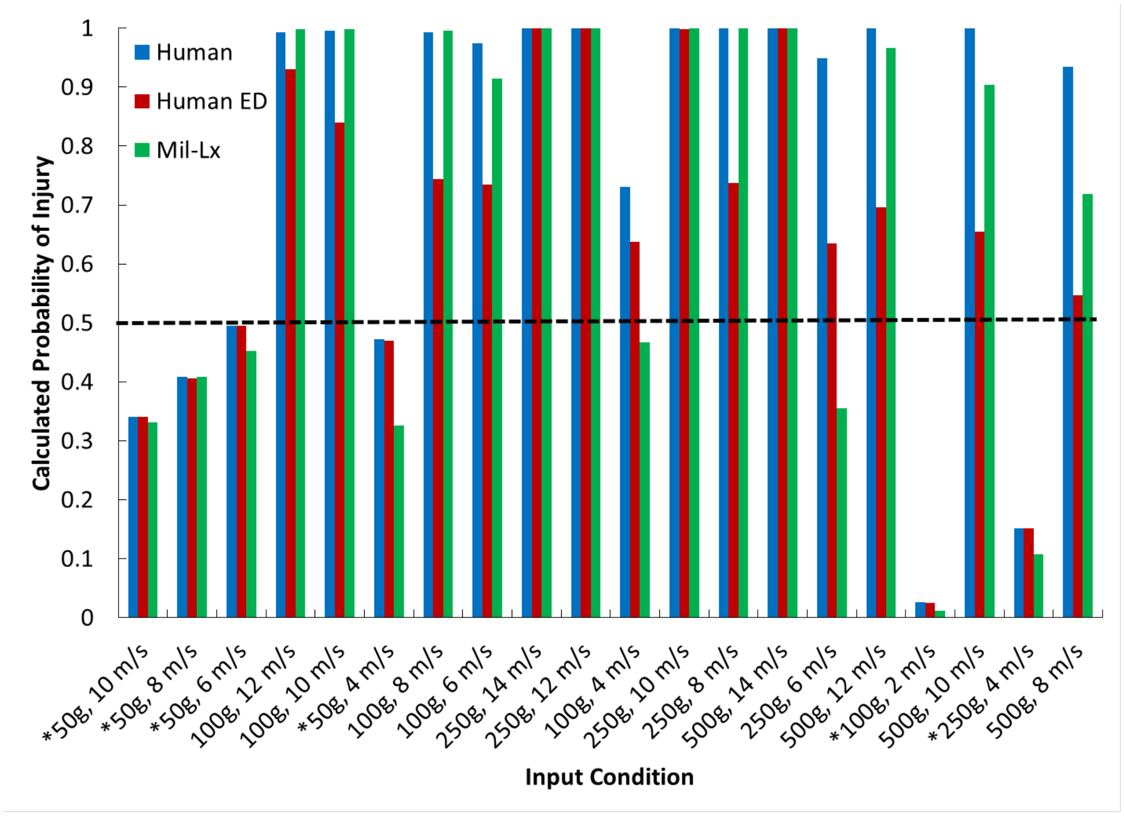

Figure 7.39. Probability of injury calculated using the proposed injury risk function is shown for the optimized Mil-Lx and human FE models. For the human FE model, probability of injury was calculated using force and impulse measured at time of peak force for the case were element deletion was turned off, and for time of fracture and time of peak force for the case were element elimination was used. Note that input conditions are ordered from low to high frequency (left to right).

For all except the 100g, 4 m-s^{-1} and 250g, 6 m-s^{-1} conditions, the optimized Mil-Lx would have accurately predicted injury outcome assuming a 50-percent probability of injury cut-off point. Sub-injurious cases were correctly predicted by the injury risk function, however, injury probability predicted by the Mil-Lx was lower than for the human model with and without element deletion. For all injurious cases except the 100 g, 4 m-s^{-1} and 250g, 6 m-s^{-1} conditions, the Mil-Lx overestimated the injury probability calculated for the human model with element deletion. This was expected since the Mil-Lx optimization was designed to maximize the CORA score for the Mil-Lx model and the human FE model without element deletion. For the injurious cases with element deletion, the peak forces are expected to be lower than those for the human model without element deletion as was discussed in Chapter 4. There was no apparent frequency dependence in the ability of the optimized Mil-Lx to estimate probability of injury.

For the incorrectly-classified injury cases, the 100g, 4 m-s^{-1} and 250g, 6 m-s^{-1} conditions, the footplate force experienced a double peak. Since the peak footplate force was reduced by this phenomena, the probability of injury was under-estimated. Despite improving the overall ability to predict footplate and proximal tibia force response, the optimized Mil-Lx cannot provide a reliable estimate of injury risk. The inaccuracy of the response of the optimized Mil-Lx does not seem to be frequency-dependent for the loading conditions used, so no conclusion can be reached regarding the range of frequencies for which this modified model can provide an accurate assessment of injury risk.

The observations made regarding the ability of the optimized Mil-Lx FE model to fit both the force response for the plantar and proximal or mid-tibia locations reinforce the conclusions from the lumped-mass model analysis. To best replicate the response of the human leg, the ATD leg must mimic both the stiffness and damping qualities, as well as the mass distribution. Designing an ATD leg using the information obtained from modelling the human leg as a LMM in Chapter 5 would theoretically produce better results than the approach taken here. As evidenced by the Mil-Lx LMM exercise in Section 7.3, weighting the objective function toward providing a better fit of one force versus another would undoubtedly produce a different set of optimal material parameters, and a better fit of the force for which the optimization was biased. For the FE Mil-Lx optimization, the weighting of the objection function was chosen such that the Mil-Lx could continue to use the injury risk function developed by McKay and Bir which uses the upper tibia force, as well as the plantar force based injury risk function proposed by this dissertation. In theory, if both proximal and distal forces could be matched by the ATD, the ATD could use a future injury criterion with the ability to distinguish between proximal and distal injuries.

7.5.1 Selection of Materials for Adapting the Mil-Lx ATD

After finding optimized properties for the Mil-Lx, an attempt was made to identify existing materials for the compliant element and heel pad which may improve the current performance of the Mil-Lx. Changing the materials used for these parts rather than completely redesigning the Mil-Lx would suffice as a cheap and time-efficient solution to ATD leg development for use with the proposed injury criterion, particularly if existing materials could be used.

First, a literature review was performed to find material properties for existing materials with properties similar to those estimated by the FE optimization. Material cards were then created using LS-Dyna *MAT_SIMPLIFIED_RUBBER for various existing rubber materials. A summary of these materials is provided in Table 7.14, and stress-strain curves for the materials are supplied in the Appendix.

Table 7.14. Summary of FE materials used for discrete optimization of Mil-Lx biofidelity

Material	Density (kg-mm^{-3})	Bulk Modulus (GPa)	Shear Modulus (GPa)
90 Durometer Polyurethane	1.3e-6	5.0	1.40e-2
80 Durometer Polyurethane	1.2e-6	5.0	1.40e-2
60 Durometer Polyurethane	1.15e-6	5.0	8.60e-3
40 Durometer Polyurethane	1.15e-6	5.0	8.40e-3
20 Durometer Polyurethane	1.12e-6	5.0	7.40e-3
70 Durometer Neoprene	9.6e-7	1.36	2.72e-3
65 Durometer Neoprene	9.6e-7	1.36	2.72e-3
60 Durometer Neoprene	9.6e-7	1.36	2.72e-3
70 Durometer Sorbothane	1.364e-6	4.140	
50 Durometer Sorbothane	1.364e-6	4.710	
30 Durometer Sorbothane	1.364e-6	4.710	

A trial and error methodology was used to iterate through different combinations of the materials summarized in Table 7.14. Five conditions were chosen from the 28 conditions used for the parametric study to use for comparing the plantar and upper tibia force response of the Mil-Lx to the human leg FE model response. The materials for the heel pad insert and tibia compliant element were substituted into the model using a trial and error method and using the combined CORA score for the plantar and proximal tibia force to determine whether the material provided an improvement over the previous combination of materials. As with the LMM approach to optimizing the biofidelity of the Mil-Lx, none of the combinations provided both a good fit of both the plantar and proximal tibia forces. Since the proposed injury risk function is based on plantar force, the decision was made to choose the material combination which provided the best fit of the plantar force.

The best fit of the plantar force was observed when the heel pad rubber was replaced with 70 durometer neoprene, and 90 durometer polyurethane was used for the tibia compliant element. Sample plots comparing the response of the modified Mil-Lx FE model and the human leg FE model response are provided in Figure 7.40. Plots for the remaining input conditions are located in Appendix 10.7.3.

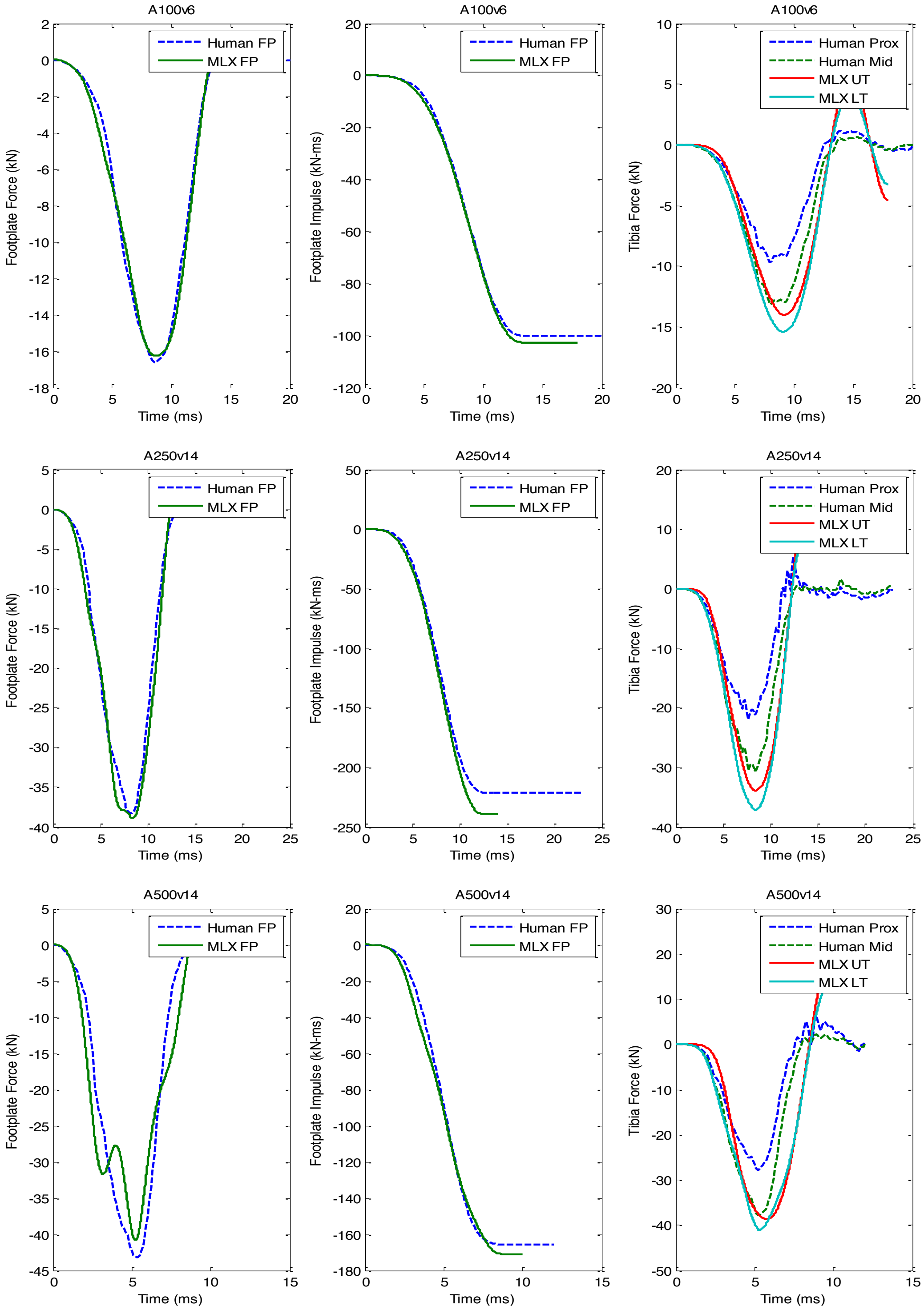

Figure 7.40. Comparison of human leg plantar force and impulse and modified Mil-Lx plantar force and impulse from finite element models. Heel pad and tibia compliant element materials were replaced with 70-durometer neoprene and 90-durometer rubber, respectively.

The input conditions for the first two sets of plots shown in Figure 7.40 show that the modified Mil-Lx model is able to capture both the peak and timing of the footplate force, but the upper tibia force slightly overestimates the peak human mid-tibia force. The third set of plots shows the double peak behavior that occurs for the footplate force for higher frequency loading conditions, though shows that the impulse is essentially unaffected by the double peak. The upper tibia force again slightly overestimates the peak mid-tibia force and relaxes slower than the human leg mid-tibia force.

A summary of peak forces for all input conditions is provided in Figure 7.41. With a few exceptions, the peak Mil-Lx upper tibia force overestimated the peak human mid-tibia force. The average percent difference between the human mid-tibia force and Mil-Lx upper tibia force was 37% for all loading conditions. An average difference of 49% was observed between the peak human proximal tibia force and peak Mil-Lx upper tibia force. For loading durations less than 5 ms, the average percent difference between peak footplate forces was 4% compared to 12% for higher frequencies. This aligns with the observations from the LMM study which concluded that the mass distribution of the Mil-Lx and placement of the compliant puck predisposes the Mil-Lx to poor estimate of footplate force for higher loading frequencies.

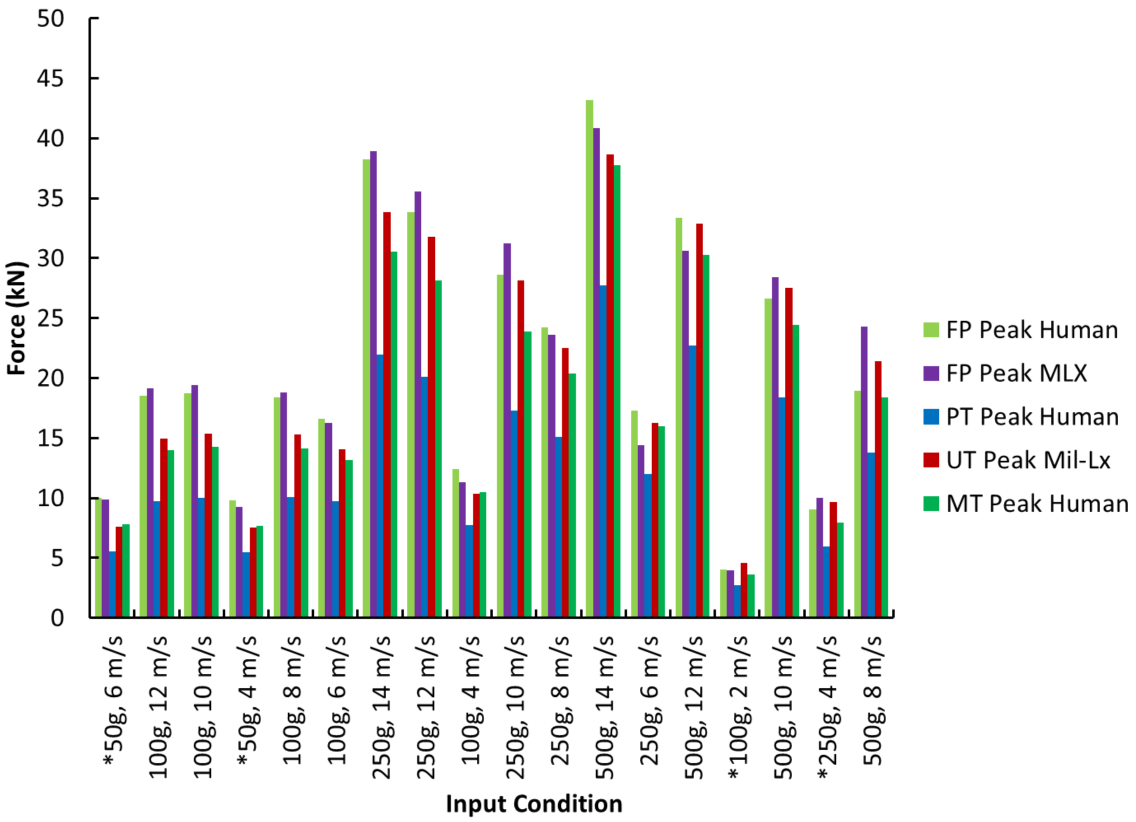

Figure 7.41. Summary of peak forces for the Mil-Lx model using 90 durometer polyurethane for the tibia compliant element and 70 durometer neoprene for the heel pad and the human FE model for footplate (FP), proximal tibia (PT), upper tibia (UT), and mid-tibia (MT) forces.

CORA scores support the observations from the peak force analysis. The summary of the weighted overall CORA scores for the modified Mil-Lx model (Figure 7.42) shows that footplate force and impulse are predicted with reasonable accuracy less than 4.5 ms (250g, 6 m/s). This range of frequencies aligns with the range of frequencies for which the Mil-Lx based LMM was able to accurately predict human leg force response (see Section 7.3). High CORA scores are observed for the comparison of the Mil-Lx upper tibia and human mid-tibia forces as well, though CORA scores greater than 0.8 persist for a larger range of durations (less than 3.8 ms).

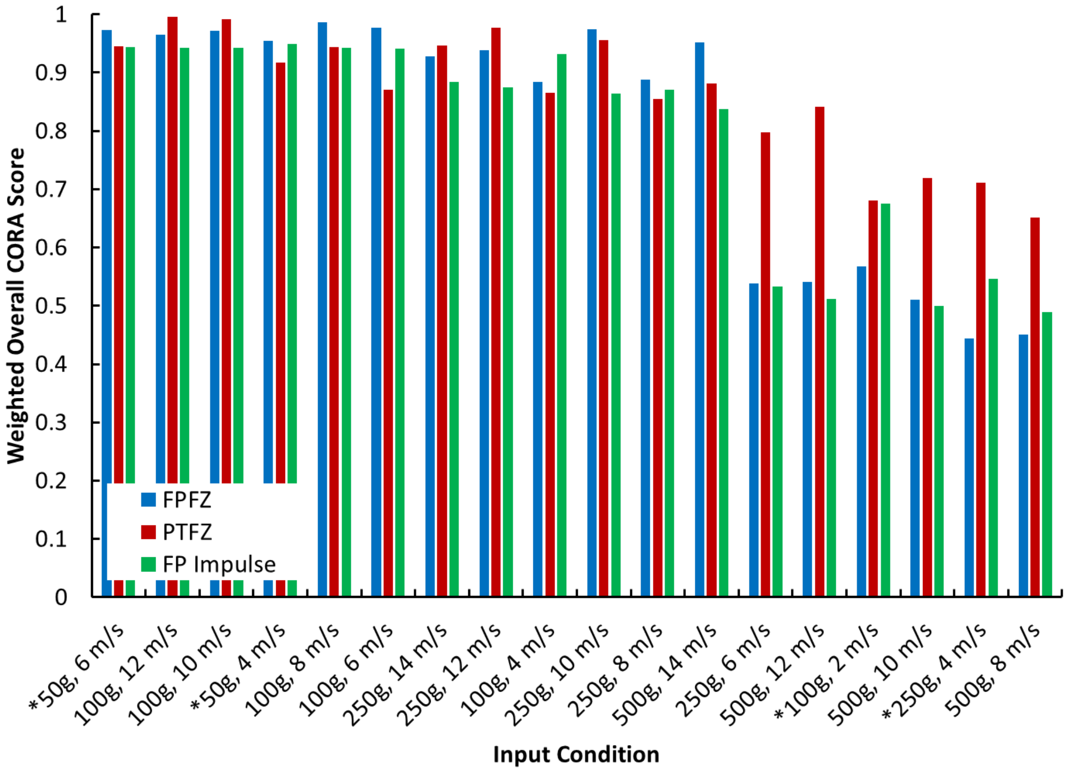

Figure 7.42. Weighted CORA scores for the comparison of the Mil-Lx model results using 90 durometer polyurethane for the tibia compliant element and 70 durometer neoprene for the heel pad and the human FE model results for footplate force (FPFZ), proximal tibia force (PTFZ), and footplate impulse (FP Impulse).

Though the FE-optimized Mil-Lx model is better able to produce both biofidelic footplate and proximal tibia forces, the discretely optimized model is more suited for predicting injury probability using the proposed force-impulse injury risk function. Injury probability was calculated using the proposed force-impulse injury risk function based on the results from the discretely optimized Mil-Lx and human (with element deletion) FE models. Since the Mil-Lx FE model was optimized to reproduce the response of the human FE model without element deletion, it is expected that the Mil-Lx should over-predict the injury risk estimated using the results of the human FE model with element deletion. For each injurious condition, the Mil-Lx over-predicted the injury risk associated with the human response except for the 250g, 6 m-s^{-1} condition. Further investigation revealed that a double peak occurred for the Mil-Lx footplate force, causing the peak force to be underestimated. As previously discussed, this condition falls outside of the range of frequencies for which the modified Mil-Lx was able to produce biofidelic forces. For the sub-injurious conditions, the injury risk estimated using the modified Mil-Lx was within an average of 3.6% of that estimated using the human FE model response.

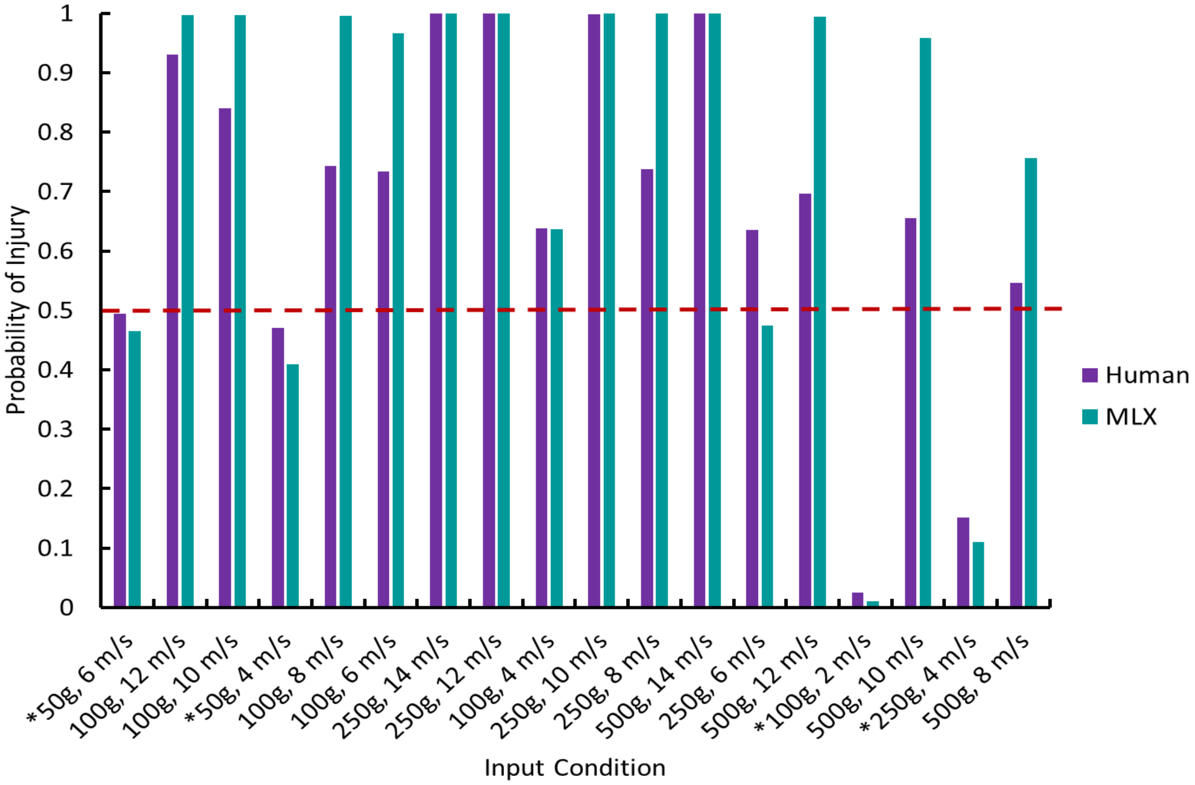

Figure 7.43. Injury probability calculated using the force-impulse injury risk function and the results of the modified Mil-Lx and human FE models. An asterisk denotes the sub-injurious conditions.

The ability of the modified Mil-Lx design to predict both the peak force and timing of the force response is an improvement from the previous Mil-Lx design. The amount of improvement for injury prediction cannot be completely established using the human FE model response since it only represents one response from the population in terms of injury or no injury. Instead, the evaluation must be based on the ability of the modified Mil-Lx FE model to predict the peak plantar force and impulse measured in the human FE model for matched loading conditions. Several assumptions are necessary to draw conclusions from these models. While the human FE model was benchmarked using PMHS response data for several different loading conditions, the FE model of the Mil-Lx was only benchmarked using the forces and displacements from four experimental drop tower tests, which were of similar rates of loading. Thus, to draw conclusions from this FE model, the assumption must be made that the FE model is valid across each of the loading frequencies used in the parametric study.

7.5.2 Comparison of Modified Mil-Lx Response to PMHS Response

In order to compare the response of the original and modified Mil-Lx designs, each of the finite element models was run using the footplate acceleration from a matched pair PMHS and Mil-Lx test condition (Drop Tower A). The proximal tibia and footplate forces are shown for each of the three models: the original Mil-Lx FE model (Mil-Lx FE); the Mil-Lx FE model modified using discrete optimization for real material properties (Discrete Opt. Mil-Lx); the Mil-Lx FE model modified using continuous variable optimization (FE Opt. Mil-Lx); and the experimental Mil-Lx and PMHS corridors (Mil-Lx Exp. and PMHS). This plot shows that the discrete optimized model under-predicted the peak PMHS average proximal tibia force, while the FE optimized model over-predicted the average PMHS force. CORA scores comparing each of the three model forces to the PMHS average proximal tibia force showed that both of the optimized models provided a better fit of the PMHS force than the original Mil-Lx FE model, with weighted overall CORA scores of 0.738, 0.783, and 0.810 for the original, FE optimized, and discrete optimized models, respectively. The modified Mil-Lx designs also showed an improvement over the experimental Mil-Lx results, which yielded a modified overall CORA score of 0.7669.

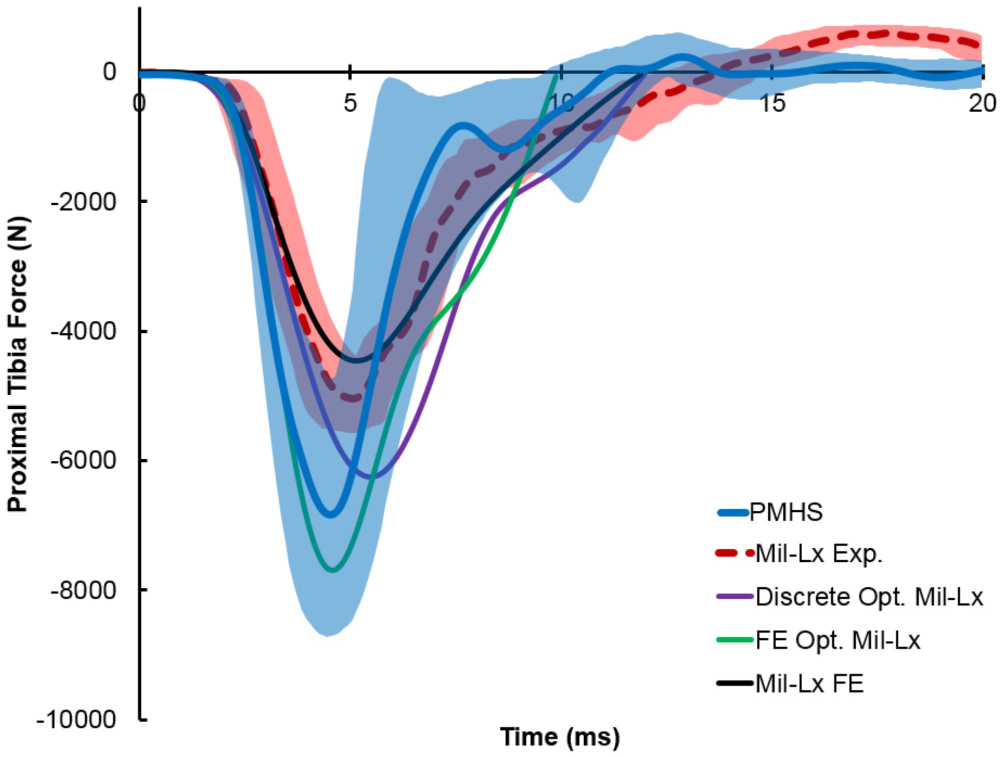

Figure 7.44.Comparison of experimental Mil-Lx and PMHS corridors to the finite element proximal tibia forces from the original, FE optimized, and discrete optimized Mil-Lx models for the Drop Tower A test condition.

The same comparison was performed for plantar forces since the goal was to improve the Mil-Lx's ability to replicate human proximal tibia and plantar forces (Figure 7.45). Weighted overall CORA scores for the original, FE optimized, and discrete optimized model plantar forces compared to the PMHS average plantar force were 0.632, 0.709, and 0.827, respectively. Though the CORA scores were not as high as for the idealized, single-frequency acceleration inputs from the parametric study, the fact that the optimized models had higher CORA scores than those for the original Mil-Lx design for this experimental condition suggests that the observed design improvement extends to more realistic test conditions with content from multiple loading frequencies.

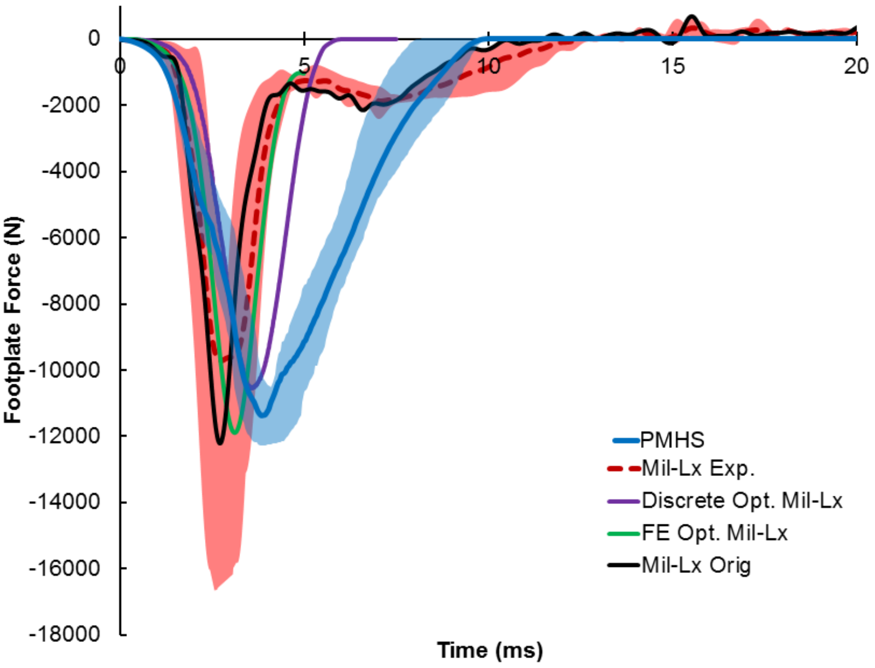

Figure 7.45. Comparison of experimental Mil-Lx and PMHS corridors to the finite element footplate (plantar) forces from the original, FE optimized, and discrete optimized Mil-Lx models for the Drop Tower A test condition.

These comparisons suggest that while the modified Mil-Lx FE models are able to provide a more biofidelic response than the current (original) Mil-Lx design, there is room for further improvement. It is important to note that making these material changes to the Mil-Lx may improve biofidelity for the loading conditions used in the optimization, but further adjustments to the design of the Mil-Lx structure may be necessary to achieve biofidelity across the desired range of loading conditions in the automotive and military environments. Additionally, while a large range of single loading frequencies were used in the optimization matrix, real-world acceleration pulses from automotive intrusion and UBB contain a spectrum of frequencies with varying power throughout the loading phase, which may include frequencies beyond the range of frequencies used in the optimization. Thus, it is imperative that further testing be performed to investigate the effects of these additional frequencies.

7.6 Application of Injury Criterion to Modified Mil-Lx ATD

The inability of the current design of the Mil-Lx to predict human plantar and proximal tibia force simultaneously prevents the proposed injury risk function from being applied directly in its current form. The importance of being able to predict the time history rather than the peak force alone enhances the challenge of developing a biofidelic ATD leg for a large range of loading frequencies. An additional complication is that the Mil-Lx currently does not measure plantar force. Despite these pitfalls of the current Mil-Lx design, the ability to easily replace the heel pad and tibia compliant element with readily available materials allows for convenient use of the proposed injury risk function in its current form, with only slight modification. By using the Mil-Lx hindfoot z-acceleration and the lower tibia force, plantar force can be calculated for purely axial loading conditions using Eqn. 7.15.

The Mil-Lx has little axial compliance in the ankle joint, which allows for the estimation of plantar force using the lower tibia load cell. For the case where loading is primarily vertical (SAE-z) and the Mil-Lx tibia is in a neutral position perpendicular to the footplate, the estimation of the plantar force using the Mil-Lx hindfoot acceleration and the lower tibia force is trivial. The calculation can be performed simply by determining the mass located distal to the lower tibia load cell as indicated by Eqn. 7.15. In this case, we assume that the plantar force vector is perpendicular to the footplate and that the plantar surface of the foot lays flat against the plate. The global coordinate system is with respect to the footplate, where the z-direction is perpendicular to the plate and the x-direction points in the direction the toes of the Mil-Lx are pointing while in contact with the plate (Figure 7.46).

$$\mathrm{F}_{\mathrm{plantar}_z} = \mathrm{F}_{\mathrm{LT}_z} + (\mathrm{m}_{\mathrm{foot}} + \mathrm{m}_{\mathrm{below\ LTLC}})\mathrm{a}_{\mathrm{foot}_z} \qquad \text{Eqn. 7.15}$$

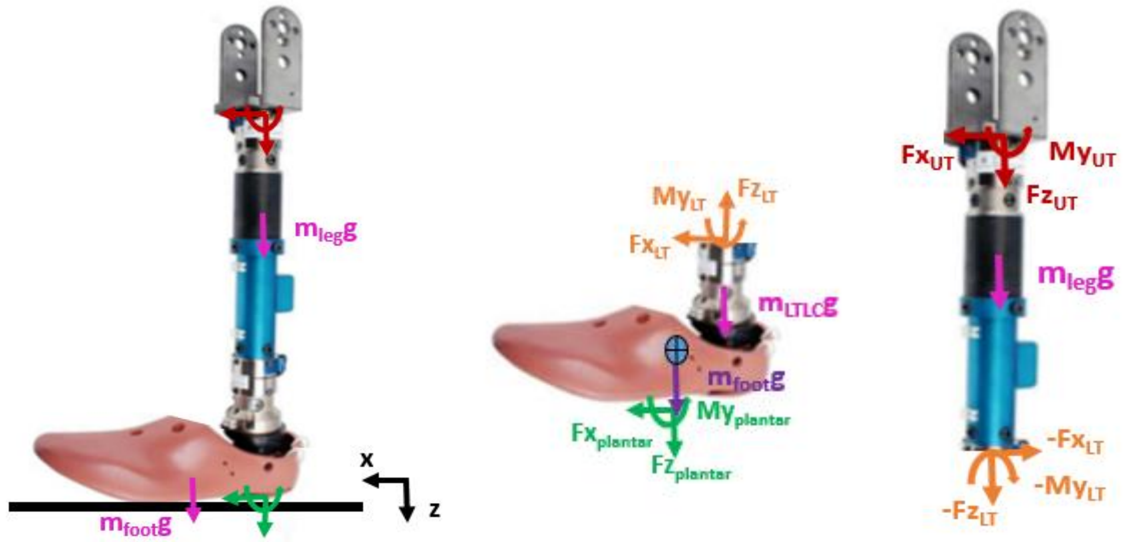

Figure 7.46. Free body diagram of the Mil-Lx leg showing forces (F) and moments (M) in the x-z plane for the plantar surface of the foot (plantar), upper tibia (UT), and lower tibia (LT).

One key assumption of using this approach to estimate plantar force is that the ankle joint remains in one position and that the foot and section of the tibia below the lower tibia load cell can be treated as a rigid body. In reality, the loading of the foot may result in ankle rotation or flexion. As the ankle angle changes, the SAE-z component of the acceleration no longer aligns with the axial force vector in the tibia. Similarly, if the Mil-Lx tibia is not aligned with the loading vector, the tibia force can no longer be used to predict the plantar force. For the case where the leg is in a primarily neutral position with the tibia aligned with the load vector from the footplate, it may be reasonable to assume that the ankle angle changes after the vertical loading is complete.

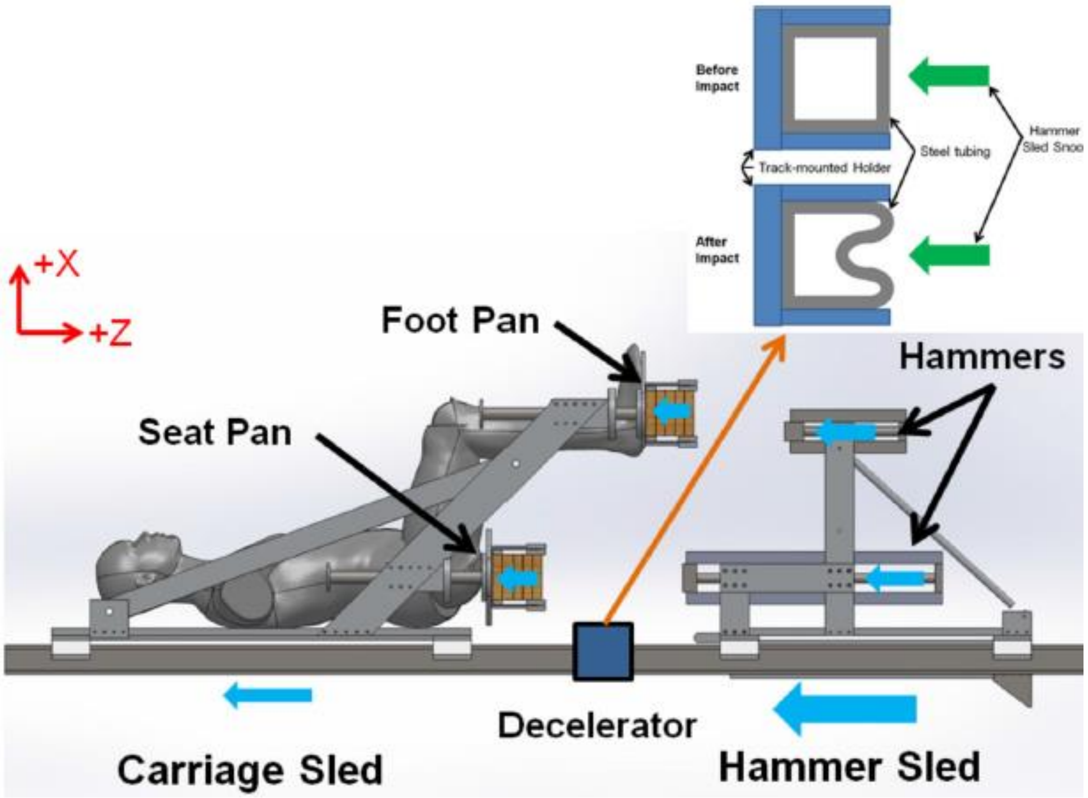
Before Impact
Track-mounted Holder
Steel tubing
Hammer Sled Snoo
After Impact
+X
+Z
Foot Pan
Hammers
Seat Pan
Decelerator
Carriage Sled
Hammer Sled

Figure 7.47. Odyssey UBB-simulator test rig consisting of a hammer sled with two hammers which impact the seat and foot pans of the carriage sled separately. The mass of the hammer sled is decelerated by crushing a steel tube mounted to the tracks of a Via sled system. (Annals of biomedical engineering by BIOMEDICAL ENGINEERING SOCIETY Reproduced with permission of SPRINGER NEW YORK LLC in the format Thesis/Dissertation via Copyright Clearance Center.)[9]

To investigate the timing of ankle rotation during loading typical of UBB, data from previous whole body UBB-simulator (Odyssey) laboratory experiments was used (Figure 7.47). These tests used a Via Systems model 713 sled system to deliver axial impacts to the floor and seat of a horizontal sled in which both PMHS and ATD tests subjects were positioned. The ATD tests used a Hybrid-III outfitted with a Mil-Lx leg on the right side and a Hybrid-III leg on the left side. Time of noticeable foot rotation was collected from high speed video and compared to timing of forces and accelerations in the Mil-Lx leg. Two test conditions are shown in Figure 7.48: a sub-injurious 278 g in 2.11 ms footplate acceleration condition (8.09 m-s^{-1}) and an injurious 516.7 in 1.26 ms footplate acceleration condition (13.98 m-s^{-1}). For each case, the Mil-Lx tibia was aligned with the loading vector. The time at which the ankle began to dorsiflex is indicated in the plot, and occurs after the loading phase. Thus, at least for a primarily vertical loading scenario with the tibia perpendicular to the load, the foot acceleration and lower tibia force vectors should be aligned with minimal rotation prior to peak force. Hence, Eqn. 7.15 is deemed sufficient for estimating peak plantar force and impulse for these primarily axial loads.

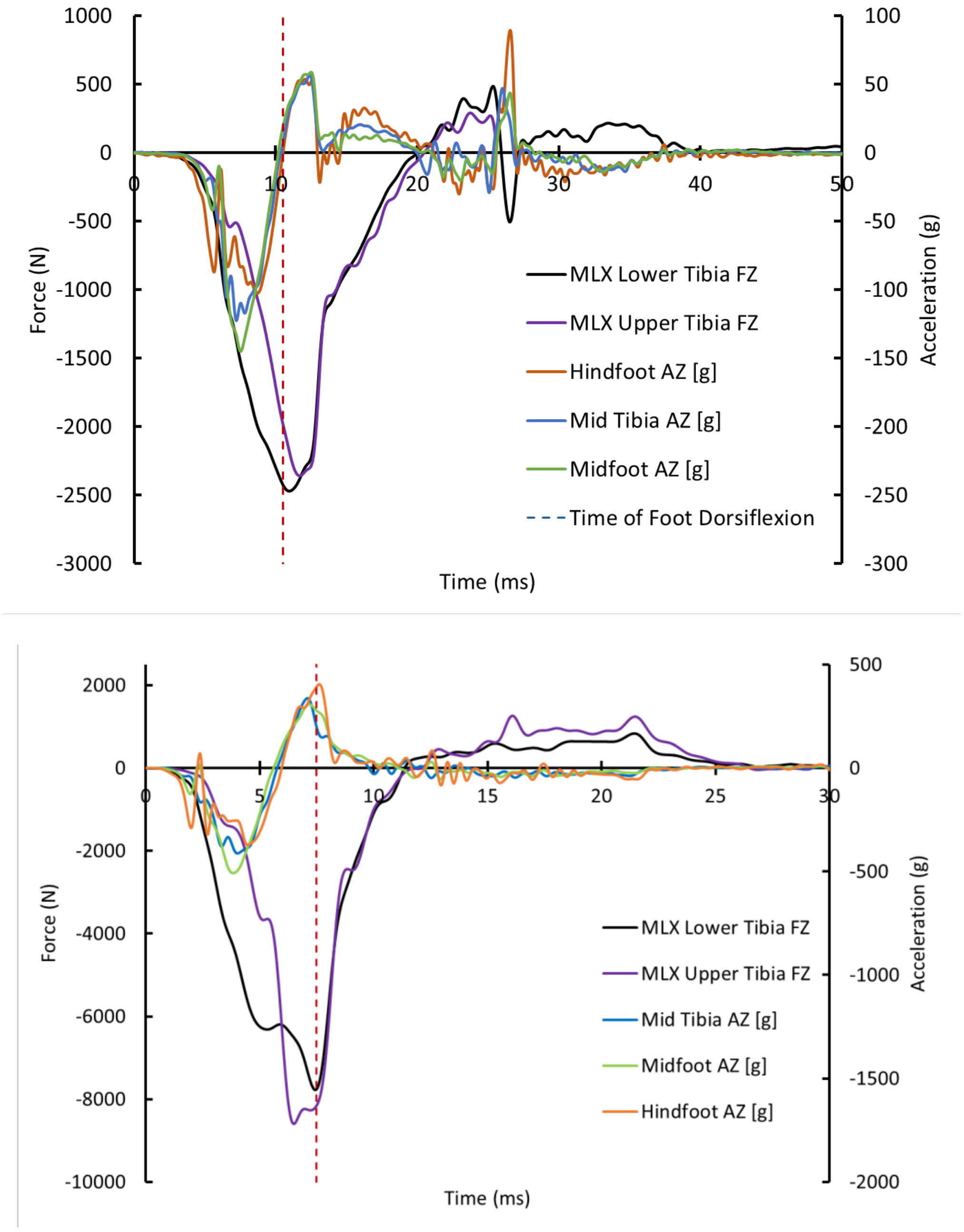

Figure 7.48. Mil-Lx force and acceleration response to a sub-injurious (top) and injurious (bottom) footplate loading condition from tests performed by Bailey et al. using the Odyssey blast simulator. Time of noticeable ankle dorsiflexion is indicated in each plot.

The previous method for estimating footplate force from the Mil-Lx applies only the vertical loading scenarios in which the loading vector is aligned with the tibia shaft and the ankle is ina neutral position. Though, underbody blast loading is typically vertical in nature, the vehicle occupants may be positioned such that alternative load vectors are introduced. The Odyssey test series did not incorporate alternative leg positions into the whole body test matrix, however, a study presented by Danelson et al. investigated the changes in cadaveric and ATD response to controlled live-fire UBB loads for different seating postures (Figure 7.47). Though Mil-Lx legs were not used, the study outlined the change in PMHS leg rotation as a function of time and indicates that a significant amount of leg rotation is expected during the event. In order to provide a useful tool for estimating injury risk in these events, the Mil-Lx leg must be able to provide an estimate of plantar force even for these alternative postures.

Estimating the footplate force using the Mil-Lx lower tibia force for alternative leg positions is more difficult than the approach outlined for the nominal posture. The Mil-Lx was specifically designed and validated for the vertical loading direction, so it is not expected that the Mil-Lx will produce biofidelic responses for non-vertical loads, particularly because of the presence of the compliant element in the tibia shaft. Thus, the use of the Mil-Lx for predicting injury due to combined axial and bending loads using an additional injury criterion similar to the tibia index would require further testing and likely a redesign of the positioning of the compliant element. Moreover, the lack of instrumentation such as angular rate sensors and an ankle potentiometer prevents the estimation of plantar force using rigid body dynamics. Nonetheless, the process for estimating plantar force using the Mil-Lx placed in an out-of-position posture will be discussed, assuming that additional instrumentation such as angular rate sensors may be attached to the leg without extensive alterations to the leg's structure.

For vertical loading, it was assumed that the foot and tibia below the lower tibia load cell could be treated as a rigid body. For non-vertical loads, the system must either be modelled using multibody dynamics, or assumptions must be made about the behavior of the ankle joint. For simplicity, the ankle joint will be treated as a spherical joint which cannot transmit moments. In reality, the Mil-Lx contains the Hybrid-III ankle joint, which has a rotational stiffness that changes as a function of rotation angle.[159] For small angles, however, the rotational stiffness is negligible. It is also necessary to assume that the ankle joint does not deform while transmitting forces. The distal portion of the tibia and the foot must also be treated as separate rigid bodies connected by the spherical joint.

Using these assumptions, rigid body dynamics can be used to calculate the forces transmitted through the ankle joint. To do this, additional instrumentation must be installed on the Mil-Lx, including angular rate sensors on the tibia to calculate angular acceleration of the tibia (α_{LT}), and a rotary potentiometer on the ankle to measure the angle of the tibia relative to the foot (θ). This instrumentation is included on the Thor-Lx, though the intent to use the Mil-Lx in primarily vertical loading applications may have been the purpose for excluding it.

In addition to extra instrumentation, the location of the Mil-Lx's center of pressure must be estimated for the case of vertical loads applied to the plantar surface of the foot. This location must be known in order to calculate the moment induced by the vertical load application to the foot, which influences the rotation of the foot during these loads. Data from a previous study by Van Tuyl et al. was used to calculate the location of the center of pressure for a load applied to the plantar surface of the Hybrid-III foot is located 2.5 mm lateral of the mid-line of the foot, and 74.3 mm anterior of the heel of the foot.[206] These dimensions will be used as the estimate of the center of pressure for the Mil-Lx foot. Previous studies have shown that the center of pressure varies for the human knee and ankle joints when posture is varied.[74] The location of the ankle joint center does not change for the Mil-Lx since it is constructed using a simple ball joint. It is important to note that this difference may be a source of error when attempting to estimate human leg response for alternative postures using an ATD which does not account for these changes.

Center of mass of the Mil-Lx foot is located 29.4 mm above the footplate, 5.4 mm to the right of the anterior-posterior centerline of the foot, and 119.3 mm anterior of the posterior surface of the foot. The center of the ankle joint is located 49 mm posterior of, 4 mm to the left of, and 50 mm proximal to the foot center of mass. These dimensions are depicted in Figure 7.49. The location of the center of pressure is also depicted.

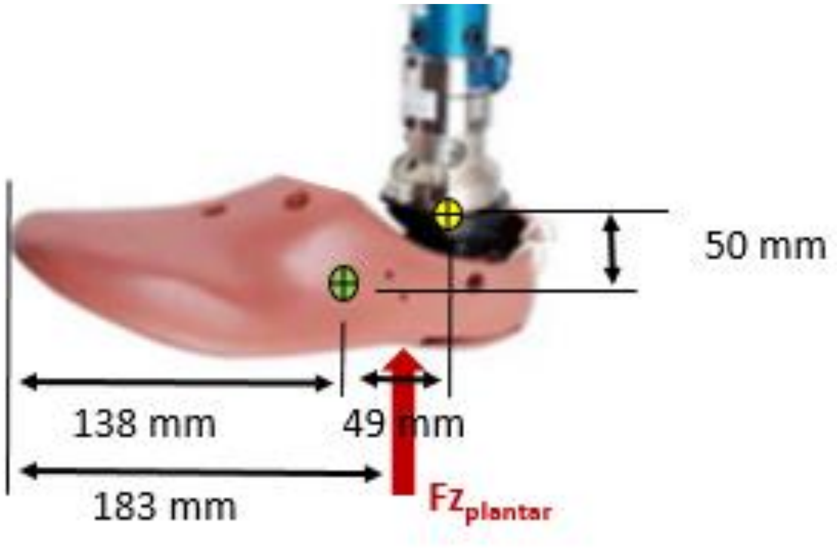

Figure 7.49. Estimated location of the center of mass, center of pressure, and center of ankle rotation location for the Mil-Lx.

Eqn. 7.19 through Eqn. 7.21 provide the system of equations for calculating the forces at the ankle joint in the x-z plane, and Eqn. 7.23 provides the equation for estimating the plantar force. The unknown variables are highlighted in blue, and variables that require additional instrumentation to measure are highlighted in red. The green variables are those associated with the plantar force, which are the desired values from this calculation. Using these equations, the forces applied to the foot through the ankle joint can be calculated using the equations of motion for the Mil-Lx distal tibia segment (Eqn. 7.19-Eqn. 7.21). Since the acceleration at the lower tibia's center of gravity is not directly measured, Eqn. 7.22 will be used to calculate it based on the acceleration of the ankle, lower tibia angular acceleration and velocity, and the position vector between the ankle joint and tibia, which will be assumed equal to the acceleration of the foot. After calculating the ankle forces, Eqn. 7.16 through Eqn. 7.18 can be used to calculate the plantar forces and moments. The equation for plantar force has been simplified and is provided separately in Eqn. 7.23.

Equations of motion for the Mil-Lx foot:

$$\sum F_x = m_{foot} a_{foot_x} = -F_{Fr_x} - F_{ank_x} \qquad \text{Eqn. 7.16}$$

$$\sum F_z = m_{foot} a_{foot_z} = -F_{plantar_z} - F_{ank_z} + m_{foot} g \qquad \text{Eqn. 7.17}$$

$$\sum \mathrm{M_y} = \mathrm{I_{foot_y}} \alpha_{\mathrm{foot_y}}$$

$$= \mathrm{F_{ankle_z}} \mathrm{x_{ank/cg}} - \mathrm{F_{ank_x}} \mathrm{z_{ank/cg}} + \mathrm{F}_{Fr_{\mathrm{x}}} \mathrm{z_{cg}} + \mathrm{F}_{Plantar_{\mathrm{z}}} \mathrm{x_{cp/cg}}$$

$$+ M_{plantar_y}$$

Eqn. 7.18

Equations of motion for the Mil-Lx distal tibia:

$$\sum \mathrm{F_x} = \mathrm{m_{LT}} \mathrm{a_{LT_x}} = \mathrm{F_{LT_x}} \sin \theta - \mathrm{F_{ank_x}}$$

Eqn. 7.19

$$\sum \mathrm{F_z} = \mathrm{m_{LT}} \mathrm{a_{LT_z}} = \mathrm{F_{LT_z}} \cos \theta - \mathrm{F_{ank_z}} + \mathrm{m_{LT}} \mathrm{g}$$

Eqn. 7.20

$$\sum \mathrm{M_y} = \mathrm{I_{LT_y}} \alpha_{\mathrm{LT_y}} = \mathrm{F_{ank_z}} \mathrm{x_{ank/cg}} - \mathrm{F_{LT_z}} \mathrm{x_{LT/cg}} - \mathrm{F_{ank_x}} \mathrm{z_{ank/cg}} + \mathrm{F_{LT_x}} \mathrm{z_{LT/cg}}$$

Eqn. 7.21

$$\mathbf{a_{LT}} = \mathbf{a_{foot}} + \boldsymbol{\alpha}_{\mathbf{LT}} \times \mathbf{r_{LT/foot}} + \boldsymbol{\omega}_{\mathbf{LT}} \times (\boldsymbol{\omega}_{\mathbf{LT}} \times \mathbf{r_{LT/foot}})$$

Eqn. 7.22

$$\mathrm{F_{Plantar_z}} = \mathrm{F_{ank_z}} + (\mathrm{m_{foot}}) \mathrm{a_{foot_z}}$$

Eqn. 7.23

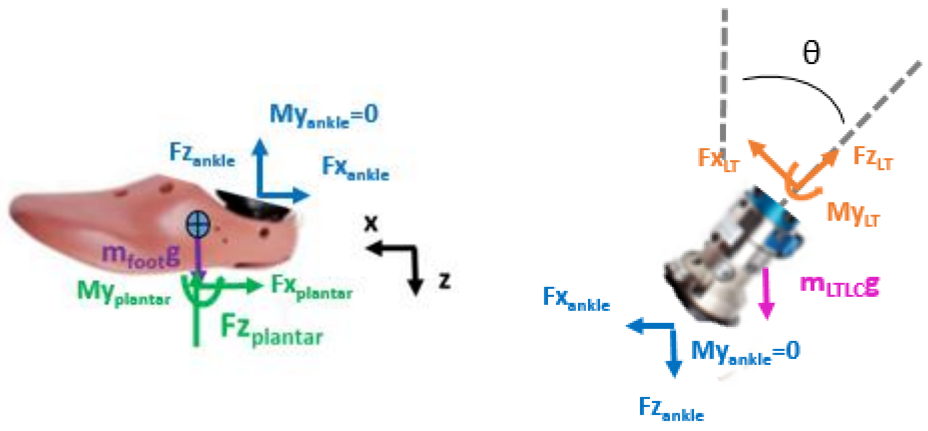

Figure 7.50. Free body diagrams for the foot and distal portion of the tibia below the lower tibia load cell. Note that θ represents the angle between the tibia shaft and the normal to the footplate.

It is important to note that, though it is possible to estimate the footplate force using the methods described above, the Mil-Lx has not been validated for alternative postures. Since the Mil-Lx was intended for use in vertical loading scenarios, little effort has been placed on benchmarking the response of the Mil-Lx for alternative knee or ankle angles. The equations above have assumed that no force is generated by the ankle joint. However, the ankle joint includes a rotational stiffness and joint stops which have been ignored up to this point. Thus, it is recommended that the Mil-Lx be used for primarily axial loading applications for which the ankle angle is small. Further, injury criteria such as the tibia index and the ankle joint injury criteria described by Kuppa et al. should not be used with the Mil-Lx until further validation efforts have taken place to ensure the correct response of the ATD compared to the human leg. Previous work by Pandelani et al. has shown that the tibia index developed for the Hybrid-III yields different results than the Hybrid-III for the same loading condition.[157]

To reiterate the limitations and guidelines for using the proposed injury criterion, the force-impulse injury criterion should be used for primarily axial loading environments for which the applied load is aligned within +/- ten degrees of the SAE z-axis of the ATD tibia and only for load durations ranging from 5-90 ms. Estimated or measured plantar forces should be baseline shifted and filtered to SAE J-211 filter class CFC1000. The force data should be mass-scaled to a 50th percentile male in order to estimate probability of injury for different percentiles of the population prior to using the injury risk function. Eqn. 6.36 can then be used to calculate the probability of injury at each time step. The maximum probability of injury from all time steps should be used to estimate the overall probability of injury associated with the event.

7.7 Discussion

Data from previous literature and from experimental tests from the present study showed that the current form of the Mil-Lx is unable to reproduce both the plantar and proximal tibia forces measured for the human leg for all loading frequencies of interest. The lumped mass model and finite element model optimization exercises performed in this chapter highlighted the weaknesses associated with the current design. First and foremost, the placement of the tibia compliant element is located proximal of the majority of the compliance in the human leg. Ideally, the compliant element would represent the compliance of the ankle, but because much of the mass of the Mil-Lx is located distal to the compliant element, mass is recruited faster in the Mil-Lx than it is for the human leg. This fault is most obvious when the Mil-Lx is loaded with high frequency loads which cause a double peak in the plantar force trace. Lower frequency loads, associated with larger displacements, engage more mass in the human leg than higher frequency loads. Further, for lower frequencies, the placement of the compliant element matters less since the mass is recruited more gradually.

The second fault of the Mil-Lx is that it was only designed to match the upper tibia force to the PMHS mid-tibia force for vertical loading. The lower tibia load cell has no significance in terms of estimating the response or probability of injury of the human leg. Moreover, the Mil-Lx cannot measure forces in the foot, despite foot and ankle fractures being the most common injuries in UBB events. The fact that the Mil-Lx was designed for high rate applications, but has no ability to measure the larger localized forces due to inertial differences prevents the Mil-Lx from providing sufficient information to distinguish between the injuries applicable to UBB and those applicable to automotive rates.

Designing an ATD leg to match the response of the human leg perfectly would require a more continuous structure which matches both the mass and compliance of the human leg. Unfortunately the difficulty lies in designing the ATD such that it can withstand higher loads than the human leg. Many current ATD leg designs have utilized strong materials such as steel and aluminum in series with a durable polymer in order to produce the desired overall compliance of the human leg. In the case of the Mil-Lx, location of the compliant element and overall mass distribution of the leg produces a different frequency response than the human leg. To improve the Mil-Lx design, it is recommended that the leg be reconfigured in terms of mass distribution, which requires moving the compliant tibia element to a more distal location. The lumped mass models developed in Chapter 5 provide a reasonable guide for the breakdown of mass and the compliances necessary to produce a biofidelic response across a wider range of loading frequencies than the current Mil-Lx can provide.

In the meantime, a modified version of the Mil-Lx may be used with the proposed force-impulse injury risk function to obtain estimates of injury probability. It is recommended that the tibia compliant element be replaced with 90 durometer polyurethane and the heel pad be replaced by 70 durometer neoprene. As discussed, these material changes yielded biofidelic footplate forces for loading durations as small as 4.5 ms. Further, additional instrumentation is necessary to calculate the footplate force using the Mil-Lx lower tibia load cell. This instrumentation includes ankle potentiometers and angular rate sensors mounted to the tibia and foot. The eventual goal for development of an improved ATD leg for this expanded range of loading applications is the inclusion of a plantar foot load cell, or perhaps a heel and forefoot load cell. In this case, it would be necessary to distinguish between the proportion of force transmitted through the heel versus the forefoot in the PMHS experiments and scale the injury criterion accordingly in terms of peak force and impulse. Previous studies have shown that a majority of the load is transmitted through the hindfoot, rather than the forefoot.[191,206]

Though the modifications to the Mil-Lx improve the ability of the Mil-Lx to replicate the force response of the human leg, the overall stiffness of the leg is also important. As discussed in Section 7.2 and Figure 7.1, the ability to accurately predict the response of the human using an ATD relies on the ability of the ATD to interact with injury mitigation materials in the same way, which is reliant on the overall stiffness of the ATD compared to the human leg. Thus, the ATD must respond similarly to the human leg in terms of compression response as well as in terms of force response. The Mil-Lx's mass distribution prevents it from replicating both force (plantar and proximal tibia) and overall compression response, which limits the use of the modified Mil-Lx in terms of use with uncharacterized injury mitigation materials.

Nonetheless, other existing ATD legs such as the Hybrid-III and Thor-Lx are also unable to replicate the force-deflection of the human leg for such a wide range of loading frequencies.

7.7.1 Discussion of Modified ATD Design

Limitations were placed on the assumed validity of the modified Mil-Lx in terms of the frequencies for which it can accurately estimate human footplate force. No limitations have been assigned to the current Mil-Lx design or the injury criteria associated with the upper tibia force. The purpose of this discussion is to compare the injury probabilities estimated by the original and modified Mil-Lx using their respective injury risk functions. Injury risk estimated using the human leg model with element deletion was also calculated. Injury probability estimated by the McKay injury criterion predicted injury for the 250g, 4 m-s^{-1} and 50g, 6 m-s^{-1} cases for which injury did not occur in the human FE model, though the original Mil-Lx only incorrectly predicted injury for the 50g, 6 m-s^{-1}. The original Mil-Lx also failed to predict injury for the 100g, 4 m-s^{-1} case, for which the probability of injury predicted by the original Mil-Lx was more than 20 percent less than the probability of injury predicted using the modified Mil-Lx and force-impulse injury criterion.

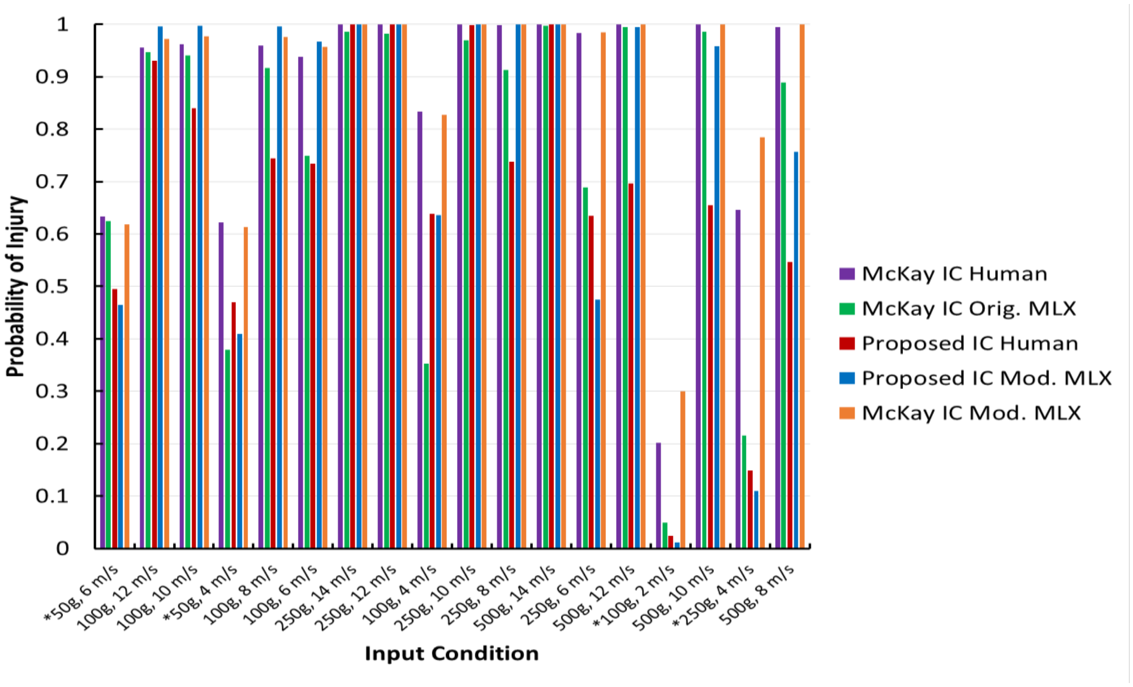

Figure 7.51. Probability of injury calculated using the McKay and Bir injury criterion and the proposed force-impulse injury criterion for the original and modified Mil-Lx FE model. Input conditions with asterisks indicate that failure occurred in the human FE model.[136]

In terms of injury risk estimated using each of the injury criteria and the forces measure in the human FE model, the McKay injury criterion predicted higher probability of injury for all conditions, with an average difference in injury probability of 19 percent. The reason for the McKay injury criterion over-predicting probability of injury is likely due to the fact that it was developed based on data from PMHS tests which likely included artefactual fractures, which would tend to lower the force at fracture. Additionally, forces were measured at the mid-shaft of the tibia using implanted load cells for the McKay and Bir study.[136] Since these tests were performed at high rates, it would be expected that the forces measured at the mid-shaft of the tibia would be less than the force applied to the foot at the footplate surface due to inertia. Thus, the forces associated with fracture in the McKay and Bir study would be less than those which actually caused the fractures, leading to an injury risk function which over-predicts the probability of injury.

Large differences were observed between the peak human mid-tibia force and the peak Mil-Lx upper tibia forces for the original Mil-Lx model compared to the modified Mil-Lx model. For long duration input conditions (12.8-100 ms), peak upper tibia forces were comparable to the original and modified Mil-Lx FE models and forces were within 2 kN of the peak mid-tibia force measured in the human FE model. In general, the original Mil-Lx force peaks tended to be closer to the peak forces for the human model with element deletion, while the modified Mil-Lx model tended to predict the peaks of the human model without element deletion. It is also important to note that the probability of injury estimated using the human FE model does not accurately represent the population, but only one possible response of the human leg.

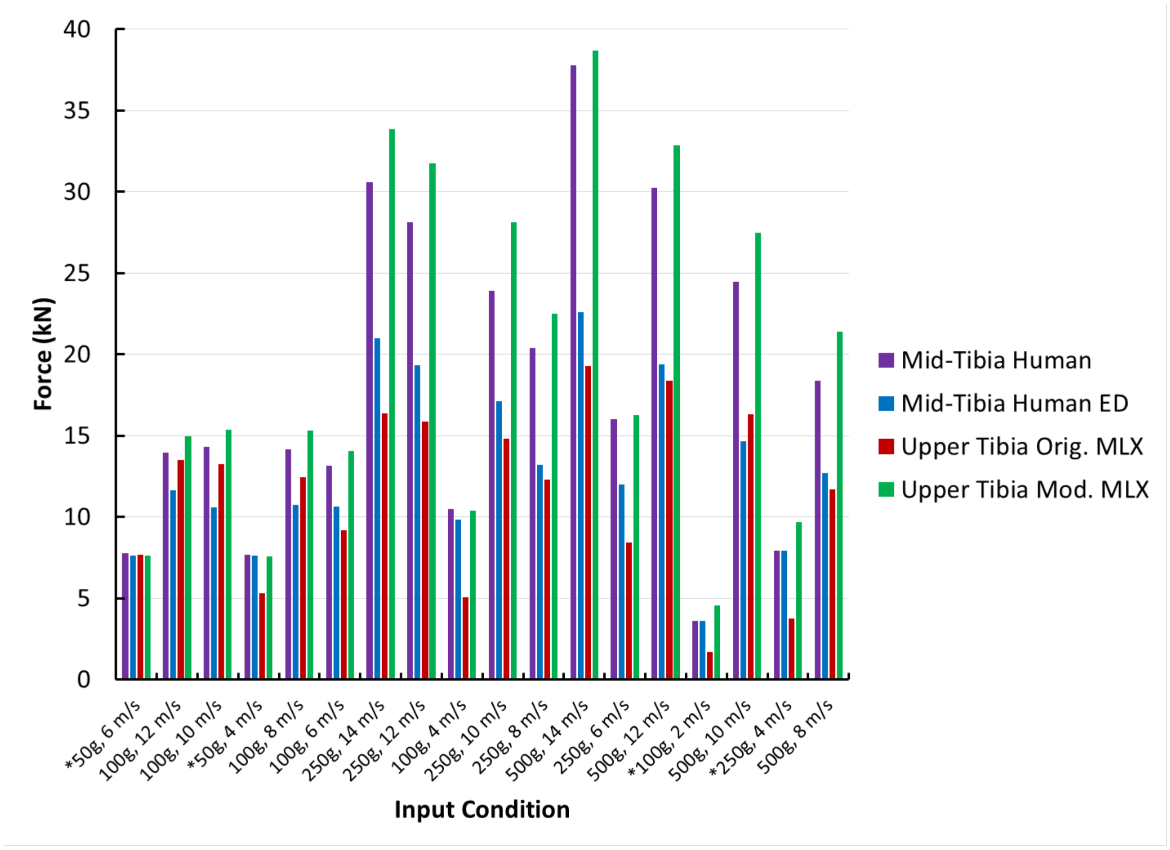

Figure 7.52. Difference between human mid-tibia force and the forces estimated using the original and modified Mil-Lx FE models. Human FE model response with element deletion (ED) is also reported.

These two Mil-Lx models represent two different theories in terms of how to model human response. The original Mil-Lx seems to model the effect of injury, while the modified Mil-Lx models the assumed response of the human leg without injury. In terms of using the proposed injury risk function, the modified Mil-Lx model is better suited for predicting the severity of the event, though it would be unlikely to match the probability of injury associated with the peak force and impulse from the human leg since peak force and impulse would be over-predicted for cases where fracture occurred in the human leg. On the other hand, the original Mil-Lx may not be able to match the response of the human leg for cases where fracture does not occur.

A comparison of the peak force and impulse at peak force for each of the Mil-Lx models and human FE model with and without element deletion is provided in Figure 7.53. Some of points for the human model with element deletion follow the curved pattern established for the force at fracture from the parametric study. Others, for which the peak force exceeded the force at fracture are shown in the region beyond the "theoretical injury line" for which force at fracture and peak force were one in the same. For these data points, peak force occurred after the fracture in the model, meaning that the input contained enough energy to continue to reload the leg after release of energy from the fracture. This phenomena was observed in some of the PMHS tests discussed in the previous chapter, but to a much smaller degree than was observed in the FE model. Based on the observations from the PMHS studies, the peak forces would not exceed the force at fracture to the extent observed in the model, but instead would be likely to produced additional fractures beyond the initial fracture.

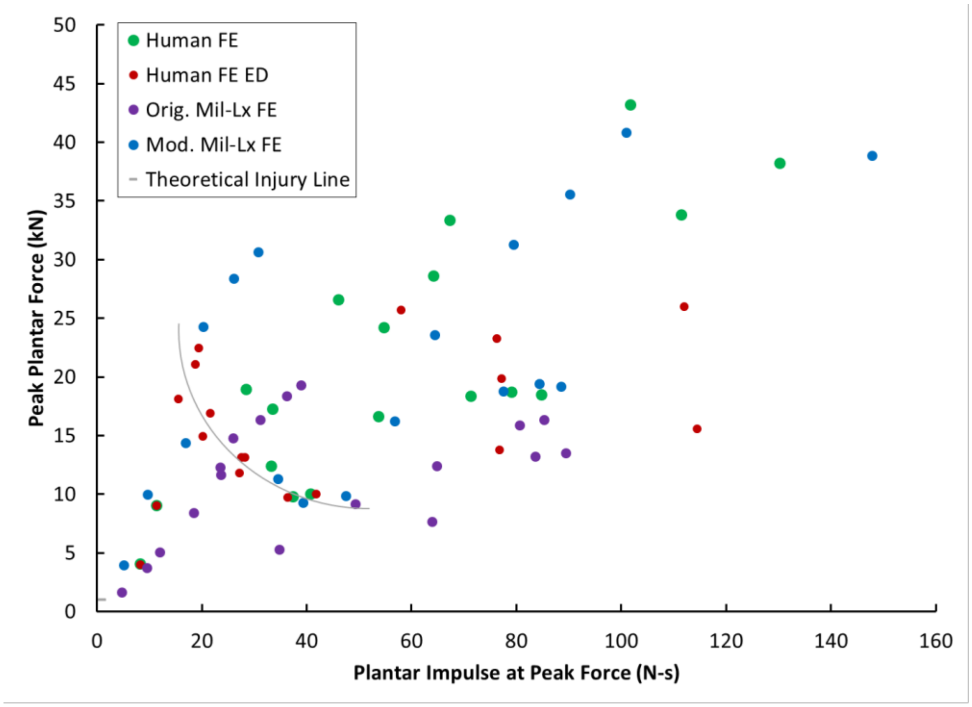

Figure 7.53. Peak force and impulse at peak force for the original and modified Mil-Lx FE models and for the human leg FE model with and without element deletion (ED). Individual data points are shown each of the input conditions used for the human model parametric study.

A contour plot showing the line for 50% probability of injury for age 27 as defined by the proposed injury risk function is provided in Figure 7.54. Injury data points (outlined in black) and "no-injury" data points (outlined in white) are plotted for the response of the human FE model with and without element deletion (ED) and for the original and modified Mil-Lx FE model. "No-injury" points are shown to be below the 50% threshold for both Mil-Lx models, but the probability of injury predicted using the original Mil-Lx is significantly lower than the probability of injury predicted by the modified Mil-Lx and using the results of the human FE model. Additionally, the original Mil-Lx model predicted less than 50% probability of injury for three injury data points. For one injury case, less than 50% probability of injury was calculated using the human model with element deletion, with the modified Mil-Lx model predicting a similar probability of injury below 50% for the same input condition.

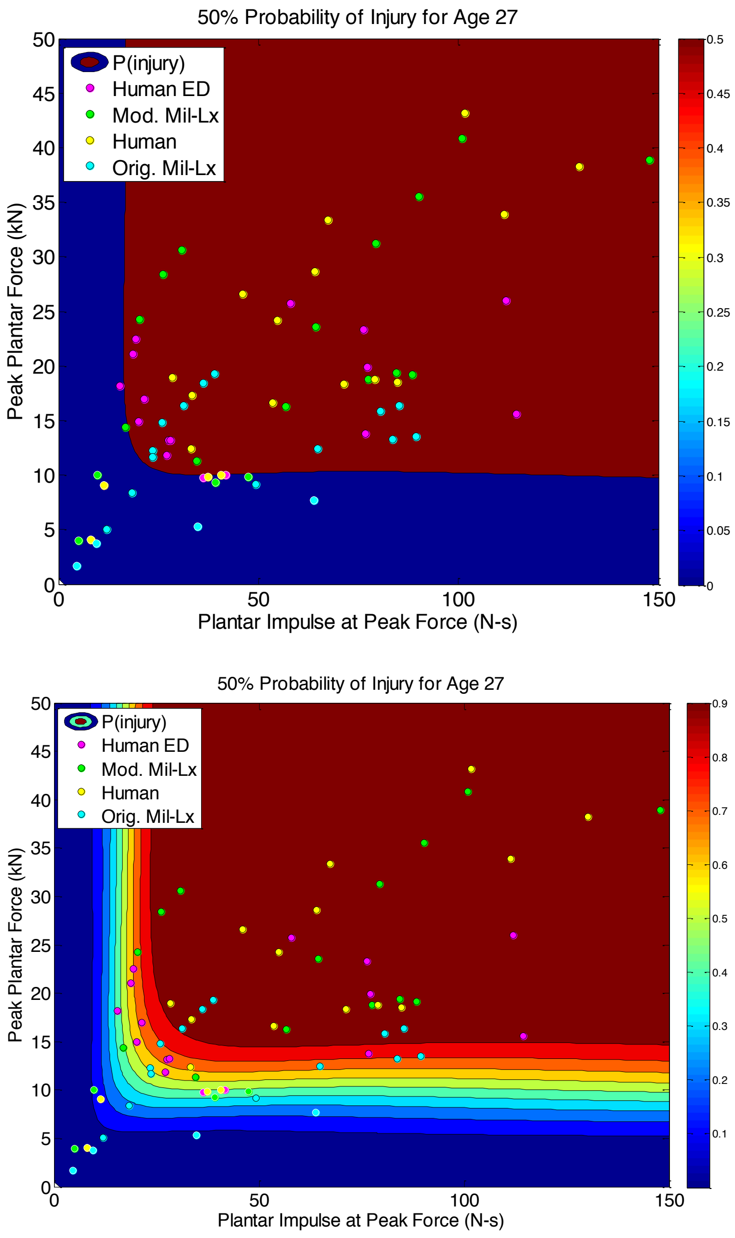

Figure 7.54. Contour for 50% probability of injury for age 27 as defined by the proposed injury risk function. Injury data points (outlined in black) and no-injury data points (outlined in white) are plotted for the response of the human FE model with and without element deletion (ED) and for the original and modified Mil-Lx FE model. The second plot (bottom) provides the same data, but with additional contour lines.

7.7.2 Cost-Benefit Analysis of Mil-Lx Redesign

Both the purchase and design of anthropomorphic test devices are costly. A General Motors engineer stated that crash test ATDs can range in cost from $100,000 to $500,000 depending on the type of ATD and the degree to which the ATD is instrumented.[91] The National Highway Traffic Safety Administration spent over $11 million on biomechanics research, which funded testing and evaluation of the Thor ATD in addition to development of injury criteria for various body regions.[112] As ATDs become more sophisticated and additional instrumentation is added, these costs will likely increase.

The Warrior Injury Assessment Manakin (WIAMan) Program was established by the U.S. Department of Defense to design an ATD specifically for military applications such as underbody blast. This program began in 2010, and was allotted an $88 million budget over a 5-year span. The complexity and expansiveness of the project required an additional $98 million of funding in 2015.[88] While the WIAMan project is atypical of ATD design in that ATD development for crash testing purposes has taken place over decades rather than in a concentrated effort, the cost of developing the Hybrid-III and Thor ATDs and associated injury criteria may be comparable.

Understanding that a redesign of the ATD leg is only a portion of the whole body ATD and would only cost a fraction of the overall budget for design of an ATD, using the guidelines provided in this dissertation to improve upon the biofidelity of the Mil-Lx would greatly reduce the cost of completely redesigning the leg. Further, adapting the design of the Mil-Lx leg by replacing only the heel pad and compliant element materials eliminates the need to buy a completely new set of ATD legs. The cost of altering the Mil-Lx leg by changing the materials used for the compliant element and heel pad would cost an estimated $500 for materials and machining costs. On the other hand, buying a completely new, redesigned ATD leg could cost more than $52,600 (the current cost of a pair of Thor-Lx legs).[238] Changing the placement of the compliant element in the tibia shaft would increase the cost of improving the Mil-Lx design, however, a cost-benefit analysis should be used to determine whether to pursue a completely new design that includes a foot load cell.

Having summarized the costs associated with designing an ATD and buying a new pair of ATD legs, it is apparent that the current strategy for improving the Mil-Lx's biofidelity offers financial benefits over other options that cannot be ignored. Further, the methodology and reasoning behind designing the ATD leg to be biofidelic at both low and high frequencies typical of automotive intrusion and UBB provides advantages over the WIAMan ATD leg which is currently aimed at providing biofidelity for UBB scenarios only. In theory, tuning the WIAMan ATD leg using higher frequency pulses could potentially cause the ATD to provide inaccurate results when floor mats are incorporated into the vehicle or if the ATD is fitted with different boots.

8 Summary

The goal of this dissertation was to provide a set of tools which could be used to estimate the injury risk of the human leg exposed to axial impacts characteristic of underbody blast and automotive intrusion. Existing injury criteria and anthropomorphic test devices fail to account for the effect of load duration and frequency, which limits the validity of individual risk functions and ATDs to a small subset of the frequencies applicable to UBB. For this reason, the same ATD and injury criteria may not be valid for both mitigated and unmitigated UBB scenarios. Tasks described in this dissertation were performed with the objective of combining UBB and automotive leg data with the hope of developing a single injury risk function and ATD which could be used in both loading environments.

PMHS axial impact tests were performed and used to validate a pre-existing finite element model of the human leg. The model was then used to perform a parametric study to demonstrate the duration-dependence of fracture force. Lumped mass models were constructed based on the response of the human leg FE model for a range of sinusoidal footplate acceleration pulses with durations ranging from 2-100 ms. These lumped mass models and the results of the FE parametric study were used to characterize the relationship between fracture force and duration which was used to develop a duration-dependent injury risk function for the leg exposed to axial impact loading.

The duration-dependent injury risk function used data obtained from the PMHS tests as well as a collection of additional axial loading tests from the literature to optimize for survival model parameters using a force- and impulse-based predictor variable. The injury risk function was shown to improve injury prediction accuracy compared to existing injury risk functions which used peak force as the injury predictor.

An existing ATD leg, the Mil-Lx, was assessed for its ability to predict injury using the proposed injury risk function. A finite element model of the Mil-Lx was developed and exercised to estimate the range of loading durations for which the Mil-Lx can predict human plantar and proximal tibia force. The Mil-Lx FE model provided a good fit (CORA>0.80) of plantar force for footplate acceleration pulse durations ranging from frequencies ranging from 2.5-5.0 ms, but failed to provide a satisfactory estimation of tibia force for the same durations. The Mil-Lx was then modified to provide biofidelic forces at the plantar surface of the foot. Insight into the limitations of the current Mil-Lx configuration was obtained from the development of additional lumped mass models based on the mass distribution of the Mil-Lx. Conclusions from lumped mass model and Mil-Lx finite element model optimization exercises revealed that the placement of the tibia compliant element limits the ability of the Mil-Lx to produce biofidelic force response at both the plantar and proximal tibia locations.

A discrete optimization approach was used to choose alternative materials for the tibia compliant element and heel pad to improve the biofidelity of the Mil-Lx's plantar force. Results from this analysis revealed that replacing the heel pad material with 70-durometer neoprene and the tibia compliant element with 90-durometer polyurethane rubber improves the biofidelity of both the proximal tibia and plantar forces for the range of footplate acceleration durations from 4.5-100 ms. Additional recommendations were made in terms of adding additional instrumentation to the Mil-Lx in order to estimate plantar force without a foot load cell.

8.1 Limitations and Use

Though great progress has been made in understanding the duration-dependence of injury for axial loading of the leg, additional data would benefit the field in terms of validation of the proposed injury risk function. Despite efforts to validate the injury risk function using cross-validation and statistical comparisons using subsets of the combined data set, reliable validation of the injury risk function requires an independent data set. Nonetheless, the statistical analysis used to vet the proposed injury risk function goes beyond analyses performed for previous leg injury risk functions in terms of estimating predictive accuracy.

The form of the equation relating force and impulse that was used in the development of the injury risk function requires further attention. While the equation was able to provide a good fit of the finite element model and lumped mass model response surfaces relating force and impulse to leg compressions and strains, the derivation of the relationship between leg compression and these two parameters for the multiple-degree-of-freedom lumped parameter model may improve the fit of the injury data. The analytical form of the equation relating force, impulse, and compression would allow for the equation parameters to be based on actual LMM mass, stiffness, and damping parameters which could eventually be altered to scale the injury criterion for subject-specific injury risk estimates. These parameters may also be used to provide a better method for scaling the injury risk based on bone geometry and bone material characteristics if the force-impulse formulation were altered.

The strain-rate dependency of the yield strength of bone was assumed negligible for this study. From experimental tests, strain rates in the tibia and calcaneus were found to be less than 2000 μS-ms^{-1} for the high impactor test condition, which only amounts to a three percent increase in yield strength according to the relationship established by Carter and Hayes.[37] The presence of the heel pad dampens the load delivered to the bony structures of the foot, which prevents these strain rates from yielding significant effects on the force at fracture. Moreover, the presence of boots for the case of UBB is also likely to prevent strain rates from exceeding those used in the development of the injury criterion. Application of the injury criterion to loading environments such as those encountered during an anti-personnel landmine detonation would require additional investigation of the effect of strain rate.[20] For this reason, bounds have been placed on the range of frequencies and peak forces for which the proposed injury risk function is valid.

Though the Mil-Lx was primarily intended for vertical loading scenarios with a neutral posture, this dissertation provides a methodology for estimating Mil-Lx plantar force using the Mil-Lx lower tibia force when the Mil-Lx is loaded in an alternative posture. The Mil-Lx, however, has not been validated for such postures, and the results of the calculation should be treated carefully, since the effect of ankle positions was not considered in the development of the injury risk function. Previous studies have concluded that foot and ankle fracture force increases with dorsiflexion angle as a result of changes in joint contact area.[15,35,71,81,109] Alternative postures may also lead to off-axis and combined loading scenarios, which were also not considered in this study. Future studies must investigate how axial force and duration tolerance is affected by these additional loading vectors and account for the possibility that ankle position may change the injury mechanism from axial compression to bending. The tibia index, which uses tibia forces and moments, is currently used to assess tibia injury probability for combined loading using the Hybrid-III. It is recommended that future ATD legs use a similar measure in addition to the proposed axial loading IRF to estimate injury risk since tibia bending is not factored into the proposed IRF. The lack of validation for the Mil-Lx exposed to non-vertical loading conditions prevents the application of even a modified revised tibia index for estimation of tibia fracture. Moreover, using a modified tibia index requires simultaneous biofidelity of plantar and proximal tibia forces, which the proposed modifications to the Mil-Lx cannot fully satisfy. To summarize, the following guidelines should be used for the injury risk function and suggested modifications to the Mil-Lx design:

1. Limit use to vertical loading where the angle between the tibia and footplate is within 80-100 degrees.
2. Limit the use of the injury criterion for force durations ranging between 5 and 90 ms.
3. Limit the use of the modified Mil-Lx design between footplate acceleration durations of 4.5-100 ms.
4. Mass normalization[62] may be used to scale the injury risk function for anthropometries other than the 50th percentile male.

While improvements were made to the Mil-Lx ATD design by changing the heel pad and compliant element materials, other options exist for further maximizing the biofidelity of the ATD’s response. Mass distribution of the leg due to the placement of the compliant tibia element is one major drawback of the current Mil-Lx design. While the optimal design for an ATD leg would match both the mass distribution and compliance of the human leg, moving the compliant puck to a more distal location would require redesigning the Mil-Lx structure. This type of redesign would be more costly than the proposed modifications to the Mil-Lx leg, which simply involves changing out easily-replaceable parts. It should be noted, however, that this modification does not guarantee biofidelity outside the stated range of acceleration frequencies since even and ATD-to-human transfer function does not guarantee an accurate estimate of human response. Mismatches in stiffness between the human and ATD legs cause these transfer functions only to be valid for cases in which an additional compliance is not present between the impacting structure and the leg. This is a major flaw with current ATDs which often produce different compressions of floor mats, knee bolsters, etc., which lead to a differences in the forces measured in the ATD compared to the forces experienced by the human leg. Without first characterizing the materials or structures interacting with the leg, a transfer function is not helpful for interpreting ATD response.

Further design effort may be focused on the leg flesh for the Mil-Lx as the coupling of this mass to the leg may be useful for modulating the force response for certain frequencies of loading. While the parameter-dependent LMM attempted to account for the effect of the soft tissue by using a parallel mass, a PMHS study specifically aimed at measuring the rate at which the soft tissue mass is recruited may be necessary to fully characterize the leg's response to different loading frequencies. This may be of particular importance when attempting to scale the injury criteria for anthropometries such as the 5th percentile female.

8.2 Future Work

The impact of this work has potential to improve the ability to predict foot and leg injury in both military and automotive environments by providing an injury criterion that is not tied to particular loading durations or boundary conditions. Though this dissertation outlines steps that should be taken to improve the design of the Mil-Lx so that it may be used with the proposed injury criterion, the long-term solution to improving injury prediction in these environments requires further research.

The ideal approach for implementing the research from this dissertation would be to collaborate with an ATD manufacturer to incorporate the design specifications from this dissertation into a military ATD. The conclusions from this dissertation indicate that measurement of plantar force in an ATD leg would allow for a reduction in inertial effects present between the location of force measurement and the most common location of injury, the foot and ankle. Further, it is recommended that an ATD leg designed for the military environment also be able to provide a biofidelic response for longer duration loads to accommodate the changes to the load that may be caused by different injury mitigation schemes. The lumped mass models and finite element optimizations presented in this dissertation provide a starting point and suggest approaches for designing an ATD leg which can provide biofidelic responses across an expanded range of load durations and frequencies. Implementing these approaches as part of the ATD design process could save both time and money by providing a simplified, efficient means for estimating the material properties and mass distribution necessary to achieve a biofidelic response. Further, if the ATD leg were designed to span both military and automotive environments, the leg could be used in a more versatile manner which would encourage a more widespread use of the ATD leg in both academic and commercial environments. In turn, this would provide a more cohesive base of literature for understanding the response of the leg when in the presence of different floor padding or boots.

While the main focus of the dissertation was to develop an injury criterion for the foot/leg, the lumped mass models provide a path forward for future ATD development and vehicle safety optimization. Though simple second-order systems were investigated for their ability to fit human leg force and displacement responses, use of more complicated constitutive models such as combinations of Kelvin-Voigt or generalized Maxwell units may improve these models. Future efforts for ATD design may utilize these models to simplify and characterize the human leg response in order to optimize the range of frequencies for which future ATDs can behave biofidelically. Further use of these models, coupled with the force and duration based injury risk function, may include a limiting performance study to estimate the best case scenario (largest reduction in injury probability) for floor mats or boots with specific geometric constraints such as thickness.

Though the human foot and leg finite element model used in this study was shown to fit the PMHS corridors developed for five different test conditions, the model lacked articular cartilage in the ankle joint and did not significantly distinguish between ligamentous material properties. Cutting edge finite element models have added detail to the soft tissue of the ankle joint.[68,110,149] Future work should be aimed at updating these finite element models to include high rate material properties, and then comparing to the PMHS corridors provided by this dissertation.

This dissertation did not explore the effects of alternative postures and non-vertical loading, but the models developed and validated as part of this dissertation offer valuable tools for investigating these effects. For example, the human leg and Mil-Lx finite element models may be used to estimate the effect of changing the ankle position in terms of the difference between plantar and tibia forces. These modelling results may be helpful in further establishing the bounds for which the proposed injury criterion is valid in terms of predicting calcaneus versus tibia fractures. Additional validation efforts would be required to ensure that the load transmission through the ankle joint is biofidelic for these alternative postures.

8.3 Contributions

This dissertation contributes 54 additional PMHS leg axial loading tests to the literature, which provide valuable information about the timing and progression of foot and ankle fracture, and are the first lower extremity PMHS tests to use high speed x-ray. The test matrix design of the impactor tests allowed direct comparison of force at fracture for two different load duration groups, which demonstrated that force at fracture is not constant across all load durations. Though this concept had been previously demonstrated for other body regions, this study was the first to verify its applicability to the leg. Biofidelity corridors for forces and displacements generated from the PMHS experimental data were also produced, and provide additional data for validating ATDs and human leg finite element models for different loading rates.

Secondly, a set of lumped mass models of the human leg were developed to characterize the leg's frequency response. These models revealed that the human leg response to axial loading can be characterized for single loading frequencies ranging from 5 to 156 Hz using a three-mass model, and for 5 to 130 Hz using a two-mass model. These models provide guidelines for future ATD development since ATDs currently use a series of metal and polymer materials to replicate the overall compliance of the leg. Implementing ATD design changes to match the human-based lumped mass model characteristics would reduce the need for multiple ATDs to cover different loading frequencies. Further, designing the ATD leg in this manner would reduce the complications that arise from differing responses when floor mats or other compliant materials are present which can respond differently when in the presence of legs with different stiffnesses.

The major contribution of this dissertation is an injury risk function for the leg exposed to axial impact loads that accounts for duration-dependence of fracture force. While previous IRFs have used peak force to predict injury, the aforementioned PMHS experimentation revealed that force at fracture decreases with duration of the load for high frequencies, and force-at-fracture is less dependent on time for low frequencies. These findings are consistent with previous theoretical literature and injury models for other body regions,[140,197,208,215] though this study is the first to demonstrate this phenomenon for the leg. In light of these findings, a force and impulse-based injury risk function was developed for the leg, which spans a larger range of load durations (5.1 to 89.9 ms) than previous IRFs and demonstrates a high level of accuracy for injury prediction (81.8%).

The contributions of this injury risk function have far-reaching implications for both military and automotive loading environments, particularly when considering that accurate assessment of injury risk using ATDs requires biofidelity of plantar force magnitudes and durations. For underbody blast applications, which can span a large range of load durations depending on the type of vehicle, PPE, or vehicle floor design, it is imperative that loading duration be accounted for in the injury risk function. For example, a force-based injury criterion developed for high amplitude, short duration unmitigated blasts may over-estimate the force required to cause injury for mitigated blast cases where floor mats may lengthen the duration; this could potentially lead to underestimation of injury probability. The proposed injury criterion offers the ability to predict injury accurately for a larger range of loading durations, which ensures that when floor mats or PPE are used for injury mitigation in UBB, a single injury criterion can be used to predict risk of injury.

Furthermore, accuracy of injury prediction for the proposed IRF was shown to be greater than that of previous injury risk functions in the literature, by 8% for Yoganandan 2015 data set, 18% for the Funk 2002 data set, and by 5% for the combined data set. Statistics also showed that the proposed force-impulse IRF provided better injury prediction accuracy than a strictly plantar force-based IRF developed using the same set of data. The proposed injury criterion was shown to improve injury prediction accuracy compared to the Kuppa et al., Yoganandan et al., and Funk et al. injury risk functions for both the large combined data set and smaller data sets encompassing narrower ranges of load durations and frequencies.[73,116,230,231]

The introduction of a duration-dependent injury risk function necessitates the development of an improved ATD leg which can provide a biofidelic response for the range of loading frequencies covered by the injury risk function. A finite element model of the Mil-Lx estimated that the current design of the Mil-Lx is only capable of predicting injury using the proposed injury criterion between acceleration durations of 2.5-3.2 ms. It should be noted that Mil-Lx proximal tibia forces were not biofidelic for this range of frequencies. The Mil-Lx was then modified to estimate biofidelic forces at both the plantar surface of the foot and upper tibia. Replacing the heel pad and compliant element materials with 70-durometer neoprene and 90-durometer polyurethane, respectively, expanded the Mil-Lx's plantar force and proximal tibia force biofidelity to durations ranging from 4.5 to 100 ms. This modification to the current Mil-Lx enables the use of the proposed injury risk function for this limited range of frequencies until a new ATD can be designed with a more biofidelic mass and compliance distribution. Moreover, the suggested Mil-Lx modifications serve as a quick, low-cost solution for improving an existing ATD which prevents the immediate need to purchase new ATD legs which may be designed to perform for only a limited range of loading frequencies.

A methodology for applying the proposed injury criterion to the Mil-Lx is supplied, which utilizes multibody dynamics to estimate plantar force using the lower tibia force measured by the Mil-Lx. For primarily vertical loads, it is possible to estimate the plantar force with the instrumentation currently installed on the Mil-Lx. For non-neutral initial ankle positions, it is recommended that additional instrumentation be added to the Mil-Lx to estimate plantar force accurately. This instrumentation includes angular rate sensors on the Mil-Lx tibia and foot so that the rotation characteristics of these parts may be measured. This additional instrumentation should also be included on future ATD legs which do not contain foot load cells.

In summary, the duration-dependent leg injury risk function described in this dissertation increases the injury prediction accuracy by up to 18% compared to previous injury risk functions, and expands the range of load durations for which a single leg injury risk function may be used, encompassing load durations of 5.1-89.9 ms. Further, Mil-Lx modifications outlined in the dissertation provide a temporary solution for providing an ATD which can utilize the proposed injury criterion. The lumped-mass modeling efforts outlined a simplified approach for further expanding ATD biofidelity. These contributions are the first step toward establishing more accurate assessment of the effectiveness of injury mitigation schemes for underbody blast, and have the potential to inform the design process for military vehicles.

Summary of Contributions:

1. First PMHS leg tests using high speed x-ray to track fracture progression
2. Biofidelity corridors for force and displacement
3. Lumped-mass models for the human leg
4. Duration-dependent injury risk function valid for plantar force durations of 5-90 ms.
5. Recommendations for changes to the Mil-Lx design using both lumped-parameter and finite element models to expand the range of load duration for which it can be used.

8.4 Publications

8.4.1 Conference Proceedings/Presentations

1. Bailey, A, Poplin, G, McMurry, T, Salzar, R, Crandall, J, Improved Survival Model for Foot/Ankle/Leg High Rate Axial Impact Injury Data, Association for the Advancement of Automotive Medicine Conference, Philadelphia, PA, October 4-7, 2015.
2. Bailey, A, Panzer, M, Salzar, R, Development of a Transfer Function for Interpreting Hybrid-III Leg Data from Axial Loading, Proceedings of the International Conference on the Biomechanics of Impact, Berlin, Germany, 2014.
3. Bailey, A, Panzer, M, Salzar, R, Development of a Hybrid-III to Human Leg Transfer Function for Axial Loading, Ohio State University Injury Biomechanics Symposium, Columbus, OH, 2014.
4. Perry, B, Gabler, L, Bailey, A, Henderson, K, Brozoski, F, Salzar, S. Lower Extremity Characterization and Injury Mitigation. Proceedings of the International Conference on the Biomechanics of Impact, Berlin, Germany, 2014.
5. Perry, B, Bailey, A, Gabler, L, Henderson, K, Brozoski, F, Salzar, R, Optimization of Combat Boot Properties to Mitigate Underbody Blast Injuries to the Lower Extremity, Personal Armor Systems Symposium, Cambridge, UK, September 8-12, 2014.
6. Bailey, A, Christopher, J, Henderson, K, Brozoski, F, & Salzar, R. Comparison of Hybrid-III and PMHS Response to Simulated Underbody Blast Loading Conditions. Proceedings of the International Conference on the Biomechanics of Impact, Goteborg, Sweden, 2013.
7. Henderson, K, Bailey, A, Christopher, J, Brozoski, F, & Salzar, R. Biomechanical Response of the Leg Under High Rate Loading. Proceedings of the International Conference on the Biomechanics of Impact, Goteburg, Sweden, 2013.

8. Bailey, A, Boruah, S, Christopher, J, Shafieian, M, Cronin, D, Salzar, R, Finite Element Analysis of the Injury Potential of Shock-Induced Compressive Waves on Human Bone, Ohio State University Injury Biomechanics Symposium, Columbus, OH, 2012.
9. Bailey, A, Boruah, S, Christopher, J, Shafieian, M, Cronin, D, Salzar, R, Injury Potential of Shock Induced Compressive Waves on Human Bone, International Congress & Exposition on Experimental and Applied Mechanics, Costa Mesa, CA, USA, June 11-14, 2012.
10. Funk, J, Rudd, R, King, R, Srinivasan, S, Bailey, A, Crandall, J, Injuries caused by brake pedal loading of the midfoot, Rocky Mountain Bioengineering Symposium, Blacksburg, VA, March 23-24, 2012.

8.4.2 Journal Publications

1. Bailey, A, Salzar, R, Crandall, J, Optimization of Anthropomorphic Test Device Leg Biofidelity using Analytical and Finite Element Models, *International Journal of Impact Engineering.*
2. Bailey, A, McMurry, T, Salzar, R, Crandall, J, An Injury Risk Function for the Leg Exposed to Axial Impact Loading using Force and Impulse, *Journal of Biomechanical Engineering*.
3. Bailey, A, Perry, B, Salzar, R, Response and Injury of the Human Leg for a Range of Axial Impact Durations, *Journal of Crashworthiness*.
4. Bailey, A, Poplin, G, McMurry, T, Salzar, R, Crandall, J, Improved Survival Model for Foot/Ankle/Leg High Rate Axial Impact Injury Data, *Traffic Injury Prevention*, 16, pages S96-S102, 2015*.*
5. Bailey, A, Christopher, J, Salzar, R, Brozoski, F, Comparison of Hybrid-III and Post Mortem Human Surrogate Response to Simulated Underbody Blast Loading, *Journal of Biomechanical Engineering*, 137(5), 2015.

6. Salzar, R, Lievers, B, Bailey, A, Crandall, J, Leg, “Foot, and Ankle Injury Biomechanics,” *Accidental Injury – Biomechanics and Prevention,* 3rd Edition, Springer New York, pages 499-547, 2015.
7. Bailey, A, Christopher, J, Salzar, R, Brozoski, F, Post Mortem Human Surrogate Injury Response to Simulated Underbody Blast, *Annals of Biomedical Engineering*, 43(8), pages 1907-1917, 2015.
8. Bailey, A, Boruah, S, Christopher, J, Shafieian, M, Cronin, D, Salzar, R, Injury Potential of Shock Induced Compressive Waves on Human Bone, *Dynamic Behavior of Materials*, 1, pp. 149-156, Springer New York, 2013.
9. Funk, J, Rudd, R, King, R, Srinivasan, S, Bailey, A, Crandall, J, Injuries caused by brake pedal loading of the midfoot, *Biomedical Sciences Instrumentation* 48:134, 2012.

9 References

1. Administration, N. H. T. S., and others. National automotive sampling system (NASS) general estimates system (GES) analytical users Manual 1988-2005. *US Dep. Transp.* , 2006.
2. Aerts, P., R. F. Ker, D. De Clercq, D. W. Ilsley, and R. M. Alexander. The mechanical properties of the human heel pad: a paradox resolved. *J. Biomech.* 28:1299–1308, 1995.
3. Alvarez, C. J. Epidemiology of Blast Injuries in Current Operations. , 2011.
4. Alvarez, C. J. Epidemiology of Blast Injuries in Current Operations. *Surv. Blast Inj. Full Landsc. Mil. Sci.* , 2011.
5. Ammann, P., and R. Rizzoli. Bone Strength and its Determinants. *Osteoporos. Int.* 14:S13–S18, 2003.
6. Andrews, D. M., and J. J. Dowling. Mechanical modeling of tibial axial accelerations following impulsive heel impact. *J. Appl. Biomech.* 16:276, 2000.
7. Andrews, D. M., and J. J. Dowling. Mechanical modeling of tibial axial accelerations following impulsive heel impact. *J. Appl. Biomech.* 16:276, 2000.
8. Austin, R. A. Lower extremity injuries and intrusion in frontal crashes. National Center for Statistics and Analysis, 2012.
9. Bailey, A. M., J. J. Christopher, F. Brozoski, and R. S. Salzar. Post Mortem Human Surrogate Injury Response of the Pelvis and Lower Extremities to Simulated Underbody Blast. *Ann. Biomed. Eng.* , 2014.doi:10.1007/s10439-014-1211-5
10. Bailey, A. M., J. J. Christopher, K. Henderson, F. Brozoski, and R. Salzar. Comparison of Hybrid-III and PMHS response to simulated underbody blast loading conditions. , 2013.at <http://www.ircobi.org/downloads/irc13/pdf_files/25.pdf>

11. Bailey, A. M., J. J. Christopher, R. S. Salzar, and F. Brozoski. Comparison of Hybrid-III and Postmortem Human Surrogate Response to Simulated Underbody Blast Loading. *J. Biomech. Eng.* 137:51009, 2015.
12. Bailey, A. M., T. McMurry, G. S. Poplin, R. S. Salzar, and J. R. Crandall. Survival model for foot and leg high rate axial impact injury data. *Traffic Inj. Prev.* 16:S96–S102, 2015.
13. Bailey, A. M., M. B. Panzer, and R. S. Salzar. Development of a Transfer Function for Interpreting Hybrid-III Lower Leg Data from Axial Loading. , 2014.at <http://www.ircobi.org/downloads/irc14/pdf_files/28.pdf>
14. Bailey, A. M., B. J. Perry, and R. S. Salzar. Response and Injury of the Human Leg for a Range of Axial Impact Durations. *Ann. Biomed. Eng.* , Under Review.
15. Bailey, Ann, McMurry, Timothy, Poplin, Gerald, Salzar, Robert, and Crandall, Jeff. Survival Model for Foot and Leg High Rate Axial Impact Injury Data. *Traffic Inj. Prev.* , 2015.
16. Balazs, G. C., E. M. Polfer, A. M. Brelin, and W. T. Gordon. High Seas to High Explosives: The Evolution of Calcaneus Fracture Management in the Military. *Mil. Med.* 179:1228–1235, 2014.
17. Banglmaier, R. F., T. E. Oniang'o, and R. C. Haut. Axially compressive impacts to the human tibiofemoral joint. *ASME-Publ.-BED* 42:673–674, 1999.
18. Barbir, A. Validation of lower limb surrogates as injury assessment tools in floor impacts due to anti-vehicular landmine explosions. *Wayne State Univ. Theses* , 2005.at <http://digitalcommons.wayne.edu/oa_theses/287>
19. Barr, J. S., R. H. Draeger, and W. W. Sager. Solid blast personnel injury; a clinical study. *Mil. Surg.* 98:1, 1946.

20. Bass, C., B. Folk, R. Salzar, M. Davis, R. Harris, M. S. Rountree, T. Harcke, E. Rouse, B. Oliver, and E. Sanderson. Development of a test methodology to evaluate mine protective footwear. DTIC Document, 2004.
21. Beck, T. J., C. B. Ruff, R. A. Shaffer, K. Betsinger, D. W. Trone, and S. K. Brodine. Stress fracture in military recruits: gender differences in muscle and bone susceptibility factors. *Bone* 27:437–444, 2000.
22. Bediz, B., H. N. Özgüven, and F. Korkusuz. Vibration measurements predict the mechanical properties of human tibia. *Clin. Biomech.* 25:365–371, 2010.
23. Begeman, P., and K. Aekbote. 'Axial Load Strength and Some Ligament Properties of the Ankle Joint. , 1996.
24. Begeman, P. C., and P. Prasad. Human ankle impact response in dorsiflexion. Society of Automotive Engineers, 1990.
25. Begeman, P., and P. Prasad. Human ankle response in dorsiflexion. *Prog. Technol.* 56:535–550, 1996.
26. Benesch, B. Utilizing Vehicle Response Data from Underbody Blast Tests. , 2011.
27. Bir, C., A. Barbir, F. Dosquet, M. Wilhelm, M. van der Horst, and G. Wolfe. Validation of lower limb surrogates as injury assessment tools in floor impacts due to anti-vehicular land mines. *Mil. Med.* 173:1180–1184, 2008.
28. Bluman, E. M., J. R. Ficke, and D. C. Covey. War wounds of the foot and ankle: causes, characteristics, and initial management. *Foot Ankle Clin.* 15:1–21, 2010.
29. Boone, D. C., and S. P. Azen. Normal range of motion of joints in male subjects. *J Bone Jt. Surg Am* 61:756–759, 1979.
30. Brown, D. Weaknesses of Impact Testing. , 1997.

31. Bruckner, J. Variations in the human subtalar joint. *J. Orthop. Sports Phys. Ther.* 8:489–494, 1987.
32. Burghele, N., and K. Schuller. Strength of calcaneus and astragalus. *Z. Für Orthop. Ihre Grenzgeb.* 107:447, 1970.
33. Byfield, M., and S. Paramasivam. Murrah building collapse: reassessment of the transfer girder. *J. Perform. Constr. Facil.* 26:371–376, 2011.
34. Calhoun, J. H., F. Li, B. R. Ledbetter, and S. F. Viegas. A comprehensive study of pressure distribution in the ankle joint with inversion and eversion. *Foot Ankle Int.* 15:125–133, 1994.
35. Calhoun, J. H., F. Li, B. R. Ledbetter, and S. F. Viegas. A comprehensive study of pressure distribution in the ankle joint with inversion and eversion. *Foot Ankle Int.* 15:125–133, 1994.
36. Carothers, C. O., F. C. Smith, and P. Calabrisi. The elasticity and strength of some long bones of the human body. Naval Medical Research Institute, National Naval Medical Center, 1949.
37. Carter, D. R., and W. C. Hayes. Bone compressive strength: the influence of density and strain rate. *Science* 194:1174–1176, 1976.
38. Carter, D. R., and W. C. Hayes. Bone compressive strength: the influence of density and strain rate. *Science* 194:1174–1176, 1976.
39. Carter, D. R., and W. C. Hayes. The compressive behavior of bone as a two-phase porous structure. *J. Bone Jt. Surg.* 59:954–962, 1977.

40. Celander, H., C.-J. CLEMENDSON, U. A. Ericsson, and H. E. HULTMAN. A study on the relation between the duration of a shock wave and the severity of the blast injury produced by it. *Acta Physiol. Scand.* 33:14–18, 1955.
41. Champion, H. R., R. F. Bellamy, C. P. Roberts, and A. Leppaniemi. A profile of combat injury. *J. Trauma Acute Care Surg.* 54:S13–S19, 2003.
42. Cheng, Z., J. R. Crandall, K. Darvish, and W. D. Pilkey. Limiting performance analysis of toepan padding for mitigating lower limb injuries. *Proc. Inst. Mech. Eng. Part J. Automob. Eng.* 218:619–628, 2004.
43. Cheng, Z., J. R. Crandall, K. Darvish, and W. D. Pilkey. Limiting performance analysis of toepan padding for mitigating lower limb injuries. *Proc. Inst. Mech. Eng. Part J. Automob. Eng.* 218:619–628, 2004.
44. Cheng, Z. Q., W. D. Pilkey, J. A. Pellettiere, and A. L. Rizer. Limiting performance analysis of biomechanical systems for optimal injury control – Part 1: Theory and methodology. *Int. J. Crashworthiness* 10:567–577, 2005.
45. Chi, K.-J., and D. Schmitt. Mechanical energy and effective foot mass during impact loading of walking and running. *J. Biomech.* 38:1387–1395, 2005.
46. Clarke, H. J., J. D. Michelson, Q. G. Cox, and R. H. Jinnah. Tibio-talar stability in bimalleolar ankle fractures: a dynamic in vitro contact area study. *Foot Ankle Int.* 11:222–227, 1991.
47. Clemedson, C.-J. Blast injury. *Physiol. Rev.* 36:336–354, 1956.
48. Commandeur, J., R. J. Derksen, D. MacDonald, and R. Breederveld. Identical fracture patterns in combat vehicle blast injuries due to improvised explosive devices; a case series. *Bmc Emerg. Med.* 12:1, 2012.

49. Costner, H. L. Criteria for measures of association. *Am. Sociol. Rev.* 341–353, 1965.
50. Coughlin, M. J. Calcaneal Fractures in the Industrial Patient. *Foot Ankle Int.* 21:896–905, 2000.
51. Courtney, M. W., and A. C. Courtney. Working toward exposure thresholds for blast-induced traumatic brain injury: thoracic and acceleration mechanisms. *Neuroimage* 54:S55–S61, 2011.
52. Crandall, J. R., J. R. Funk, R. W. Rudd, and L. J. Tourret. The tibia index: a step in the right direction. In: Human Biomechanics and Injury Prevention. Springer, 2000, pp. 29–40.at <http://link.springer.com/chapter/10.1007/978-4-431-66967-8_4>
53. Crandall, J. R., A. Jordan, C. R. Bass, G. S. Klopp, W. D. Pilkey, and E. M. Sieveka. Reproducing the Structural Intrusion of Frontal Offset Crashes in the Laboratory Sled Test Environment. SAE Technical Paper, 1995.at <http://papers.sae.org/950643/>
54. Crandall, J. R., S. M. Kuppa, G. S. Klopp, G. W. Hall, W. D. Pilkey, and S. R. Hurwitz. Injury mechanisms and criteria for the human foot and ankle under axial impacts to the foot. *Int. J. Crashworthiness* 3:147–162, 1998.
55. Crandall, J. R., P. G. Martin, E. M. Sieveka, G. S. Klopp, T. P. Kuhlmann, W. D. Pilkey, P. C. Dischinger, A. R. Burgess, T. D. O'quinn, and C. B. Schmidhauser. The influence of footwell intrusion on lower extremity response and injury in frontal crashes. , 1995.
56. Crandall, J. R., P. G. Martin, E. M. Sieveka, W. D. Pilkey, P. C. Dischinger, A. R. Burgess, T. D O'Quinn, and C. B. Schmidhauser. Lower limb response and injury in frontal crashes. *Accid. Anal. Prev.* 30:667–677, 1998.

57. Crandall, J. R., L. Portier, P. Petit, G. W. Hall, C. R. Bass, G. S. Klopp, S. Hurwitz, W. D. Pilkey, X. Trosseille, C. Tarrière, and others. Biomechanical response and physical properties of the leg, foot, and ankle. SAE Technical Paper, 1996.
58. Crandall, J. R., X. Ye, D. Bose, A. Forbes, S. R. Hurwitz, J. R. Funk, G. Shaw, M. Sochor, A. Rizzo, R. Freeth, R. W. Rudd, and M. Scarboro. Longitudinal Trends in the Patterns of Distal Lower Extremity Injuries Sustained in Frontal Motor Vehicle Crashes. , 2012.
59. Daftary, A., A. H. Haims, and M. R. Baumgaertner. Fractures of the Calcaneus: A Review with Emphasis on CT 1. *Radiographics* 25:1215–1226, 2005.
60. Danelson, K. A., A. R. Kemper, M. J. Mason, M. Tegtmeyer, S. A. Swiatkowski, J. H. Bolte, W. N. Hardy, and others. Comparison of ATD to PMHS Response in the Under-Body Blast Environment. *Stapp Car Crash J.* 59:445–520, 2015.
61. Dischinger, P. C., K. M. Read, J. A. Kufera, T. J. Kerns, C. A. Burch, N. Jawed, S. M. Ho, and A. R. Burgess. Consequences and costs of lower extremity injuries. , 2004.
62. Eppinger, R. H., J. H. Marcus, and R. M. Morgan. Development of dummy and injury index for NHTSA's thoracic side impact protection research program. SAE Technical Paper, 1984.
63. Eppinger, R. H., J. H. Marcus, and R. M. Morgan. Development of dummy and injury index for NHTSA's thoracic side impact protection research program. SAE Technical Paper, 1984.at <http://papers.sae.org/840885/>
64. Erdemir, A., M. L. Viveiros, J. S. Ulbrecht, and P. R. Cavanagh. An inverse finite-element model of heel-pad indentation. *J. Biomech.* 39:1279–1286, 2006.
65. Evans, F. G. Mechanical properties of bone. Charles C. Thomas Publisher, 1973.

66. Fan, W. R., R. J. Vargovick, and J. J. King. Femur load injury criteria~ a realistic approach. , 1973.

67. Farley, C. T., and O. Gonzalez. Leg stiffness and stride frequency in human running. *J. Biomech.* 29:181–186, 1996.

68. Fielding, R. A., R. H. Kraft, A. Przekwas, and X. G. Tan. Development of a lower extremity model for high strain rate impact loading. *Int. J. Exp. Comput. Biomech.* 3:161–186, 2015.

69. Fitzpatrick, D. C., J. K. Otto, T. O. McKinley, J. L. Marsh, and T. D. Brown. Kinematic and contact stress analysis of posterior malleolus fractures of the ankle. *J. Orthop. Trauma* 18:271–278, 2004.

70. Funk, J. R. The Axial Injury Tolerance of the Human Foot/Ankle Complex and the Effect of Achilles Tension. *J. Biomech. Eng.* 124:750, 2002.

71. Funk, J. R. Ankle injury mechanisms: Lessons learned from cadaveric studies. *Clin. Anat.* 24:350–361, 2011.

72. Funk, J. R. The Effect of Active Muscle Tension on the Axial Impact Tolerance of the Human Foot/Ankle Complex

73. Funk, J. R., J. R. Crandall, L. J. Tourret, C. B. MacMahon, C. R. Bass, J. T. Patrie, N. Khaewpong, and R. H. Eppinger. The Axial Injury Tolerance of the Human Foot/Ankle Complex and the Effect of Achilles Tension. *J. Biomech. Eng.* 124:750–757, 2002.

74. Funk, J. R., R. W. Rudd, J. R. Kerrigan, and J. R. Crandall. The Effect of Tibial Curvature and Fibular Loading on the Tibia Index. *Traffic Inj. Prev.* 5:164–172, 2004.

75. Funk, J. R., L. J. Tourret, S. E. George, and J. R. Crandall. The role of axial loading in malleolar fractures. SAE Technical Paper, 2000.

76. Gabler, L. F. Sorbothane Material Characterization. Charlottesville, VA: Center for Applied Biomechanics, 2014.
77. Gabler, L. F., H. Joodaki, J. R. Crandall, and M. B. Panzer. Toward Development of a Single-Degree-of-Freedom Mechanical Model for Predicting Brain Injury. , 2016.
78. Gabler, L. F., M. B. Panzer, and R. S. Salzar. High-Rate Mechanical Properties of Human Heel Pad for Simulation of a Blast Loading Condition. , 2013.
79. Gadd, C. W. Criteria for injury potential. *Impact Accel. Stress* 977:141, 1962.
80. Gadd, C. W. Use of a Weighted-Impulse Criterion for Estimatéjlnjury Hazard. , 1966.at <http://www.snell-helmets.net/docs/articles/hic/Gadd_1966_Weighted-Impulse_Criterion_for_Estimating_Injury_H.pdf>
81. Gallenberger, K. Foot And Ankle Injuries In Variable Energy Impacts. , 2013.
82. Gallenberger, K., N. Yoganandan, and F. Pintar. Biomechanics of foot/ankle trauma with variable energy impacts. *Ann. Adv. Automot. Med.* 57:123, 2013.
83. Gans, L., and T. Kennedy. Management of unique clinical entities in disaster medicine. *Emerg. Med. Clin.* 14:301–326, 1996.
84. Gayzik, F. S., N. A. Vavalle, D. P. Moreno, and J. D. Stitzel. An Evaluation of Objective Rating Methods for Full Body Finite Element Model Comparison to PMHS Testsat <http://www-nrd.nhtsa.dot.gov/pdf/BIO/Proceedings/2012_40/40-4.pdf>
85. Gehre, C., H. Gades, and P. Wernicke. Objective rating of signals using test and simulation responses. , 2009.
86. Gennarelli, T. A. Abbreviated injury scale. American Association for Automotive Medicine, 1985.

87. von Gierke, H. Transient acceleration, vibration and noise problems in space flight. In: Bioastronautics. Macmillan New York, 1964, pp. 27–75.

88. Gilmore, J. M. FY 2015 Annual Report. U.S. Department of Operational Test and Evaluation, .

89. Goh, J. C., E. Lee, E. Ang, P. Bayon, and R. Pho. Biomechanical Study on the Load-Bearing Characteristics of t... : Clinical Orthopaedics and Related Research

90. Gray, H. Gray's Anatomy: With original illustrations by Henry Carter. Arcturus Publishing, 2009.

91. Hall, H. GM engineer: Today's crash test dummies cost up to $500K, saving more lives. , 2015.at <http://engineering.vanderbilt.edu/news/2015/gm-engineer-todays-crash-test-dummies-cost-up-to-500k-saving-more-lives/>

92. Hallquist, J. LS Dyna User's Manual Version 971. , 2007.

93. Harrell, F. Regression Modeling Strategies: With Applications to Linear Models, Logistic and Ordinal Regression, and Survival Analysis. Springer, 2015, 598 pp.

94. Henderson, K., A. Bailey, J. Christopher, F. Brozoski, and R. Salzar. Biomechanical response of the lower leg under high rate loading. , 2013.

95. Hobatho, M. C., R. Darmana, P. Pastor, J. J. Barrau, S. Laroze, and J. P. Morucci. Development of a three-dimensional finite element model of a human tibia using experimental modal analysis. *J. Biomech.* 24:371–383, 1991.

96. Hougaard, P., and P. Hougaard. Analysis of multivariate survival data. Springer New York, 2000.

97. Humanetics Innovative Solutions. Mil-LX Leg Model 585-0000 Technical Data Sheetat <http://www.humaneticsatd.com/sites/default/files/file/MIL-LX_Leg_TPS.pdf>

98. Inman, V. T. The joints of the ankle. Williams & Wilkins, 1976.

99. Isman, R. E., V. T. Inman, and P. M. Poor. Anthropometric studies of the human foot and ankle. *Bull Prosthet Res* 11:97–108, 1969.

100. ISO. Road vehicles--procedure to construct injury risk curves for the evaluation of occupant protection in crash tests. International Organization for Standardization, 2014.

101. Jaffredo, A. S., P. Potier, S. R. Robin, J. Y. Le Coz, and J. P. Lassau. Cadaver lower limb dynamic response in inversion-eversion. , 2000.

102. Kajzer, J., E. Tanaka, and H. Yamada. Human Biomechanics and Injury Prevention. Springer, 2000.

103. Kemper, A., C. McNally, E. Kennedy, S. Manoogian, and S. Duma. The material properties of human tibia cortical bone in tension and compression: Implications for the tibia index. , 2007.

104. Kent, R., J. Patrie, F. Poteau, F. Matsuoka, and C. Mullen. Development of an age-dependent thoracic injury criterion for frontal impact restraint loading. , 2003.at <http://www-nrd.nhtsa.dot.gov/Pdf/ESV/esv18/CD/Files/18ESV-000072.pdf>

105. Khalil, T. B., D. C. Viano, and L. A. Taber. Vibrational characteristics of the embalmed human femur. *J. Sound Vib.* 75:417–436, 1981.

106. Kim, T., J. Shin, X. Ye, J. Crandall, C. Knospe, and J. Funk. Evaluation of methods for the development of representative responses and corridors from biomechanical data using mechanical models. *Int. J. Crashworthiness* 18:633–646, 2013.

107. Kimizuka, M., H. Kurosawa, and T. Fukubayashi. Load-bearing pattern of the ankle joint. *Arch. Orthop. Trauma. Surg.* 96:45–49, 1980.

108. Kitagawa, Y. I. Lower leg injuries caused by dynamic axial loading and muscle testing. , 1998.

109. Klopp, G. S., J. R. Crandall, G. W. Hall, W. D. Pilkey, S. R. Hurwitz, and S. M. Kuppa. Mechanisms of injury and injury criteria for the human foot and anklein dynamic axial impacts to the foot. , 1997.

110. Kraft, R. H., M. L. Lynch, W. Pino, A. Jean, R. Radovitzky, and S. Socrate. Computational Failure Modeling of Accelerative Injuries to the Lower Leg Below the Knee. DTIC Document, 2013.

111. Kulkarni, K., J. Ramalingam, and R. Thyagarajan. Assessment of the accuracy of certain reduced order models used in the prediction of occupant injury during under-body blast events. DTIC Document, 2014.at <http://oai.dtic.mil/oai/oai?verb=getRecord&metadataPrefix=html&identifier=ADA599846>

112. Kunze, S. Budget Estimates Fiscal Year 2017. National Highway Traffic Safety Administration, 2016.

113. Kuppa, S., M. Haffner, R. Eppinger, and J. Saunders. Lower extremity response and trauma assessment using the Thor-Lx/HIIIr and the Denton leg in frontal offset vehicle crashes. , 2001.

114. Kuppa, S. M., G. S. Klopp, J. R. Crandall, G. Hall, N. Yoganandan, F. A. Pintar, R. H. Eppinger, E. Sun, N. Khaewpong, and M. Kleinberger. Axial impact characteristics of dummy and cadaver lower limbs. , 1998.

115. Kuppa, S. M., and E. M. Sieveka. Dynamic Motion of the Floor Pan and Axial Loading through the Feet in Frontal Crash Tests. , 1995.

116. Kuppa, S., J. Wang, M. Haffner, R. Eppinger, and others. Lower extremity injuries and associated injury criteria. , 2001.at <http://www-nrd.nhtsa.dot.gov/pdf/ESV/esv17/Proceed/00160.pdf>

117. Kura, H., H. B. Kitaoka, Z.-P. Luo, and K.-N. An. Measurement of surface contact area of the ankle joint. *Clin. Biomech.* 13:365–370, 1998.

118. Lallement, G., and D. J. Inman. A tutorial on complex eigenvalues. , 1995.at <http://sh.st/st/787f28ed3e745c14417e4aec27303038/sem-proceedings.com/13i/sem.org-IMAC-XIII-13th-13-13-2-A-Tutorial-Complex-Eigenvalues.pdf>

119. Lang, T. F., J. H. Keyak, M. W. Heitz, P. Augat, Y. Lu, A. Mathur, and H. K. Genant. Volumetric quantitative computed tomography of the proximal femur: precision and relation to bone strength. *Bone* 21:101–108, 1997.

120. Lau, I. V., and D. C. Viano. The viscous criterion-bases and applications of an injury severity index for soft tissues. SAE Technical Paper, 1986.at <http://papers.sae.org/861882/>

121. Launey, M. E., M. J. Buehler, and R. O. Ritchie. On the mechanistic origins of toughness in bone. *Annu. Rev. Mater. Res.* 40:25–53, 2010.

122. Lemonick, D. M. Bombings and blast injuries: a primer for physicians. *Am J Clin Med* 8:134–140, 2011.

123. Lessley, D., J. Crandall, G. Shaw, R. Kent, and J. Funk. A normalization technique for developing corridors for individual subject force-deflection responses. , 2004.

124. Levine, R. S., A. Manoli, and P. Prasad. Ankle and foot injury scales: AFIS-S & AFIS-I. , 1995.

125. Li, J., and H. Hao. Numerical study of concrete spall damage to blast loads. *Int. J. Impact Eng.* 68:41–55, 2014.

126. LINDSJÖ, U., G. DANCKWARDT-LILLIESTRÖM, and B. O. Sahlstedt. Measurement of the motion range in the loaded ankle. *Clin. Orthop.* 199:68–71, 1985.

127. Liu, W., and B. M. Nigg. A mechanical model to determine the influence of masses and mass distribution on the impact force during running. *J. Biomech.* 33:219–224, 2000.

128. MacKenzie, E. J., A. Damiano, T. Miller, and S. Luchter. The development of the functional capacity index. *J. Trauma Acute Care Surg.* 41:799–807, 1996.

129. Madeley, N. J., C. M. S. Srinivasan, J. R. Crandall, S. Hurwitz, and J. R. Funk. Retrospective analysis of malleolar fractures in an impact environment. , 2004.

130. Manning, P., A. Wallace, C. Owen, A. Roberts, C. Oakley, and R. Lowne. Dynamic response and injury mechanism in the human foot and ankle and an analysis of dummy biofidelity. , 1998.at <http://www-nrd.nhtsa.dot.gov/Pdf/ESV/esv16/98S9O11.PDF>

131. Manoli, A., P. Prasad, and R. S. Levine. Foot and ankle severity scale (FASS). *Foot Ankle Int.* 18:598–602, 1997.

132. McCalden, R. W., J. A. McGeough, and others. Age-Related Changes in the Compressive Strength of Cancellous Bone. The Relative Importance of Changes in Density and Trabecular Architecture*. *J. Bone Jt. Surg.* 79:421–7, 1997.

133. McElhaney, J. H. Dynamic response of bone and muscle tissue. *J. Appl. Physiol.* 21:1231–1236, 1966.

134. Mckay, B. J. Development of lower extremity injury criteria and biomechanical surrogate to evaluate military vehicle occupant injury during an explosive blast event. , 2010.

135. McKay, B. J., and C. A. Bir. Lower extremity injury criteria for evaluating military vehicle occupant injury in underbelly blast events. *Stapp Car Crash J.* 53:229–249, 2009.

136. McKay, B. J., and C. A. Bir. Lower extremity injury criteria for evaluating military vehicle occupant injury in underbelly blast events. *Stapp Car Crash J.* 53:229, 2009.

137. McMahon, T. A., and G. C. Cheng. The mechanics of running: how does stiffness couple with speed? *J. Biomech.* 23:65–78, 1990.

138. McMaster, J., C. G. Moran, W. A. Wallace, and L. Wheeler. Foot and ankle injury mechanisms in frontal car collisions. *J. Orthop. Trauma* 14:144–145, 2000.

139. Mertz, H. J. Injury assessment values used to evaluate Hybrid III response measurements. *NHTSA Docket* 74:14, 1984.

140. Mertz, H. J. Injury assessment values used to evaluate Hybrid III response measurements. *NHTSA Docket* 74:14, 1984.

141. Mertz, H. J. Anthropomorphic test devices. In: Accidental Injury. Springer, 1993, pp. 66–84.at <http://link.springer.com/chapter/10.1007/978-1-4757-2264-2_4>

142. Metz, C. E. Basic principles of ROC analysis. , 1978.

143. Misra, J. C., and S. Samanta. A mathematical analysis of the vibration characteristics of the human tibia. *Comput. Math. Appl.* 16:1017–1026, 1988.

144. Morgan, R. M., R. H. Eppinger, and B. C. Hennessey. Ankle joint injury mechanism for adults in frontal automotive impact. SAE Technical Paper, 1991.at <http://papers.sae.org/912902/>

145. Natali, A. N., C. G. Fontanella, and E. L. Carniel. Constitutive formulation and analysis of heel pad tissues mechanics. *Med. Eng. Phys.* 32:516–522, 2010.

146. National Highway Traffic Safety Administration. Thor-Lx Advanced Lower Extremity (Thor-LX/HIIIr)at <http://www.nhtsa.gov/Research/Biomechanics+&+Trauma/Thor-Lx(HIIIr)+Advanced+Lower+Extremity>

147. Newell, N., S. D. Masouros, A. D. Pullen, and A. M. J. Bull. The comparative behaviour of two combat boots under impact. *Inj. Prev.* 18:109–112, 2012.

148. Newell, N., R. Salzar, A. M. Bull, and S. D. Masouros. A validated numerical model of a lower limb surrogate to investigate injuries caused by under-vehicle explosions. *J. Biomech.* , 2016.at <http://www.sciencedirect.com/science/article/pii/S0021929016301075>

149. Nie, B., M. B. Panzer, A. Mane, A. R. Mait, J.-P. Donlon, J. L. Forman, and R. W. Kent. A framework for parametric modeling of ankle ligaments to determine the in situ response under gross foot motion. *Comput. Methods Biomech. Biomed. Engin.* 1–12, 2015.

150. Nieves, J. W., C. Formica, J. Ruffing, M. Zion, P. Garrett, R. Lindsay, and F. Cosman. Males Have Larger Skeletal Size and Bone Mass Than Females, Despite Comparable Body Size. *J. Bone Miner. Res.* 20:529–535, 2005.

151. North Atlantic Treaty Organization. Procedures for evaluating the protection level of armored vehicles—IED threat, NATO Standard AEP-55. , 2011.

152. Otte, D., H. Von Rheinbaben, and H. Zwipp. Biomechanics of injuries to the foot and ankle joint of car drivers and improvements for an optimal car floor development. SAE Technical Paper, 1992.

153. Otte, D., H. Von Rheinbaben, and H. Zwipp. Biomechanics of injuries to the foot and ankle joint of car drivers and improvements for an optimal car floor development. SAE Technical Paper, 1992.at <http://papers.sae.org/922514/>

154. Pain, M. T., and J. H. Challis. The role of the heel pad and shank soft tissue during impacts: a further resolution of a paradox. *J. Biomech.* 34:327–333, 2001.

155. Pandelani, T. Evaluation of dynamic response characteristics of the MiL-Lx leg compared to the Thor-Lx leg. , 2011.at <http://researchspace.csir.co.za/dspace/handle/10204/5955>

156. Pandelani, T. An investigation of the forces within the tibiae at typical blast loading rates–with different boots. , 2014.at <http://researchspace.csir.co.za/dspace/handle/10204/7986>

157. Pandelani, T., D. Reinecke, and F. Beetge. In pursuit of vehicle landmine occupant protection: Evaluating the dynamic response characteristic of the military lower extremity leg (MiL-Lx) compared to the Hybrid III (HIII) lower leg. , 2010.at <http://researchspace.csir.co.za/dspace/handle/10204/4263>

158. Pandelani, T., D. Reinecke, M. Philippens, F. Dosquet, and F. Beetge. Practical evaluation of the MiL-Lx lower leg when subjected to simulated vehicle under belly blast load conditions. , 2010.at <http://researchspace.csir.co.za/dspace/handle/10204/4488>

159. Pandelani, T., J. D. Reinecke, T. J. Sono, R. Ahmed, F. J. Beetge, P. Nkosi, P. Dicks, and G. N. Nurick. The design of a modified lower limb impactor to assess lower limb injury at typical blast loading rates. , 2014.at <http://researchspace.csir.co.za/dspace/handle/10204/7657>

160. Pandelani, T., T. J. Sono, J. D. Reinecke, and G. N. Nurick. Impact loading response of the MiL-Lx leg fitted with combat boots. *Int. J. Impact Eng.* , 2015.at <http://www.sciencedirect.com/science/article/pii/S0734743X15000408>

161. Panzer, M. B., R. Cameron, K. A. Rafaels, J. Shridharani, and B. P. Capehart. Primary blast survival and injury risk assessment for repeated blast exposures. *J. Trauma Acute Care Surg.* 72:454–466, 2012.

162. Panzer, M. B., L. F. Gabler, E. J. Rodenberger, H. Joodaki, and J. R. Crandall. Assessment of Brian Injury Criterion (BrIC). National Highway Traffic Safety Administration, 2016.

163. Parenteau, C. S., D. C. Viano, and P. Y. Petit. Biomechanical properties of human cadaveric ankle-subtalar joints in quasi-static loading. *J. Biomech. Eng.* 120:105–111, 1998.

164. Pereira, D. S., K. J. Koval, R. B. Resnick, S. C. Sheskier, F. Kummer, and J. D. Zuckerman. Tibiotalar contact area and pressure distribution: the effect of mortise widening and syndesmosis fixation. *Foot Ankle Int.* 17:269–274, 1996.

165. Perry, B. J., L. Gabler, A. Bailey, K. Henderson, F. Brozoski, and R. S. Salzar. Lower Extremity Characterization and Injury Mitigation

166. Petit, P., L. Portier, J.-Y. Foret-Bruno, X. Trosseille, C. S. Parenteau, C. Tarriere, and J. Lassau. Quasistatic characterization of the human foot-ankle joints in a simulated tensed state and updated accidentological data. , 1997.

167. Pithioux, M., D. Subit, and P. Chabrand. Comparison of compact bone failure under two different loading rates: experimental and modelling approaches. *Med. Eng. Phys.* 26:647–653, 2004.

168. Portier, L., P. Petit, A. Domont, X. Trosseille, J.-Y. Le Coz, C. Tarriere, and J.-P. Lassau. Dynamic biomechanical dorsiflexion responses and tolerances of the ankle joint complex. , 1997.

169. Putnam, J. B., J. T. Somers, and C. D. Untaroiu. Development, Calibration, and Validation of a Head–Neck Complex of THOR Mod Kit Finite Element Model. *Traffic Inj. Prev.* 15:844–854, 2014.

170. Quenneville, C. E., and C. E. Dunning. Evaluation of the Biofidelity of the HIII and MIL-Lx Lower Leg Surrogates Under Axial Impact Loading. *Traffic Inj. Prev.* 13:81–85, 2012.

171. Quenneville, C. E., G. S. Fraser, and C. E. Dunning. Development of an Apparatus to Produce Fractures From Short-Duration High-Impulse Loading With an Application in the Lower Leg. *J. Biomech. Eng.* 132:014502–014502, 2009.

172. Quenneville, C. E., S. D. McLachlin, G. S. Greeley, and C. E. Dunning. Injury Tolerance Criteria for Short-Duration Axial Impulse Loading of the Isolated Tibia: *J. Trauma Inj. Infect. Crit. Care* 70:E13–E18, 2011.

173. Rafaels, K., C. R. “Dale” Bass, R. S. Salzar, M. B. Panzer, W. Woods, S. Feldman, T. Cummings, and B. Capehart. Survival Risk Assessment for Primary Blast Exposures to the Head. *J. Neurotrauma* 28:2319–2328, 2011.

174. Ramasamy, A., A. M. Hill, S. Masouros, I. Gibb, A. M. J. Bull, and J. C. Clasper. Blast-related fracture patterns: a forensic biomechanical approach. *J. R. Soc. Interface* 8:689–698, 2011.

175. Ramasamy, A., A. M. Hill, R. Phillip, A. M. J. Bull, and J. C. Clasper. The Modern Deck-Slap Injuries: 3-Year Outcomes of Calcaneal Blast Fractures. *Orthop. Proc.* 94–B:27–27, 2012.

176. Ramasamy, A., A. M. Hill, R. Phillip, I. Gibb, A. M. Bull, and J. C. Clasper. The modern "deck-slap" injury—calcaneal blast fractures from vehicle explosions. *J. Trauma Acute Care Surg.* 71:1694–1698, 2011.

177. Ramasamy, A., S. D. Masouros, N. Newell, A. M. Hill, W. G. Proud, K. A. Brown, A. M. J. Bull, and J. C. Clasper. In-vehicle extremity injuries from improvised explosive devices: current and future foci. *Philos. Trans. R. Soc. B Biol. Sci.* 366:160–170, 2011.

178. Ramasamy, M. A., C. A. M. Hill, S. Masouros, L.-C. Iain Gibb, L.-C. Rhodri Phillip, A. M. J. Bull, and C. J. C. Clasper. Outcomes of IED Foot and Ankle Blast Injuries. *J. Bone Jt. Surg. Am.* 95:e25 1, 2013.

179. Rhule, H. H., M. R. Maltese, B. R. Donnelly, R. H. Eppinger, J. K. Brunner, J. H. Bolte, and others. Development of a new biofidelity ranking system for anthropomorphic test devices. *Stapp Car Crash J.* 46:477–512, 2002.

180. Ritchie, R. O., M. J. Buehler, and P. Hansma. Plasticity and toughness in bone. *Phys Today* 62:41–47, 2009.

181. Roberts, D., B. Donnelly, C. Severin, and J. Medige. Injury mechanisms and tolerance of the human ankle joint. *Cent. Dis. Control* , 1993.

182. Rudd, R., J. Crandall, and J. Butcher. Biofidelity Evaluation of Dynamic and Static Response Characteristics of the Thor Lx Dummy Lower Extremity. *Int. J. Crashworthiness* 5:127–140, 2000.

183. Ruff, C. B., and W. C. Hayes. Sex differences in age-related remodeling of the femur and tibia. *J. Orthop. Res.* 6:886–896, 1988.

184. Rupp, J. D., C. A. Flannagan, and S. M. Kuppa. Injury risk curves for the skeletal knee–thigh–hip complex for knee-impact loading. *Accid. Anal. Prev.* 42:153–158, 2010.

185. Rupp, J. D., C. S. Miller, M. P. Reed, N. H. Madura, K. D. Klinich, and L. W. Schneider. Characterization of knee-thigh-hip response in frontal impacts using biomechanical testing and computational simulations. *Stapp Car Crash J.* 52:421, 2008.

186. Rupp, J. D., M. P. Reed, N. H. Madura, S. Kuppa, and L. Schneider. Comparison of Knee/Femur Force-Deflection Response of the THOR, Hybrid III, and Human Cadaver to Dynamic Frontal Impact Knee Loading. , 2003.at <http://www-nrd.nhtsa.dot.gov/pdf/esv/esv18/CD/proceed/00015.pdf>

187. Rupp, J. D., M. P. Reed, C. A. Van Ee, S. Kuppa, S. C. Wang, J. A. Goulet, and L. W. Schneider. The tolerance of the human hip to dynamic knee loading. , 2002.at <http://www.nhtsa.gov/DOT/NHTSA/NRD/Multimedia/PDFs/Biomechanics%20%26%20Trauma/HipStappFINAL.pdf>

188. SAE, J. 211/1, Instrumentation for Impact Test–Part 1–Electronic Instrumentation. *Soc. Automot. Eng. Warrendale PA* , 2003.

189. Salzar, R. S., W. B. Lievers, A. M. Bailey, and J. R. Crandall. Leg, Foot, and Ankle Injury Biomechanics. In: Accidental Injury, edited by N. Yoganandan, A. M. Nahum, J. W. Melvin, and T. M. C. of W. I. on behalf of N. Yoganandan. Springer New York, 2015, pp. 499–547.at <http://link.springer.com/chapter/10.1007/978-1-4939-1732-7_18>

190. Scherer, R., C. Felczak, and S. Halstead. Vehicle and crash-dummy response to an underbelly blast event. , 2010.at

<https://blastinjuryresearch.amedd.army.mil/docs/ubb/Vehicle_and_Crash_Dummy_response_to_an_underbelly_blast_event.pdf>

191. Schueler, F., R. Mattern, F. Zeidler, and D. Scheunert. Injuries of the lower legs-foot, ankle joint, tibia; mechanisms, tolerance limits, injury-criteria evaluation of a recent biomechanic experiment series (impact tests with a pneumatic-biomechanic impactor). , 1995.

192. Shewchenko, N. ATD Lower Leg Surrogate Selection and the Effects on the Evaluation of Blast Energy Attenuating Floor Matsat <https://www.researchgate.net/profile/Nicholas_Shewchenko/publication/271136210_ATD_Lower_Leg_Surrogate_Selection_and_the_Effects_on_the_Evaluation_of_Blast_Energy_Attenuating_Floor_Mats/links/54be9c5b0cf2f6bf4e037f99.pdf>

193. Shin, J., and C. D. Untaroiu. Biomechanical and injury response of human foot and ankle under complex loading. *J. Biomech. Eng.* 135:101008, 2013.

194. Shin, J., and C. D. Untaroiu. Biomechanical and injury response of human foot and ankle under complex loading. *J. Biomech. Eng.* 135:101008, 2013.

195. Siegler, S., J. K. Udupa, S. I. Ringleb, C. W. Imhauser, B. E. Hirsch, D. Odhner, P. K. Saha, E. Okereke, and N. Roach. Mechanics of the ankle and subtalar joints revealed through a 3D quasi-static stress MRI technique. *J. Biomech.* 38:567–578, 2005.

196. Smith, B. R., P. C. Begeman, R. Leland, R. Meehan, R. S. Levine, K. H. Yang, and A. I. King. A mechanism of injury to the forefoot in car crashes. *Traffic Inj. Prev.* 6:156–169, 2005.

197. Stech, E. L., and P. R. Payne. Dynamic models of the human body. DTIC Document, 1969.at

<http://oai.dtic.mil/oai/oai?verb=getRecord&metadataPrefix=html&identifier=AD0701383>

198. Stewart, C., S. Center, and C. Stewart. Blast Injuries" True Weapons of Mass Destruction". *Work* 918:660–2828, 2009.

199. Stitzel, J. D. Global human body models consortium (GHBMC) male 50th percentile (M50) occupant model manual. *Va. Tech—Wake For. Univ. Cent. Inj. Biomech.* , 2011.

200. Stitzel, J. D. Global human body models consortium (GHBMC) male 50th percentile (M50) occupant model manual. , 2011.

201. Takebe, K., A. Nakagawa, H. Minami, H. Kanazawa, and K. Hirohata. Role of the Fibula in Weight-bearing. : Clinical Orthopaedics and Related Research

202. Taylor, W. R., E. Roland, H. Ploeg, D. Hertig, R. Klabunde, M. D. Warner, M. C. Hobatho, L. Rakotomanana, and S. E. Clift. Determination of orthotropic bone elastic constants using FEA and modal analysis. *J. Biomech.* 35:767–773, 2002.

203. Thomsen, J. J. Modelling human tibia structural vibrations. *J. Biomech.* 23:215–228, 1990.

204. Thyagarajan, R., J. Ramalingam, and K. B. Kulkarni. Comparing the Use of Dynamic Response Index (DRI) and Lumbar Load as Relevant Spinal Injury Metrics. DTIC Document, 2014.at <http://oai.dtic.mil/oai/oai?verb=getRecord&metadataPrefix=html&identifier=ADA591409>

205. U.S. Department of Defense. 2014 Demographics: Profile of the Military Community. 2014.

206. Van Tuyl, J. T. DEVELOPMENT OF A FORCE SENSING INSOLE TO QUANTIFY IMPACT LOADING TO THE FOOT IN VARIOUS POSTURES. , 2014.at <https://macsphere.mcmaster.ca/handle/11375/15981>

207. Vavalle, N. A., B. C. Jelen, D. P. Moreno, J. D. Stitzel, and F. S. Gayzik. An evaluation of objective rating methods for full-body finite element model comparison to PMHS tests. *Traffic Inj. Prev.* 14:S87–S94, 2013.

208. Viano, D. C. Considerations for a femur injury criterion. SAE Technical Paper, 1977.at <http://papers.sae.org/770925/>

209. Viano, D. C. Considerations for a femur injury criterion. SAE Technical Paper, 1977.at <http://papers.sae.org/770925/>

210. Viano, D. C., and T. B. Khalil. Investigation of impact response and fracture of the human femur by finite element modeling. SAE Technical Paper, 1976.at <http://papers.sae.org/760773/>

211. Viano, D. C., and A. I. King. Biomechanics of chest and abdomen impact. *Biomed. Eng. Handb.* 1:369–380, 2000.

212. Viano, D. C., A. I. King, J. W. Melvin, and K. Weber. Injury biomechanics research: an essential element in the prevention of trauma. *J. Biomech.* 22:403–417, 1989.

213. Viano, D. C., and I. V. Lau. A viscous tolerance criterion for soft tissue injury assessment. *J. Biomech.* 21:387–399, 1988.

214. Von Gierke, H. E. Biodynamic response of the human body. *Appl. Mech. Rev.* 17:951–958, 1964.

215. Von Gierke, H. E. Biodynamic response of the human body. *Appl. Mech. Rev.* 17:951–958, 1964.

216. von Gierke, H. E. Biodynamic models and their applications. *J. Acoust. Soc. Am.* 50:1397–1413, 1971.

217. Wakeling, J. M., and B. M. Nigg. Modification of soft tissue vibrations in the leg by muscular activity. *J. Appl. Physiol.* 90:412–420, 2001.

218. Wakeling, J. M., B. M. Nigg, and A. I. Rozitis. Muscle activity damps the soft tissue resonance that occurs in response to pulsed and continuous vibrations. *J. Appl. Physiol.* 93:1093–1103, 2002.

219. Wang, J., R. Bird, B. Swinton, and A. Krstic. Protection of lower limbs against floor impact in army vehicles experiencing landmine explosion. *J Battlef. Tech* 4:11–5, 2001.

220. Weis Jr, E. B., N. P. Clarke, and J. W. Brinkley. Human response to several impact acceleration orientations and patterns. DTIC Document, 1963.at <http://oai.dtic.mil/oai/oai?verb=getRecord&metadataPrefix=html&identifier=AD0727923>

221. Wellbourne, E. R., and N. Shewchenko. Improved measures of foot ankle injury risk from the Hybrid III tibia. , 1998.at <http://www-nrd.nhtsa.dot.gov/pdf/ESV/esv16/98S7O11.PDF>

222. Wellbourne, E. R., and N. Shewchenko. Improved measures of foot ankle injury risk from the Hybrid III tibia. , 1998.at <http://www-nrd.nhtsa.dot.gov/pdf/ESV/esv16/98S7O11.PDF>

223. Wiktorsson-Moller, M., B. Öberg, J. Ekstrand, and J. Gillquist. Effects of warming up, massage, and stretching on range of motion and muscle strength in the lower extremity. *Am. J. Sports Med.* 11:249–252, 1983.

224. Wood, J. L. Dynamic response of human cranial bone. *J. Biomech.* 4:1–12, 1971.

225. World Health Organization. Prevention and management of osteoporosis: report of a WHO scientific group. Diamond Pocket Books (P) Ltd., 2003.

226. Wu, G., F. C. T. van der Helm, H. E. J. (DirkJan) Veeger, M. Makhsous, P. Van Roy, C. Anglin, J. Nagels, A. R. Karduna, K. McQuade, X. Wang, F. W. Werner, and B. Buchholz. ISB recommendation on definitions of joint coordinate systems of various joints for the reporting of human joint motion—Part II: shoulder, elbow, wrist and hand. *J. Biomech.* 38:981–992, 2005.

227. Ye, X., J. Funk, A. Forbes, S. Hurwitz, G. Shaw, J. Crandall, R. Freeth, C. Michetti, R. Rudd, and M. Scarboro. Case series analysis of hindfoot injuries sustained by drivers in frontal motor vehicle crashes. *Forensic Sci. Int.* 254:18–25, 2015.

228. Yi, J., M. C. Boyce, G. F. Lee, and E. Balizer. Large deformation rate-dependent stress–strain behavior of polyurea and polyurethanes. *Polymer* 47:319–329, 2006.

229. Yoganandan, N., M. W. J. Arun, F. A. Pintar, and A. Szabo. Optimized Lower Leg Injury Probability Curves From Postmortem Human Subject Tests Under Axial Impacts. *Traffic Inj. Prev.* 15:S151–S156, 2014.

230. Yoganandan, N., M. W. Arun, F. A. Pintar, and A. Banerjee. Lower leg injury reference values and risk curves from survival analysis for male and female dummies: meta-analysis of postmortem human subject tests. *Traffic Inj. Prev.* 16:S100–S107, 2015.

231. Yoganandan, N., F. A. Pintar, M. Boynton, P. Begeman, P. Prasad, S. M. Kuppa, R. M. Morgan, and R. H. Eppinger. Dynamic axial tolerance of the human foot-ankle complex. SAE Technical Paper, 1996.

232. Yoganandan, N., F. A. Pintar, S. Kumaresan, and M. Boynton. Axial impact biomechanics of the human foot-ankle complex. *Trans.-Am. Soc. Mech. Eng. J. Biomech. Eng.* 119:433–437, 1997.

233. Zhang, W., E. Chen, D. Xue, H. Yin, and Z. Pan. Risk factors for wound complications of closed calcaneal fractures after surgery: a systematic review and meta-analysis. *Scand. J. Trauma Resusc. Emerg. Med.* 23:, 2015.

234. Zhao, P. D., Y. Wang, J. Y. Du, L. Zhang, Z. P. Du, and F. Y. Lu. Using split Hopkinson pressure bars to perform large strain compression tests on neoprene at intermediate and high strain rates. , 2013.

235. THOR Certification Manual, Rev. 2005-2. Report No: GESAC-05-04. , 2005.

236. Test Methodology for Protection of Vehicle Occupants Against Anti-Vehicular Landmine Effects. North Atlantic Treaty Organization, 2007.

237. Hybrid-III 50th Male Dummy. Human Innovative Solutions, 2013.

238. Federal Register | Anthropomorphic Test Devices; Instrumented Lower Legs for Hybrid III-50M and -5F Dummiesat <https://www.federalregister.gov/articles/2002/05/03/02-11050/anthropomorphic-test-devices-instrumented-lower-legs-for-hybrid-iii-50m-and--5f-dummies#h-12>

10 Appendices

10.1 Coordinate Transformations and Scaling

10.1.1 Tibia Coordinate System

The local coordinate system for the tibias was defined using the lateral and medial malleoli, the intercondylar eminence, and the tibial tuberosity. The Z-axis was defined as the vector connecting the midpoint of the malleoli and the intercondylar eminence, with positive pointing away from the intercondylar eminence. The X-vector was defined as a vector perpendicular to the Z-vector and passing through the tibial tuberosity (with positive pointing anteriorly). The Y-vector was defined as the cross-product of the X- and Z- vectors (with positive pointing toward the right). The center of the coordinate systems was set on the Z-axis at the projected location of the midpoint of the accelerometer mounting plate.

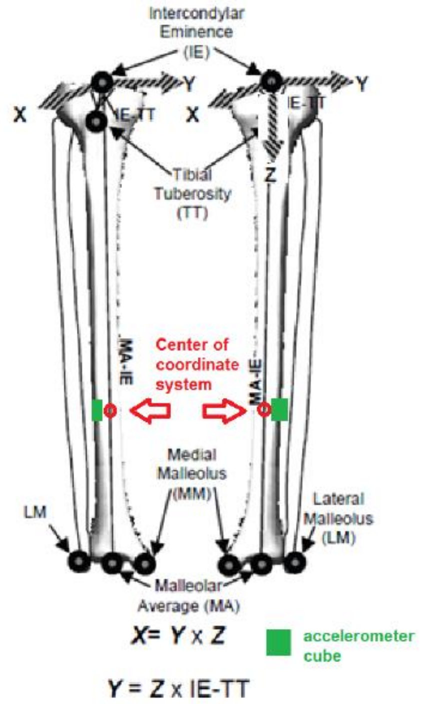
Intercondylar Eminence (IE)
X
Y
IE-TT
X
Y
IE-TT
Z
Tibial Tuberosity (TT)
MA-IE
Center of coordinate system
MA-IE
Medial Malleolus (MM)
LM
Lateral Malleolus (LM)
Malleolar Average (MA)
X= Y x Z
🟩 accelerometer cube
Y = Z x IE-TT

Figure 10.1. Local coordinate system for the tibia, aligned with the SAE J211 coordinate system.

This coordinate system was aligned with the coordinate system outlined by the Society of Automotive Engineers (SAE) J-211 document.[188] The SAE coordinate system uses Cartesian coordinates to define the motion of the human body.

10.1.2 PMHS Data Scaling

Data scaling was performed using the methods described by Eppinger et al.[63] This scaling technique involves an equal mass-equal velocity normalization scheme for which the normalized response would have the same velocity as the original trace. Additionally, the mass-density and elastic modulus would be assumed invariant between test subjects. The following equations outline the relationship between the scaled data (with an 's' subscript) and the individual unscaled data traces (with a 'u' subscript). The mass scale factor is represented by λ_m, while a, v, t, F, and l represent acceleration, velocity, time, force, and length, respectively.

$$\lambda_m = {}^{m_s}/_{m_u} \quad \text{Eqn. 10.1}$$

$$v_s = v_u \quad \text{Eqn. 10.2}$$

$$F_s = \lambda_m^{2/3} F_u \quad \text{Eqn. 10.3}$$

$$t_s = \lambda_m^{1/3} t_u \quad \text{Eqn. 10.4}$$

$$a_s = \lambda_m^{-1/3} a_u \quad \text{Eqn. 10.5}$$

$$l_s = \lambda_m^{1/3} l_u \quad \text{Eqn. 10.6}$$

10.2 Injury Summary

A summary of the injuries from the PMHS impactor test series and drop tower test series is provided in Table 10.1. Images from x-ray and CT are provided in the smaller tables that follow, which provide a more detailed description of the injuries shown in the radiographs.

Table 10.1. Summary of Impactor Test Injuries

Test	Specimen	INJURY	AFIS Verbage	AFIS-S	AFIS-I
1	**578L**	Calcaneus	calcaneal fx, non-articular, undisplaced	2	0
		Tibia	tibial pilon fx, displaced	6	4
2	**545R**	NO INJURY	NO INJURY	0	0
3	**647L**	NO INJURY	NO INJURY	0	0
4	**579L**	NO INJURY	NO INJURY	0	0
5	**674R**	Calcaneus	calcaneal fx, non-articular, undisplaced	2	0
6	**695L**	NO INJURY	NO INJURY	0	0
7	**576R**	NO INJURY	NO INJURY	0	0
8	**574R**	Calcaneus	calcaneal fx, non-articular, displaced	2	1
		Tibia	tibial pilon fx, displaced	6	4
		Talus	Talar fx, body, undisplaced	3	2
9	**573L**	Calcaneus	calcaneal fx, articular, displaced	5	3
10	**532R**	NO INJURY	NO INJURY	0	0
11	**674L**	NO INJURY	NO INJURY	0	0
12	**695R**	NO INJURY	NO INJURY	0	0
13	**538R**	Calcaneus	calcaneal fx, non-articular, undisplaced	2	0
		talus	talar fx, body, undisplaced	3	2
		Tibia	tibial pilon fx, undisplaced	4	2
		Fibula	Fibula fx, diaphysis, displaced	2	1
14	**539L**	NO INJURY	NO INJURY	0	0
15	**541R**	Calcaneus	calcaneal fx, non-articular, undisplaced	2	0
		Tibia	tibial pilon fx, displaced	6	4
16	**529L**	NO INJURY	NO INJURY	0	0
17	**529R**	NO INJURY	NO INJURY	0	0
18	**546L**	NO INJURY	NO INJURY	0	0
19	**577R**	NO INJURY	NO INJURY	0	0
20	**577L**	NO INJURY	NO INJURY	0	0
21	**647R**	NO INJURY	NO INJURY	0	0
22	**542R**	Tibia	tibial pilon fx, displaced	6	4
		Fibula	Fibula fx, diaphysis, displaced	2	1
23	**554R**	Calcaneus	calcaneal fx, articular, displaced	5	3
24	**555L**	Calcaneus	calcaneal fx, articular, displaced	5	3
25	**565R**	Calcaneus	calcaneal fx, non-articular, displaced	2	1
		Tibia	tibial pilon fx, displaced	6	4
26	**575L**	Calcaneus	calcaneal fx, articular, displaced	5	3
		talus	talar fx, body, undisplaced	3	2
27	**578R**	Calcaneus	calcaneal fx, articular, displaced	5	3
28	**554L**	Calcaneus	calcaneal fx, articular, displaced	5	3
29	**555R**	Calcaneus	calcaneal fx, articular, displaced	5	3
30	**565L**	Calcaneus	calcaneal fx, articular, displaced	5	3
31	**574L**	Calcaneus	calcaneal fx, non-articular, undisplaced	2	0
		Tibia	tibial pilon fx, displaced	6	4
32	**575R**	Calcaneus	calcaneal fx, non-articular, undisplaced	2	0
		Tibia	tibial pilon fx, displaced	6	4
33	**576L**	Calcaneus	calcaneal fx, articular, displaced	5	3
34	**538L**	Calcaneus	calcaneal fx, articular, displaced	5	3
		talus	talar fx, neck, displaced	5	3
35	**539R**	Calcaneus	calcaneal fx, non-articular, undisplaced	2	0
		Tibia	tibial pilon fx, displaced	6	4
36	**541L**	Calcaneus	calcaneal fx, articular, displaced	5	3
		Lateral malleous	lateral malleolus fx, undisplaced	1	0
37	**542L**	Calcaneus	calcaneal fx, articular, displaced	5	3
		Talus	talus fx, with dislocation of fragment	5	3
		Lateral malleous	lateral malleolus fx, undisplaced	1	0
38	**573R**	Calcaneus	calcaneal fx, articular, displaced	5	3

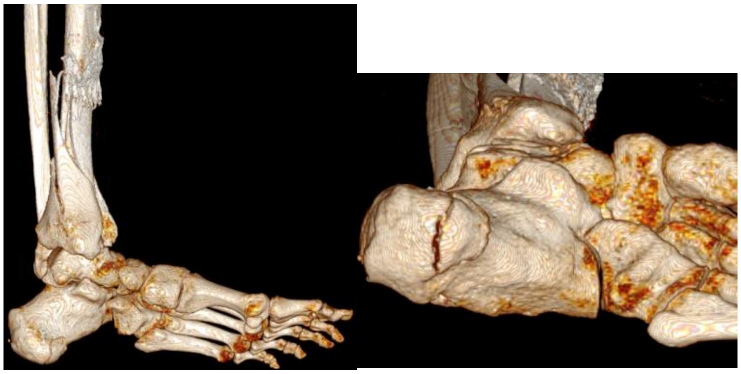

Test: Impactor 01

Condition: Medium

Specimen: 578L

Injury Description:
calcaneal fx, non-articular, undisplaced
tibial pilon fx, displaced

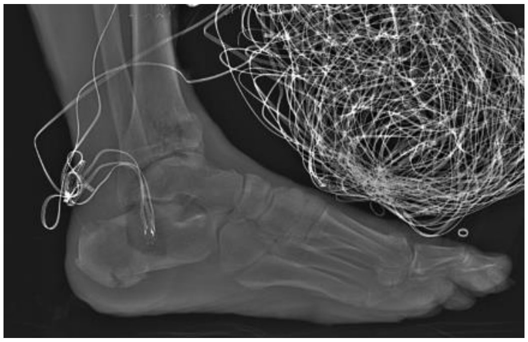

Test: Impactor 05

Condition: Low

Specimen: 674R

Injury Description:
calcaneal fx, non-articular, undisplaced

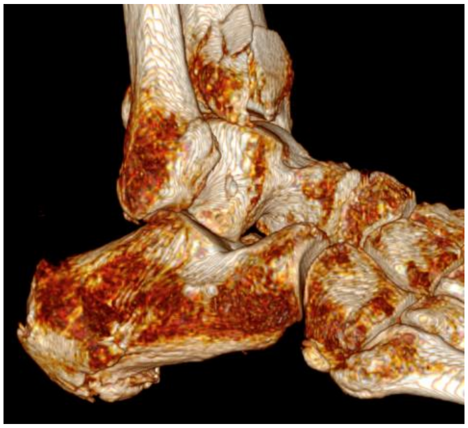

Test: Impactor 08

Condition: Medium

Specimen: 574R

Injury Description:
calcaneal fx, non-articular, displaced
tibial pilon fx, displaced
talar fx, body, undisplaced

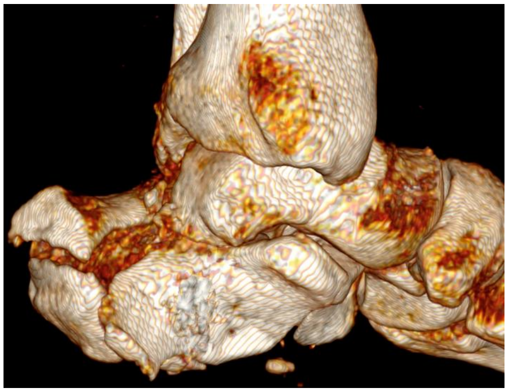	Test: Impactor 09
	Condition: Medium
	Specimen: 573L
	Injury Description: calcaneal fx, articular, displaced

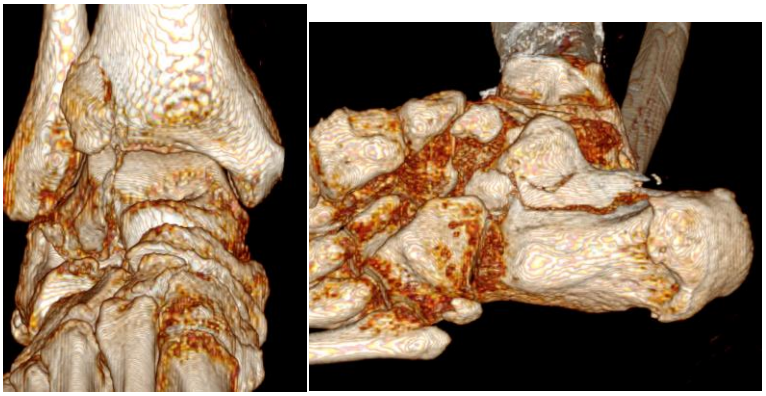	Test: Impactor 13
	Condition: Medium
	Specimen: 538R
	Injury Description: calcaneal fx, non-articular, undisplaced talar fx, body, undisplaced tibial pilon fx, undisplaced fibula fx, diaphysis, displaced

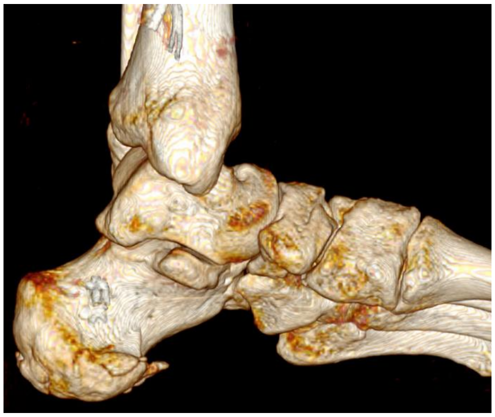	Test: Impactor 14
	Condition: Medium
	Specimen:539L
	Injury Description: NO INJURY

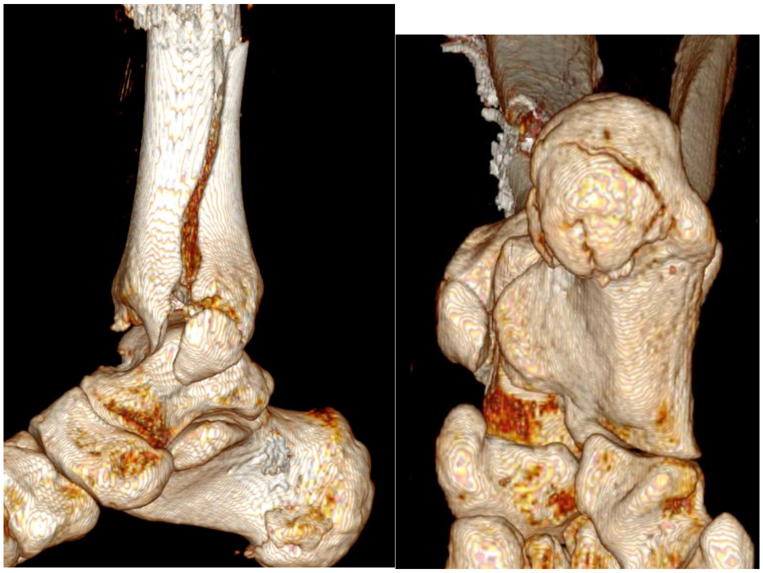	Test: Impactor 15
	Condition: Medium
	Specimen: 541R
	Injury Description: calcaneal fx, non-articular, undisplaced tibial pilon fx, displaced

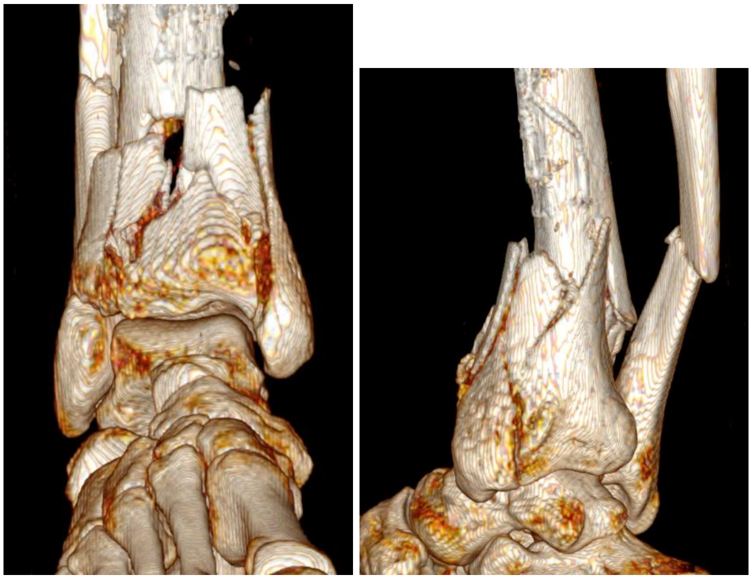	Test: Impactor 22
	Condition: Medium
	Specimen: 542R
	Injury Description: tibial pilon fx, displaced Fibula fx, diaphysis, displaced

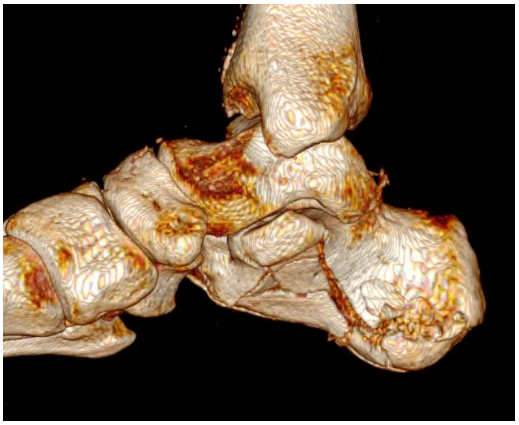	Test: Impactor 23
	Condition: Medium
	Specimen: 554R
	Injury Description: calcaneal fx, articular, displaced

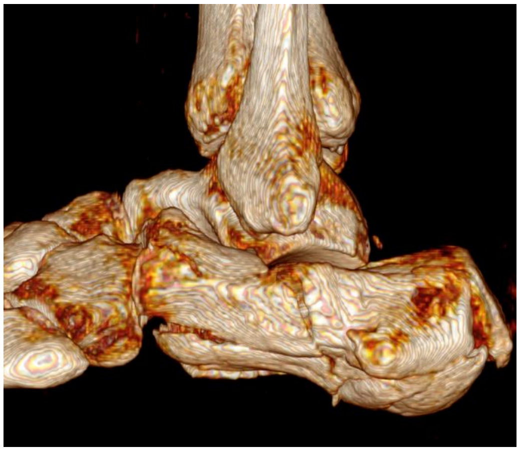	Test: Impactor 24
	Condition: Medium
	Specimen: 555L
	Injury Description: calcaneal fx, articular, displaced

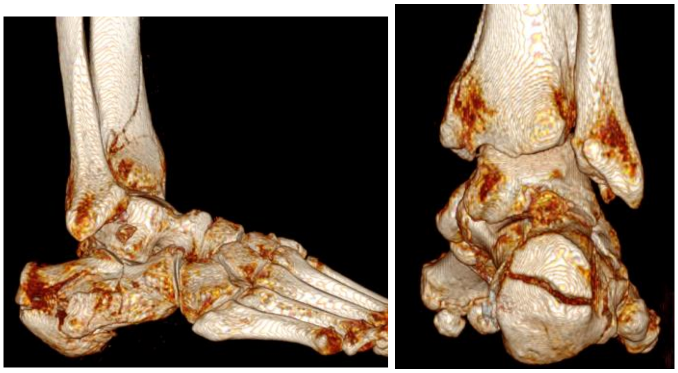	Test: Impactor 25
	Condition: Medium
	Specimen: 565R
	Injury Description: calcaneal fx, non-articular, displaced tibial pilon fx, displaced

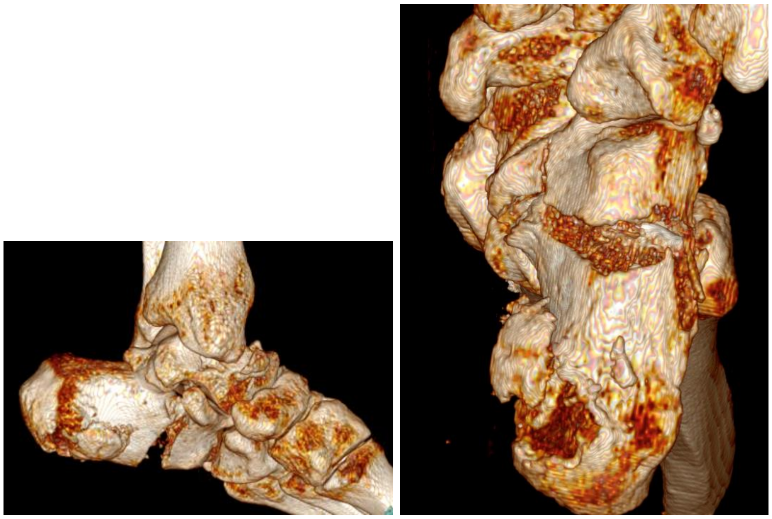

Test: Impactor 26

Condition: Medium

Specimen: 575L

Injury Description:
calcaneal fx, articular, displaced
talar fx, body, undisplaced

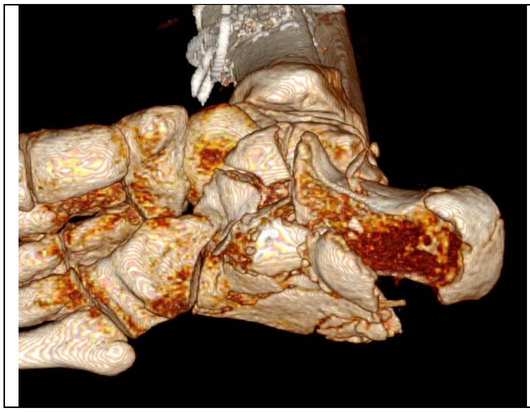

Test: Impactor 27

Condition: High

Specimen: 578R

Injury Description:
calcaneal fx, articular, displaced

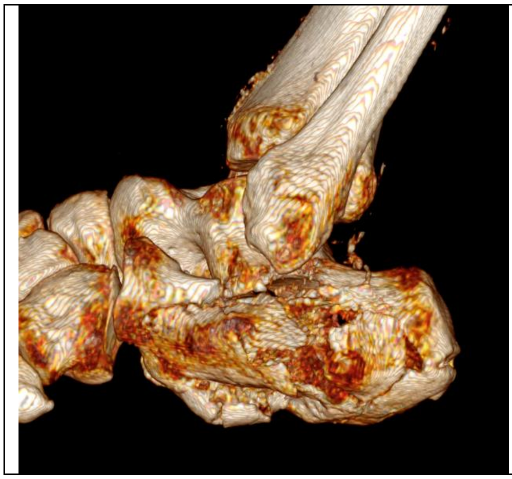

Test: Impactor 28

Condition: High

Specimen: 554L

Injury Description:
calcaneal fx, articular, displaced

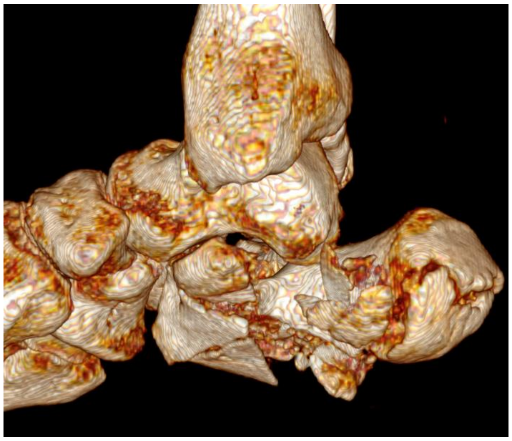	Test: Impactor 29
	Condition: High
	Specimen: 555R
	Injury Description: calcaneal fx, articular, displaced

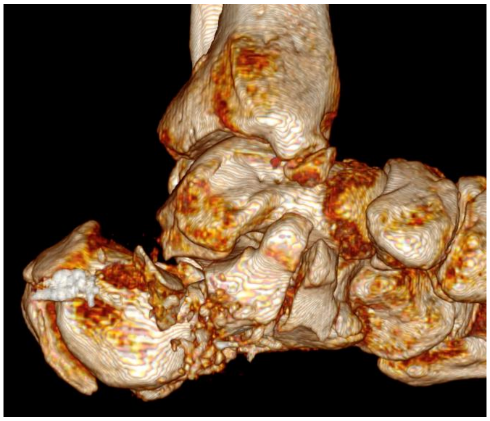	Test: Impactor 30
	Condition: High
	Specimen: 565L
	Injury Description: calcaneal fx, articular, displaced

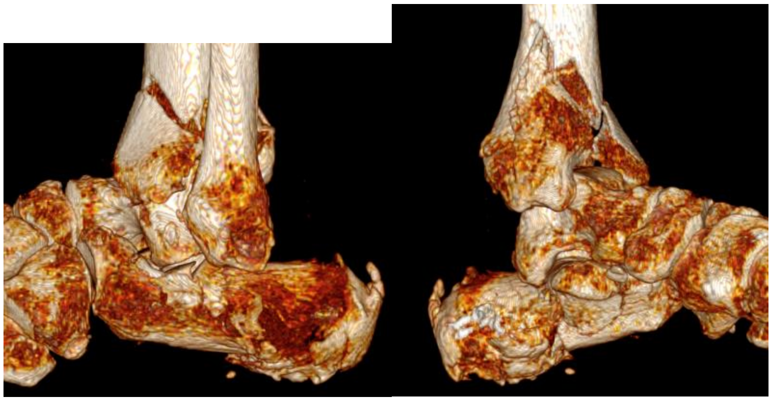	Test: Impactor 31
	Condition: High
	Specimen: 574L
	Injury Description: calcaneal fx, non-articular, undisplaced tibial pilon fx, displaced

<table>
<tr><td rowspan="4">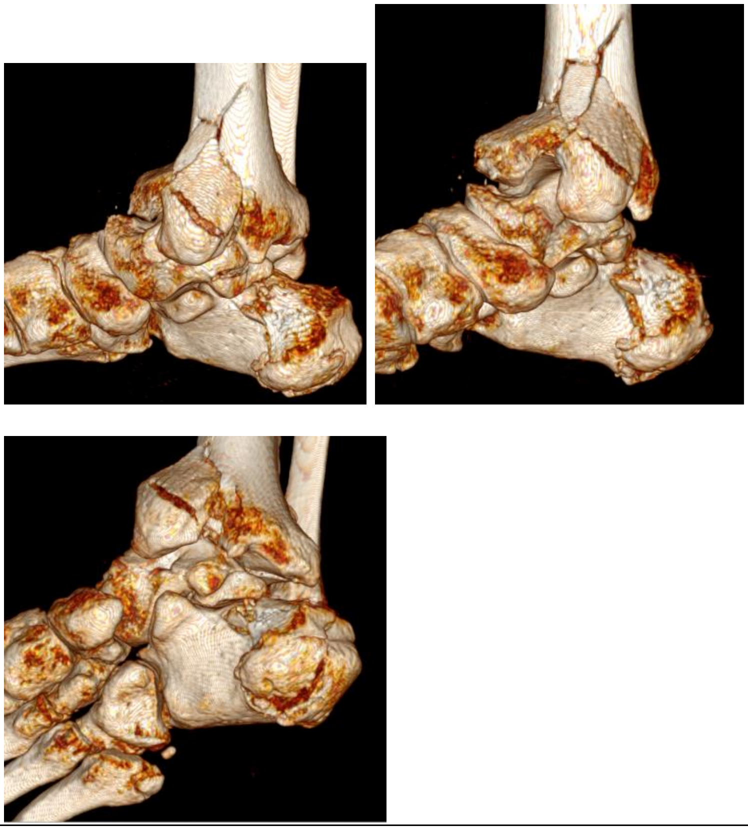</td><td>Test: Impactor 32</td></tr>
<tr><td>Condition: High</td></tr>
<tr><td>Specimen: 575R</td></tr>
<tr><td>Injury Description:
calcaneal fx, articular, displaced
tibial pilon fx, displaced</td></tr>
</table>

<table>
<tr><td rowspan="4">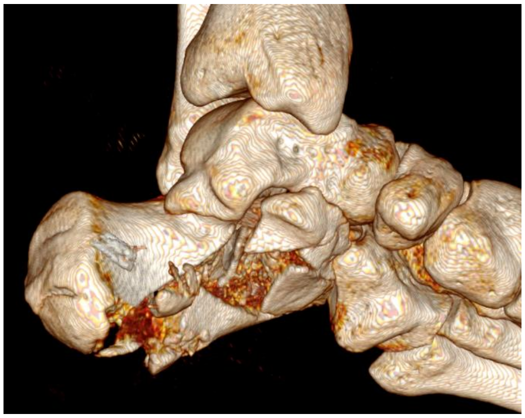</td><td>Test: Impactor 33</td></tr>
<tr><td>Condition: High</td></tr>
<tr><td>Specimen: 576L</td></tr>
<tr><td>Injury Description:
calcaneal fx, non-articular, displaced</td></tr>
</table>

<table>
<tr><td rowspan="4">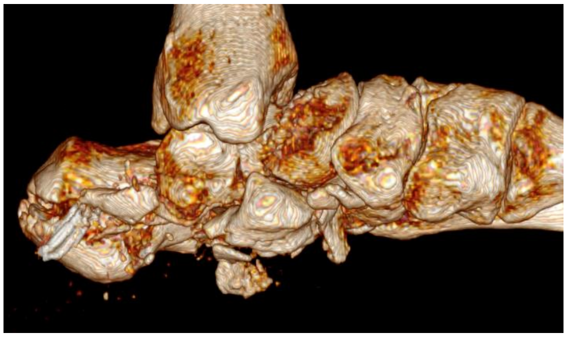
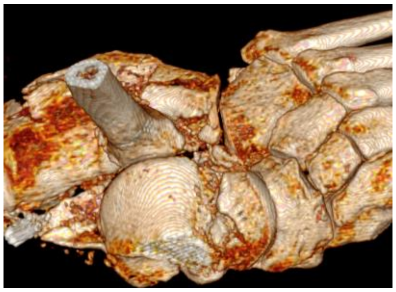</td><td>Test: Impactor 34</td></tr>
<tr><td>Condition: High</td></tr>
<tr><td>Specimen: 538L</td></tr>
<tr><td>Injury Description:</td></tr>
</table>

<table>
<tr><td rowspan="4">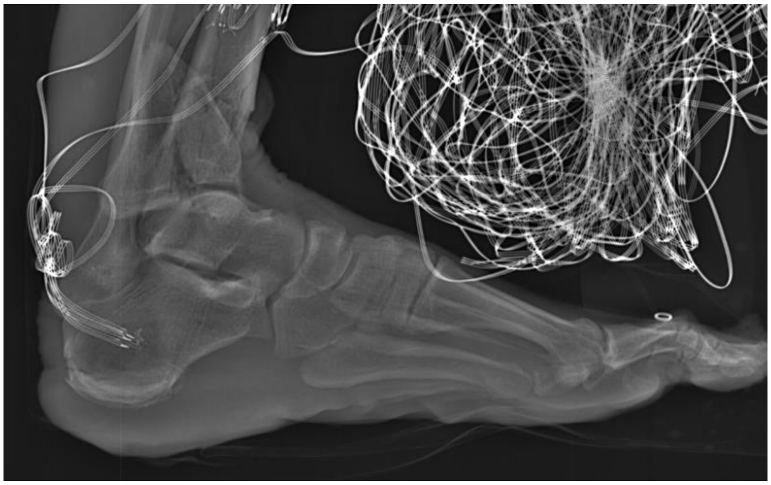</td><td>Test: Impactor 35</td></tr>
<tr><td>Condition: High</td></tr>
<tr><td>Specimen: 539R</td></tr>
<tr><td>Injury Description:
calcaneal fx, non-articular, undisplaced
tibial pilon fx, displaced</td></tr>
</table>

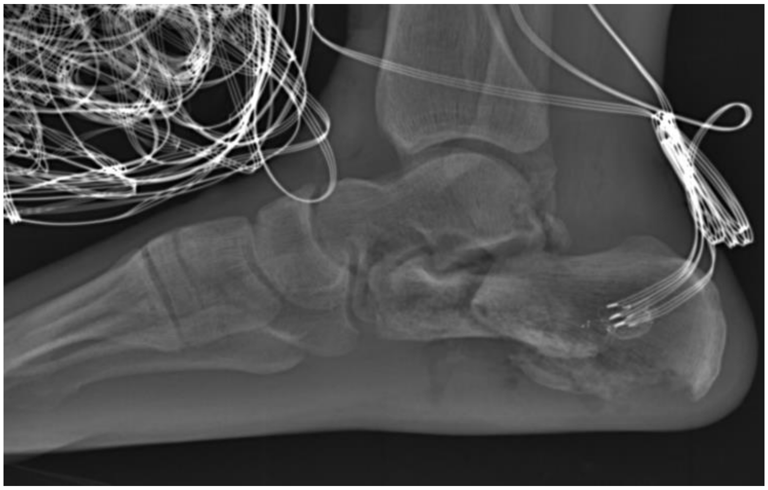

Test: Impactor 36

Condition: High

Specimen: 541L

Injury Description:
Calcaneus fx, articular, displaced
Lateral mallolus fx, undisplaced

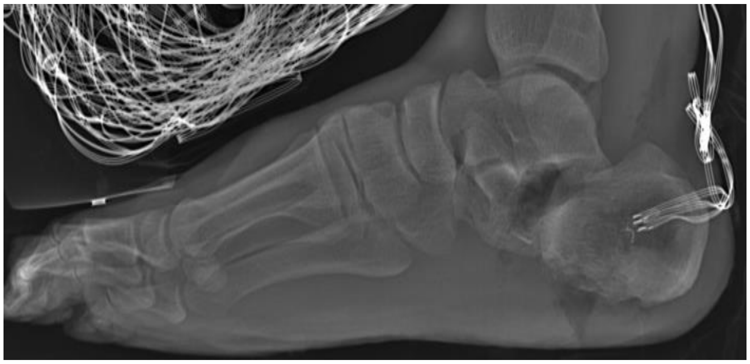

Test: Impactor 37

Condition: High

Specimen: 542L

Injury Description:
Calcaneus fx, articular, displaced
Talus fx, with dislocation of fragment
Lateral mallolus fx, undisplaced

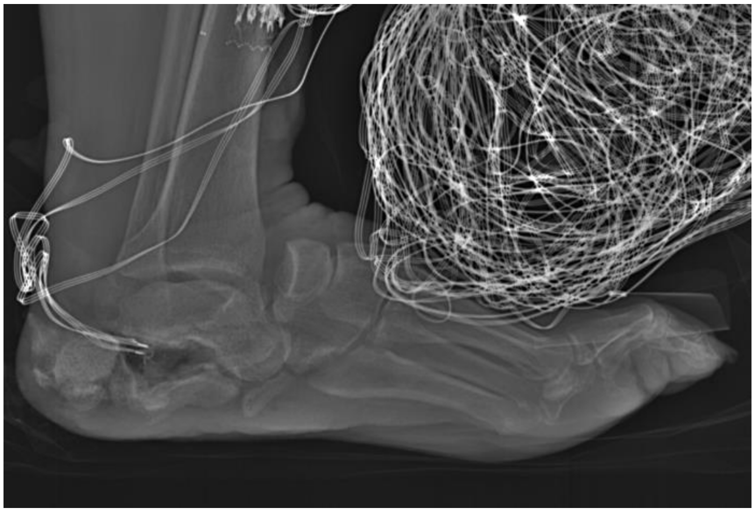

Test: Impactor 38

Condition: High

Specimen: 573R

Injury Description:
Calcaneus fx, articular, displaced

10.3 Data Summary from PMHS Tests

The following plots show the footplate force response and the leg compression calculated using the difference in displacement between the footplate and proximal tibia displacements as calculated from the double integration of the acceleration at those locations for each of the three impactor loading conditions. Plots are also provided for the leg compression and proximal tibia force for the two drop tower test conditions. Forces were inertially-compensated using half the mass of the load cell.

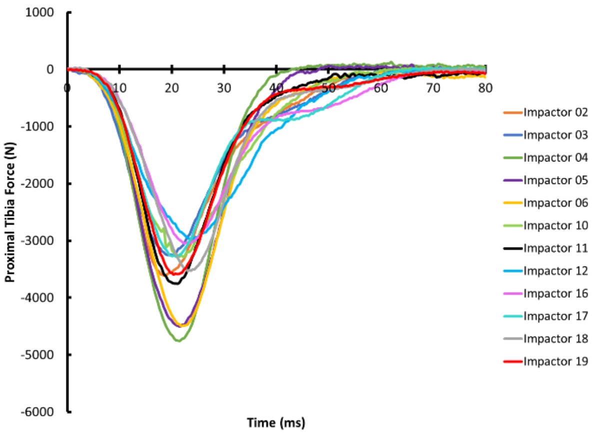

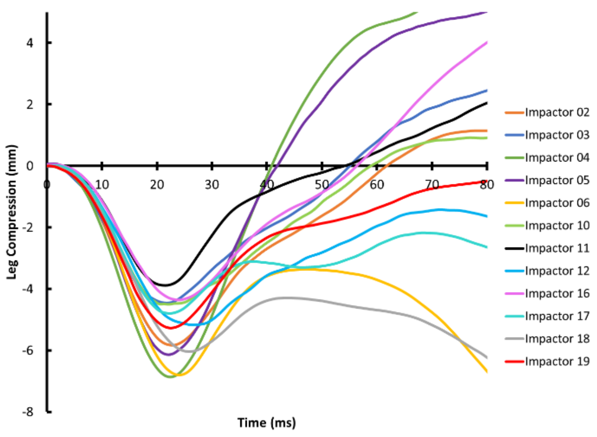

Figure 10.2. Mass-compensated footplate force for low impactor tests

Figure 10.3. Leg compression for low impactor tests calculated using footplate and proximal tibia accelerometers

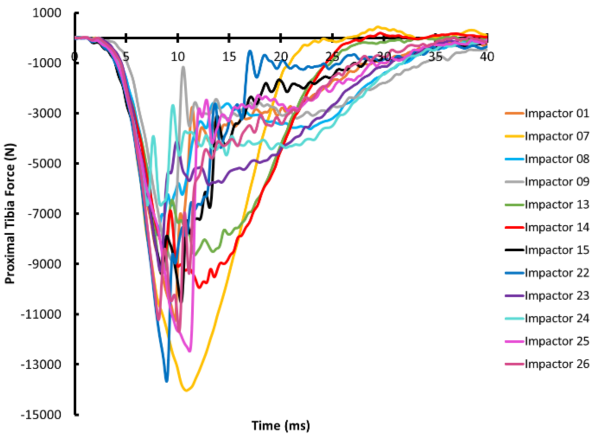

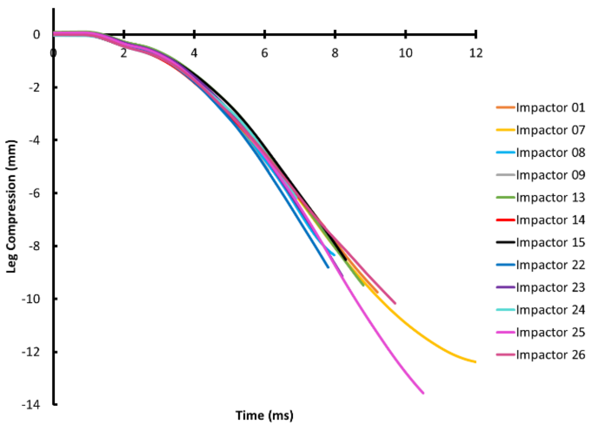

Figure 10.4. Mass-compensated footplate force for medium impactor tests

Figure 10.5. Leg compression for medium impactor tests calculated using footplate and proximal tibia accelerometers

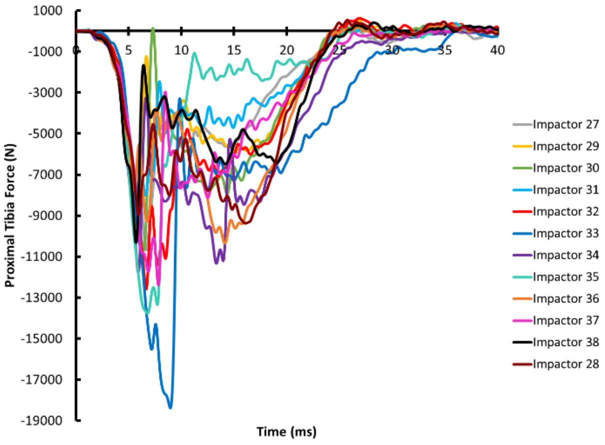

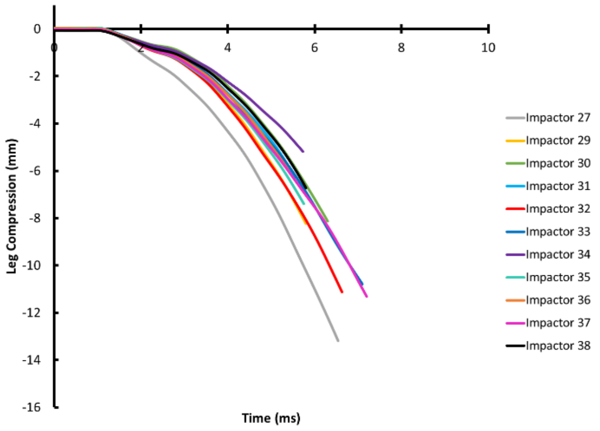

Figure 10.6. Proximal tibia force for high impactor tests

Figure 10.7. Leg compression for high impactor tests calculated using footplate and proximal tibia accelerometers

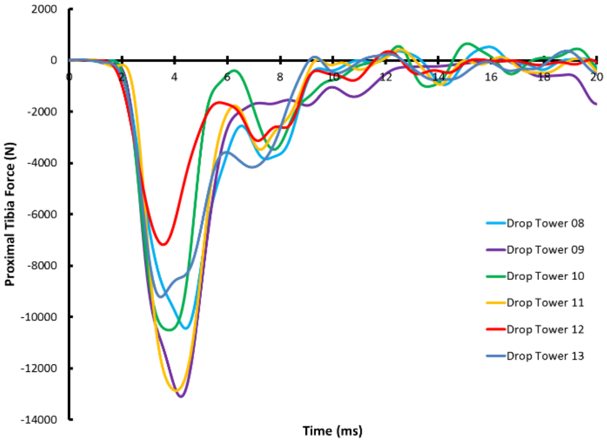

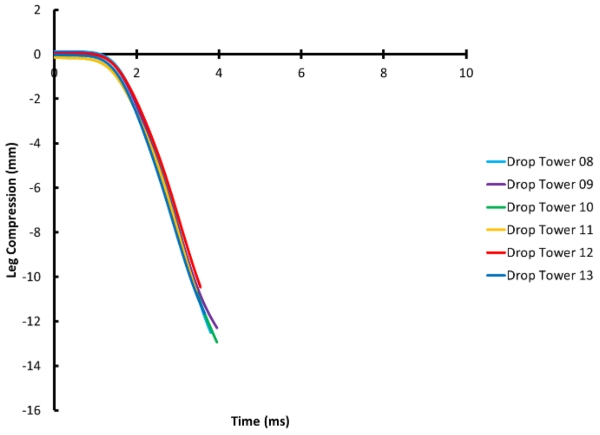

Figure 10.8. Mass-compensated proximal tibia force for Drop Tower A tests.

Figure 10.9. Leg compression for Drop Tower A tests calculated using footplate and proximal tibia accelerometers

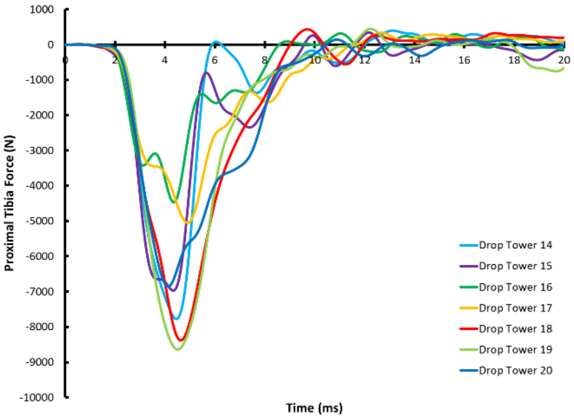

Figure 10.10. Mass-compensated proximal tibia force for Drop Tower B tests.

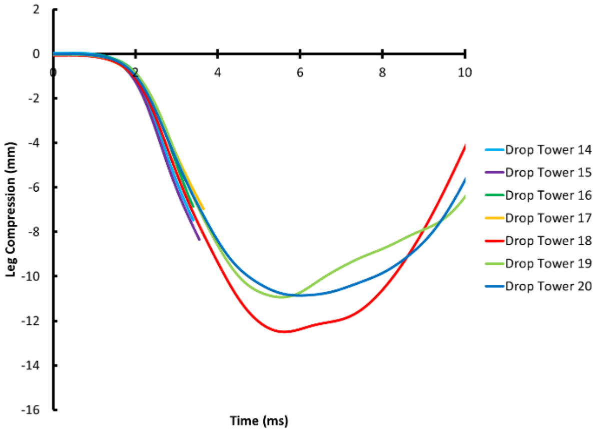

Figure 10.11. Leg compression for Drop Tower B tests calculated using footplate and proximal tibia accelerometers.

10.3.1 Fracture Timing

Time of fracture was established using the force, strain, and acoustic data traces from each of the impactor tests. The availability of the high speed x-ray footage allowed for additional comparison and confirmation of fracture location. Plots of these traces are overlaid in the following plots to show the overlap of peak forces, acoustic emission spikes, and discontinuities in the strain. In cases where multiple fractures occurred, the acoustic sensor on the respective bones (tibia and calcaneus) spiked at different times and aligned with the time estimated for fracture using the high speed x-ray.

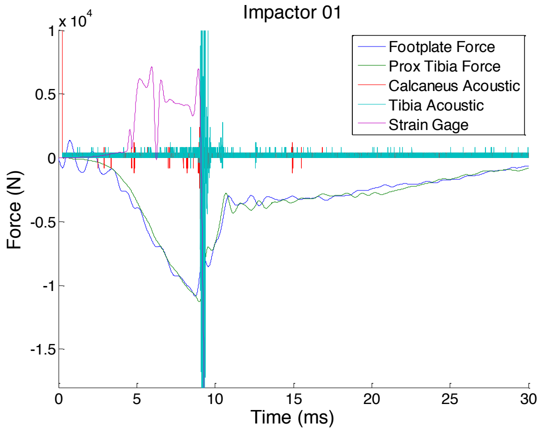
Impactor 01
x 10^4
1
0.5
0
-0.5
-1
-1.5
Force (N)
0
5
10
15
20
25
30
Time (ms)
Footplate Force
Prox Tibia Force
Calcaneus Acoustic
Tibia Acoustic
Strain Gage

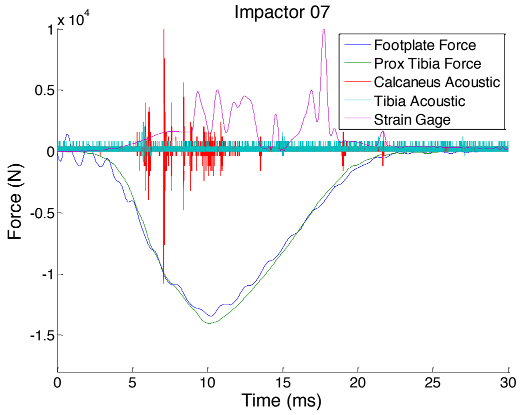
Impactor 07
x 10^4
1
0.5
0
-0.5
-1
-1.5
Force (N)
0
5
10
15
20
25
30
Time (ms)
Footplate Force
Prox Tibia Force
Calcaneus Acoustic
Tibia Acoustic
Strain Gage

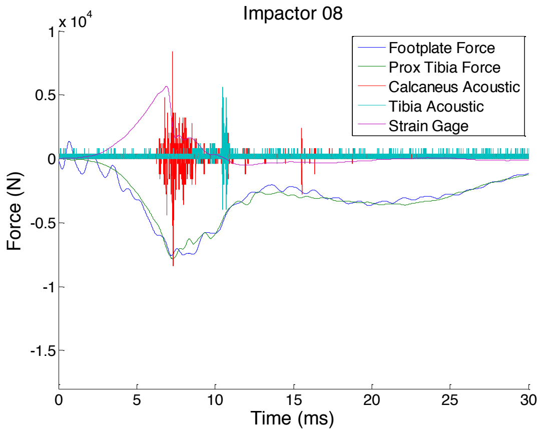
Impactor 08
x 10^4
1
0.5
0
-0.5
-1
-1.5
Force (N)
0
5
10
15
20
25
30
Time (ms)
Footplate Force
Prox Tibia Force
Calcaneus Acoustic
Tibia Acoustic
Strain Gage

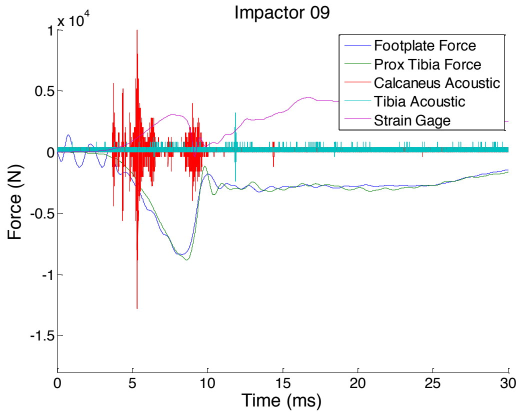
Impactor 09
x 10^4
1
0.5
0
-0.5
-1
-1.5
Force (N)
0
5
10
15
20
25
30
Time (ms)
Footplate Force
Prox Tibia Force
Calcaneus Acoustic
Tibia Acoustic
Strain Gage

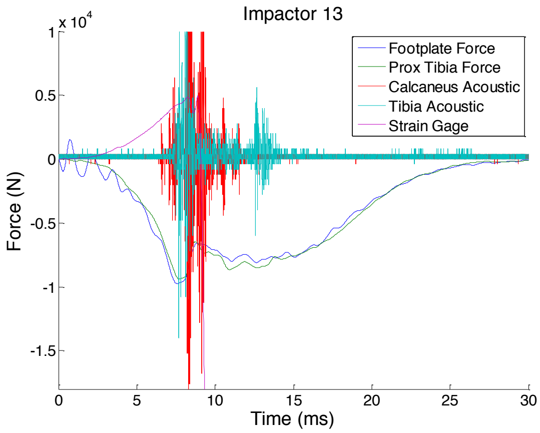
Impactor 13
x 10^4
1
0.5
0
-0.5
-1
-1.5
Force (N)
0
5
10
15
20
25
30
Time (ms)
Footplate Force
Prox Tibia Force
Calcaneus Acoustic
Tibia Acoustic
Strain Gage

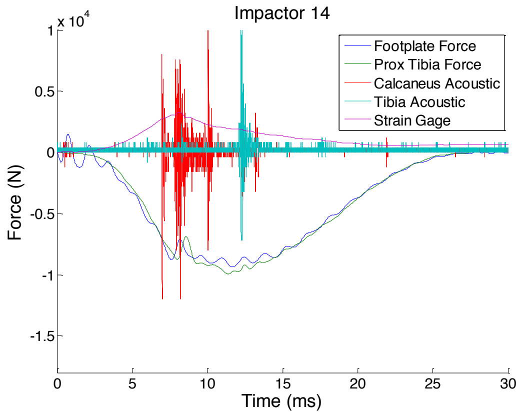
Impactor 14
x 10^4
1
0.5
0
-0.5
-1
-1.5
Force (N)
0
5
10
15
20
25
30
Time (ms)
Footplate Force
Prox Tibia Force
Calcaneus Acoustic
Tibia Acoustic
Strain Gage

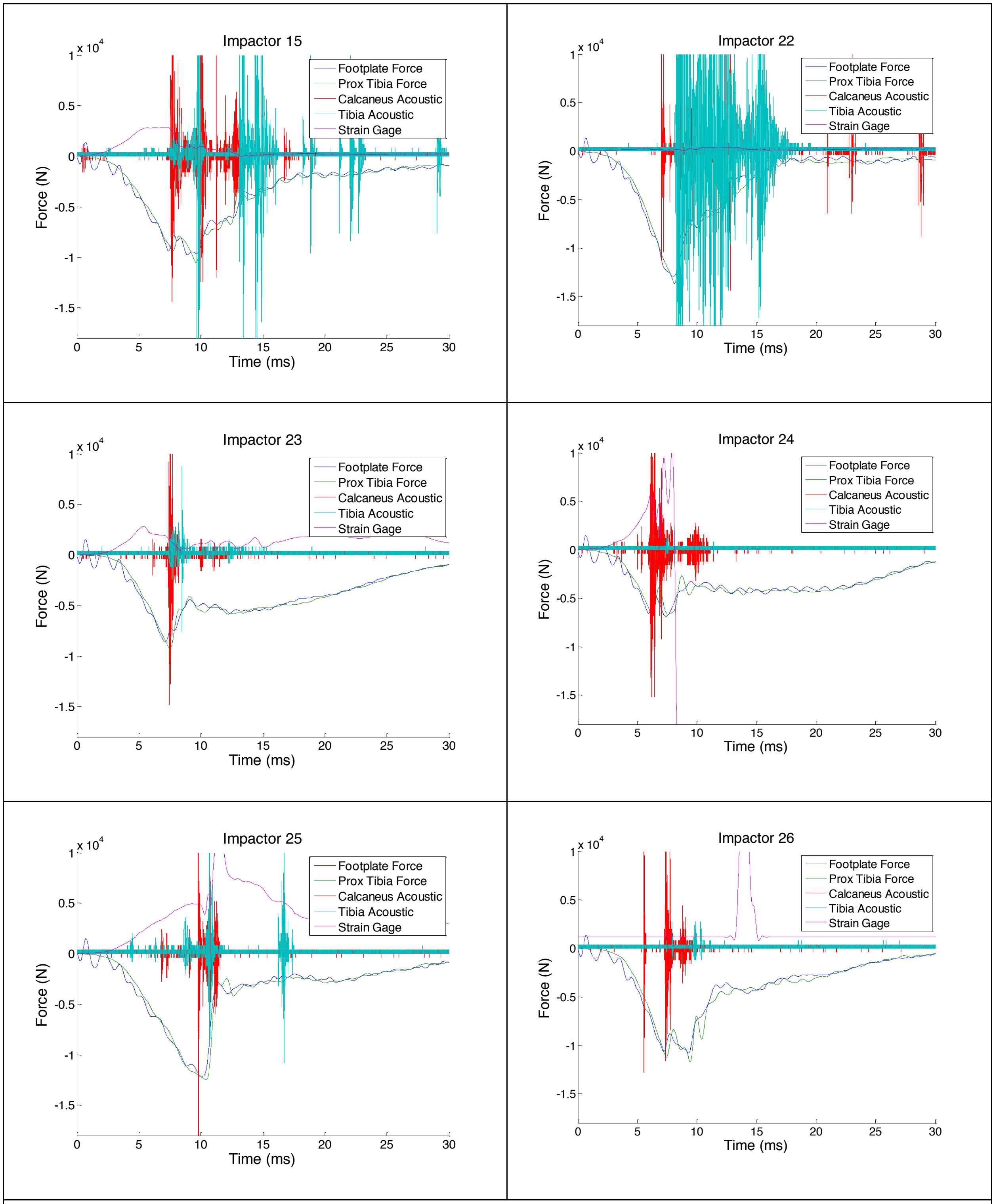

Impactor 15

Impactor 22

Impactor 23

Impactor 24

Impactor 25

Impactor 26

Figure 10.12. Medium Impactor condition fracture timing plots with tibia and calcaneus acoustic data and calcaneus maximum principal strain plotted over footplate and proximal tibia forces.

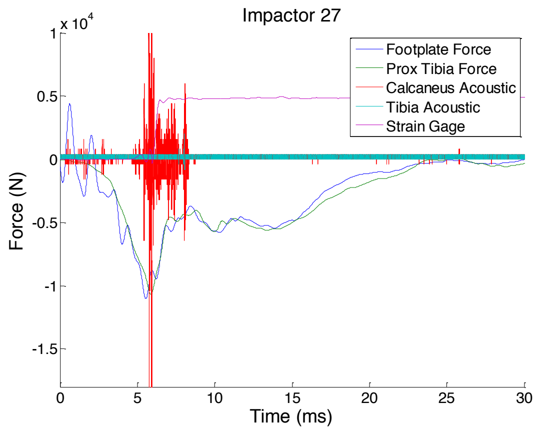
Impactor 27
x 10^4
1
0.5
0
-0.5
-1
-1.5
Force (N)
0
5
10
15
20
25
30
Time (ms)
Footplate Force
Prox Tibia Force
Calcaneus Acoustic
Tibia Acoustic
Strain Gage

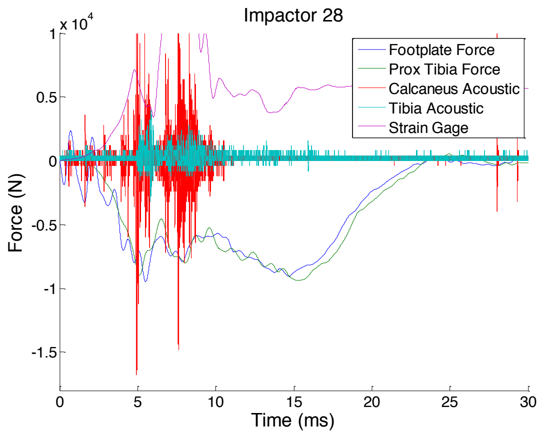
Impactor 28
x 10^4
1
0.5
0
-0.5
-1
-1.5
Force (N)
0
5
10
15
20
25
30
Time (ms)
Footplate Force
Prox Tibia Force
Calcaneus Acoustic
Tibia Acoustic
Strain Gage

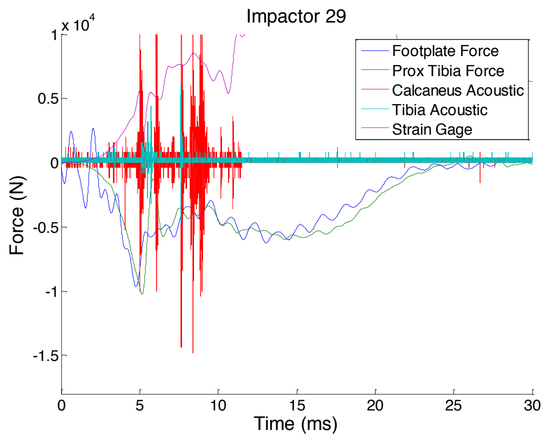
Impactor 29
x 10^4
1
0.5
0
-0.5
-1
-1.5
Force (N)
0
5
10
15
20
25
30
Time (ms)
Footplate Force
Prox Tibia Force
Calcaneus Acoustic
Tibia Acoustic
Strain Gage

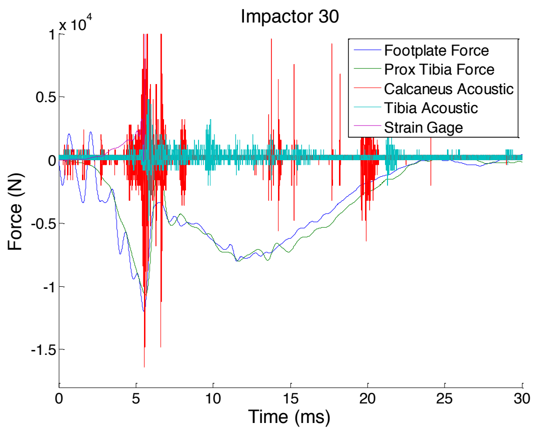
Impactor 30
x 10^4
1
0.5
0
-0.5
-1
-1.5
Force (N)
0
5
10
15
20
25
30
Time (ms)
Footplate Force
Prox Tibia Force
Calcaneus Acoustic
Tibia Acoustic
Strain Gage

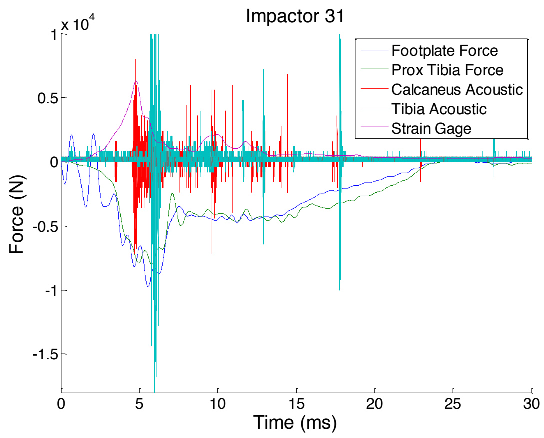
Impactor 31
x 10^4
1
0.5
0
-0.5
-1
-1.5
Force (N)
0
5
10
15
20
25
30
Time (ms)
Footplate Force
Prox Tibia Force
Calcaneus Acoustic
Tibia Acoustic
Strain Gage

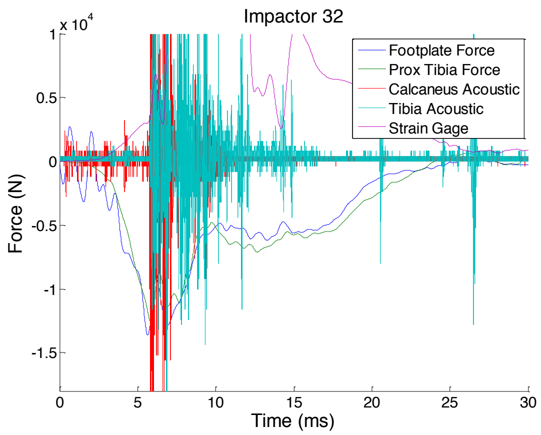
Impactor 32
x 10^4
1
0.5
0
-0.5
-1
-1.5
Force (N)
0
5
10
15
20
25
30
Time (ms)
Footplate Force
Prox Tibia Force
Calcaneus Acoustic
Tibia Acoustic
Strain Gage

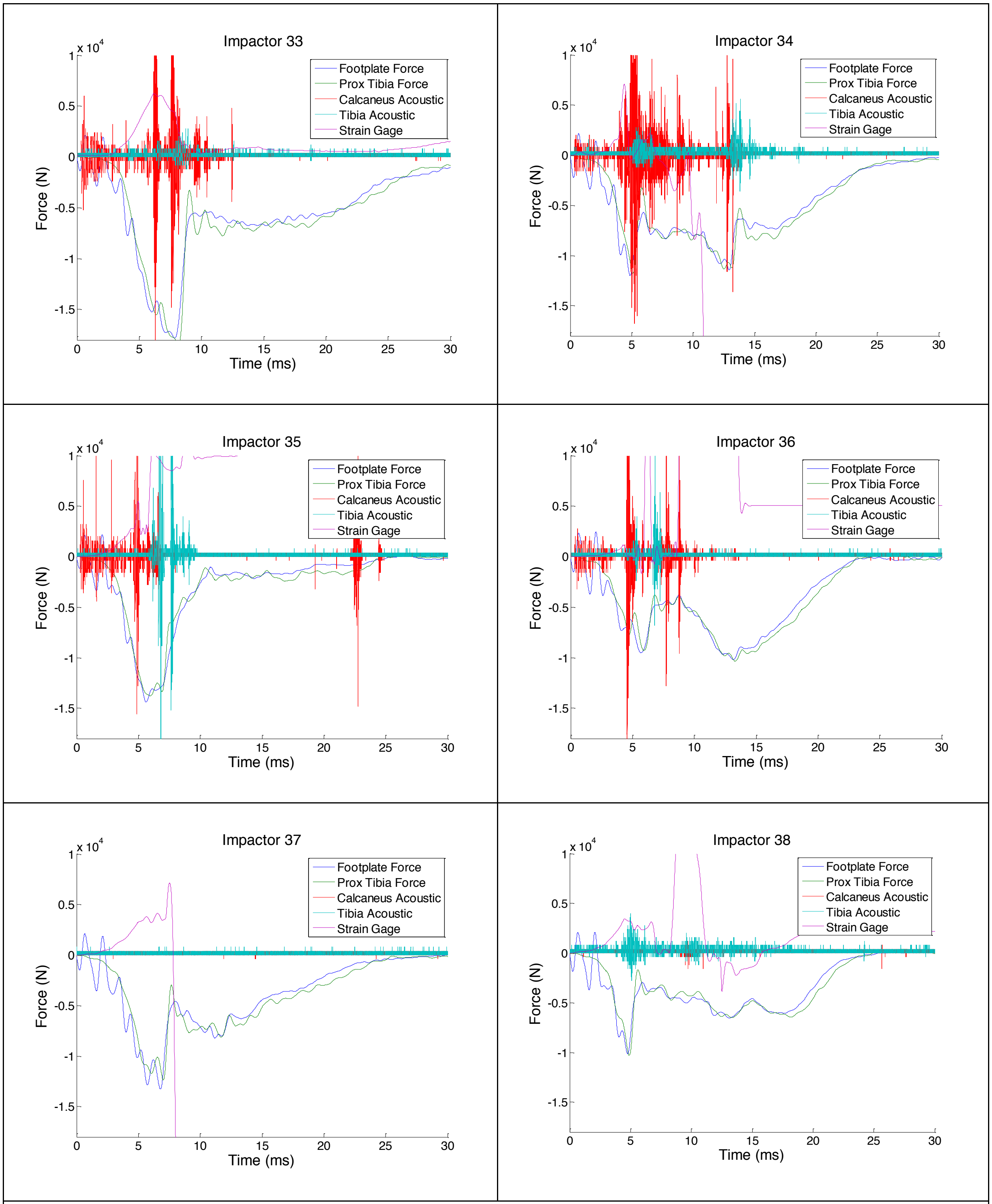

Figure 10.13. High Impactor condition fracture timing plots with tibia and calcaneus acoustic data and calcaneus maximum principal strain plotted over footplate and proximal tibia forces.

10.4 Human Finite Element Model Results

The following are results of a comparison of the modified Human leg finite element model simulations for the case with and without element deletion. It should be noted that while element deletion was used to predict/simulate fracture in the model, the results are not necessarily representative of reality. Nonetheless, these results provide some idea of the ability of the leg to reload after fracture occurs and thus provide an estimation of the peak forces that may be observed in at the plantar surface of the foot and mid- and proximal tibia. . Plots are labeled with the peak acceleration and velocity (A#v*) such that # is the peak acceleration and * is the peak velocity of the footplate input. The sinusoidal inputs from the parametric study were used. Footplate (plantar surface of the foot), mid-tibia, and proximal tibia forces are presented in the following plots.

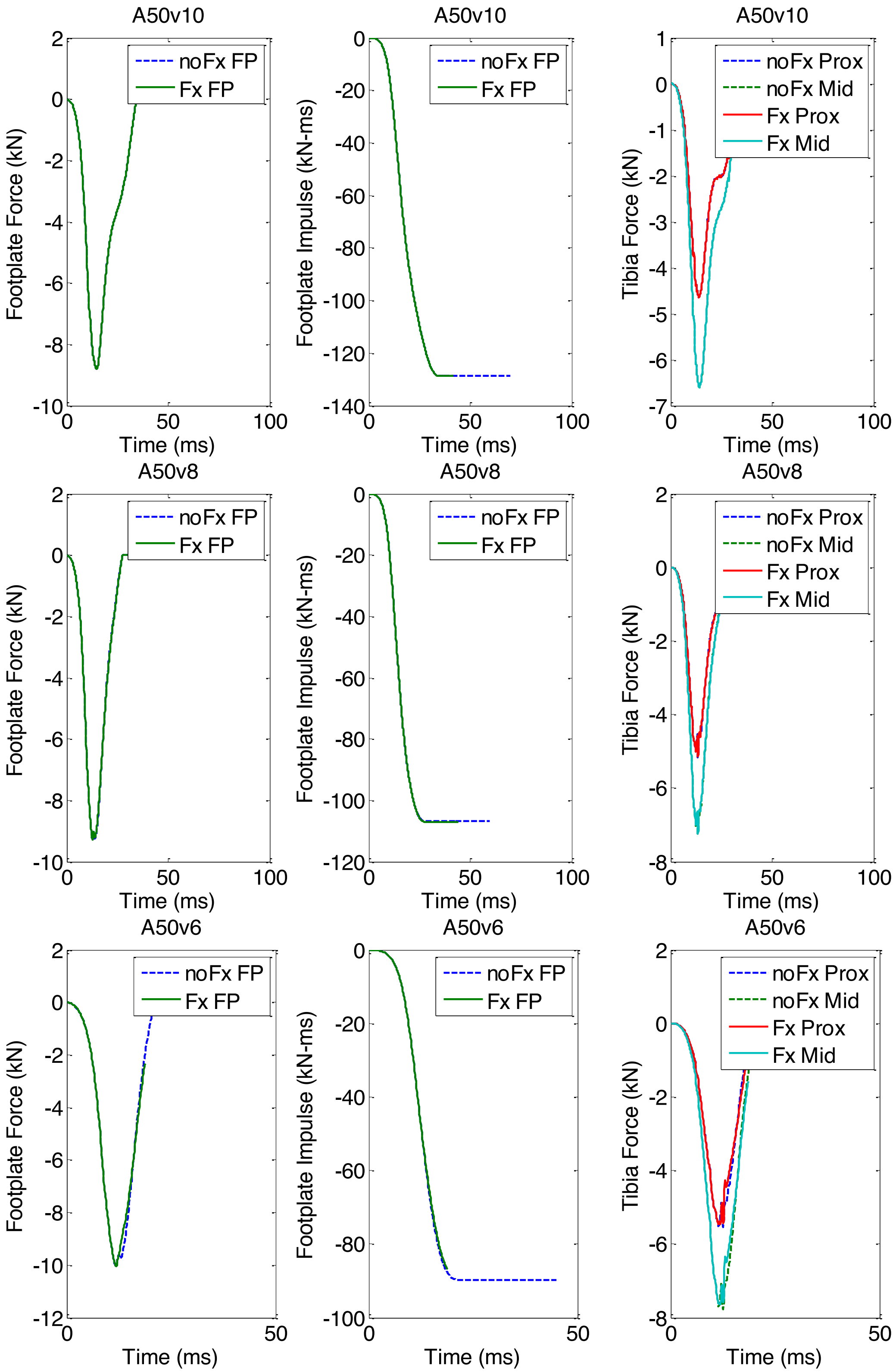
A50v10
Footplate Force (kN)
Time (ms)
noFx FP
Fx FP
2
0
-2
-4
-6
-8
-10
0
50
100
A50v10
Footplate Impulse (kN-ms)
Time (ms)
noFx FP
Fx FP
0
-20
-40
-60
-80
-100
-120
-140
A50v10
Tibia Force (kN)
Time (ms)
noFx Prox
noFx Mid
Fx Prox
Fx Mid
1
0
-1
-2
-3
-4
-5
-6
-7
A50v8
Footplate Force (kN)
Time (ms)
noFx FP
Fx FP
A50v8
Footplate Impulse (kN-ms)
Time (ms)
noFx FP
Fx FP
-120
A50v8
Tibia Force (kN)
Time (ms)
noFx Prox
noFx Mid
Fx Prox
Fx Mid
2
0
-2
-4
-6
-8
A50v6
Footplate Force (kN)
Time (ms)
noFx FP
Fx FP
-12
0
50
A50v6
Footplate Impulse (kN-ms)
Time (ms)
noFx FP
Fx FP
-100
A50v6
Tibia Force (kN)
Time (ms)
noFx Prox
noFx Mid
Fx Prox
Fx Mid

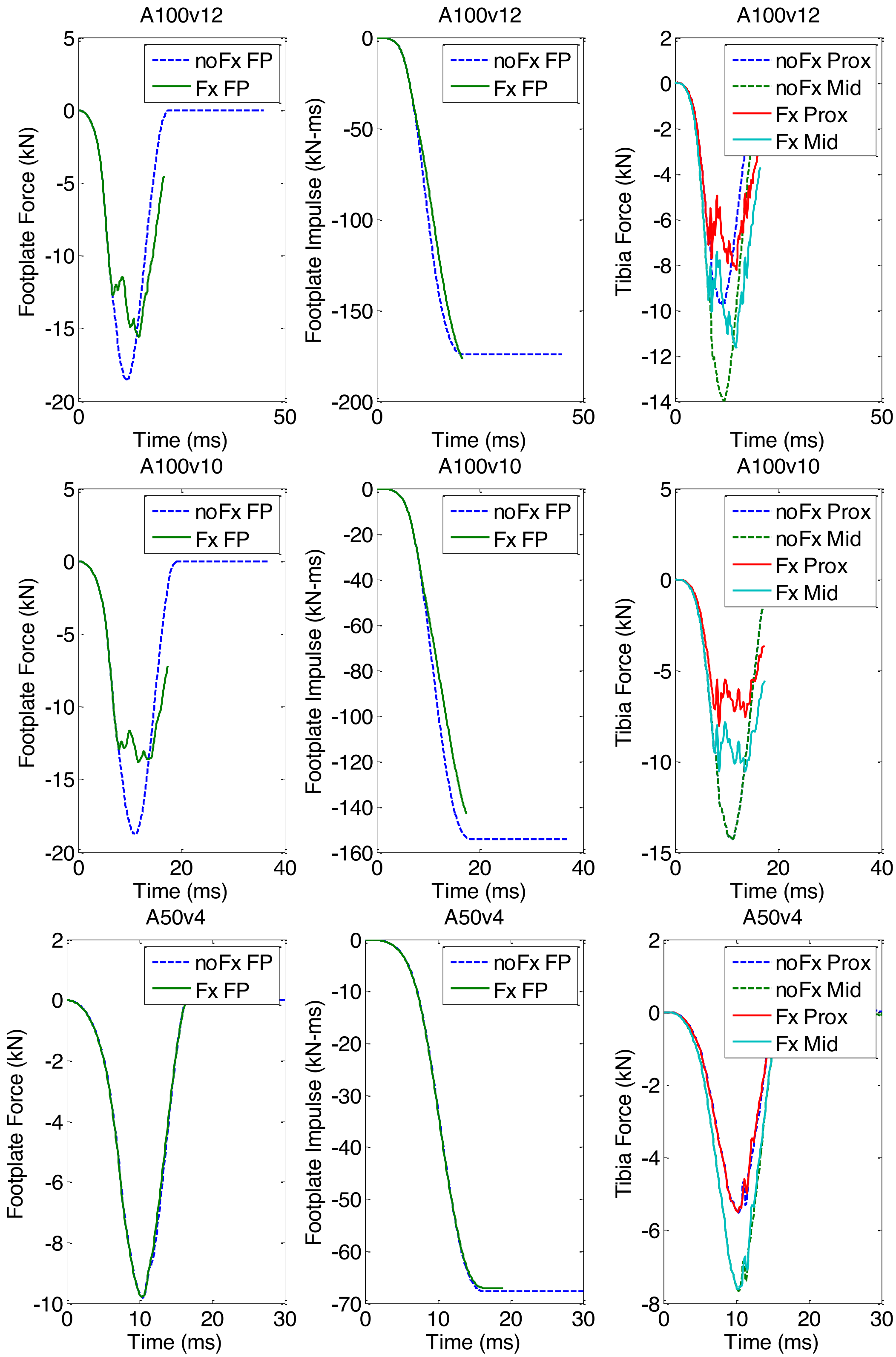
A100v12
Footplate Force (kN)
Time (ms)
noFx FP
Fx FP
5
0
-5
-10
-15
-20
0
50
A100v12
Footplate Impulse (kN-ms)
Time (ms)
noFx FP
Fx FP
0
-50
-100
-150
-200
0
50
A100v12
Tibia Force (kN)
Time (ms)
noFx Prox
noFx Mid
Fx Prox
Fx Mid
2
0
-2
-4
-6
-8
-10
-12
-14
0
50
A100v10
Footplate Force (kN)
Time (ms)
noFx FP
Fx FP
5
0
-5
-10
-15
-20
0
20
40
A100v10
Footplate Impulse (kN-ms)
Time (ms)
noFx FP
Fx FP
0
-20
-40
-60
-80
-100
-120
-140
-160
0
20
40
A100v10
Tibia Force (kN)
Time (ms)
noFx Prox
noFx Mid
Fx Prox
Fx Mid
5
0
-5
-10
-15
0
20
40
A50v4
Footplate Force (kN)
Time (ms)
noFx FP
Fx FP
2
0
-2
-4
-6
-8
-10
0
10
20
30
A50v4
Footplate Impulse (kN-ms)
Time (ms)
noFx FP
Fx FP
0
-10
-20
-30
-40
-50
-60
-70
0
10
20
30
A50v4
Tibia Force (kN)
Time (ms)
noFx Prox
noFx Mid
Fx Prox
Fx Mid
2
0
-2
-4
-6
-8
0
10
20
30

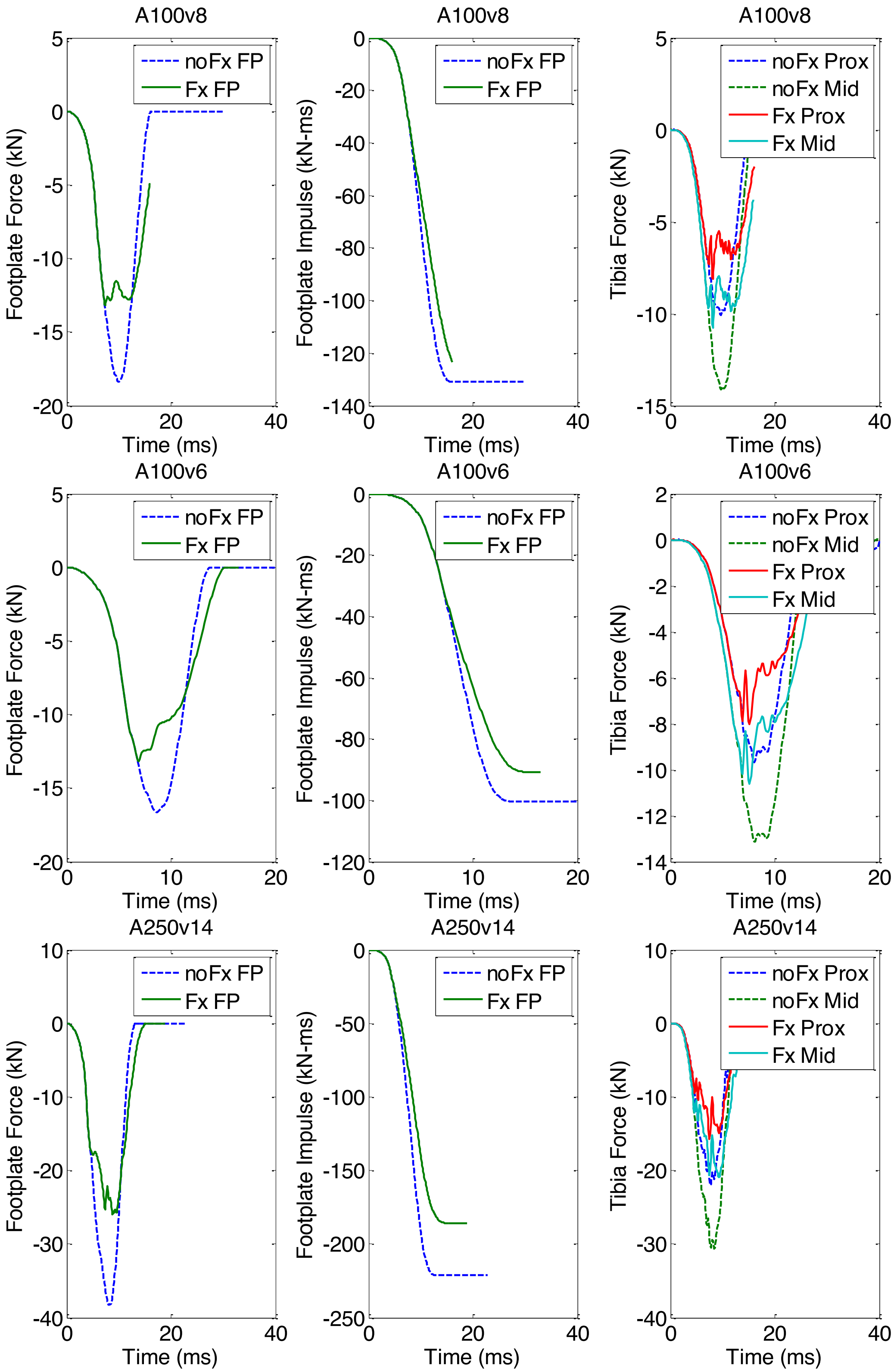
A100v8
Footplate Force (kN)
Time (ms)
noFx FP
Fx FP
A100v8
Footplate Impulse (kN-ms)
Time (ms)
noFx FP
Fx FP
A100v8
Tibia Force (kN)
Time (ms)
noFx Prox
noFx Mid
Fx Prox
Fx Mid
A100v6
Footplate Force (kN)
Time (ms)
noFx FP
Fx FP
A100v6
Footplate Impulse (kN-ms)
Time (ms)
noFx FP
Fx FP
A100v6
Tibia Force (kN)
Time (ms)
noFx Prox
noFx Mid
Fx Prox
Fx Mid
A250v14
Footplate Force (kN)
Time (ms)
noFx FP
Fx FP
A250v14
Footplate Impulse (kN-ms)
Time (ms)
noFx FP
Fx FP
A250v14
Tibia Force (kN)
Time (ms)
noFx Prox
noFx Mid
Fx Prox
Fx Mid

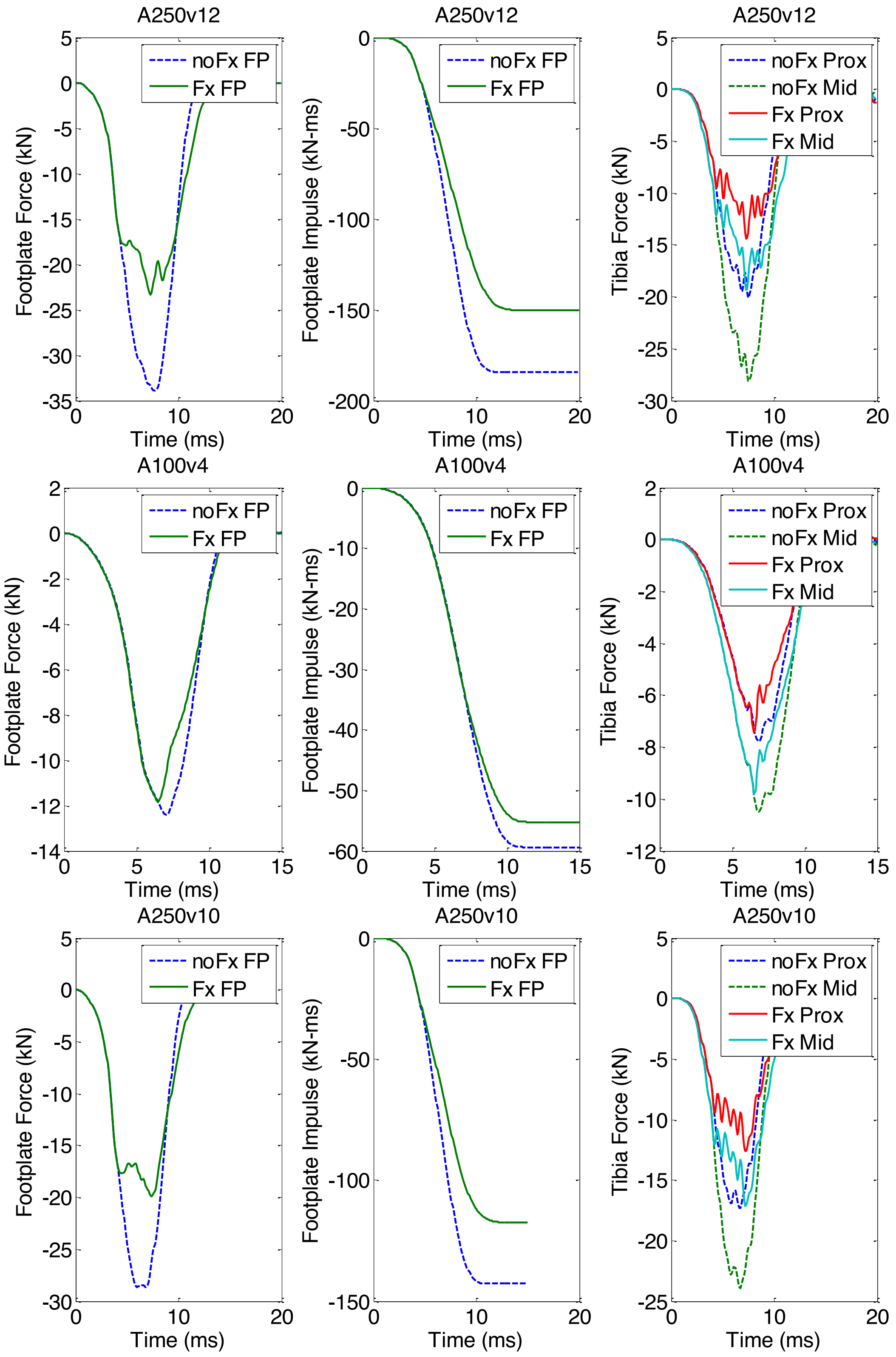
A250v12
Footplate Force (kN)
Time (ms)
noFx FP
Fx FP
Footplate Impulse (kN-ms)
Tibia Force (kN)
noFx Prox
noFx Mid
Fx Prox
Fx Mid
5
0
-5
-10
-15
-20
-25
-30
-35
-50
-100
-150
-200
10
20
A100v4
2
-2
-4
-6
-8
-12
-14
-40
-60
15
A250v10

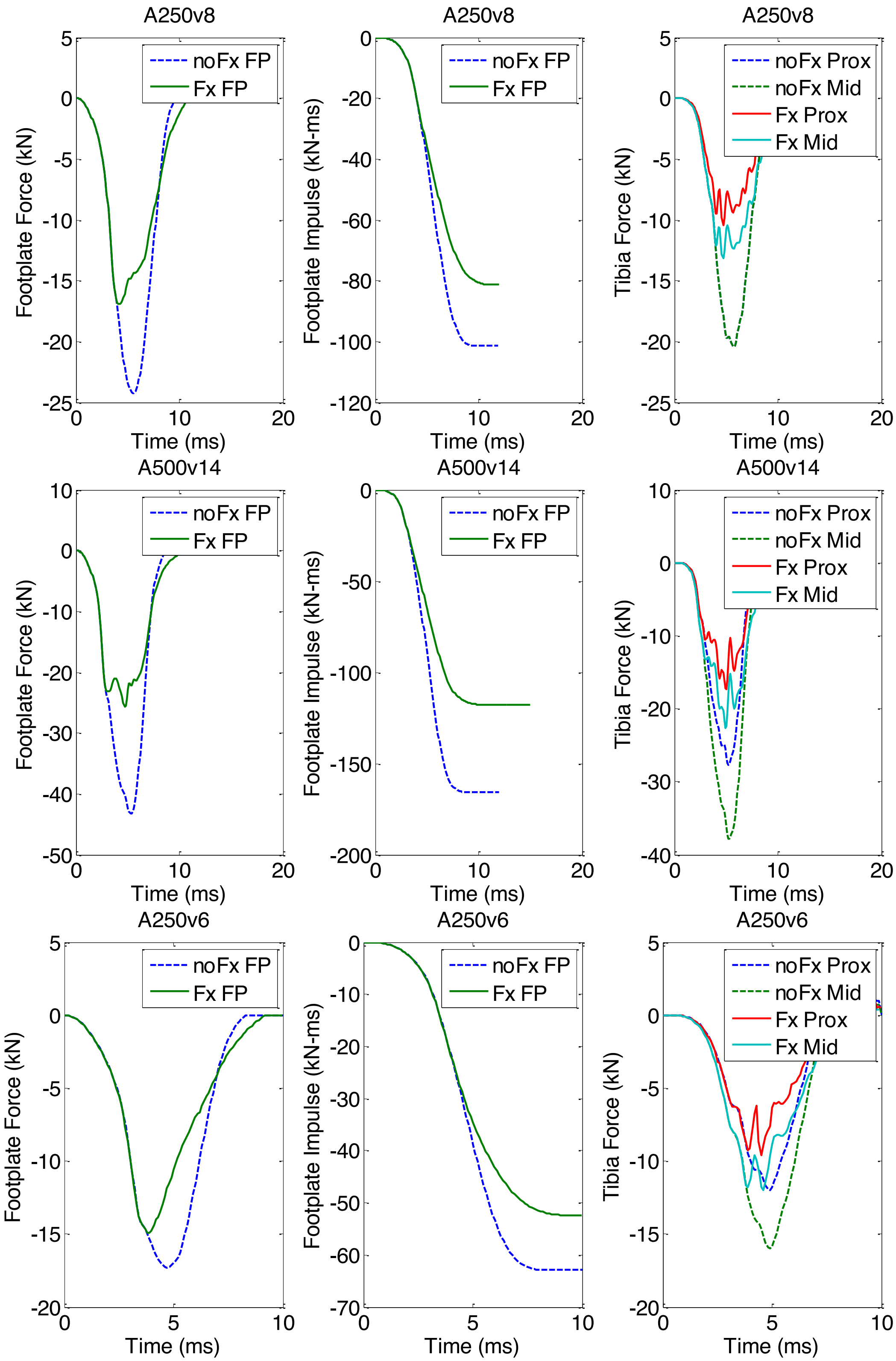
A250v8
Footplate Force (kN)
Time (ms)
noFx FP
Fx FP
5
0
-5
-10
-15
-20
-25
0
10
20
A250v8
Footplate Impulse (kN-ms)
Time (ms)
noFx FP
Fx FP
0
-20
-40
-60
-80
-100
-120
A250v8
Tibia Force (kN)
Time (ms)
noFx Prox
noFx Mid
Fx Prox
Fx Mid
A500v14
Footplate Force (kN)
Time (ms)
noFx FP
Fx FP
10
0
-10
-20
-30
-40
-50
A500v14
Footplate Impulse (kN-ms)
Time (ms)
noFx FP
Fx FP
0
-50
-100
-150
-200
A500v14
Tibia Force (kN)
Time (ms)
noFx Prox
noFx Mid
Fx Prox
Fx Mid
10
0
-10
-20
-30
-40
A250v6
Footplate Force (kN)
Time (ms)
noFx FP
Fx FP
5
0
-5
-10
-15
-20
0
5
10
A250v6
Footplate Impulse (kN-ms)
Time (ms)
noFx FP
Fx FP
0
-10
-20
-30
-40
-50
-60
-70
A250v6
Tibia Force (kN)
Time (ms)
noFx Prox
noFx Mid
Fx Prox
Fx Mid
5
0
-5
-10
-15
-20

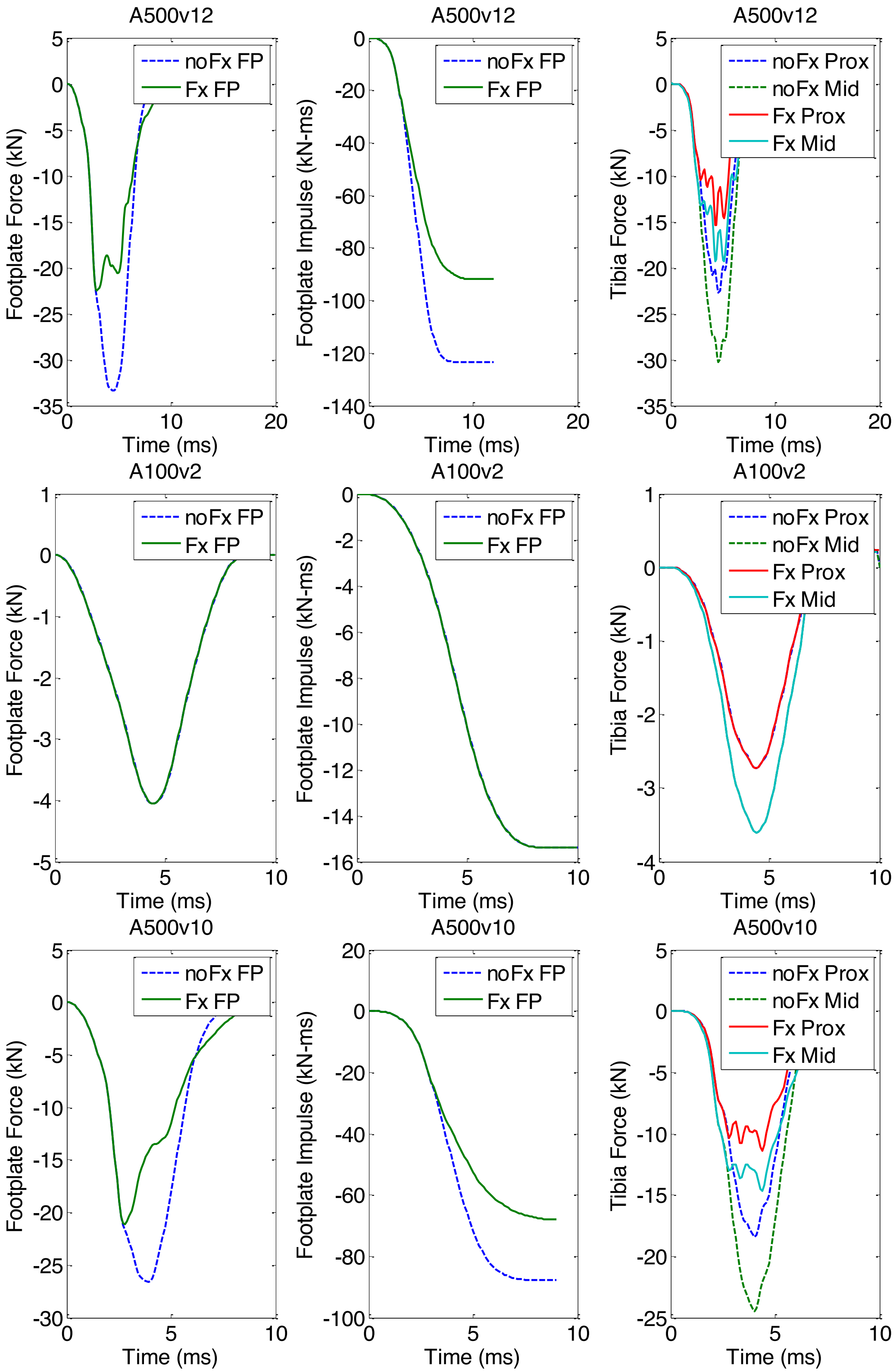
A500v12
Footplate Force (kN)
Time (ms)
noFx FP
Fx FP
5
0
-5
-10
-15
-20
-25
-30
-35
0
10
20
A500v12
Footplate Impulse (kN-ms)
Time (ms)
noFx FP
Fx FP
0
-20
-40
-60
-80
-100
-120
-140
0
10
20
A500v12
Tibia Force (kN)
Time (ms)
noFx Prox
noFx Mid
Fx Prox
Fx Mid
5
0
-5
-10
-15
-20
-25
-30
-35
0
10
20
A100v2
Footplate Force (kN)
Time (ms)
noFx FP
Fx FP
1
0
-1
-2
-3
-4
-5
0
5
10
A100v2
Footplate Impulse (kN-ms)
Time (ms)
noFx FP
Fx FP
0
-2
-4
-6
-8
-10
-12
-14
-16
0
5
10
A100v2
Tibia Force (kN)
Time (ms)
noFx Prox
noFx Mid
Fx Prox
Fx Mid
1
0
-1
-2
-3
-4
0
5
10
A500v10
Footplate Force (kN)
Time (ms)
noFx FP
Fx FP
5
0
-5
-10
-15
-20
-25
-30
0
5
10
A500v10
Footplate Impulse (kN-ms)
Time (ms)
noFx FP
Fx FP
20
0
-20
-40
-60
-80
-100
0
5
10
A500v10
Tibia Force (kN)
Time (ms)
noFx Prox
noFx Mid
Fx Prox
Fx Mid
5
0
-5
-10
-15
-20
-25
0
5
10

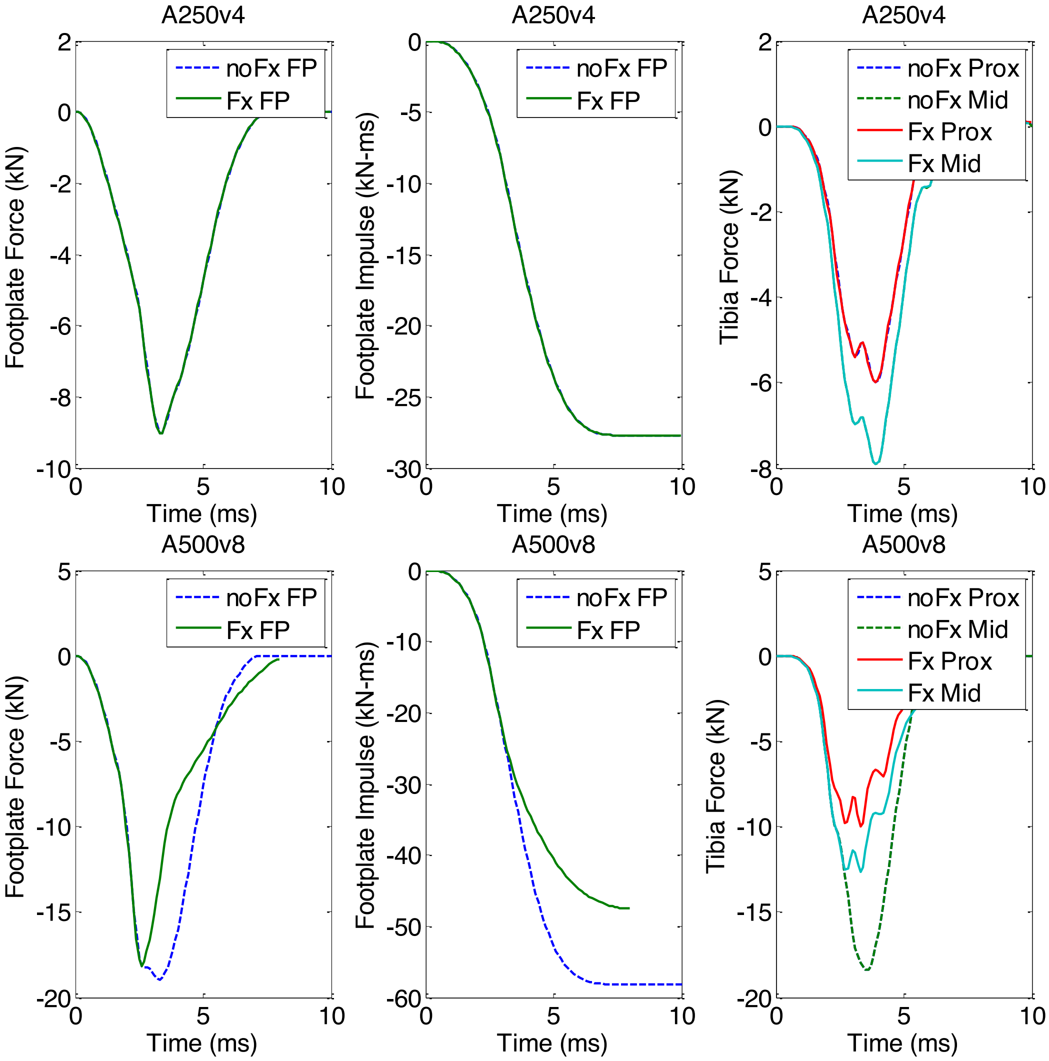

10.5 Statistics Equations

The following equations provide measures for evaluating the predictive capabilities of a model. In particular, these equations were used in the dissertation to assess the ability of the injury criterion to correctly identify injury and no injury cases from previous experimental tests.

Accuracy:	
$\text{Acc} = \frac{\text{TP} + \text{TN}}{\text{Total}}$	Eqn. 10.7
True Positive Ratio (also Sensitivity):	
$\text{TPR} = \frac{\text{TP}}{\text{\# Injured Tests}}$	Eqn. 10.8
False Negative Ratio:	
$\text{FNR} = \frac{\text{FN}}{\text{\# Injured Tests}}$	Eqn. 10.9
False Positive Ratio:	
$\text{FPR} = \frac{\text{FP}}{\text{\# No} - \text{injury Tests}}$	Eqn. 10.10
True Negative Ratio (also Specificity):	
$\text{TNR} = \frac{\text{TN}}{\text{\# No} - \text{injury Tests}}$	Eqn. 10.11
Positive Predictive Value:	
$\text{PPV} = \frac{\text{TP}}{\text{\# Predicted Injuries}}$	Eqn. 10.12
False Discovery Rate:	
$\text{FDR} = \frac{\text{FP}}{\text{\# Predicted Injuries}}$	Eqn. 10.13
Negative Predictive Value:	
$\text{NPV} = \frac{\text{TN}}{\text{\# No} - \text{injury Predictions}}$	Eqn. 10.14
False Omission Ratio:	
$\text{FOR} = \frac{\text{FN}}{\text{\# No} - \text{injury Predictions}}$	Eqn. 10.15

10.6 Material Property Summary

This appendix provides an overview of the properties of materials which were considered as candidates for replacing the heel pad and compliant element in the tibia of the

Mil-Lx. Stress-strain plots were digitized from existing literature and are provided for reference. Additionally, a summary of the materials and key material properties from the literature are provided in Table 10.2.

Table 10.2. Summary of materials considered as candidates for replacing components in the Mil-Lx.

Material	**Density (kg-mm^{-3})**	**Bulk Modulus (GPa)**	**Shear Modulus (GPa)**
90 Durometer Polyurethane	1.3e-6	5.0	1.40e-2
80 Durometer Polyurethane	1.2e-6	5.0	1.40e-2
60 Durometer Polyurethane	1.15e-6	5.0	8.60e-3
40 Durometer Polyurethane	1.15e-6	5.0	8.40e-3
20 Durometer Polyurethane	1.12e-6	5.0	7.40e-3
70 Durometer Neoprene	9.6e-7	1.36	2.72e-3
65 Durometer Neoprene	9.6e-7	1.36	2.72e-3
60 Durometer Neoprene	9.6e-7	1.36	2.72e-3
70 Durometer Sorbothane	1.364e-6	4.140	
50 Durometer Sorbothane	1.364e-6	4.710	
30 Durometer Sorbothane	1.364e-6	4.710	

10.6.1 Polyurethane

Dynamic stress-strain curves were digitized from two versions of polyurethane rubber (Polyurethane-A and Polyurethane-B) generated by Yi et al. (Figure 10.15, Figure 10.16).[228] Stress-strain data was collected from quasi-static and dynamic compression tests. Stress-strain curves are also presented for polyurethane rubber ranging from 20 to 90 durometer. This data was obtained from a data sheet from Polyurethane Products.

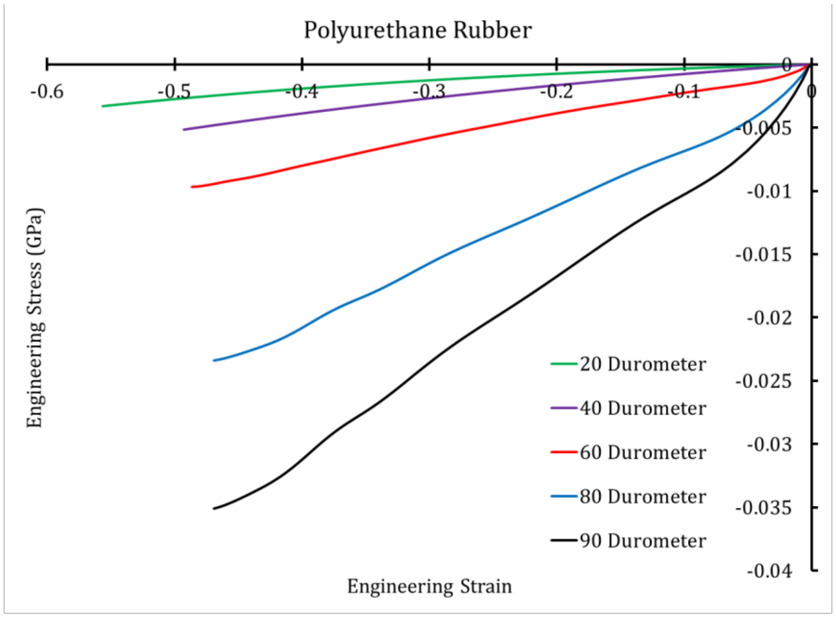

Figure 10.14. Polyurethane rubber engineering stress versus strain for different durometers ranging from 20 to 90 durometer. (Data from polyurethane products).

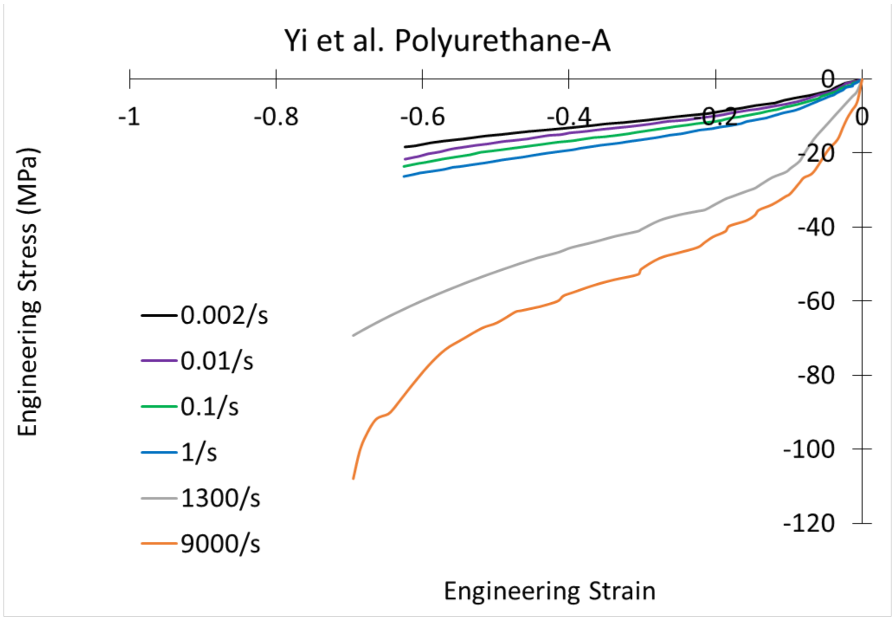

Figure 10.15. Polyurethane rubber stress versus strain for strain rates ranging from quasi-static to 9000 s^{-1}. (Data from Yi et al.)[228]

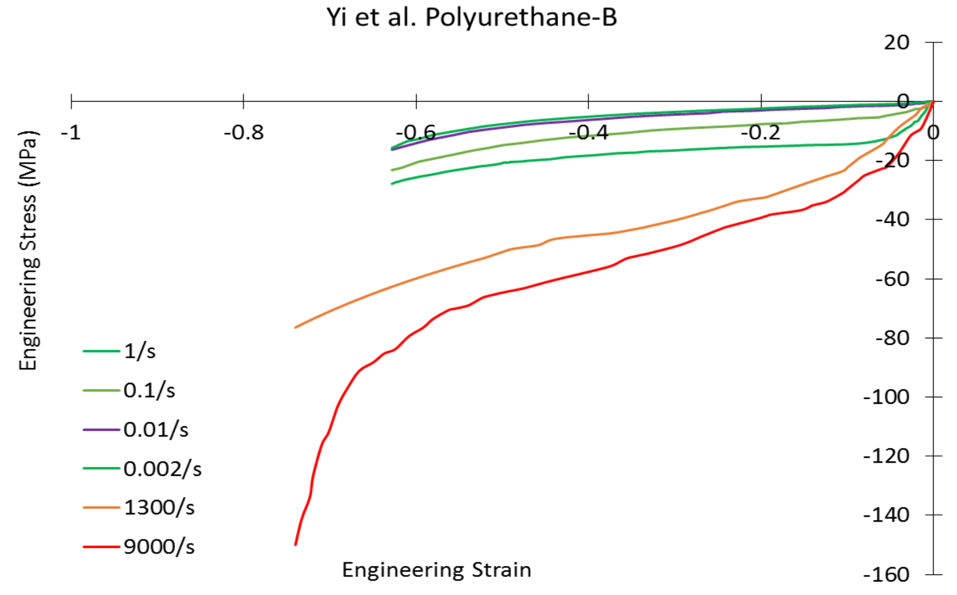

Figure 10.16. Polyurethane rubber stress versus strain for strain rates ranging from quasi-static to 9000 s^{-1}. (Data from Yi et al.)[228]

10.6.2 Other Materials

Other materials considered for the replacement of the Mil-Lx heel pad and tibia compliant element included nitrile rubber and neoprene. Stress-strain curves 60-, 65-, and 70-durometer neoprene were collected from a study by Zhao et al.[234]

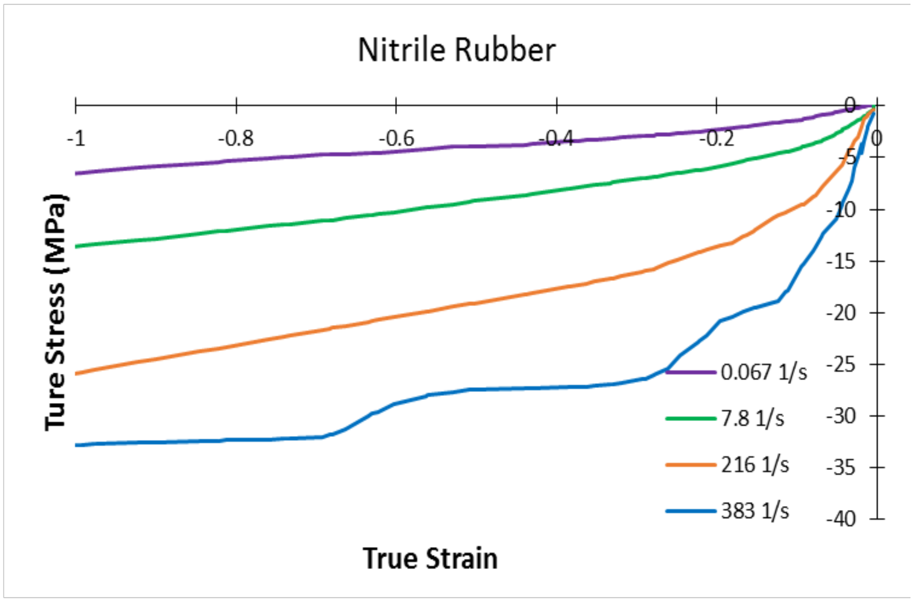

Figure 10.17. Nitrile rubber stress versus strain for strain rates ranging from 0.067 to 383 s^{-1}.

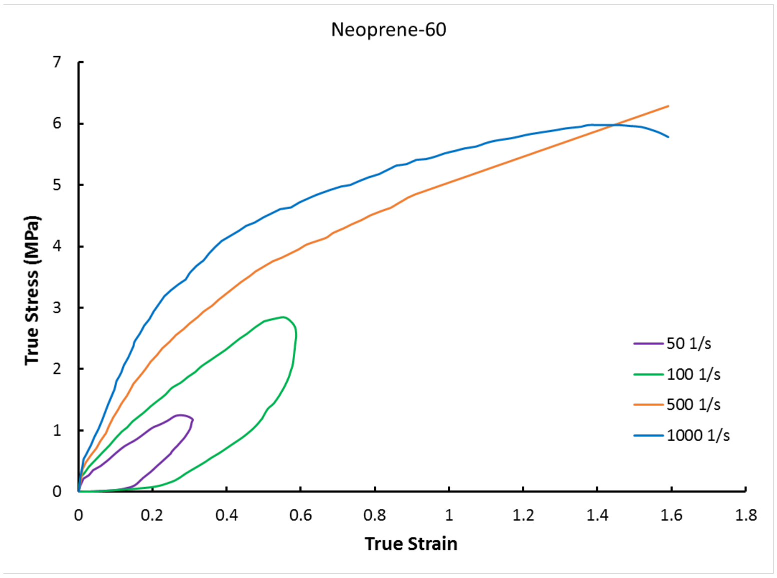

Figure 10.18. Neoprene 60-durometer rubber compressive stress versus strain for strain rates ranging from 50 to 1000 s^{-1}. Reproduced from Zhao et al.[234]

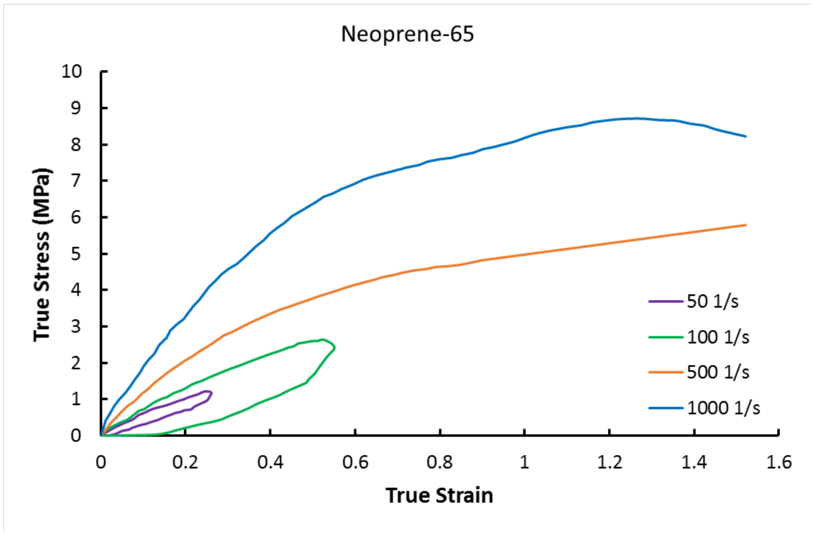

Figure 10.19. Neoprene 65-durometer rubber compressive stress versus strain for strain rates ranging from 50 to 1000 s^{-1}. Reproduced from Zhao et al.[234]

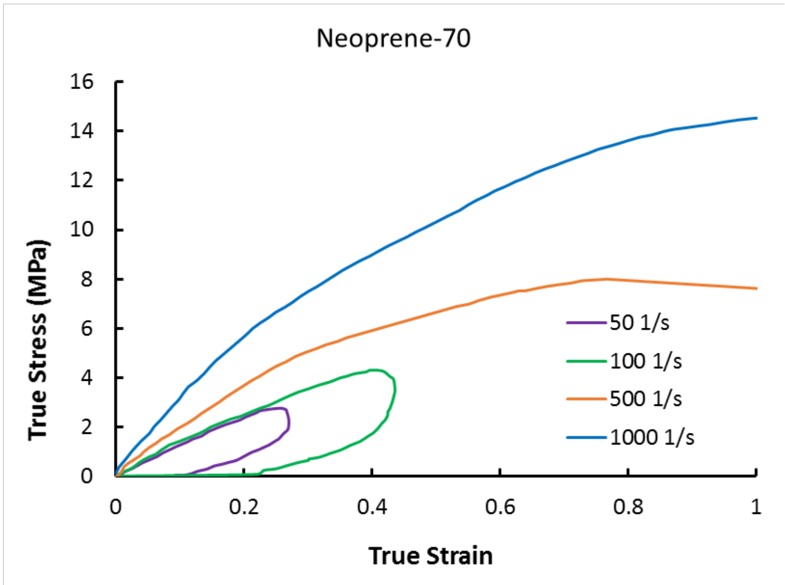

Figure 10.20. Neoprene 70-durometer rubber compressive stress versus strain for strain rates ranging from 50 to 1000 s^{-1}. Reproduced from Zhao et al.[234]

10.7 Mil-Lx FE Model Response

The following plots are results from the original and optimized versions of the Mil-Lx model subjected to the prescribed footplate accelerations from the human finite element model parametric study. Each Mil-Lx response (footplate force, footplate impulse, upper tibia force, and lower tibia force) was plotted with the human FE model (without element deletion) response for the same input condition.

10.7.1 Mil-Lx FE Original

The following plots are force and impulse responses from the Mil-Lx FE model exposed to axial loading from various footplate acceleration frequencies and amplitudes. The FE model contains the material properties of the current Mil-Lx design, the characteristics of which are summarized in Section 7.4. Plots are labeled with the peak acceleration and velocity (A#v*) such that # is the peak acceleration and * is the peak velocity of the footplate input. The sinusoidal inputs from the parametric study were used. Force and impulses from the optimized Mil-Lx FE model and the human leg FE model (without element deletion) are presented. Lower and upper tibia forces are denoted as *LT* and *UT*, respectively, while footplate forces are abbreviated as *FP*.

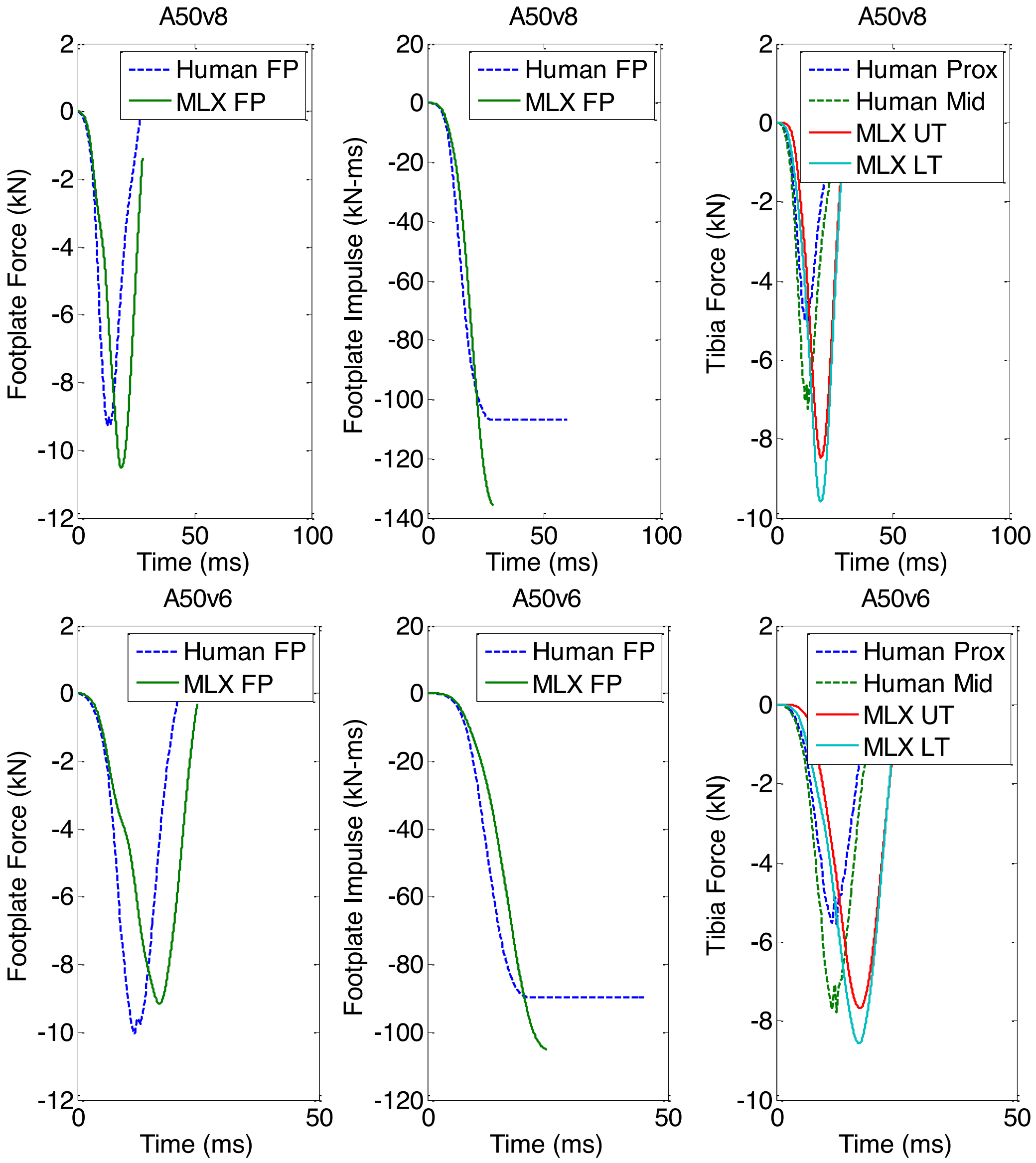
A50v8
Footplate Force (kN)
Human FP
MLX FP
2
0
-2
-4
-6
-8
-10
-12
0
50
100
Time (ms)
A50v8
Footplate Impulse (kN-ms)
Human FP
MLX FP
20
0
-20
-40
-60
-80
-100
-120
-140
0
50
100
Time (ms)
A50v8
Tibia Force (kN)
Human Prox
Human Mid
MLX UT
MLX LT
2
0
-2
-4
-6
-8
-10
0
50
100
Time (ms)
A50v6
Footplate Force (kN)
Human FP
MLX FP
2
0
-2
-4
-6
-8
-10
-12
0
50
Time (ms)
A50v6
Footplate Impulse (kN-ms)
Human FP
MLX FP
20
0
-20
-40
-60
-80
-100
-120
0
50
Time (ms)
A50v6
Tibia Force (kN)
Human Prox
Human Mid
MLX UT
MLX LT
2
0
-2
-4
-6
-8
-10
0
50
Time (ms)

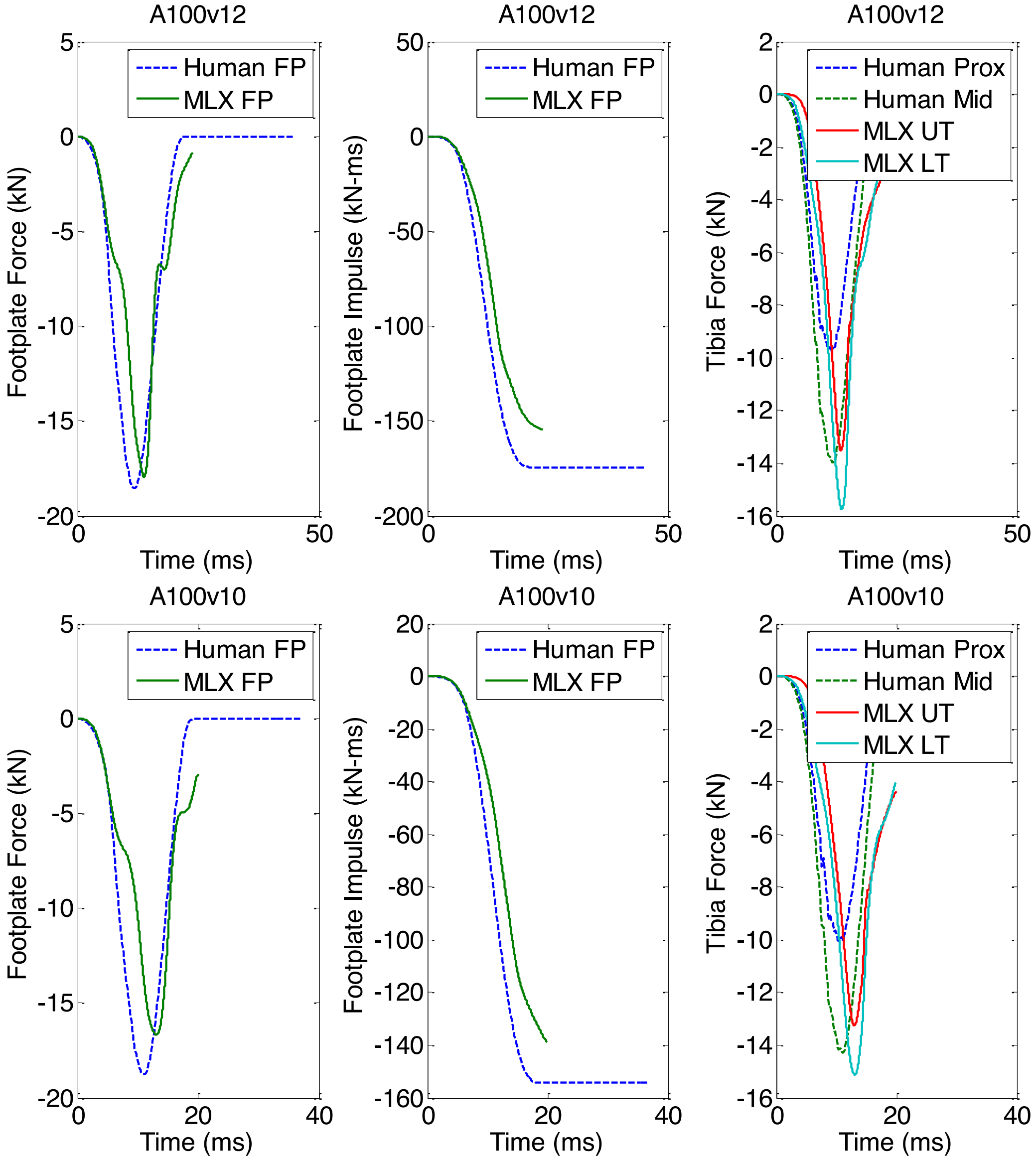
A100v12
Footplate Force (kN)
5
0
-5
-10
-15
-20
0
50
Time (ms)
Human FP
MLX FP
A100v12
Footplate Impulse (kN-ms)
50
0
-50
-100
-150
-200
0
50
Time (ms)
Human FP
MLX FP
A100v12
Tibia Force (kN)
2
0
-2
-4
-6
-8
-10
-12
-14
-16
0
50
Time (ms)
Human Prox
Human Mid
MLX UT
MLX LT
A100v10
Footplate Force (kN)
5
0
-5
-10
-15
-20
0
20
40
Time (ms)
Human FP
MLX FP
A100v10
Footplate Impulse (kN-ms)
20
0
-20
-40
-60
-80
-100
-120
-140
-160
0
20
40
Time (ms)
Human FP
MLX FP
A100v10
Tibia Force (kN)
2
0
-2
-4
-6
-8
-10
-12
-14
-16
0
20
40
Time (ms)
Human Prox
Human Mid
MLX UT
MLX LT

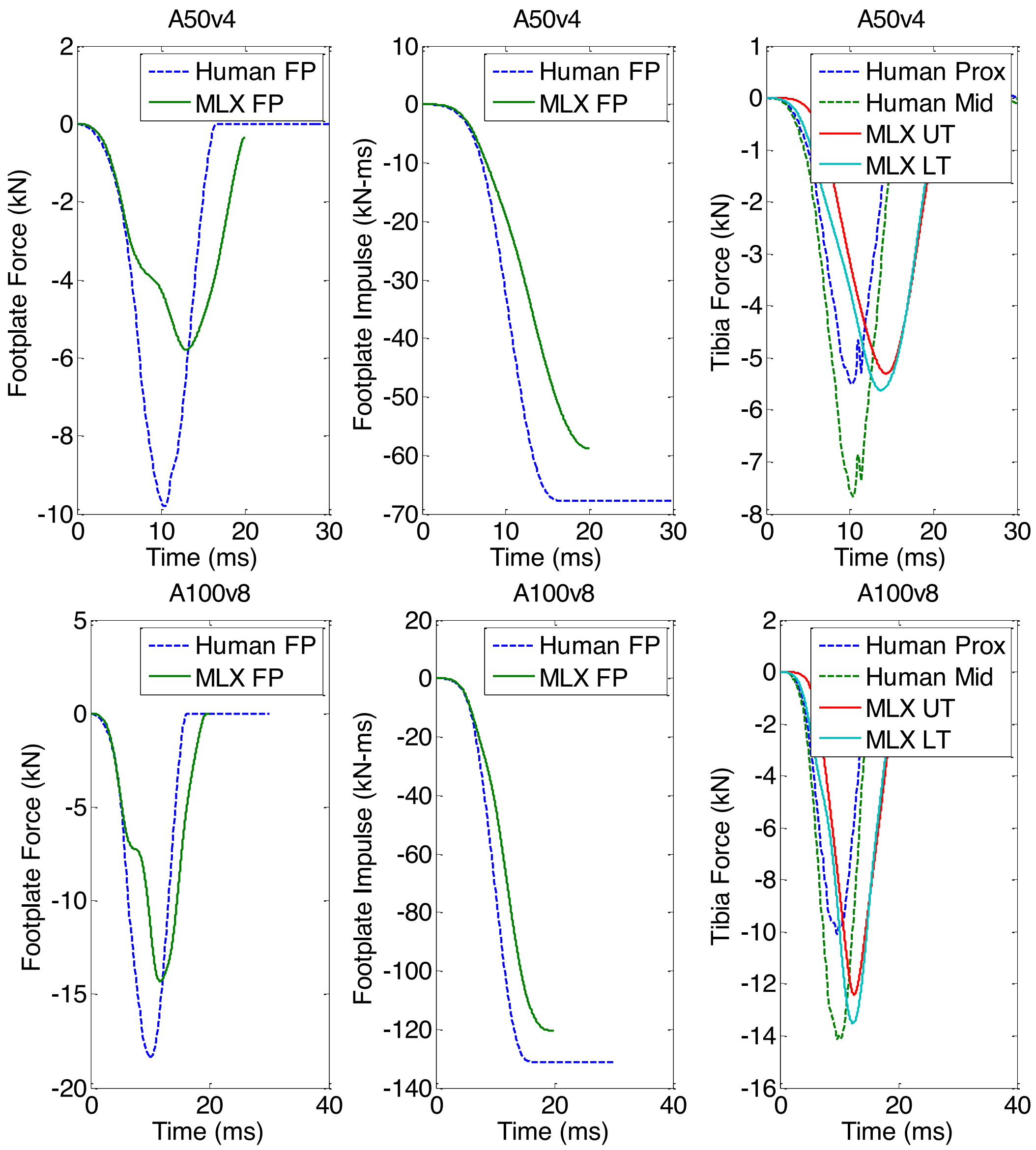
A50v4
Footplate Force (kN)
Time (ms)
Human FP
MLX FP
2
0
-2
-4
-6
-8
-10
0
10
20
30
A50v4
Footplate Impulse (kN-ms)
Time (ms)
Human FP
MLX FP
10
0
-10
-20
-30
-40
-50
-60
-70
0
10
20
30
A50v4
Tibia Force (kN)
Time (ms)
Human Prox
Human Mid
MLX UT
MLX LT
1
0
-1
-2
-3
-4
-5
-6
-7
-8
0
10
20
30
A100v8
Footplate Force (kN)
Time (ms)
Human FP
MLX FP
5
0
-5
-10
-15
-20
0
20
40
A100v8
Footplate Impulse (kN-ms)
Time (ms)
Human FP
MLX FP
20
0
-20
-40
-60
-80
-100
-120
-140
0
20
40
A100v8
Tibia Force (kN)
Time (ms)
Human Prox
Human Mid
MLX UT
MLX LT
2
0
-2
-4
-6
-8
-10
-12
-14
-16
0
20
40

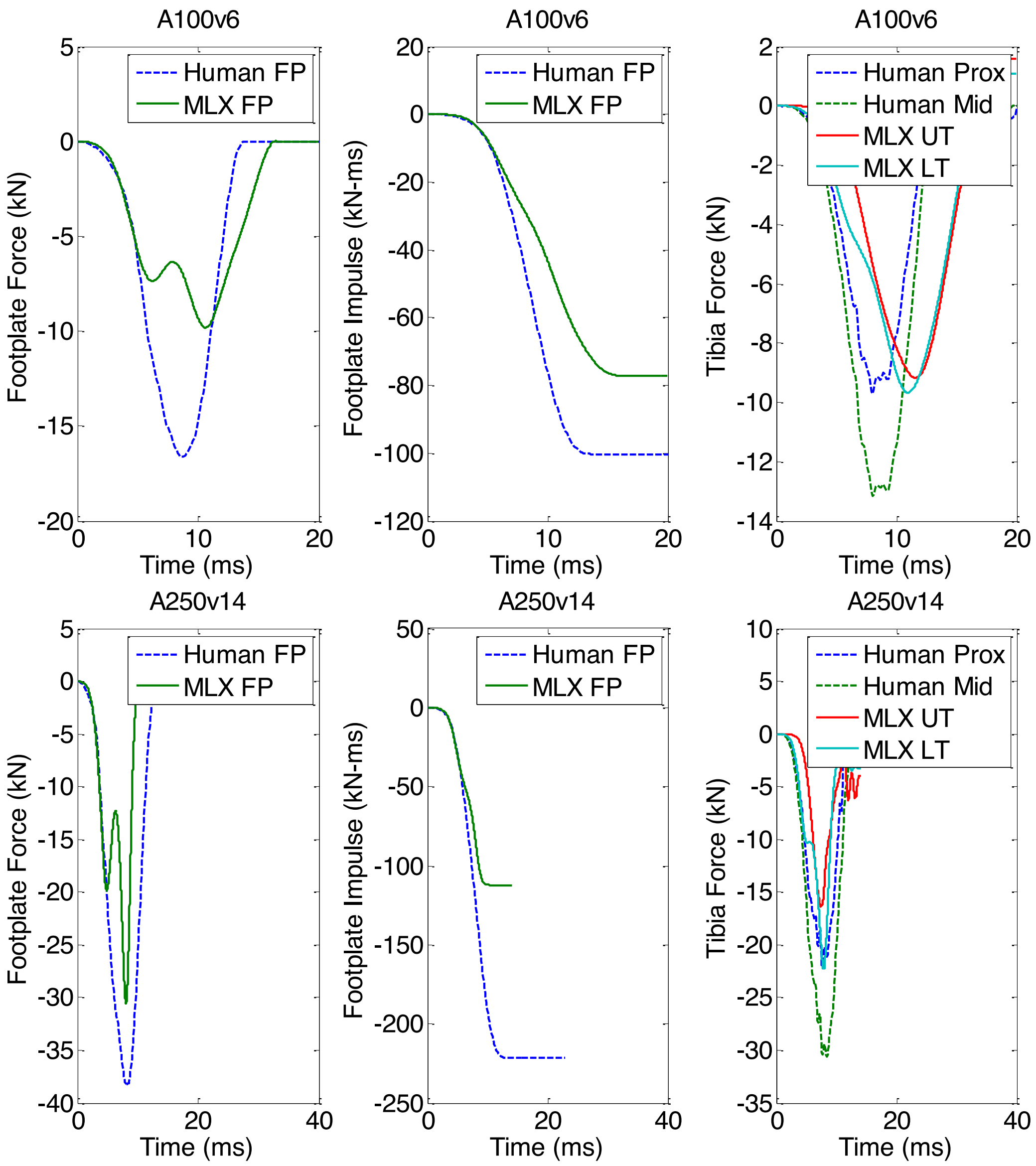
A100v6
Footplate Force (kN)
Time (ms)
Human FP
MLX FP
A100v6
Footplate Impulse (kN-ms)
Time (ms)
Human FP
MLX FP
A100v6
Tibia Force (kN)
Time (ms)
Human Prox
Human Mid
MLX UT
MLX LT
A250v14
Footplate Force (kN)
Time (ms)
Human FP
MLX FP
A250v14
Footplate Impulse (kN-ms)
Time (ms)
Human FP
MLX FP
A250v14
Tibia Force (kN)
Time (ms)
Human Prox
Human Mid
MLX UT
MLX LT

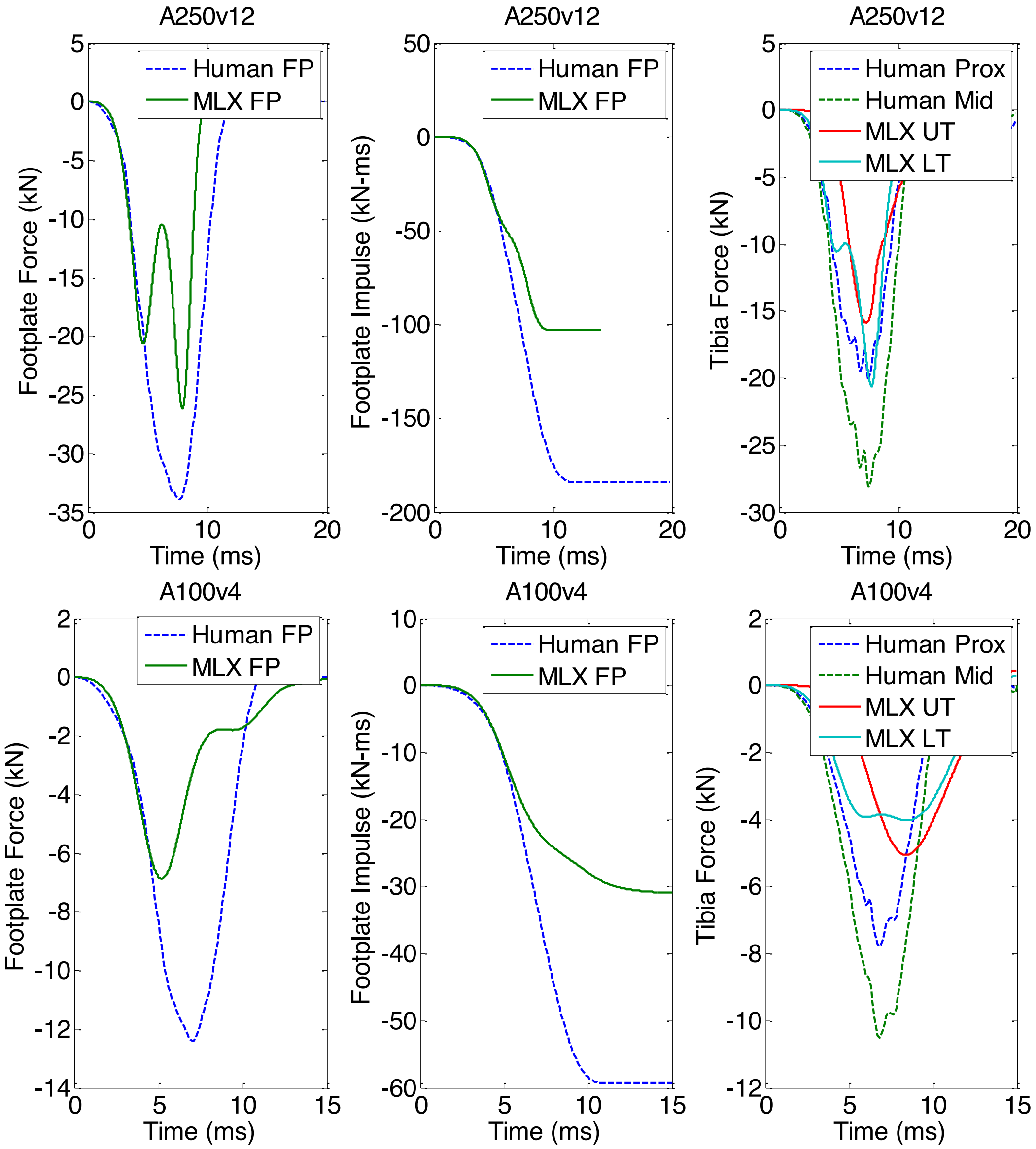

A250v12
Footplate Force (kN)
Human FP
MLX FP
5
0
-5
-10
-15
-20
-25
-30
-35
0
10
20
Time (ms)
A250v12
Footplate Impulse (kN-ms)
Human FP
MLX FP
50
0
-50
-100
-150
-200
0
10
20
Time (ms)
A250v12
Tibia Force (kN)
Human Prox
Human Mid
MLX UT
MLX LT
5
0
-5
-10
-15
-20
-25
-30
0
10
20
Time (ms)
A100v4
Footplate Force (kN)
Human FP
MLX FP
2
0
-2
-4
-6
-8
-10
-12
-14
0
5
10
15
Time (ms)
A100v4
Footplate Impulse (kN-ms)
Human FP
MLX FP
10
0
-10
-20
-30
-40
-50
-60
0
5
10
15
Time (ms)
A100v4
Tibia Force (kN)
Human Prox
Human Mid
MLX UT
MLX LT
2
0
-2
-4
-6
-8
-10
-12
0
5
10
15
Time (ms)

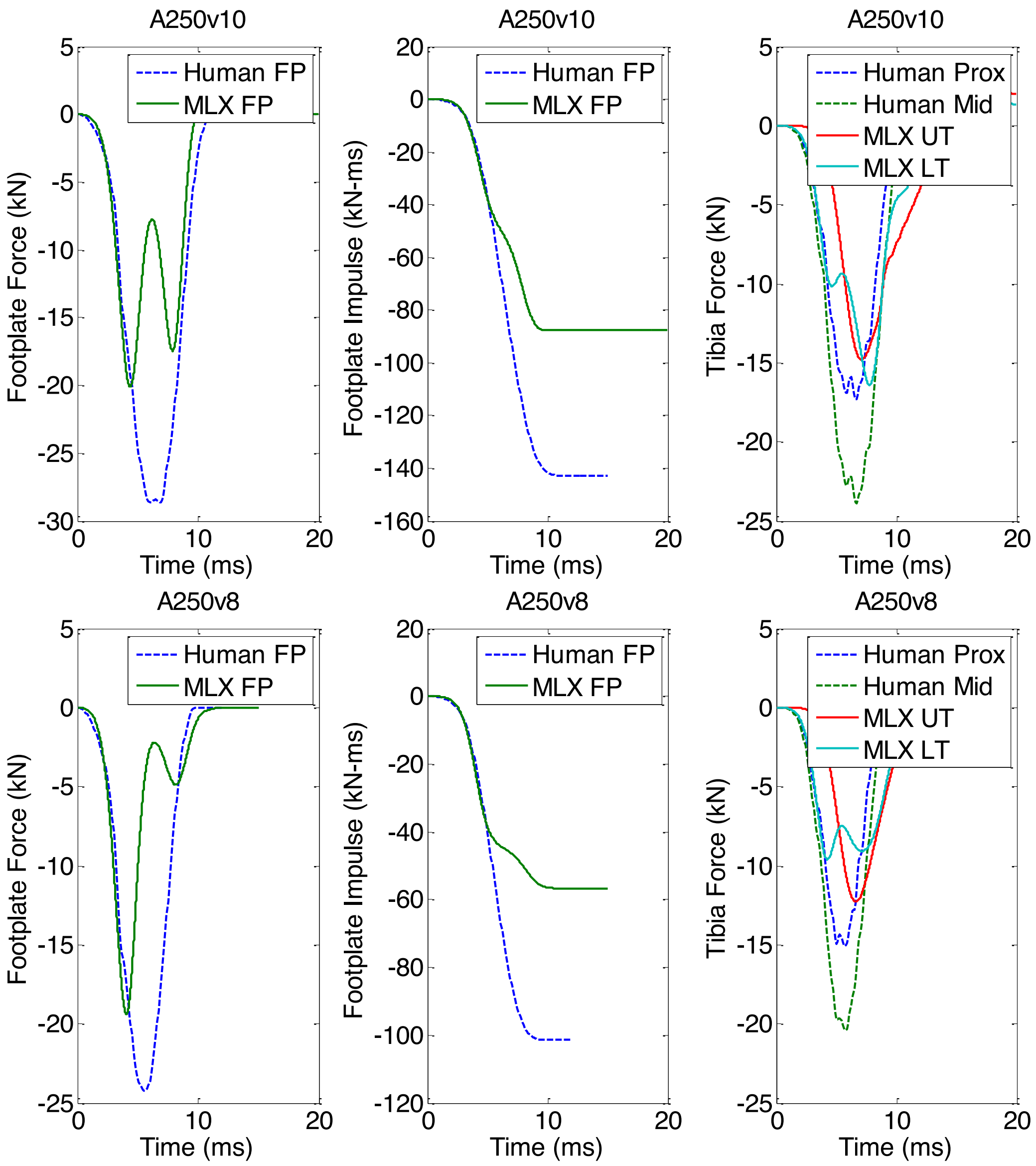
A250v10
Footplate Force (kN)
Time (ms)
Human FP
MLX FP
5
0
-5
-10
-15
-20
-25
-30
0
10
20
A250v10
Footplate Impulse (kN-ms)
Time (ms)
Human FP
MLX FP
20
0
-20
-40
-60
-80
-100
-120
-140
-160
A250v10
Tibia Force (kN)
Time (ms)
Human Prox
Human Mid
MLX UT
MLX LT
5
0
-5
-10
-15
-20
-25
A250v8
Footplate Force (kN)
Time (ms)
Human FP
MLX FP
A250v8
Footplate Impulse (kN-ms)
Time (ms)
Human FP
MLX FP
A250v8
Tibia Force (kN)
Time (ms)
Human Prox
Human Mid
MLX UT
MLX LT

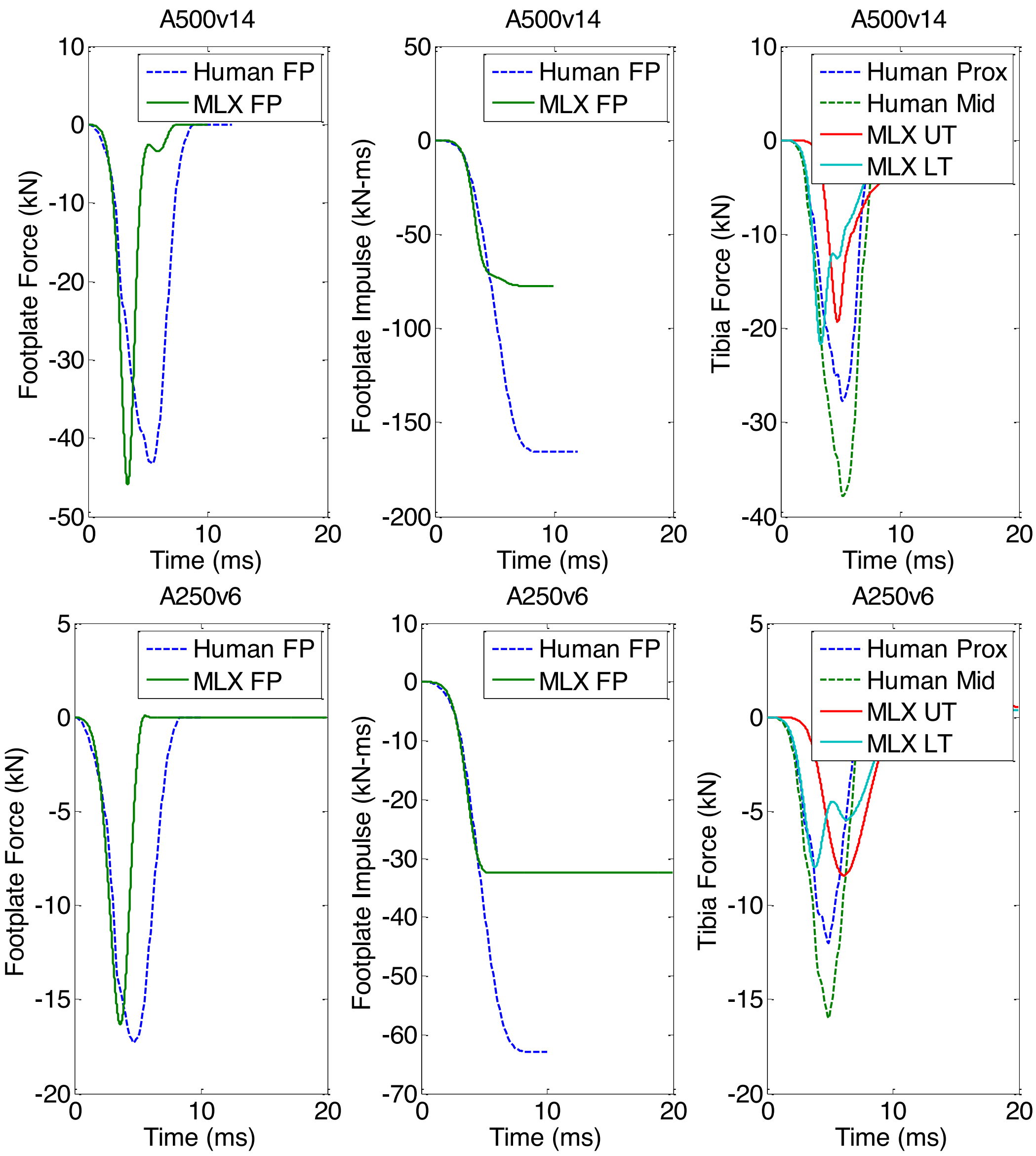
A500v14
Footplate Force (kN)
10
0
-10
-20
-30
-40
-50
Time (ms)
0
10
20
Human FP
MLX FP
A500v14
Footplate Impulse (kN-ms)
50
0
-50
-100
-150
-200
Time (ms)
0
10
20
Human FP
MLX FP
A500v14
Tibia Force (kN)
10
0
-10
-20
-30
-40
Time (ms)
0
10
20
Human Prox
Human Mid
MLX UT
MLX LT
A250v6
Footplate Force (kN)
5
0
-5
-10
-15
-20
Time (ms)
0
10
20
Human FP
MLX FP
A250v6
Footplate Impulse (kN-ms)
10
0
-10
-20
-30
-40
-50
-60
-70
Time (ms)
0
10
20
Human FP
MLX FP
A250v6
Tibia Force (kN)
5
0
-5
-10
-15
-20
Time (ms)
0
10
20
Human Prox
Human Mid
MLX UT
MLX LT

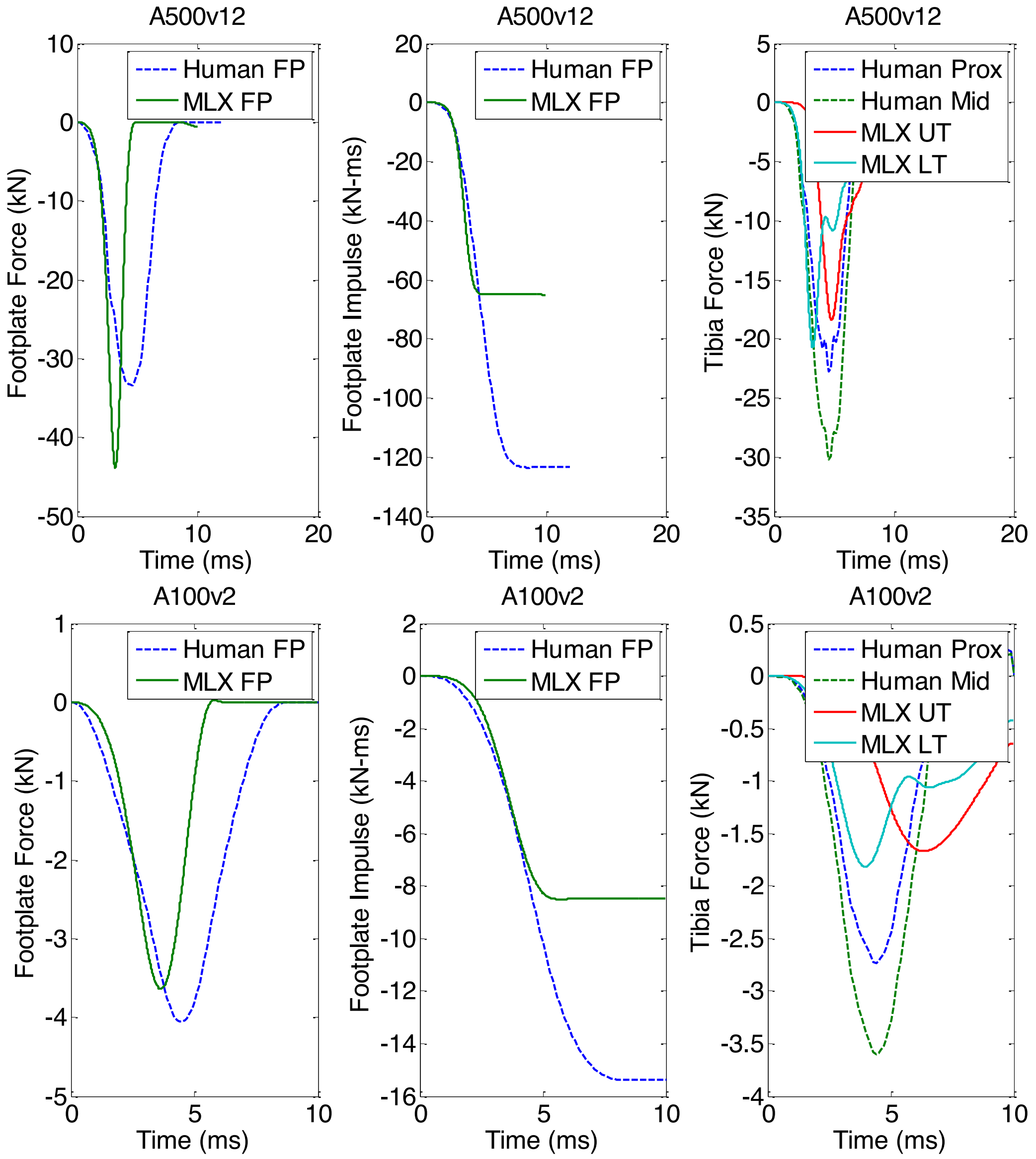
A500v12
Footplate Force (kN)
Time (ms)
Human FP
MLX FP
10
0
-10
-20
-30
-40
-50
0
10
20
A500v12
Footplate Impulse (kN-ms)
Time (ms)
Human FP
MLX FP
20
0
-20
-40
-60
-80
-100
-120
-140
0
10
20
A500v12
Tibia Force (kN)
Time (ms)
Human Prox
Human Mid
MLX UT
MLX LT
5
0
-5
-10
-15
-20
-25
-30
-35
0
10
20
A100v2
Footplate Force (kN)
Time (ms)
Human FP
MLX FP
1
0
-1
-2
-3
-4
-5
0
5
10
A100v2
Footplate Impulse (kN-ms)
Time (ms)
Human FP
MLX FP
2
0
-2
-4
-6
-8
-10
-12
-14
-16
0
5
10
A100v2
Tibia Force (kN)
Time (ms)
Human Prox
Human Mid
MLX UT
MLX LT
0.5
0
-0.5
-1
-1.5
-2
-2.5
-3
-3.5
-4
0
5
10

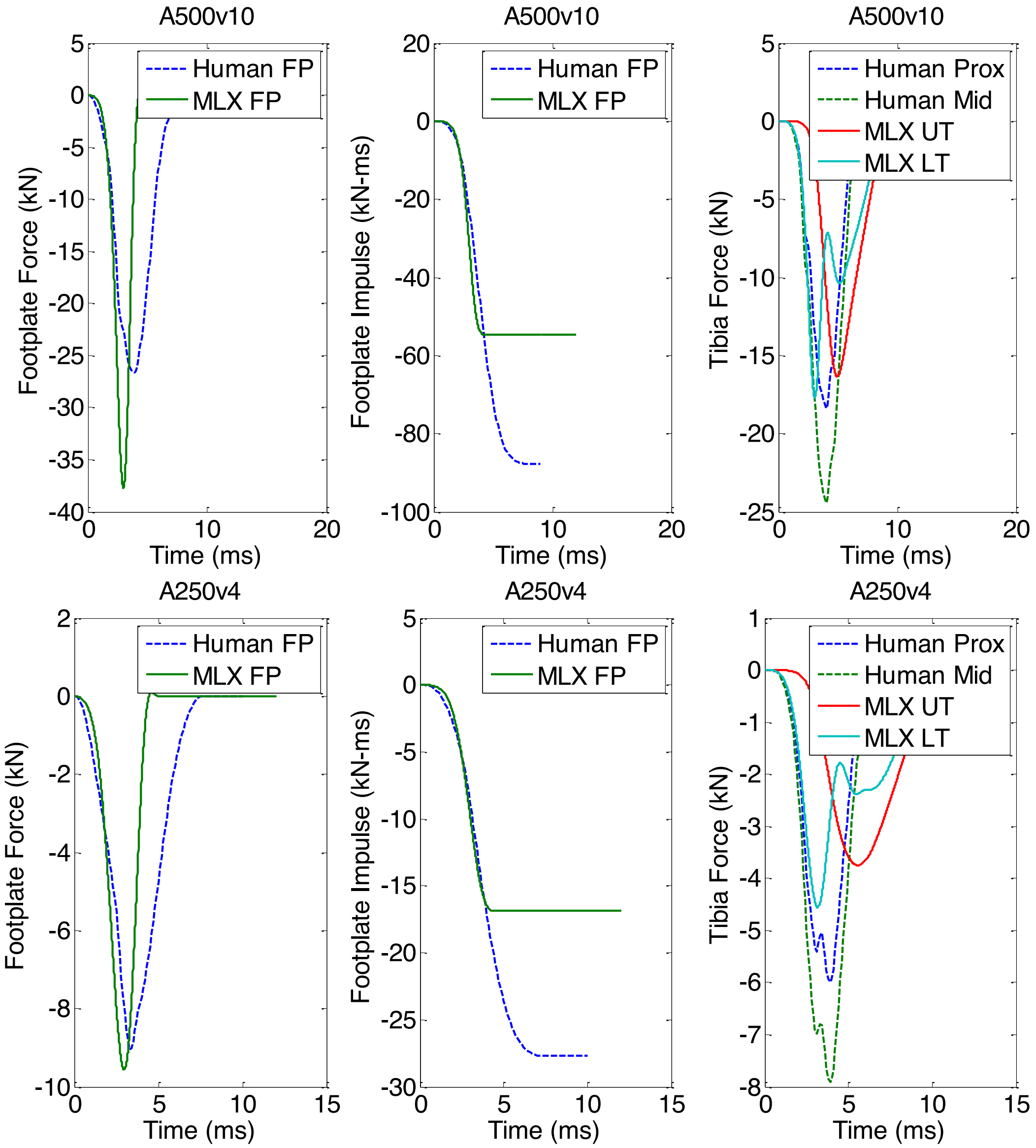
A500v10
Footplate Force (kN)
Time (ms)
Human FP
MLX FP
5
0
-5
-10
-15
-20
-25
-30
-35
-40
0
10
20
A500v10
Footplate Impulse (kN-ms)
Time (ms)
Human FP
MLX FP
20
0
-20
-40
-60
-80
-100
0
10
20
A500v10
Tibia Force (kN)
Time (ms)
Human Prox
Human Mid
MLX UT
MLX LT
5
0
-5
-10
-15
-20
-25
0
10
20
A250v4
Footplate Force (kN)
Time (ms)
Human FP
MLX FP
2
0
-2
-4
-6
-8
-10
0
5
10
15
A250v4
Footplate Impulse (kN-ms)
Time (ms)
Human FP
MLX FP
5
0
-5
-10
-15
-20
-25
-30
0
5
10
15
A250v4
Tibia Force (kN)
Time (ms)
Human Prox
Human Mid
MLX UT
MLX LT
1
0
-1
-2
-3
-4
-5
-6
-7
-8
0
5
10
15

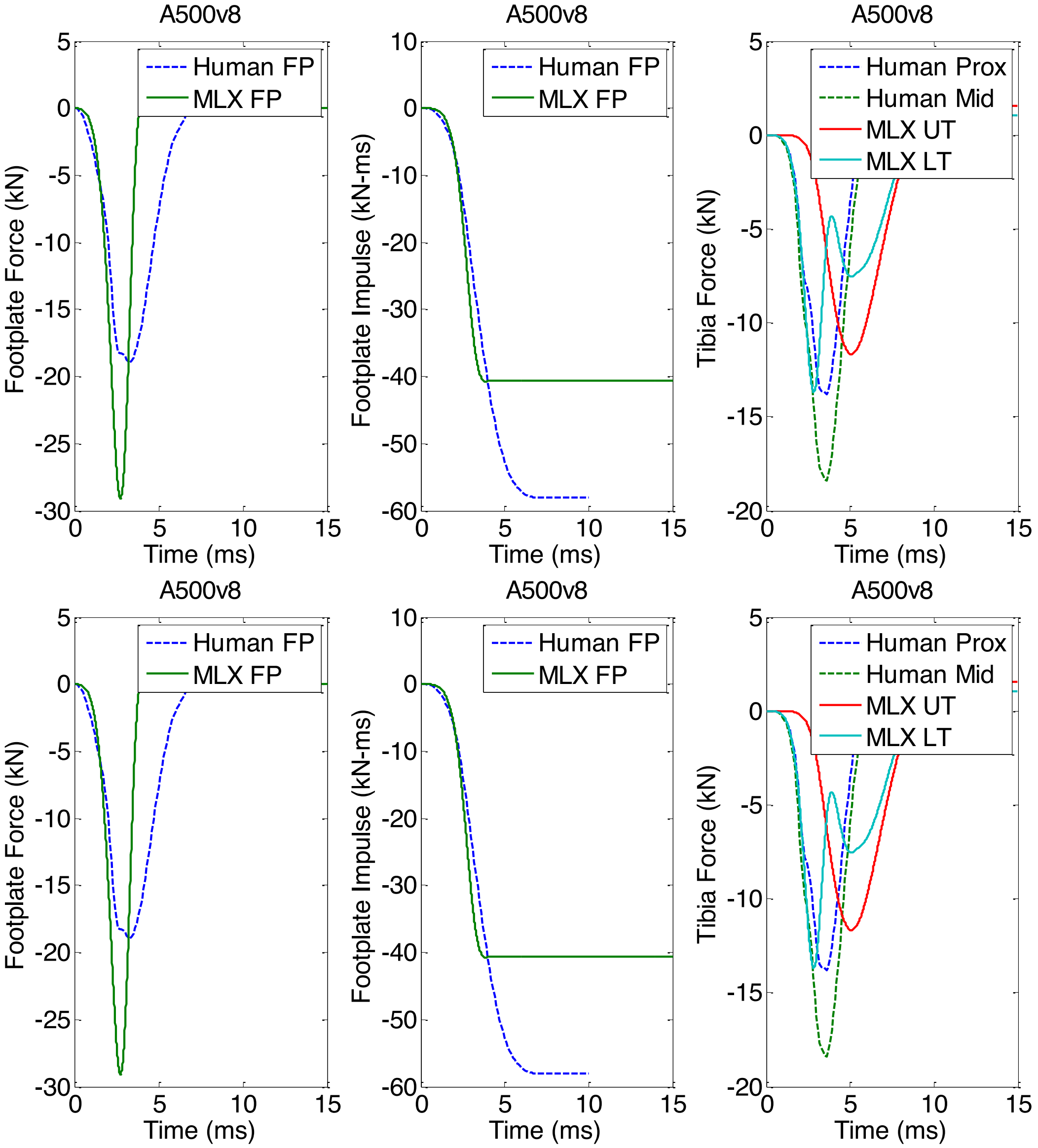

10.7.2 FE-Based Optimization

The following plots are results from the FE optimization for improving the response of the Mil-Lx under various loading frequencies. Plots are labeled with the peak acceleration and velocity (A#v*) such that # is the peak acceleration and * is the peak velocity of the footplate input. The sinusoidal inputs from the parametric study were used. Force and impulses from the optimized Mil-Lx FE model and the human leg FE model (without element deletion) are presented. Lower and upper tibia forces are denoted as *LT* and *UT*, respectively, while footplate forces are abbreviated as *FP*.

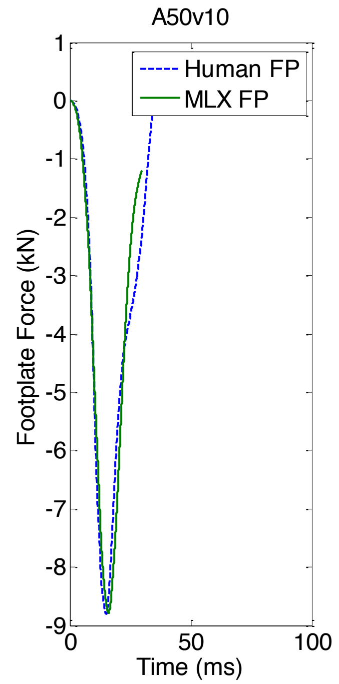
A50v10

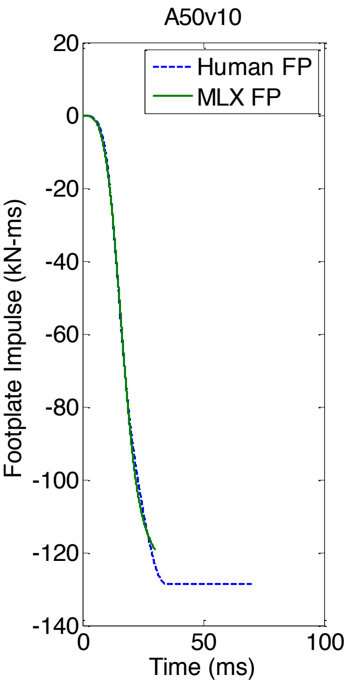
A50v10

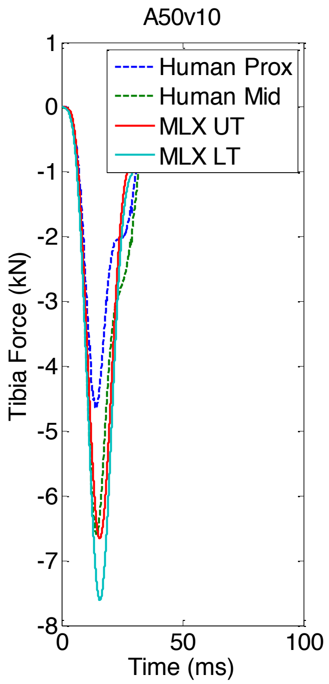
A50v10

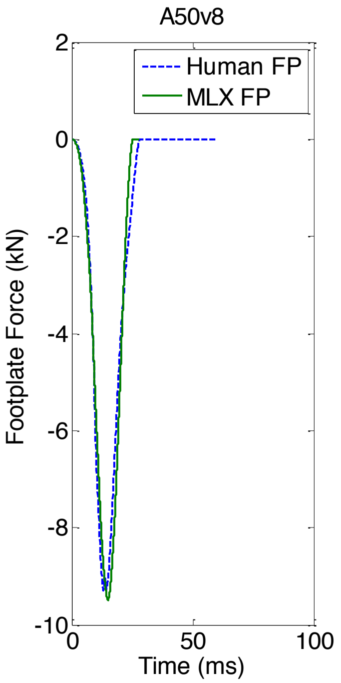
A50v8

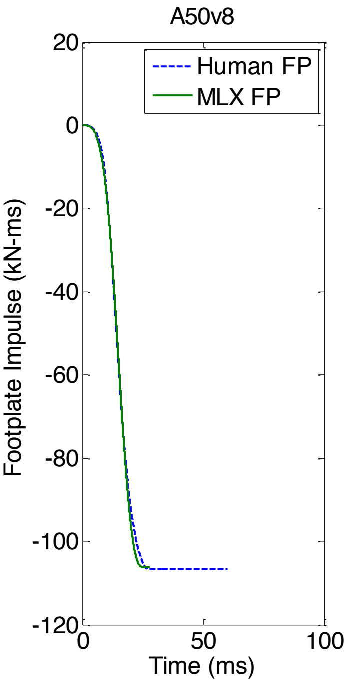
A50v8

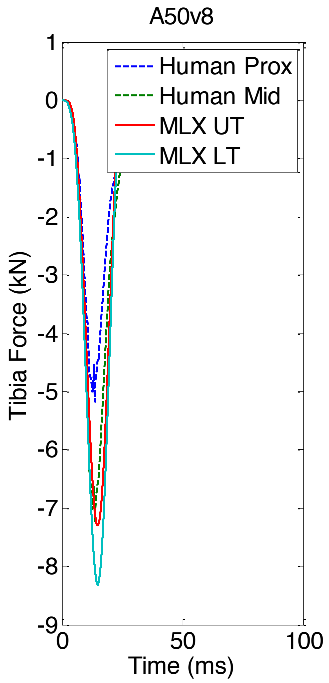
A50v8

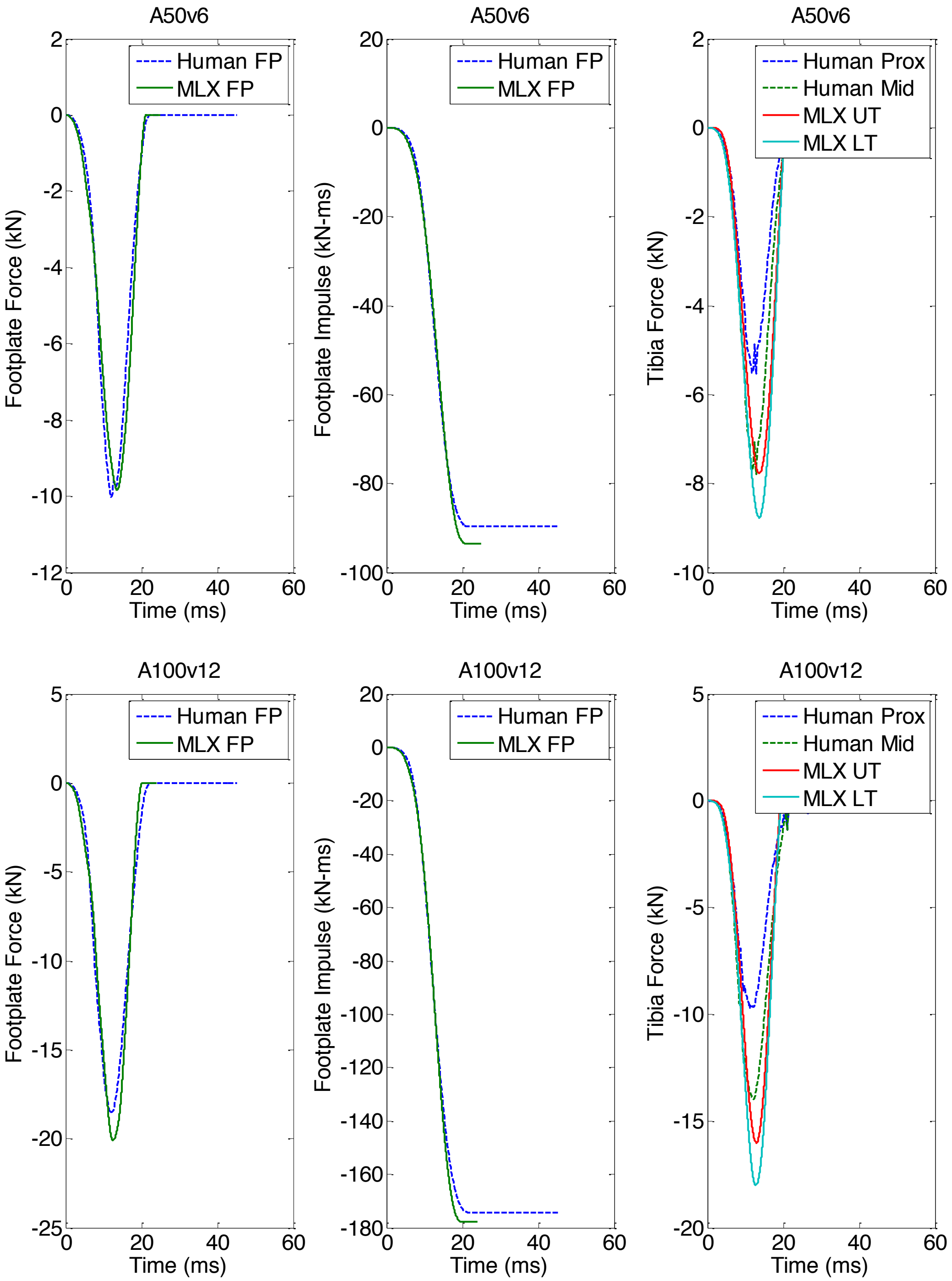
A50v6
Footplate Force (kN)
Time (ms)
Human FP
MLX FP
2
0
-2
-4
-6
-8
-10
-12
0
20
40
60
A50v6
Footplate Impulse (kN-ms)
Time (ms)
Human FP
MLX FP
20
0
-20
-40
-60
-80
-100
A50v6
Tibia Force (kN)
Time (ms)
Human Prox
Human Mid
MLX UT
MLX LT
2
0
-2
-4
-6
-8
-10
A100v12
Footplate Force (kN)
Time (ms)
Human FP
MLX FP
5
0
-5
-10
-15
-20
-25
A100v12
Footplate Impulse (kN-ms)
Time (ms)
Human FP
MLX FP
20
0
-20
-40
-60
-80
-100
-120
-140
-160
-180
A100v12
Tibia Force (kN)
Time (ms)
Human Prox
Human Mid
MLX UT
MLX LT
5
0
-5
-10
-15
-20

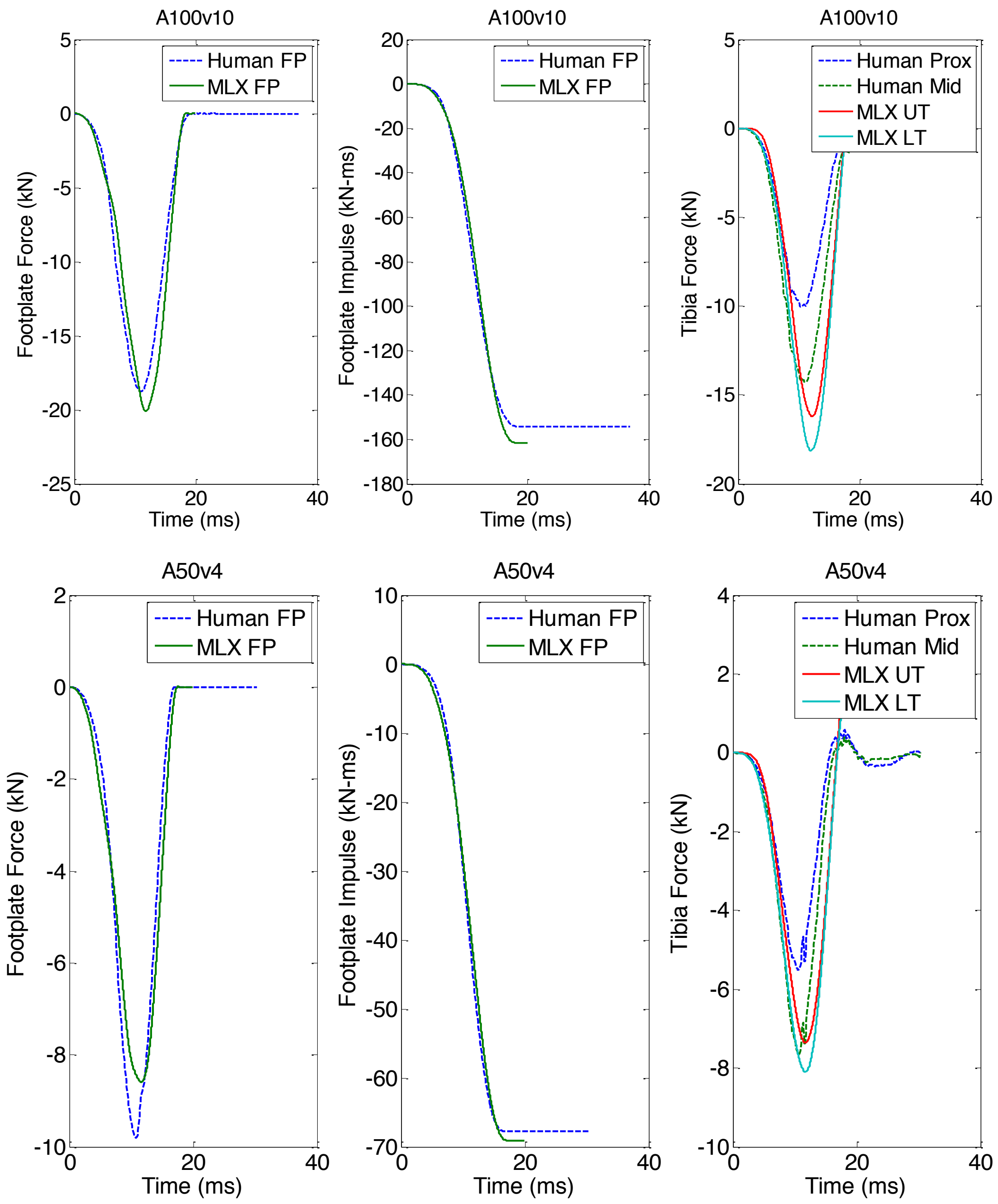
A100v10
Footplate Force (kN)
Time (ms)
Human FP
MLX FP
5
0
-5
-10
-15
-20
-25
0
20
40
A100v10
Footplate Impulse (kN-ms)
Time (ms)
Human FP
MLX FP
20
0
-20
-40
-60
-80
-100
-120
-140
-160
-180
A100v10
Tibia Force (kN)
Time (ms)
Human Prox
Human Mid
MLX UT
MLX LT
A50v4
Footplate Force (kN)
Time (ms)
Human FP
MLX FP
2
0
-2
-4
-6
-8
-10
A50v4
Footplate Impulse (kN-ms)
Time (ms)
Human FP
MLX FP
10
0
-10
-20
-30
-40
-50
-60
-70
A50v4
Tibia Force (kN)
Time (ms)
Human Prox
Human Mid
MLX UT
MLX LT
4
2
0
-2
-4
-6
-8
-10

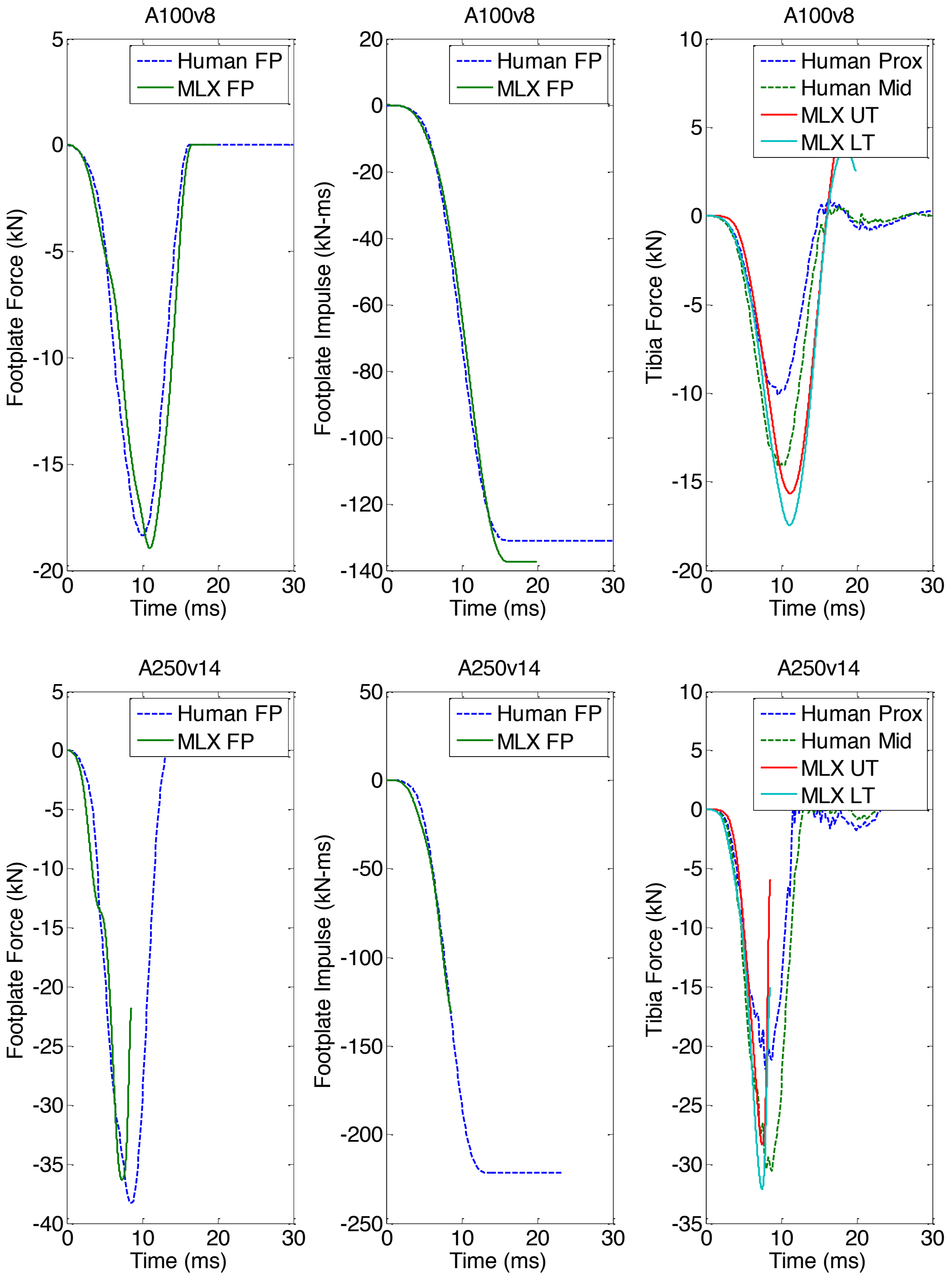
A100v8
Footplate Force (kN)
Time (ms)
Human FP
MLX FP
5
0
-5
-10
-15
-20
0
10
20
30
A100v8
Footplate Impulse (kN-ms)
Time (ms)
Human FP
MLX FP
20
0
-20
-40
-60
-80
-100
-120
-140
A100v8
Tibia Force (kN)
Time (ms)
Human Prox
Human Mid
MLX UT
MLX LT
10
5
0
-5
-10
-15
-20
A250v14
Footplate Force (kN)
Time (ms)
Human FP
MLX FP
5
0
-5
-10
-15
-20
-25
-30
-35
-40
A250v14
Footplate Impulse (kN-ms)
Time (ms)
Human FP
MLX FP
50
0
-50
-100
-150
-200
-250
A250v14
Tibia Force (kN)
Time (ms)
Human Prox
Human Mid
MLX UT
MLX LT
10
5
0
-5
-10
-15
-20
-25
-30
-35

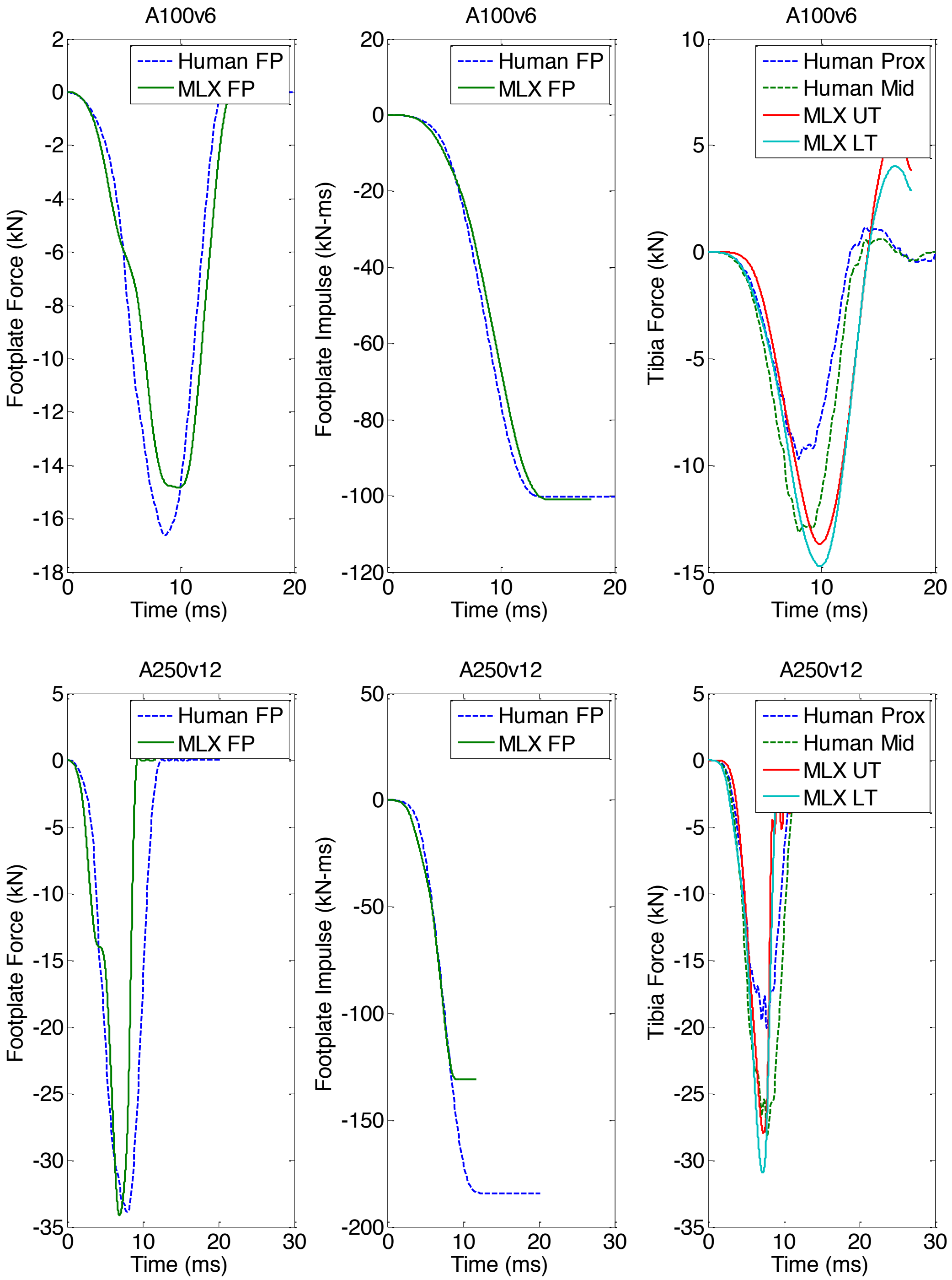
A100v6
Footplate Force (kN)
Time (ms)
Human FP
MLX FP
2
0
-2
-4
-6
-8
-10
-12
-14
-16
-18
0
10
20
A100v6
Footplate Impulse (kN-ms)
Time (ms)
Human FP
MLX FP
20
0
-20
-40
-60
-80
-100
-120
0
10
20
A100v6
Tibia Force (kN)
Time (ms)
Human Prox
Human Mid
MLX UT
MLX LT
10
5
0
-5
-10
-15
0
10
20
A250v12
Footplate Force (kN)
Time (ms)
Human FP
MLX FP
5
0
-5
-10
-15
-20
-25
-30
-35
0
10
20
30
A250v12
Footplate Impulse (kN-ms)
Time (ms)
Human FP
MLX FP
50
0
-50
-100
-150
-200
0
10
20
30
A250v12
Tibia Force (kN)
Time (ms)
Human Prox
Human Mid
MLX UT
MLX LT
5
0
-5
-10
-15
-20
-25
-30
-35
0
10
20
30

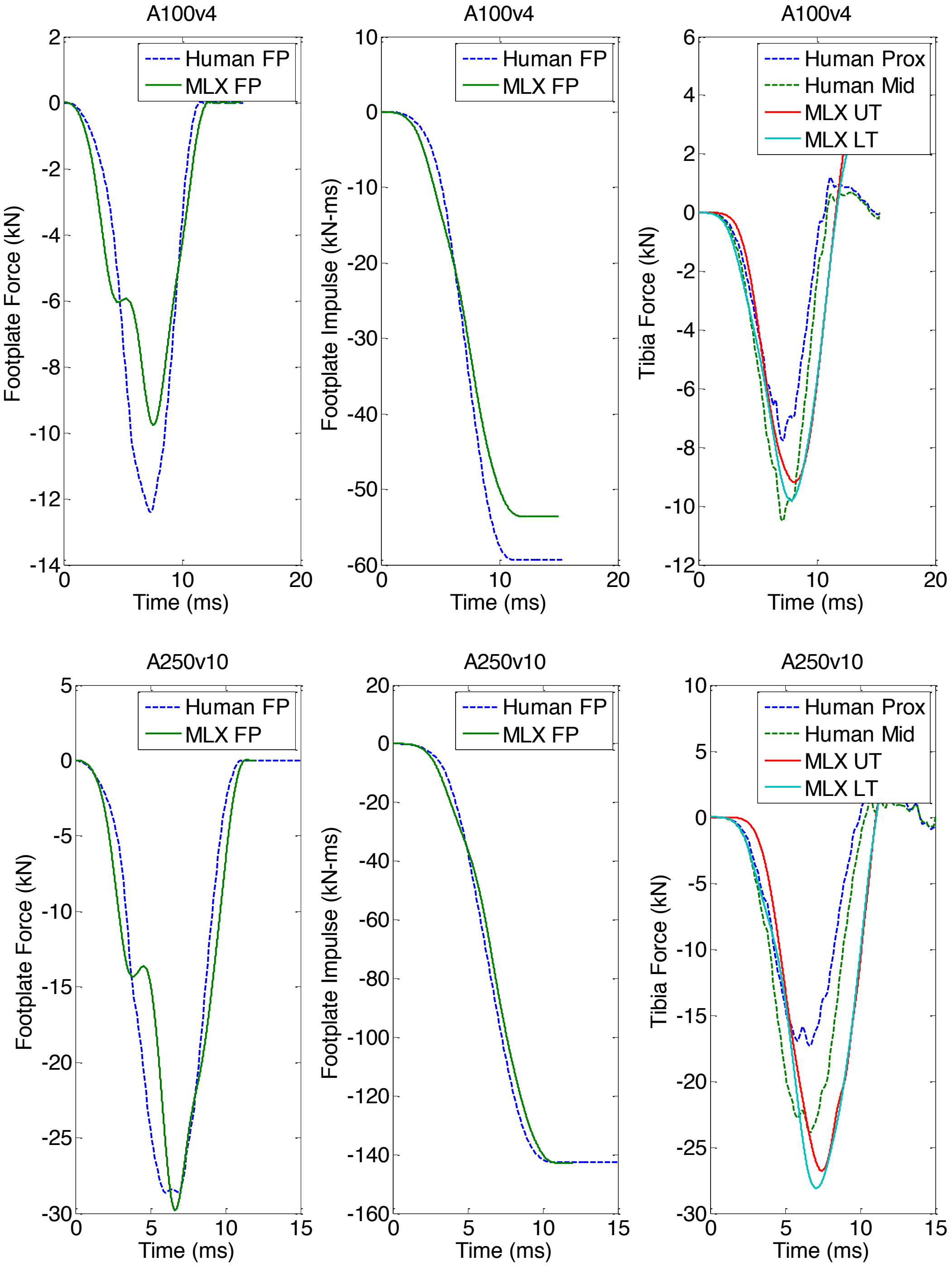
A100v4
Human FP
MLX FP
Footplate Force (kN)
Time (ms)
2
0
-2
-4
-6
-8
-10
-12
-14
0
10
20
A100v4
Human FP
MLX FP
Footplate Impulse (kN-ms)
Time (ms)
10
0
-10
-20
-30
-40
-50
-60
0
10
20
A100v4
Human Prox
Human Mid
MLX UT
MLX LT
Tibia Force (kN)
Time (ms)
6
4
2
0
-2
-4
-6
-8
-10
-12
0
10
20
A250v10
Human FP
MLX FP
Footplate Force (kN)
Time (ms)
5
0
-5
-10
-15
-20
-25
-30
0
5
10
15
A250v10
Human FP
MLX FP
Footplate Impulse (kN-ms)
Time (ms)
20
0
-20
-40
-60
-80
-100
-120
-140
-160
0
5
10
15
A250v10
Human Prox
Human Mid
MLX UT
MLX LT
Tibia Force (kN)
Time (ms)
10
5
0
-5
-10
-15
-20
-25
-30
0
5
10
15

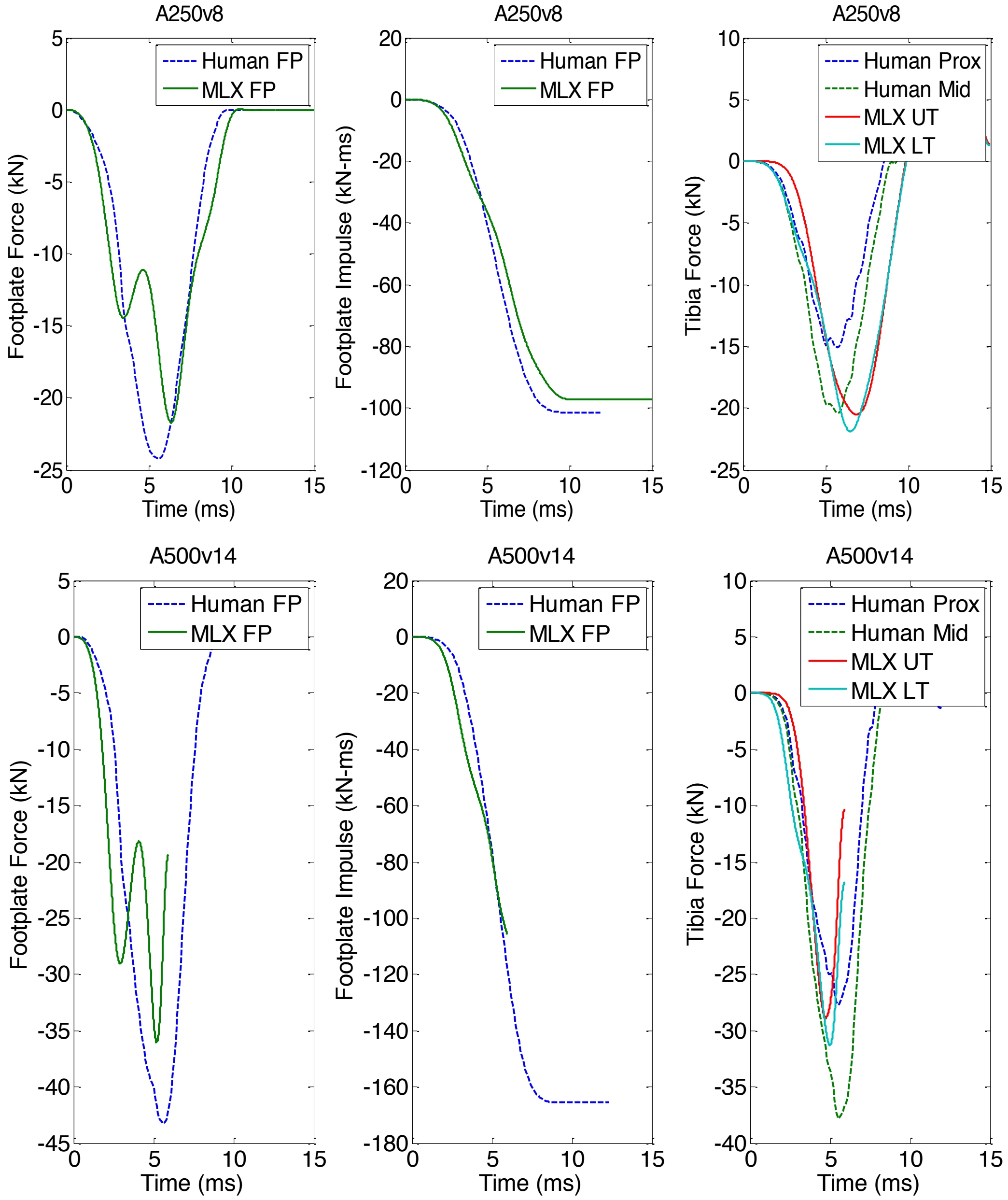
A250v8
Footplate Force (kN)
Time (ms)
Human FP
MLX FP
5
0
-5
-10
-15
-20
-25
0
5
10
15
A250v8
Footplate Impulse (kN-ms)
Time (ms)
Human FP
MLX FP
20
0
-20
-40
-60
-80
-100
-120
A250v8
Tibia Force (kN)
Time (ms)
Human Prox
Human Mid
MLX UT
MLX LT
10
A500v14
Footplate Force (kN)
Time (ms)
Human FP
MLX FP
-30
-35
-40
-45
A500v14
Footplate Impulse (kN-ms)
Time (ms)
Human FP
MLX FP
-140
-160
-180
A500v14
Tibia Force (kN)
Time (ms)
Human Prox
Human Mid
MLX UT
MLX LT

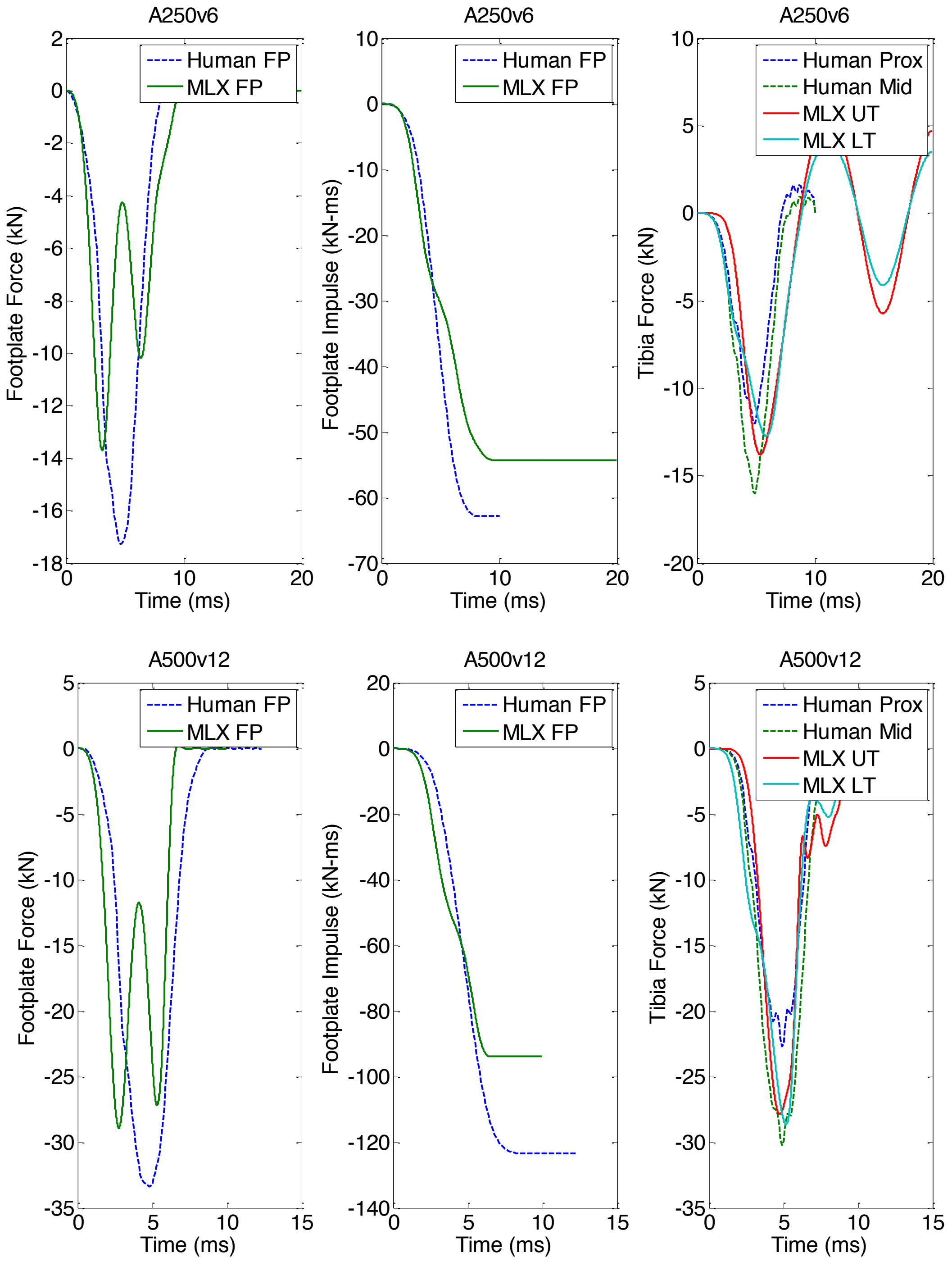
A250v6
Footplate Force (kN)
Time (ms)
Human FP
MLX FP
2
0
-2
-4
-6
-8
-10
-12
-14
-16
-18
0
10
20
A250v6
Footplate Impulse (kN-ms)
Time (ms)
Human FP
MLX FP
10
0
-10
-20
-30
-40
-50
-60
-70
0
10
20
A250v6
Tibia Force (kN)
Time (ms)
Human Prox
Human Mid
MLX UT
MLX LT
10
5
0
-5
-10
-15
-20
0
10
20
A500v12
Footplate Force (kN)
Time (ms)
Human FP
MLX FP
5
0
-5
-10
-15
-20
-25
-30
-35
0
5
10
15
A500v12
Footplate Impulse (kN-ms)
Time (ms)
Human FP
MLX FP
20
0
-20
-40
-60
-80
-100
-120
-140
0
5
10
15
A500v12
Tibia Force (kN)
Time (ms)
Human Prox
Human Mid
MLX UT
MLX LT
5
0
-5
-10
-15
-20
-25
-30
-35
0
5
10
15

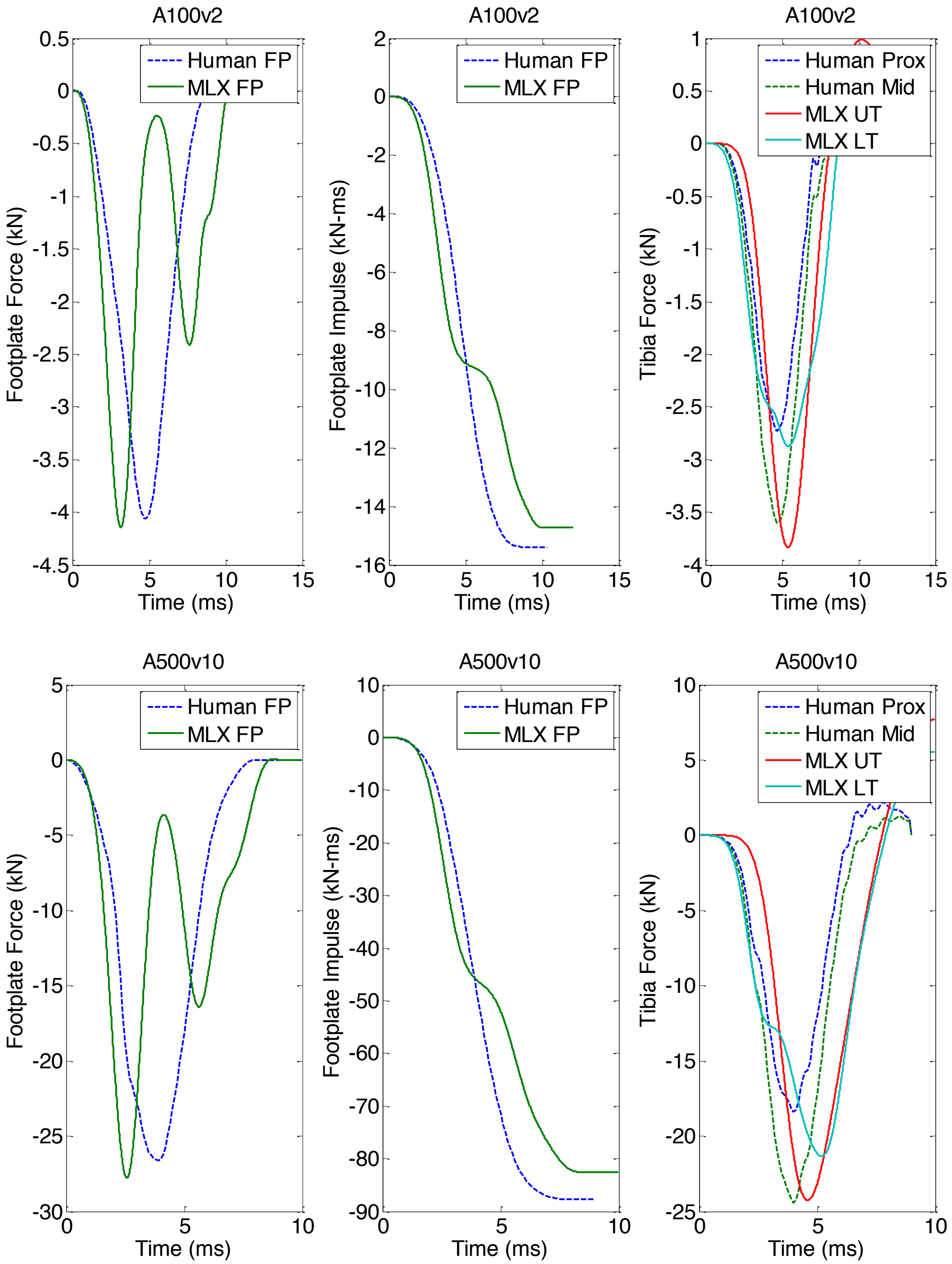
A100v2
Footplate Force (kN)
0.5
0
-0.5
-1
-1.5
-2
-2.5
-3
-3.5
-4
-4.5
0
5
10
15
Time (ms)
Human FP
MLX FP
A100v2
Footplate Impulse (kN-ms)
2
0
-2
-4
-6
-8
-10
-12
-14
-16
0
5
10
15
Time (ms)
Human FP
MLX FP
A100v2
Tibia Force (kN)
1
0.5
0
-0.5
-1
-1.5
-2
-2.5
-3
-3.5
-4
0
5
10
15
Time (ms)
Human Prox
Human Mid
MLX UT
MLX LT
A500v10
Footplate Force (kN)
5
0
-5
-10
-15
-20
-25
-30
0
5
10
Time (ms)
Human FP
MLX FP
A500v10
Footplate Impulse (kN-ms)
10
0
-10
-20
-30
-40
-50
-60
-70
-80
-90
0
5
10
Time (ms)
Human FP
MLX FP
A500v10
Tibia Force (kN)
10
5
0
-5
-10
-15
-20
-25
0
5
10
Time (ms)
Human Prox
Human Mid
MLX UT
MLX LT

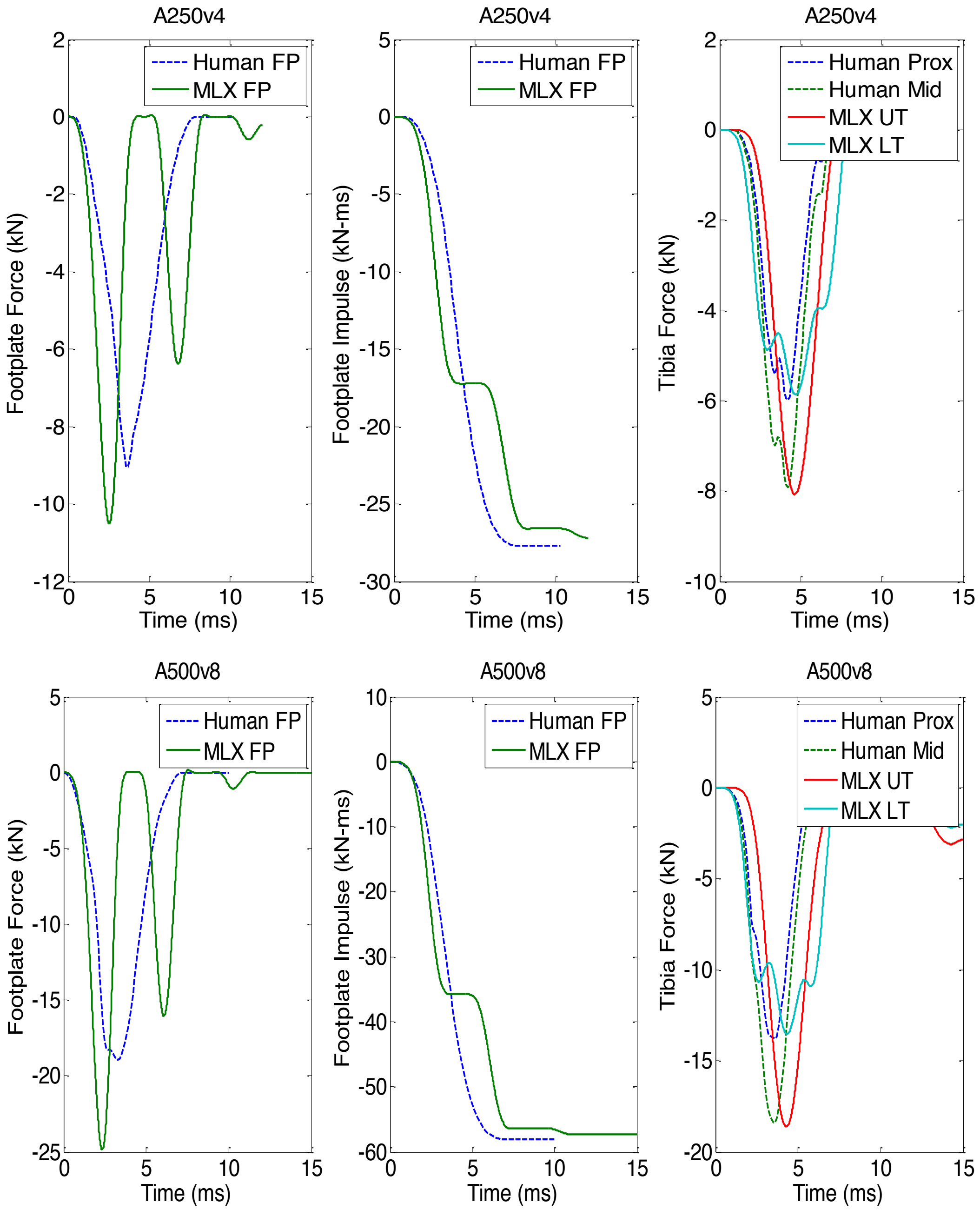

10.7.3 Discrete Material Optimization of Mil-Lx

The following plots show the response of the Mil-Lx leg FE model for which the tibia compliant element has been replaced with 90-durometer polyurethane rubber, and the heel pad has been replaced with 70-durometer neoprene. Footplate force and impulse for the Mil-Lx FE model are plotted against the human FE model (without element elimination) footplate force and impulse for each of the loading conditions. Mil-Lx upper and lower tibia forces and human mid- and proximal tibia forces are provided in a third plot for each input condition. Again, the plots are labeled with the peak acceleration and velocity (A#v*) such that # is the peak acceleration and * is the peak velocity of the footplate input. Lower and upper tibia forces are denoted as *LT* and *UT*, respectively, while footplate forces are abbreviated as *FP*.

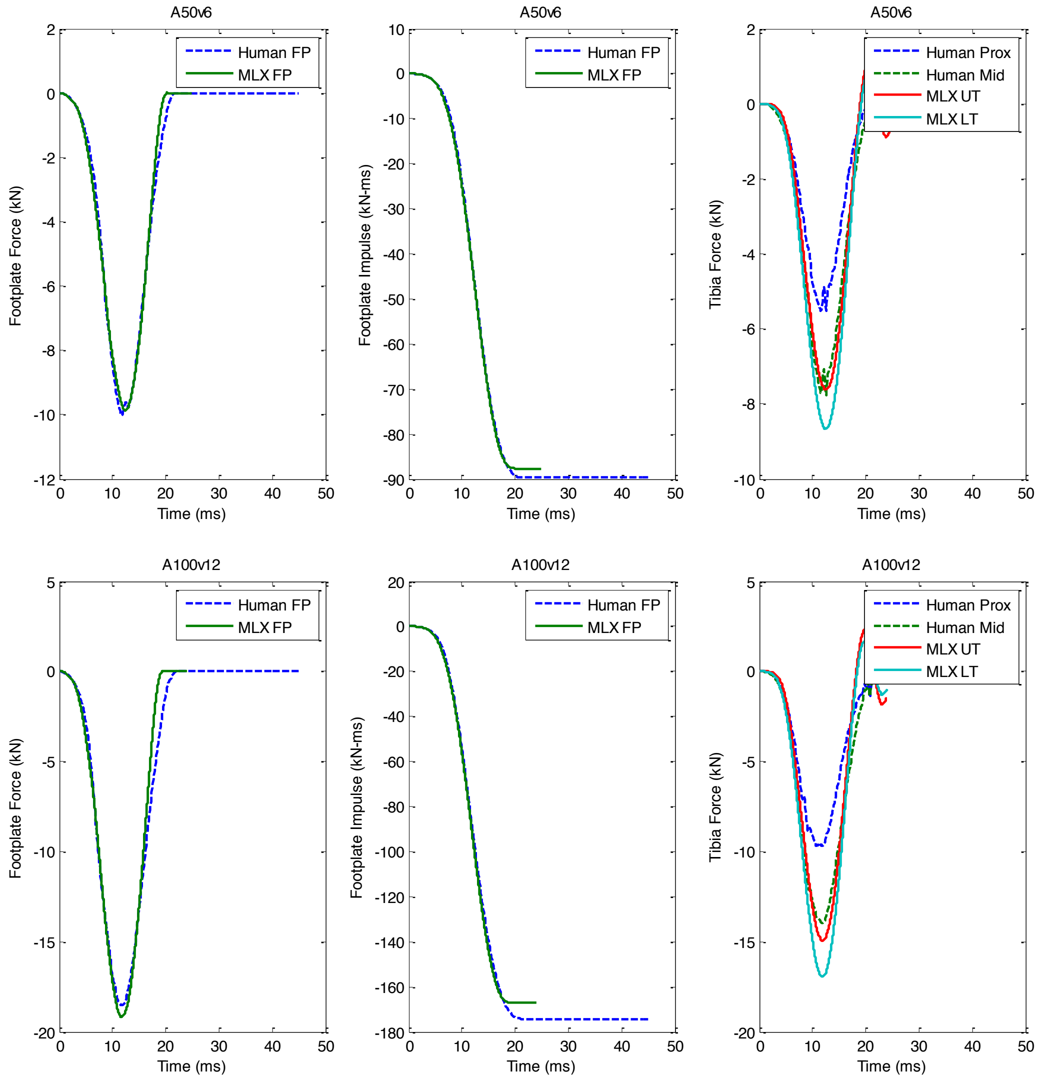

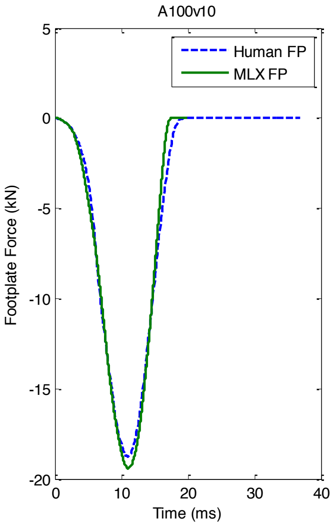
A100v10

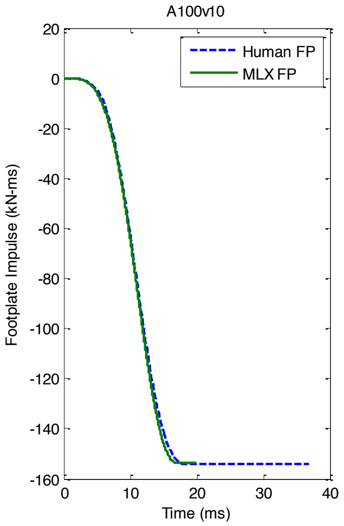
A100v10

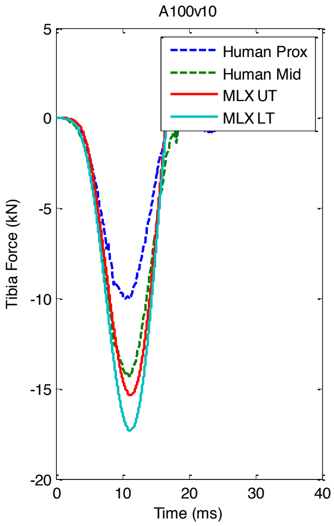
A100v10

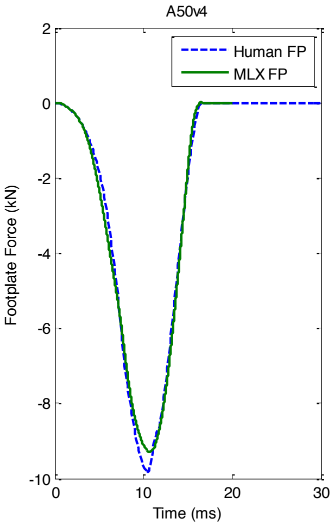
A50v4

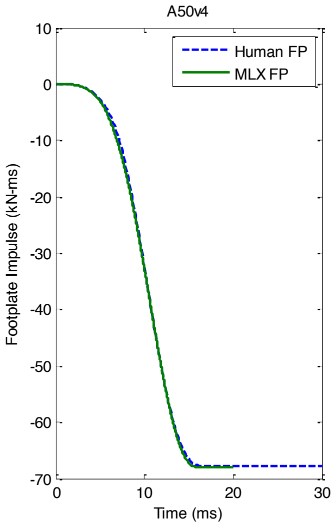
A50v4

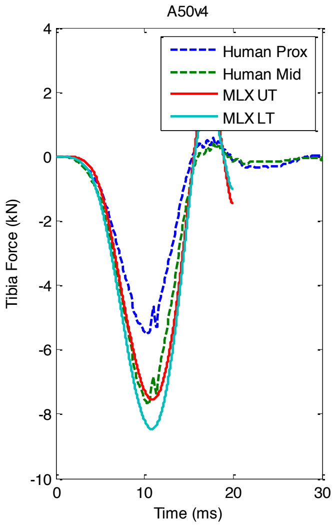
A50v4

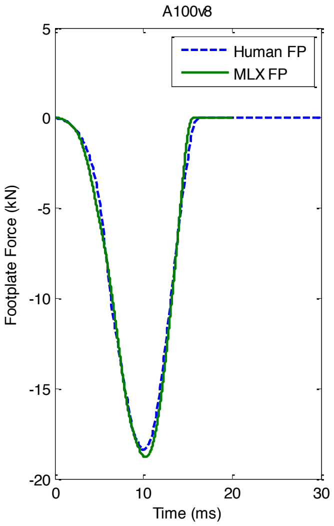
A100v8

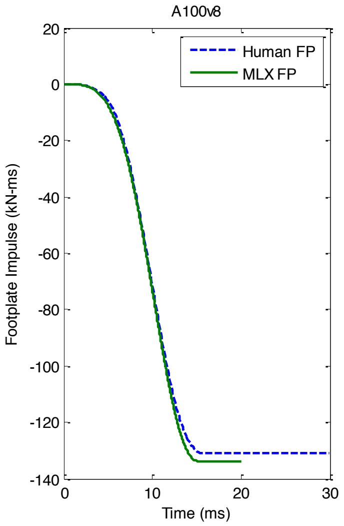
A100v8

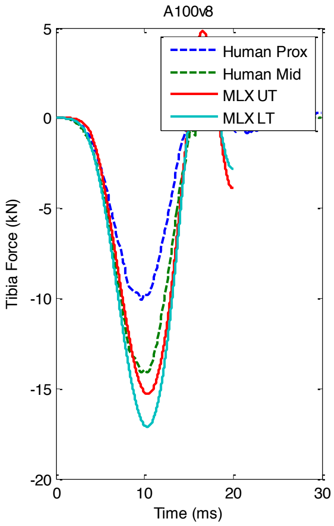
A100v8

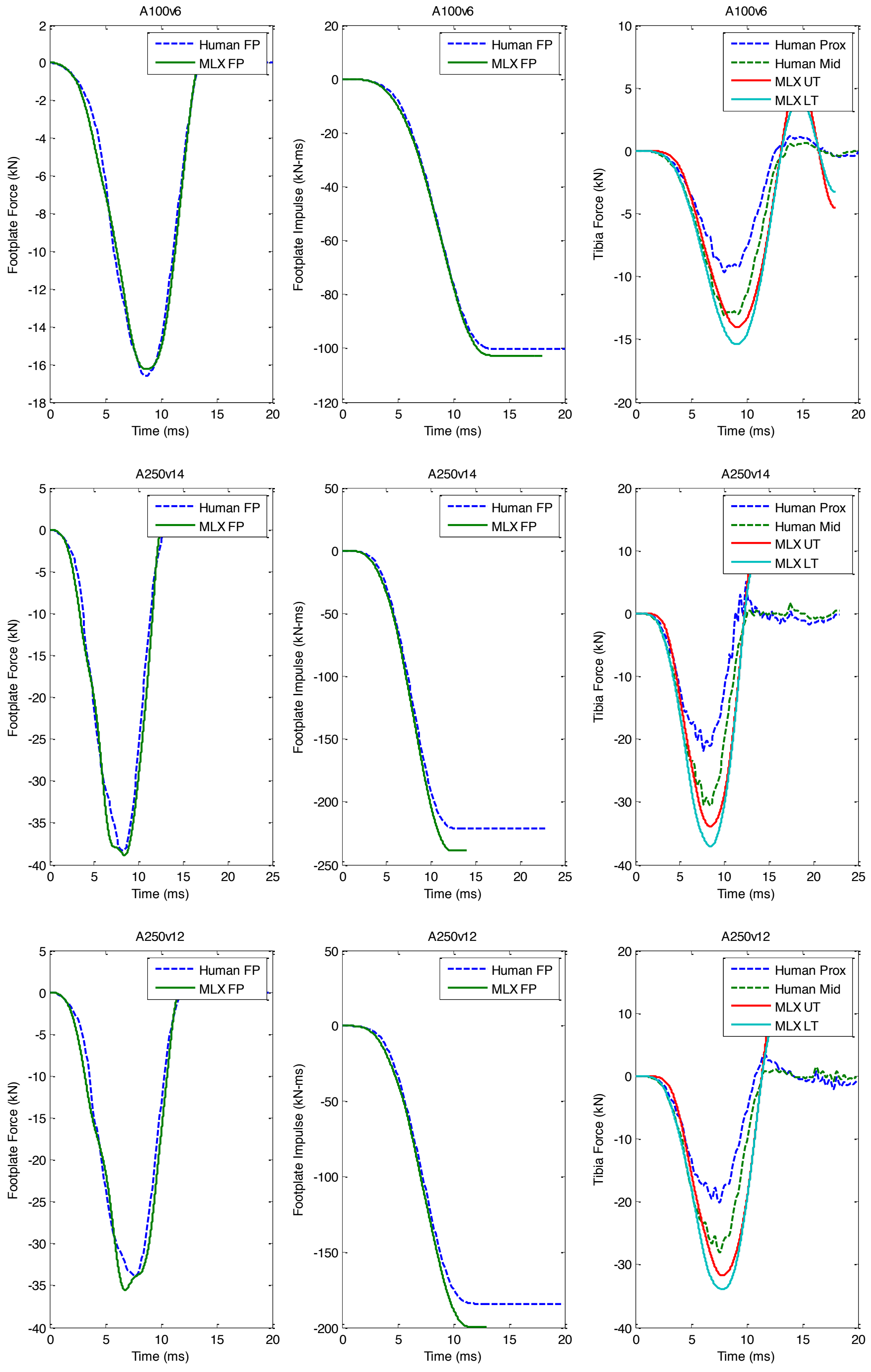
A100v6
Footplate Force (kN)
2
0
-2
-4
-6
-8
-10
-12
-14
-16
-18
Time (ms)
0
5
10
15
20
Human FP
MLX FP
A100v6
Footplate Impulse (kN-ms)
20
0
-20
-40
-60
-80
-100
-120
Time (ms)
Human FP
MLX FP
A100v6
Tibia Force (kN)
10
5
0
-5
-10
-15
-20
Time (ms)
Human Prox
Human Mid
MLX UT
MLX LT
A250v14
Footplate Force (kN)
5
0
-5
-10
-15
-20
-25
-30
-35
-40
Time (ms)
0
5
10
15
20
25
Human FP
MLX FP
A250v14
Footplate Impulse (kN-ms)
50
0
-50
-100
-150
-200
-250
Time (ms)
Human FP
MLX FP
A250v14
Tibia Force (kN)
20
10
0
-10
-20
-30
-40
Time (ms)
Human Prox
Human Mid
MLX UT
MLX LT
A250v12
Footplate Force (kN)
5
0
-5
-10
-15
-20
-25
-30
-35
-40
Time (ms)
0
5
10
15
20
Human FP
MLX FP
A250v12
Footplate Impulse (kN-ms)
50
0
-50
-100
-150
-200
Time (ms)
Human FP
MLX FP
A250v12
Tibia Force (kN)
20
10
0
-10
-20
-30
-40
Time (ms)
Human Prox
Human Mid
MLX UT
MLX LT

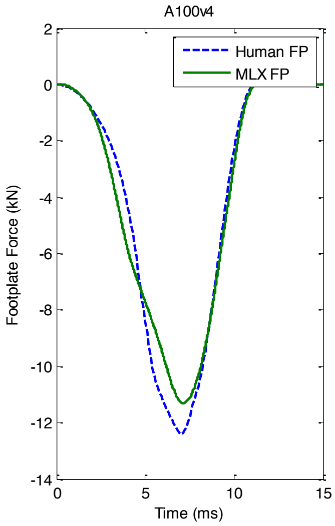
A100v4
Human FP
MLX FP
Footplate Force (kN)
2
0
-2
-4
-6
-8
-10
-12
-14
0
5
10
15
Time (ms)

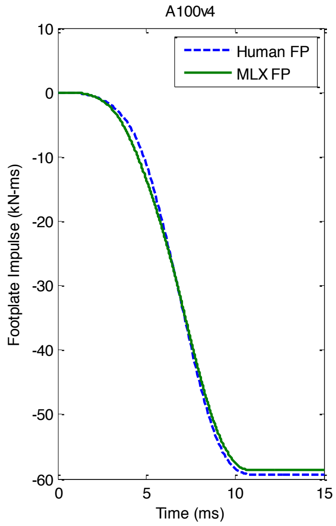
A100v4
Human FP
MLX FP
Footplate Impulse (kN-ms)
10
0
-10
-20
-30
-40
-50
-60
0
5
10
15
Time (ms)

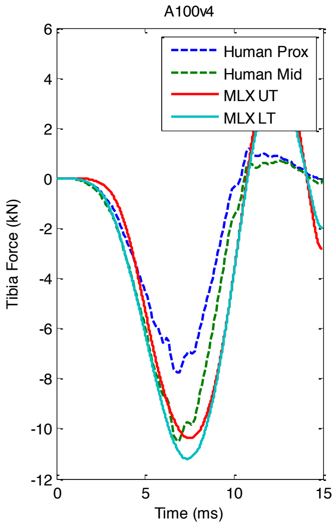
A100v4
Human Prox
Human Mid
MLX UT
MLX LT
Tibia Force (kN)
6
4
2
0
-2
-4
-6
-8
-10
-12
0
5
10
15
Time (ms)

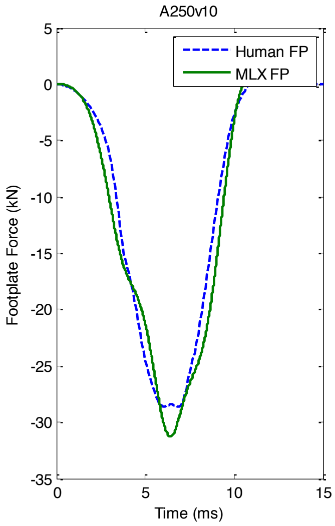
A250v10
Human FP
MLX FP
Footplate Force (kN)
5
0
-5
-10
-15
-20
-25
-30
-35
0
5
10
15
Time (ms)

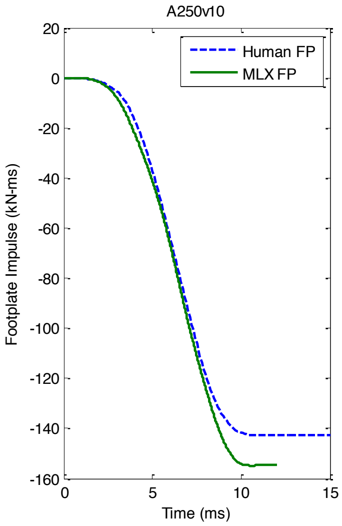
A250v10
Human FP
MLX FP
Footplate Impulse (kN-ms)
20
0
-20
-40
-60
-80
-100
-120
-140
-160
0
5
10
15
Time (ms)

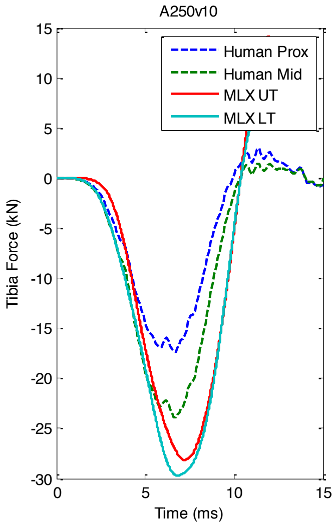
A250v10
Human Prox
Human Mid
MLX UT
MLX LT
Tibia Force (kN)
15
10
5
0
-5
-10
-15
-20
-25
-30
0
5
10
15
Time (ms)

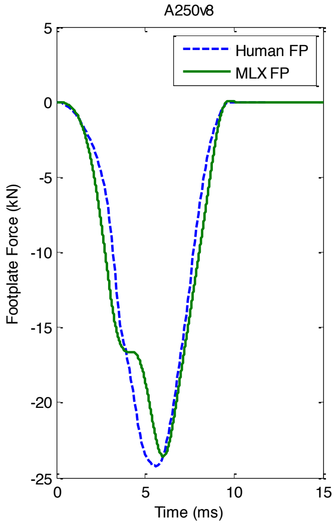
A250v8
Human FP
MLX FP
Footplate Force (kN)
5
0
-5
-10
-15
-20
-25
0
5
10
15
Time (ms)

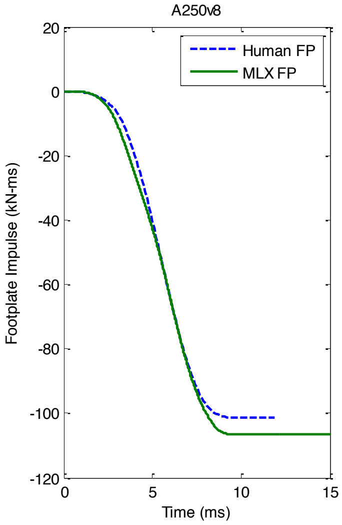
A250v8
Human FP
MLX FP
Footplate Impulse (kN-ms)
20
0
-20
-40
-60
-80
-100
-120
0
5
10
15
Time (ms)

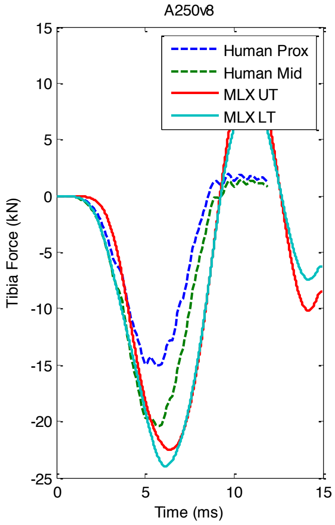
A250v8
Human Prox
Human Mid
MLX UT
MLX LT
Tibia Force (kN)
15
10
5
0
-5
-10
-15
-20
-25
0
5
10
15
Time (ms)

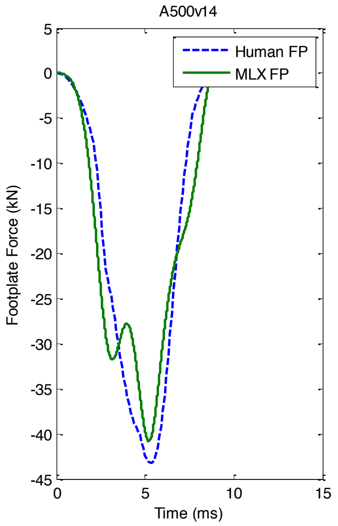
A500v14
Human FP
MLX FP
Footplate Force (kN)
5
0
-5
-10
-15
-20
-25
-30
-35
-40
-45
0
5
10
15
Time (ms)

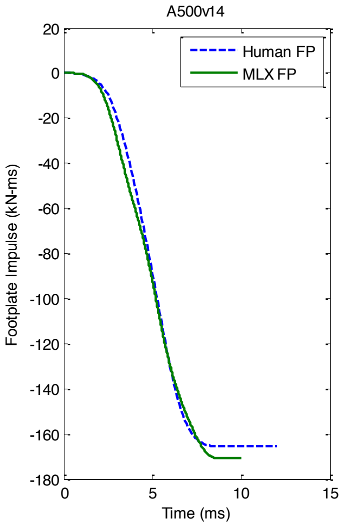
A500v14
Human FP
MLX FP
Footplate Impulse (kN-ms)
20
0
-20
-40
-60
-80
-100
-120
-140
-160
-180
0
5
10
15
Time (ms)

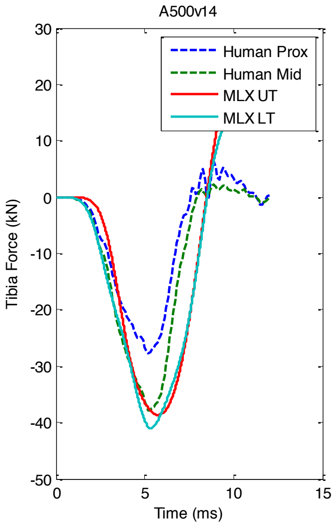
A500v14
Human Prox
Human Mid
MLX UT
MLX LT
Tibia Force (kN)
30
20
10
0
-10
-20
-30
-40
-50
0
5
10
15
Time (ms)

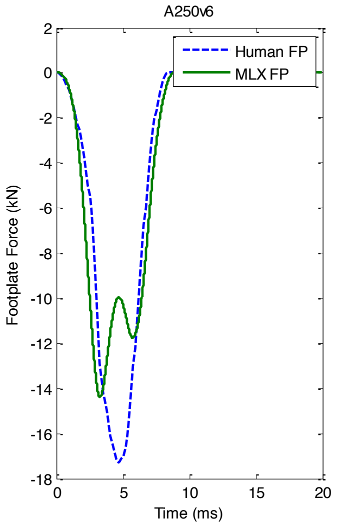
A250v6
Human FP
MLX FP
Footplate Force (kN)
2
0
-2
-4
-6
-8
-10
-12
-14
-16
-18
0
5
10
15
20
Time (ms)

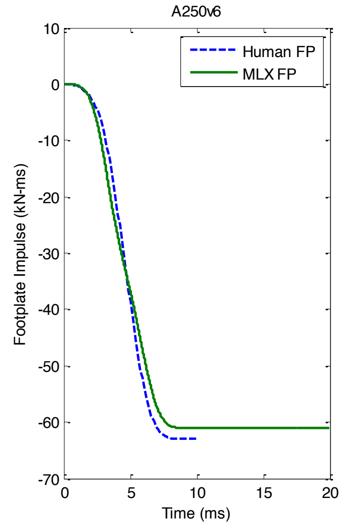
A250v6
Human FP
MLX FP
Footplate Impulse (kN-ms)
10
0
-10
-20
-30
-40
-50
-60
-70
0
5
10
15
20
Time (ms)

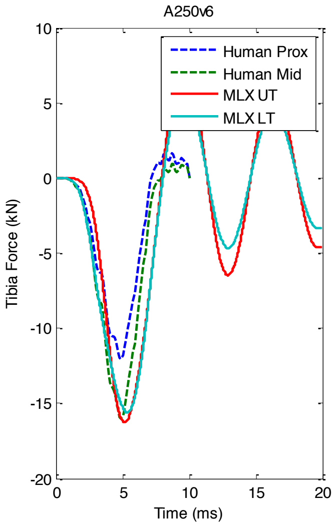
A250v6
Human Prox
Human Mid
MLX UT
MLX LT
Tibia Force (kN)
10
5
0
-5
-10
-15
-20
0
5
10
15
20
Time (ms)

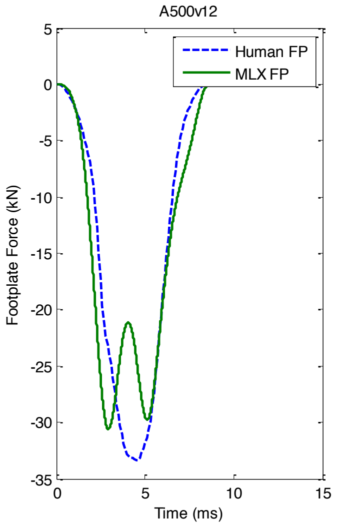
A500v12
Human FP
MLX FP
Footplate Force (kN)
5
0
-5
-10
-15
-20
-25
-30
-35
0
5
10
15
Time (ms)

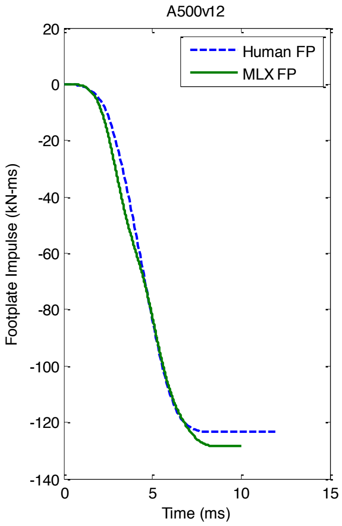
A500v12
Human FP
MLX FP
Footplate Impulse (kN-ms)
20
0
-20
-40
-60
-80
-100
-120
-140
0
5
10
15
Time (ms)

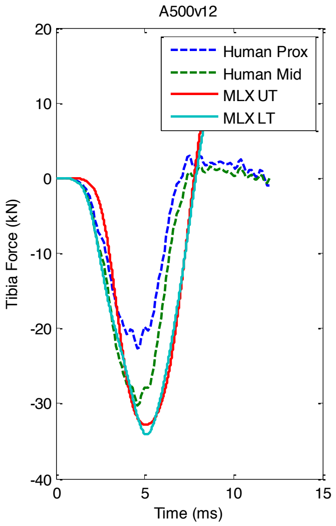
A500v12
Human Prox
Human Mid
MLX UT
MLX LT
Tibia Force (kN)
20
10
0
-10
-20
-30
-40
0
5
10
15
Time (ms)

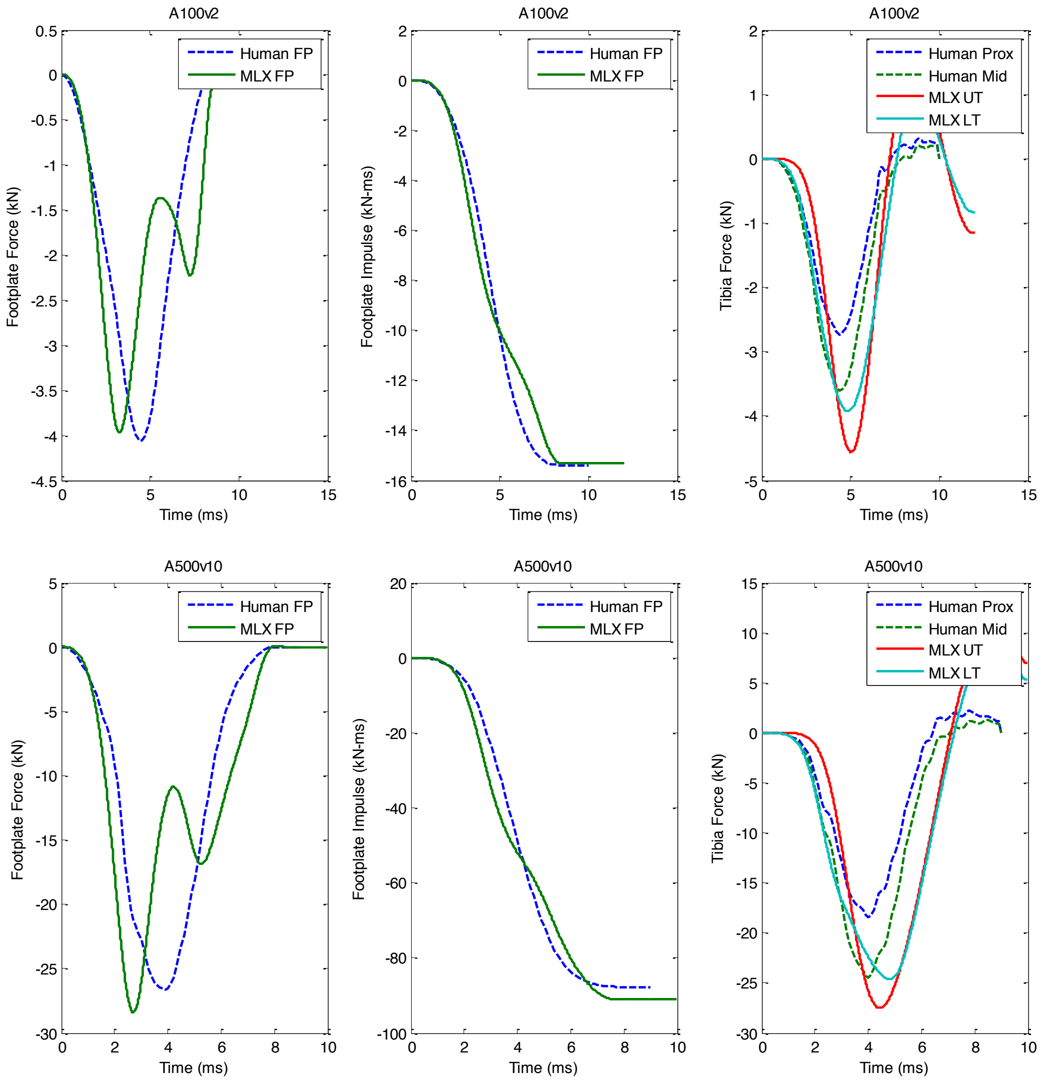
A100v2
Footplate Force (kN)
Time (ms)
Human FP
MLX FP
0.5
0
-0.5
-1
-1.5
-2
-2.5
-3
-3.5
-4
-4.5
0
5
10
15
A100v2
Footplate Impulse (kN-ms)
Time (ms)
Human FP
MLX FP
2
0
-2
-4
-6
-8
-10
-12
-14
-16
A100v2
Tibia Force (kN)
Time (ms)
Human Prox
Human Mid
MLX UT
MLX LT
2
1
0
-1
-2
-3
-4
-5
A500v10
Footplate Force (kN)
Time (ms)
Human FP
MLX FP
5
0
-5
-10
-15
-20
-25
-30
0
2
4
6
8
10
A500v10
Footplate Impulse (kN-ms)
Time (ms)
Human FP
MLX FP
20
0
-20
-40
-60
-80
-100
A500v10
Tibia Force (kN)
Time (ms)
Human Prox
Human Mid
MLX UT
MLX LT
15
10
5
0
-5
-10
-15
-20
-25
-30

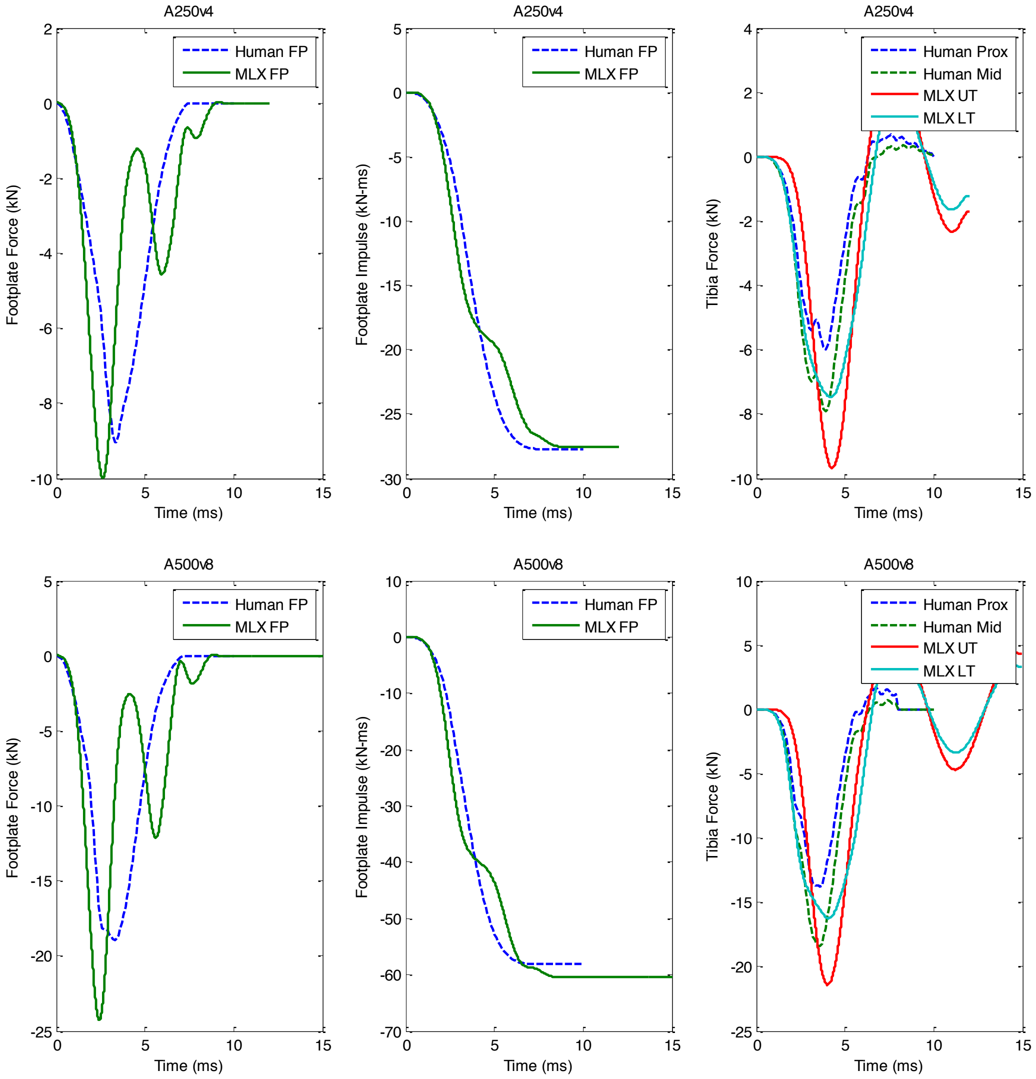
A250v4
Footplate Force (kN)
Human FP
MLX FP
2
0
-2
-4
-6
-8
-10
0
5
10
15
Time (ms)
A250v4
Footplate Impulse (kN-ms)
Human FP
MLX FP
5
0
-5
-10
-15
-20
-25
-30
Time (ms)
A250v4
Tibia Force (kN)
Human Prox
Human Mid
MLX UT
MLX LT
4
2
0
-2
-4
-6
-8
-10
Time (ms)
A500v8
Footplate Force (kN)
Human FP
MLX FP
5
0
-5
-10
-15
-20
-25
Time (ms)
A500v8
Footplate Impulse (kN-ms)
Human FP
MLX FP
10
0
-10
-20
-30
-40
-50
-60
-70
Time (ms)
A500v8
Tibia Force (kN)
Human Prox
Human Mid
MLX UT
MLX LT
10
5
0
-5
-10
-15
-20
-25
Time (ms)